ASSESSING CELLULAR MICROSTRUCTURE IN BIOLOGICAL TISSUES USING *IN VIVO* DIFFUSION-WEIGHTED MAGNETIC RESONANCE

EDITED BY: Julien Valette, Itamar Ronen and Sune Nørhøj Jespersen

PUBLISHED IN: Frontiers in Physics and Frontiers in Neuroscience

frontiers Research Topics

ISSN 1664-8714
ISBN 978-2-88945-841-7
DOI 10.3389/978-2-88945-841-7

About Frontiers

Frontiers is more than just an open-access publisher of scholarly articles: it is a pioneering approach to the world of academia, radically improving the way scholarly research is managed. The grand vision of Frontiers is a world where all people have an equal opportunity to seek, share and generate knowledge. Frontiers provides immediate and permanent online open access to all its publications, but this alone is not enough to realize our grand goals.

Frontiers Journal Series

The Frontiers Journal Series is a multi-tier and interdisciplinary set of open-access, online journals, promising a paradigm shift from the current review, selection and dissemination processes in academic publishing. All Frontiers journals are driven by researchers for researchers; therefore, they constitute a service to the scholarly community. At the same time, the Frontiers Journal Series operates on a revolutionary invention, the tiered publishing system, initially addressing specific communities of scholars, and gradually climbing up to broader public understanding, thus serving the interests of the lay society, too.

Dedication to Quality

Each Frontiers article is a landmark of the highest quality, thanks to genuinely collaborative interactions between authors and review editors, who include some of the world's best academicians. Research must be certified by peers before entering a stream of knowledge that may eventually reach the public - and shape society; therefore, Frontiers only applies the most rigorous and unbiased reviews.
Frontiers revolutionizes research publishing by freely delivering the most outstanding research, evaluated with no bias from both the academic and social point of view. By applying the most advanced information technologies, Frontiers is catapulting scholarly publishing into a new generation.

What are Frontiers Research Topics?

Frontiers Research Topics are very popular trademarks of the Frontiers Journals Series: they are collections of at least ten articles, all centered on a particular subject. With their unique mix of varied contributions from Original Research to Review Articles, Frontiers Research Topics unify the most influential researchers, the latest key findings and historical advances in a hot research area! Find out more on how to host your own Frontiers Research Topic or contribute to one as an author by contacting the Frontiers Editorial Office: researchtopics@frontiersin.org

ASSESSING CELLULAR MICROSTRUCTURE IN BIOLOGICAL TISSUES USING *IN VIVO* DIFFUSION-WEIGHTED MAGNETIC RESONANCE

Topic Editors:
Julien Valette, Commissariat à l'Energie Atomique et aux Energies Alternatives, France
Itamar Ronen, Leiden University, Netherlands
Sune Nørhøj Jespersen, Aarhus University, Denmark

Magnetic resonance imaging (MRI) and spectroscopy (MRS) techniques have opened new doors for examining biological tissues in vivo. By combining sensitization to diffusion using magnetic field gradients with a variety of imaging and localization schemes, diffusion-weighted MRI and diffusion-weighted MRS allow investigating translational diffusion of endogenous molecules, such as water or metabolites, in biological tissues, most commonly the brain but also other organs such as the prostate.

The typical voxel resolution of MRI or MRS is in the millimeter to centimeter range, much lower than the cellular scale. However, as molecules are typically diffusing over just a few µm during the duration of the measurement (the "diffusion time") and encounter numerous biological membranes at these scales, the average cellular microstructure has a critical influence on the measured diffusion signal. Hence, diffusion-weighted MRI and diffusion-weighted MRS are sensitive to tissue microstructure at a scale well below the nominal imaging resolution. However, the connection between diffusion properties and tissue microstructure remains indirect, so any attempt to quantify microstructure will rely on modeling.

The goal of this Research Topic was to gather experts in various acquisition and modeling strategies and show how these approaches, despite their own strengths and weaknesses, can yield unique information about cellular microstructure, and sometimes complement each other.

Citation: Valette, J., Ronen, I., Jespersen, S. N., eds. (2019). Assessing Cellular Microstructure in Biological Tissues using *In Vivo* Diffusion-Weighted Magnetic Resonance. Lausanne: Frontiers Media. doi: 10.3389/978-2-88945-841-7

Table of Contents

frontiers in Physics

EDITORIAL
published: 21 March 2019
doi: 10.3389/fphy.2019.00037

Editorial: Assessing Cellular Microstructure in Biological Tissues Using *in vivo* Diffusion-Weighted Magnetic Resonance

Julien Valette[1,2]*, *Itamar Ronen*[3] and *Sune Nørhøj Jespersen*[4,5]

[1] MIRCen, Commissariat à l'Energie Atomique et aux Energies Alternatives, Fontenay-aux-Roses, France, [2] Neurodegenerative Diseases Laboratory, Centre National de la Recherche Scientifique, Université Paris-Sud, Université Paris-Saclay, UMR 9199, Fontenay-aux-Roses, France, [3] C. J. Gorter Center for High Field MRI, Department of Radiology, Leiden University Medical Center, Leiden, Netherlands, [4] Center of Functionally Integrative Neuroscience and MINDLab, Department of Clinical Medicine, Aarhus University, Aarhus, Denmark, [5] Department of Physics and Astronomy, Aarhus University, Aarhus, Denmark

Keywords: medical imaging, cell morphology, diffusion-weighted (DW), MRI, NMR, diffusion, microstructure

Editorial on the Research Topic

Assessing Cellular Microstructure in Biological Tissues Using *in vivo* Diffusion-Weighted Magnetic Resonance

Since the seminal works of Stejskal and Tanner in the 1960s [1], the study of molecular self-diffusion by diffusion-weighted (DW) nuclear magnetic resonance (NMR) has emerged as a dynamic and rich research field. Initially introduced as a tool to measure diffusion in materials and to estimate microstructural properties of materials by modeling deviations from free diffusion caused by microstructural barriers [2], DW-NMR was soon proposed as a tool to characterize cellular microstructure in biological tissues [3]. It was then quite a natural—although challenging—step to endow magnetic resonance imaging (MRI) with diffusion-weighting capabilities to map water diffusion *in vivo* [4], which almost immediately revolutionized the diagnosis of brain ischemic stroke [5–7]. This partial historical account of the early days highlights the different "flavors" still characterizing our research field at the interface of physics, chemistry, biology, computer science, and medical imaging: a unique blend of powerful concepts and theories, cutting-edge methodological, and technical innovations, ideally leading to highly-relevant biological insights or clinical applications.

Various approaches, each with their own strengths and weaknesses, have been developed over the years to probe microstructure with ever higher degrees of sensitivity and specificity. The goal of this Research Topic was to gather experts in various acquisition and modeling strategies and show how these approaches can yield unique and complementary information about cellular microstructure. In parallel to the topics discussed here, other developments are also driving *in vivo* DW-NMR forward. Important examples are the ever increasing field strength and gradient performance of MRI scanners, boosting signal-to-noise, and enabling larger and better temporally resolved diffusion-weighting, respectively [8, 9]. However, these technical innovations also come with new difficulties or limitations, e.g., increased tissue heating, decreased transverse relaxation times, increased sensitivity to motion and field fluctuations, decreased field homogeneity and increased geometrical distortions at high fields [10, 11], and increased peripheral nerve stimulation by powerful gradients [9]. The drawbacks resulting from these technical innovations are partially offset by parallel developments in coil and pulse sequence technology. Such technical innovations and solutions are not discussed in this Research Topic.

OPEN ACCESS

Edited and reviewed by:
Ewald Moser,
Medical University of Vienna, Austria

***Correspondence:**
Julien Valette
julien.valette@cea.fr

Specialty section:
This article was submitted to Biomedical Physics, a section of the journal Frontiers in Physics

Received: *12 February 2019*
Accepted: *27 February 2019*
Published: *21 March 2019*

Citation:
Valette J, Ronen I and Jespersen SN (2019) Editorial: Assessing Cellular Microstructure in Biological Tissues Using in vivo Diffusion-Weighted Magnetic Resonance. Front. Phys. 7:37. doi: 10.3389/fphy.2019.00037

Many fundamental questions remain open about the relationships existing between the diffusion-weighted signal and its derived diffusion metrics on one hand, and the underlying microstructural features on the other hand. Approximately half of the papers of this research topic aim at addressing such fundamental questions, using different approaches.

Some rely primarily on theoretical considerations. Özarslan et al. revisit the q^{-1} decay in narrow fibers, taking curvature into account. The problem is examined in three distinct temporal regimes of the Stejskal-Tanner pulse-field gradient experiment. For smaller cells, the q^{-1} decay of the orientationally-averaged signal is only predicted for straight fibers. This decay is more general for cells with longer projections, but fades away for curvy structures as gradient pulse duration increases. The authors stress that the q^{-1} decay could represent an intermediate range, as the true asymptotic behavior is governed by a steeper attenuation. Laun et al. tackle another kind of diffusion experiments, where the time-dependence of the apparent diffusion coefficient (ADC) is measured. In the short diffusion time (t_d) regime, the ADC is known to decrease as the square root of t_d multiplied by the surface to volume ratio (S/V). The next term in the expansion is proportional to t_d multiplied by a factor depending on permeability and curvature. Laun et al. show that this term is identically zero for oscillating gradients, meaning that permeability and curvature cannot be easily measured with these sequences, while S/V term may be easier to quantify than with pulsed-field gradients. Ozarslan et al. present a new perspective for the representation of restricted diffusion that is highly suitable for diffusion experiments performed with commonly available gradient hardware, for example on clinical scanners. Diffusion experiments under such conditions are typically performed with long gradient pulses, thus blurring the information necessary for the characterization of the restricting pore. The approach presented here assumes that diffusion occurs in an effective quadratic potential landscape, thus resulting in a linear (Hookean) dependence of the stochastic effective force on the center-of-mass position. The implications that this approach may have on the interpretation of diffusion experiments performed with long diffusion gradients are discussed, together with possible extensions of this theoretical framework to potential landscapes other than quadratic.

Theoretical analysis typically relies on idealized assumptions for mathematical tractability, and therefore struggle to evaluate the quantitative impact of complex structural features in realistic acquisition conditions. In that case, numerical simulations may help. Ginsburger et al. describe simulations in synthetic white matter mimicking axonal bundles (Ginsburger et al.), with a small set of parameters controlling the level of tissue complexity and disorder. Their results show that angular dispersion and most importantly axonal beading have non-negligible effects on extracellular diffusion which may be measured using DW-MRI clinical protocols with oscillating gradients.

A major limitation of both theoretical analysis and numerical simulation may be the insufficient knowledge about the precise nature or magnitude of some features potentially affecting diffusion (such as the properties and detailed distribution of membranes or the existence of molecular pools with different relaxation times), thus precluding solid theoretical or numerical approaches. In such situations, we must rely on experiments for gaining further fundamental insights about what diffusion measurements reflect. Shemesh investigates the microstructural correlates of fractional anisotropy (FA) and microscopic FA (μFA) using high resolution double-diffusion encoding (DDE) and double oscillating gradient diffusion encoding (DODE) experiments in fixed spinal cords. The results indicate that μFA(DODE) mostly depend on axon sizes and myelin water fraction, whereas μFA(DDE), FA(DODE), and FA(DDE) correlate to a much lesser extent with those cellular features. This is promising for future interpretations of these metrics in health and disease. Valette et al. recapitulate how intracellular metabolite diffusion has been measured in the brain, using DW-NMR spectroscopy *in vivo*, from t_d<1 ms to t_d>1 sec, and how the picture emerges that metabolites are not confined into subcellular compartments, but are instead diffusing in long fibers with some long-range complexity. Some possible future directions to extend the range of diffusion times, and what information about cell structure can be gleaned, are also discussed. As a final illustration of how well-thought experiments may yield fundamental insight, Lemberskiy et al. exploit data obtained in the prostate at multiple t_d and echo times to select and combine two different models, which allows disentangling the cellular compartment (exhibiting shorter relaxation time T2 and associated with diffusion through extended disorder) from the lumen (exhibiting longer T2 and associated with the short-time S/V limit). Beyond fundamental understanding, data modeling allows extracting lumen diameter, fiber diameter and membrane permeability, with possible application to non-invasive diagnosis and staging of prostate cancer with MRI.

The potential relevance for applications of DW-NMR *in vivo* certainly underlies all works in our field, even those aiming at gaining fundamental knowledge, but some works more directly aim toward applications in animals or humans. Such more "application-driven" papers, either describing optimized methods to measure biologically/clinically relevant parameters, or evaluating the value of these methods under various conditions (e.g., in disease), represent approximately another half of this research topic.

Hansen and Jespersen review fast kurtosis imaging protocols, which are capable of estimating the mean, axial and radial kurtosis (i.e., deviations from Gaussian diffusion when q is varied at constant t_d) with only a few diffusion directions. The review describes the theoretical foundations for these methods, technical and practical considerations, and potential applications mostly related to peripheral nerve or white matter microstructure. In a similar vein, Jelescu and Budde review popular models of diffusion in white matter to extract parameters such as axonal orientation dispersion, axon diameter, and extracellular volume fraction, from the q-dependence at constant t_d. Assumptions and required data are detailed for each model, before examining how these models can be validated using numerical simulations, phantoms, or *ex vivo* microscopy. Zeng et al. consider the fitting quality of multi-exponential signal expressions to diffusion data from white matter in healthy volunteers. Specifically, they propose to describe water diffusion in white matter in terms

of a modified tri-exponential expression; a biexponential plus a "dot" compartment, i.e., a water pool having zero diffusivity. The latter component is interpreted as restricted diffusion, and the modified tri-exponential is found to have lower corrected Akaike criterion than both free tri-exponential and biexponential signal representations in several white matter ROIs.

Mériaux et al. present an original method which, unlike other papers of this research topic, does not assess diffusion by gradient-induced diffusion-weighting, but by dynamically acquiring concentration maps of contrast agents as they diffuse through the extracellular space (as more traditionally performed with optical imaging) to evaluate the ADC and tortuosity in the extracellular space. One original point of their approach is that the agent is delivered to the brain after i.v. injection and ultrasound-induced blood-brain barrier opening, avoiding invasive intracerebral injection. This technique may be useful to characterize the alterations of extracellular space diffusion properties in pathologies such as Alzheimer's disease, and also to predict drug biodistribution.

Some methods may prove particularly relevant for specific pathologies, such as tumors. Reynaud starts by reviewing the fundamentals of time-dependent diffusion in the short-time regime and near the tortuosity limit. The main three geometrical models (IMPULSED, POMACE, VERDICT) implemented so far to describe tumor cells as spheres are then reviewed, and their applications for estimating tumor intra- and extracellular volume fraction and cell size is then presented and discussed. Budde et al. present an optimization of pulse sequences for imaging of spinal cord injury. The authors consider orientationally invariant DDE, filter probe DDE and filter probe single-diffusion encoding (SDE), in which the idea of a filter probe is basically to suppress extra-axonal water with a diffusion gradient perpendicular to the cord. They find that filter probe SDE coupled with reduced field-of-view excitation is the best protocol with highest signal-to-noise ratio and with high sensitivity to injury, without contamination from edema and cerebrospinal fluid. This is demonstrated with simulations, and *in vivo* rat and human spinal cord imaging. Finally, one important clinical use of MRI is in assessing tissue damage and prospective recovery in ischemic stroke. Question remains as to what are the most meaningful diffusion metrics in ischemic stroke, that is, those that most sensitively reflect microstructural characteristics of tissue affected by ischemia. Galazzo et al. consider a set of indices obtained from the Simple Harmonic Oscillator Based Reconstruction and Estimation (SHORE). Assessment of quantities associated with the SHORE formalism are investigated in a tract-based fashion in white matter and region-of-interest analysis in gray matter in patients and controls, providing insight into the potential benefits of adopting the SHORE model and some of its metrics in the clinic.

In conclusion, this research topic illustrates the multifaceted nature of cellular microstructure assessment using DW-NMR. While no particular method can grasp the full complexity of cellular microstructure, each of them can shed light on different aspects and find specific applications. In the long term, some approaches will certainly prove more insightful or useful than others. For now, the present collection of works pays tribute to the vitality and diversity of our research field.

AUTHOR CONTRIBUTIONS

JV drafted the first version of the editorial. IR and SJ revised the first draft and made contributions about papers they edited.

REFERENCES

1. Stejskal EÖ, Tanner JE. Spin diffusion measurements: spin echoes in the presence of a time-dependent field gradient. *J Chem Phys.* (1965) **42**:288. doi: 10.1063/1.1695690
2. Tanner JE, Stejskal EO. Restricted self-diffusion of protons in colloidal systems by pulsed-gradient spin-echo method. *J Chem Phys.* (1968) **49**:1768. doi: 10.1063/1.1670306
3. Tanner JE. Self diffusion of water in frog muscle. *Biophys J.* (1979) **28**:107–16. doi: 10.1016/S0006-3495(79)85162-0
4. Lebihan D, Breton E, Lallemand D, Grenier P, Cabanis E, Lavaljeantet M. Mr imaging of intravoxel incoherent motions - application to diffusion and perfusion in neurologic disorders. *Radiology.* (1986) **161**:401–7. doi: 10.1148/radiology.161.2.3763909
5. Le Bihan D, Breton E, Lallemand D, Aubin ML, Vignaud J, Laval-Jeantet M. Separation of diffusion and perfusion in intravoxel incoherent motion MR imaging. *Radiology.* (1988) **168**:497–505. doi: 10.1148/radiology.168.2.3393671
6. Moseley ME, Kucharczyk J, Mintorovitch J, Cohen Y, Kurhanewicz J, Derugin N, et al. Diffusion-weighted MR imaging of acute stroke: correlation with T2-weighted and magnetic susceptibility-enhanced MR imaging in cats. *AJNR Am J Neuroradiol.* (1990) **11**:423–9.
7. Warach S, Chien D, Li W, Ronthal M, Edelman RR. Fast magnetic resonance diffusion-weighted imaging of acute human stroke. *Neurology.* (1992) **42**:1717–23.
8. Le Bihan D, Schild T. Human brain MRI at 500MHz, scientific perspectives and technological challenges. *Superconduct Sci Technol.* (2017) **30**:033003. doi: 10.1088/1361-6668/30/3/033003
9. Jones DK, Alexander DC, Bowtell R, Cercignani M, Dell'Acqua F, McHugh DJ, et al. Microstructural imaging of the human brain with a 'super-scanner': 10 key advantages of ultra-strong gradients for diffusion MRI. *Neuroimage.* (2018) **182**:8–38. doi: 10.1016/j.neuroimage.2018.05.047
10. Moser E, Stahlberg F, Ladd ME, Trattnig S. 7-T MR–from research to clinical applications? *NMR Biomed.* (2012) **25**:695–716. doi: 10.1002/nbm.1794
11. Ladd ME, Bachert P, Meyerspeer M, Moser E, Nagel AM, Norris DG, et al. Pros and cons of ultra-high-field MRI/MRS for human application. *Prog Nucl Magn Reson Spectrosc.* (2018) **109**:1–50. doi: 10.1016/j.pnmrs.2018.06.001

Conflict of Interest Statement: The authors declare that the research was conducted in the absence of any commercial or financial relationships that could be construed as a potential conflict of interest.

frontiers in Physics

HYPOTHESIS AND THEORY
published: 02 March 2018
doi: 10.3389/fphy.2018.00017

Influence of the Size and Curvedness of Neural Projections on the Orientationally Averaged Diffusion MR Signal

Evren Özarslan[1,2]*, *Cem Yolcu*[1], *Magnus Herberthson*[3], *Hans Knutsson*[1] and *Carl-Fredrik Westin*[1,4]

[1] Department of Biomedical Engineering, Linköping University, Linköping, Sweden, [2] Center for Medical Image Science and Visualization, Linköping University, Linköping, Sweden, [3] Division of Mathematics and Applied Mathematics, Department of Mathematics, Linköping University, Linköping, Sweden, [4] Laboratory for Mathematics in Imaging, Department of Radiology, Brigham and Women's Hospital, Harvard Medical School, Boston, MA, United States

OPEN ACCESS

Edited by:
Julien Valette,
Commissariat à l'Energie Atomique et aux Energies Alternatives (CEA), France

Reviewed by:
Silvia Capuani,
Consiglio Nazionale Delle Ricerche (CNR), Italy
Gernot Reishofer,
Medical University of Graz, Austria
Sune Nørhøj Jespersen,
Aarhus University, Denmark

***Correspondence:**
Evren Özarslan
evren.ozarslan@liu.se

Specialty section:
This article was submitted to Biomedical Physics, a section of the journal Frontiers in Physics

Received: 29 September 2017
Accepted: 09 February 2018
Published: 02 March 2018

Citation:
Özarslan E, Yolcu C, Herberthson M, Knutsson H and Westin C-F (2018) Influence of the Size and Curvedness of Neural Projections on the Orientationally Averaged Diffusion MR Signal. Front. Phys. 6:17. doi: 10.3389/fphy.2018.00017

Neuronal and glial projections can be envisioned to be tubes of infinitesimal diameter as far as diffusion magnetic resonance (MR) measurements via clinical scanners are concerned. Recent experimental studies indicate that the decay of the orientationally-averaged signal in white-matter may be characterized by the power-law, $\bar{E}(q) \propto q^{-1}$, where q is the wavenumber determined by the parameters of the pulsed field gradient measurements. One particular study by McKinnon et al. [1] reports a distinctively faster decay in gray-matter. Here, we assess the role of the size and curvature of the neurites and glial arborizations in these experimental findings. To this end, we studied the signal decay for diffusion along general curves at all three temporal regimes of the traditional pulsed field gradient measurements. We show that for curvy projections, employment of longer pulse durations leads to a disappearance of the q^{-1} decay, while such decay is robust when narrow gradient pulses are used. Thus, in clinical acquisitions, the lack of such a decay for a fibrous specimen can be seen as indicative of fibers that are curved. We note that the above discussion is valid for an intermediate range of q-values as the true asymptotic behavior of the signal decay is $\bar{E}(q) \propto q^{-4}$ for narrow pulses (through Debye-Porod law) or steeper for longer pulses. This study is expected to provide insights for interpreting the diffusion-weighted images of the central nervous system and aid in the design of acquisition strategies.

Keywords: diffusion, magnetic resonance, anisotropy, Stejskal-Tanner, curvature, curvilinear, power-law, powder

1. INTRODUCTION

Diffusion-sensitized magnetic resonance acquisitions have been employed to recover the microscopic building blocks of complex nervous tissue. Simplified models exploiting the compartmentalized structure of the tissue are instrumental in this endeavor. Water molecules in the intra- and extra-cellular spaces have been envisioned to form separate compartments with different signal characteristics [2]. The intracellular signal is also thought to represent the superposition of contributions from cells of different types, shapes, and orientations [3]. The same argument has been employed even for a single neuron wherein each neurite has been considered to comprise

a collection of straight compartments [4]. Such representation of neurites as slender cylinders distributed in random orientations within the voxel is perhaps the model most relevant to the current study.

The diameter of neurites, and in fact all neural projections, is so small that diffusion in the transverse plane may be negligible. More explicitly, a cylinder with the same diameter as a neurite would not suffer any signal loss in a typical clinical diffusion MRI measurement when the diffusion gradients are applied in the direction perpendicular to the cylinder's axis. This justifies assigning zero value to transverse diffusivity for molecules confined in the cylinder. Such behavior [5] was indeed observed for N-acetyl-L-aspartate (NAA) diffusion in the brain [6] and have been employed for water in recent models [7].

In this work, we consider the pulsed field gradient measurement introduced by Stejskal and Tanner [8] featuring diffusion encoding gradients $\boldsymbol{G}$ of duration δ, whose leading edges are separated from each other by duration Δ (see **Figure 1A** for the effective gradient waveform). We define $\boldsymbol{q} = \gamma\delta\boldsymbol{G}$, where γ is the gyromagnetic ratio and note that for sufficiently small values of $q = |\boldsymbol{q}|$, the signal for each compartment can be approximated with a Gaussian, i.e.,

$$E(\boldsymbol{q}) \approx e^{-\boldsymbol{q}^{\mathsf{T}}\boldsymbol{V}\boldsymbol{q}}. \tag{1}$$

Considering the form (Equation 1) of the signal, $\boldsymbol{V}$ can be referred to as the signal decay tensor[1]. The geometric parameters of the compartment have typically a complicated relation to $\boldsymbol{V}$; the exact form of such relation is dictated by the temporal parameters (δ and Δ) of the diffusion encoding pulse sequence. For axially symmetric $\boldsymbol{V}$, we shall denote by $v_{\parallel}$ and $v_{\perp}$ the eigenvalues of $\boldsymbol{V}$ associated with directions parallel and perpendicular to the symmetry axis, respectively.

Our focus in this work is the orientationally-averaged signal, which can be obtained by computing the "isotropic component" of the signal, as was referred to in Özarslan and Basser [10] and actually estimated as a byproduct of the q-space signal representation in Özarslan et al. [11]. Alternatively, the signal values measured over all gradient directions at a particular q-value can be averaged [12, 13] so that any dependence on the direction of the gradient vector is lost. Repeating this procedure for all q-values reduces the data collected over the three-dimensional q-space into a one-dimensional profile, which does not contain any information on ensemble (macroscopic) anisotropy[2]. The estimated signal profile represents the decay for the so-called "powdered" specimen, which contains an isotropic distribution of each and every compartment in the original specimen [19, 20]. The orientationally-averaged signal for axisymmetric compartments, each of which contributes according to Equation (1), is thus the same as the signal for an isotropic ensemble of such compartments, and is given by [6, 21, 22]

$$\bar{E}(q) = \frac{\sqrt{\pi}\, e^{-q^2 v_{\perp}}\, \mathrm{erf}(q\sqrt{v_{\parallel} - v_{\perp}})}{2q\sqrt{v_{\parallel} - v_{\perp}}}. \tag{2}$$

This expression predicts a squared exponential decay in general. However, if signal loss is limited to only the fiber direction ($v_{\perp} = 0$), a much slower decay emerges. A power law of the form $\bar{E} \propto q^{-1}$, to be specific. Therefore, the appearance of this particular power-law can be used as an indicator of vanishing transverse diffusivity, in other words, the signal decay tensor $\boldsymbol{V}$ being of rank 1. We note that the problem of characterizing the orientationally averaged signal is considerably more complicated when Equation (1) cannot be used to represent the compartmental signal; addressing this issue is one of our goals in this study.

The $\bar{E} \propto q^{-1}$ decay alluded to above was recently reported in white matter [1, 23]. These studies have found that in

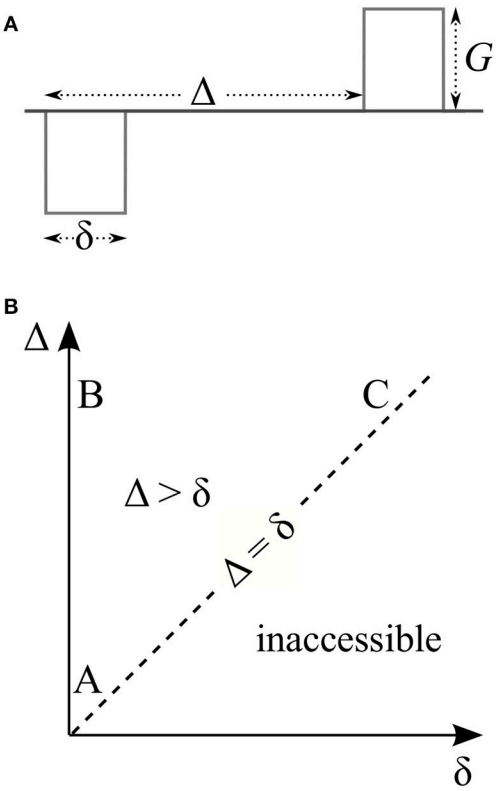

FIGURE 1 | (A) Stejskal and Tanner's pulsed field gradient experiment features a pair of rectangular gradient pulses of duration δ whose leading edges are separated by Δ. **(B)** The timing parameters of this experiment lie on or above the dashed line since the separation of the two pulses (Δ) has to be at least as long as the duration of each of them (δ). Thus, the experiment has three distinct regimes (labeled A, B, and C) based on whether these timing parameters are short or long. These are the three regimes that exhibit all interesting features of the signal. The same features are expected to be observed to various degrees in the intermediate region between these three regimes.

[1]We note that the decay tensor is closely related to an apparent diffusion tensor (ADT) whose time-dependence has been shown to be sufficient for describing (approximately-)Gaussian diffusion via general gradient waveforms [9]. In this study, it proves convenient to employ the $\boldsymbol{V}$-tensor, which encapsulates all dependencies other than that on the $\boldsymbol{q}$-vector.

[2]Yet another approach would involve employing alternative gradient waveforms for isotropic diffusion weighting [14–18]. However, we do not discuss such sequences here because of the complicated dependence of the signal intensity on the gradient waveform.

white-matter-dominated regions of the brain, the orientationally averaged signal exhibits a decay $\sim q^{-c}$ with an exponent c close to 1, in support of cylindrical neural projections as remarked above. In gray-matter-dominated regions, McKinnon et al. [1] have observed a larger exponent $c \approx 1.8 \pm 0.2$. They proposed that the apparent breakdown of the cylinder model may indicate a significantly larger permeability of the cellular membranes in gray matter vs. white matter. Here, we investigate an alternative hypothesis. Namely, the departure of the exponent c from 1 can well be due to impermeable but *curved* projections. To assess this point, we studied the influence of neural projections' size and shape on the orientationally-averaged diffusion MR signal. Due to the large variability in the geometric features of the neural cells, all temporal regimes of the Stejskal-Tanner sequence were considered, and the problem was studied both in the small-q regime as well as at larger q-values for which Equation (1) and thus Equation (2) are inaccurate.

Investigation of power-like tails in the diffusion MR signal goes back to Köpf et al. [24], where large values of the wave vector were achieved using a fringe field method. A range of exponents (roughly between -1.8 and -4.6) were observed across various nonneural tissue types, as well as stretched exponential behavior, which was ascribed to fractional Brownian motion. In a subsequent study, Yablonskiy et al. [25] predicted an exponent of -2 for specimens featuring compartments with a distribution of diffusivities. Jian et al. [26] considered a parametric tensor distribution, which suggested a signal decay with a general power-law tail. These studies, however, observe or predict the signal decay for measurements along a single direction. As for the orientationally (powder) averaged signal, a quite general statement regarding an asymptotic power-law decay in the diffusion MR signal is the Debye-Porod law [27]. Here, the orientationally averaged signal measured using narrow pulses is predicted to follow a q^{-4} tail under quite general considerations. In our discussion, we take up apparent violations of this.

Although the influence of fiber curvature on the MR signal has been considered [28–33] in various contexts, to our knowledge, this is the first study to provide explicit expressions for the signal decay for diffusion along a general parametrized curve and study its effect on the orientationally averaged signal.

In the next section, we provide explicit expressions for the MR signal for diffusion on curves in three distinct temporal regimes of the Stejskal-Tanner measurement. In the subsequent section, we discuss the implications of our theoretical findings as they relate to the morphology of neural cells and recent experimental observations. The article is concluded following a brief discussion of what observed power-law tails in the powder averaged signal may represent in that context, as well as from the perspective of the Debye-Porod law.

2. COMPARTMENTAL AND ORIENTATIONALLY-AVERAGED SIGNAL FOR DIFFUSION ALONG CURVES

The effective gradient waveform of a traditional Stejskal-Tanner measurement is shown in **Figure 1A**. In this work, we consider three distinct regimes of this pulse sequence based on whether δ and Δ are short or long. These regimes are indicated by the letters A, B, and C on the δ-Δ plane in **Figure 1B**. We note that the essential features of the signal at these three extreme situations are exhibited to some extent for more general timing values, i.e., within the interior of the triangle whose vertices are at A, B, and C.

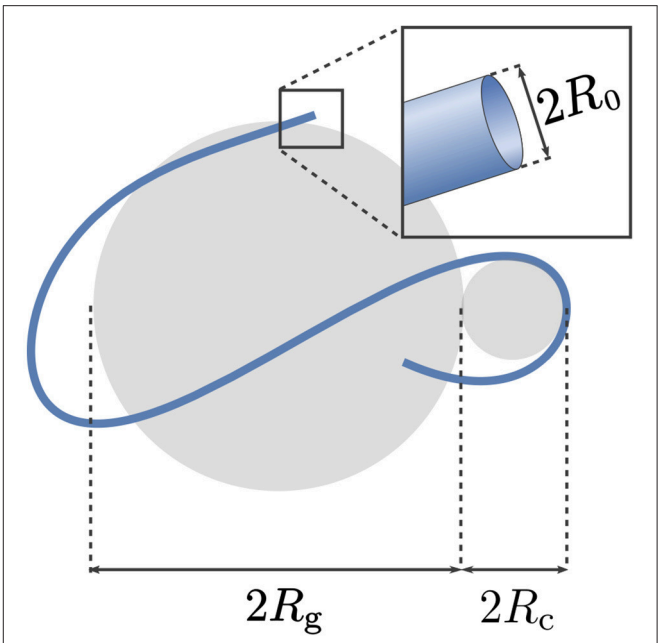

FIGURE 2 | The relevant size parameters of a simplified neural projection (ignoring branchings and other features such as beading patterns [34]) are: its contour length denoted by ℓ, its radius of gyration R_g, the characteristic radius of curvature R_c, and the radius of the projection's cross-section R_0.

The relevant size parameters of a simplified neural projection (ignoring branchings and other features such as beading patterns [34]) are: its contour length denoted by ℓ, its radius of gyration R_g, its characteristic curvature radius R_c, and the radius of the projection's cross-section R_0. These parameters are illustrated for a representative projection in **Figure 2**. As mentioned in Introduction, R_0 is typically so small that $qR_0 \ll 1$ for clinical MRI; this justifies representing the neurites and glial projections via one-dimensional curves. Thus, we shall consider diffusion taking place on a curve $\boldsymbol{r}(s) = (r_1(s), r_2(s), r_3(s))^\intercal$ parameterized by its arclength s, where $0 \leqslant s \leqslant \ell$.

2.1. Regime A: Short Diffusion-Time

In the first case, diffusion is observed for such a short time that the hindrances have not been encountered. This condition implies that the pulse durations are short as well. In fact, when $D\Delta \ll R_c^2$, spins spread so little that even the most curved point along the projection seems like a straight segment[3]. Thus, the

[3]The "most curved point" should be taken with a grain of salt. Even though, mathematically, the approximations in this regime would require a diffusion length $\sqrt{D\Delta}$ much smaller than the smallest radius of curvature along the curve, R_c is not

compartmental signal occurs as the average, over the curve, of the signals originating from the tangents of the curve:

$$E(\boldsymbol{q}) = \frac{1}{\ell}\int_0^\ell \mathrm{d}s\, e^{-D\Delta \boldsymbol{q}^\intercal \hat{\boldsymbol{t}}(s)\hat{\boldsymbol{t}}^\intercal(s)\boldsymbol{q}}\,, \tag{3}$$

where

$$\hat{\boldsymbol{t}}(s) = \frac{\mathrm{d}\boldsymbol{r}(s)}{\mathrm{d}s} \tag{4}$$

is the unit tangent to the curve.

As shown in Appendix A (see the Supplementary Material), the very small-q behavior of the orientationally-averaged signal ($q^2 D\Delta \ll 1$) is given by $\bar{E}(q) \approx e^{-q^2 D\Delta/3}$. Thus, the decay rate is determined solely by the (intracellular) diffusivity, and bears no geometric feature of the neural arborization in this regime.

For a more general analysis involving larger q-values, one can still employ Equations (1, 2) as follows. We are interested in the orientational average of the compartmental signal in Equation (3), i.e.,

$$\bar{E}(q) = \frac{1}{\ell}\int_0^\ell \mathrm{d}s\, \left\langle e^{-D\Delta \boldsymbol{q}^\intercal \hat{\boldsymbol{t}}(s)\hat{\boldsymbol{t}}^\intercal(s)\boldsymbol{q}}\right\rangle\,, \tag{5}$$

where the order of integration and orientational averaging, indicated by the angular brackets, was changed. However, the expression within the angular brackets is of the Gaussian form (Equation 1) with a rank-1 decay tensor whose non-vanishing eigenvalue is $D\Delta$. Consequently, the signal for the powdered specimen is given through Equation (2) by setting $v_\perp = 0$, and $v_\parallel = D\Delta$ to be

$$\bar{E}(q) = \frac{\sqrt{\pi}\,\mathrm{erf}(q\sqrt{D\Delta})}{2q\sqrt{D\Delta}}\,. \tag{6}$$

Clearly, for larger q-values, the orientationally-averaged signal decay in regime A is proportional to q^{-1} irrespective of the shape of the curve as long as $R_c^2 \gg D\Delta$. It can be observed that Equation (5) has the form of a signal arising from a uniform orientational distribution of "sticks". Hence the emergence of q^{-1} at large q-values can be justified alternatively by Veraart et al.'s arguments [23].

2.1.1. Incorporating Curvature Effects

The above expression holds when the diffusion distance is much smaller than R_c as pointed out earlier. Here, we would like to generalize this expression to larger timing parameters, Δ and δ, to allow for the possibility that the diffusion distance during the course of the experiment is long enough for the molecules to traverse an approximately circular arc along the curve. Moreover, we assume that there is a single characteristic radius of curvature that represents the effective curvedness of the entire projection. This characteristic curvature is denoted by R_c.

Let $E_{\mathrm{arc}}(\hat{\boldsymbol{n}}, \varphi, \boldsymbol{q})$ denote the signal for a single such arc, where $\hat{\boldsymbol{n}}$ is the unit vector normal to its plane and φ is the polar coordinate of the center of the arc in a cylindrical reference frame oriented along $\hat{\boldsymbol{n}}$. The orientationally averaged signal can then be written as the average of $E_{\mathrm{arc}}(\hat{\boldsymbol{n}}, \varphi, \boldsymbol{q})$, over all possible realizations of a single arc, i.e.,

$$\bar{E}(q) = \frac{1}{4\pi}\int_{S_2} \mathrm{d}\hat{\boldsymbol{n}}\, \frac{1}{2\pi}\int_0^{2\pi} \mathrm{d}\varphi\, E_{\mathrm{arc}}(\hat{\boldsymbol{n}}, \varphi, \boldsymbol{q})\,, \tag{7}$$

where S_2 denotes the unit sphere. The second average simply defines the signal for a full circle of radius R_c. If we denote by $E_{\mathrm{circ}}(\hat{\boldsymbol{n}}, \boldsymbol{q})$ the signal for such a circle whose plane has the normal vector $\hat{\boldsymbol{n}}$, the orientationally averaged signal can be expressed as

$$\bar{E}(q) = \frac{1}{4\pi}\int_{S_2} \mathrm{d}\hat{\boldsymbol{n}}\, E_{\mathrm{circ}}(\hat{\boldsymbol{n}}, \boldsymbol{q})\,. \tag{8}$$

Due to its axial symmetry, the signal for the circle has the functional dependence $E_{\mathrm{circ}}(\hat{\boldsymbol{n}}\cdot\hat{\boldsymbol{q}}, q)$, where $\hat{\boldsymbol{q}} = \boldsymbol{q}/q$. Since $\hat{\boldsymbol{n}}\cdot\hat{\boldsymbol{q}}$ is invariant under exchange of the unit vectors $\hat{\boldsymbol{n}}$ and $\hat{\boldsymbol{q}}$, one is free to replace the integration variable above with $\hat{\boldsymbol{q}}$ and fix $\hat{\boldsymbol{n}}$ instead [19] . With the variable θ defined through $\hat{\boldsymbol{n}}\cdot\hat{\boldsymbol{q}} = \cos\theta$, we moreover note that since there is no motion and hence no signal attenuation in the direction along $\hat{\boldsymbol{n}}$, the integrand's functional dependence may further be reduced to $E_{\mathrm{circ}}(q\,\sin\theta)$, namely, the signal obtained when a $\boldsymbol{q}$-vector of magnitude $q\,\sin\theta$ is applied in the plane of the circle. Upon taking these observations into account, we obtain

$$\bar{E}(q) = \int_0^{\pi/2} \mathrm{d}\theta\, \sin\theta\, E_{\mathrm{circ}}(q\,\sin\theta)\,. \tag{9}$$

2.1.1.1. Narrow Pulses

First, we shall consider the scenario involving narrow pulses, i.e., $D\delta \ll R_c^2$, but allow for the possibility that $D\Delta \approx R_c^2$. For arbitrary Δ, the signal for a full circle is given by Özarslan et al. [28]

$$E_{\mathrm{circ}}(q) = J_0(qR_c)^2 + 2\sum_{n=1}^{\infty} e^{-n^2 D\Delta/R_c^2} J_n(qR_c)^2\,, \tag{10}$$

where J_n denotes the nth order Bessel function. This expression yields, via Equation (9), the orientationally-averaged signal to be

$$\begin{aligned}\bar{E}(q) = {} & J_0(2qR_c) + \frac{\pi}{2}\left[J_1(2qR_c)\mathbf{H}_0(2qR_c) - J_0(2qR_c)\mathbf{H}_1(2qR_c)\right] \\ & + 2\sum_{n=1}^{\infty} e^{-n^2 D\Delta/R_c^2}\frac{(qR_c)^{2n}}{(2n+1)!} \\ & {}_1F_2\left(n+\frac{1}{2}; n+\frac{3}{2}, 2n+1; -q^2R_c^2\right)\,,\end{aligned} \tag{11}$$

where $\mathbf{H}_\alpha$ is the Struve function of order α and ${}_1F_2$ represents the generalized hypergeometric function. We note that this orientationally averaged signal in the narrow pulse regime has the asymptotic behavior

$$\bar{E}(q) \sim \frac{\sqrt{\pi}\,\mathrm{erf}(q\sqrt{D\Delta})}{2q\sqrt{D\Delta}} + \frac{(D\Delta)^2 q^2 e^{-D\Delta q^2}}{6R_c^2} - \mathcal{O}(R_c^{-4})\,. \tag{12}$$

such a strict measure. Rather, it is the minimal radius of curvature that the curve exhibits along a portion of it significant enough to influence the signal.

This expression contains the curvature-related correction to Equation (6), which is valid for straight fibers, and suggests that curvature induced effects are rather limited for the case of narrow pulses, as the $\bar{E}(q) \propto q^{-1}$ dependence is unaffected at larger q-values.

2.1.1.2. Longer pulse durations

To investigate the influence of longer pulse durations, we numerically evaluated the integral in Equation (9) using Simpson's rule [35]. We adapted the multiple correlation (MCF) framework to the problem of diffusion on a circle. The details of this procedure are provided in Appendix B (see the Supplementary Material).

In **Figure 3**, we illustrate the signal decay curves at different pulse durations. In these simulations, the $D\Delta$ value was set equal to R_c^2; during a time interval of duration Δ, the spread of molecules on the circle is about 80°. When the pulse duration is short, we verified that the decay obeys the expressions in Equations (11) and (12) (results not shown). The power-law, $E(q) \propto q^{-1}$, which is valid in the narrow pulse regime does *not* prevail when the pulses are prolonged.

2.2. Regime B: Long Diffusion-Time and Narrow Pulses

When diffusion is probed via a pair of impulses (or, when $D\delta \ll R_c^2$) separated from each other by a duration long enough for the molecules to reach all points within the curve, i.e., $D\Delta \gg \ell^2$, the signal is given simply by the expression $E(\boldsymbol{q}) = |\tilde{\rho}(\boldsymbol{q})|^2$, where $\tilde{\rho}(\boldsymbol{q})$ is the Fourier transform of the density

$$\rho(\boldsymbol{r}) = \frac{1}{\ell}\int_0^\ell \mathrm{d}s\, \delta(\boldsymbol{r} - \boldsymbol{r}(s))\,, \tag{13}$$

which is uniform along the curve. The orientationally averaged signal decay is thus obtained by averaging $|\tilde{\rho}(\boldsymbol{q})|^2$, and is given by

$$\bar{E}(q) = \frac{1}{\ell^2}\int_0^\ell \mathrm{d}s \int_0^\ell \mathrm{d}s' \, \frac{\sin\left[q\,|\boldsymbol{r}(s) - \boldsymbol{r}(s')|\right]}{q\,|\boldsymbol{r}(s) - \boldsymbol{r}(s')|}\,. \tag{14}$$

This expression is referred to as the Debye scattering equation [36], which is widely utilized in studies employing small angle scattering experiments for characterizing the structure of polymers. The essential features of the resulting $\bar{E}(q)$ curve are well-understood [37, 38]. As shown in Appendix A (see the Supplementary Material), the small-q regime ($qR_g \ll 1$, the "Guinier regime" of scattering experiments) is described by the relationship $\bar{E}(q) \approx e^{-(qR_g)^2/3}$. As for larger q-values, such studies indicate that depending on the structure of the polymer, different sections of the curve could be characterized by different power-laws. For example, Gaussian chains undergo q^{-2} decay, while fractional exponents are obtained for curves exhibiting fractality. Perhaps the most relevant finding, however, is that wormlike structures (i.e., those characterized by a so-called persistence length over which the polymer is likely to retain its direction) are characterized by a decay $\propto q^{-1}$ at q-values about the reciprocal of the chain's persistence length [39]. Thus, even a class of non-straight structures exhibit q^{-1} decay in Regime B.

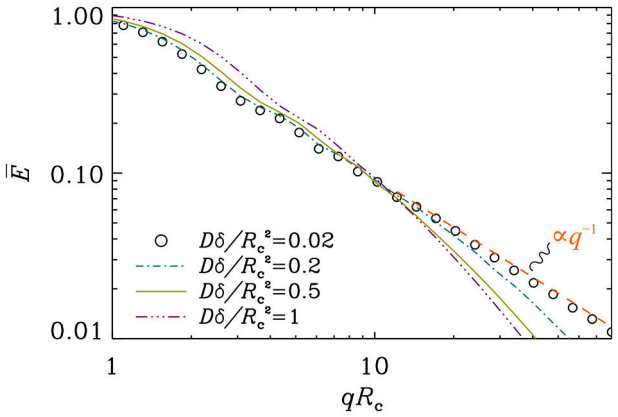

FIGURE 3 | Signal attenuation curves for different values of the pulse duration. The separation of pulses was taken so that $D\Delta = R_c^2$. The q^{-1} decay, visible at short pulse durations, disappears as the pulses are prolonged.

2.3. Regime C: Long Pulse-Duration

For the traditional Stejskal-Tanner measurement utilizing a pair of identical pulses in opposite directions, the compartmental signal has the form

$$E = \left\langle e^{-i\boldsymbol{q}\cdot(\boldsymbol{\xi}_2 - \boldsymbol{\xi}_1)} \right\rangle_{\text{paths}}\,, \tag{15}$$

where the averaging is performed over all trajectories, with

$$\boldsymbol{\xi}_n = \frac{1}{\delta}\int_{t_n}^{t_n+\delta} \boldsymbol{r}(t)\,\mathrm{d}t \tag{16}$$

being the center of mass coordinate [40] of the fragment of trajectory coinciding with each pulse ($t_1 = 0$ and $t_2 = \Delta$). Therefore, the MR signal (Equation 15) elicited by flat gradient pulses is not sensitive to the Brownian trajectories instant by instant but only in a time averaged sense.

In the limit $D\delta/\ell^2 \to \infty$, the two random variables lose correlation and the explicit dependence on Δ disappears, leading to the signal intensity [40]

$$E = \left|\tilde{p}_{\text{cm}}(\boldsymbol{q}, \delta)\right|^2\,, \tag{17}$$

where

$$\tilde{p}_{\text{cm}}(\boldsymbol{q}, \delta) = \int p_{\text{cm}}(\boldsymbol{\xi}, \delta) e^{-i\boldsymbol{q}\cdot\boldsymbol{\xi}}\,\mathrm{d}\boldsymbol{\xi} \tag{18}$$

is the Fourier transform of the center of mass distribution. Moreover, in this limit, the distribution for the random variable $\boldsymbol{\xi}$ approaches a Gaussian due to the central limit theorem [41][4]. Consequently, the signal (Equation 17) also approaches a quadratic exponential form, encoding no more structural information than the variance of $p_{\text{cm}}(\boldsymbol{\xi}, \delta)$. Whether the domain

[4]This non-obvious statement, whose rigorous proof can be found in mathematics literature [42], was instrumental in our identification of an effective potential for restricted diffusion [43].

is an irregularly curved fiber or a much more regular shape like a sphere, its fine structural features will find no representation in the signal acquired this way, since the length of the time averaging (pulse) has suppressed all short-scale (high q) variation encoded in the cumulants higher than the second.

Hence, the compartmental signal has the form Equation (1). Here, though, $\boldsymbol{V}$ is the variance tensor for the center of mass coordinate (Equation 16) for a trajectory of (long) duration δ. This variance can be calculated for diffusion along a general continuous curve following Mitra and Halperin's [40] derivation in the case of slab geometry, with slight modifications. One finds

$$V_{ij} = \frac{2}{D\delta}\int_0^\ell \mathrm{d}s\, r_i(s)\int_0^\ell \mathrm{d}s'\, r_j(s')\left\{B_2\left(\frac{|s-s'|}{2\ell}\right)+B_2\left(\frac{s+s'}{2\ell}\right)\right. \\ \left. +\frac{\ell^2}{3D\delta}\left[B_4\left(\frac{|s-s'|}{2\ell}\right)+B_4\left(\frac{s+s'}{2\ell}\right)\right]\right\}, \quad (19)$$

where $B_n(\cdot)$ denotes the nth order Bernoulli polynomial, and $D\delta/\ell^2 \gg 1$. Here, the exponentially decaying terms are ignored as their contribution is negligible at even moderate durations. The details of the derivation of the above expression is provided in Appendix A (see the Supplementary Material). We note that alternative representations of the final result (Equation 19) can be given in terms of polylogarithmic or Hurwitz zeta functions. We verified that Equation (19) correctly reproduces Mitra and Halperin's expression [40] in the same regime for the slab geometry, i.e., for a straight line.

As were in the previous cases, the signal decay tensor for long pulse duration is not rank-1 for a general curve. However, unlike in previous regimes, the compartmental signal decay is truly Gaussian. Consequently, the orientationally averaged signal in this regime suffers q^{-1} decay if and only if the fibers are straight.

3. RESULTS AND DISCUSSION

3.1. Summary

The above findings can be summarized as follows: For narrow pulses ($D\delta \ll R_c^2, \ell^2$) in regimes A and B, the orientationally averaged signal exhibits a slow q^{-1} tail for large q for diffusion along curved as well as straight 1 dimensional structures. As the pulse duration is prolonged, as we have studied for regime A, the slow q^{-1} tail gives way to a steeper drop for substantially curved fibers, by which we mean $R_c \lesssim \sqrt{D\delta}$. Indeed, the signal may be expected to bear less features of diffusion along a 1D structure and more of diffusion in a 3D domain (i.e., a steep decay), since a long pulse serves to average the motion of the spin carriers over a length $\sim \sqrt{D\delta}$ along the path curved in 3D space. Fibers much shorter than the averaging length ($\ell \ll \sqrt{D\delta}$) fall into regime C and may contribute to an exponent of -1 in the orientationally averaged signal *only* if they are straight ($R_c \gg \ell$).

3.2. Clinical Relevance

An important question to ask is: What regime is the most relevant for clinical MR examinations of the brain? There is no clear answer to this question, essentially because of the extremely wide variability in the size and shapes of cells within the brain [44][5]. Consequently, it is impossible to suggest that diffusion within all neural cells takes place in a single experimental regime. We can, nonetheless, argue that regime B is the least relevant one as it is impossible to meet the narrow pulse condition along with the long diffusion time condition when $\delta \approx \Delta$ as in clinical acquisitions performed at larger (in a practical sense) b-values, where $b = q^2(\Delta - \delta/3)$. The diffusion distance $\sqrt{2D\Delta}$ is expected to be about 10–20 μm in such acquisitions, which will place longer ($\ell \gg \sqrt{D\Delta}$) arborizations toward regime A while the shorter ($\ell \ll \sqrt{D\Delta}$) ones will tend to exhibit features of regime C. If the longer structures furthermore exhibit curvature radii safely above the "averaging length" ($R_c \gg \sqrt{D\delta}$), the q^{-1} signature will be possible to observe over a range of large q-values without requiring strict straightness, as demonstrated in **Figure 3**. For structures whose radii of curvature are small ($R_c \lesssim \sqrt{D\delta}$) the appearance of the slow decay q^{-1} becomes sensitive to curvature, and is not retained for as wide a range of q-values (see **Figure 4**). At the extreme end of the spectrum, for structures so short that $\ell \ll \sqrt{D\delta}$, entering into regime C, no curvature is tolerated if the tail q^{-1} is to appear. These considerations will have to be revisited if one measures the diffusion of molecules other than water, due to differences in their diffusion characteristics [48–50].

3.3. On Experimental Findings

In light of the above deliberations, we can revisit the experimental observations of McKinnon et al. [1] who have reported the powder averaged signals stemming from various brain regions dominated by white- or gray-matter. In white-matter regions, they have measured a decay q^{-c} for large q with c values in the neighborhood $c \approx 1.1 \pm 0.1$, whereas in gray-matter regions, the decay was significantly faster, with $c \approx 1.8 \pm 0.2$. Concerning the faster decay observed in gray-matter, they propose an explanation based on permeability differences in white and gray-matter regions. If one assumes impermeable membranes, as we did in this study, the following alternative interpretation seems adequate: In white-matter, the observation of the tail q^{-1} is compatible with regimes A and C, suggesting a substantial presence of fibers that fall into these regimes. The former implies long fibers ($\ell \gg \sqrt{D\Delta}$) that could in fact be modestly curved (as long as $R_c \gg \sqrt{D\delta}$ remains valid). The latter implies short fibers ($\ell \ll \sqrt{D\delta}$) that are straight. In gray-matter regions, the loss of the slow q^{-1} decay suggests that the signal originates predominantly from fibers that fall outside these descriptions, i.e., exhibiting strong curvature ($R_c \lesssim \sqrt{D\delta}$). Indeed, gray-matter is rich in dendrites and unmyelinated axons, which will exhibit a fair amount of bending distributed across any voxel. The gray box in **Figure 4** depicts roughly the q range used in McKinnon et al.'s study, where it is seen that while modest curvatures do exhibit the exponent -1 for a while, strong curvature yields a steeper decay for most of the range.

[5] A collection of neuron images for various species and anatomical regions can be found in the Neuromorpho database, which can be accessed through its web site, http://www.neuromorpho.org. For a recent review on the findings based on this database, see Parekh and Ascoli [45]. We also note [46] wherein the authors employ the approach taken in Jespersen et al. [47] on this database to relate the neuronal morphology in gray-matter to the MR signal at very low diffusion sensitivity.

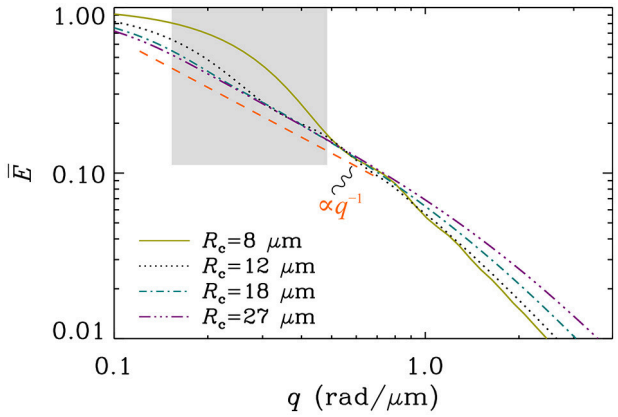

FIGURE 4 | Simulation of the orientationally averaged signal for diffusion along an arc of various curvature radii. The contour length was taken to be infinite so that the results for Regime A are employed. The timing parameters were taken to be clinically realistic for high b-value acquisitions ($\delta = 50$ ms and $\Delta = 60$ ms), and the diffusion coefficient was set to $D = 3\ \mu m^2/ms$. The gray box depicts roughly the range of b-values between 1 and 10 ms/μm^2. It is seen that the larger the curvature radius, the wider the range over which the exponent -1 can be observed. Conversely, below a cutoff determined by the averaging length $\sqrt{D\delta}$, a steeper decay of the signal becomes very prominent.

Another potential explanation involves glial cells, which constitute a substantial portion of all neural cells. Similar to neurons, glial cells exhibit an extraordinary level of diversity in their size and shape throughout the brain. Their relative number and distribution is the subject of ongoing debate [51]. Thus, an accurate assessment of their influence on the detected diffusion MR signal is infeasible at this time. It is known, however, that the glial cells tend to be smaller than neurons, they lack axons, and many of them are star-shaped [52]. These structural features tend to disfavor the emergence of a q^{-1} decay. However, recent studies have suggested that the glial cells are significantly more prevalent in cerebral white-matter compared to gray-matter [53]. Thus, it can be argued that their contribution to the overall MR signal must be rather limited. We note that the vast variation in neuronal and glial morphology along with the reported regional differences justify future studies performed at high spatial resolutions, for understanding the influence of compositional variations on the diffusion MR signal.

3.4. Immobile Water

The detected orientationally-averaged signal would typically include contributions from many different compartments besides the neural projections, including extracellular matrix, cell bodies, and molecules trapped within very small regions (e.g., within certain organelles, between myelin layers, etc.). Among these, molecules diffusing relatively freely (for instance, between the neural processes) are expected to yield a decay rate faster than q^{-1} so that much of their contribution is expected to disappear at larger q values. Conversely, there would be no significant loss of signal for truly restricted particles. Presence of a substantial portion of signal originating from such compartments as well as noise-induced bias associated with employing magnitude-valued data would make the decay appear slower [54, 55] than q^{-1} . The decay exponent $c \approx 1.1 \pm 0.1$ reported by McKinnon et al. [1] suggests that contributions from such immobile spins could be negligible in their acquisitions. This can be attributed [23] to the relatively short transverse relaxation times those spins are expected to have, along with the long echo times employed at larger q-value acquisitions via clinical scanners.

3.5. A Possible Error

One may be tempted to employ Equation (1) for the compartmental signal, as it always has a Gaussian form for sufficiently small q values, and then to attribute the emergence of the q^{-1} behavior of the orientationally averaged signal through Equation (2) to the rank of the decay tensor $\boldsymbol{V}$ being 1. However, this may be permissible for large q only in regime C. This attribution would therefore be erroneous for large q in regimes A and B. Specifically, in regimes A and B, the q range in which Equation (1) applies is similar to the q range in which the orientational average (Equation 2) exhibits a Gaussian tail no matter the rank of the tensor $\boldsymbol{V}$ (see Appendix A in the Supplementary Material). Thus, the q^{-1} behavior is *not* a consequence of the signal decay tensor having rank 1. Importantly, such behavior naturally emerges at larger q-values in regimes A and B for reasonable shapes of neural projections.

3.6. Debye-Porod Law

The powder averaged signal may be envisioned as having originated from a porous specimen which is macroscopically isotropic, in which case one expects an asymptote of the form q^{-4} due to the Debye-Porod law [27] (see Appendix C in the Supplementary Material), while a steeper decay is predicted for longer pulses as the process approaches a Gaussian (Regime C). Since this behavior arises from quite general considerations, the observation of a tail of q^{-1} appears questionable. Indeed, the observed power is most likely valid only in an *intermediate* range, as opposed to the strict $q \to \infty$ limit. The asymptotic expansion, whose leading term gives the Debye-Porod law, contains terms that decay faster than any pure power (e.g., exponential). These terms may very well exhibit decays slower than q^{-4} over a certain stretch of q-values, before the Debye-Porod asymptote takes over, which happens when q begins to compete with the inverse length of the smallest dimension of the pore geometry. Alas, the q values used in McKinnon et al.'s experiments are of the order 0.1 μm^{-1} which is far from large enough compared to the inverse length scale of 1 μm^{-1} afforded by the axon diameter.

3.7. Unaccounted Factors

One of the hallmarks of neuronal morphology is the axonal and dendritic branchings [56], which are not accounted for in our treatment of diffusion on curves. Although an accurate assessment of the influence of branchings could be achieved via careful numerical studies [57], the insight gained from our description above can be employed to some extent for making some predictions. For long structures, each branch can be considered a separate segment along which diffusion takes place. Thus, the presence of branchings would not impact the formulation for projections in regime A. However, since the total

contour length can be considerably increased in the presence of branchings, it may be more difficult to satisfy the long pulse duration condition of regime C. When this condition is met, however, the rank of the signal decay tensor would almost certainly be greater than one. In other words, detecting q^{-1} decay in regime C would be nearly impossible for smaller cells unless most arborizations run parallel within a narrow cylindrical region.

The detected MR signal is known to be dependent on factors other than those accounted for in this work. Among these, spatial heterogeneity of magnetic susceptibility within the tissue have been reported to influence the diffusion decay [58, 59] as well. In fact, suppressing [60] or taking advantage [61, 62] of effects due to susceptibility variations is an active area of research. We note that the presence of internal gradients could be investigated as yet another mechanism that could explain the reported features in the orientationally averaged signal; doing so would require an extension of existing studies relating the diffusion MR signal to microscopic perturbations in susceptibility [63, 64].

4. CONCLUSION

In an attempt to interpret new experimental findings, we studied the influence of diffusion along parameterized curves on orientationally-averaged diffusion MR signal. We examined the problem in three distinct temporal regimes of the Stejskal-Tanner experiment and investigated the appearance of a slow decay. We have found that for smaller cells, the q^{-1} decay of the orientationally-averaged signal is predicted only for straight fibers. This decay is more general for cells with longer projections, while it fades away for curvy structures as the pulse duration of the gradient sequence increases. Finally, we stressed that the q^{-1} decay could represent an intermediate range as the true asymptotic behavior is governed by a steeper attenuation. The findings of this paper are expected to provide insight into the link between the diffusion weighted MR acquisitions and geometry of the neural cells.

AUTHOR CONTRIBUTIONS

EÖ conceptualized the problem, and performed the main derivations. EÖ and CY developed and refined the theory, performed the numerical simulations, and wrote the manuscript. MH and HK provided inputs to the theory while C-FW provided guidelines. All authors collaborated in bringing the manuscript to its final state.

FUNDING

This study was supported by the Swedish Foundation for Strategic Research AM13-0090, the Swedish Research Council CADICS Linneaus research environment, the Swedish Research Council 2015-05356 and 2016-04482, Linköping University Center for Industrial Information Technology (CENIIT), VINNOVA/ITEA3 13031 BENEFIT, and National Institutes of Health P41EB015902, R01MH074794, P41EB015898.

SUPPLEMENTARY MATERIAL

The Supplementary Material for this article can be found online at: https://www.frontiersin.org/articles/10.3389/fphy.2018.00017/full#supplementary-material

REFERENCES

1. McKinnon ET, Jensen JH, Glenn GR, Helpern JA. Dependence on b-value of the direction-averaged diffusion-weighted imaging signal in brain. *Magn Reson Imaging* (2017) **36**:121–7. doi: 10.1016/j.mri.2016.10.026
2. Assaf Y, Freidlin RZ, Rohde GK, Basser PJ. New modeling and experimental framework to characterize hindered and restricted water diffusion in brain white matter. *Magn Reson Med.* (2004) **52**:965–78. doi: 10.1002/mrm.20274
3. Stanisz GJ, Szafer A, Wright GA, Henkelman RM. An analytical model of restricted diffusion in bovine optic nerve. *Magn Reson Med.* (1997) **37**:103–11.
4. Jespersen SN, Kroenke CD, Østergaard L, Ackerman JJH, Yablonskiy DA. Modeling dendrite density from magnetic resonance diffusion measurements. *NeuroImage* (2007) **34**:1473–86. doi: 10.1016/j.neuroimage.2006.10.037
5. Behrens TEJ, Woolrich MW, Jenkinson M, Johansen-Berg H, Nunes RG, Clare S, et al. Characterization and propagation of uncertainty in diffusion-weighted MR imaging. *Magn Reson Med.* (2003) **50**:1077–88. doi: 10.1002/mrm.10609
6. Kroenke CD, Ackerman JJH, Yablonskiy DA. On the nature of the NAA diffusion attenuated MR signal in the central nervous system. *Magn Reson Med.* (2004) **52**:1052–9. doi: 10.1002/mrm.20260
7. Zhang H, Schneider T, Wheeler-Kingshott CA, Alexander DC. NODDI: practical *in vivo* neurite orientation dispersion and density imaging of the human brain. *NeuroImage* (2012) **61**:1000–16. doi: 10.1016/j.neuroimage.2012.03.072
8. Stejskal EO, Tanner JE. Spin diffusion measurements: spin echoes in the presence of a time-dependent field gradient. *J Chem Phys.* (1965) **42**:288–92.
9. Jensen JH. Sufficiency of diffusion tensor in characterizing the diffusion MRI signal to leading order in diffusion weighting. *NMR Biomed.* (2014) **27**:1005–7. doi: 10.1002/nbm.3145
10. Özarslan E, Basser PJ. Microscopic anisotropy revealed by NMR double pulsed field gradient experiments with arbitrary timing parameters. *J Chem Phys.* (2008) **128**:154511. doi: 10.1063/1.2905765
11. Özarslan E, Koay CG, Shepherd TM, Komlosh ME, İrfanoğlu MO, Pierpaoli C, et al. Mean apparent propagator (MAP) MRI: a novel diffusion imaging method for mapping tissue microstructure. *NeuroImage* (2013) **78**:16–32. doi: 10.1016/j.neuroimage.2013.04.016
12. Kaden E, Kruggel F, Alexander DC. Quantitative mapping of the per-axon diffusion coefficients in brain white matter. *Magn Reson Med.* (2016) **75**:1752–63. doi: 10.1002/mrm.25734
13. Szczepankiewicz F, Westin CF, Knutsson H. A measurement weighting scheme for optimal powder average estimation. *Proc Intl Soc Mag Reson Med.* (2017) **26**:3345.
14. Mori S, van Zijl PC. Diffusion weighting by the trace of the diffusion tensor within a single scan. *Magn Reson Med.* (1995) **33**:41–52.
15. Wong EC, Cox RW, Song AW. Optimized isotropic diffusion weighting. *Magn Reson Med.* (1995) **34**:139–43.
16. Eriksson S, Lasič S, Topgaard D. Isotropic diffusion weighting in PGSE NMR by magic-angle spinning of the q-vector. *J Magn Reson.* (2013) **226**:13–18. doi: 10.1016/j.jmr.2012.10.015
17. Westin CF, Knutsson H, Pasternak O, Szczepankiewicz F, Özarslan E, van Westen D, et al. Q-space trajectory imaging for multidimensional diffusion MRI of the human brain. *NeuroImage* (2016) **135**:345–62. doi: 10.1016/j.neuroimage.2016.02.039
18. Lampinen B, Szczepankiewicz F, Mørtensson J, van Westen D, Sundgren PC, Nilsson M. Neurite density imaging versus imaging of microscopic anisotropy in diffusion MRI: a model comparison using spherical tensor encoding. *NeuroImage* (2017) **147**:517–31. doi: 10.1016/j.neuroimage.2016.11.053

19. Özarslan E. Compartment shape anisotropy (CSA) revealed by double pulsed field gradient MR. *J Magn Reson.* (2009) **199**:56–67. doi: 10.1016/j.jmr.2009.04.002
20. Lawrenz M, Finsterbusch J. Double-wave-vector diffusion-weighted imaging reveals microscopic diffusion anisotropy in the living human brain. *Magn Reson Med.* (2013) **69**:1072–82. doi: 10.1002/mrm.24347
21. Yablonskiy DA, Sukstanskii AL, Leawoods JC, Gierada DS, Bretthorst GL, Lefrak SS, et al. Quantitative *in vivo* assessment of lung microstructure at the alveolar level with hyperpolarized ^{3}He diffusion MRI. *Proc Natl Acad Sci USA* (2002) **99**:3111–6. doi: 10.1073/pnas.052594699
22. Anderson AW. Measurement of fiber orientation distributions using high angular resolution diffusion imaging. *Magn Reson Med.* (2005) **54**:1194–206. doi: 10.1002/mrm.20667
23. Veraart J, Fieremans E, Novikov DS. Universal power-law scaling of water diffusion in human brain defines what we see with MRI. arXiv 1609.09145. (2016).
24. Köpf M, Corinth C, Haferkamp O, Nonnenmacher TF. Anomalous diffusion of water in biological tissues. *Biophys J.* (1996) **70**:2950–8.
25. Yablonskiy DA, Bretthorst GL, Ackerman JJH. Statistical model for diffusion attenuated MR signal. *Magn Reson Med.* (2003) **50**:664–9. doi: 10.1002/mrm.10578
26. Jian B, Vemuri BC, Özarslan E, Carney PR, Mareci TH. A novel tensor distribution model for the diffusion-weighted MR signal. *NeuroImage* (2007) **37**:164–76. doi: 10.1016/j.neuroimage.2007.03.074
27. Sen PN, Hürlimann MD, de Swiet TM. Debye-Porod law of diffraction for diffusion in porous media. *Phys Rev B* (1995) **51**:601–4.
28. Özarslan E, Koay CG, Basser PJ. Remarks on q-space MR propagator in partially restricted, axially-symmetric, and isotropic environments. *Magn Reson Imaging* (2009) **27**:834–44. doi: 10.1016/j.mri.2009.01.005
29. Nørhøj Jespersen S, Buhl N. The displacement correlation tensor: microstructure, ensemble anisotropy and curving fibers. *J Magn Reson.* (2011) **208**:34–43. doi: 10.1016/j.jmr.2010.10.003
30. Nilsson M, Lätt J, Støahlberg F, van Westen D, Hagslätt H. The importance of axonal undulation in diffusion MR measurements: a Monte Carlo simulation study. *NMR Biomed.* (2012) **25**:795–805. doi: 10.1002/nbm.1795
31. Reisert M, Kellner E, Kiselev VG. About the geometry of asymmetric fiber orientation distributions. *IEEE Trans Med Imaging* (2012) **31**:1240–9. doi: 10.1109/TMI.2012.2187916
32. Pizzolato M, Wassermann D, Boutelier T, Deriche R. Exploiting the phase in diffusion MRI for microstructure recovery: Towards axonal tortuosity via asymmetric diffusion processes. In: *International Conference on Medical Image Computing and Computer-Assisted Intervention* (Cham: Springer International Publishing) (2015). p. 109–16.
33. Cetin S, Özarslan E, Unal G. Elucidating intravoxel geometry in diffusion-MRI: asymmetric orientation distribution functions (AODFs) revealed by a cone model. In: *International Conference on Medical Image Computing and Computer-Assisted Intervention* (Cham: Springer International Publishing) (2015). p. 231–8.
34. Budde MD, Frank JA. Neurite beading is sufficient to decrease the apparent diffusion coefficient after ischemic stroke. *Proc Natl Acad Sci USA* (2010) **107**:14472–7. doi: 10.1073/pnas.1004841107
35. Press WH, Teukolsky SA, Vetterling WT, Flannery BP. *Numerical Recipes in C: The Art of Scientific Computing*. Cambridge: Cambridge Press (1992).
36. Debye P. Zerstreuung der röntgenstrahlen. *Ann Phys.* (1915) **46**:809–24.
37. Glatter O, Kratky O (eds.). *Small Angle X-Ray Scattering*. London: Academic Press (1982).
38. Feigun LA, Svergun DI. *Structure Analysis by Small-Angle X-Ray and Neutron Scattering*. New York, NY: Springer Science + Business Media (1987).
39. des Cloizeaux J. Form factor of an infinite Kratky-Porod chain. *Macromolecules* (1973) **6**:403–7.
40. Mitra PP, Halperin BI. Effects of finite gradient-pulse widths in pulsed-field-gradient diffusion measurements. *J Magn Reson A* (1995) **113**:94–101.
41. Neuman CH. Spin echo of spins diffusing in a bounded medium. *J Chem Phys.* (1974) **60**:4508–11.
42. Baxter JR, Brosamler GA. Energy and the law of the iterated logarithm. *Math Scand.* (1976) **38**:115–36.
43. Özarslan E, Yolcu C, Herberthson M, Westin CF, Knutsson H. Effective potential for magnetic resonance measurements of restricted diffusion. *Front Phys.* (2017) **5**:68. doi: 10.3389/fphy.2017.00068
44. Schoonover C. *Portraits of the Mind*. New York, NY: Abrams (2010).
45. Parekh R, Ascoli GA. Quantitative investigations of axonal and dendritic arbors: development, structure, function, and pathology. *Neuroscientist* (2015) **21**:241–54. doi: 10.1177/1073858414540216
46. Hansen MB, Jespersen SN, Leigland LA, Kroenke CD. Using diffusion anisotropy to characterize neuronal morphology in gray matter: the orientation distribution of axons and dendrites in the NeuroMorpho.org database. *Front Integr Neurosci.* (2013) **7**:31. doi: 10.3389/fnint.2013.00031
47. Jespersen SN, Leigland LA, Cornea A, Kroenke CD. Determination of axonal and dendritic orientation distributions within the developing cerebral cortex by diffusion tensor imaging. *IEEE Trans Med Imaging* (2012) **31**:16–32. doi: 10.1109/TMI.2011.2162099
48. Najac C, Branzoli F, Ronen I, Valette J. Brain intracellular metabolites are freely diffusing along cell fibers in grey and white matter, as measured by diffusion-weighted MR spectroscopy in the human brain at 7 T. *Brain Struct Funct.* (2016) **221**:1245–54. doi: 10.1007/s00429-014-0968-5
49. Palombo M, Ligneul C, Najac C, Le Douce J, Flament J, Escartin C, et al. New paradigm to assess brain cell morphology by diffusion-weighted MR spectroscopy *in vivo*. *Proc Natl Acad Sci USA* (2016) **113**:6671–6. doi: 10.1073/pnas.1504327113
50. Palombo M, Ligneul C, Valette J. Modeling diffusion of intracellular metabolites in the mouse brain up to very high diffusion-weighting: diffusion in long fibers (almost) accounts for non-monoexponential attenuation. *Magn Reson Med.* (2017) **77**:343–50. doi: 10.1002/mrm.26548
51. Hilgetag CC, Barbas H. Are there ten times more glia than neurons in the brain? *Brain Struct Funct.* (2009) **213**:365–6. doi: 10.1007/s00429-009-0202-z
52. Purves D, Augustine GJ, Fitzpatrick D, Katz LC, LaMantia AS, McNamara JO, et al. (eds.). *Neuroscience, 2nd Edn.* Sunderland, MA: Sinauer Associates (2001).
53. Herculano-Houzel S, Lent R. Isotropic fractionator: a simple, rapid method for the quantification of total cell and neuron numbers in the brain. *J Neurosci.* (2005) **25**:2518–21. doi: 10.1523/JNEUROSCI.4526-04.2005
54. Koay CG, Özarslan E, Basser PJ. A signal transformational framework for breaking the noise floor and its applications in MRI. *J Magn Reson.* (2009) **197**:108–19. doi: 10.1016/j.jmr.2008.11.015
55. Özarslan E, Shepherd TM, Koay CG, Blackband SJ, Basser PJ. Temporal scaling characteristics of diffusion as a new MRI contrast: findings in rat hippocampus. *NeuroImage* (2012) **60**:1380–93. doi: 10.1016/j.neuroimage.2012.01.105
56. Cajal SR. *Histologie Du Systeme Nerveux De L'Homme Et Des Vertebretes*. Paris: Maloine (1911).
57. Van Nguyen D, Grebenkov D, Le Bihan D, Li JR. Numerical study of a cylinder model of the diffusion MRI signal for neuronal dendrite trees. *J Magn Reson.* (2015) **252**:103–13. doi: 10.1016/j.jmr.2015.01.008
58. Palombo M, Gabrielli A, De Santis S, Capuani S. The γ parameter of the stretched-exponential model is influenced by internal gradients: validation in phantoms. *J Magn Reson.* (2012) **216**:28–36. doi: 10.1016/j.jmr.2011.12.023
59. Caporale A, Palombo M, Macaluso E, Guerreri M, Bozzali M, Capuani S. The γ-parameter of anomalous diffusion quantified in human brain by MRI depends on local magnetic susceptibility differences. *NeuroImage* (2017) **147**:619–31. doi: 10.1016/j.neuroimage.2016.12.051
60. Zheng G, Price WS. Suppression of background gradients in (B_0 gradient-based) NMR diffusion experiments. *Concept Magn Reson A* (2007) **30**:261–77. doi: 10.1002/cmr.a.20092
61. Song YQ, Ryu S, Sen PN. Determining multiple length scales in rocks. *Nature* (2000) **406**:178–81. doi: 10.1038/35018057
62. Álvarez GA, Shemesh N, Frydman L. Internal gradient distributions: a susceptibility-derived tensor delivering morphologies by magnetic resonance. *Sci Rep.* (2017) **7**:3311. doi: 10.1038/s41598-017-03277-9
63. Pathak AP, Ward BD, Schmainda KM. A novel technique for modeling susceptibility-based contrast mechanisms for arbitrary microvascular geometries: the finite perturber method. *NeuroImage* (2008) **40**:1130–43. doi: 10.1016/j.neuroimage.2008.01.022

64. Kurz FT, Kampf T, Buschle LR, Schlemmer HP, Bendszus M, Heiland S, et al. Generalized moment analysis of magnetic field correlations for accumulations of spherical and cylindrical magnetic perturbers. *Front Phys.* (2016) **4**:46. doi: 10.3389/fphy.2016.00046
65. Tanner JE, Stejskal EO. Restricted self-diffusion of protons in colloidal systems by the pulsed-gradient, spin-echo method. *J Chem Phys.* (1968) **49**:1768–77.
66. Robertson B. Spin-echo decay of spins diffusing in a bounded region. *Phys Rev.* (1966) **151**:273–7.
67. Barzykin AV. Theory of spin echo in restricted geometries under a step-wise gradient pulse sequence. *J Magn Reson.* (1999) **139**:342–53. doi: 10.1006/jmre.1999.1778.575
68. Grebenkov DS. NMR survey of reflected Brownian motion. *Rev Mod Phys.* (2007) **79**:1077–137. doi: 10.1103/RevModPhys.79.1077
69. Özarslan E, Shemesh N, Basser PJ. A general framework to quantify the effect of restricted diffusion on the NMR signal with applications to double pulsed field gradient NMR experiments. *J Chem Phys.* (2009b) **130**:104702. doi: 10.1063/1.3082078
70. Grebenkov DS. Analytical solution for restricted diffusion in circular and spherical layers under inhomogeneous magnetic fields. *J Chem Phys.* (2008) **128**:134702. doi: 10.1063/1.2841367
71. Torrey HC. Bloch equations with diffusion terms. *Phys Rev.* (1956) **104**:563–5.
72. Hörmander L. *The Analysis of Linear Partial Differential Operators I, (Distribution Theory and Fourier Analysis), 2nd Edn.* Berlin: Springer-Verlag (1990).
73. Yolcu C, Memiç M, Şimşek K, Westin CF, Özarslan E. NMR signal for particles diffusing under potentials: from path integrals and numerical methods to a model of diffusion anisotropy. *Phys Rev E* (2016) **93**:052602.

Conflict of Interest Statement: The authors declare that the research was conducted in the absence of any commercial or financial relationships that could be construed as a potential conflict of interest.

frontiers in Physics

ORIGINAL RESEARCH
published: 14 November 2017
doi: 10.3389/fphy.2017.00056

On the Vanishing of the *t*-term in the Short-Time Expansion of the Diffusion Coefficient for Oscillating Gradients in Diffusion NMR

Frederik B. Laun[1], *Kerstin Demberg*[2], *Armin M. Nagel*[1], *Micheal Uder*[1] *and Tristan A. Kuder*[2]*

[1] *Institute of Radiology, University Hospital Erlangen, Erlangen, Germany,* [2] *Medical Physics in Radiology, German Cancer Research Center, Heidelberg, Germany*

Nuclear magnetic resonance (NMR) diffusion measurements can be used to probe porous structures or biological tissues by means of the random motion of water molecules. The short-time expansion of the diffusion coefficient in powers of $t^{1/2}$, where t is the diffusion time related to the duration of the diffusion-weighting magnetic field gradient profile, is universally connected to structural parameters of the boundaries restricting the diffusive motion. The $t^{1/2}$-term is proportional to the surface to volume ratio. The t-term is related to permeability and curvature. The short time expansion can be measured with two approaches in NMR-based diffusion experiments: First, by the use of diffusion encodings of short total duration and, second, by application of oscillating gradients of long total duration. For oscillating gradients, the inverse of the oscillation frequency becomes the relevant time scale. The purpose of this manuscript is to show that the oscillating gradient approach is blind to the t-term. On the one hand, this prevents fitting of permeability and curvature measures from this term. On the other hand, the t-term does not bias the determination of the $t^{1/2}$-term in experiments.

Keywords: magnetic resonance imaging, diffusion, short-time limit, surface-to-volume ratio, gradient profile, oscillating gradients

OPEN ACCESS

Edited by:
Sune Nørhøj Jespersen, Aarhus University, Denmark

Reviewed by:
Valerij G. Kiselev, Universitätsklinikum Freiburg, Germany
Junzhong Xu, Vanderbilt University, United States

***Correspondence:**
Tristan A. Kuder
t.kuder@dkfz.de

Specialty section:
This article was submitted to Biomedical Physics, a section of the journal Frontiers in Physics

Received: *03 August 2017*
Accepted: *24 October 2017*
Published: *14 November 2017*

Citation:
Laun FB, Demberg K, Nagel AM, Uder M and Kuder TA (2017) On the Vanishing of the t-term in the Short-Time Expansion of the Diffusion Coefficient for Oscillating Gradients in Diffusion NMR. Front. Phys. 5:56. doi: 10.3389/fphy.2017.00056

INTRODUCTION

This article builds on and extends a previous article [1], which investigated the term linear in time of the short-time expansion of the diffusion coefficient [2–5] which is given by:

$$D(t) = D_0\left(1 - \frac{4}{3d\sqrt{\pi}}\frac{S}{V}\sqrt{D_0 t} + \left(\frac{1}{d}\frac{S}{V}\kappa + \frac{1}{2d}\frac{S}{V}\varrho - \frac{1}{12}\frac{S}{V}D_0\overline{R^{-1}}\right)t + O\left(t^{3/2}\right)\right), \quad (1)$$

where D_0 is the free diffusion coefficient, S/V is the surface-to-volume ratio, κ is the surface permeability, ϱ is the surface relaxivity, $\overline{R^{-1}}$ is a mean curvature term, d is the spatial dimension, and t is the observation time. This universal expansion is valuable, since it connects a measurable quantity, i.e., $D(t)$, to structural parameters of barriers restricting the diffusive motion.

Using magnetic resonance diffusion experiments [6–9], information about the diffusive motion of spin-bearing particles can be encoded into the signal by using diffusion-weighting magnetic

field gradient pulses. Regarding the diffusion time t linked to the total duration of the diffusion-weighting gradient profile, one often considers the long-time and short-time limit. In the first case, the limit of long diffusion time, detailed information about the porous structure of the investigated material can be obtained [10–12] such as actual pore shapes [13–15]. On the other hand, $D(t)$ can be measured in the short-time limit to obtain the structural parameters in Equation (1). For this purpose, a pair of bipolar gradient pulses is applied to achieve diffusion encoding [16]. In the short gradient pulse approximation [6, 17], the measured diffusion coefficient in such experiments is $D(t)$ (Equation 1). If the gradient pulses cannot be considered to be short, Equation (1) must be modified to take into account the effect of the gradient pulse duration and of the temporal evolution of the gradients $G(t)$ [18–22]:

$$D_{\text{app}}(t) = D_0\left(1 - c_1\frac{4}{3d\sqrt{\pi}}\frac{S}{V}\sqrt{D_0 t} + c_2\left(\frac{1}{d}\frac{S}{V}\kappa - \frac{1}{12}\frac{S}{V}D_0\overline{R^{-1}}\right)t + O\left(t^{3/2}\right)\right) \quad (2)$$

Here, the influence of the temporal gradient profile is expressed solely by the constants c_1 and c_2, which can be computed from $G(t)$, so that an elegant decoupling takes place. Note that surface relaxation is neglected in Equation (2) and in the remainder of the manuscript, thus avoiding the difficulties in the mathematical treatment [23], and that t is the total duration of the diffusion gradients in Equation (2).

In Laun et al. [1], it was shown that c_2 can be tuned to values between 0 and 1. Tuning c_2 to zero can be advantageous, for example, if the aim of the experiment is to measure the $\sqrt{t}$-term without bias from the t-term.

A striking result [24–30] is that the short-time expansion is moreover valid for the diffusion spectrum $\mathfrak{D}(\omega)$, or $\mathfrak{D}_{\text{app}}(\tau) := \mathfrak{D}\left(\frac{2\pi}{\tau}\right)$, that can be measured by the use of oscillating gradients. Note that $\mathfrak{D}_{\text{app}}(\tau)$ and $D_{\text{app}}(t)$ are different functions as outlined in more detail below. Then Equation (1) can be cast in a similar form for the diffusion spectrum, where t is replaced by the duration τ of one gradient oscillation:

$$\mathfrak{D}_{\text{app}}(\tau) = D_0\left(1 - C_1\frac{4}{3d\sqrt{\pi}}\frac{S}{V}\sqrt{D_0\tau} + C_2\left(\frac{1}{d}\frac{S}{V}\kappa - \frac{1}{12}\frac{S}{V}D_0\overline{R^{-1}}\right)\tau + O\left(\tau^{3/2}\right)\right) \quad (3)$$

The constants C_n in Equation (3) are printed in capital letters because they differ, in general, from the constants c_n of Equation (2) as will be described below.

Equations (2) and (3) were successfully applied in experiments to obtain information about the first order term and thus about the surface-to-volume ratio [27, 28, 31–37]. The thereto necessary constants C_1 were derived for some gradient waveforms such as the bipolar waveform and oscillating gradients [18, 27, 29, 38].

The aim of the work at hand is to investigate the constant C_2. For this purpose, Equation (3) is derived starting from Equation (1).

MATERIALS AND METHODS

Numerical simulations were performed as in Laun et al. [1][1]. The diffusion coefficient $D_{\text{app}}(t)$ and the diffusion spectrum $\mathfrak{D}_{\text{app}}(\tau)$ [using the signal decrease as recalled in Equation (A13) in Appendix A (Supplementary Material)] were computed using the multiple correlation function (MCF) approach [22, 39–45] (using Equation 114 in Grebenkov [42]). The MCF approach decomposes the magnetization into the eigenfunctions of the Laplace operator. One important parameter is the number N_λ of employed eigenfunctions, which should be sufficiently large to ensure numerical accuracy. In the presented results, the accuracy was verified by increasing N_λ and checking whether numerical results remained unchanged. A detailed description of the MCF approach is beyond the scope of this article, but can be found in Grebenkov and Grebenkov [46, 47], for example.

The following closed domains were considered: slab, cylinder, sphere, "bi-slab" (see **Figure 1**). The bi-slab domain consists of three parallel planes. The inner plane is permeable, while the two outer ones are impermeable. Particles only reside within the volume between the two impermeable slabs. The radii of cylinder and sphere were 5 μm, the separation of the slabs was 10 μm, and the separation of the planes of the bi-slab domain was 10 μm (thus the bi-slab domain was in total 20 μm wide). The free diffusion coefficient D_0 was set to 1 μm^2/ms. The boundaries were fully reflecting except for the inner wall of the bi-slab domain, which had a permeability of 50 μm/s. N_λ was 100 for the bi-slab domain, 500 for slab domain and cylinder, and 200 for the sphere. Oscillating cosine gradients were simulated with a total duration $T_{\cos}$ of 0.05, 0.1, and 0.5 s. The number of oscillations N was varied in twenty steps. For bipolar gradients, δ was set to 10^{-3} ms and t was varied between 0.1 and 15 ms.

Additionally, the difference between simulated diffusion coefficients and first order short time expansion was calculated. This difference is labeled ΔD in the plots and represents $D_{\text{app,simulated}}(t) - D_0 - M_1 c_1 t^{1/2}$ or $\mathfrak{D}_{\text{app,simulated}}(\tau) - D_0 - M_1 C_1 \tau^{1/2}$.

RESULTS

Derivation of the *t*-Term for Oscillating Gradients

First, a shorthand-notation for Equation (2) is introduced:

$$D(t) = \sum\nolimits_{n=0} M_n c_n t^{n/2} \quad (4)$$

with the coefficients

$$M_0 = D_0$$
$$M_1 = -\frac{4}{3d\sqrt{\pi}}\frac{S}{V}D_0^{3/2}$$
$$M_2 = \frac{1}{d}\frac{S}{V}\kappa D_0 - \frac{1}{12}\frac{S}{V}\overline{R^{-1}}D_0^2$$

[1] A considerable overlap of the Methods sections with the corresponding sections of the earlier article is present.

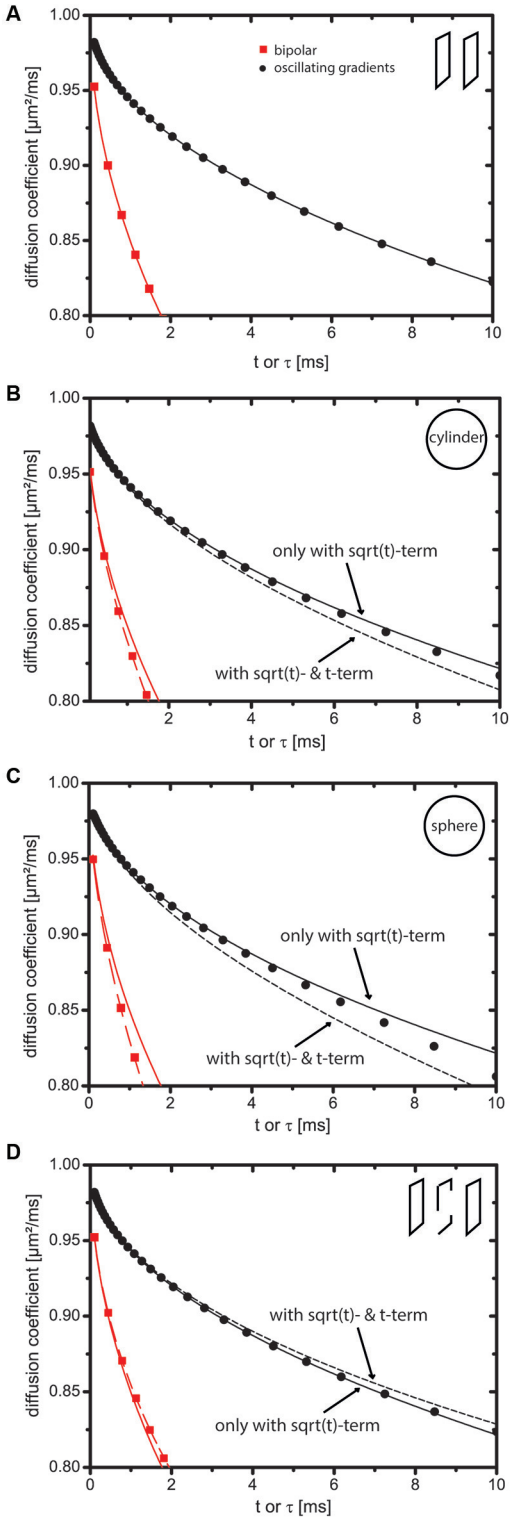

FIGURE 1 | Impact of the *t*-term on the short-time expansion of the diffusion coefficient. Markers indicate values obtained by numerical simulations. Solid lines represent the short-time expansion to order $\sqrt{t}$ and dotted lines represent it to order *t*. Red square markers represent bipolar gradients (i.e., $D_{\text{app}}(t)$) and black circular markers represent oscillating cosine gradients (i.e., $\mathfrak{D}_{\text{app}}(\tau)$). *(Continued)*

FIGURE 1 | Continued
(A) Slab domain. The *t*-term is zero because curvature and permeability of the sample are zero. **(B–D)** Cylinder, sphere, and bi-slab. In case of oscillating cosine gradients, the *t*-term is zero, because C_2 is zero. For this reason, the markers stay close to the solid line in contrast to the markers indicating the bipolar gradients, which stay close to the dotted line. T_{cos} was 500 ms.

and so on (with $c_0 = 1$).

As outlined in Appendix A (Supplementary Material), the short-time expansion for the position correlation function that generates an experimentally detectable signal attenuation reads:

$$\langle x(t_2)x(t_1)\rangle = -D\left(|t_{21}|\right)\cdot|t_{21}| = -\sum\nolimits_{n=0} M_n\,|t_{21}|^{1+n/2} \quad (5)$$

with $t_{21} = t_2 - t_1$, where the brackets $\langle\ldots\rangle$ denote the expectation value. Note that the terms $\langle x(t_2)^2\rangle$ and $\langle x(t_1)^2\rangle$ where neglected in Equation (5) because they do not contribute to the signal attenuation. Equation (5) can be related to the diffusion spectrum $\mathfrak{D}(\omega)$ (see Appendix A in Supplementary Material) via:

$$\begin{aligned}\frac{\mathfrak{D}(\omega)}{\omega^2} &= \frac{1}{2}\int_{-\infty}^{\infty}\langle x(t_2)\,x(t_1)\rangle\; e^{-i\omega t_{21}}\,dt_{21}\\ &= -\frac{1}{2}\sum\nolimits_{n=0}\int_{-\infty}^{\infty} M_n|t_{21}|^{1+n/2}e^{-i\omega t_{21}}\,dt_{21}. \quad (6)\end{aligned}$$

This Fourier integral exists (see Appendix B in Supplementary Material):

$$\frac{1}{2}\int_{-\infty}^{\infty}|t_{21}|^{1+n/2}e^{-i\omega t_{21}}\,dt_{21} = -\omega^{-2-\frac{n}{2}}\cos\left(\frac{n\pi}{4}\right)\Gamma\left(2+\frac{n}{2}\right),\quad \omega>0,\ n\geq 0 \quad (7)$$

and thus by inserting Equation (7) in Equation (6), one finds:

$$\mathfrak{D}(\omega) = D_0 + M_1\sqrt{\frac{\pi}{2}}\frac{3}{4\omega^{1/2}} + 0\cdot M_2 + 0\left(\omega^{-3/2}\right). \quad (8)$$

Note that the gamma function Γ makes the constants c_n increase swiftly at larger *n*. Defining the time parameter $\tau = t/n$, entailing $\omega = 2\pi/\tau$, one finds:

$$\mathfrak{D}_{\text{app}}(\tau) := \mathfrak{D}\left(\frac{2\pi}{\tau}\right) = D_0 + M_1\frac{3}{8}\tau^{1/2} + 0\cdot M_2 + O\left(\tau^{3/2}\right) \quad (9)$$

with $\mathfrak{D}_{\text{app}}(\tau)$ being identical to $\mathfrak{D}(\omega)$ except for taking a different argument. $\mathfrak{D}_{\text{app}}(\tau)$ has exactly the form of Equation (3) as desired and one can read off the coefficients C_n directly: $C_1 = 3/8$ and $C_2 = 0$. Note that the value of C_1 was reported previously (e.g., in Novikov and Kiselev [29]). The vanishing of C_2 has not been reported so far to our knowledge.

Using the expression for M_1, one finds:

$$\mathfrak{D}(\omega) = D_0 - \frac{D_0}{d\sqrt{2}}\frac{S}{V}\sqrt{\frac{D_0}{\omega}} + O\left(\omega^{-3/2}\right), \quad (10)$$

$$\mathfrak{D}_{\text{app}}(\tau) := \mathfrak{D}\left(\frac{2\pi}{\tau}\right) = D_0 - \frac{D_0}{2d\sqrt{\pi}}\frac{S}{V}\sqrt{D_0}\tau^{1/2} + O\left(\tau^{3/2}\right). \quad (11)$$

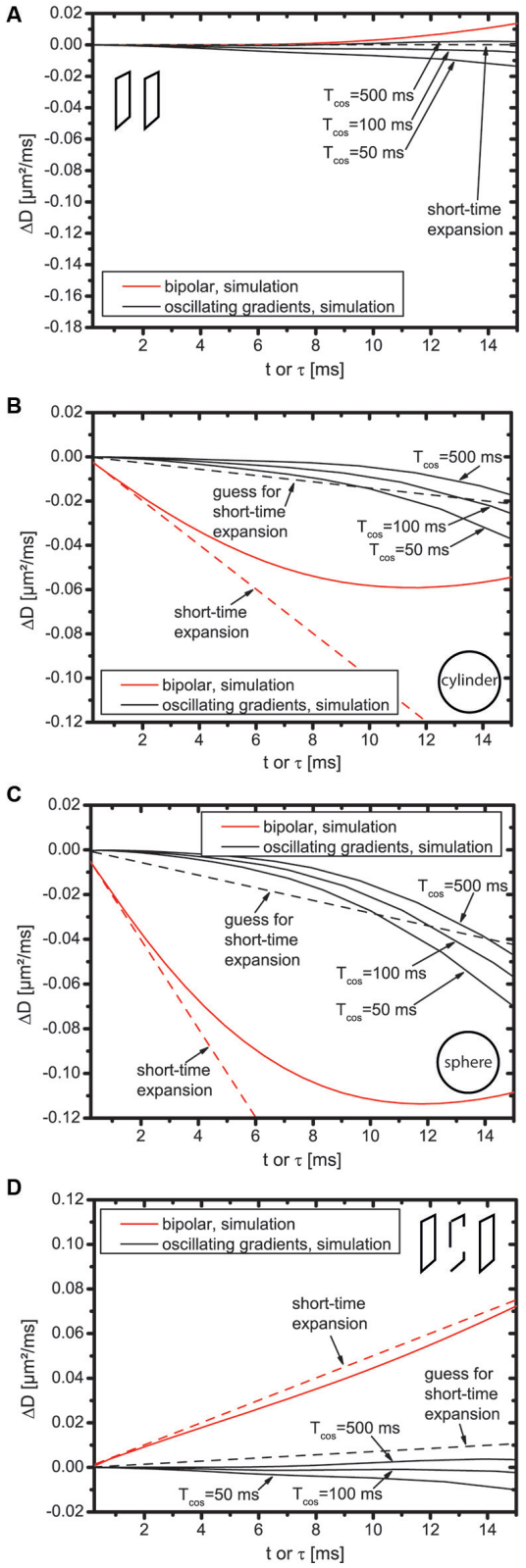

FIGURE 2 | Difference between simulated diffusion coefficients and first order short time diffusion expansion for slab domain **(A)**, cylinder **(B)**, sphere **(C)**, and bi-slab **(D)**.

It is interesting to calculate the coefficients c_1 and c_2 for a short-time cosine gradient with one oscillation [with methods as described, e.g., in Laun et al. [1] and references therein]. We find $c_1 = 3 \cdot \left(4\pi \text{ FresnelC}(2) + 3 \text{ FresnelS}(2)\right)/16/\pi \approx 0.428$ and $c_2 = 0$. These values bear great similarity to $C_1 \approx 0.375$ and $C_2 = 0$. It should be noted that c_2 of oscillating cosine gradients with any number of oscillations equals zero because they are "flow-compensated," i.e., because their first moment vanishes [1].

Validation with Simulations

Figure 1 displays $D_{\text{app}}(t)$ and $\mathfrak{D}_{\text{app}}(\tau)$. Markers indicate simulation results using the MCF approach and lines represent the short-time expansion. For $D_{\text{app}}(t)$, solid lines equal $M_0 + M_1 c_1 t^{1/2}$ and dotted lines equal $M_0 + M_1 c_1 t^{1/2} + M_2 c_2 t$. For $\mathfrak{D}_{\text{app}}(\tau)$, solid lines equal $M_0 + M_1 C_1 \tau^{1/2}$ and dotted lines equal $M_0 + M_1 C_1 \tau^{1/2} + M_2 C_1^2 \tau$. The term $M_2 C_1^2 \tau$ shall represent a reasonable "guess" for the t-term with an effective diffusion time $\tau_{\text{eff}} = C_1^2 \tau$, where the coefficient C_2 was set to one. The intention is to visualize a line with $C_2 \neq 0$, although this term does not occur in reality. Some remarks on effective diffusion times can be found in Appendix C (Supplementary Material).

For the slab domain (**Figure 1A**), $M_{n>1} = 0$ holds true (see [42]). Hence, **Figure 1A** does not display a dotted line and markers stay close to the solid lines.

In **Figures 1B,C** (cylinder, sphere) and **Figure 1D** (bi-slab), it is clearly visible that the markers for the bipolar gradients (with $c_2 = 1 \neq 0$) stay close to the dotted lines indicating the importance of the t-term. The markers of the oscillating cosine gradients stay close to the solid line indicating that the t-term does not influence $\mathfrak{D}_{\text{app}}(\tau)$. Owing to higher order terms, deviations between the short-time expansion and markers are present at larger t.

Figure 2 shows ΔD, i.e., the difference between simulated diffusion coefficients and first order short time expansion. The dotted line represents the t-term, i.e., $M_2 c_2 t$ for the bipolar gradients. For the oscillating gradients, the black dotted line shall represent an educated guess for the t-term, i.e., $M_2 C_1^2 \tau$, as in **Figure 1**.

First, the bipolar gradients displayed in **Figure 2** are discussed (displayed in red color). For the slab domain (**Figure 2A**), the dotted line is flat because $M_2 = 0$. However, deviations of ΔD from zero are well visible for $t > 10$ ms. This does not result from the influence of higher order terms because all higher order terms are zero. It rather indicates the breakdown of the short-time expansion. For cylinder, sphere, and bi-slab (**Figures 2B–D**), the slope of ΔD is identical to that of the dotted line at $t = 0$, but starts deviating already roughly at $t = 2$ ms indicating that either higher order terms are needed or, again, that the short-time expansion breaks down. This deviation is more pronounced for cylinder and sphere than for the bi-slab.

Next, the oscillating gradients in **Figure 2** are discussed (displayed in black color). For cylinder, sphere, and bi-slab, ΔD does have zero slope at $t = 0$ and does not follow the dotted line for any of these domains, which supports the finding that $C_2 = 0$. This holds true for $T_{\text{cos}} = 500$ ms, but also for reduced total duration of the oscillating gradients, i.e., for smaller T_{cos}. The difference of ΔD between $T_{\text{cos}} = 500$ ms and $T_{\text{cos}} = 50$ ms is

smaller than 0.015 $\mu m^2/ms$ for all domains at $\tau = 10\,ms$, which is roughly equally large as the guessed t-term, but an order of magnitude smaller than the $\sqrt{t}$-term. Thus, for the considered domains, $T_{cos} = 50\,ms$ still appears to be well suited for investigations of the $\sqrt{t}$-term, even with as few as five oscillations.

DISCUSSION

The main result of this work is that oscillating cosine gradients are blind with respect to the t-term of the short-time expansion of the apparent diffusion coefficient.

Oscillating gradients and extensions [48–51] have been used in several research studies [27, 28, 32, 35, 38, 52–65], among them applications to human brains *in vivo* [66]. Comparing oscillating gradients to pulsed gradients, the advantage of the oscillating gradients is that the obtainable b-value is higher allowing the assessment of shorter times. This is particularly useful if strong gradient amplitudes are not available or if the structure of interest is too small. The disadvantage is the need for longer echo times entailing decreased signal-to-noise ratio due to transversal relaxation, which also entails a longer acquisition time.

As oscillating gradients are blind to the t-term, estimates of S/V as in Reynaud et al. [36] are not biased by this term, but, obviously, the membrane permeability, for example, cannot be estimated using the t-term. This is in line with the findings by Li et al. [67], who reported that the membrane permeability has little effect on oscillating gradient derived diffusion coefficients at high frequencies. This is presumably not a major limitation given the smallness of the t-term that is visible in **Figures 1**, **2**, which makes a fit challenging. The permeability information must have some influence on $\mathfrak{D}_{app}(\tau)$ at long τ; otherwise diffusion in the bi-slab would have to be identical to that of a single slab domain of double size. Therefore, the estimation of membrane permeability using oscillating gradients might in principle be possible.

As different versions of Equations (10) and (11) can be found in the literature, a comparison is worthwhile. Equation (10) is identical to Equation 10 of the article by Novikov and Kiselev [29]. Except for a small deviation, which may be due to numerics, Equation (10) is also identical to Equation (3) of the article by Xu et al. [35], but, to our understanding, not to the respective equations in an earlier article [27]. In general, care must be taken concerning the definition of τ. For example, Zielinski et al. [38] use the definition $\tau_{Zielinski} = \tau/2$, which is closer to the classical timing definitions of CPMG echo trains than our definition. Considering this difference in definitions, their respective coefficient C_1 for the CPMG condition as stated in their Equation (6) is almost identical to 3/8, which is in agreement with the finding that the difference between C_1 of CPMG and cosine gradients should be almost negligible as stated in section 3.3 of Novikov and Kiselev [29]. Further, we found our coefficient C_1 to be a factor of six smaller than the one stated in Equation 14 in the article by Stepišnik et al. [28]. This difference was noted by the authors themselves and in Novikov and Kiselev [29].

Interestingly, the disappearance of the t-term in the Mitra expansion of Equation (3) using oscillating gradients is due to its disappearance in $\mathfrak{D}(\omega)$, or $\mathfrak{D}_{app}(2\pi/\tau)$, respectively. Thus, optimizing oscillating gradient profiles instead of using, for example, just cosine gradients, which was a successful approach in other regards [68, 69], does not help to make the t-term reappear in the signal attenuation.

In practice, diffusion measurements use spin echoes and hence two gradients at both sides of the refocusing pulse (as in Baron and Beaulieu [66]). This effectively introduces an extra variable, i.e., the separation of two gradients, which can affect the spectrum of diffusion gradients. When interpreting oscillating gradient experiments, this effect must be taken into account.

A limitation of the presented simulations is that they cannot prove the disappearance of the t-term. In principle, a very small t-term might be present and go unnoticed.

In conclusion, oscillating gradients are blind to the t-term and hence no bias in fits of the surface-to-volume ratio arises from the t-term.

AUTHOR CONTRIBUTIONS

FL performed the simulations and initial computations. TK and MU were involved in the design of the evaluations. TK, AN, KD, and FL were involved in implementation and testing of the MCF code and of the mathematical derivations.

FUNDING

Financial support by the DFG (grant numbers SFB TRR 125/2 R01 and KU 3362/1-1) is gratefully acknowledged.

SUPPLEMENTARY MATERIAL

The Supplementary Material for this article can be found online at: https://www.frontiersin.org/articles/10.3389/fphy.2017.00056/full#supplementary-material

REFERENCES

1. Laun FB, Kuder TA, Zong F, Hertel S, Galvosas P. Symmetry of the gradient profile as second experimental dimension in the short-time expansion of the apparent diffusion coefficient as measured with NMR diffusometry. *J Magn Reson.* (2015) **259**:10–9. doi: 10.1016/j.jmr.2015.07.003
2. Mitra PP, Sen PN, Schwartz LM, Ledoussal P. Diffusion propagator as a probe of the structure of porous-media. *Phys Rev Lett.* (1992) **68**:3555–8. doi: 10.1103/PhysRevLett.68.3555
3. Mitra PP, Sen PN, Schwartz LM. Short-time behavior of the diffusion-coefficient as a geometrical probe of porous-media. *Phys Rev B.* (1993) **47**:8565–74. doi: 10.1103/PhysRevB.47.8565
4. Sen PN, Schwartz LM, Mitra PP, Halperin BI. Surface relaxation and the long-time diffusion coefficient in porous media: periodic geometries. *Phys Rev B Condens Matter.* (1994) **49**:215–25. doi: 10.1103/PhysRevB.49.215
5. Sen PN. Time-dependent diffusion coefficient as a probe of geometry. *Concepts Magn Reson Part A.* (2003) **23**:1–21. doi: 10.1002/cmr.a.20017

6. Callaghan PT. *Translational Dynamics and Magnetic Resonance*. New York, NY: Oxford University Press (2011).
7. Jones DK. *Diffusion MRI: Theory, Methods, and Applications*. New York, NY: Oxford University Press (2011).
8. Laun FB, Fritzsche KH, Kuder TA, Stieltjes B. Introduction to the basic principles and techniques of diffusion-weighted imaging. *Radiologe* (2011) **51**:170–9. doi: 10.1007/s00117-010-2057-y
9. Freitag MT, Bickelhaupt S, Ziener C, Meier-Hein K, Radtke JP, Mosebach J, et al. Selected clinically established and scientific techniques of diffusion-weighted MRI. In the context of imaging in oncology. *Radiologe* (2016) **56**:137–47. doi: 10.1007/s00117-015-0066-6
10. Novikov DS, Jensen JH, Helpern JA, Fieremans E. Revealing mesoscopic structural universality with diffusion. *Proc Natl Acad Sci USA*. (2014) **111**:5088–93. doi: 10.1073/pnas.1316944111
11. Sigmund EE, Novikov DS, Sui D, Ukpebor O, Baete S, Babb JS, et al. Time-dependent diffusion in skeletal muscle with the random permeable barrier model (RPBM): application to normal controls and chronic exertional compartment syndrome patients. *NMR Biomed.* (2014) **27**:519–28. doi: 10.1002/nbm.3087
12. Lemberskiy G, Rosenkrantz AB, Veraart J, Taneja SS, Novikov DS, Fieremans E. Time-dependent diffusion in prostate cancer. *Invest Radiol.* (2017b) **52**:405–11. doi: 10.1097/RLI.0000000000000356
13. Laun FB, Kuder TA, Wetscherek A, Stieltjes B, Semmler W. NMR-based diffusion pore imaging. *Phys Rev E Stat Nonlin Soft Matter Phys.* (2012) **86**:021906. doi: 10.1103/PhysRevE.86.021906
14. Kuder TA, Bachert P, Windschuh J, Laun FB. Diffusion pore imaging by hyperpolarized xenon-129 nuclear magnetic resonance. *Phys Rev Lett.* (2013). **111**:028101. doi: 10.1103/PhysRevLett.111.028101
15. Demberg K, Laun FB, Windschuh J, Umathum R, Bachert P, Kuder TA. Nuclear magnetic resonance diffusion pore imaging: experimental phase detection by double diffusion encoding. *Phys Rev E.* (2017) **95**:022404. doi: 10.1103/PhysRevE.95.022404
16. Stejskal EO, Tanner JE. Spin diffusion measurements: spin echoes in the presence of a time-dependent field gradient. *J Chem Phys.* (1965) **42**:288–92. doi: 10.1063/1.1695690
17. Stejskal EO. Use of spin echoes in a pulsed magnetic-field gradient to study anisotropic, restricted diffusion and flow. *J Chem Phys.* (1965) **43**:3597–603. doi: 10.1063/1.1696526
18. De Swiet TM, Sen PN. Decay of nuclear magnetization by bounded diffusion in a constant field gradient. *J Chem Phys.* (1994) **100**:5597–604. doi: 10.1063/1.467127
19. Fordham EJ, Gibbs SJ, Hall LD. Partially restricted diffusion in a permeable sandstone: observations by stimulated echo PFG NMR. *Magn Reson Imaging.* (1994) **12**:279–84. doi: 10.1016/0730-725X(94)91536-9
20. Fordham EJ, Mitra PP, Latour LL. Effective diffusion times in multiple-pulse PFG diffusion measurements in porous media. *J Magn Reson Ser A.* (1996) **121**:187–92. doi: 10.1006/jmra.1996.0159
21. Sen PN, Andre A, Axelrod S. Spin echoes of nuclear magnetization diffusing in a constant magnetic field gradient and in a restricted geometry. *J Chem Phys.* (1999) **111**:6548–55. doi: 10.1063/1.480009
22. Axelrod S, Sen PN. Nuclear magnetic resonance spin echoes for restricted diffusion in an inhomogeneous field: methods and asymptotic regimes. *J Chem Phys.* (2001) **115**:6878–95. doi: 10.1063/1.1356010
23. Grebenkov DS. Multiple Correlation function approach: rigorous results for simple geometries. *Diff Fundam.* (2007a) **5**:1–34. Available online at: http://diffusion.uni-leipzig.de/contents_vol5.html; http://ul.qucosa.de/landing-page/?tx_dlf[id]=http%3A%2F%2Fubl.qucosa.de%2Fapi%2Fqucosa%253A14264%2Fmets
24. Gross B, Kosfeld R. Anwendung der spin-echo-methode der messung der selbstdiffusion. *Messtechnik* (1969) **77**:171–7.
25. Stepišnik, J. Analysis of Nmr self-diffusion measurements by a density-matrix calculation. *Physica* (1981) **104**:350–64. doi: 10.1016/0378-4363(81)90182-0
26. Stepišnik, J. Time-dependent self-diffusion by NMR spin-echo. *Physica B* (1993) **183**:343–50. doi: 10.1016/0921-4526(93)90124-O
27. Parsons EC, Does MD, Gore JC. Temporal diffusion spectroscopy: theory and implementation in restricted systems using oscillating gradients. *Magn Reson Med.* (2006) **55**:75–84. doi: 10.1002/mrm.20732
28. Stepišnik J, Lasic S, Mohoric A, Sersa I, Sepe A. Spectral characterization of diffusion in porous media by the modulated gradient spin echo with CPMG sequence. *J Magn Reson.* (2006) **182**:195–9. doi: 10.1016/j.jmr.2006.06.023
29. Novikov DS, Kiselev VG. Surface-to-volume ratio with oscillating gradients. *J Magn Reson.* (2011) **210**:141–5. doi: 10.1016/j.jmr.2011.02.011
30. Sukstanskii, A. L. Exact analytical results for ADC with oscillating diffusion sensitizing gradients. *J Magn Reson.* (2013) **234**:135–40. doi: 10.1016/j.jmr.2013.06.016
31. Latour LL, Svoboda K, Mitra PP, Sotak CH. Time-dependent diffusion of water in a biological model system. *Proc Natl Acad Sci USA.* (1994) **91**:1229–33. doi: 10.1073/pnas.91.4.1229
32. Schachter M, Does MD, Anderson AW, Gore JC. Measurements of restricted diffusion using an oscillating gradient spin-echo sequence. *J Magn Reson.* (2000) **147**:232–7. doi: 10.1006/jmre.2000.2203
33. Vogt C, Galvosas P, Klitzsch N, Stallmach F. Self-diffusion studies of pore fluids in unconsolidated sediments by PFG NMR. *J Appl Geophys.* (2002) **50**:455–67. doi: 10.1016/S0926-9851(02)00195-7
34. Parsons EC, Does MD, Gore JC. Modified oscillating gradient pulses for direct sampling of the diffusion spectrum suitable for imaging sequences. *Magn Reson Imaging.* (2003) **21**:279–85. doi: 10.1016/S0730-725X(03)00155-3
35. Xu JZ, Xie JP, Jourquin J, Colvin DC, Does MD, Quaranta V, et al. Influence of cell cycle phase on apparent diffusion coefficient in synchronized cells detected using temporal diffusion spectroscopy. *Magn Reson Med.* (2011) **65**:920–6. doi: 10.1002/mrm.22704
36. Reynaud O, Winters KV, Hoang DM, Wadghiri YZ, Novikov DS, Kim SG. Surface-to-volume ratio mapping of tumor microstructure using oscillating gradient diffusion weighted imaging. *Magn Reson Med.* (2016b) **76:**237–47. doi: 10.1002/mrm.25865
37. Lemberskiy G, Baete SH, Cloos MA, Novikov DS, Fieremans E. Validation of surface-to-volume ratio measurements derived from oscillating gradient spin echo on a clinical scanner using anisotropic fiber phantoms. *MR Biomed.* (2017a). **30**:e3708. doi: 10.1002/nbm.3708
38. Zielinski LJ, Hurlimann MD. Probing short length scales with restricted diffusion in a static gradient using the CPMG sequence. *Jo Magn Reson.* (2005) **172**:161–7. doi: 10.1016/j.jmr.2004.10.006
39. Caprihan A, Wang LZ, Fukushima E. A multiple-narrow-pulse approximation for restricted diffusion in a time-varying field gradient. *J Magn Reson Series A.* (1996) **118**:94–102. doi: 10.1006/jmra.1996.0013
40. Callaghan PT. A simple matrix formalism for spin echo analysis of restricted diffusion under generalized gradient waveforms. *J Magn Reson.* (1997) **129**:74–84. doi: 10.1006/jmre.1997.1233
41. Barzykin AV. Theory of spin echo in restricted geometries under a step-wise gradient pulse sequence. *J Magn Reson.* (1999) **139**:342–53. doi: 10.1006/jmre.1999.1778
42. Grebenkov DS. NMR survey of reflected Brownian motion. *Rev Modern Phys.* (2007b) **79**:1077–137. doi: 10.1103/RevModPhys.79.1077
43. Grebenkov DS. Analytical solution for restricted diffusion in circular and spherical layers under inhomogeneous magnetic fields. *J Chem Phys.* (2008a) **128**:134702. doi: 10.1063/1.2841367
44. Özarslan E, Shemesh N, Basser PJ. A general framework to quantify the effect of restricted diffusion on the NMR signal with applications to double pulsed field gradient NMR experiments. *J Chem Phys.* (2009) **130**:104702. doi: 10.1063/1.3082078
45. Laun FB. Restricted diffusion in NMR in arbitrary inhomogeneous magnetic fields and an application to circular layers. *J Chem Phys.* (2012) **137**:044704. doi: 10.1063/1.4736849
46. Grebenkov DS. Laplacian eigenfunctions in NMR. I. A numerical tool. *Concepts Magn Reson A.* (2008b) **32A**:277–301. doi: 10.1002/cmr.a.20117
47. Grebenkov DS. Laplacian eigenfunctions in NMR. II. Theoretical advances. *Concepts Magne Resona A.* (2009) **34A**:264–96. doi: 10.1002/cmr.a.20145
48. Shemesh N, Westin CF, Cohen Y. Magnetic resonance imaging by synergistic diffusion-diffraction patterns. *Phys Rev Lett.* (2012) **108**:058103. doi: 10.1103/PhysRevLett.108.058103
49. Shemesh N, Alvarez GA, Frydman L. Measuring small compartment dimensions by probing diffusion dynamics via Non-uniform Oscillating-Gradient Spin-Echo (NOGSE) NMR. *J Magn Reson.* (2013) **237**:49–62. doi: 10.1016/j.jmr.2013.09.009

50. Lundell H, Sonderby CK, Dyrby TB. Diffusion weighted imaging with circularly polarized oscillating gradients. *Magn Reson Med.* (2015) **73**:1171–6. doi: 10.1002/mrm.25211
51. Shemesh N, Alvarez GA, Frydman L. (2015). Size distribution imaging by non-uniform oscillating-gradient spin echo (NOGSE) MRI. *PLoS ONE* **10**:e0133201. doi: 10.1371/journal.pone.0133201
52. Does MD, Parsons EC, Gore JC. Oscillating gradient measurements of water diffusion in normal and globally ischemic rat brain. *Magn Reson Med.* (2003) **49**:206–15. doi: 10.1002/mrm.10385
53. Aggarwal M, Jones MV, Calabresi PA, Mori S, Zhang JY. Probing mouse brain microstructure using oscillating gradient diffusion MRI. *Magn Reson Med.* (2012) **67**:98–109. doi: 10.1002/mrm.22981
54. Xu JZ, Li K, Smith RA, Waterton JC, Zhao P, Chen HD et al. Characterizing tumor response to chemotherapy at various length scales using temporal diffusion spectroscopy. *PLoS ONE* (2012) **7**:e41714. doi: 10.1371/journal.pone.0041714
55. Ianus A, Siow B, Drobnjak I, Zhang H, Alexander DC. Gaussian phase distribution approximations for oscillating gradient spin echo diffusion MRI. *J Magn Reson.* (2013) **227**:25–34. doi: 10.1016/j.jmr.2012.11.021
56. Aggarwal M, Burnsed J, Martin LJ, Northington FJ, Zhang JY. Imaging neurodegeneration in the mouse hippocampus after neonatal hypoxia-ischemia using oscillating gradient diffusion MRI. *Magn Reson Med.* (2014) **72**:829–40. doi: 10.1002/mrm.24956
57. Li H, Gore JC, Xu JZ. Fast and robust measurement of microstructural dimensions using temporal diffusion spectroscopy. *J Magn Reson.* (2014) **242**:4–9. doi: 10.1016/j.jmr.2014.02.007
58. Portnoy S, Fichtner ND, Dziegielewski C, Stanisz MP, Stanisz GJ. *In vitro* detection of apoptosis using oscillating and pulsed gradient diffusion magnetic resonance imaging. *NMR Biomed.* (2014) **27**:371–80. doi: 10.1002/nbm.3070
59. Van AT, Holdsworth SJ, Bammer R. *In vivo* investigation of restricted diffusion in the human brain with optimized oscillating diffusion gradient encoding. *Magn Reson Med.* (2014) **71**:83–94. doi: 10.1002/mrm.24632
60. Wu D, Martin LJ, Northington FJ, Zhang JY. Oscillating gradient diffusion MRI reveals unique microstructural information in normal and hypoxia-ischemia injured mouse brains. *Magn Reson Med.* (2014) **72**:1366–74. doi: 10.1002/mrm.25441
61. Xu JZ, Li H, Harkins KD, Jiang XY, Xie JP, Kang H, et al. Mapping mean axon diameter and axonal volume fraction by MRI using temporal diffusion spectroscopy. *Neuroimage* (2014) **103**:10–9. doi: 10.1016/j.neuroimage.2014.09.006
62. Li H, Jiang XY, Wang F, Xu JZ, Gore JC. Structural information revealed by the dispersion of ADC with frequency. *Magn Reson Imaging* (2015) **33**:1083–90. doi: 10.1016/j.mri.2015.06.009
63. Drobnjak I, Zhang H, Ianus A, Kaden E, Alexander DC. PGSE, OGSE, and sensitivity to axon diameter in diffusion MRI: insight from a simulation study. *Magn Reson Med.* (2016) **75**:688–700. doi: 10.1002/mrm.25631
64. Jiang XY, Li H, Xie JP, Zhao P, Gore JC, Xu JZ. Quantification of cell size using temporal diffusion spectroscopy. *Magn Reson Med.* (2016) **75**:1076–85. doi: 10.1002/mrm.25684
65. Reynaud O, Winters KV, Hoang DM, Wadghiri YZ, Novikov DS, Kim SG. Pulsed and oscillating gradient MRI for assessment of cell size and extracellular space (POMACE) in mouse gliomas. *NMR Biomed.* (2016a) **29**:1350–63. doi: 10.1002/nbm.3577
66. Baron CA, Beaulieu C. Oscillating gradient spin-echo (OGSE) diffusion tensor imaging of the human brain. *Magn Reson Med.* (2014) **72**:726–36. doi: 10.1002/mrm.24987
67. Li H, Jiang XY, Xie JP, McIntyre JO, Gore JC, Xu JZ. Time-dependent influence of cell membrane permeability on MR diffusion measurements. *Magn Reson Med.* (2016) **75**:1927–34. doi: 10.1002/mrm.25724
68. Drobnjak I, Siow B, Alexander DC. Optimizing gradient waveforms for microstructure sensitivity in diffusion-weighted MR. *J Magn Reson.* (2010) **206**:41–51. doi: 10.1016/j.jmr.2010.05.017
69. Siow B, Drobnjak I, Chatterjee A, Lythgoe MF, Alexander DC. Estimation of pore size in a microstructure phantom using the optimised gradient waveform diffusion weighted NMR sequence. *J Magn Reson.* (2012) **214**:51–60. doi: 10.1016/j.jmr.2011.10.004

Conflict of Interest Statement: The authors declare that the research was conducted in the absence of any commercial or financial relationships that could be construed as a potential conflict of interest.

The handling Editor declared a past co-authorship with the authors TK and FL.

frontiers in Physics

PERSPECTIVE
published: 19 December 2017
doi: 10.3389/fphy.2017.00068

Effective Potential for Magnetic Resonance Measurements of Restricted Diffusion

Evren Özarslan[1]*, *Cem Yolcu*[1], *Magnus Herberthson*[2], *Carl-Fredrik Westin*[1,3] and *Hans Knutsson*[1]

[1] Department of Biomedical Engineering, Linköping University, Linköping, Sweden, [2] Division of Mathematics and Applied Mathematics, Department of Mathematics, Linköping University, Linköping, Sweden, [3] Laboratory for Mathematics in Imaging, Department of Radiology, Harvard Medical School, Brigham and Women's Hospital, Boston, MA, United States

The signature of diffusive motion on the NMR signal has been exploited to characterize the mesoscopic structure of specimens in numerous applications. For compartmentalized specimens comprising isolated subdomains, a representation of individual pores is necessary for describing restricted diffusion within them. When gradient waveforms with long pulse durations are employed, a quadratic potential profile is identified as an effective energy landscape for restricted diffusion. The dependence of the stochastic effective force on the center-of-mass position is indeed found to be approximately linear (Hookean) for restricted diffusion even when the walls are sticky. We outline the theoretical basis and practical advantages of our picture involving effective potentials.

Keywords: diffusion, magnetic resonance, anisotropy, microscopic, local, confinement, tensor, parabolic

OPEN ACCESS

Edited by:
Itamar Ronen,
Leiden University, Netherlands

Reviewed by:
Silvia Capuani,
Consiglio Nazionale Delle Ricerche (CNR), Italy
Christian Herbert Ziener,
German Cancer Research Center, Germany

***Correspondence:**
Evren Özarslan
evren.ozarslan@liu.se

Specialty section:
This article was submitted to Biomedical Physics, a section of the journal Frontiers in Physics

Received: *29 September 2017*
Accepted: *08 December 2017*
Published: *19 December 2017*

Citation:
Özarslan E, Yolcu C, Herberthson M, Westin C-F and Knutsson H (2017) Effective Potential for Magnetic Resonance Measurements of Restricted Diffusion. Front. Phys. 5:68. doi: 10.3389/fphy.2017.00068

1. INTRODUCTION

Recovering the mesoscopic structure of porous media and biological tissues via diffusion sensitized NMR methods has been an active area of research since 1960s [1, 2]. As a molecule diffuses within the medium, its magnetic moment acquires a certain phase depending upon the particle's trajectory and the impressed magnetic field gradient profile. The total signal generated by all molecules can be expressed mathematically as

$$E = \left\langle e^{-i\gamma \int_0^t \mathrm{d}s\, \boldsymbol{G}(s)\cdot\boldsymbol{x}(s)} \right\rangle, \tag{1}$$

where γ is the gyromagnetic ratio while $\boldsymbol{G}$ and $\boldsymbol{x}$ denote the time-dependent magnetic field gradient and the position of the particle, respectively. The average is taken over all particle trajectories.

Conventional techniques for relating the NMR signal above to microstructural features of the medium vary from "localized" models in which the aggregate signal is envisioned to arise from isolated (e.g., restricted) compartments [3, 4] to more "global" models, which attempt to capture the medium's disorder [5, 6]. Here, we propose to approach the problem of relating the NMR signal to microstructural features of the medium with an alternative paradigm wherein diffusion is thought to be taking place within a potential energy landscape.

When the gradient waveform, $\boldsymbol{G}(s)$, comprises two well-separated pulses of infinitesimal durations, the relationship between the NMR signal and the compartment shape is the same as that in scattering experiments. For closed pores, the signal intensity is given by $E(\boldsymbol{q}) = |\tilde{\rho}(\boldsymbol{q})|^2$, *i.e.*,the

power spectrum of the equilibrium distribution of spins $\rho(\boldsymbol{r})$. Here, the wavevector $\boldsymbol{q}$ is taken to be the time integral of each gradient pulse multiplied by γ. As the pulse duration is prolonged, the oscillatory diffraction pattern of the signal stretches toward larger q-values ($q = |\boldsymbol{q}|$), and eventually becomes unobservable [7, 8]. This is a manifestation of the loss of information in experiments featuring long pulses; such information loss is key to our endeavor to identify an effective potential for the diffusion process.

In this Perspective, we argue that the theory of diffusion under a Hookean restoring force [7, 9–13] can be regarded as the *effective theory of restricted diffusion* for a wide class of highly relevant NMR signal acquisition scenarios. This is evident at the macroscopic scale when one considers the dependence of the signal on experimental parameters for sequences featuring long gradient pulses or plots the average effective force experienced by the particles against their mean position (center of mass of their trajectories) during the application of a long pulse. For NMR examinations of microscopic diffusion anisotropy [14, 15], the quadratic potential profile is ideally suited to represent the observable properties of small pores making up a compartmentalized medium.

2. EFFECTIVE POTENTIAL FOR RESTRICTED DIFFUSION

Here we demonstrate that, under certain experimental conditions, the influence of restricted diffusion is essentially the same as that for the Hookean potential model, which was studied in-depth recently [13]. After the theoretical grounds for the effective theory are established, we proceed with presenting simulation results that provide additional justification.

2.1. Long-Pulse Train

Consider a pulse sequence which consists of N rectangular gradient pulses of varying (vector) magnitudes $\boldsymbol{G}_n$ and durations δ_n. With the definition

$$\boldsymbol{q}_n = \gamma \boldsymbol{G}_n \delta_n, \tag{2}$$

the NMR signal (Equation 1) is given by

$$E = \left\langle \exp\left\{ -i \sum_{n=1}^{N} \frac{1}{\delta_n} \int_{t_n}^{t_n+\delta_n} \boldsymbol{q}_n \cdot \boldsymbol{x}(t) \mathrm{d}t \right\} \right\rangle, \tag{3}$$

where t_n denotes the leading edge of the nth pulse. Angular brackets indicate averaging over the possible trajectories $\boldsymbol{x}(t)$.

Further, introducing the stochastic center-of-mass of the particle trajectory [7] during the nth pulse through

$$\boldsymbol{\xi}_n = \frac{1}{\delta_n} \int_{t_n}^{t_n+\delta_n} \boldsymbol{x}(t)\, \mathrm{d}t, \tag{4}$$

the stochastic signal can be rewritten as

$$E = \left\langle e^{-i(\boldsymbol{q}_1 \cdot \boldsymbol{\xi}_1 + \boldsymbol{q}_2 \cdot \boldsymbol{\xi}_2 + \ldots + \boldsymbol{q}_N \cdot \boldsymbol{\xi}_N)} \right\rangle. \tag{5}$$

In words, the NMR signal elicited by spatially constant gradient pulses of finite duration is sensitive to the center of mass (average position) of Brownian trajectories, rather than instantaneous coordinates. The duration of the pulses therefore serve to smear out fine spatial features.

Let $p_{\mathrm{cm}}(\boldsymbol{\xi}, \delta)$ denote the distribution of the center of mass during a time interval of duration δ. In the long duration regime, $\delta_n \to \infty$, the dependence on the pulse separation disappears and the signal intensity (Equation 5) factorizes, leading to

$$E = \tilde{p}_{\mathrm{cm}}(\boldsymbol{q}_1, \delta_1)\, \tilde{p}_{\mathrm{cm}}(\boldsymbol{q}_2, \delta_2) \ldots \tilde{p}_{\mathrm{cm}}(\boldsymbol{q}_N, \delta_N), \tag{6}$$

where

$$\tilde{p}_{\mathrm{cm}}(\boldsymbol{q}, \delta) = \int p_{\mathrm{cm}}(\boldsymbol{\xi}, \delta) e^{-i\boldsymbol{q}\cdot\boldsymbol{\xi}}\, \mathrm{d}^3\xi \tag{7}$$

is the Fourier transform of the center of mass distribution. Due to its construction (Equation 4), the random variable $\boldsymbol{\xi}$ has a distribution $p_{\mathrm{cm}}(\boldsymbol{\xi}, \delta)$ that approaches a Gaussian in the limit of long duration[1]. Therefore, both its Fourier transform (Equation 7) and hence the signal (Equation 6) approach Gaussians as well.

The Gaussian distribution is determined simply by its variance matrix (with its mean set to zero for convenience). The relevance of this fact here is that when a train of long pulses is employed, the signal has no means of encoding for fine features of the microscopic environment where diffusion takes place[2]. What survives in the signal is merely that component of the microscopic forces that provide a stable equilibrium (since the particles do not escape to infinity) for the center of mass and no more. More specifically, a Hookean force.

While restricted diffusion becomes a difficult problem to tackle in higher dimensions for all but a few special geometries, diffusion under a Hookean force is much more tractable, and it behooves one to adopt the latter model when its features are all that can be observed, as argued above. Hence we consider the case of diffusing particles subject to a (dimensionless) parabolic confining potential $U(\boldsymbol{x}) = (1/2)\boldsymbol{x}^{\mathsf{T}}\boldsymbol{C}\boldsymbol{x}$, where $\boldsymbol{C}$ is the confinement tensor [13]. Under this potential, the magnetization density evolves according to the Bloch-Torrey-Smoluchowski equation [13, 17, 18]. For this process, the center of mass distribution is Gaussian for *any* duration, and its Fourier transform is given by

$$\tilde{p}_{\mathrm{cm}}(\boldsymbol{q}, \delta) = e^{-\frac{1}{2}\boldsymbol{q}^{\mathsf{T}} V \boldsymbol{q}}, \tag{8}$$

with the variance matrix

$$\boldsymbol{V} = 2(D\delta)^{-2}\boldsymbol{C}^{-3}(D\boldsymbol{C}\delta + e^{-DC\delta} - 1), \tag{9}$$

which is just a straightforward generalization of an expression in Mitra and Halperin [7] to higher dimensions. Via Equation (6), the signal encodes the confinement tensor, $\boldsymbol{C}$, for the restricted region.

[1] A rigorous proof of this can be found in the mathematics literature [16].

[2] Indicated also by the absence of powers of "momentum" $\boldsymbol{q}$ higher than 2 in its cumulant expansion.

2.2. Insights from the One-Dimensional Problem

The eigenvalues of the inverse of the confinement tensor $\boldsymbol{C}$ can be associated with the square of three lengths pertaining to the overall size of a 3-dimensional region. Of course, these three lengths cannot characterize the irregular boundary of a general 3-dimensional region, as alluded to above. However, for the illustration of the size-confinement correspondence, we momentarily take up the simple 1-dimensional example of diffusion restricted by two parallel plates separated by a distance L. The variance of the center of mass position is provided by Mitra and Halperin [7] to be

$$\left\langle \xi(\delta)^2 \right\rangle_{\text{res}} = \frac{16L^4}{\pi^6 D\delta} \sum_{n=1,3,5,\ldots}^{\infty} \frac{1}{n^6} \left[1 - \frac{1 - e^{-\pi^2 n^2 D\delta/L^2}}{\pi^2 n^2 D\delta/L^2} \right], \tag{10}$$

where the subscript stands for restricted diffusion[3].

In the long pulse duration regime wherein the statistics of the restricted problem approach those of the confinement problem, the variances of the center of mass position for the two problems are found by taking the long time limit of Equations (9) and (10), respectively,

$$\left\langle \xi(\delta)^2 \right\rangle_{\text{con}} \sim \frac{2}{C^2 D\delta}, \quad \delta \to \infty, \tag{11}$$

$$\left\langle \xi(\delta)^2 \right\rangle_{\text{res}} \sim \frac{L^4}{60 D\delta}, \quad \delta \to \infty. \tag{12}$$

Demanding that the two variances above agree results in the relation

$$C = \frac{\sqrt{120}}{L^2}, \tag{13}$$

meaning that the confinement model with parameter C becomes the appropriate effective theory for the restriction model (the "true" theory) with length L, yielding the same observed quantities under the coarse-graining furnished by the long averaging pulse.

While in the above it was the long pulse duration that ensured the Gaussianity of the signal (through the center of mass distribution) for restricted diffusion, an alternative situation is one where the gradient strength is so small that qL is much smaller than unity. Because the observed signal is Gaussian for such q values, the confinement model would perfectly represent the data, yet Equation (13) would not apply since the pulse duration is not necessarily long. If one adopts a matching scenario as above, a correspondence can be obtained numerically for general pulse durations. As shown in **Figure 1A**, the effective confinement value obtained by matching the variances of the center-of-mass distributions for the two problems, which is equivalent to matching the signals in an experiment employing well-separated pulses, varies within a very narrow range, namely between $C = 12/L^2$ and $C = \sqrt{120}/L^2$. Therefore, employing the asymptotic correspondence (Equation 13) in lieu of the numerical one (blue curve in **Figure 1A**) would still provide an acceptable estimate of L.

[3]Coordinates are chosen such that $\langle \xi \rangle = \langle x \rangle = 0$.

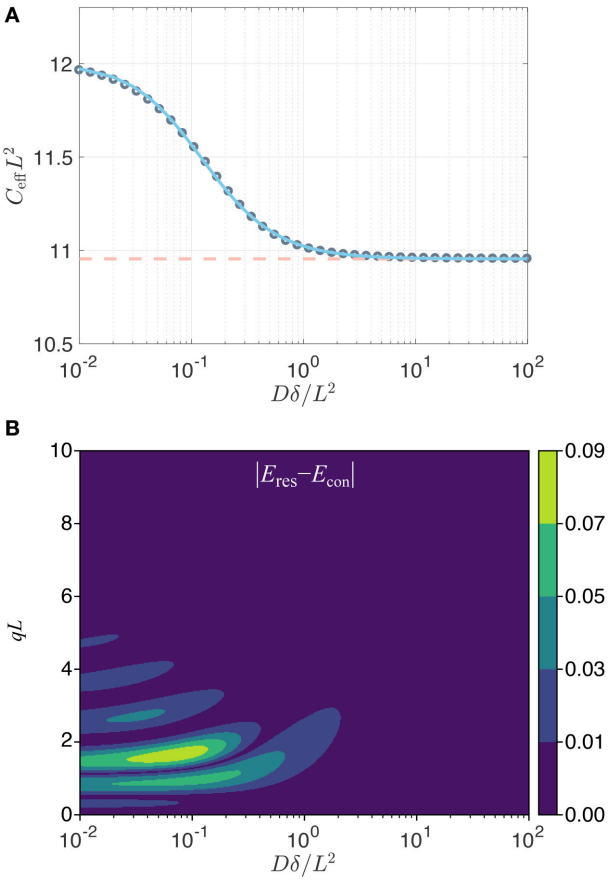

FIGURE 1 | (A) Effective dimensionless confinement value (gray circles) computed by matching the variances of the center of mass distributions in the two problems plotted vs. the dimensionless time $D\delta/L^2$. The variation in $C_{\text{eff}}L^2$ value is well-captured (error less than 0.12%) by the expression $y = 12 - (12 - \sqrt{120})(\alpha x)^{k\gamma}[1 + (\alpha x)^k]^{-\gamma}$, with $\alpha = 9.495$, $\gamma = 1.210$, and $k = 1.266$ (blue line). The dashed line indicates the asymptotic value $\sqrt{120}$. **(B)** The absolute value of the difference in the normalized signals implied by the two problems (restricted diffusion with separation L, and the Hookean potential with a confinement value taken to be $C = \sqrt{120}L^{-2}$) for a traditional Stejskal-Tanner sequence [32] with two gradient pulses whose leading edges are separated by Δ with $D\Delta/L^2 = 100$. The restricted diffusion signal was computed using the multiple correlation function method [33, 34].

Contrary to the two cases above, the signal for restricted diffusion is not Gaussian for other values of q or δ. Thus, the signal profile afforded by the confinement model can only be an approximation to the true signal when the pulses are not long. To investigate the discrepancy, it is insightful to compare the signal for the restricted diffusion problem (for a slab geometry of separation L) to that for the Hookean model featuring the long-time asymptotic value (Equation 13) of the effective confinement. In **Figure 1B**, we show that the error (defined as the difference in the normalized signal intensities implied by the restriction and confinement pictures) is below 0.01 for a very large portion of the relevant parameter space that could be probed. Such differences are not detectable when the signal-to-noise ratio is 100 or less, thus justifying the confinement description as a

reliable substitute in studies involving restricted diffusion. In fact, the most significant exception to this statement is at the peaks of the diffraction pattern, which occur roughly at $qL = 3/2, 5/2, \ldots$ for very short pulses (i.e., along the left edge of this figure) and at slighly larger qL values for longer durations. For long pulse durations, the diffraction pattern does not prevail, and the confinement model eventually provides an accurate description of the detectable signal.

Consider, e.g., a 4 μm pore—roughly the size of a yeast cell. Assuming a bulk diffusivity value of 2 μm^2/ms, and for a pulse duration of 20 ms, which is typical for diffusion measurements via clinical scanners, the $D\delta/L^2$ value is 2.5. Thus, the signal response of the confinement picture would be indistinguishable from a much more elaborate theory involving restricted diffusion. The situation is even more favorable for smaller sized compartments. In laboratory spectrometers, however, pulse durations an order of magnitude shorter are feasible; in such scenarios, detectable differences between the restricted diffusion and confinement pictures can be encountered unless the pores are smaller. However, let us remark once more that it is only in this simplified one-dimensional scenario that there exists a single unambiguous size of the region, allowing a one-to-one correspondence to be drawn between C and L. In higher dimensions, one's measurements have access simply to the tensor $\boldsymbol{C}$; the actual dimensions of the region can only be speculated upon to the extent that its geometry is known.

2.3. Boundary Force: Simulations

The confinement model is based on a Hookean force assumption, i.e., the presence of a restoring force whose magnitude increases linearly as the particles move away from an attractive center. We shall define an effective force, F_{eff}, based on the impulse the particles experience during a time interval of duration δ, i.e.,

$$F_{\text{eff}}\delta = \int_0^\delta F(t)\,\mathrm{d}t. \tag{14}$$

Because the time-dependent force $F(t)$ is proportional to $-Cx(t)$ for particles subject to a quadratic potential, the effective force is proportional to $-C\xi(\delta)$, implying a perfectly linear dependence on the center-of-mass of *each and every* trajectory. On the other hand for restricted diffusion, the effective force is proportional to $-\Delta N/\delta$, where ΔN denotes the number of collisions the particle makes with the wall on the left subtracted from that with the wall on the right.

By performing random walk simulations, we investigated whether a similar (Hookean) force model could emerge for the restricted diffusion process as well. In the top panel of **Figure 2A**, we plot the histograms of mean particle position for different durations. As expected, the center of mass distribution approaches a Gaussian as the time is prolonged. Note that the net force is a stochastic variable just like the mean position of the trajectories. Thus, in the bottom panel of **Figure 2A**, we plot the average of the net effective force against the mean trajectory position. Remarkably, the effective force is linearly related to the mean position for an overwhelming portion of the particles even for moderate times. Moreover, by repeating the simulations for different L values (results not shown), we found that the slope of the curves at long durations, i.e., the effective force constant, is proportional to L^{-2} just like in Equation (13). These findings further support the idea of employing a Hookean force model as a substitute for restricted diffusion at long durations. Importantly, the Hookean model is valid even for more complicated problems, which are difficult to treat analytically. We illustrate this point by introducing stickiness to the walls of the same restricted geometry. As shown in **Figure 2B**, the same conclusions can be drawn for this scenario albeit for a different value of the effective confinement.

3. DISCUSSION AND CONCLUSION

While characterizing a compartmentalized specimen or biological tissue via diffusion NMR, one is faced with the problem of determining a reliable representation of the local compartment. An accurate mathematical description of the pore shape would typically necessitate numerous parameters. However, such parameters are simply unavailable in diffusion NMR measurements featuring long gradients as a result of coarse-graining associated with the diffusion process taking place during the application of the gradients. The confinement tensor model [13] contains *just the right number of parameters* as dictated by the central limit theorem.

Similar to the diffusion tensor, the confinement tensor is real and symmetric, thus is described by 6 independent numbers. However, the confinement tensor *model* has at least one extra parameter—the bulk diffusivity, which can be scalar (isotropic) or tensorial. For the latter case, the diffusion tensor model emerges simply in the $C \to 0$ limit [13]. It is common to express the detected NMR signal for complex specimens as the sum of contributions from Gaussian and restricted compartments [3]. Our work implies that, when appropriate acquisition parameters are employed, both these compartments could be represented by the confinement tensor model though with different confinement values.

Diffusion tensors have also been employed for representing diffusion in microscopic compartments [4, 19, 20]. Since the two models (employing diffusion and confinement tensors) have the same q dependence for traditional Stejskal-Tanner measurements performed with varying gradient vectors, their predictions of the signal would be the same, and one model cannot be preferred over the other; this was observed when the confinement tensor is employed to represent the voxel-level signal [21] similar to what is done in diffusion tensor imaging [22]. However, the diffusion tensor model is based on free diffusion, and exhibits a time-dependence which is *paradoxical* for a compartmentalized structure. Manifestations of the difference in time-dependencies would be observable, e.g., when the timing parameters of the measurements are varied [23]. In fact, the influence of the gradient waveform on the free-diffusion signal is fully captured [24] by a measurement tensor, referred to as the b-matrix [25]. Thus, any set of acquisitions featuring the same b-matrix would yield the same signal value if diffusion tensor model is employed. However, the quadratic potential profile would lead to qualitatively different signal profiles, approximating the response

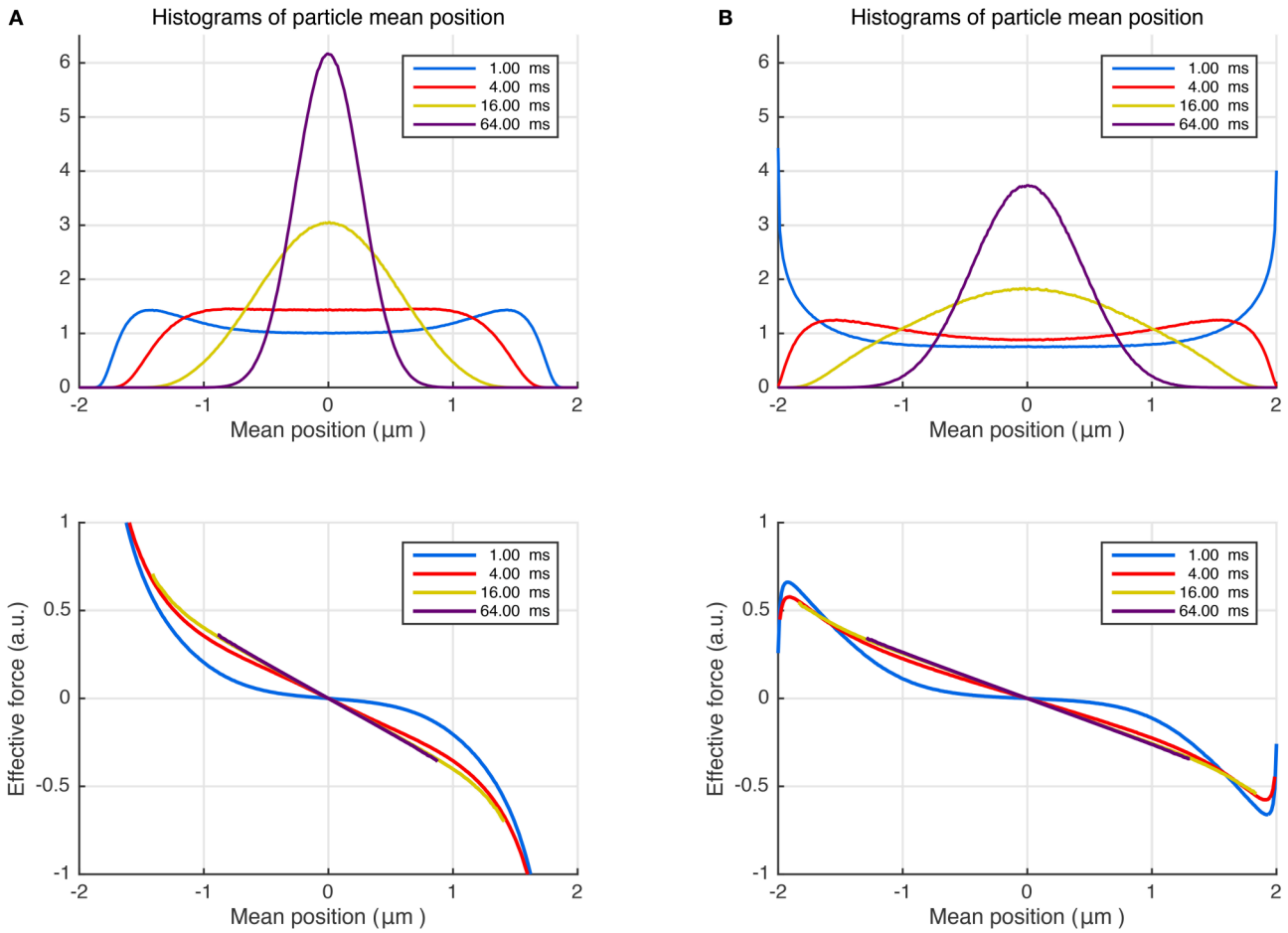

FIGURE 2 | (A) Random walk simulations for particles trapped between non-sticky parallel plates separated by 4 μm, diffusing with bulk diffusivity $D = 1.0\ \mu m^2/ms$. Different curves represent different time intervals, which can be associated with durations of the pulses in NMR measurements. The distributions of the positions of the center of mass are shown at the top. The average effective force exerted on the diffusing particles plotted vs. the trajectories' center of mass (bottom). **(B)** The simulations were repeated by introducing surface adsorption effect so that the particles spend, on average, 25% of the time stuck at the walls.

of a restricted diffusion process, which is more consistent with the underlying compartmentalized structure.

From a practical point of view, treating restricted diffusion is quite difficult even for simple geometries. For example, if we consider an ellipsoidal pore—the simplest geometry with the same number of parameters as a general confinement tensor—the problem would be very difficult to solve analytically. We argue that doing so would also be unnecessary if long pulses are employed. The *separability* of the confinement model enables one to write [13] the expected signal simply in terms of the solution of the one-dimensional Hookean problem, provided that we work in a frame of reference whose axes coincide with those of the ellipsoid; in this frame, $\boldsymbol{C}$ is diagonal. Such simplicity due to separation of variables in the confinement model is valid even for more complicated shapes since the statistics of the center of mass converge to Gaussian as long as the durations of the gradient pulses are long.

We would like to note that, as shown by Bauer et al. [26] accumulation of Gaussian phase, if true, implies a propagator (not just stationary distribution) that is Gaussian. In fact, the Ornstein-Uhlenbeck propagator [17, 27, 28] associated with the quadratic potential profile is the general form following the basic properties of the process: diffusive, Markovian, stationary, with Gaussian transition probabilities [26].

In a very recent study [29], some of us considered a general potential energy landscape, $U(\boldsymbol{x})$, in which all disturbances to otherwise free diffusion are envisioned to originate from the variations in this landscape. For this scenario, the equilibrium density of the particles is governed by Maxwell-Boltzmann statistics, i.e., $\rho(\boldsymbol{x}) \propto e^{-U(\boldsymbol{x})}$, which could account for inhomogeneities in the bulk, and incorporate the effects of boundaries if needed, in a mathematically wieldy manner. We demonstrated that pulse sequences involving very short and long pulses [30, 31] could be employed to map this underlying landscape. Here, we have extended this finding to *effective* potential energy landscapes associated with restricted diffusion, which can be mapped without narrow pulses.

In conclusion, we have presented a new perspective in which findings of common and relevant NMR signal acquisition scenarios can be interpreted. At the heart of this perspective lies modeling the diffusion as taking place in an effective quadratic potential landscape instead of a restricted domain. We have argued that when probed via waveforms featuring long pulses, the two models become indistinguishable, and the signal should rather be taken to reflect the parameters of such an effective model. Simulations suggest that the stochastic effective force has a linear (Hookean) dependence on the average particle position. The signal for quadratic potential indeed provides a very good approximation to that for restricted diffusion in small (micron-scale) pores when examined via commonly available hardware (see **Figure 1B**). This observation can be generalized in a straightforward way to higher dimensions, thus making the confinement tensor model [13] relevant for applications such as clinical and pre-clinical MRI.

AUTHOR CONTRIBUTIONS

EÖ conceptualized the problem. EÖ, CY, MH, and HK developed and refined the perspective. HK and EÖ performed the numerical simulations. CY and EÖ wrote the manuscript. C-FW provided guidelines. All authors collaborated in bringing the manuscript to its final state.

FUNDING

This study was supported by the Swedish Foundation for Strategic Research AM13-0090, the Swedish Research Council CADICS Linneaus research environment, the Swedish Research Council 2015-05356 and 2016-04482, Linköping University Center for Industrial Information Technology (CENIIT), VINNOVA/ITEA3 13031 BENEFIT, and National Institutes of Health P41EB015902, R01MH074794, P41EB015898.

REFERENCES

1. Price WS. *NMR Studies of Translational Motion.* Cambridge: Cambridge University Press (2009). doi: 10.1017/CBO9780511770487
2. Callaghan PT. *Translational Dynamics and Magnetic Resonance: Principles of Pulsed Gradient Spin Echo NMR.* New York, NY: Oxford University Press (2011). doi: 10.1093/acprof:oso/9780199556984.001.0001
3. Assaf Y, Freidlin RZ, Rohde GK, Basser PJ. New modeling and experimental framework to characterize hindered and restricted water diffusion in brain white matter. *Magn Reson Med.* (2004) **52**:965–78. doi: 10.1002/mrm.20274
4. Jian B, Vemuri BC, Özarslan E, Carney PR, Mareci TH. A novel tensor distribution model for the diffusion-weighted MR signal. *NeuroImage* (2007) **37**:164–76. doi: 10.1016/j.neuroimage.2007.03.074
5. Özarslan E, Basser PJ, Shepherd TM, Thelwall PE, Vemuri BC, Blackband SJ. Observation of anomalous diffusion in excised tissue by characterizing the diffusion-time dependence of the MR signal. *J Magn Reson.* (2006) **183**:315–23. doi: 10.1016/j.jmr.2006.08.009
6. Ning L, Özarslan E, Westin CF, Rathi Y. Precise inference and characterization of structural organization (PICASO) of tissue from molecular diffusion. *NeuroImage* (2017) **146**:452–73. doi: 10.1016/j.neuroimage.2016.09.057
7. Mitra PP, Halperin BI. Effects of finite gradient-pulse widths in pulsed-field-gradient diffusion measurements. *J Magn Reson A* (1995) **113**:94–101. doi: 10.1006/jmra.1995.1060
8. Callaghan PT. A simple matrix formalism for spin echo analysis of restricted diffusion under generalized gradient waveforms. *J Magn Reson.* (1997) **129**:74–84. doi: 10.1006/jmre.1997.1233
9. Stejskal EO. Use of spin echoes in a pulsed magnetic-field gradient to study anisotropic, restricted diffusion and flow. *J Chem Phys.* (1965) **43**:3597–603. doi: 10.1063/1.1696526
10. Tanner JE, Stejskal EO. Restricted self-diffusion of protons in colloidal systems by the pulsed-gradient, spin-echo method. *J Chem Phys.* (1968) **49**:1768–77. doi: 10.1063/1.1670306
11. Callaghan PT, Pinder DN. Dynamics of entangled polystyrene solutions studied by pulsed field gradient nuclear magnetic resonance. *Macromolecules* (1980) **13**:1085–92. doi: 10.1021/ma60077a012
12. Le Doussal P, Sen PN. Decay of nuclear magnetization by diffusion in a parabolic magnetic field: an exactly solvable model. *Phys Rev B* (1992) **46**:3465–85. doi: 10.1103/PhysRevB.46.3465
13. Yolcu C, Memiç M, Şimşek K, Westin CF, Özarslan E. NMR signal for particles diffusing under potentials: from path integrals and numerical methods to a model of diffusion anisotropy. *Phys Rev E* (2016) **93**:052602. doi: 10.1103/PhysRevE.93.052602
14. Cheng Y, Cory DG. Multiple scattering by NMR. *J Am Chem Soc.* (1999) **121**:7935–6. doi: 10.1021/ja9843324
15. Özarslan E. Compartment shape anisotropy (CSA) revealed by double pulsed field gradient MR. *J Magn Reson.* (2009) **199**:56–67. doi: 10.1016/j.jmr.2009.04.002
16. Baxter JR, Brosamler GA. Energy and the law of the iterated logarithm. *Math Scand.* (1976) **38**:115–36. doi: 10.7146/math.scand.a-11622
17. Smoluchowski M. Über Brownsche Molekularbewegung unter Einwirkung äußerer Kräfte und deren Zusammenhang mit der verallgemeinerten Diffusionsgleichung. *Ann Phys.* (1916) **353**:1103–12. doi: 10.1002/andp.19163532408
18. Torrey HC. Bloch equations with diffusion terms. *Phys Rev.* (1956) **104**:563–5. doi: 10.1103/PhysRev.104.563
19. Callaghan PT, Komlosh ME. Locally anisotropic motion in a macroscopically isotropic system: displacement correlations measured using double pulsed gradient spin-echo NMR. *Magn Reson Chem.* (2002) **40**:S15–9. doi: 10.1002/mrc.1122
20. Westin CF, Knutsson H, Pasternak O, Szczepankiewicz F, Özarslan E, van Westen D, et al. Q-space trajectory imaging for multidimensional diffusion MRI of the human brain. *NeuroImage* (2016) **135**:345–62. doi: 10.1016/j.neuroimage.2016.02.039
21. Afzali M, Yolcu C, Özarslan E. Characterizing diffusion anisotropy for molecules under the influence of a parabolic potential: a plausible alternative to DTI. *Proc Intl Soc Mag Reson Med.* (2015) **23**:2795.
22. Basser PJ, Mattiello J, LeBihan D. MR diffusion tensor spectroscopy and imaging. *Biophys J.* (1994) **66**:259–67. doi: 10.1016/S0006-3495(94)80775-1
23. Zucchelli M, Afzali M, Yolcu C, Westin CF, Menegaz G, Özarslan E. The confinement tensor model improves characterization of diffusion-weighted magnetic resonance data with varied timing parameters. In: *2016 IEEE 13th International Symposium on Biomedical Imaging (ISBI)*. Prague: IEEE (2016). p. 1093–6.
24. Özarslan E, Westin CF, Mareci TH. Characterizing magnetic resonance signal decay due to Gaussian diffusion: the path integral approach and a convenient computational method. *Concepts Magn Reson Part A* (2015) **44**:203–13. doi: 10.1002/cmr.a.21354
25. Mattiello J, Basser PJ, LeBihan D. Analytical expressions for the b-matrix in NMR diffusion imaging and spectroscopy. *J Magn Reson A* (1994) **108**:131–41. doi: 10.1006/jmra.1994.1103
26. Bauer WR, Ziener CH, Jakob PM. Non-Gaussian spin dephasing. *Phys Rev A* (2005) **71**:053412. doi: 10.1103/PhysRevA.71.053412
27. Smoluchowski M. Einige Beispiele Brown'scher Molekularbewegung unter Einfluss äusserer Kräfte. *Bull Int Acad Sci Cracovie Cl Sci Math Natur.* (1913) 418.
28. Uhlenbeck GE, Ornstein LS. On the theory of the Brownian motion. *Phys Rev.* (1930) **36**:823–41. doi: 10.1103/PhysRev.36.823

29. Özarslan E, Şimşek K, Yolcu C, Westin CF. Imaging energy landscapes. *Proc Intl Soc Mag Reson Med.* (2017) **25**:1830.
30. Laun FB, Kuder TA, Semmler W, Stieltjes B. Determination of the defining boundary in nuclear magnetic resonance diffusion experiments. *Phys Rev Lett.* (2011) **107**:048102. doi: 10.1103/PhysRevLett.107.048102
31. Laun FB, Kuder TA, Wetscherek A, Stieltjes B, Semmler W. NMR-based diffusion pore imaging. *Phys Rev E Stat Nonlin Soft Matter Phys.* (2012) **86**:021906. doi: 10.1103/PhysRevE.86.021906
32. Stejskal EO, Tanner JE. Spin diffusion measurements: spin echoes in the presence of a time-dependent field gradient. *J Chem Phys.* (1965) **42**:288–92. doi: 10.1063/1.1695690
33. Barzykin AV. Exact solution of the Torrey-Bloch equation for a spin echo in restricted geometries. *Phys Rev B* (1998) **58**:14171–4. doi: 10.1103/PhysRevB.58.14171
34. Grebenkov DS. NMR survey of reflected Brownian motion. *Rev Mod Phys.* (2007) **79**:1077–137. doi: 10.1103/RevModPhys.79.1077

Conflict of Interest Statement: The authors declare that the research was conducted in the absence of any commercial or financial relationships that could be construed as a potential conflict of interest.

frontiers in Physics

ORIGINAL RESEARCH
published: 20 February 2018
doi: 10.3389/fphy.2018.00012

Improving the Realism of White Matter Numerical Phantoms: A Step toward a Better Understanding of the Influence of Structural Disorders in Diffusion MRI

Kévin Ginsburger[1,2], Fabrice Poupon[2,3], Justine Beaujoin[1,2], Delphine Estournet[1,2], Felix Matuschke[4], Jean-François Mangin[2,3,5], Markus Axer[4] and Cyril Poupon[1,2]*

[1] CEA DRF/ISVFJ/Neurospin/UNIRS, Gif-sur-Yvette, France, [2] Université Paris-Saclay, Orsay, France, [3] CEA DRF/ISVFJ/Neurospin/UNATI, Gif-sur-Yvette, France, [4] Research Centre Jülich, Institute of Neuroscience and Medicine, Jülich, Germany, [5] CATI, Multicenter Neuroimaging Platform, Orsay, France

OPEN ACCESS

Edited by:
Julien Valette, Commissariat à l'Energie Atomique et aux Energies Alternatives (CEA), France

Reviewed by:
Olivier Reynaud, École Polytechnique Fédérale de Lausanne, Switzerland
Marco Palombo, University College London, United Kingdom

***Correspondence:**
Kévin Ginsburger
kginsburger@gmail.com

Specialty section:
This article was submitted to Biomedical Physics, a section of the journal Frontiers in Physics

Received: 29 November 2017
Accepted: 02 February 2018
Published: 20 February 2018

Citation:
Ginsburger K, Poupon F, Beaujoin J, Estournet D, Matuschke F, Mangin J-F, Axer M and Poupon C (2018) Improving the Realism of White Matter Numerical Phantoms: A Step toward a Better Understanding of the Influence of Structural Disorders in Diffusion MRI. Front. Phys. 6:12. doi: 10.3389/fphy.2018.00012

White matter is composed of irregularly packed axons leading to a structural disorder in the extra-axonal space. Diffusion MRI experiments using oscillating gradient spin echo sequences have shown that the diffusivity transverse to axons in this extra-axonal space is dependent on the frequency of the employed sequence. In this study, we observe the same frequency-dependence using 3D simulations of the diffusion process in disordered media. We design a novel white matter numerical phantom generation algorithm which constructs biomimicking geometric configurations with few design parameters, and enables to control the level of disorder of the generated phantoms. The influence of various geometrical parameters present in white matter, such as global angular dispersion, tortuosity, presence of Ranvier nodes, beading, on the extra-cellular perpendicular diffusivity frequency dependence was investigated by simulating the diffusion process in numerical phantoms of increasing complexity and fitting the resulting simulated diffusion MR signal attenuation with an adequate analytical model designed for trapezoidal OGSE sequences.This work suggests that angular dispersion and especially beading have non-negligible effects on this extracellular diffusion metrics that may be measured using standard OGSE DW-MRI clinical protocols.

Keywords: diffusion time-dependence, white matter microstructure, trapezoidal OGSE sequences, axonal diameter, Monte-Carlo simulations, biomimicking numerical phantoms

1. INTRODUCTION

Diffusion-weighted magnetic resonance imaging (dMRI), sensitized to the diffusive motion of water along the direction of an applied magnetic field gradient, has become a well-established technique to non-invasively probe the cellular organization of tissues *in vivo*. Diffusion NMR measurements embed some information about the inhibition of particles motion due to the presence of barriers in the local environment, and can therefore be exploited to map some specific microstructural features characterizing the brain white matter ultrastructure at cellular scales. While Pulsed Gradient Spin Echo (PGSE) sequences [1] are still widely used in clinical routine, alternative schemes such as Oscillating Gradient Spin Echo (OGSE) sequences seem a promising

approach since they enable to explore the diffusion pattern in the frequency domain dual to the diffusion time domain and are able to probe shorter diffusion times compared to conventional PGSE. Some OGSE studies have reported that, at frequencies below 400 Hz, the OG-measured extra-axonal diffusivity transverse to axons in white matter is linearly dependent on the frequency of the employed OGSE sequence [2], whereas state-of-the art multi-compartment models of white matter relying on PGSE or OGSE sequences usually assume a Gaussian diffusion in the extra-axonal space [3–6]. A theoretical explanation was given in Burcaw et al. [7], where the observed frequency-dependence is interpreted as resulting from the extra-axonal 2D short-range disorder of axonal packings in the plane transverse to white matter fibers.

The extra-axonal perpendicular diffusivity transverse to axons was thus written as

$$D(t) = D_\infty + A.\frac{\ln(t/t_c)}{t}, \quad t_c \ll t \tag{1}$$

and, equivalently, in the frequency domain:

$$\mathrm{Re}\mathcal{D}(\omega) \sim D_\infty + A.\frac{\pi}{2}|\omega|, \quad |\omega| t_c \ll 1 \tag{2}$$

where t is the diffusion time, ω is the dual frequency and t_c represents the time to diffuse across the correlation length l_c of the packing geometry (l_c closely follows the mean external radius r_{ext} of the axon packing [7, 8]).

Similar to recent models accounting for extra-axonal time-dependence in the case of single diffusion encoding sequences [9], a multi-compartment model for cosine OGSE sequences was proposed in Ginsburger et al. [10] which added a frequency-dependent term in the extra-axonal diffusion tensor perpendicular diffusivity based on Equation (2), showing a significant improvement of the model fit quality.

The first contribution of this article is to show the relevance of such a frequency-dependent correction using clinically feasible cosine trapezoidal OGSE sequences. The theoretically predicted linear relationship between the extracellular perpendicular diffusivity and the OGSE frequency was observed using 3D simulations of the diffusion process with different values of signal-to-noise ratios (SNR).

Having introduced a physically plausible frequency-dependent correction in our model, the next step is to study the dependence of its scaling coefficient A (Equation 2) to the geometrical features of the extracellular space. Indeed, to our knowledge, this dependence is very little known. An empirical law $A \sim l_c^2$ relating A to the correlation length l_c was given in Burcaw et al. [7] and Fieremans et al. [8] but is not sufficient to catch the complexity of the scaling coefficient A. The value of A is a measure of the strength of the structural disorder [7, 11], thus related to the geometrical properties characterizing the spatial organization of white matter at various scales. A possible approach to decipher the complex relationship between A and white matter features is to perform Monte-Carlo simulations of the diffusion process in diffusing media with increasing level of structural disorder.

The simulation of the diffusion process in state-of-the-art Monte-Carlo simulators such as CAMINO [12] and DMS [13] is decomposed into three main steps: (1) the generation of a 3D numerical phantom representing the diffusion medium (2) the Monte-Carlo simulation of the Brownian motion of spins (3) the synthesis of a DW-NMR signal. Simulators like CAMINO or DMS are able to extract triangle meshes from histological samples in step (1) in order to simulate diffusion in ultra-realistic media. However, this approach does not allow to have access to the plethora of possible geometries but only to the limited set of configurations provided by the reduced set of histological samples. Beside the possibility to use geometries extracted from histological samples in step (1), state-of-the-art simulators can only generate a limited number of geometries which might not represent white matter sufficiently well. For instance, the CAMINO and DMS simulators are able to simulate the diffusion process in any triangle mesh, but the algorithm used to construct simulation meshes from input geometrical parameters only generates substrates with straight cylinders of various diameters (including crossing between two populations of fibers). Other simulation tools like Fiberfox [14] rely on analytical models associated to each particular cell geometry, including various combinations of sticks, tensors, zeppelins, balls, dots, and astrosticks. They are inherently limited by the realism of the used geometries and the employed analytical models do not account for the presence of structural disorder in the extracellular space. There is thus a real need to propose alternative generative algorithms able to create more complex geometries while controlling the parameters driving the various sources of geometrical disorder to explore more extensively the vast domain of possible geometries.

The main contribution of this article is therefore the development of a novel algorithm to produce a wide variety of biomimicking numerical phantoms representing more realistic white matter tissue configurations from a reduced set of control parameters. Embedded in the Diffusion Microscopist Simulator (DMS) [13], this algorithm enables to control the degree of complexity of the generated geometrical configurations (induction of global angular dispersion and local tortuosity, presence of Ranvier nodes along the axonal membrane, presence of beading) with few design parameters, and without the necessity of any input histological sample. Such numerical white matter phantoms are then used to perform Monte-Carlo simulations of the diffusion process from which simulated diffusion-weighted NMR signals can be synthesized using trapezoidal OGSE sequences at different values of SNR. The obtained signal is fed into our analytical model to explore the evolution of the structural disorder coefficient A for various well-characterized geometrical configurations of the extracellular space.

2. MATERIALS AND METHODS

2.1. White Matter Numerical Phantoms

Actual simulation tools rely either on membrane surfaces extracted from manual or automatic segmentations of microscopic imaging data stemming from histological tissue samples or on algorithms generating designs of axonal

membranes built from a distribution of rectilinear cylinders (possibly with angular dispersion) which diameters d follow a Gamma distribution h. The function h can be tuned using a α shape parameter and a β inverse scale parameter such that:

$$h(d;\alpha,\beta) = \frac{\beta^{\alpha} d^{\alpha-1} e^{-\beta d}}{\Gamma(\alpha)} \tag{3}$$

where Γ is a complete Gamma function. The first approach is hard to achieve and generally yields a limited collection of membrane configurations, whereas the second approach provides over-simplistic representations of white matter. Here, we propose a novel framework to design more realistic membrane geometries better mimicking white matter structure. One of the challenging issue of such an approach is to design a tool enabling to cover a wide range of actual geometries while using a limited number of parameters. Several observations can be taken into account to improve the development of more realistic white matter geometries:

- Several heterogeneous populations of fibers can populate the field of view (FOV) of interest; whatever the target FOV (from mesoscale to millimeter scale), complex configurations of fibers are likely to happen and several studies in the field of diffusion MRI have reported a percentage of around 60 percent of voxels containing crossing, kissing or splitting fibers at the conventional millimeter resolution of diffusion MRI data [15].
- Each fiber population is composed of myelinated or unmyelinated axons which diameters follow the previous Gamma distribution (Equation 3) but the shape and inverse scale parameters can vary from a population to another; in addition, each population is characterized by its mean orientation in the 3D space and by its volume fraction.
- Myelinated axons are regularly interrupted by Ranvier nodes along the axon main direction [16]; the internode distance d has been extensively studied in Rushton [17] leading to the maximum conduction relationship

$$\frac{d}{D} = kg\sqrt{\log\left(\frac{1}{g}\right)} \tag{4}$$

  where k is a constant, D is the external diameter of the axon (including the myelin sheath) and g is the g-ratio defined as the ratio between the axonal membrane and the external myelin sheath outer membrane diameters.
- The fibers of a given population depict a macroscopic angular dispersion that corresponds to the global misalignment of the axons which has previously been modeled both in ActiveAx [4] and NODDI [5] models using Watson's or Bingham's distributions relying on the knowledge of the principal orientation and of one or two concentration parameters respectively, thus imposing a strong assumption on the nature of angular dispersion.
- The fibers of a given population also depict local tortuosity than can be simply measured by the ratio between the geodesic distance along the curvilinear frame defined by the centroid axis of the fiber and the Euclidean distance between the two extremities of the fiber.
- It is not clear whether the axon diameter and myelin sheath thickness remain constant along the axon; several studies have assumed this absence of variation [18, 19] whereas there is no clear assessment of such a property; in particular, it is known that membrane injury can induce axonal beading for instance due to cytoskeletal damage. According to Budde and Frank [20], beading-induced changes in cell-membrane morphology are sufficient to significantly hinder water mobility and thereby decrease the apparent diffusion coefficient; it is therefore recommended to account for this and allow axon diameter variation.

Accounting for all these observations, we propose an algorithm relying on a six-fold strategy to design white matter mimicking numerical phantoms, that do not present the actual limitations of existing phantom design tools. Such phantoms will allow to go further into the study of the impact of both intra- and extra-axonal compartments on the diffusion signal. In particular, current achievable numerical phantoms do not provide the possibility to induce local fiber tortuosity, which might have a significant impact on the signal stemming from the extra-axonal compartment by modifying the parallel and transverse diffusivities along and perpendicular to the fibers.

The phantom generation algorithm takes a maximal number of $14N_{Populations} + 2$ parameters to generate complex axonal geometries, where $N_{Populations}$ is the number of fiber populations ($N_{Populations} > 1$ in the case of crossing fibers). The list of control parameters used to design a fiber population is summarized in **Table 1**.

Step 1—During the first step of the phantom construction, similarly to state-of-the-art simulation tools, a set of over-simplistic fiber populations is constructed, each fiber population corresponding to a set of rectilinear and parallel outer envelopes. To each population corresponds an orientation, a Gamma distribution of fiber envelope diameters (defined by a mean diameter D and a standard deviation σ_D related to the shape α and scale β of the Gamma distribution, such that $\alpha\beta = D$ and $\alpha\beta^2 = \sigma_D$), and an intracellular fraction, amounting to 4 parameters (**Figure 1A**). In the case of multiple populations, the degree of interweaving of axons from different populations is ruled by 2 scale parameters which control the distance between axons within the same population, thus enabling to create aggregated structures or a sheet organization [21] where axons find their way amongst other populations. At each step of the algorithm, the absence of intersection between the outer envelopes of fibers populating the phantom is ensured using a 3D collision algorithm.

Step 2—Once the fiber populations composed of parallel, rectilinear axons are constructed, the second step of the algorithm consists in the induction of global orientation dispersion requiring one further parameter per fiber population. As depicted in **Figure 1B**, global angular dispersion is created by selecting randomly one fiber among a fiber population. The fiber population is randomly selected among those that did not reach their target angular dispersion yet. Then, a center of rotation is selected along this fiber, following a Gaussian distribution to ensure that most of the selected rotation centers

TABLE 1 | List of control parameters names associated to each step of the phantom generation algorithm.

Geometrical characteristics	Control parameters names	Parameters description
Axon diameter distribution	u	Mean orientation of the population
	Φ	Target volume fraction of the population
	$< D >$	Axon diameter mean value
	σ_D	Axon diameter standard deviation
Global angular dispersion	GAD	Target global angular dispersion
Local tortuosity	LAD	Additional angular dispersion due to tortuosity
Ranvier nodes	$< R >$	Mean ratio (internodal length) / (node width)
	σ_R	Ratio standard deviation
Beading	$< BS >$	Beading spacing mean value
	σ_{BS}	Beading spacing standard deviation
	$< BA >$	Beading amplitude mean value
	σ_{BA}	Beading amplitude standard deviation
Myelin sheath	$< g >$	Mean g-ratio value
	σ_g	g-ratio standard deviation

belong to the central part of the fibers (see **Figure 1B**). A perturbation vector g is then added to the orientation vector **u** of the considered fiber, resulting in a rotation around the center and in a new orientation vector **u'**. Each component of g is obtained randomly, following a Gaussian distribution whose variance is proportional to the target angular dispersion. The proposed rotation is accepted if and only if the modified fiber does not collide with another fiber. The global angular dispersion **AD** is computed as follows:

$$\mathbf{AD} = \frac{1}{\sum_{P\in\mathcal{P}} Card(P)} \sum_{P\in\mathcal{P}} \sum_{f\in P} \theta(u'_f, u_P) \tag{5}$$

where u'_f is the new orientation vector of fiber f in fiber population P, u_P is the principal orientation vector of fiber population P, $\theta(u'_f, u_P)$ is the angle between the two lines supported by u'_f and u_P vectors, $\mathcal{P}$ denotes the ensemble of all fiber populations in the considered field of view and $Card(P)$ corresponds to the number of fibers in each fiber population P.

Step 3—The third step of the phantom generation algorithm consists in the induction of local tortuosity in the geometry. To this aim, one population is randomly selected from the set of populations that did not reach their target angular dispersion yet. One fiber of this population and a point along this fiber are then selected randomly. A random orthonormal trieder (x, y, z) is built such that z corresponds to the local direction u_f of the fiber f. The y-axis of the direct trieder defines the direction along which is applied the tortuosity deformation on the fiber (see **Figure 1C**). This deformation follows a Gaussian distribution with a zero mean and a variance proportional to the tortuosity perturbation value provided as an input. It moves all the points of the fiber in the neighborhood of the selected point that is defined using a tortuosity neighborhood size given as an input parameter of the algorithm for each fiber population. The neighborhood size controls the frequency of the undulations, e.g., the larger this size, the smoother the undulations. Provided that all the deformed points remain in the field of view and that the modified fiber does not collide with any other fiber, the Gaussian deformation is accepted. The induction of local tortuosity is a computationally complex problem. Indeed, the total number of points N_{Points} in the field of view is given by

$$N_{Points} = N_{Populations} \cdot \sum_{P\in\mathcal{P}} \sum_{f\in P} Card(f) \tag{6}$$

where $N_{Populations}$ is the number of fiber populations and $Card(f)$ stands for the number of control points of the centroid of a given fiber f. A typical order of magnitude of N_{Points} is 10^4 which means that at each step of the induction of local tortuosity, the algorithm must check at 10^4 points whether the fibers are colliding, which can be computationally heavy. Thus, our algorithm is based on the construction of a look-up table (LUT) which is updated at each step of the tortuosity induction and whose size is optimized so that we check the intersection at each point of the fiber only with all the points in a neighborhood of this very point. The LUT size must be adequately chosen to optimize the computation time. If the LUT size is too small, collisions might be missed whereas a too large LUT size will drastically increase the computation time.

Step 4—Our phantom generation algorithm also enables to distinguish the myelin sheath from the axon. The axon membrane is created within the fiber envelope with a radius computed from a predefined g-ratio, corresponding to the ratio between the axon membrane diameter and the outer fiber diameter. For each population, the g-ratio follows a Gamma distribution, thus adding two further control parameters for each fiber population. The myelin sheath corresponds to the space between the axon membrane and the outer envelope of the fiber (see **Figure 1D**).

Step 5—The algorithm also accounts for the presence of Ranvier nodes along the myelin sheath (**Figure 1E**). The internodal distance d is set using Equation (4) (maximal conduction relationship [17]). The width w_R of each Ranvier node corresponds to a fraction α_R of the internodal length d such that $w_R = \alpha_R.d$, with α_R typically equal to 10^{-3}, as described in Salzer [16]. This fraction follows a Gamma distribution adding two further control parameters.

Step 6—Finally, our algorithm gives the possibility to represent beading caused by cytoskeletal damage of the axon membrane: the contours of both axonal and outer myelin membranes are swollen using adequate bell-shaped functions like sine functions (see **Figure 1F**). The amplitude and spacing of those lobes both follow a Gamma distribution (adding four control parameters for each fiber population).

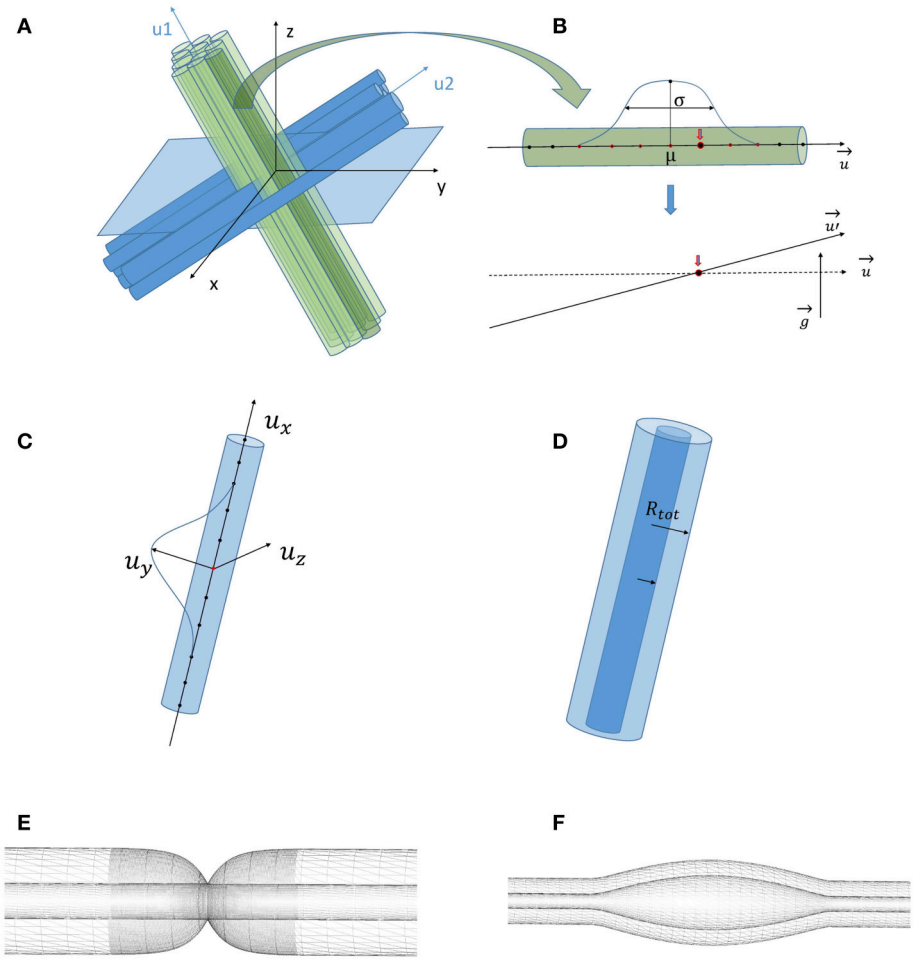

FIGURE 1 | (A) Phantom generation for two populations (blue and green) with orientations u_i **(B)**. Global angular dispersion is created by selecting randomly an axon among a given fiber and a point on this axon which will be the center of rotation of the fiber. The selection of the rotation center follows a Gaussian distribution with mean μ and variance σ. A perturbation vector g whose components follow a Gaussian distribution with a variance proportional to the target angular dispersion is added to the orientation vector u, resulting in a rotation around the selected fixed point and in a new orientation vector u'. **(C)** Local angular dispersion is induced by deforming each axon separately. A point on the axon (in red) and a direct trieder (u_x, u_y, u_z) are chosen randomly. u_y defines the direction of the tortuosity deformation whose amplitude follows a Gaussian distribution with a variance depending on the number of points which are affected by the deformation around the central red point. **(D)** Creation of the myelin sheath. Inside each cylinder of radius R_{tot}, an inner cylinder of radius $R = g.R_{tot}$ (g is the g-ratio) is created which represents the axonal membrane, and the external cylinder represents the outer layer of myelin sheath. **(E)** Creation of Ranvier nodes. The resolution of the fiber mesh around each Ranvier node is refined to better account for the exponential decay of the myelin thickness around the node. **(F)** Beading generation. Both the axonal contour (inner mesh) and the myelin sheath (external mesh) are swollen with a sine function. The myelin sheath thickness is preserved since beading comes from the swelling of the axonal membrane due to injury.

2.2. Multi-compartmental Model for Trapezoidal OG Measurements

Oscillating gradient spin echo (OGSE) sequences are sensitive to diffusion on the time scale of the oscillation period rather than the interval between the pulses and can thus enhance the sensitivity to small axonal restrictions. Recently, an ActiveAx OGSE model was proposed in Ginsburger et al. [10] which accounts for the frequency-dependence of the diffusivity transverse to axons in the extra-axonal space using cosine OGSE schemes. A frequency-dependence correction was proposed for the extra-axonal tensor and showed significant reduction of the fit error. However, the correction derived in Ginsburger et al. [10] is only valid for sinusoidal waveforms, while square (or in practice trapezoidal) wave oscillating gradients maximize sensitivity to smaller pore sizes in comparison with sinusoidal sequences. Indeed, they yield the highest diffusion weighting within one period compared to other periodic waveforms [22], which also makes trapezoidal sequences more clinically feasible. The aim of this section is thus to adapt the previous model proposed in Ginsburger et al. [10] to trapezoidal waveforms.

2.2.1. General Model

White matter tissues are modeled using three tissue compartments embedding three types of micro-structural

environments: intra-cellular, extra-cellular, and cerebro-spinal fluid (CSF) compartments. A common assumption of effectively impermeable axonal walls is used [3–5]. Thus each compartment provides a separate normalized MR signal and no exchange between the populations of water molecules occurs. The resulting model for the diffusion MR signal S can thus be written as

$$S = (1 - \nu_{iso})(\nu_{ic} S_{ic} + (1 - \nu_{ic}) S_{ec}) + \nu_{iso} S_{iso} \tag{7}$$

where S_{ic} and ν_{ic} are the normalized signal and volume fraction of the intra-cellular compartment, S_{ec} is the normalized signal of the extra-cellular compartment, and S_{iso} and ν_{iso} are the normalized signal and volume fraction of the CSF compartment. The model for S_{iso} assumes an isotropic Gaussian distribution of displacements [23]. Water diffusion in the intra-cellular compartment is restricted by axonal walls and further restricted by myelin sheath in case of myelinated fibers. Fibers are assumed to be parallel and oriented along a single direction **n**. Hence, one computes the intra-cellular signal S_{ic} using the Gaussian Phase Distribution approximation of the signal from particles trapped inside a cylinder, which has been derived for trapezoidal OGSE sequences [6, 24]. Diffusion in the extra-axonal compartment is assumed to be hindered. This compartment is generally characterized by a 3D Gaussian displacement distribution:

$$S_{ec} = e^{b\mathbf{G}^T D_{ec}(\mathbf{n}, \nu_{ic})\mathbf{G}} \tag{8}$$

where b is the diffusion sensitization for a given tuning of a diffusion-weighted NMR sequence, **G** represents the gradient magnitude and D_{ec} is the extracellular diffusion tensor. Assuming that the diffusion tensor is cylindrically symmetric, D_{ec} is defined as [5, 25]

$$D_{ec}(\mathbf{n}, \nu_{ic}) = (d - d_\perp(\nu_{ic}))\mathbf{n}\mathbf{n}^T + d_\perp(\nu_{ic}) I \tag{9}$$

where $d_\perp$ is the apparent diffusion coefficient perpendicular to axons and I is the identity tensor [5].

2.2.2. Frequency Dependence of Extra-Axonal Space with Trapezoidal OGSE Sequences

In Ginsburger et al. [10], a correction to the $d_\perp$ component of the extracellular diffusion tensor D_{ec} which describes diffusion perpendicular to the fibers was proposed for cosine OGSE, making the diffusion transverse to the fiber bundle in the extra-axonal space $d_\perp$ dependent on the frequency of the OGSE sequence ω_0 :

$$d_\perp(\omega_0) = d_{\perp,\infty} + A\frac{\pi}{2}|\omega_0| \tag{10}$$

where $d_{\perp,\infty}$ is the bulk diffusion constant [5].

Equation (10) was obtained combining two observations. First, the signal attenuation can be written as a function of the dispersive diffusivity $\mathcal{D}(\omega)$ [26]

$$-\ln S \sim \int \frac{d\omega}{2\pi} q_{-\omega} \mathcal{D}(\omega) q_\omega \tag{11}$$

where q_ω is the Fourier transform of the integral $\int_0^t dt'\, g(t')$ of the applied Larmor frequency gradient $g(t)$. Second, the Fourier transform q_ω of the integral $\int_0^t dt'\, g(t')$ of the applied Larmor frequency gradient $g(t)$ can be written as follows

$$q_\omega = \frac{i\pi\gamma g_0}{\omega_0}\left[\delta(\omega - \omega_0) - \delta(\omega + \omega_0)\right] \tag{12}$$

where δ is the Dirac distribution, for an OG profile $g(t) = g_0 \cos(\omega_0 t)$ and for a sufficiently large number of oscillations $[\frac{\omega_0 T}{2\pi} \gg 1$, T being the total duration of the gradient train $g(t)]$.

Indeed, the presence of these Dirac distributions in q_ω leads to the much simplified expression of the signal attenuation

$$-\ln S(T) \sim b.\, Re\mathcal{D}(\omega_0) \tag{13}$$

which, combined with Equation (2), results in Equation (10).

In the case of cosine trapezoidal OGSE (OGSE-CT), the peak frequency (frequency at which q_ω reaches its maximum) will be the same as for a cosine OGSE (OGSE-C) sequence with the same frequency ω, since the Fourier expansion of the OGSE-CT $f_{trap}(t)$ is a infinite sum of odd cosine functions

$$f_{trap}(\omega t) = \sum_{n=0}^{\infty} a_{2n+1} \cos((2n+1)\omega t) \tag{14}$$

where $|a_{2n+1}|$ is a decreasing sequence. However, it is not *a priori* clear whether the frequency selectivity (which is characterized by both the full-width-half-maximum of the main lobe and the maximum ratio between the side lobes and main lobe amplitudes) will be preserved using OGSE-CT, which might potentially prevent the use of Equation (12) for OGSE-CT. This question was disambiguated in Van et al. [27] who compared the encoding spectrum $F(\omega)$ of both sequences. The encoding spectrum for a OGSE-C sequence is:

$$|F(\omega)|^2 = \left(\frac{\pi\gamma G}{\omega_0}\right)^2 [\delta(\omega + \omega_0) + \delta(\omega - \omega_0)] \tag{15}$$

It was shown that the differences between the encoding spectra of OGSE-CT and OGSE-C waveforms with equal frequency are minimal, thus justifying as well the use of Equation (12) for OGSE-CT sequences having a high selectivity around the frequency ω_0 of interest (see also **Figure 2**).

Consequently, the same frequency-dependence correction of the extra-axonal space tensor (Equation 10) can be used for both OGSE-C and OGSE-CT waveforms.

2.3. Monte-Carlo Simulations and NMR Signal Synthesis

The Diffusion Microscopist Simulator (DMS) [13] relies on a three-fold architecture:

- a 3D phantom generation engine
- a Monte-Carlo simulator engine
- a DW-NMR signal synthesizer

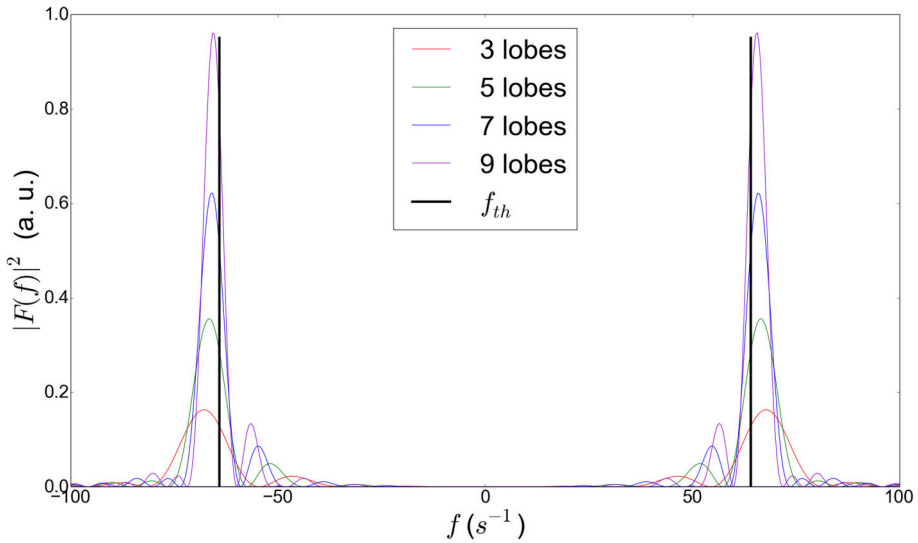

FIGURE 2 | Power modulation spectra for trapezoidal cosine OGSE gradient waveforms at 64 Hz for different number of half periods (or lobes), showing the influence of the number of lobes on the frequency selectivity. The theoretical peak frequency is denoted as f_{th}. We observe that the difference between this theoretical peak and the actual frequency peak of the sequence decreases with increasing number of lobes. The actual frequency peak (not the theoretical one) of the OGSE sequences employed in this article is fed in our model for better precision.

The 3D phantom generation engine, improved using our novel algorithm to produce biomimicking numerical phantoms, creates the 3D triangulated surfaces from the fiber descriptions. It includes two non-linearly sampled curves (also called axon and outer myelin sheath membrane centroids), and two profiles of radii to represent the axon membrane and the outer myelin sheath membrane, respectively.

The Monte-Carlo simulator engine is composed of several element that have to be individually tuned:

- A scene modeler that contains the description of the evolving simulated space, including the dimensions of the simulation domain corresponding to a global bounding box set to $(-60, +60, -60, +60, -60, +60\,\mu\text{m})$ in all our simulations, the temporal resolution set to 10 μs, the number of simulation steps set to 50,000, the set of membranes generated by the 3D phantom generation engine and the set of particles used to perform the Monte-Carlo simulation (10^6 particles in our simulations).
- A motion model that drives the motion of particles, set to a Brownian random walk model tuned using a parameter corresponding to the diffusivity of the medium (2.0×10^{-9} m^2/s in our simulations).
- A membrane model built for each individual axon or outer myelin membrane that integrates:
  - the triangulated surface itself
  - a particle-to-membrane interaction model set to the total reflexion interaction in our case
  - a vertex evolution function set to static in our case (DMS is also able to deal with a temporal evolution of the membranes that is not used in this work)
  - a polygon cache that facilitates and speeds up the computation of the list of the closest membrane triangles likely to interact with a particle of arbitrary position in the simulation domain
  - a particle or random-walker model that represents water molecules moving in the simulation domain. Particles are randomly distributed either over the whole simulation domain, or only in the intra- or extra-cellular space. In this work, two types of simulations were performed, either with particles randomly distributed in the whole domain or restricted to the extra-cellular space (see **Figure 3**), since the present study is focused on the characterization of the extracellular space signal for different levels of structural disorder.

The trajectories of random walkers computed using the Monte-Carlo simulator engine are fed into the diffusion-weighted NMR signal synthesizer, which synthesizes a volume of DW-MRI signals for a given DW-MRI sequence and for a specific tuning of the sequence parameters. The DW-NMR signal synthesizer is also composed of several elements that have to be individually tuned:

- A DW-NMR sequence factory that allows to simulate the chronograms of gradients and radio-frequency pulses; several schemes are available (bipolar double STEAM sequence, bipolar STEAM sequence, multiple PGSE sequence, single PGSE sequence, twice refocused spin echo sequence, OGSE sequence); in this work, a trapezoidal OGSE sequence was tuned (see **Figure 4**), requiring to define the period of oscillating gradients (varying in this study), the gradient time resolution (10.0 μs), the maximum gradient slew rate and the

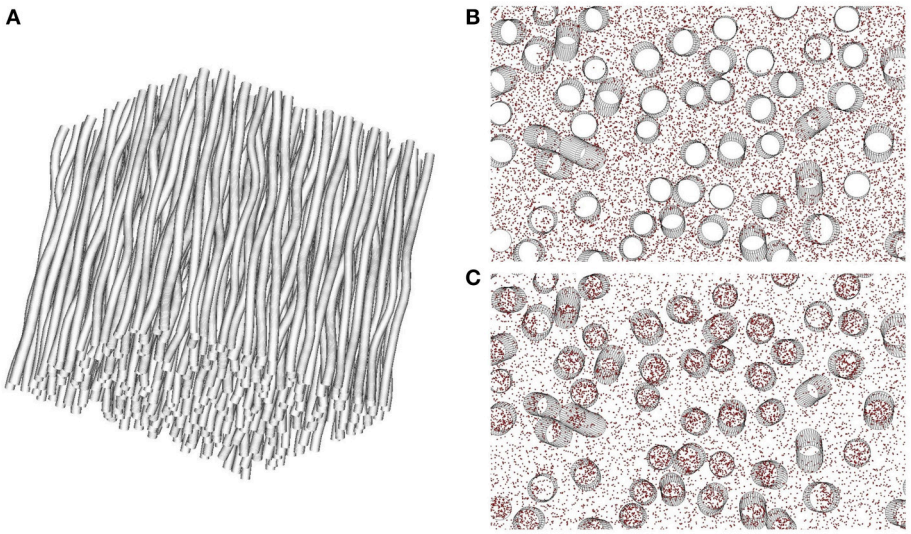

FIGURE 3 | Illustration of the two simulation modalities available in DMS on an example mesh **(A)** with intracellular volume fraction of 0.2 and 5° angular dispersion induced by tortuosity. In **(B)** corresponding to a cross-section of **(A)**, random walkers for Monte-Carlo simulation of the diffusion process are placed only in the extra-axonal space, with impermeable membranes. The obtained signal thus stems exclusively from the extracellular space. In **(C)**, particles are initially placed in both intra- and extra-cellular compartments, with impermeable membranes. The diffusion process is thus simulated in both compartments, without exchange between them.

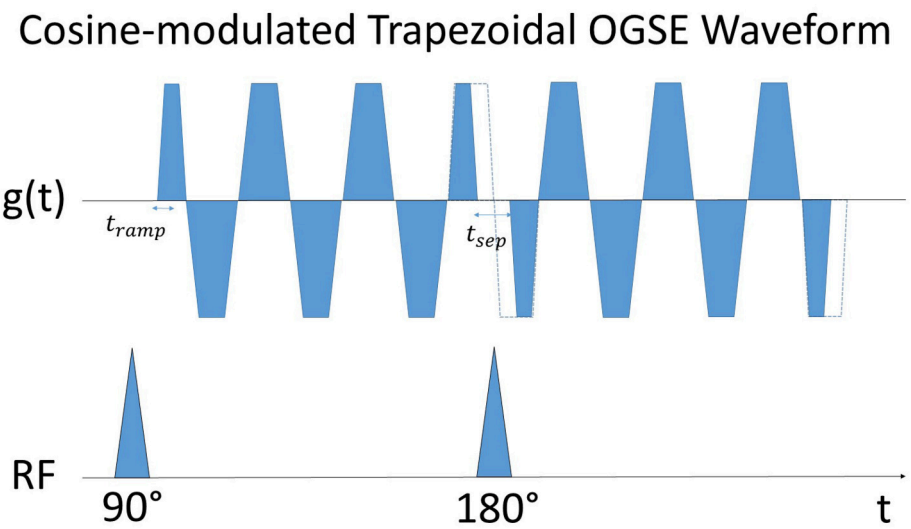

FIGURE 4 | Schematic representation of the employed trapezoidal cosine OGSE gradient waveform, here with six lobes (half-periods) before and after the 180° refocusing pulse. The separation between gradient waveforms, t_{sep}, is required to accomodate the 180° RF pulse, and has been set to allow a continuous single frequency oscillating gradient to be drawn between the two waveforms to obtain a narrower peak at the desired frequency [28]. The duration of the shorter lobes are increased by half the gradient ramp time, t_{ramp}, to ensure zero cumulative gradient area.

maximum gradient magnitude (respectively 200 T/m/s and 80 mT/m corresponding to the latest Connectome gradient coils available for 3T MRI systems on the market).

- A Cartesian grid defined within the MC simulation domain using a local bounding box and the 3D volume size; in our case, to avoid boundary effects, the local bounding box was chosen slightly smaller than the global bounding box of the MC domain and set to (−55, +55, −55, +55, −55, +55 μm).
- A noise model to simulate the actual level of noise corrupting the signal of real acquisitions; the analysis of the impact of the noise on the signal of the extra-cellular space and on the inference of the structural white matter disorder has been done for four different values of SNR in this study: an infinite value corresponding to the absence of noise, a SNR of 30 corresponding to state-of-the-art experimental conditions with the latest 3T clinical MRI systems available on the market,

and SNR of 20 and 10 corresponding to worse experimental conditions.
- A spin model associated to each random walker in charge of accumulating the net phase evolution induced by the trapezoidal OGSE sequence and seen by the random walker along its trajectory. Although they clearly influence the SNR when long echo times are chosen, the effects of T1/T2 relaxation have not been taken into account by the spin model in the performed simulations.

The synthesized DW-MR image consists of a 3D volume corresponding to the T_2 reference volume at $b = 0$ s/mm^2 (set to 10,000 in our case) and a 4D volume corresponding to the employed trapezoidal OGSE sequence along a set of uniformly distributed diffusion directions over the unit sphere (300 directions in our case).

2.4. Estimation of the Scaling Coefficient *A* with Simulations

Monte-Carlo Simulations were launched by placing 10^6 particles in the extra-axonal space of each studied white matter numerical phantom. The employed phantoms composed of a single fiber population, listed in **Table 2**, have an intracellular volume fraction of 0.2 and the fiber radii follow a Gamma distribution whose shape and scale parameters α and β are set to obtain a mean diameter $\alpha\beta = 2.0\,\mu$m and a standard deviation $\alpha\beta^2 = 0.2\,\mu$m. The signal obtained from diffusion MRI data synthesis comes only from the extra-axonal space, since the fiber membranes were set to be impermeable. Thus, the intra-cellular volume fraction was set to 0 in the employed multi-compartment model. For each studied geometrical configuration, 4D DW-volumes were synthesized for five distinct frequency values of the employed trapezoidal OGSE sequence : 60, 70, 80, 90, and 100 Hz. In order to have a constant b-value of 200 s/mm^2 and a constant TE of 116ms, the gradient magnitude was varied up to 80 mT/m (corresponding to the maximum achievable gradient magnitude of modern clinical 3T MRI systems) and the number of lobes (half-periods of the OGSE sequence) on each side of the refocusing pulse was also varied, as follows: 6, 8, 8, 10, and 12 lobes/50, 57, 70, 75, and 80 mT/m for encoding frequencies of 60, 70, 80, 90, and 100 Hz. **Figure 4** gives an illustration of the employed trapezoidal OGSE sequence. The multiple-frequency sampling enables to perform a linear fitting procedure on Equation (10) in order to obtain reliable estimates of the scaling coefficient A of the extra-axonal perpendicular diffusivity linear-in-frequency term. The error associated to the linear fit was assessed using the covariance matrix returned by the linear least-square procedure employed to estimate the scaling

TABLE 2 | Values of the control parameters of the phantom generation algorithm for each studied configuration (C1 to C5).

	C1	**C2** $C2_{1.5°}$|$C2_{2.5°}$| $C2_{3.5°}$|$C2_{4.5°}$	**C3** $C3_{5°}$|$C3_{10°}$| $C3_{15°}$|$C3_{20°}$	**C4** $C4_{R32}$|$C4_{R16}$| $C4_{R8}$|$C4_{R4}$	**C5** $C5_{BS80}$|$C5_{BS60}$| $C5_{BS40}$|$C5_{BS20}$
u	(0.0, 0.0, 1.0)	(0.0, 0.0, 1.0)	(0.0, 0.0, 1.0)	(0.0, 0.0, 1.0)	(0.0, 0.0, 1.0)
Φ	0.2	0.2	0.2	0.2	0.2
$< D >$	2.0 μm	2.0 μm	2.0 μm	2.0 μm	2.0 μm
σ_D	0.2 μm	0.2 μm	0.2 μm	0.2 μm	0.2 μm
GAD	0°	1.5°|2.5°| **3.5°**|4.5°	3.5°	3.5°	3.5°
LAD	0°	2.5°	5°|10°| **15°**|20°	15°	15°
$< R >$	Ø	Ø	Ø	**100** 32|16| 8 | 4	100
σ_R	Ø	Ø	Ø	5	5
$< BS >$	Ø	Ø	Ø	Ø	80.0 μm|60.0 μm| 40.0 μm|**20.0** μm
σ_{BS}	Ø	Ø	Ø	Ø	20.0 μm|15.0 μm| 10.0 μm|**5.0** μm
$< BA >$	Ø	Ø	Ø	Ø	1.5
σ_{BA}	Ø	Ø	Ø	Ø	0.5
$< g >$	Ø	Ø	Ø	0.6	0.6
σ_g	Ø	Ø	Ø	0.05	0.05

*In configurations C2–C5, one or two parameters are varied: GAD for C2, LAD for C3, $< R >$ for C4, $< BS >$ and σ_{BS} for C5. The parameter value in bold corresponds to the default value used to generate each configuration, which are employed in **Figure 9** to study the evolution of the scaling coefficient A for different types of structural disorder. Other values below correspond to variants of each configuration, which are employed in **Figure 10** to study the evolution of A with respect to the variation of one given geometrical parameter, associated to one specific disorder type.*

coefficient A in Equation (10). These fitting errors are represented by error bars in figures giving estimated values of A for various geometric configurations (see section 3).

The evolution of the scaling coefficient A with respect to the various sources of disorder is explored by simulating the diffusion process within the geometric configurations presented in **Table 2** (configurations C1–C5, as well as some variants of those configurations). **Table 2** provides the list of all the control parameters as well as their values employed for the construction of the numerical phantoms. The purpose is to catch the complex dependence of A with respect to geometrical characteristics of the diffusion medium. The degree of complexity of the employed numerical phantom is fully monitored using the DMS simulator, thus enabling a very precise study of the influence of each parameter on the fitted coefficient A.

3. RESULTS

3.1. Numerical Phantoms Mimicking White Matter

We present in this section numerical phantoms generated with our novel algorithm. **Figure 5** represents various configurations with one, two, and three fiber populations and with or without global angular dispersion. **Figure 6-1** represents a set of straight parallel fibers randomly placed in the phantom volume, with mean fiber diameter of 2.0 μm (diameter variance of 0.2 μm) and volume fraction of 0.1. In **Figure 6-2**, global angular dispersion is induced, enabling to reach 5.6° of angular dispersion (for a target value of 10°). The tortuosity induction (**Figure 6-3**) brings this angular dispersion up to the 10° target. **Figures 6-4,5** illustrate the creation of myelin sheath and Ranvier nodes which account for the actual structure of myelinated fibers. Beading -consisting in a swelling of both axonal and myelin sheath membranes—is also handled (**Figure 6-6**). In all presented surface renderings, there is no collision between the membranes. **Figure 6-6** presents a realistic geometry mimicking a complex white matter environment, taking into account all the putative deformations of membranes observed in real tissues (angular dispersion, tortuosity, myelination and creation of Ranvier nodes, beadings). We note that the generated phantoms have been presented here in the case of multiple fiber populations for more generality. However, the simulations performed to study the structural disorder of white matter in next sections only used phantoms with a single fiber population. While essential to make our approach directly applicable to most white matter regions, the study of the structural disorder induced in crossing areas of multiple fiber populations is out of the scope of this study. This topic is addressed in the section 4.

3.2. Measuring Structural Disorder in the Extra-Axonal Space

3.2.1. Validation of the Employed Trapezoidal OGSE Model

A linear relationship between the extra-axonal perpendicular diffusivity and the frequency of the employed trapezoidal OGSE sequence is shown in **Figure 8**, where the frequency was varied from 60 to 100 Hz at a constant b-value of 200 s/mm^2. This result validates the use of Equation (10).

3.2.2. Studying Different Types of Structural Disorders

Monte-Carlo simulations were run in geometries characterized by increasing structural complexity. In what follows, the different geometrical configurations were classified according to the type of structural disorder they represent, from configurations C1 to C5. **Table 2** lists all the employed geometrical configurations and gives the associated set of control parameters.

In configuration C1 (**Figure 7**), parallel axons are randomly placed in the simulation volume. The centers of the cross section of the cylinders representing the axons follow a uniform distribution. The diameters follow a Gamma distribution, with a mean axonal diameter of 2.0 μm. The value of the scaling coefficient A reaches its maximum value of 9.09 μm^2 (all the values of A are given for a SNR of 30) in this configuration which corresponds exactly to the 2D short-range disorder geometry described in Burcaw et al. [7] and Novikov et al. [11] . From C1 to C2, the induction of global angular dispersion (fibers remain straight but are rotated to induce angular dispersion) of 3.5° yields to a substantial diminution of the scaling coefficient from 9.09 down to 8.54 μm^2. Local tortuosity is induced in configuration C3 (fibers are deformed to induce angular dispersion), enabling to reach an angular dispersion value of 15° and yielding a moderate decrease of the scaling coefficient from 8.54 down to 8.26 μm^2. The addition of Ranvier nodes along the myelin sheath (with a g-ratio of 0.6) in configuration C4 does not significantly change the value of the estimated A coefficient with respect to the previous configuration ($A = 8.24\,\mu$m^2 vs. $A = 8.26\,\mu$m^2 in configuration C3, which is negligible given the fitting uncertainty at a SNR of 30). From C4 to C5, beading is introduced (swelling of the axonal membrane and myelin sheath) with amplitudes equal to 1.5 times the fiber radii in average, and mean spacing of 20.0 μm, yielding a significant decrease of A (up to 19% with A going from 8.32 to 6.76 μm^2).

It appears from **Figures 7A–D**. that the diffusion signal variation between configuration C1 and configurations C2–C5 is stronger for diffusion sensitization directions perpendicular to fibers, meaning that most of the information stemming from the increasing complexity of the studied geometrical configurations is included in the evolution of perpendicular diffusivity. **Figure 7** also clearly indicates that beading (corresponding to configuration C5) has the strongest effect on the perpendicular diffusivity. This result can be directly related to the important variations of A observed in configuration C5, as reported previously.

3.3. Understanding the Quantitative Influence of Each Disorder Parameter

The different configurations studied in **Figure 9** correspond to qualitatively different geometric configurations. The quantitative evolution of the structural disorder coefficient A with respect to each geometrical parameter has also been studied (see **Figure 10**), by varying one geometrical parameter in each configuration separately. The evolution of each parameter is explained in **Table 2**.

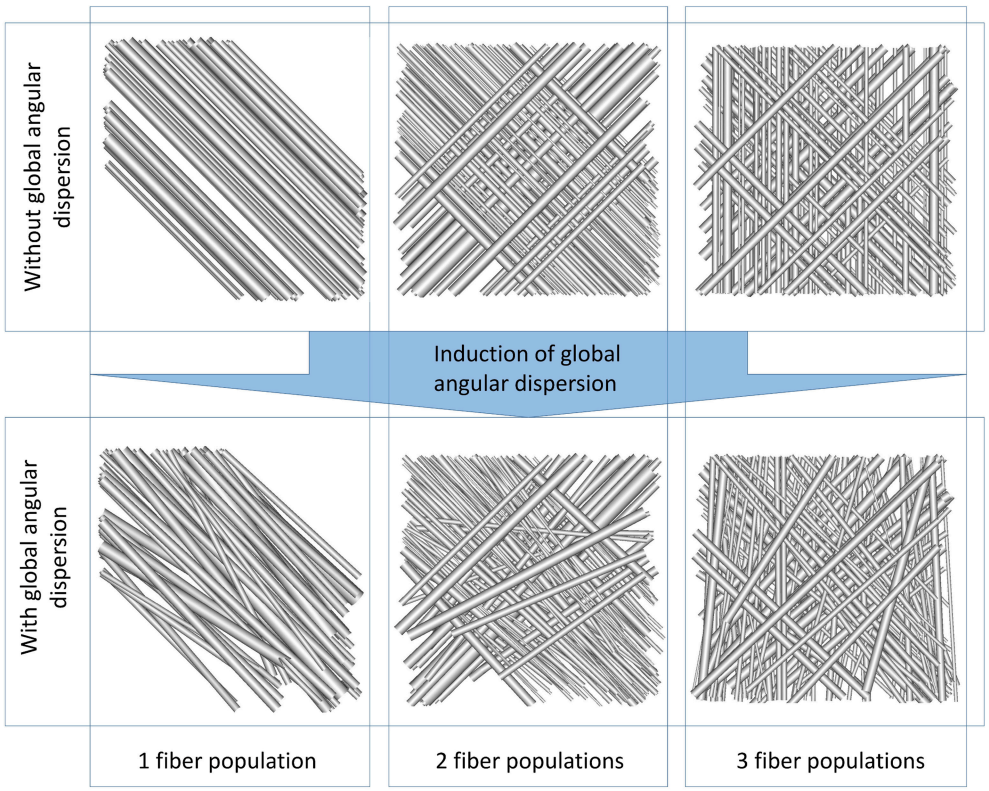

FIGURE 5 | (Top) Surface renderings of outer fiber envelopes corresponding to one (left), two (middle), and three (right) fiber populations with intracellular fraction of 0.06 for one population, 0.03 each for the two populations, 0.02 each for the three populations and mean diameters 2.5 μm (one population), 1.5 and 2.5 μm (two populations), 1.5, 2.0, and 2.5 μm (three populations). **Bottom** same as top. with global angular dispersion of 10° for the single population, 5.5 and 8.5° for the two populations, 5.5, 6.7, and 8.5° for the three populations (for a target angular dispersion of 10° each).

The induction of global angular dispersion from 0° to 4.5° in configuration C2 (see **Table 2**) results in a decrease of the scaling coefficient A (see **Figure 10A**) from 9.09 to 8.43 μm^2 for the biggest value of global angular dispersion of 4.5°. The diminution of A gets stronger for increasing values of global angular dispersion. However, the study of the influence of global angular dispersion on A was limited to small values of angular dispersion, owing to the fact that higher values of angular dispersion were not reachable for the specific fiber density and radii distribution of C2. These values of angular dispersion are far from the values of microscopic misalignments of axons estimated up to 18° [29]. One possibility to reach this target is to decrease the intracellular volume fraction. Another option consists in increasing angular dispersion using local tortuosity, as was done in configuration C3. The induction of tortuosity in this configuration causes a moderate decrease of the scaling coefficient from 8.54 μm^2 corresponding to configurations C2 (global angular dispersion of 3.5°) to 8.24 μm^2 for the biggest tortuosity value (20° of angular dispersion), as shown in **Figure 10B**.

In configuration C4 (corresponding to a global angular dispersion of 3.5° and to a total angular dispersion of 15° after the induction of tortuosity, with the presence of Ranvier nodes), a small increase of the scaling coefficient is observed due to demyelination, from 8.24 up to 8.32 μm^2 for a demyelination ratio of 25% (see **Figure 10C**), which is not significant given the uncertainties of the estimated values of A at a SNR of 30.

The introduction of beading in configuration C5 causes important variations of the scaling coefficient A (**Figure 10D**). As mentioned previously, a mean beading spacing of 20.0 μm yields a significant decrease of A (up to 19% with A going from 8.32 to 6.76 μm^2 The scaling coefficient $A = 7.95\,\mu m^2$ is still 4.5% smaller for a beading spacing of 100.0 μm, corresponding to a low density of beads, than in the absence of beading where $A = 8.32\,\mu m^2$.

4. DISCUSSION

4.1. White Matter Biomimicking Numerical Phantoms

Designing realistic numerical phantoms of white matter tissue seems to be a promising approach to study the influence of various structural properties of white matter on the measured diffusion signal. Being able to construct biomimicking simulations geometries without using histological samples is an essential step toward the comprehension of the specific effect of

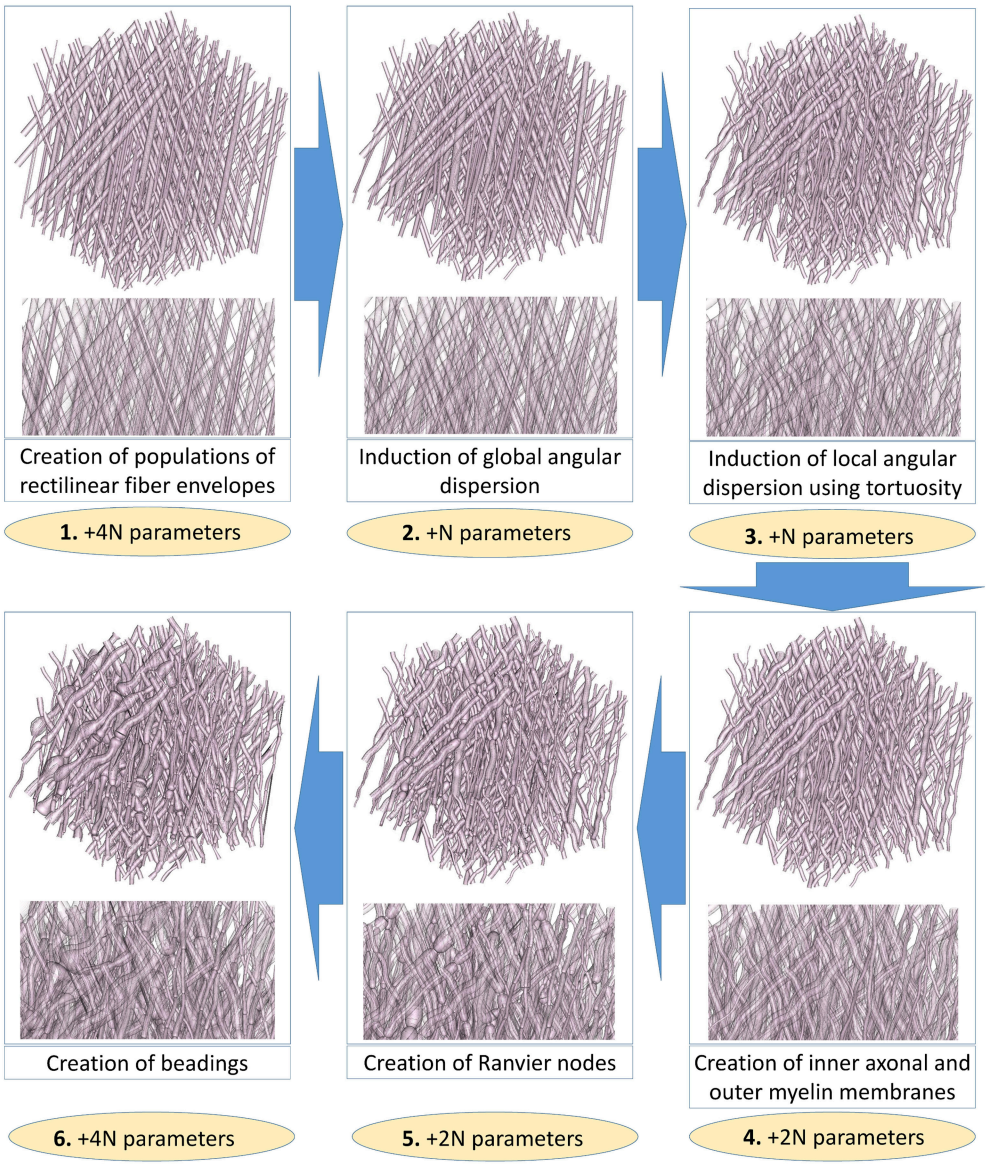

FIGURE 6 | (1) Surface renderings corresponding to three fiber populations with mean diameters 1.5, 2.0, and 3.0 μm, respectively with intracellular volume fraction of 0.05 each. *N* is the number of populations in general (here $N = 3$). **(2)** Global angular dispersion is induced (4.7, 2.5, and 2.8° per population). **(3)** Tortuosity is induced, enabling to reach 10° of angular dispersion for each population. **(4)** Creation of the myelin sheath. **(5)** Creation of Ranvier nodes with mean ratio 1,000 between internodal length and node width. **(6)** Creation of beadings with 20.0 μm mean inter-beading length and beading magnitude ratios of 1.7, 1.5, and 1.2, respectively.

each geometrical characteristic of the diffusing medium on the obtained signal. An important aspect of our phantom generation algorithm is its ability to deal with multiple fiber populations, which was reported to represent up to 60% of the number of voxels of a mask of the brain white matter at a spatial resolution of 2 mm [15]. However, generating phantoms with multiple fiber populations come with additional difficulties, notably related to the generation of global angular dispersion. Phantoms presented in **Figure 5** exhibit geometrical configurations with multiple fiber populations. In **Figure 5**, the target angular dispersion value of 10° can be reached only in the single population case for an intra-cellular fraction of 0.2. The maximum reachable global angular dispersion strongly depends on the number of fiber populations, on the distribution of radii and on the target intra-cellular volume fractions of these populations (for instance, the lower the intra-cellular fraction, the higher the reachable angular dispersion). The use of tortuosity is essential to reach high values of angular dispersion in multiple population configurations. Indeed, in **Figure 6-2**, the induction of global dispersion enables to reach 5.6° of angular dispersion (for a target of 10°). The tortuosity induction (**Figure 6-3**) brings this angular dispersion up to the 10° target.

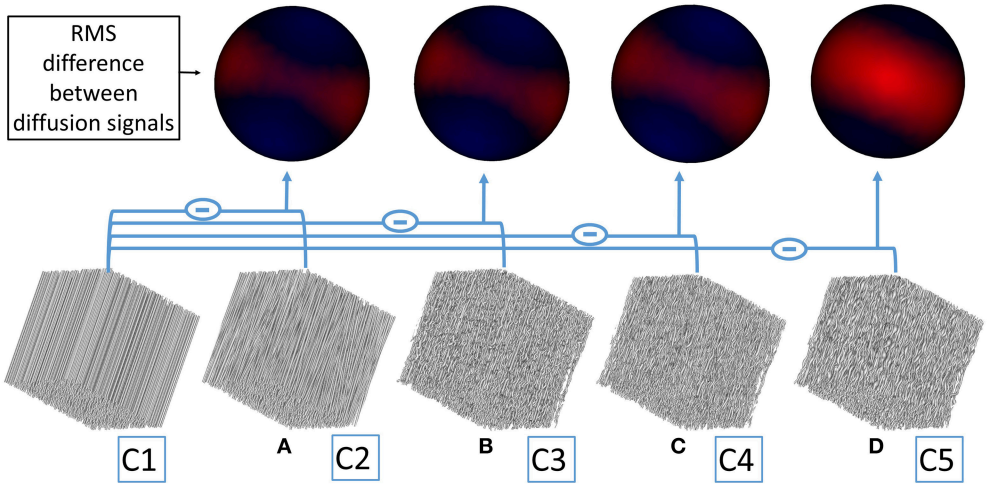

FIGURE 7 | From left to right, simulation domains corresponding to different geometrical configurations (from C1 to C5) are shown. A 3D rendering of the root-mean-squared difference (represented by the minus sign) between the diffusion signal stemming from each configuration and the "reference" configuration C1 (most left configuration composed of straight parallel cylinders) is shown on a spherical surface. **(A)** The RMS signal difference is computed between configuration C1 and C2. The red area where the diffusion signal difference is the strongest corresponds to diffusion sensitization directions perpendicular to fibers. Blue areas correspond to directions parallel to fibers where the signal differences are weaker but not null, and originate from the variations of diffusion properties around those directions when structural disorder is added. **(B–D)** Represent the same RMS signal differences between configurations C1 and C3, C1 and $C4_{R4}$ (corresponding to configuration C4 with a demyelination ratio of 25%, see **Table 2**), C1 and C5, respectively.

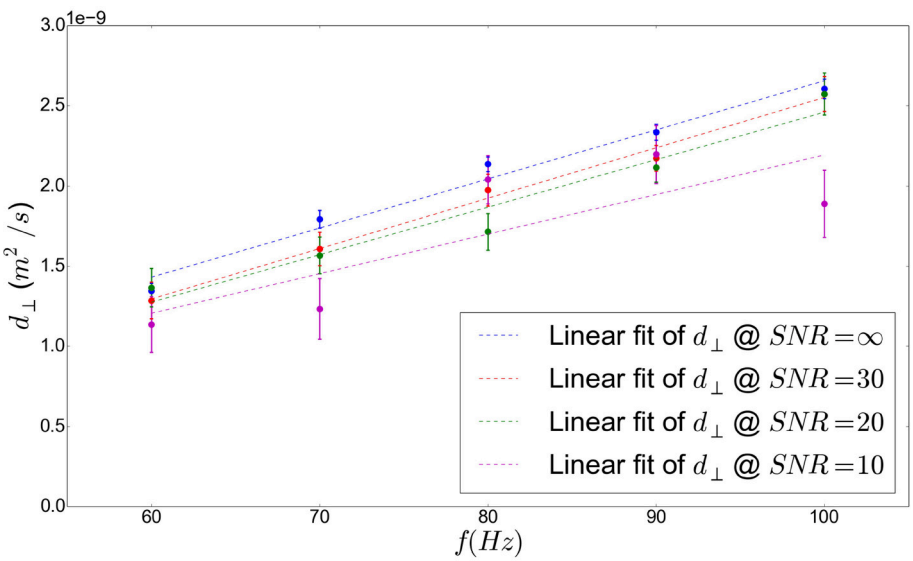

FIGURE 8 | Frequency-dependent perpendicular diffusivity in the extracellular space measured by performing Monte-Carlo simulations with diffusing particles in the extracellular space of configuration C1 (see **Table 2**), plotted against the frequency of the employed OGSE-CT sequence. A linear fit is also plotted which shows the linear dependence of diffusivity to frequency.

4.2. Characterizing Structural Disorder with *A*

As shown in **Figure 7**, the differences between diffusion signals obtained by simulating the diffusion process in the extra-axonal space of various geometrical configurations are predominant in the diffusion direction perpendicular to fibers, although there exists differences in all directions. This observation shows that most of the structural disorder effects are caught by the diffusion signal around the equator perpendicular to the mean fiber orientation. Modeling structural disorder using an additional term in the extra-axonal perpendicular diffusivity thus appears to be physically reasonable.

Across all configurations, at a SNR of 30, the values of the scaling coefficient A vary between 9.09 and 6.77 μm^2 which is

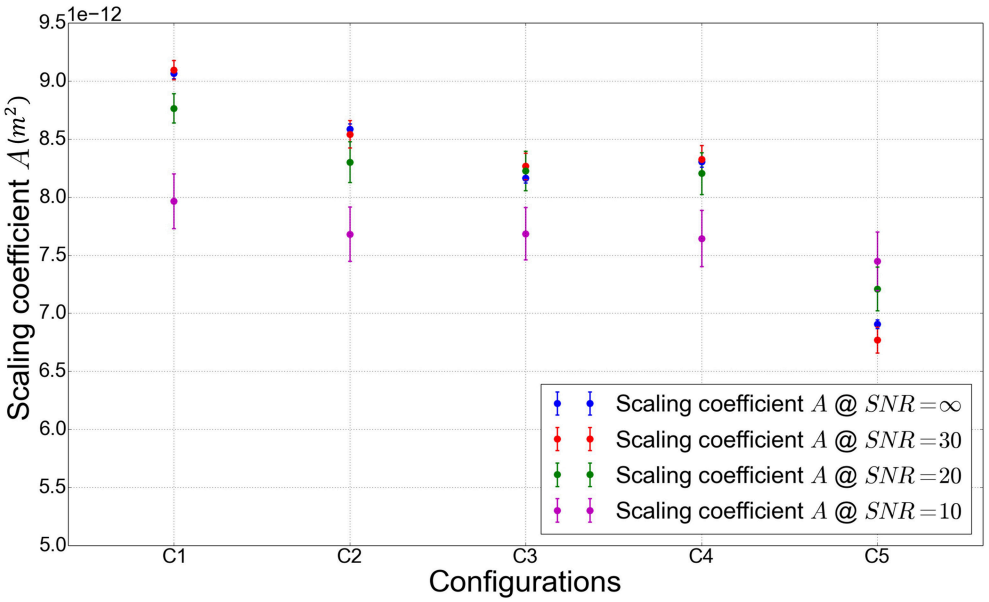

FIGURE 9 | Value of the scaling coefficient A in m^2 for geometric configurations with increasing structural disorder. The simulation are performed in configurations C1–C5, whose design parameters are summarized in **Table 2**.

consistent with previous studies [7, 8] reporting the empirical law $A \sim l_c^2$ were the correlation length l_c closely follows the mean external radius of the fibers. Indeed, in our case the mean axonal diameter is equal to 2.0 µm yielding $l_c \sim 1.0\,\mu m$, which leads to $A \sim 1.0\,\mu m^2$. This value corresponds to the order of magnitude of the fitted values of A.

As reported in Fieremans et al. [8], the effect of angular dispersion introduced in configurations C2 and C3 on the estimated perpendicular diffusivity can be understood by considering the diffusion process along each fiber in the presence of orientational dispersion. When the orientation of a given fiber differs from the mean orientation of the fibers population, the diffusion process along this fiber yields a local parallel diffusivity whose projection on the plane perpendicular to the mean fiber population direction is not null. Due to this projection effect, the existence of longitudinal frequency-dependence along each elementary fiber will yield a frequency-dependence of the global perpendicular diffusivity. Thus, the frequency-dependence observed in our work might not only originate from the 2D short-range disorder in the plane transverse to axons, but might also be partly explained by the contamination of the perpendicular diffusivity (and thus of the scaling coefficient A) with longitudinal diffusion frequency-dependence. As a consequence, in addition to modeling the 2D short-range disorder in the plane perpendicular to fibers, the estimated scaling coefficient A might also embed some information related to physical properties along the fibers. While this hypothesis makes the physical interpretation of the coefficient A tricky, it would enable to obtain information from both parallel and perpendicular extra-axonal diffusion processes by measuring only one coefficient. The interest of such an approach is that the estimation of A relies on a simple and robust fitting procedure. It only requires to perform data acquisition using trapezoidal OGSE sequences with a sufficient number of frequencies to be able to fit the data properly, which is clinically feasible.

The introduction of Ranvier nodes in configuration C4 does not yield to a significant change in the scaling coefficient A. This is not surprising since Ranvier nodes correspond to a very low volume fraction of the extracellular space, due to their low width, reported to correspond on average to a few thousandths of the internodal length [16], which is amplified by the low intracellular fraction of 0.2 employed in our simulations. In **Figure 10C**, demyelination is mimicked by progressively increasing the width of the Ranvier nodes, from 1 to 25% of the internodal length. The observed increase of the scaling coefficient A is again small (up to 3% for the maximal demyelination ratio of 25%, roughly corresponding to the percentage of demyelinated areas observed in the cerebral cortex of multiple sclerosis patients [30]).

In this study, only the structural effects of Ranvier nodes and demyelination on diffusion properties in the extra-axonal space were studied. However, from the diffusion point of view, the most interesting feature of Ranvier nodes and unmyelinated regions areas is that they represent those regions along a myelinated axon where the exchange between intra- and extra-axonal water is the fastest. The analysis of the effect of such an increased exchange would be of great interest to thoroughly study the effect of Ranvier nodes and demyelination on the scaling constant A. Indeed, in the Appendix F of Burcaw et al. [7], the authors theoretically tackled this problem and their prediction is that the values of the scaling constant A may or may not be affected by the exchange, depending on the exchange regime (slow, intermediate, or fast). Their theoretical analysis

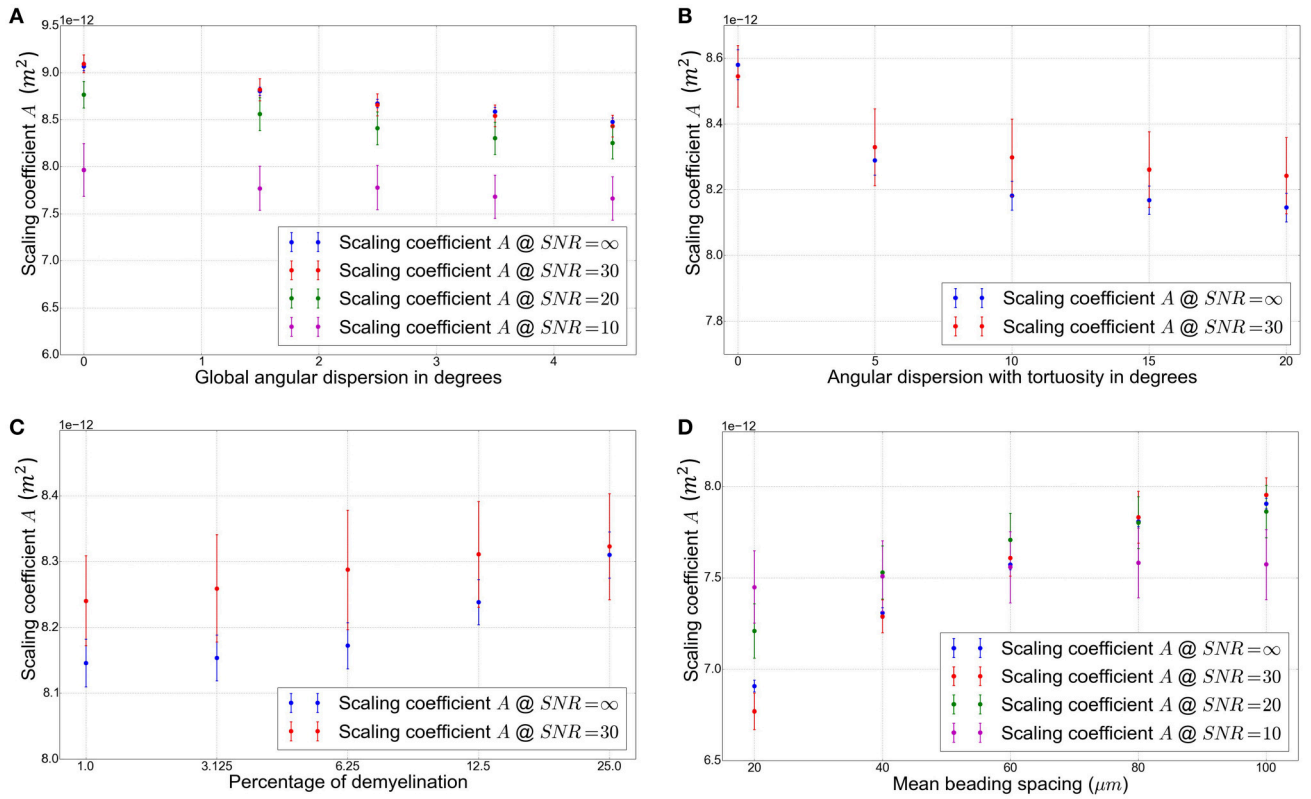

FIGURE 10 | (A) Value of the scaling coefficient *A* in m^2 plotted against the global angular dispersion. The simulations were performed in variants of configuration C2 by varying the global angular dispersion value (see **Table 2**). **(B)** Value of the scaling coefficient *A* plotted against the angular dispersion. The simulations were performed in variants of configuration C3 by varying the local tortuosity value (see **Table 2**). **(C)** Value of the scaling coefficient *A* plotted against the percentage of demyelination. The simulations were performed in variants of configuration C4 by varying the percentage of demyelination, directly related to the width of Ranvier nodes (see **Table 2**). **(D)** Value of the scaling coefficient *A* plotted against the mean beading spacing. The simulations were performed in variants of configuration C5 by varying the value of the mean beading spacing (see **Table 2**). A bigger spacing yields to a lower beading density.

takes into account a general uniform exchange of molecules between intra- and extra-axonal space. However, the Ranvier nodes and demyelination around them would introduce a local exchange linked to the disorder with which the Ranvier nodes occurs within the voxel. In this condition, it is not clear if the argument in Burcaw et al. [7] still holds. This question will be investigated in a future work.

4.3. The Strong Influence of Beading on the Scaling Coefficient *A*

The value of the scaling coefficient *A* appears to be mostly influenced by the local enlargement of both axonal and myelin membranes, also called beading. Indeed, **Figure 9** shows a significant decrease of *A* (up to 19%) in the presence of beading.

According to **Figure 10D** the scaling coefficient is still 4.5% smaller for a beading spacing of 100.0 µm than in the absence of beading, suggesting that *A* could be a putative marker of the presence of beading, since *A* is significantly reduced even for a lower density of beadings within the phantom.

The influence of beading on the diffusion signal has been extensively studied in Budde and Frank [20], where it was emphasized that neurite beading might explain the decrease of the apparent diffusion coefficient after ischemic stroke. Our results point in the same direction, since the significant decrease of the coefficient *A* in case of beading induces a net decrease of the transverse diffusivity which results in a diminution of the apparent diffusion coefficient. However, in Budde and Frank [20], simulations were run on numerical phantoms with an hexagonal packing of fibers and periodic restrictions along the fiber. The periodicity of the employed simulation domain might affect the realism of the obtained diffusion signal since it does not reflect the 1D short-range disorder along white matter fibers nor the 2D short-range disorder in the plane transverse to fibers [7, 11]. In our simulations, short-range disorder effects are expected to be accounted for, since the spacing between each beading is highly variable (as shown in **Table 2**, the variance of the spacing distribution is equal to one fourth of the spacing value) and the fibers are randomly placed in the phantom, thus mimicking transverse short-range disorder better representing actual brain white matter tissues.

The extracellular diffusion signal obtained from our simulations thus gives a more realistic view of the effect of beading on the transverse diffusion coefficient, which appears to be quantitatively significant. As discussed earlier, the effect of

beading on the scaling coefficient A might partly originate from the hindrance of extra-axonal diffusion along the beaded fibers, due to the projection of parallel diffusivity on the transverse plane, as a consequence of angular dispersion.

The effect of beadings on the intra-cellular diffusion process -which is not studied in this work- might also be quantitatively substantial, as suggested in Marco et al. [31]. In this work, the sensitivity of the diffusion signal of intracellular metabolites with respect to beaded structures was studied using Monte-Carlo simulation of brain metabolites dynamics, which can be compared, from the numerical simulation point of view, with the waters one after proper scaling. A clear dependence of both radial and axial intracellular dispersive diffusivities with respect to the frequency of the employed OGSE sequence in the presence of beadings was observed. Moreover, results of MC molecular diffusion simulations in complex synthetic substrates mimicking the presence of beads showed a clear $1/\sqrt{t}$ dependence of the axial intracellular Apparent Diffusion Coefficient due to 1D short-range disorder introduced in the axial direction by the randomly placed beads, in good accordance with theoretical predictions in Burcaw et al. [7] and Novikov et al. in [11]. Indeed, beadings are supposed to primarily affect the diffusion process along the fibers and a $1/\sqrt{t} \sim \sqrt{\omega}$ frequency-dependence of the parallel diffusivity in the intra-cellular space of beaded axons is expected. Similarly to what was done in Marco et al. [31] for intracellular metabolites, an interesting approach would be to capture directly the effect of beading on the intra-cellular parallel diffusivity $\sqrt{\omega}$ term, by performing 3D Monte-Carlo simulations of spin dynamics in the intra-cellular space and fitting the scaling factor of the $\sqrt{\omega}$ term for various beaded geometrical configurations. The amount of variation of this "intra-cellular disorder" scaling factor in the presence of beading could be compared to the variation of the scaling factor A studied in this work. Moreover, since it has been observed in this study that A depends (mostly) both on angular dispersion and beading, further information from an intracellular model accounting for beading would enable to disentangle the influence of angular dispersion and beading on the coefficient A.

In any case, the presented approach provides a reliable way to detect beading-induced modifications of the diffusion process, which are measurable for a SNR greater or equal to 20, as shown in **Figure 9**.

The estimation of A was performed using a linear fit with five values of the perpendicular diffusivity corresponding to five distinct OGSE frequencies. The degradation of the estimation of A while reducing the number of measurements (by using only three OGSE frequencies for instance) should also be studied in order to reduce acquisition time. However, a protocol relying on a single b-value at five different OGSE frequencies and along 60 directions already meets the requirements of a clinical research protocol and will be used in the future to assess all the findings presented in this work. The range of explored OGSE frequencies from 60 to 100 Hz allows to obtain a sufficiently short echo time ($<$ 120 ms) that enables to preserve at least 23% of the magnetization before diffusion-weighting, when considering an average T_2 value of 80 ms at $3T$. A diffusion sensitization of 200 s/mm^2 still preserves 20% of the signal after T_2 relaxation and diffusion decay for a diffusion coefficient of 0.7×10^{-9} m^2/s. Therefore, it seems possible, if the voxel spatial resolution is kept on the order of $2mm$, to apply this imaging protocol on a clinical 3T MRI system *in vivo* in human subjects.

4.4. Effect of SNR

In order to invoke practical conclusions from the numerical simulation results reported here, the present study addressed the impact of noise on the quality of the A scaling coefficient fit. Indeed, Gaussian noises with equal standard deviations were added to the real and imaginary parts of the complex NMR signal before computing its magnitude which corresponds to the simulated diffusion-weighted signal, resulting in a Rician noise corruption, as expected. Three different values of SNR were employed: SNR = 30 (corresponding to good experimental conditions with the latest 3T clinical MRI systems available on the market), SNR = 20 (intermediate experimental conditions), and SNR = 10 (worse experimental conditions). As shown in **Figure 8**, our noise analysis suggests that a SNR of 10 does not enable to fit the scaling coefficient A properly since the estimation of the perpendicular diffusivity for each frequency value has a too large uncertainty: the differences between the obtained values of A for the different geometrical configurations (shown in **Figures 9**, **10**) are strongly mitigated by noise. However, this analysis suggests that it is possible to reliably detect changes in perpendicular diffusivity and estimate the corresponding scaling coefficient A for a SNR greater or equal to 20 (see again **Figures 8**–**10**). The algorithm employed to estimate the parameters of the model presented in this work is part of a framework which maximizes a Rician log-likelihood function using a robust Expectation Maximization algorithm. In the presence of noise in DW data, the use of such a framework enables to alleviate the fit error of the model parameters.

4.5. Limitations

An intracellular fraction of 0.2 was employed to generate our numerical phantoms, which is not realistic since values of intracellular fraction are reported in the range (0.6–0.8). The choice of such a low fraction was deliberately made because it enables an important variation of both global and local angular dispersion as well as beading amplitude which is not possible at higher intracellular fractions. Those geometrical considerations are a major difficulty when trying to design realistic numerical phantoms, which becomes even stronger in the case of multiple populations.

The simulations performed in this article only used phantoms with a single fiber population, thus omitting the effect of crossing fibers on the scaling coefficient A. Studying the effect of multiple fiber populations on our model is essential and will be possible since our algorithm to design numerical phantoms enables to generate multiple populations geometries. However, we chose to restrict this study to single populations because (1) this study has never been performed, even in the case of a single population; understanding the various structural disorder effects for one population is, in our opinion, already a major challenge (2) it enables a more important variation of both global and local

angular dispersion whose effects are of interest and (3) choosing a proper adaptation of our model to multiple fiber configurations requires a thorough investigation which should be the object of a complete study. Indeed, there are at least two distinct approaches to adapt our model to fiber crossing configurations. The first approach relies on the hypothesis formulated in Burcaw et al. [7] that the behavior of Equation (2) will persist in fiber crossing regions because as long as the neurites of each tract are randomly positioned, the dynamical exponent will remain equal to 1, thus still leading to a $|\omega|$ frequency dependence in the extra-axonal space. However, in the case of fiber crossing, Equation (2) will no longer describe the frequency-dependence of the sole perpendicular diffusivity. Indeed, the fact of introducing fibers with multiple directions leads to a 3D disorder, while in the case of parallel fibers, the disorder was 2D, in the plane perpendicular to fibers. Thus, Equation (2) will apply not only to the diffusion coefficient transverse to axons—the perpendicular diffusivity—but to the overall diffusion coefficient. The second approach assumes that there is not a qualitative change of the underlying physics when introducing fiber crossings. In this case, an adaptation of our model to fiber crossings would draw from similar adaptations of state-of-the art microstructure models to deal with multiple fiber configurations, such as AMICOx [32] which estimates axon diameter indices in two fiber orientations (synthetic data only, using ActiveAx model in two orientations [5]). A second approach [33] introduced the spherical mean technique, capable of factoring out the effects of fiber crossing to estimate per-axon parallel and perpendicular effective diffusion coefficients, and subsequently extract fiber orientation using spherical deconvolution. Similarly, estimation of NODDI in two directions [34] for tractography uses fiber orientation estimates from neighboring voxels.

5. CONCLUSION

In this article, a novel tool to design more realistic phantoms of white matter was presented, enabling to study the influence of different geometrical features on the linear-in-frequency dependence of the extra-axonal perpendicular diffusivity, weighted by a scaling coefficient A .

By performing Monte-Carlo simulations in the extracellular space of numerical phantoms with increasing geometrical complexity, it was observed that this scaling coefficient A is sensitive to the modification of geometrical properties of the diffusing medium, such as the introduction of global angular dispersion and tortuosity. The presence of Ranvier nodes and demyelinated areas along the axons in the numerical phantom did not seem to significantly change the fitted value of A and further simulations in both intra- and extra-axonal spaces taking into account the high level of exchange around unmyelinated areas have to be performed to possibly observe as stronger effect on the coefficient A. The introduction of beading in the numerical phantoms was by far the most impacting geometrical modification, with a strong deviation of the fitted scaling coefficient A from geometries without beaded structures.

Future work will consist in studying the effect of multiple fibers populations on the estimation of the scaling coefficient A, since crossing configurations represent at least 60% of white matter regions. The effect of further geometrical characteristics on the structural disorder coefficient A, such as the presence of astrocytes and oligodendrocytes which could slow down the diffusion in the extra-axonal space, should also be considered by introducing those geometries in our numerical phantom generation algorithm. Further developments are also needed to be able to reach higher values of angular dispersion and beading at high and realistic intracellular volume fractions (>0.7).

This simulation study shows the importance of the generation of more realistic numerical phantoms in order to catch the complexity of the underlying diffusion biophysics. Analytical models such as the one employed in this article enable to assess the degree of realism needed to perform Monte-Carlo simulations reflecting the actual diffusion process in white matter without adding dispensable and computationally costly details in the phantoms geometry. This is a necessary step towards the construction of dictionaries of simulated biomimicking geometries to inversely decode white matter microstructure.

AUTHOR CONTRIBUTIONS

KG, CP, J-FM, and MA: Designed research; KG, JB, and CP: Performed analytical calculations; KG, FP, DE, and FM: Performed numerical calculations; KG, JB, and CP: Analyzed data; KG and CP: Wrote the paper.

FUNDING

This project has received funding from the European Union's Horizon 2020 Framework Programme for Research and Innovation under Grant Agreement No 720270 (Human Brain Project SGA1).

REFERENCES

1. Stejskal EO, Tanner JE. Spin diffusion measurements: spin echoes in the presence of a time-dependent field gradient. *J Chem Phys*. (1965) **42**:288–92.
2. Portnoy S, Flint J, Blackband S, Stanisz G. Oscillating and pulsed gradient diffusion magnetic resonance microscopy over an extended b-value range: implications for the characterization of tissue microstructure. *Magn Reson Med*. (2013) **69**:1131–45. doi: 10.1002/mrm.24325
3. Assaf Y, Blumenfeld-Katzir T, Yovel Y, Basser PJ. AxCaliber: a method for measuring axon diameter distribution from diffusion MRI. *Magn Reson Med*. (2008) **59**:1347–54. doi: 10.1002/mrm.21577
4. Alexander DC, Hubbard PL, Hall MG, Moore EA, Ptito M, Parker GJ, et al. Orientationally invariant indices of axon diameter and density from diffusion MRI. *Neuroimage* (2010) **52**:1374–89. doi: 10.1016/j.neuroimage.2010.05.043
5. Zhang H, Schneider T, Wheeler-Kingshott CA, Alexander DC. NODDI: practical *in vivo* neurite orientation dispersion and density

imaging of the human brain. *Neuroimage* (2012) **61**:1000–16. doi: 10.1016/j.neuroimage.2012.03.072
6. Ianuş A, Siow B, Drobnjak I, Zhang H, Alexander DC. Gaussian phase distribution approximations for oscillating gradient spin echo diffusion MRI. *J Magn Reson.* (2013) **227**:25–34. doi: 10.1016/j.jmr.2012.11.021
7. Burcaw LM, Fieremans E, Novikov DS. Mesoscopic structure of neuronal tracts from time-dependent diffusion. *Neuroimage* (2015) **114**:18–37. doi: 10.1016/j.neuroimage.2015.03.061
8. Fieremans E, Burcaw LM, Lee HH, Lemberskiy G, Veraart J, Novikov DS. *In vivo* observation and biophysical interpretation of time-dependent diffusion in human white matter. *Neuroimage* (2016) **129**:414–27. doi: 10.1016/j.neuroimage.2016.01.018
9. De Santis S, Jones DK, Roebroeck A. Including diffusion time dependence in the extra-axonal space improves *in vivo* estimates of axonal diameter and density in human white matter. *Neuroimage* (2016) **130**:91–103. doi: 10.1016/j.neuroimage.2016.01.047
10. Ginsburger K, Poupon F, Mangin JF, Poupon C. "Frequency dependence of the extra-axonal diffusion coefficient for OGSE sequences," in *Proceedings of ESMRMB 2017*. Barcelona (2017).
11. Novikov DS, Jensen JH, Helpern JA, Fieremans E. Revealing mesoscopic structural universality with diffusion. *Proc Natl Acad Sci USA*. (2014) **111**:5088–93. doi: 10.1073/pnas.1316944111
12. Hall MG, Alexander DC. Convergence and parameter choice for Monte-Carlo simulations of diffusion MRI. *IEEE Trans Med Imaging* (2009) **28**:1354–64. doi: 10.1109/TMI.2009.2015756
13. Yeh CH, Schmitt B, Le Bihan D, Li-Schlittgen JR, Lin CP, Poupon C. Diffusion microscopist simulator: a general Monte Carlo simulation system for diffusion magnetic resonance imaging. *PLoS ONE* (2013) **8**:e76626. doi: 10.1371/journal.pone.0076626
14. Neher PF, Laun FB, Stieltjes B, Maier-Hein KH. Fiberfox: facilitating the creation of realistic white matter software phantoms. *Magn Reson Med*. (2014) **72**:1460–70. doi: 10.1002/mrm.25045
15. Behrens TE, Berg HJ, Jbabdi S, Rushworth MF, Woolrich MW. Probabilistic diffusion tractography with multiple fibre orientations: what can we gain? *Neuroimage* (2007) **34**:144–55. doi: 10.1016/j.neuroimage.2006.09.018
16. Salzer JL. Clustering sodium channels at the node of Ranvier: close encounters of the axon-glia kind. *Neuron* (1997) **18**:843–46.
17. Rushton WAH. A theory of the effects of fibre size in medullated nerve. *J Physiol*. (1951) **115**:101–22.
18. Beaulieu C. The basis of anisotropic water diffusion in the nervous system-a technical review. *NMR Biomed*. (2002) **15**:435–55. doi: 10.1002/nbm.782
19. Daducci A, Dal Palú A, Descoteaux M, Thiran JP. Microstructure informed tractography: pitfalls and open challenges. *Front Neurosci*. (2016) **10**:247. doi: 10.3389/fnins.2016.00247
20. Budde MD, Frank JA. Neurite beading is sufficient to decrease the apparent diffusion coefficient after ischemic stroke. *Proc Natl Acad Sci USA*. (2010) **107**:14472–7. doi: 10.1073/pnas.1004841107
21. Wedeen VJ, Rosene DL, Wang R, Dai G, Mortazavi F, Hagmann P, et al. The geometric structure of the brain fiber pathways. *Science* (2012) **335**:1628–34. doi: 10.1126/science.1215280
22. Drobnjak I, Zhang H, Ianuş A, Kaden E, Alexander DC. PGSE, OGSE, and sensitivity to axon diameter in diffusion MRI: insight from a simulation study. *Magn Reson Med.* (2016) **75**:688–700. doi: 10.1002/mrm.25631
23. Barazany D, Basser PJ, Assaf Y. *In vivo* measurement of axon diameter distribution in the corpus callosum of rat brain. *Brain* (2009) **132**:1210–20. doi: 10.1093/brain/awp042
24. Xu J, Does MD, Gore JC. Sensitivity of MR diffusion measurements to variations in intracellular structure: effects of nuclear size. *Magn Reson Med.* (2009) **61**:828–33. doi: 10.1002/mrm.21793
25. Jespersen SN, Kroenke CD, Østergaard L, Ackerman JJ, Yablonskiy DA. Modeling dendrite density from magnetic resonance diffusion measurements. *Neuroimage* (2007) **34**:1473–86. doi: 10.1016/j.neuroimage.2006.10.037
26. Novikov DS, Kiselev VG. Surface-to-volume ratio with oscillating gradients. *J Magn Reson.* (2011) **210**:141–5. doi: 10.1016/j.jmr.2011.02.011
27. Van AT, Holdsworth SJ, Bammer R. *In vivo* investigation of restricted diffusion in the human brain with optimized oscillating diffusion gradient encoding. *Magn Reson Med.* (2014) **71**:83–94. doi: 10.1002/mrm.24632
28. Baron CA, Beaulieu C. Oscillating gradient spin-echo (OGSE) diffusion tensor imaging of the human brain. *Magn Reson Med*. (2014) **72**:726–36. doi: 10.1002/mrm.24987
29. Ronen I, Budde M, Ercan E, Annese J, Techawiboonwong A, Webb A. Microstructural organization of axons in the human corpus callosum quantified by diffusion-weighted magnetic resonance spectroscopy of N-acetylaspartate and post-mortem histology. *Brain Struct Funct*. (2014) **219**:1773–85. doi: 10.1007/s00429-013-0600-0
30. Bø L, Vedeler CA, Nyland HI, Trapp BD, Mørk SJ. Subpial demyelination in the cerebral cortex of multiple sclerosis patients. *J Neuropathol Exp Neurol*. (2003) **62**:723–32. doi: 10.1093/jnen/62.7.723
31. Palombo M, Ligneul C, Valette J, Hernández-Garzón E. Can we detect the effect of spines and leaflets on the diffusion of brain intracellular metabolites? *Neuroimage* (2017). doi: 10.1016/j.neuroimage.2017.05.003
32. Auría A, Romascano D, Canales-Rodriguen E, Wiaux Y, Dirby T, Alexander D, et al. "Accelerated microstructure imaging via convex optimisation for regions with multiple fibres (AMICOx)," in *2015 IEEE International Conference on Image Processing (ICIP)*. Quebec City, QC (2015) p. 1673–76.
33. Kaden E, Kruggel F, Alexander DC. Quantitative mapping of the per-axon diffusion coefficients in brain white matter. *Magn Reson Med*. (2016) **75**:1752–63. doi: 10.1002/mrm.25734
34. Reddy CP, Rathi Y. Joint multi-fiber NODDI parameter estimation and tractography using the unscented information filter. *Front Neurosci*. (2016) **10**:166. doi: 10.3389/fnins.2016.00166

Conflict of Interest Statement: The authors declare that the research was conducted in the absence of any commercial or financial relationships that could be construed as a potential conflict of interest.

The handling editor declared a shared affiliation, though no other collaboration, with the authors KG, FP, JB, DE, JF-M, CP.

frontiers in Physics

ORIGINAL RESEARCH
published: 08 June 2018
doi: 10.3389/fphy.2018.00049

Axon Diameters and Myelin Content Modulate Microscopic Fractional Anisotropy at Short Diffusion Times in Fixed Rat Spinal Cord

*Noam Shemesh**

Champalimaud Neuroscience Programme, Champalimaud Centre for the Unknown, Lisbon, Portugal

Mapping tissue microstructure accurately and noninvasively is one of the frontiers of biomedical imaging. Diffusion Magnetic Resonance Imaging (MRI) is at the forefront of such efforts, as it is capable of reporting on microscopic structures orders of magnitude smaller than the voxel size by probing restricted diffusion. Double Diffusion Encoding (DDE) and Double Oscillating Diffusion Encoding (DODE) in particular, are highly promising for their ability to report on microscopic fractional anisotropy (μFA), a measure of the pore anisotropy in its own eigenframe, irrespective of orientation distribution. However, the underlying correlates of μFA have insofar not been studied. Here, we extract μFA from DDE and DODE measurements at ultrahigh magnetic field of 16.4T with the goal of probing fixed rat spinal cord microstructure. We further endeavor to correlate μFA with Myelin Water Fraction (MWF) derived from multiexponential T_2 relaxometry, as well as with literature-based spatially varying axon diameter. In addition, a simple new method is presented for extracting unbiased μFA from three measurements at different *b*-values. Our findings reveal strong anticorrelations between μFA (derived from DODE) and axon diameter in the distinct spinal cord tracts; a moderate correlation was also observed between μFA derived from DODE and MWF. These findings suggest that axonal membranes strongly modulate μFA, which—owing to its robustness toward orientation dispersion effects—reflects axon diameter much better than its typical FA counterpart. μFA varied when measured via oscillating or blocked gradients, suggesting selective probing of different parallel path lengths and providing insight into how those modulate μFA metrics. Our findings thus shed light into the underlying microstructural correlates of μFA and are promising for future interpretations of this metric in health and disease.

Keywords: microscopic anisotropy, MRI, microstructure, diffusion MRI, myelin water fraction, spinal cord, axon diameter

OPEN ACCESS

Edited by:
Julien Valette, Commissariat à l'Energie Atomique et aux Energies Alternatives (CEA), France

Reviewed by:
Pascal Sati, National Institutes of Health (NIH), United States
Tim B. Dyrby, Copenhagen University Hospital, Denmark

***Correspondence:**
Noam Shemesh
noam.shemesh@neuro.fchampalimaud.org

Specialty section:
This article was submitted to Biomedical Physics, a section of the journal Frontiers in Physics

Received: *22 December 2017*
Accepted: *07 May 2018*
Published: *08 June 2018*

Citation:
Shemesh N (2018) Axon Diameters and Myelin Content Modulate Microscopic Fractional Anisotropy at Short Diffusion Times in Fixed Rat Spinal Cord. Front. Phys. 6:49. doi: 10.3389/fphy.2018.00049

INTRODUCTION

Diffusion Magnetic Resonance Imaging (MRI) has become a mainstay of contemporary microstructural imaging in biomedical applications. Diffusion MRI can provide rich information on the sample's microstructure by interrogating micron-scale dimensions within millimeter-scale voxels [1]. In the hierarchical scaling of dimensions in biological systems, the micron-scale is

fortuitously a characteristic length scale of many (sub)cellular structures of interest, such as axons, dendrites or cell bodies, which cannot be accessed using routine spatial resolutions in MRI. Most diffusion MRI methods utilize variants of Stejskal and Tanner's [2] Single Diffusion Encoding (SDE) technique [3], which probes diffusion using a single diffusion epoch spanned by diffusion-sensitizing gradient waveforms. The flexibility of SDE in terms of parameter space led to numerous variants [4], as well as diffusion models [5, 6], that have been devised to probe different aspects of the microstructure. For example, Diffusion Tensor Imaging (DTI) models diffusion using a single tensor [7, 8] under the assumption of (time-dependent) Gaussian diffusion, and the tensor's rotationally invariant properties can then report on diffusion anisotropy and parallel/perpendicular diffusivities. Other methods, such as q-space imaging [9, 10] or diffusion spectrum imaging [11] utilize Fourier relationships between the diffusion propagator and signal decay with the *q*-value (where $\mathbf{q} = \frac{1}{2\pi}\gamma\delta\mathbf{G}$ is the wavevector, γ is the gyromagnetic ratio, δ represents the gradient duration, and $|\boldsymbol{G}|$ is the gradient amplitude) to extract information on pore size or orientation distributions, respectively. Diffusion time- and/or frequency-dependence can also provide much insight into the restricting geometry by probing the way in which the diffusion path is modulated with time and/or the diffusion spectrum, respectively [12–19]. Furthermore, more advanced biophysical modeling has been recently put forth to characterize specific microstructural components such as neurite density [20, 21], or water fractions tentatively associated with axons in white matter [19] from specific acquisition schemes. Such SDE methods have been widely useful in neuroscience [22] and biomedical applications, typically targeting longitudinal processes such as stroke, learning, or chronic disease progression [1].

One interesting metric that can be probed by diffusion is the microscopic diffusion anisotropy (μA) [23–25], from which its normalized counterpart – the microscopic fractional anisotropy (μFA) – can be derived. μFA defines a single compartment's anisotropy in its own eigenframe [26], e.g., for a sphere μFA = 0 while for an infinite cylinder μFA can approach 1. However, in practice, the MRI signal will always originate from an ensemble, thereby making it necessary to account for orientation dispersion within the ensemble [27]. In systems comprising coherently-aligned anisotropic objects where orientation dispersion is ideally zero, μFA would be equivalent to the fractional anisotropy (FA) derived from DTI. However, in conventional SDE methods, when orientation dispersion is significant, estimated FA values typically do not represent the true anisotropy, or μFA, as they are conflated with orientation dispersion [28, 29]. For example, in ideal randomly oriented infinite cylinders, the averaging of anisotropic compartments results in FA = 0, which—without a-priori knowledge or extensive modeling—would suggest that the microscopic geometry is spherical.

In recent years, the Double Diffusion Encoding (DDE) methodology (**Figure 1**) has been gaining increasing attention for its potential to refine and identify microstructural aspects not so easily probed by SDE [25, 30]. Unlike SDE, DDE probes diffusion correlations using—as its name suggests—two diffusion encoding periods, spanned by two independent gradient wavevectors, which are separated by a mixing time (τ_m). Comparing q-space-like signal decays using parallel and perpendicular relative gradient orientations, Cheng and Cory have been able to measure the sizes of randomly oriented elongated (anisotropic) yeast cells, and distinguish them from spherical cells [24]. Similarly, Callaghan and Komlosh have shown that diffusivities extracted from parallel vs. perpendicular DDE experiments could provide insight into μFA in randomly oriented liquid crystals characterized by Gaussian diffusion [23]. Such measurements provided the first clues that μFA (termed using many divergent terms [3])

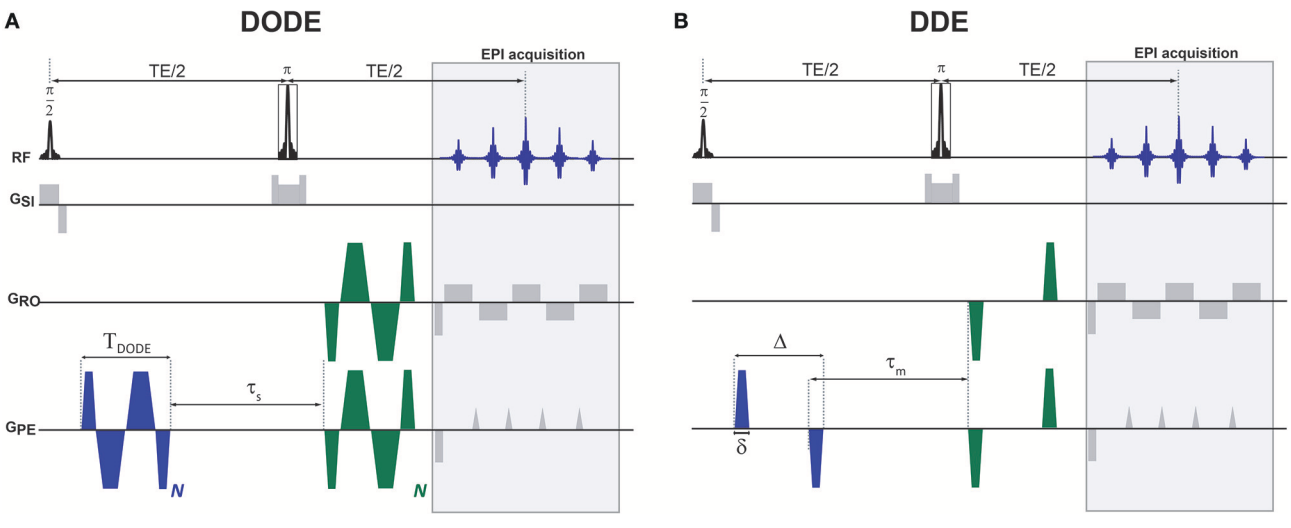

FIGURE 1 | Diffusion MRI pulse sequences used in this study. **(A)** DODE and **(B)** DDE weightings were overlaid on a basic SE-EPI sequence. The diffusion gradient orientations are independent and can vary in any of the axes, the particular instantiation here represents one particular case where G_1 is oriented along the PE axis and G_2 is at an angle in the PE-RO plane. Other than the relative orientations that varied, identical waveforms were used for the two diffusion encodings.

could be recovered from DDE irrespective of orientation dispersion.

Mitra [25], and later Özarlsan [31] derived exact solutions for DDE signals, and have identified the importance of the mixing time in decoupling μA from other effects. In the short mixing time regime, interesting diffusion-diffraction phenomena can be produced [32–36], and angular dependencies can provide insight into pore sizes as shown experimentally first by Koch and Finsterbusch [37, 38] and then by others [39–41]; however, by analyzing the displacement correlation tensor [42], the short τ_m angular DDE experiment aiming to measure compartment sizes was found by Jespersen to be equivalent to a time-dependent SDE experiment [43]. By contrast, in the long mixing time regime, the second order term in the displacement correlation tensor, from which sizes are measured, is decoupled from μA, making its measurement much less complicated [25, 31]. The ability to measure accurate μA values was validated in Shemesh et al. [34] and its importance was shown in biological systems such as *ex-vivo* neural tissues [44], yeast cells [45], and preclinical *in-vivo* experiments [46], where the orientational variance of the measurements was highlighted. Lawrenz et al. have proposed rotationally invariant schemes for mapping an index of μA [47, 48], and Jespersen et al. subsequently generalized rotationally invariant DDE measurements up to 5th order (in *q*-values) via a measurement scheme termed DDE 5-design [26]. Numerous promising studies have also been performed on human scanners [37, 38, 48–51], suggesting quite promising potential for disentangling μFA from the underlying orientation dispersion. Additional recent experiments have even extended the DDE methodology toward MR spectroscopy, aiming to impart specificity toward specific cell populations via cellular-specific metabolites [52, 53].

As alluded to above, the diffusion process in biological tissues is highly time-dependent, and thus the filter with which the diffusion experiment is performed can be important. Oscillating Diffusion Encoding (ODE) experiments [14, 54, 55] have been widely used in SDE to enhance contrast in neural tissue, likely since they access shorter diffusion time than could be reached using pulsed-gradient-spin-echo methods [56]. Additionally, ODE has been shown to be highly beneficial for mapping axonal sizes in rat spinal cord [57, 58] as well as for contrasting malignancy in tissues [59, 60]. More recently, the DDE framework was extended toward accommodation of oscillating gradients, termed Double Oscillating Diffusion Encoding (DODE, **Figure 1A**), first in theory [61], and more recently, in experiment [62]. Importantly, DODE enables the time/frequency-dependence of μFA to be studied. Furthermore, DODE sequences reach the long mixing time regimes much more easily than their DDE counterparts, thereby making the experiments less mixing-time dependent [61], and, as a result, offering the benefit of reduced echo times. This property is likely due to the mixing beginning already from the first gradient pair, and accumulating over the entire gradient waveform. Such DODE experiments were recently reported for the first time in the *ex-vivo* mouse brain, and μFA maps derived from DODE indeed showed richer contrast than those of their DDE-derived counterparts [62].

Many studies have investigated the underlying microstructural correlates of FA, mainly in white matter (for a classical review, the reader is referred to Beaulieu [63]). It is clear that although myelin strongly modulates FA, it is not necessary for detection of anisotropy in biological systems. Axonal membranes, for example, can impede the diffusion processes with orientational preference and thus can contribute to FA. However, in most studies attempting to investigate the origins of restriction in tissues, orientation dispersion was conflated with SDE-driven metrics; an interesting question is therefore whether μFA, which should not suffer from orientation dispersion effects, could be associated with microstructural features to different extents than FA. *The goal of this study was therefore to investigate how μFA and FA correlate underlying microstructural features such as myelin water fraction (MWF) or axonal diameters.* As well, we aimed to investigate whether these parameters are differently correlated, and to qualitatively assess the importance of orientation dispersion, especially in the white matter. The final goal of this study was to determine whether μFA is modulated when different length scales are probed via DODE and DDE sequences. A well-characterized system, namely, fixed spinal cord—which has been extensively used in the past to study diffusion [15, 58, 64–66] or relaxation [67–70] microstructural correlates—was used for these investigations. Our findings demonstrate interesting differences in correlations between μFA and FA and MWF, as well as with the a-priori known axonal sizes in white matter, when measured using DODE or DDE. Interesting findings in gray matter tissues are also presented. Implications for D(O)DE contrasts and future routes for investigations of the origin of μFA in neural tissue, are discussed.

THEORY

Most DDE-MRI studies up to date have used only a single *b*-value to extract μFA. However, very recently, Ianus et al. showed that for most plausible microstructural scenarios, μFA obtained in such a way can be highly biased due to neglecting the higher-order terms in the signal decay [62]. Ianus et al. proposed to more accurately estimate μFA in both DDE and DODE methodologies by performing D(O)DE experiments at multiple *b*-values, and fitting both μA (from which μFA is then calculated) and the higher-order term via polynomial fits. That is, the D(O)DE signal decay at long mixing times can be expanded with b-value as:

$$\frac{1}{12}\sum \log\left(S_{\parallel}(b)\right) - \frac{1}{60}\sum \log\left(S_{\perp}(b)\right) = \mu A^2 b^2 + P_3 b^3,$$

where $\mu A^2 = \frac{3}{5}\mathrm{var}(\sigma_i)$, $\sigma_{i=1,2,3}$ are the diffusion tensor eigenvalues, $S_{\parallel}$ and $S_{\perp}$ represent the D(O)DE signals acquired using parallel and perpendicular gradients, respectively, and P_3 contains the higher-order terms up to third order (even higher-order terms are neglected). Ianus et al. showed that polynomial fitting can be used to estimate μA^2 and P_3 from Equation 1. When the mean diffusivity (MD) is additionally measured at lower *b*-values (e.g., from fitting a tensor to the 12 parallel

orientations in the 5-design), μFA can be directly calculated from Eq. 2:

$$\mu FA = \sqrt{\frac{3}{2}\frac{\mu A^2}{\mu A^2 + \frac{3}{5}MD^2}}.$$

Although polynomial fitting probably yields more accurate estimates of μA^2, it should be noted that ideally, many *b*-value shells would be required for robust fitting. An alternative approach would be to acquire a much more minimalistic dataset and still be able to quantify μA^2 and P_3. Setting $\frac{1}{12}\sum \log\left(S_{\parallel}(b)\right) - \frac{1}{60}\sum \log\left(S_{\perp}(b)\right) \equiv \tilde{\epsilon}(b)$, Eq. 1 can be rewritten for two different *b*-values b_1 and b_2:

$$\begin{cases} \tilde{\epsilon}\left(b_1\right) = \mu A^2 b_1^2 + P_3 b_1^3 \\ \tilde{\epsilon}\left(b_2\right) = \mu A^2 b_2^2 + P_3 b_2^3 \end{cases}.$$

It is then straightforward to show that from two measurements at different *b*-values, μA^2 can be directly obtained from

$$\widetilde{\mu A^2} = \frac{\tilde{\epsilon}\left(b_2\right) - \tilde{\epsilon}\left(b_1\right)\frac{b_2^3}{b_1^3}}{b_2^2 - \frac{b_2^3}{b_1}},$$

which can then be plugged into Equation 2 to obtain μFA directly. Note that we use the tilde to distinguish the extracted $\widetilde{\mu A^2}$ from the real μA^2. This approach for accurate μFA extraction thus requires, in principle, only two measurements, one at low *b*-value, from which MD and $\tilde{\epsilon}\left(b_1\right)$ would be obtained, and another at higher *b*-value, where $\tilde{\epsilon}\left(b_2\right)$ would be obtained. However, since at low *b*-values required for accurate estimation of MD, $\tilde{\epsilon}\left(b_1\right)$ may be very small and comparable to noise levels, it is more appropriate to acquire $\tilde{\epsilon}\left(b_1\right)$ and $\tilde{\epsilon}\left(b_2\right)$ at somewhat higher *b*-values (where the b^2 terms are more dominant) and perform a separate, third acquisition for extracting MD at lower *b*-values. This 3-shell approach was thus preferred in this study.

MATERIALS AND METHODS

This study was carried out in accordance with the recommendations of the directive 2010/63/EU of the European Parliament of the Council, authorized by the Champalimaud Centre for the Unknown's Animal Welfare Body, and approved by the national competent authority (Direcção Geral de Alimentação e Veterinária, DGAV).

Specimen Preparation

Spinal cord specimens were obtained from adult male Wistar rats ($N = 2$) weighing ∼300 gr. The rats underwent standard transcardial perfusion under deep pentobarbital anesthesia. Cervical spinal cords were extracted, washed in PBS, and kept in 4% paraformaldehyde (PFA) for 24 h at 4°C. The samples were then placed in freshly prepared phosphate buffer saline (PBS) for at least 48 h prior to MRI experiments. The samples were cut to ∼1 cm segments and placed in a 5 mm NMR tube filled with fluorinert (Sigma Aldrich, Lisbon, Pt).

MRI Experiments

All MRI experiments were performed on a vertical 16.4T (700 MHz ^{1}H frequency) Aeon Ascend scanner (Bruker, Karlsruhe, Germany) interfaced with a Bruker AVANCE IIIHD console. A Micro5 probe equipped with a 5 mm birdcage coil for transmit and receive functions and a gradient system capable of producing amplitudes of up to 3T/m isotropically was used. The sample was kept at a constant temperature of 23°C throughout the experiments by means of air flow, and the samples were allowed to equilibrate with the surrounding temperature for at least 4 h before acquiring any diffusion or relaxation experiments.

All diffusion sequences were written in-house and were based on an Echo Planar Imaging (EPI) readout. For both DODE and DDE, the same acquisition parameters were used, namely, two-shot and double-sampled EPI with a readout bandwidth of 555.555 kHz, Field of View (FOV) of 6 × 4 mm^2 and in-plane matrix size of 120 × 80, leading to an isotropic in-plane resolution of 50 × 50 μm^2. The slice thickness was 500 μm, and TR/TE = 2,500/52 ms. For both DODE and DDE acquisitions, Jespersen's 5-design sampling scheme [26] was used for the diffusion weighted images, and, additionally, eight images with zero *b*-value were acquired, such that the total number of images acquired in a given scan was 80. For both DODE and DDE, three separate acquisitions were performed with different *b*-values, namely, 2b = 1.2, 2.4 and 3.0 ms/μm^2 (where the factor of 2 reflects the accumulated diffusion weighting along the two diffusion epochs). The specific *b*-values were chosen based on signal-to-noise and contrast considerations: on the one hand, they have to be sufficiently low such that even higher-order terms do not contribute, but on the other hand, they have to be high enough for μFA contrast to be detectable. The lowest *b*-value scans were acquired with 12 averages, while the other two *b*-value shells were acquired with 32 averages each. The DODE diffusion parameters were: $T_{DODE} = 13$ ms, $N = 5$, $\tau_s = 2$ ms. The DDE diffusion parameters were $\Delta/\delta = 12/1$ ms, $\tau_m = 12$ ms, see **Figure 1** for definitions of the parameters.

Additional experiments were performed for mapping myelin water fraction. Those consisted of a Carr-Purcell-Meiboom-Gill (CPMG)-based acquisition performed using a modified pulse multi-slice-multi-echo (MSME) sequence. The same slice was acquired as in the diffusion images with identical in-plane resolution and FOV. The acquisition bandwidth for the pulse sequence was 100 kHz, and the pulses used for slice-selective excitation and refocusing had durations of 1.16 ms (Shinnar-Le-Roux design) and 50 μs (Gaussian shape), respectively. The respective bandwidths of the excitation and refocusing pulses were 3625 and 32,100 Hz, respectively, such that the refocusing pulse provided complete refocusing on the entire slice. The ΔTE that could be achieved using these parameters was 2.85 ms, and 96 echoes were acquired from 2.85 to 273.6 ms. The repetition time was 2500 ms and two averages were acquired.

Diffusion Data Preprocessing

All preprocessing and analyses were performed using MatLab® (The MathWorks, Inc., Natick, Massachusetts, United States). Raw images were registered using an implementation of

Guizar-Sicairos et al. [71] found in https://goo.gl/3bGU8b. The images were then denoised using Veraart's method based on Marchenko-Pastur distributions in Principal Component Analysis of redundant data [72]. Gibbs unringing was performed using Kellner's method [73] implemented in Matlab. Finally, the denoised and unrung images were very slightly smoothed using a [2 2] median filter.

Relaxation Data Preprocessing

The preprocessing steps for the relaxation data were identical to the diffusion data preprocessing steps, except for an additional step in the very beginning of the pipeline whereby the magnitude data was converted to real data using Eichner's method [74]. All steps listed above including denoising, unringing and median filter smoothing were then executed in sequence.

Diffusion Data Analysis

The first analysis step for D(O)DE data was to fit the diffusion tensor. Diffusivities were computed using a simple linear fitting of $S_{\|}$ data acquired at the lowest *b*-value experiments followed by diagonalization and extraction of the diffusion tensor eignevalues and eigenvectors. The mean diffusivity and fractional anisotropy were then calculated from the tensor eigenvalues as $MD = \frac{1}{3}(\lambda_1 + \lambda_2 + \lambda_3)$ and $FA = \sqrt{\frac{3}{2}\frac{(\lambda_1-MD)^2+(\lambda_2-MD)^2+(\lambda_3-MD)^2}{\lambda_1^2+\lambda_2^2+\lambda_3^2}}$, where λ_i represent the tensor eigenvalues.

The second step in the analysis was to use the data from the two higher *b*-values to extract μFA. First, $\widetilde{\mu A^2}$ was extracted directly from Eq. 4; the mean diffusivity estimate was then used along with the extracted $\widetilde{\mu A^2}$ to obtain μFA via Equation 2.

Relaxation Data Analysis

Following the preprocessing steps listed above, the filtered relaxation data were subject to a voxelwise inverse Laplace Transform (iLT) using 150 T_2 components log-spaced between 2.1 and 328.3 ms. The T_2 spectra were smoothed by minimum-curvature constraint as in Dula et al. [75] and extended phase graph analysis was performed to account for any B_1^+ inhomogeneity and ensuing stimulated echoes [76]. The myelin water fraction (MWF) was computed from each spectrum as the fraction of signal originating from components with peak T_2 smaller than 17 ms. ROIs were drawn manually on the raw data closely following Dula et al. [75], and the ROI data underwent the same analysis using the mean signal decay in each ROI.

Statistical Analysis

Gray matter and white matter masks were created by thresholding MWF maps with MWF < 0.22 for gray matter and MWF > 0.25 for white matter. The histograms in **Figure 4** were then generated for each metric/method using Matlab's *histogram* function which automatically selects the bin width to represent the underlying distribution in the most accurate way. Parameter means and standard deviations are reported in the text and Tables.

Correlation analyses between different diffusion metrics were performed using automatic outlier rejection (Grubbs test for outliers) followed by calculation of Spearman's ρ (μFA and FA data from all methods were not normally distributed). An analysis of variance (ANOVA) was performed to compare μFA and FA arising from DODE and DDE methods, with *post-hoc* Bonferroni tests corrected for multiple comparisons.

To correlate MWF with μFA or FA extracted from the different methods, the diffusion maps were registered to the MWF using Matlab's *imregister* function using a *multimodal* configuration, initial radius of 1e-5, maximum number of iterations = 1,000, and allowing for affine transformations due to the small differences in image geometry arising from EPI-based (diffusion) and line-by-line (relaxation) acquisitions.

When linear fits are presented (**Figure 8**), Matlab's *robustfit* function was used to extract the coefficients.

RESULTS

Diffusion data quality can be appraised in **Figure 2**, which plots representative raw data from one of the spinal cords, obtained from experiments with zero *b*-value (**Figure 2A**), parallel (**Figure 2B**), and perpendicular (**Figure 2C**) diffusion orientations at the highest *b*-value used in this study. Before denoising, the worst-case signal to noise ratio (SNR)—measured at the highest *b*-value and with significant diffusion weighting gradients in the direction parallel to the spinal cord's principal axis—was ∼20 in white matter. The middle column in **Figure 2** shows the corresponding preprocessed data and the ensuing enhancement of image quality from denoising and Gibbs unringing (**Figures 2D–F**). **Figures 2G–I** show the result of subtracting raw and denoised images. The lack of structure in the subtracted images suggest that indeed only noise was removed and that no significant signal components were lost during denoising [72]. The SNR of the preprocessed images was enhanced by a factor of ∼2.

To assess the different maps obtained in this study, representative μFA and FA maps derived from DODE as well as DDE experiments (hereafter referred to as μFA_{DODE} and μFA_{DDE} or FA_{DODE} and FA_{DDE}, respectively) are shown in **Figure 3.** Several interesting qualitative features can be highlighted from these images: (1) both μFA_{DODE} and μFA_{DDE} maps (**Figures 3A,C**) have higher values than their FA_{DODE} and FA_{DDE} counterparts (**Figures 3B,D**) in white matter, as well as in gray matter; (2) μFA_{DDE} is higher and less tract-specific when compared with μFA_{DODE} (for approximate definitions of tract locations and spinal cord anatomy, the reader is referred to **Figure 3E**); (3) μFA_{DDE} appears quite homogeneous in the WM while μFA_{DODE} shows more variation within WM; (4) similarly, FA_{DDE} is more homogeneous in white matter compared with FA_{DODE}, which shows a greater variance in different tracts. To provide a more quantitative view on these features, **Figure 4** plots histograms of μFA and FA in white matter and gray matter (c.f. **Figures 4A,B** for the ROI masks). In white matter, μFA_{DODE} is higher than its FA_{DODE} counterpart (**Figure 4C**), while in gray matter, μFA_{DODE} is distributed at much higher values compared to FA_{DODE} (**Figure 4D**). Similar trends were observed for DDE but with μFA or FA shifted toward somewhat higher values (**Figures 4E,F**).

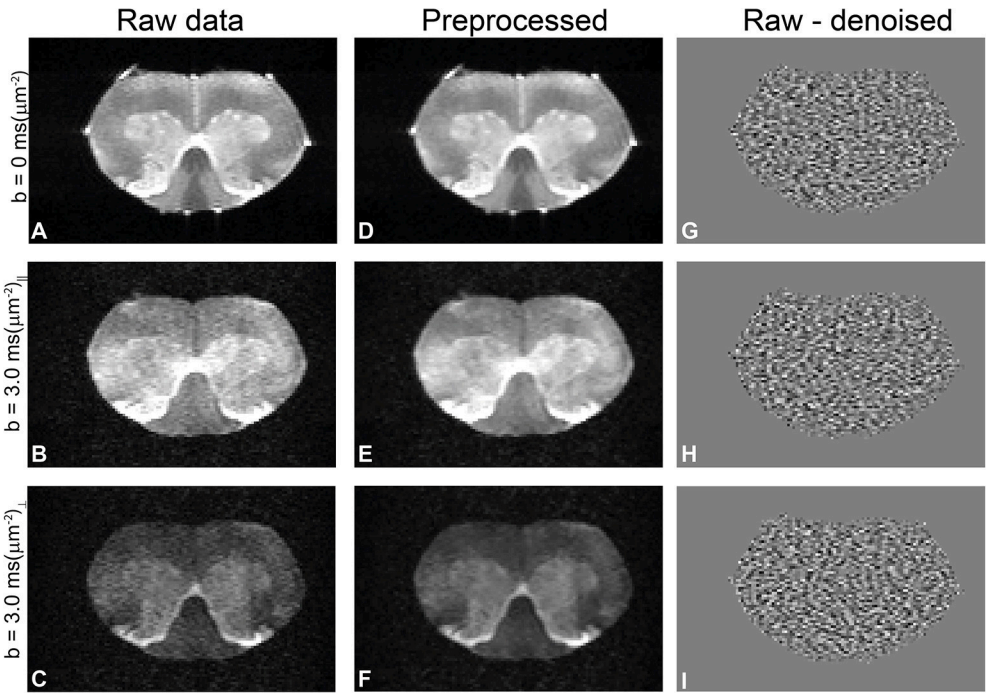

FIGURE 2 | Quality of diffusion MRI data and preprocessing in a representative spinal cord. **(A–C)** Raw data with zero *b*-value, parallel, and perpendicular waveforms acquired at the highest *b*-value, respectively. In this particular direction, the perpendicular waveform had more significant components along the spinal cord principal axis and thus show greater attenuation. **(D–F)** Results of preprocessing the data in **A–C** (denoising and Gibbs unringing). Notice how the noise is highly reduced in the preprocessed images without adverse effects to image quality. **(G–I)** Subtraction of denoised and raw data, showing only noise and thus demonstrating that no significant signal components were removed during Marchenko-Pastur PCA denoising.

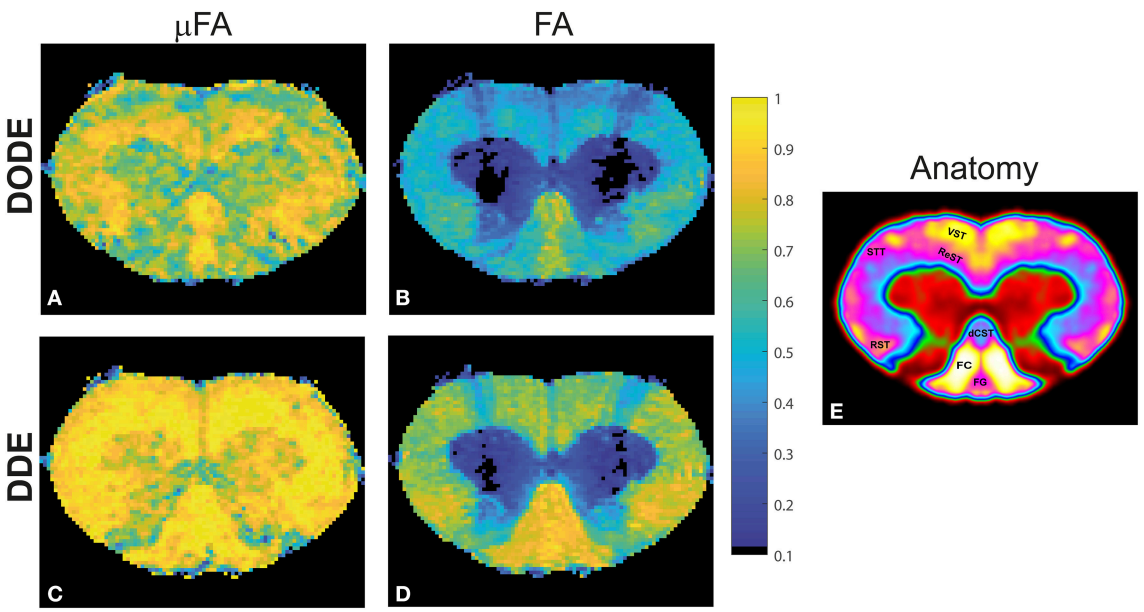

FIGURE 3 | Parameter maps for a representative spinal cord. **(A)** μFA_{DODE}; **(B)** FA_{DODE}; **(C)** μFA_{DDE}; **(D)** FA_{DDE}. Notice the differences in contrast both in white and in gray matter tissues both between metrics and between sequences. Most notably, μFA is higher than FA and DDE-driven metrics are higher than DODE-driven metrics, especially in white matter. **(E)** Anatomy of the spinal cord for reference, displayed over a smoothed false-color image of the cervical segment. The gray matter is shown in red and green, while the tracts are highlighted on the left side of the cord.

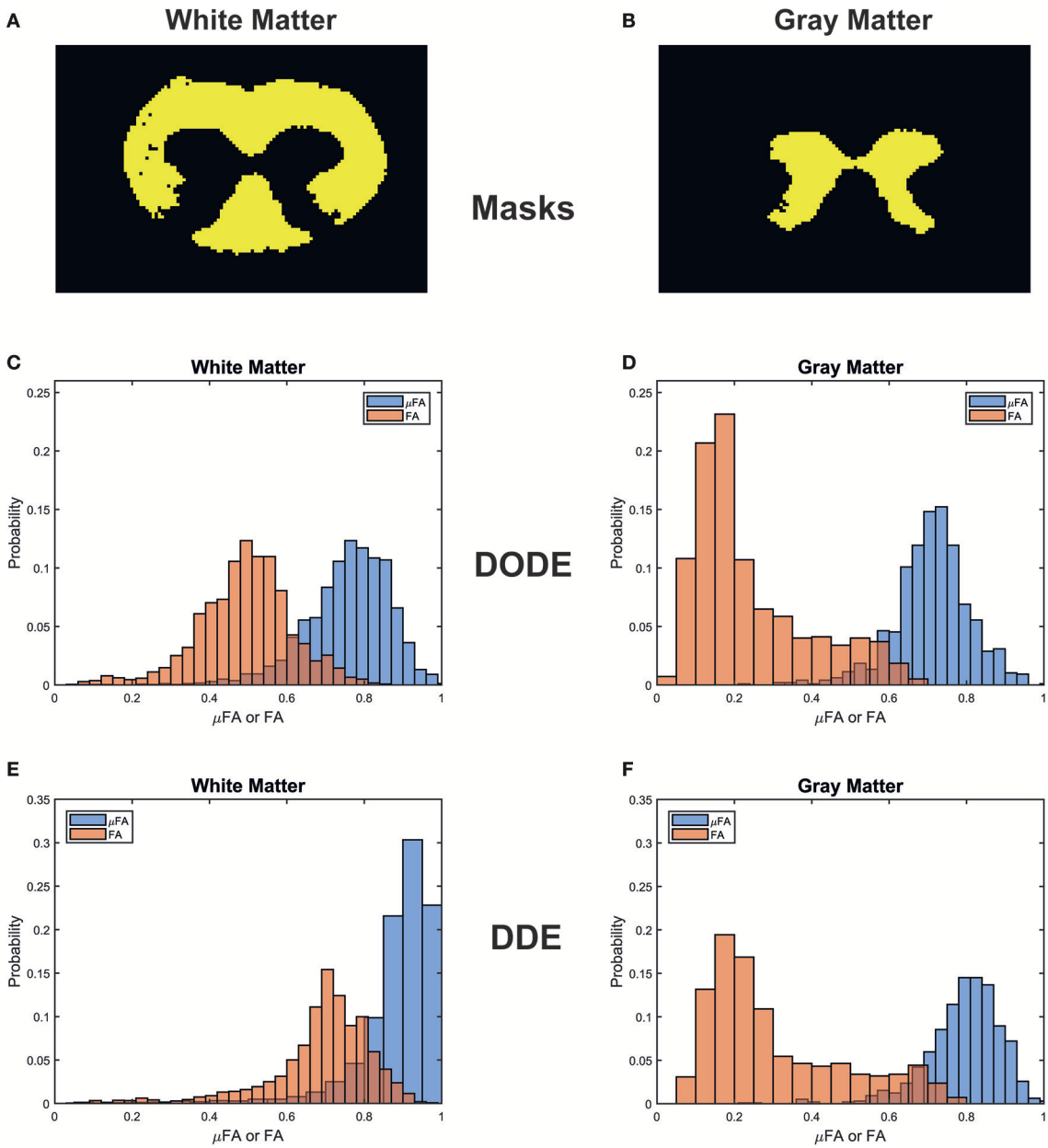

FIGURE 4 | Histogram distributions of the different metrics in white matter and gray matter. **(A,B)** Masks for the white and gray matter tissues, respectively. **(C,D)** μFA_{DODE} and FA_{DODE} for white and gray matter. **(E,F)** μFA_{DDE} and FA_{DDE} for white and gray matter. Notice the different distributions in white matter for both DODE- and DDE-driven metrics, as well as the higher μFA as compared to FA in all tissues.

It is also interesting to compare differences between methods within the same tissue type (e.g., comparing same-color distributions down the columns of **Figure 4**). μFA_{DODE} is clearly lower and more widely distributed compared with μFA_{DDE} in white matter. In gray matter, μFA_{DDE} is high, while μFA_{DODE} is somewhat smaller. Another interesting finding in gray matter, is that FA_{DODE} and FA_{DDE} values are only slightly different. The means and standard deviations of μFA and FA for each method are tabulated in **Table 1**.

A statistical analysis of these data is given in **Figure 5**, which presents box plots of the data. A one-way ANOVA revealed that in each tissue type (e.g., white matter or gray matter), all four metrics are highly statistically significantly different from each other (corrected $p < 1e\text{-}12$, *post-hoc* Bonferroni test). However, it should be noted that although the metrics are different, they are not completely uncorrelated. **Table 1** reports Spearman's ρ and its significance levels when comparing μFA and FA (extracted by the same method) in each ROI. While μFA_{DODE}

TABLE 1 | White matter and gray matter microscopic and fractional anisotropies, along with their spearman correlation coefficient and significance.

	μFA DODE	FA DODE	Spearman's ρ	*p*-value	μFA DDE	FA DDE	Spearman's ρ	*p*-value
White Matter			0.41	$<10^{-10}$			0.19	$<10^{-10}$
Mean σ	0.77 ± 0.10	0.49 ± 0.12			0.89 ± 0.16	0.69 ± 0.13		
Gray Matter			0.22	$<10^{-10}$			−0.10	<0.002
Mean σ	0.71 ± 0.10	0.24 ± 0.15			0.79 ± 0.10	0.31 ± 0.18		

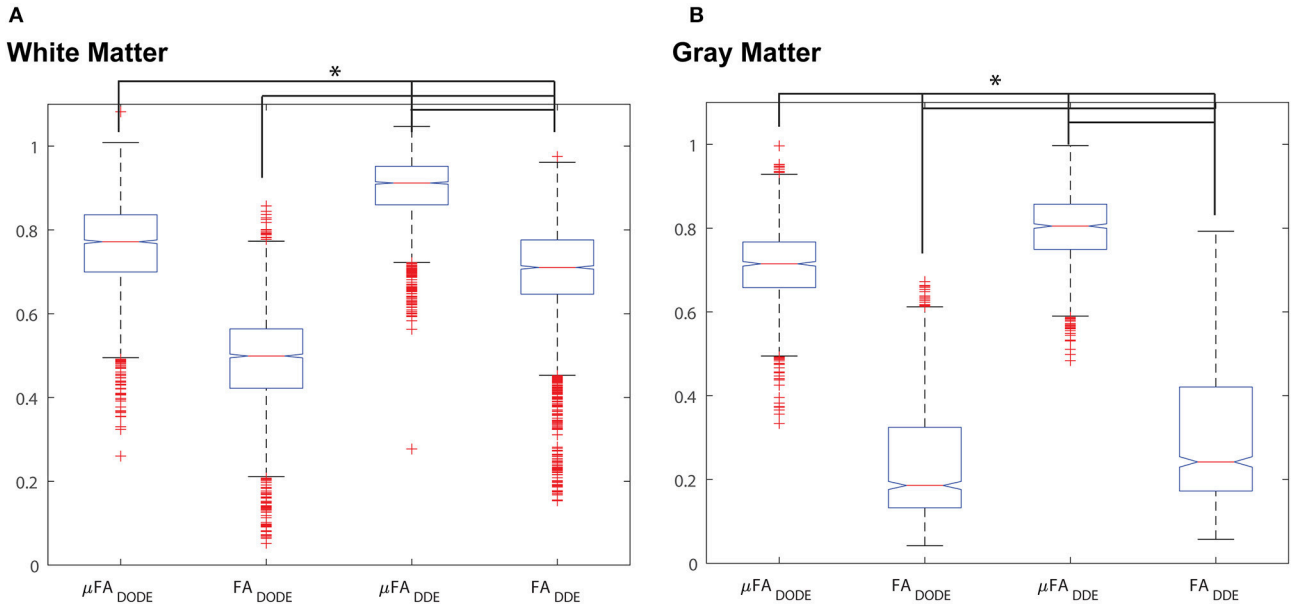

FIGURE 5 | Box-and-whisker plots of the different metrics. **(A)** White matter analysis. **(B)** Gray matter analysis. *$p < 10^{-12}$ between all pairs from ANOVA with Bonferroni *post-hoc* comparison and corrected for multiple comparisons.

and FA_{DODE} are correlated in white matter (Spearman's $\rho = \sim 0.41$), μFA_{DDE} and FA_{DDE} metrics are only weakly correlated (Spearman's $\rho = \sim 0.19$). In gray matter, the correlations between μFA and FA were weak for both methods and (Spearman's $\rho = 0.22$ and -0.10 for DODE and DDE, respectively). Note that although outlier rejection was used, in all cases $< \sim 1\%$ of the data were identified as outliers and rejected.

To establish whether and how myelin modulates the anisotropy metrics, Carr-Purcell-Meiboom-Gill (CPMG) MRI experiments were performed on the same slice with the same resolution as the diffusion experiments. To assess the quality of the data, **Figures 6A,B** show the preprocessed data at short and very short TE of 2.9 ms and very long TE of 142.5 ms, respectively, in a representative spinal cord. Even at the very long TE, the SNR remains very high, especially after denoising. Denoising and unringing procedures were validated and found to have no negative impact on the quality of T_2 fitting procedure (data not shown), while improving the fits significantly. **Figure 6C** shows ROIs drawn in the major tracts of the spinal cord, while **Figures 6D,E** show the T_2 decays (with the ordinate drawn in log scale) and the resultant T_2 spectra (with the abscissa drawn in linear scale), respectively. The decays in white matter are clearly non-linear, and the myelin water can be seen as an early peak in the T_2 spectrum with its peak T_2 around ∼10 ms.

A representative myelin water fraction (MWF) map arising from pixel-by-pixel quantification of the spectra is shown in **Figure 7A.** Note the sharp contrast between the different tracts in MWF: for example, the dCST shows the lowest MWF (MWF∼0.30) while VST and FC exhibit the highest MWF (MWF∼0.45). Scatter plots between MWF and μFA or FA in white matter are shown in **Figure 7** for DODE (**Figure 7B**) and DDE (**Figure 7C**), respectively. **Table 2** summarizes the correlation coefficients and associated statistics. A moderate anticorrelation between MWF and μFA_{DODE} is observed in the white matter (Spearman's $\rho = \sim -0.36$), while FA_{DODE} did not correlate with MWF in a statistically significant manner. The DDE counterparts μFA_{DDE} and FA_{DDE} exhibited weak anti-correlation and correlation, respectively. **Figures 7D,E** show similar plots as described above, but for gray matter. Notably, correlations between MWF and FA_{DODE}, as well as FA_{DDE} were very weak and their statistical significance not very high; on the contrary, μFA_{DODE} was found to correlate somewhat with MWF,

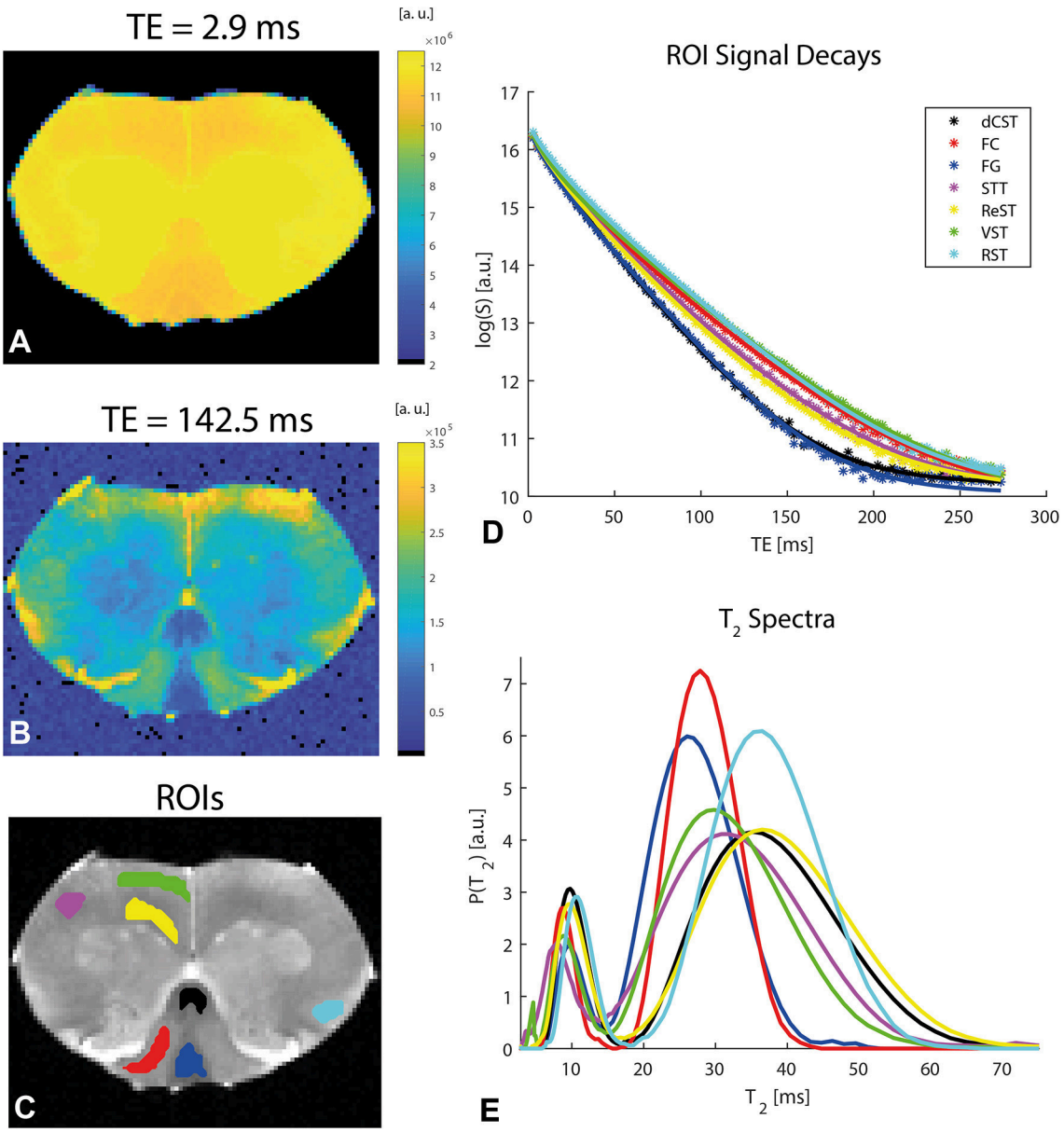

FIGURE 6 | Relaxation data and analysis in a representative spinal cord. **(A,B)** Preprocessed data at short and long TEs, respectively, reveal excellent SNR. **(C)** ROI definitions. **(D)** Mean ROI signal decays with TE (symbols) along with their respective fits (solid lines). N.b. the log scale in the ordinate. **(E)** T_2 spectra (plotted in log scale in the abscissa) extracted from an iLT fit to the ROI data. The myelin water is associated with the peak corresponding to shorter T_2 values. The ROI colors in **(C)** correspond to the color of the plots in **(D,E)**.

while μFA_{DDE} correlated moderately with MWF, with very high statistical significance (c.f. **Table 2**).

Finally, the correlation of the mean μFA in the different tracts with literature regional averaged axon diameter was assessed. **Figures 8A,B** plot mean μFA and FA against the axon diameters reported in Dula et al. [75] for the different spinal cord tracts. These data, along with the values tabulated in **Table 3**, demonstrate that μFA_{DODE} exhibits very strong anticorrelation with axon diameters (Spearman's $\rho = -0.96$, $p = 0.0028$). All other metrics are not significantly correlated with axon diameter.

DISCUSSION

μFA has been recently gaining increasing attention as a potentially useful source of contrast in microstructural MRI due to its ability to disentangle anisotropy from orientation dispersion. Methods other than D(O)DE, targeting μFA such as tailoring b-tensor shapes are emerging, with many potential applications [77–80]. However, such methods may be confounded by time-dependent diffusion effects [27, 81–83], whereas D(O)DE at long mixing times naturally avoids

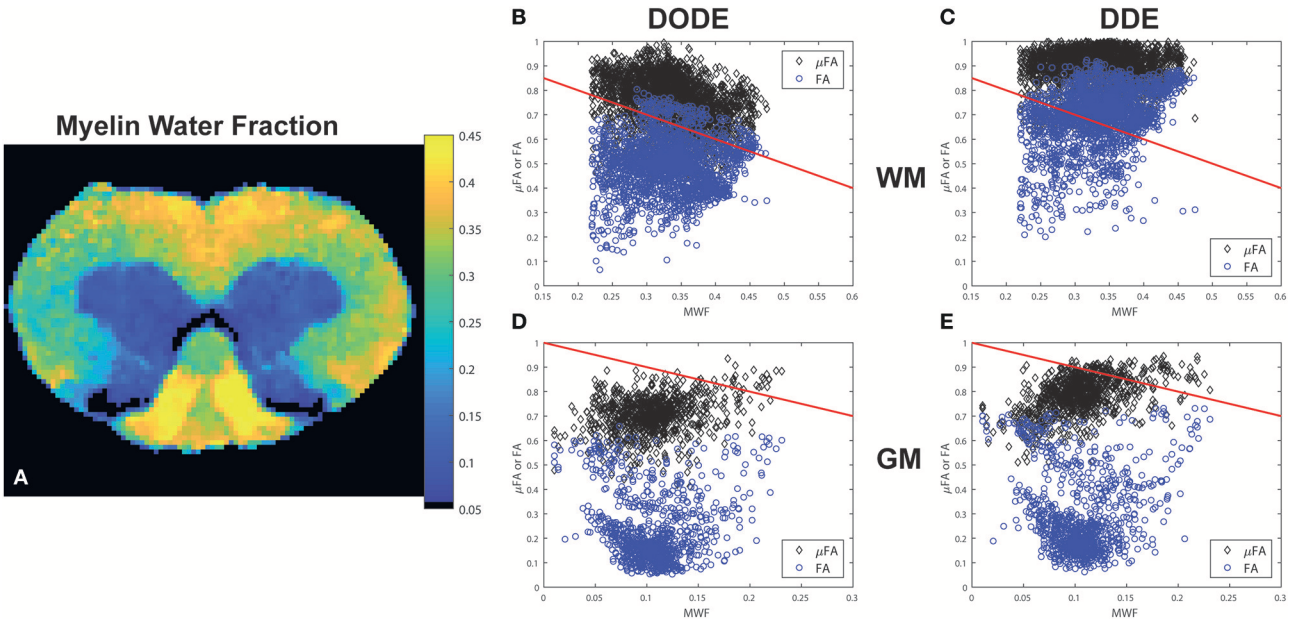

FIGURE 7 | Myelin Water Fraction (MWF) and its correlations with diffusion-derived metrics. **(A)** MWF from a representative spinal cord, showing excellent contrast between the white matter and gray matter as well as within most white matter tracts. **(B–E)** Correlations between DODE and DDE metrics with MWF in white and gray matter tissues. Blue circles represent FA whereas black diamonds represent μFA. Red lines represent−1*identity to guide the eye.

TABLE 2 | Statistical analysis of correlations between (μ)FA and myelin water fraction in white matter and gray matter.

	μFA DODE	FA DODE	μFA DDE	FA DDE
WHITE MATTER				
Spearman's ρ	−0.36	0.02	−0.07	0.30
p-value	$<10^{-10}$	NS	0.0011	$<10^{-10}$
GRAY MATTER				
Spearman's ρ	0.23	0.11	0.45	−0.1
p-value	$<10^{-10}$	0.0002	$<10^{-10}$	0.0015

these confounds [43]. It is therefore imperative to investigate how μFA may be correlated with underlying microstructural features such as axon dimensions and myelin, much like the early studies aiming to understand the sources for FA [63, 67, 84, 85]. In general, perhaps the most significant findings of prior studies on FA (conducted nearly invariably with SDE) were that (1) anisotropy in white matter depends on axonal membranes; and (2) the presence of myelin can further modulate FA metrics [63]. The application of oscillating gradients has also been shown to generate more contrast and more accurate estimations of small dimensions as compared to long diffusion time experiments, presumably due to the more efficient probing of smaller dimensions via the shorter diffusion times [58, 86, 87].

The present study aimed to investigate how μFA differs from FA in terms of correlations with myelin water and axonal diameters, and to compare those metrics when measured with DDE or DODE sequences. We first focus attention to our results arising from white matter tissue. Notably, μFA was always larger than FA (**Figures 3–5** and **Table 2**), in agreement with previous DDE experiments in fixed tissues [26] and *in-vivo* [88]. Since the μFA and FA metrics were extracted from the same acquisition, it is unlikely that other effects such as exchange or relaxation contributed to μFA > FA. Thus, our finding supports the notion that that orientation dispersion is significant even in highly structured tissues, such as spinal cord white matter. This is in excellent agreement with a recent study of SDE-derived diffusion tensor and kurtosis time-dependencies which also pointed to the same conclusion in pig spinal cord [15], as well as with histological studies attempting to measure the dispersion directly in white matter [89]. It is difficult to draw conclusions on whether the orientation dispersion arises within intra- or extra-axonal spaces (or both), or, whether undulations [90] or passing collateral fibers [91] can contribute to these observations. Performing similar spectroscopic measurements utilizing cell-specific markers such as NAA or mI [52, 53], or performing much more extensive time/frequency/b-value-dependent measurements on water [19, 59, 92], or on metabolites [93, 94] may further assist in addressing this question in the future.

Another interesting aspect when comparing μFA with FA in white matter, is that the two metrics are only moderately correlated when measured with DODE, and very weakly correlated when measured with DDE (c.f. **Table 1**). This finding suggests that when diffusion is encoded using oscillating gradients, spins experience less orientation dispersion than when they are probed using block gradients, since μFA would be perfectly correlated (and identical) to FA for perfectly aligned

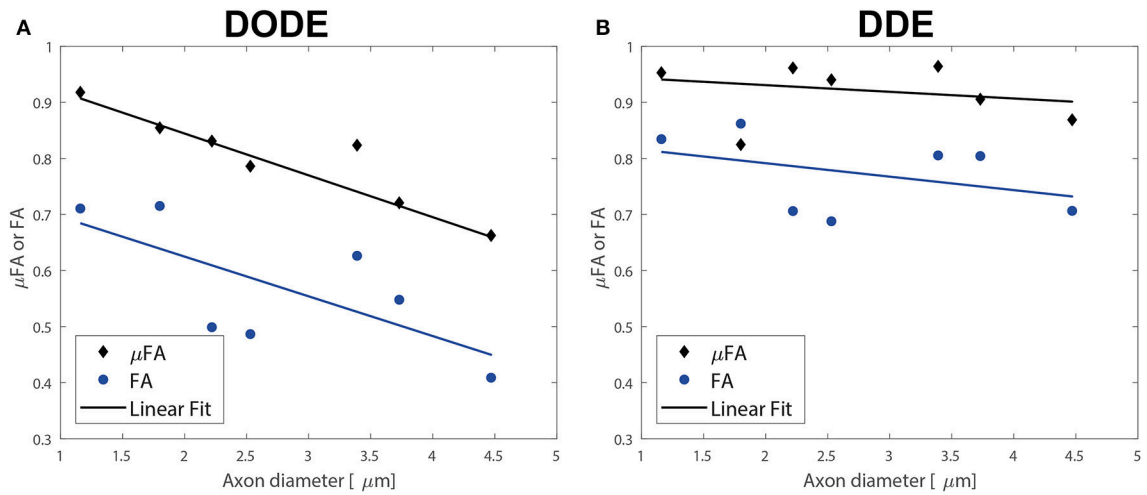

FIGURE 8 | Correlations of diffusion metrics with literature-based average axon diameters in the different white matter tracts. **(A)** Correlations of metrics derived from DODE. **(B)** Correlations derived from DDE. The best linear regressions to the experimental data are also given as solid lines. Note the excellent inverse agreement between μFA_{DODE} and axon diameter, which also had a very high anticorrelation coefficient of $\rho \sim -0.96$ while all other metrics did not show significant correlations.

TABLE 3 | Statistical analysis of correlations between (μ)FA and literature-based average axon diameter (extracted from Dula et al. [75]) in the rat spinal cord.

	μFA DODE	FA DODE	μFA DDE	FA DDE
WHITE MATTER				
Spearman's ρ, *p*-value	−0.96, 0.0028	−0.68, NS	−0.14, NS	−0.43, NS

fibers. Hence, our findings point to specific length scales for orientation dispersion that are probed differently using the different sequences.

Next, we consider the relationships between myelin and μFA. Akin to its FA counterpart–μFA is ambiguous in that a compartment with length "L" and radius "R" can give rise to the same μFA as a compartment with length 2L and radius 2R. The axial path length could be restricted due to nodes of Ranvier, non-ideal cylindrical structure, varicosities, etc. However, if the path length parallel to the (assumingly) ellipsoids is constant, then one could predict that when larger amounts of myelin surround an axon, the μFA will be smaller as the restriction will increase in the perpendicular direction. However, in our study, a moderate *negative* correlation was observed between MWF and μFA_{DODE} in white matter (**Figure 7** and **Table 2**). This can be explained by considering the dependence of MWF and axon diameter via the g-ratio [95]: the larger the axon, the thicker the myelin around it in (healthy) mammalian white matter [96]. Hence, the negative correlation between μFA_{DODE} and MWF would reflect indirectly the approximately constant g-ratio in healthy tissue, rather than enhanced restriction. Interestingly, μFA_{DDE} showed a much weaker, yet still negative correlation with MWF. Since the microstructure has not changed between measurements, this likely reflects that DODE and DDE probe different path lengths *parallel* to the spinal cord's major axis: the larger the diffusion time, the longer path will be probed in the unrestricted dimension, and thence the μFA will be larger and less reflective of axon diameter or, by proxy, its myelin thickness. FA_{DDE} showed a small positive correlation with MWF, which perhaps reflects the ambiguity of probing restriction and orientation distribution at the same time. Extracellular space contributions again cannot be neglected here, but for coherently aligned systems the arguments are similar as one could potentially treat the space between densely packed axons as potentially even more restricted than the intra-axonal space itself [45]. It is also worth mentioning that MWF extracted from multiexponential T_2 measurements, as performed in this study, have been shown in the past to reflect microstructural metrics such as axon size and myelin thickness very faithfully in white matter [67, 75, 97].

Our most striking findings in this study, perhaps, is that μFA_{DODE} showed an extremely high, and statistically significant, negative correlation with axon diameters reported by Dula et al. [75] and Harkins et al. [98] for the different tracts (**Table 3**). This observation lends further credence to the explanation above: the finite parallel length scale probed by DODE makes the measurement strongly dependent on the perpendicular restriction, which in this case is reflected through axon sizes. Although the axon diameters were obtained from literature, it is worth stressing that axon diameter dependence in healthy spinal cords is highly reproducible and that the tracts analyzed were obtained from very similar cervical slices as in Dula et al. [75]. Such a strong correlation is also highly unlikely to be obtained randomly. It is very interesting to also note that all other metrics did not correlate in a statistically significant fashion with axon diameters: μFA_{DDE} likely due to its probing of longer parallel lengths, and the FA from both methods due to its inherent conflation or restriction with orientation dispersion.

In the spinal cord gray matter, very low FA_{DODE} and FA_{DDE} values were measured, suggesting a much lower degree of restriction compared to white matter diffusion. However, the

μFA_{DODE} and μFA_{DDE} metrics in gray matter were still very high in the gray matter. In fact, the values reported in **Table 1** also reflect $\frac{\mu FA^{GM}_{DODE}}{\mu FA^{WM}_{DODE}} = \sim 0.92$ and $\frac{\mu FA^{GM}_{DDE}}{\mu FA^{WM}_{DDE}} = \sim 0.89$. Combined with the low FA values in the gray matter, our findings suggest that a significant component of gray matter tissue experiences restricted diffusion but with a large degree of orientation dispersion. This finding is also in good agreement with previous literature demonstrating significant angular DDE modulations in *ex-vivo* gray matter [44, 45]. Further studies are needed to establish which underlying biological components give rise to such high μFA in gray matter, but dendrites, astrocyte branches, and nonmyelinated or myelinated axons traversing gray matter could be suspected [93, 99]. Time-dependent or spectroscopic experiments on metabolites could provide insight into such questions in the future.

Several limitations can be identified in this study. First, we have introduced a new way of measuring $\mu\widetilde{A^2}$ harnessing the 5-design acquisition at two *b*-values to reduce the recently-reported bias in μA^2 estimation due to higher order terms. Our new method is likely inferior to a sampling of a large range of b-values and the ensuing polynomial fitting as done in Ianus et al. [62]. However, the advantage of the current approach is that it manages to avoid a prohibitively long experiment duration. Future studies will identify the accuracy and precision of the method proposed above vis-à-vis the ground-truth, and attempt to find optimal *b*-values for measuring $\mu\widetilde{A^2}$ as accurately and with as little bias as possible. Second, to compute μFA, we executed a third measurement at lower *b*-value to extract *MD*, which is then input into Eq. 2 along with $\mu\widetilde{A^2}$. However, MD itself may be conflated with higher-order terms, as pointed out recently by Chuhutin et al. [100]; in this study, this issue was not accounted for, and may induce minor biases in the measurements of μFA. Better estimation of MD could probably be performed by sampling one or more low *b*-values and fitting kurtosis and MD at the same time from spherically averaged data. In addition, we have not explored the impact of specific *b*-value selection. At too low *b*-values, the difference in the log signals is very small, while at higher *b*-values, even higher-order terms may come into play. Third, the sample size was quite small ($N = 2$ spinal cords, only a single slice per cord), such that the variability across animals was not very well sampled. However, it is worth noting that the results were actually very consistent between both spinal cords: the mean μFA and FA, for both DODE and DDE, varied <10% between the cords (both in gray and white matter tissues), and the MWF varied <6% between the tissues. Although this consistency is promising for the robustness of the approach, the small number of samples renders this study perhaps more exploratory. Fourth, the experiments were performed at a relatively long TE of 52 ms. Given that the MWF was associated with $T_2 < 20$ ms and that the other water T_2s were distributed between ∼20 and 60 ms, the diffusion experiments can be considered completely filtered for (directly contributing) myelin water, as $e^{\frac{-TE}{T_{2myelin}}} \sim 0.005$. Exchange between myelin water and intra/extra-axonal water is likely to occur, which may also confound the measurements, although it should be noted that at least for conventional DODE MRI, the relatively long TE is nearly unavoidable due to the necessity of non-negligible diffusion gradient waveform durations. Double-stimulated-echo approaches [101, 102] would thus be nearly impossible to execute for DODE, even before considering the significant SNR reduction associated with such sequences, $(1/2)^N$, where N is the number of stimulated echoes. Finally, a histological study was not here performed, and the study relies on literature reports of correlations between MRI-derived MWF and myelin thickness and the values for axon diameters. Future studies can expand the findings here and perform more direct correlations with histology, although it should be pointed out that big differences in these parameters are unlikely to be observed for healthy tissues. In addition, it would be fruitful to modulate the microstructure actively and to observe how μFA varies, e.g., using genetic mutations that alter myelin content. All these highly interesting avenues will be pursued in the future, but the present study provides the first steps in this direction.

CONCLUSIONS

This study investigated the microstructural correlates of μFA and FA using high resolution D(O)DE experiments in fixed spinal cords at 16.4 T. Our results indicate very strong anticorrelations of μFA_{DODE} with axon size, and moderate anticorrelations of μFA_{DODE} with MWF, whereas μFA_{DDE}, FA_{DODE} and FA_{DDE} correlate to a much lesser or no extent with those microstructural features. These findings shed light on the mechanisms of restriction in spinal cord white matter when investigate without conflation by orientation dispersion. The correlations of μFA_{DODE} with axon diameters and myelin water fraction are thus promising for future investigations of longitudinal variations in these properties, e.g., in disease or with learning.

AUTHOR CONTRIBUTIONS

NS designed the study, collected and analyzed data, and wrote the paper.

ACKNOWLEDGMENTS

This study was funded in part by the European Research Council (ERC) under the European Union's Horizon 2020 research and innovation programme (grant agreement No. 679058-DIRECT-fMRI). The author would like to thank Prof. Sune N. Jespersen and Mr. Jonas Lynge Olesen (Aarhus University) for providing the codes for denoising and Gibbs unringing, as well as for many insightful discussions. The author also thanks Dr. Daniel Nunes for extracting the tissues used in this study, Dr. Andrada Ianus and Ms. Teresa Serradas Duarte for providing parts of code used in the analyses performed here, and Prof. Mark D. Does from Vanderbilt University for the REMMI pulse sequence and its analysis tools, that were supported through grant number NIH EB019980.

REFERENCES

1. Johansen-Berg H, Behrens T. (2009). *Diffusion MRI: From Quantitative Measurement to in Vivo Neuroanatomy*. San Diego, CA: Academic Press.
2. Stejskal EO, Tanner JE. Spin diffusion measurements: spin echoes in the presence of a time-dependent field. *J Chem Phys*. (1965) **42**:288–92. doi: 10.1063/1.1695690
3. Shemesh N, Jespersen SN, Alexander DC, Cohen Y, Drobnjak I, Dyrby TB, et al. Conventions and nomenclature for double diffusion encoding NMR and MRI. *Magn Reson Med*. (2016) **75:** 82–7**.** doi: 10.1002/mrm.25901
4. Grebenkov DS. NMR survey of reflected Brownian motion. *Rev Mod Phys*. (2007) **79**:1077–137. doi: 10.1103/RevModPhys.79.1077
5. Assaf Y, Alexander DC, Jones DK, Bizzi A, Behrens TEJ, Clark CA, et al. The CONNECT project: combining macro- and micro-structure. *Neuroimage* (2013) **80**:273–82. doi: 10.1016/j.neuroimage.2013.05.055
6. Panagiotaki E, Schneider T, Siow B, Hall MG, Lythgoe MF, Alexander DC. Compartment models of the diffusion MR signal in brain white matter: a taxonomy and comparison. *Neuroimage* (2012) **59**:2241–54. doi: 10.1016/j.neuroimage.2011.09.081
7. Basser PJ, Jones DK. Diffusion-tensor MRI: theory, experimental design and data analysis-A technical review. *NMR Biomed*. (2002) **15**:456–67. doi: 10.1002/nbm.783
8. Mori S, Zhang J. Principles of diffusion tensor imaging and its applications to basic neuroscience research. *Neuron* (2006) **51**:527–39. doi: 10.1016/j.neuron.2006.08.012
9. Callaghan PT, Coy A, MacGowan D, Packer KJ, Zelaya FO. Diffraction-like effects in NMR diffusion studies of fluids in porous solids. *Nature* (1991) **351**:467–69. doi: 10.1038/351467a0
10. Cohen Y, Assaf Y. High b-value q-space analyzed diffusion-weighted MRS and MRI in neuronal tissues-A technical review. *NMR Biomed*. (2002) **15**:516–42. doi: 10.1002/nbm.778
11. Wedeen VJ, Hagmann P, Tseng WYI, Reese TG, Weisskoff RM. Mapping complex tissue architecture with diffusion spectrum magnetic resonance imaging. *Magn Reson Med*. (2005) **54**:1377–386. doi: 10.1002/mrm.20642
12. Clark CA, Hedehus M, Moseley ME. Diffusion time dependence of the apparent diffusion tensor in healthy human brain and white matter disease. *Magn Reson Med*. (2001) **45**:1126–9. doi: 10.1002/mrm.1149
13. Fieremans E, Burcaw LM, Lee HH, Lemberskiy G, Veraart J, Novikov DS. *In vivo* observation and biophysical interpretation of time-dependent diffusion in human white matter. *Neuroimage* (2016) **129**:414–27. doi: 10.1016/j.neuroimage.2016.01.018
14. Gore JC, Xu J, Colvin DC, Yankeelov TE, Parsons EC, Does MD. Characterization of tissue structure at varying length scales using temporal diffusion spectroscopy. *NMR Biomed*. (2010) **23**:745–56. doi: 10.1002/nbm.1531
15. Jespersen SN, Olesen JL, Hansen B, Shemesh N. Diffusion time dependence of microstructural parameters in fixed spinal cord. *Neuroimage* (2017). doi: 10.1016/j.neuroimage.2017.08.039. [Epub ahead of print].
16. Latour LL, Svoboda K, Mitra PP, Sotak CH. Time-dependent diffusion of water in a biological model system. *Proc Natl Acad Sci USA*. (1994) **91**:1229–33. doi: 10.1073/pnas.91.4.1229
17. Novikov DS, Fieremans E, Jensen JH, Helpern JA. Random walks with barriers. *Nat Phys*. (2011) **7**:508–14. doi: 10.1038/nphys1936
18. Stepišnik J, Lasič S, Mohorič A, Serša I, Sepe A. Spectral characterization of diffusion in porous media by the modulated gradient spin echo with CPMG sequence. *J Magn Reson*. (2006) **182**:195–9. doi: 10.1016/j.jmr.2006.06.023
19. Veraart J, Fieremans E, Novikov DS. Universal power-law scaling of water diffusion in human brain defines what we see with MRI. *arXiv* (2016). 1–8.
20. Jespersen SN, Kroenke CD, Østergaard L, Ackerman JJH, Yablonskiy DA. Modeling dendrite density from magnetic resonance diffusion measurements. *Neuroimage* (2007) **34**:1473–86. doi: 10.1016/j.neuroimage.2006.10.037
21. Jespersen SN, Bjarkam CR, Nyengaard JR, Chakravarty MM, Hansen B, Vosegaard T, et al. Neurite density from magnetic resonance diffusion measurements at ultrahigh field: comparison with light microscopy and electron microscopy. *Neuroimage* (2010) **49**:205–16. doi: 10.1016/j.neuroimage.2009.08.053
22. Zatorre RJ, Fields RD, Johansen-Berg H. Plasticity in gray and white: neuroimaging changes in brain structure during learning. *Nat Neurosci*. (2012) **15**:528–36. doi: 10.1038/nn.3045
23. Callaghan PT, Komlosh ME. Locally anisotropic motion in a macroscopically isotropic system: displacement correlations measured using double pulsed gradient spin-echo NMR. *Magn Reson Chem*. (2002) **40**:15–9. doi: 10.1002/mrc.1122
24. Cheng Y, Cory DG. Multiple scattering by NMR. *J Am Chem Soc*. (1999) **121**:7935–6. doi: 10.1021/ja9843324
25. Mitra PP. Multiple wave-vector extensions of the NMR pulsed-field-gradient spin-echo diffusion measurement. *Phys Rev B*. (1995) **51**:15074–8. doi: 10.1103/PhysRevB.51.15074
26. Jespersen SN, Lundell H, Sønderby CK, Dyrby TB. Orientationally invariant metrics of apparent compartment eccentricity from double pulsed field gradient diffusion experiments. *NMR Biomed*. (2013) **26**:1647–62. doi: 10.1002/nbm.2999
27. Jespersen SN, Olesen JL, Ianu A, Shemesh N. (2017b). Anisotropy in "isotropic diffusion "measurements due to nongaussian diffusion. *arXiv* 1–22.
28. Mollink J, Kleinnijenhuis M, Cappellen van Walsum AM, van Sotiropoulos SN, Cottaar M, Mirfin C, et al. Evaluating fibre orientation dispersion in white matter: comparison of diffusion MRI, histology and polarized light imaging. *Neuroimage* (2017) **157**:561–74. doi: 10.1016/j.neuroimage.2017.06.001
29. Reisert M, Kellner E, Dhital B, Hennig J, Kiselev VG. Disentangling micro from mesostructure by diffusion MRI: a bayesian approach. *Neuroimage* (2017) **147**:964–75. doi: 10.1016/j.neuroimage.2016.09.058
30. Cory DG, Garroway AN, Miller J. Applications of Spin Transport as a probe of local geometry. *Polym Preprints*. (1990) **31**:149.
31. Özarslan E. Compartment shape anisotropy (CSA) revealed by double pulsed field gradient MR. *J Magn Reson*. (2009) **199**:56–67. doi: 10.1016/j.jmr.2009.04.002
32. Laun FB, Kuder TA, Semmler W, Stieltjes B. Determination of the defining boundary in nuclear magnetic resonance diffusion experiments. *Phys Rev Lett*. (2011) **107**:2–5. doi: 10.1103/PhysRevLett.107.048102
33. Laun FB, Kuder TA, Wetscherek A, Stieltjes B, Semmler W. NMR-based diffusion pore imaging. *Phys Rev E*. (2012) **86**:021906. doi: 10.1103/PhysRevE.86.021906
34. Shemesh N, Özarslan E, Adiri T, Basser PJ, Cohen Y. Noninvasive bipolar double-pulsed-field-gradient NMR reveals signatures for pore size and shape in polydisperse, randomly oriented, inhomogeneous porous media. *J. Chem. Phys*. (2010) **133**:044705. doi: 10.1063/1.3454131
35. Shemesh N, Özarslan E, Basser PJ, Cohen Y. Detecting diffusion-diffraction patterns in size distribution phantoms using double-pulsed field gradient NMR: theory and experiments. *J Chem Phys*. (2010) **132**:034703. doi: 10.1063/1.3285299
36. Shemesh N, Westin CF, Cohen Y. Magnetic resonance imaging by synergistic diffusion-diffraction patterns. *Phys Rev Lett*. (2012) 108:058103. doi: 10.1103/PhysRevLett.108.058103
37. Koch MA, Finsterbusch J. Compartment size estimation with double wave vector diffusion-weighted imaging. *Magn Reson Med*. (2008) **60**:90–101. doi: 10.1002/mrm.21514
38. Koch MA, Finsterbusch J. Towards compartment size estimation *in vivo* based on double wave vector diffusion weighting. *NMR Biomed*. (2011) **24**:1422–32. doi: 10.1002/nbm.1711
39. Komlosh ME, Özarslan E, Lizak MJ, Horkay F, Schram V, Shemesh N, et al. Pore diameter mapping using double pulsed-field gradient MRI and its validation using a novel glass capillary array phantom. *J Magn Reson*. (2011) **208**:128–35. doi: 10.1016/j.jmr.2010.10.014
40. Morozov D, Bar L, Sochen N, Cohen Y. Microstructural information from angular double-pulsed-field-gradient NMR: from model systems to nerves. *Magn Reson Med*. (2015) **74**:25–32. doi: 10.1002/mrm.25371
41. Shemesh N, Özarslan E, Basser PJ, Cohen Y. Measuring small compartmental dimensions with low-q angular double-PGSE NMR: the effect of experimental parameters on signal decay. *J Magn Reson*. (2009) **198**:15–23. doi: 10.1016/j.jmr.2009.01.004

42. Nørhøj Jespersen S, Buhl N. The displacement correlation tensor: microstructure, ensemble anisotropy and curving fibers. *J Magn Reson*. (2011) **208**:34–43. doi: 10.1016/j.jmr.2010.10.003
43. Jespersen SN. Equivalence of double and single wave vector diffusion contrast at low diffusion weighting. *NMR Biomed*. (2012) **25**:813–18. doi: 10.1002/nbm.1808
44. Shemesh N, Cohen Y. Microscopic and compartment shape anisotropies in gray and white matter revealed by angular bipolar double-PFG MR. *Magn Reson Med*. (2011) **65**:1216–27. doi: 10.1002/mrm.22738
45. Shemesh N, Adiri T, Cohen Y. Probing microscopic architecture of opaque heterogeneous systems using double-pulsed-field-gradient NMR. *J Am Chem Soc*. (2011) **133**:6028–35. doi: 10.1021/ja200303h
46. Shemesh N, Barazany D, Sadan O, Bar L, Zur Y, Barhum Y, et al. Mapping apparent eccentricity and residual ensemble anisotropy in the gray matter using angular double-pulsed-field-gradient MRI. *Magn Reson Med*. (2012) **68**:794–806. doi: 10.1002/mrm.23300
47. Lawrenz M, Koch MA, Finsterbusch J. A tensor model and measures of microscopic anisotropy for double-wave-vector diffusion-weighting experiments with long mixing times. *J Magn Reson*. (2010) **202**:43–56. doi: 10.1016/j.jmr.2009.09.015
48. Lawrenz M, Finsterbusch J. Mapping measures of microscopic diffusion anisotropy in human brain white matter *in vivo* with double-wave-vector diffusion-weighted imaging. *Magn Reson Med*. (2015) **73**:773–83. doi: 10.1002/mrm.25140
49. Avram AV, Özarslan E, Sarlls JE, Basser PJ. *In vivo* detection of microscopic anisotropy using quadruple pulsed-field gradient (qPFG) diffusion MRI on a clinical scanner. *Neuroimage* (2013) **64**:229–39. doi: 10.1016/j.neuroimage.2012.08.048
50. Ulloa P, Wottschel V, Koch MA. Studying the extracellular contribution to the double wave vector diffusion-weighted signal. *Curr Dir Biomed Eng*. (2015) **1**:240–4. doi: 10.1515/cdbme-2015-0060
51. Finsterbusch J. Annual Reports on NMR Spectroscopy. *Multiple-Wave-Vector Diffusion-Weighted NMR*. 1st ed. Elsevier Ltd. (2011) **72**:225–99.
52. Shemesh N, Rosenberg JT, Dumez JN, Muniz JA, Grant SC, Frydman L. Metabolic properties in stroked rats revealed by relaxation-enhanced magnetic resonance spectroscopy at ultrahigh fields. *Nat Commun*. (2014) **5**:1–8. doi: 10.1038/ncomms5958
53. Shemesh N, Rosenberg JT, Dumez, J.-N., Grant SC, Frydman L. Distinguishing neuronal from astrocytic subcellular microstructures using *in vivo* double diffusion encoded 1H MRS at 21.1 T. *PLoS ONE* (2017) **12**:e0185232. doi: 10.1371/journal.pone.0185232
54. Does MD, Parsons EC, Gore JC. Oscillating gradient measurements of water diffusion in normal and globally ischemic rat brain. *Magn Reson Med*. (2003) **49**:206–15. doi: 10.1002/mrm.10385
55. Stepišnik J. Time-dependent self-diffusion by NMR spin-echo. *Phys B Phys Condens Matter* (1993) **183**:343–50. doi: 10.1016/0921-4526(93)90124-O
56. Drobnjak I, Zhang H, Ianuş A, Kaden E, Alexander DC. PGSE, OGSE, sensitivity to axon diameter in diffusion MRI: insight from a simulation study. *Magn Reson Med*. (2016) **75**:688–700. doi: 10.1002/mrm.25631
57. Xu J, Does MD, Gore JC. Quantitative characterization of tissue microstructure with temporal diffusion spectroscopy. *J Magn Reson*. (2009) **200**:189–97. doi: 10.1016/j.jmr.2009.06.022
58. Xu J, Li H, Harkins KD, Jiang X, Xie J, Kang H, et al. Mapping mean axon diameter and axonal volume fraction by MRI using temporal diffusion spectroscopy. *Neuroimage* (2014) **103**:10–9. doi: 10.1016/j.neuroimage.2014.09.006
59. Reynaud O, Winters KV, Hoang DM, Wadghiri YZ, Novikov DS, Kim SG. Surface-to-volume ratio mapping of tumor microstructure using oscillating gradient diffusion weighted imaging. *Magn Reson Med*. (2016) **76**:237–47. doi: 10.1002/mrm.25865
60. Xu J, Li K, Smith RA, Waterton JC, Zhao P, Chen H, et al. Characterizing tumor response to chemotherapy at various length scales using temporal diffusion spectroscopy. *PLoS ONE* (2012) **7**:e41714. doi: 10.1371/journal.pone.0041714
61. Ianuş A, Shemesh N, Alexander DC, Drobnjak I. Double oscillating diffusion encoding and sensitivity to microscopic anisotropy. *Magn Reson Med*. (2017) **78**:550–64. doi: 10.1002/mrm.26393
62. Ianuş A, Jespersen SN, Serradas T, Alexander DC. (2017). Accurate Estimation of Microscopic Diffusion Anisotropy and its Time Dependence in the Mouse Brain. *arxiv*.
63. Beaulieu C. The basis of anisotropic water diffusion in the nervous system-A technical review. *NMR Biomed*. (2002) **15**:435–55. doi: 10.1002/nbm.782
64. Klawiter EC, Schmidt RE, Trinkaus K, Liang HF, Budde MD, Naismith RT, et al. Radial diffusivity predicts demyelination in *ex vivo* multiple sclerosis spinal cords. *Neuroimage* (2011) **55**:1454–60. doi: 10.1016/j.neuroimage.2011.01.007
65. Komlosh ME, Lizak MJ, Horkay F, Freidlin RZ, Basser PJ. Observation of microscopic diffusion anisotropy in the spinal cord using double-pulsed gradient spin echo MRI. *Magn Reson Med*. (2008) **59**:803–09. doi: 10.1002/mrm.21528
66. Schwartz ED, Cooper ET, Chin, C.-L., Wehrli S, Tessler A, Hackney DB. *Ex vivo* evaluation of ADC values within spinal cord white matter tracts. AJNR. *Am J Neuroradiol*. (2005) **26**:390–7.
67. Kozlowski P, Liu J, Yung AC, Tetzlaff W. High-resolution myelin water measurements in rat spinal cord. *Magn Reson Med*. (2008) **59**:796–802. doi: 10.1002/mrm.21527
68. Kozlowski P, Raj D, Liu J, Lam C, Yung AC, Tetzlaff W. Characterizing white matter damage in rat spinal cord with quantitative mri and histology. *J Neurotrauma* (2008) **25**:653–76. doi: 10.1089/neu.2007.0462
69. Nunes D, Cruz TL, Jespersen SN, Shemesh N. Mapping axonal density and average diameter using non-monotonic time-dependent gradient-echo MRI. *J Magn Reson*. (2017) **277**:117–30. doi: 10.1016/j.jmr.2017.02.017
70. Wilhelm MJ, Ong HH, Wehrli SL, Li C, Tsai, P.-H., Hackney DB, et al. Direct magnetic resonance detection of myelin and prospects for quantitative imaging of myelin density. *Proc Natl Acad Sci USA*. (2012) **109**:9605–10. doi: 10.1073/pnas.1115107109
71. Guizar-Sicairos M, Thurman ST, Fienup JR. Efficient subpixel image registration algorithms. *Opt Let*. (2008) **33**:156. doi: 10.1364/OL.33.000156
72. Veraart J, Novikov DS, Christiaens D, Ades-aron B, Sijbers J, Fieremans E. Denoising of diffusion MRI using random matrix theory. *Neuroimage* (2016). **142**:394–406. doi: 10.1016/j.neuroimage.2016.08.016
73. Kellner E, Dhital B, Kiselev VG, Reisert M. Gibbs-ringing artifact removal based on local subvoxel-shifts. *Magn Reson Med*. (2016) **76**:1574–81. doi: 10.1002/mrm.26054
74. Eichner C, Cauley SF, Cohen-Adad J, Möller HE, Turner R, Setsompop K, et al. Real diffusion-weighted MRI enabling true signal averaging and increased diffusion contrast. *Neuroimage* (2015) **122**:373–84. doi: 10.1016/j.neuroimage.2015.07.074
75. Dula AN, Gochberg DF, Valentine HL, Valentine WM, Does MD. Multiexponential T2, magnetization transfer, and Quantitative histology in white matter tracts of rat spinal cord. *Magn Reson Med*. (2010) **63**:902–09. doi: 10.1002/mrm.22267
76. Prasloski T, Mädler B, Xiang QS, MacKay A, Jones C. Applications of stimulated echo correction to multicomponent T2analysis. *Magn Reson Med*. (2012) **67**:1803–14. doi: 10.1002/mrm.23157
77. De Almeida Martins JP, Topgaard D. Two-dimensional correlation of isotropic and directional diffusion using NMR. *Phys Rev Lett*. (2016) **116**:1–6. doi: 10.1103/PhysRevLett.116.087601
78. Lasič S, Szczepankiewicz F, Eriksson S, Nilsson M, Topgaard D. Microanisotropy imaging: quantification of microscopic diffusion anisotropy and orientational order parameter by diffusion MRI with magic-angle spinning of the q-vector. *Front Phys*. (2014) **2**:11. doi: 10.3389/fphy.2014.00011
79. Szczepankiewicz F, Lasič S, van Westen D, Sundgren PC, Englund E, Westin CF, et al. Quantification of microscopic diffusion anisotropy disentangles effects of orientation dispersion from microstructure: applications in healthy volunteers and in brain tumors. *Neuroimage* (2015) **104**:241–52. doi: 10.1016/j.neuroimage.2014.09.057
80. Westin CF, Knutsson H, Pasternak O, Szczepankiewicz F, Özarslan E, van Westen D, et al. Q-space trajectory imaging for multidimensional diffusion MRI of the human brain. *Neuroimage* (2016) **135**:345–62. doi: 10.1016/j.neuroimage.2016.02.039
81. De Swiet TM, Mitra PP. Possible systematic errors in single-shot measurements of the trace of the diffusion tensor. *J Magn Reson Ser B* (1996) **111**:15–22. doi: 10.1006/jmrb.1996.0055

82. Vellmer S, Edelhoff D, Suter D, Maximov II. Anisotropic diffusion phantoms based on microcapillaries. *J Magn Reson*. (2017) **279**:1–10. doi: 10.1016/j.jmr.2017.04.002
83. Vellmer S, Stirnberg R, Edelhoff D, Suter D, Stöcker T, Maximov II. Comparative analysis of isotropic diffusion weighted imaging sequences. *J Magn Reson*. (2017) **275**:137–47. doi: 10.1016/j.jmr.2016.12.011
84. Mädler B, Drabycz SA, Kolind SH, Whittall KP, MacKay AL. Is diffusion anisotropy an accurate monitor of myelination? Correlation of multicomponent T2 relaxation and diffusion tensor anisotropy in human brain. *Magn Reson Imaging* (2008) **26**:874–88. doi: 10.1016/j.mri.2008.01.047
85. West KL, Kelm ND, Carson RP, Does MD. A revised model for estimating g-ratio from MRI. *Neuroimage* (2016) **125**:1155–8. doi: 10.1016/j.neuroimage.2015.08.017
86. Álvarez GA, Shemesh N, Frydman L. Coherent dynamical recoupling of diffusion-driven decoherence in magnetic resonance. *Phys Rev Lett*. (2013) **111**:080404. doi: 10.1103/PhysRevLett.111.080404
87. Jiang X, Li H, Xie J, Zhao P, Gore JC, Xu J. Quantification of cell size using temporal diffusion spectroscopy. *Magn Reson Med*. (2016) **75**:1076–85. doi: 10.1002/mrm.25684
88. Lawrenz M, Brassen S, Finsterbusch J. Microscopic diffusion anisotropy in the human brain: age-related changes. *Neuroimage* (2016) **141**:313–25. doi: 10.1016/j.neuroimage.2016.07.031
89. Leergaard TB, White NS, De Crespigny A, Bolstad I, Dandapos Arceuil H, Bjaalie JG, et al. Quantitative histological validation of diffusion MRI fiber orientation distributions in the rat brain. *PLoS ONE* (2010) **5**:e8595. doi: 10.1371/journal.pone.0008595
90. Nilsson M, Lätt J, Ståhlberg F, van Westen D, Hagslätt H. The importance of axonal undulation in diffusion MR measurements: a monte carlo simulation study. *NMR Biomed*. (2012) **25**:795–805. doi: 10.1002/nbm.1795
91. Lundell H, Nielsen JB, Ptito M, Dyrby TB. Distribution of collateral fibers in the monkey cervical spinal cord detected with diffusion-weighted magnetic resonance imaging. *Neuroimage* (2011) **56**:923–29. doi: 10.1016/j.neuroimage.2011.02.043
92. Papaioannou A, Novikov DS, Fieremans E, Boutis GS. Observation of structural universality in disordered systems using bulk diffusion measurement. *Phys Rev E* (2017) **96**:61101. doi: 10.1103/PhysRevE.96.061101
93. Palombo M, Ligneul C, Najac C, Le Douce J, Flament J, Escartin C, et al. New paradigm to assess brain cell morphology by diffusion-weighted MR spectroscopy *in vivo*. *Proc Natl Acad Sci USA*. (2016) **113**:6671–6. doi: 10.1073/pnas.1504327113
94. Valette J, Ligneul C, Marchadour C, Najac C, Palombo M. Brain metabolite diffusion from ultra-short to ultra-long time scales: what do we learn, where should we go? *Front Neurosci*. (2018) **12**:2. doi: 10.3389/fnins.2018.00002
95. Guy J, Ellis EA, Kelley K, Hope GM. Spectra of G ratio, myelin sheath thickness, and axon and fiber diameter in the guinea pig optic nerve. *J Comp Neurol*. (1989) **287**:446–54. doi: 10.1002/cne.902870404
96. Innocenti GM. Development and evolution. Two determinants of cortical connectivity. *Prog Brain Res*. (2011) **189**:65–75. doi: 10.1016/B978-0-444-53884-0.00018-X
97. MacKay A, Laule C, Vavasour I, Bjarnason T, Kolind S, Mädler B. Insights into brain microstructure from the T2 distribution. *Magn Reson Imaging* (2006) **24**:515–25. doi: 10.1016/j.mri.2005.12.037
98. Harkins KD, Xu J, Dula AN, Li K, Valentine WM, Gochberg DF, et al. The microstructural correlates of T1 in white matter. *Magn Reson Med*. (2016) **75**:1341–5. doi: 10.1002/mrm.25709
99. Palombo M, Shemesh N, Ronen I, Valette J. (2017). Insights into brain microstructure from *in vivo* DW-MRS. *Neuroimage* doi: 10.1016/j.neuroimage.2017.11.028. [Epub ahead of print].
100. Chuhutin A, Hansen B, Jespersen SN. Precision and accuracy of diffusion kurtosis estimation and the influence of b-value selection. *NMR Biomed*. (2017) **30**:1–14. doi: 10.1002/nbm.3777
101. Jerschow A, Muller N. Suppression of convection artifacts in stimulated-echo diffusion experiments. Double-stimulated-echo experiments. *J Magn Reson*. (1997) **375**:372–5.
102. Shemesh N, Cohen Y. Overcoming apparent Susceptibility-Induced Anisotropy (aSIA) by bipolar double-Pulsed-Field-Gradient NMR. *J Magn Reson*. (2011) **212**:362–9. doi: 10.1016/j.jmr.2011.07.015

Conflict of Interest Statement: The author declares that the research was conducted in the absence of any commercial or financial relationships that could be construed as a potential conflict of interest.

frontiers in Neuroscience

PERSPECTIVE
published: 19 January 2018
doi: 10.3389/fnins.2018.00002

Brain Metabolite Diffusion from Ultra-Short to Ultra-Long Time Scales: What Do We Learn, Where Should We Go?

Julien Valette[1,2]*, *Clémence Ligneul*[1,2], *Charlotte Marchadour*[1,2], *Chloé Najac*[1,2] and *Marco Palombo*[3]

[1] Commissariat à l'Energie Atomique et aux Energies Alternatives, MIRCen, Fontenay-aux-Roses, France, [2] Neurodegenerative Diseases Laboratory, Centre National de la Recherche Scientifique, Université Paris-Sud, Université Paris-Saclay, UMR 9199, Fontenay-aux-Roses, France, [3] Department of Computer Science and Centre for Medical Image Computing, University College of London, London, United Kingdom

In vivo diffusion-weighted MR spectroscopy (DW-MRS) allows measuring diffusion properties of brain metabolites. Unlike water, most metabolites are confined within cells. Hence, their diffusion is expected to purely reflect intracellular properties, opening unique possibilities to use metabolites as specific probes to explore cellular organization and structure. However, interpretation and modeling of DW-MRS, and more generally of intracellular diffusion, remains difficult. In this perspective paper, we will focus on the study of the time-dependency of brain metabolite apparent diffusion coefficient (ADC). We will see how measuring ADC over several orders of magnitude of diffusion times, from less than 1 ms to more than 1 s, allows clarifying our understanding of brain metabolite diffusion, by firmly establishing that metabolites are neither massively transported by active mechanisms nor massively confined in subcellular compartments or cell bodies. Metabolites appear to be instead diffusing in long fibers typical of neurons and glial cells such as astrocytes. Furthermore, we will evoke modeling of ADC time-dependency to evaluate the effect of, and possibly quantify, some structural parameters at various spatial scales, departing from a simple model of hollow cylinders and introducing additional complexity, either short-ranged (such as dendritic spines) or long-ranged (such as cellular fibers ramification). Finally, we will discuss the experimental feasibility and expected benefits of extending the range of diffusion times toward even shorter and longer values.

Keywords: intracellular diffusion, brain metabolites, ADC time-dependency, microstructure, diffusion time

OPEN ACCESS

Edited by:
Sune Nørhøj Jespersen, Aarhus University, Denmark

Reviewed by:
Christopher D. Kroenke, Oregon Health & Science University, United States
Benoit Scherrer, Boston Children's Hospital, Harvard University, United States

***Correspondence:**
Julien Valette
julien.valette@cea.fr

Specialty section:
This article was submitted to Brain Imaging Methods, a section of the journal Frontiers in Neuroscience

Received: *25 September 2017*
Accepted: *03 January 2018*
Published: *19 January 2018*

Citation:
Valette J, Ligneul C, Marchadour C, Najac C and Palombo M (2018) Brain Metabolite Diffusion from Ultra-Short to Ultra-Long Time Scales: What Do We Learn, Where Should We Go? Front. Neurosci. 12:2. doi: 10.3389/fnins.2018.00002

INTRODUCTION

While water molecules are ubiquitous in the brain, many metabolites detected by magnetic resonance spectroscopy (MRS) *in vivo* are primarily intracellular, with typical extracellular concentrations ~1,000–10,000 times lower than intracellular concentrations. Moreover, works on extracts or cell cultures suggested that some metabolites exhibit preferential compartmentation in different cell types, with glutamate (Glu) and N-acetylaspartate (NAA) predominantly found in neurons, and myo-inositol (Ins) and choline compounds (tCho) preferentially found in glial cells (Simmons et al., 1991; Brand et al., 1993; Griffin et al., 2002; Le Belle et al., 2002; Choi et al., 2007) (in particular astrocytes, representing the largest volume fraction of glial cells). Hence,

measuring the brain metabolite diffusion may provide specific insight into cellular organization and microstructure.

The intracellular compartmentation of metabolites may *a priori* seem to simplify interpretation and modeling of metabolite diffusion as compared to water, because extracellular space and membrane permeability may be neglected. However, it is conceivable that metabolites are highly compartmentalized at a subcellular scale, in some subcellular regions or organelles. For example, NAA has been reported to be synthetized in mitochondria (Madhavarao et al., 2003), so that it may be primarily found in mitochondria. In this context, metabolite diffusion would reflect its subcellular metabolic compartmentation rather than diffusion within the whole cytosol and restriction by cell membrane. Here we will see how studying the time-dependency of metabolite apparent diffusion coefficient (ADC) allows clarifying the nature of the compartments where MRS-detected metabolites are diffusing, and may allow probing morphological features at different spatial scales. We will then try to explain some motivations and approaches to push further the limits of achievable diffusion times.

WHAT DOES ADC TIME-DEPENDENCY TELL ABOUT METABOLITE DIFFUSION?

To measure metabolite ADC at very short time-scales, experiments were performed in the rat (Marchadour et al., 2012) and mouse brain (Ligneul and Valette, 2017) using oscillating gradients. Measurements frequencies f went up to ∼250 Hz, corresponding to diffusion time t_d down to ∼0.5–1 ms, depending on the conversion used between f and t_d [$t_d = 1/(4f)$ based on the identification of the effective diffusion time in the b-value expression (Parsons et al., 2006), or using $t_d = 9/(64f)$ as derived in the Mitra limit when considering the surface-to-volume ratio of the restrictions (Novikov and Kiselev, 2011)]. They showed that ADC increased by ∼50% when f increased from ∼20 to 250 Hz for NAA, tCho, and tCr (also for Ins and Tau in the mouse brain), approaching ADC ∼0.2–0.30 μm^2/ms at the highest frequency. Note that, although later measurements in the mouse brain (Ligneul and Valette, 2017) suggested that early measurements in rats (Marchadour et al., 2012) may have been slightly biased by some motion artifact for some frequencies, the overall trend was preserved. The large ADC increase at short time-scales reflects significantly decreased restriction/hindrance and the progressive approach toward free diffusion. It rules out any significant contribution of active transport at these scales, which would result in the opposite trend (as the velocity autocorrelation function would be positive and decrease to 0 for increasing time Does et al., 2003). At ∼1 ms, the typical diffusion distance for metabolites is ∼1 μm, so the typical distance between obstacles/walls inducing ADC time-dependency must be in this range. More quantitatively, modeling metabolite ADC acquired in the rodent brain with oscillating gradients (Marchadour et al., 2012; Ligneul and Valette, 2017) using Stepisnik's and Callaghan's frequency-domain formalism for diffusion in cylinders or spherical pores (Stepisnik, 1981; Callaghan and Stepisnik, 1995) yields typical radii of ∼1 μm. It also allows estimating the free intracellular diffusivities to be D_{intra} ∼0.5–0.6 μm^2/ms, i.e., corresponding to a low-viscosity cytosol, less than twice the viscosity of pure water). This is in excellent agreement with fluorescence-based estimates of fluid-phase cytoplasm viscosity being quite similar to bulk water (Fushimi and Verkman, 1991; Luby-Phelps et al., 1993).

Measurements at longer t_d were achieved using pulsed-field gradients. Most DW-MRS works investigating brain metabolite diffusion were performed at a single t_d, in the 10–250 ms range, and reported ADC in the 0.1–0.25 μm^2/ms range (see for example Merboldt et al., 1993; Wick et al., 1995; Dreher et al., 2001 for measurements performed at t_d slightly longer than 10 ms, and Posse et al., 1993; Ellegood et al., 2006 for measurements at $t_d > 200$ ms). We are not aware of many works investigating t_d-dependency, except pioneer works where the high b-value attenuation of NAA was studied in the 35–305 ms range in excised rat brains (Assaf and Cohen, 1998a,b) and in the 50–100 ms range in the living rat brain (Kroenke et al., 2004). However, because acquisition and analysis differed between these studies, and some of them may be prone to artifacts (e.g., absence of scan-to-scan phase correction, incorrect b-value calculation ignoring cross-terms, signal contamination by macromolecules…), it is very difficult to see any clear pattern emerge in terms of ADC time-dependency. To specifically study ADC time-dependency at long t_d, a series of studies were performed in the rodent, primate and Human brain, all based on stimulated echo acquisitions (which are more favorable than spin echo to reach long t_d, as magnetization relaxes according to T1 during the mixing/diffusion time) and designed to minimize measurement bias (Najac et al., 2014, 2016; Palombo et al., 2016a). These studies all report very stable ADC (around 0.1 μm^2/ms, except in Human white matter where it was ∼0.15 μm^2/ms) for all metabolites as t_d is increased from a few dozen ms up to ∼700 ms in Human brain (Najac et al., 2016), and up to ∼2 s in the mouse and macaque brain (Najac et al., 2014; Palombo et al., 2016a). Note however that a slight trend to decrease can be observed (at least in the mouse and primate brain) when considering the whole time-window. The fact that ADC does not drop as t_d is increased up to 2 s is a very clear indication that metabolites are not confined in closed compartments of size equivalent to the diffusion distance (30–40 μm) or below, such as cell bodies or organelles (e.g., see Figure 3 in Najac et al., 2016). Instead, the fact that ADC remains fairly stable at approximately one third of the ADC value measured at ultra-short time-scales (**Figure 1**) is very consistent with metabolite diffusing in long fibers (in the ideal situation of infinitely long and straight fibers, and in the case of an isotropic distribution of fiber orientations, ADC would drop from D_{intra} at $t_d \sim 0$ to $D_{intra}/3$ once full restriction has been reached in the plane perpendicular to fiber axis, and then stabilize at $D_{intra}/3$ at longer t_d).

This framework of diffusion in long fibers can obviously only be considered as an approximation. First, cells do not consist of hollow tubes with smooth surfaces. The cytosol is filled with cytoskeleton and organelles which might induce

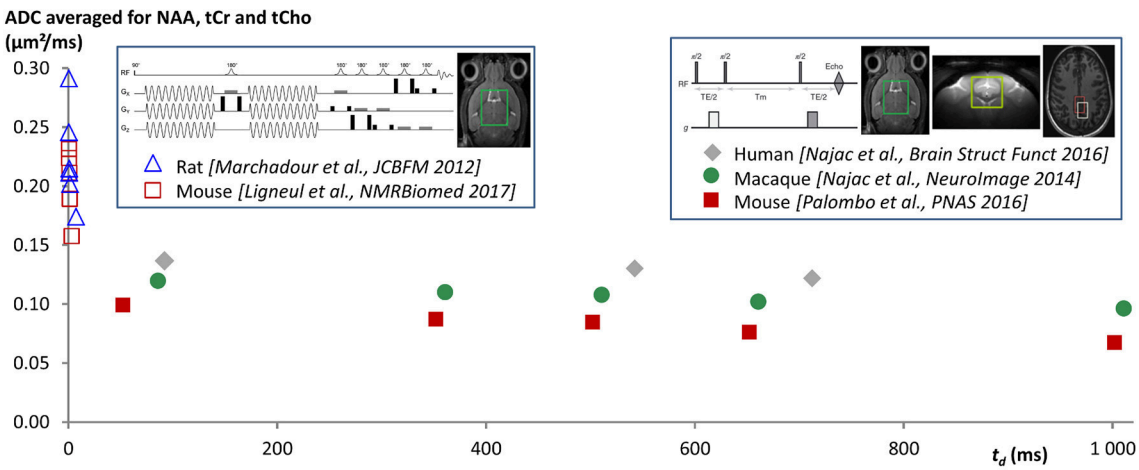

FIGURE 1 | ADC time-dependency as measured in different published works from ultra-short t_d using oscillating gradients [down to $t_d \sim 0.5$ ms when taking $t_d = 9/(64f)$ (Novikov and Kiselev, 2011), where f is the oscillating gradient frequency], up to very long $t_d \sim 1$ s using stimulated echo (data acquired at $t_d \sim 2$ s and reported in Palombo et al., 2016a are not shown here for clarity). Data points are ADC averaged for NAA, tCho, and tCr, but the trend is similar for each metabolite. The fact that ADC drops when t_d is increased at very short t_d, and then remains fairly stable at approximately one third of the ADC value measured at ultra-short times, is very consistent with metabolite diffusion mainly occurring in long and thin fibers (indeed, in the ideal situation of infinitely long and straight fibers, and in the case of an isotropic distribution of fiber orientations, ADC would drop from D_{intra} at infinitely short t_d to $D_{intra}/3$ once full restriction has been reached in the plane perpendicular to fiber axis, and then would stabilize at $D_{intra}/3$ at longer t_d, where D_{intra} is the free intracellular diffusivity). In a situation with metabolites massively confined in subcellular regions such as organelles or cell bodies, the ADC would drop to ~ 0 at long t_d over the observed time-range. Active transports would rather lead to ADC increasing with t_d, at least for the time-scales at which these transports become significant compared to diffusion.

tortuous diffusion. Similarly, dendritic spines and astrocytic leaflets, which are small protrusions along the dendrites and astrocytic processes, will slow down metabolites longitudinal diffusion, also resulting in tortuous diffusion along fiber axis. These features will result in decreased ADC plateauing at D_{intra}/τ along fibers at long t_d or, in the case of an isotropic distribution of fiber orientations or an isotropic ADC measurement (trace of the tensor), at $D_{intra}/(3\tau)$, where τ is the tortuosity along fibers. Theoretical considerations predict that this asymptotic value should be approached according to a $-1/2$ power-law in the case of a random distribution of obstacles with short-range disorder, i.e., $\mathrm{ADC}(t_d) \sim \mathrm{ADC}(t_d = \infty) + \mathrm{K}t_d^{-1/2}$, where K depends on the correlation length of the obstacles (Novikov et al., 2014). However, it is not trivial to determine when the tortuosity limit would be reached in practice, i.e., at what t_d would the ADC approach this asymptotic value within a few percent, which can be considered as a practical threshold due to limited measurement precision. Works based on numerical simulations suggested that tortuosity limit imposed by spines or similar structures with realistic densities (i.e., in the range of 0–5 μm^{-1}) would be reached within ~200 ms (Santamaria et al., 2006; Palombo et al., 2017), corresponding to a typical diffusion distance of ~10 µm along fibers. Hence the ADC value at ~200 ms could be a good estimate of $D_{intra}/(3\tau)$, which would allow extracting the tortuosity induced by short-range structures, provided D_{intra} is known. Considering the values of D_{intra} ~0.5–0.6 μm^2/ms estimated from modeling of oscillating gradients data in the rodent brain, and ADC ~ 0.1 μm^2/ms at $t_d \sim 200$ ms in the rodent brain, one gets $\tau \sim 1.6$–2, corresponding for example to 2–4 spines/leaflets per µm (see Table 1 in Palombo et al., 2017). This is however an upper estimate for τ. Indeed, other works based on the analysis of high b-value at a single t_d, using models of diffusion in cylinders, have reported D_{intra} to be rather ~0.3–0.45 μm^2/ms (Kroenke et al., 2004; Palombo et al., 2016b), which would rather correspond to a very low intracellular tortuosity $\tau \sim 1$–1.3 (corresponding to 0–1 spines or leaflets per µm), but these high-b values experiments were performed at $t_d \sim 50$–60 ms, so that D_{intra} might actually already include some tortuosity. This illustrates how the estimation of τ depends on estimation of D_{intra}, which remains indirect as it relies on some modeling.

Once the tortuosity limit imposed by short-range structures has been reached (beyond $t_d \sim 200$ ms), structural features at larger spatial scales (>~10 µm) are also expected to induce some temporal dependency of ADC, again challenging the approximation of diffusion in long cylinders. These structural features may include fiber undulation, fiber branching, and finite fiber length, which may explain the slight trend of ADC to decrease when increasing t_d up to ~2 s. The effect of undulations on intracellular diffusion has been investigated using analytical models or numerical simulations (Nilsson et al., 2012), while the effect of branching and finite length has been modeled using numerical simulations (Palombo et al., 2016a). Actually, the later approach was used to analyze experimental data, and suggested that realistic fiber branching and length were indeed quantitatively able to explain observed ADC time-dependency up to 2 s. In particular, diffusion compartments of supposedly astrocytic metabolites were found to be smaller and less complex than those of supposedly neuronal metabolites, and to be also smaller in rodents than in primates, consistently

with histology (Palombo et al., 2016a). In this latter work, an intracellular diffusion coefficient including some short-range tortuosity along fibers (equivalent to D_{intra}/τ) as discussed in the previous paragraph was also let as a free parameter in addition to morphometric parameters, and was found to be ~0.3–0.45 μm^2/ms, i.e., lower than those derived from oscillating gradient data, but very close to values derived from high-b values (Kroenke et al., 2004; Ligneul et al., 2017b), suggesting that the latter also already include short-range tortuosity. It is worth mentioning that these long-range structures are of different natures: in theory, undulation and branching would result in "long-range" tortuosity toward a non-zero ADC value, while finite length would result in full restriction with a t_d^{-1} approach toward zero. However, these different trends remain hypothetical, as they would become manifest only at very long t_d (several seconds or even tenths of seconds); at such t_d other phenomena such as intercellular trafficking, enzyme binding or biochemical transformations may become significant and obscure any long-time power law induced by structure.

WHY AND HOW TO GET FURTHER?

As discussed above, the determination of D_{intra} remains indirect and uncertain. However, it is in theory possible to directly measure D_{intra} provided ADC is measured at sufficiently short time-scales. Simulations in fibers with "realistic" spines/leaflets size and density, as performed in Palombo et al. (2017) but over an extended frequency range, suggest that oscillating gradient frequencies of at least 2,500 Hz are required to approach D_{intra} within less than 10% (assuming D_{intra} = 0.5 μm^2/ms). Reaching such high frequencies while maintaining sufficiently high b (~1 ms/μm^2 or higher) to reliably measure signal attenuation is extremely challenging. We have obtained preliminary metabolites ADC measurements up to f = 665 Hz in the rat brain (Ligneul et al., 2017a), using a gradient coil capable of reaching 1.5 T/m within 250 µs along each axis. This corresponds to t_d ~ 0.2 ms, when using $t_d = 9/(64f)$ in the Mitra limit (Novikov and Kiselev, 2011). ADC values of 0.25–0.3 μm^2/ms were measured, which actually well extend the trend toward higher ADC at higher frequencies as recently reported in the mouse brain (Ligneul and Valette, 2017), as shown in **Figure 2**. Although we are presumably far from reaching sufficiently high frequencies to directly get ADC ~ D_{intra}, it is actually tempting to estimate D_{intra} (and S/V) in the Mitra limit using the universal formula valid for oscillating gradients (Novikov and Kiselev, 2011), considering the nice linear trend when plotting ADC as a function of $f^{-1/2}$, which yields D_{intra} ~ 0.3 μm^2/ms for NAA and tCho, and ~0.35 for tCr (and S/V from 2.4 to 2.9 μm^{-1}). This seems relatively low, and compatible with the absence of short-range tortuosity when comparing to ADC values at longer t_d [ADC(t_d ~ 200 ms)~D_{intra}/3] but simulations actually show that the Mitra regime is not strictly reached yet in this frequency range, and that the estimation of D_{intra} (but not S/V) remains biased toward lower values if spines/leaflets are present (Palombo et al., 2017).

Exploring the uncharted territory from ~700 to ~2,500 Hz to reliably determine D_{intra} and the intracellular tortuosity would require extremely powerful gradients. To reach b = 1 ms/μm^2 at f = 2,500 Hz using a trapezoidal cosine waveform (Van et al., 2014) to maximize the weighting, while imposing total gradient waveform duration to be no more than 50 ms to retain some macromolecule signal (which is critical to discard datasets

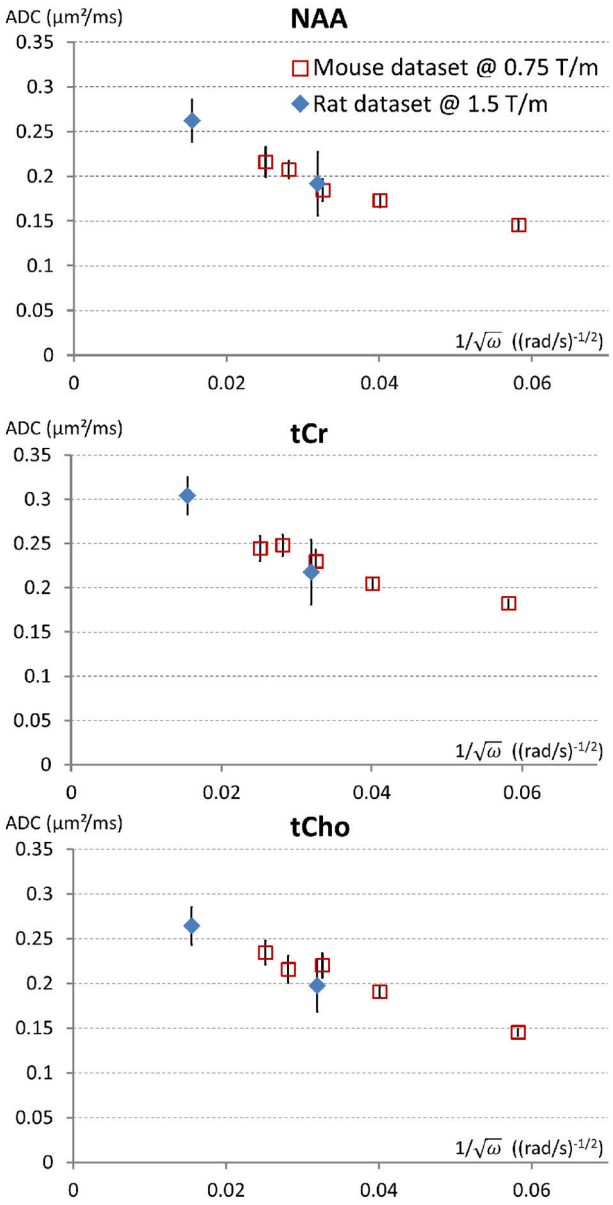

FIGURE 2 | Trying to approach the free intracellular diffusion coefficient of brain metabolites using oscillating gradients. On this figure the ADC measured for NAA, tCr, and tCho, in the mouse brain at 11.7 T using a gradient coil capable of reaching 0.75 T/m along each axis (red open squares) (Ligneul and Valette, 2017) and the rat brain at 7 T using a gradient coil capable of reaching 1.5 T/m along each axis (blue diamonds) (Ligneul et al., 2017a), are displayed as a function of the inverse of square root of the angular frequency [since a linear trend is expected for ADC($\omega^{-1/2}$) in the Mitra limit]. For better consistency between datasets, the first rat data obtained with oscillating gradients (Marchadour et al., 2012), which were probably slightly biased toward higher values due to some motion artifact, are not displayed here. Data points on the left (smallest $\omega^{-1/2}$) correspond to maximal OG frequency f = 665 Hz. Error bars stand for standard errors of the mean.

corrupted by motion artifacts; Ligneul and Valette, 2017), one would need a gradient coil capable of reaching ∼5.5 T/m within 100 µs along each axis. This appears beyond reach in Humans, and very difficult to achieve in preclinical systems. Hence, the possibility to measure the intracellular viscosity in a "model-free manner" essentially depends upon uncertain technological breakthrough, and may remain elusive.

Although going to $t_d \sim 2$ s seems to already yield some sensitivity to long-range structure (in particular fiber length), this sensitivity remains relatively poor. Indeed, the observed ADC time-dependency at long t_d, or the different time-dependency between neuronal and astrocytic metabolites, is quite close to ADC standard deviation, requiring averaging over many experiments. Further increase of t_d would allow enhancing the "ADC contrast" (relative decrease of ADC), which would subsequently lead to more reliable modeling and parameter estimation. For example, going to $t_d \sim 10$ s would approximately double the ADC contrast, for most situations with reasonable fiber length and complexity (see Figure 2 in Valette, 2014). Furthermore, going to such long t_d would help assessing the importance of phenomena that could potentially become significant at long time-scales (such as chemical exchange, intercellular exchange, active transport…) and that we have neglected so far, since structural effects alone appeared to satisfactorily explain data in the observed time-window.

Is it possible to reach $t_d \sim 10$ s (or longer)? Diffusion time is obviously limited by relaxation, and it is extremely difficult to measure diffusion much beyond metabolite T1. Increasing the magnetic field is a way to increase T1, but this gain becomes modest after 11.7 T (Lopez-Kolkovsky et al., 2016), therefore no significant jump beyond $t_d \sim 2$ s can be expected when increasing the magnetic field. However, it might be possible to observe metabolites with longer relaxation times under special conditions. For example, the ^{13}C nuclei of the carboxyl groups of glutamate and glutamine have very long T1 (∼10 vs. 1.5 s for ^{1}H at high fields), due to the absence of strong dipole-dipole interaction, as these carboxyl groups share no chemical bond with proton. ^{13}C natural abundance is too low (1.1%) to allow reliable detection in a reasonable time, however glutamate/glutamine can be labeled with ^{13}C at the C5 carboxyl group, by intravenously infusing glucose labeled at position C2 and/or C5 (Sibson et al., 2001). In that context, signal might be detectable by direct ^{13}C MRS. We actually tried to implement such an approach in the rat brain but, although some glutamate C5 signal could be detected, it remained too low for reliable ADC quantification. However, the progresses in radiofrequency coil technologies, and in particular the introduction of ^{13}C cryogenic probes, might make this strategy viable in a near future. Another possibility might reside in the "long-lived states" (Levitt, 2010) where the dipole-dipole coupling is made ineffective (for systems with only two coupled spins-1/2, this corresponds to the antisymmetric "singlet state" with total spin $I = 0$). Some molecules with a high enough degree of symmetry can be brought to (using dedicated pulse sequences exploiting J-coupling), and then maintained in such states (using spin-locking), during a time significantly exceeding T1, thus allowing diffusion measurements over longer time-scales. This approach was already suggested for slowly diffusing compounds (Cavadini and Vasos, 2008), where the gradient strength can be limiting to induce enough diffusion attenuation, which can instead be increased by increasing t_d. It is actually possible to bring some endogenous metabolites in such long-lived states. For example, taurine was shown to have long-lived state lifetime ∼3 times longer than T1 (∼2.7 vs. 1 s at 800 MHz; Ahuja et al., 2009). The extent to which long-lived state metabolite diffusion at ultra-long t_d may be measured *in vivo* remains to be explored.

CONCLUSION

Over the last years, the range of DW-MRS diffusion times has considerably increased, now spanning approximately four orders of magnitude in the rodent brain (from ∼0.2 ms to ∼2 s). These measurements concurred with the vision that intracellular metabolites are neither massively transported by active mechanisms nor massively restricted in subcellular regions, but are primarily diffusing in long fibers, and that these fibers have some short-range and long-range structures (dendritic spines and astrocytic leaflets, fiber embranchments, finite fiber length...) that may also influence ADC time-dependency. The full elucidation—and accurate quantification—of these deviations from the simple infinite cylinders model requires increasing even further the range of t_d by at least one order of magnitude (e.g., from 0.1 ms to 10 s), if not more, which appears extremely challenging, yet not absolutely impossible.

AUTHOR CONTRIBUTIONS

JV: Designed research and wrote the paper; CL, CM, CN: Performed most of the experiments described in this article and proofread the paper; MP: Performed most of the modeling described in this article and proofread the paper.

ACKNOWLEDGMENTS

JV is recipient of grant from the European Research Council about diffusion-weighted MRS (grant agreement No. 336331—INCELL project).

REFERENCES

Ahuja, P., Sarkar, R., Vasos, P. R., and Bodenhausen, G. (2009). Long-lived states in multiple-spin systems. *Chemphyschem* 10, 2217–2220. doi: 10.1002/cphc.200900335

Assaf, Y., and Cohen, Y. (1998a). *In vivo* and *in vitro* bi-exponential diffusion of N-acetyl aspartate (NAA) in rat brain: a potential structural probe? *NMR Biomed.* 11, 67–74. doi: 10.1002/(SICI)1099-1492(199804)11:2<67::AID-NBM503>3.0.CO;2-5

Assaf, Y., and Cohen, Y. (1998b). Non-mono-exponential attenuation of water and N-acetyl aspartate signals due to diffusion in brain tissue. *J. Magn. Reson.* 131, 69–85. doi: 10.1006/jmre.1997.1313

Brand, A., Richter-Landsberg, C., and Leibfritz, D. (1993). Multinuclear NMR studies on the energy metabolism of glial and neuronal cells. *Dev. Neurosci.* 15, 289–298. doi: 10.1159/000111347

Callaghan, P. T., and Stepisnik, J. (1995). Frequency-domain analysis of spin motion using modulated-gradient NMR. *J. Magn. Reson. Ser. A* 117, 118–122. doi: 10.1006/jmra.1995.9959

Cavadini, S., and Vasos, P. R. (2008). Singlet states open the way to longer time-scales in the measurement of diffusion by NMR spectroscopy. *Concepts Magn. Reson. A* 32A, 68–78. doi: 10.1002/cmr.a.20100

Choi, J. K., Dedeoglu, A., and Jenkins, B. G. (2007). Application of MRS to mouse models of neurodegenerative illness. *NMR Biomed.* 20, 216–237. doi: 10.1002/nbm.1145

Does, M. D., Parsons, E. C., and Gore, J. C. (2003). Oscillating gradient measurements of water diffusion in normal and globally ischemic rat brain. *Magn. Reson. Med.* 49, 206–215. doi: 10.1002/mrm.10385

Dreher, W., Busch, E., and Leibfritz, D. (2001). Changes in apparent diffusion coefficients of metabolites in rat brain after middle cerebral artery occlusion measured by proton magnetic resonance spectroscopy. *Magn. Reson. Med.* 45, 383–389. doi: 10.1002/1522-2594(200103)45:3<383::AID-MRM1050>3.0.CO;2-G

Ellegood, J., Hanstock, C. C., and Beaulieu, C. (2006). Diffusion tensor spectroscopy (DTS) of human brain. *Magn. Reson. Med.* 55, 1–8. doi: 10.1002/mrm.20777

Fushimi, K., and Verkman, A. S. (1991). Low viscosity in the aqueous domain of cell cytoplasm measured by picosecond polarization microfluorimetry. *J. Cell Biol.* 112, 719–725. doi: 10.1083/jcb.112.4.719

Griffin, J. L., Bollard, M., Nicholson, J. K., and Bhakoo, K. (2002). Spectral profiles of cultured neuronal and glial cells derived from HRMAS (1)H NMR spectroscopy. *NMR Biomed.* 15, 375–384. doi: 10.1002/nbm.792

Kroenke, C. D., Ackerman, J. J., and Yablonskiy, D. A. (2004). On the nature of the NAA diffusion attenuated MR signal in the central nervous system. *Magn. Reson. Med.* 52, 1052–1059. doi: 10.1002/mrm.20260

Le Belle, J. E., Harris, N. G., Williams, S. R., and Bhakoo, K. K. (2002). A comparison of cell and tissue extraction techniques using high-resolution 1H-NMR spectroscopy. *NMR Biomed.* 15, 37–44. doi: 10.1002/nbm.740

Levitt, M. H. (2010). Singlet and other states with extended lifetimes. *eMagRes.* doi: 10.1002/9780470034590.emrstm1036

Ligneul, C., Palombo, M., Flament, J., and Valette, J. (2017a). Approaching free intracellular diffusion by diffusion-weighted MRS at ultra-short time scales: initial results in the rodent brain using a 1.5 T/m gradient. *Proc. Intl. Soc. Mag. Reson. Med.* 25:1082.

Ligneul, C., Palombo, M., and Valette, J. (2017b). Metabolite diffusion up to very high b in the mouse brain *in vivo*: revisiting the potential correlation between relaxation and diffusion properties. *Magn. Reson. Med.* 77, 1390–1398. doi: 10.1002/mrm.26217

Ligneul, C., and Valette, J. (2017). Probing metabolite diffusion at ultra-short time scales in the mouse brain using optimized oscillating gradients and "short"-echo-time diffusion-weighted MRS. *NMR Biomed.* 30. doi: 10.1002/nbm.3671

Lopez-Kolkovsky, A. L., Mériaux, S., and Boumezbeur, F. (2016). Metabolite and macromolecule T1 and T2 relaxation times in the rat brain *in vivo* at 17.2T. *Magn. Reson. Med.* 75, 503–514. doi: 10.1002/mrm.25602

Luby-Phelps, K., Mujumdar, S., Mujumdar, R. B., Ernst, L. A., Galbraith, W., and Waggoner, A. S. (1993). A novel fluorescence ratiometric method confirms the low solvent viscosity of the cytoplasm. *Biophys. J.* 65, 236–242. doi: 10.1016/S0006-3495(93)81075-0

Madhavarao, C. N., Chinopoulos, C., Chandrasekaran, K., and Namboodiri, M. A. (2003). Characterization of the N-acetylaspartate biosynthetic enzyme from rat brain. *J. Neurochem.* 86, 824–835. doi: 10.1046/j.1471-4159.2003.01905.x

Marchadour, C., Brouillet, E., Hantraye, P., Lebon, V., and Valette, J. (2012). Anomalous diffusion of brain metabolites evidenced by diffusion-weighted magnetic resonance spectroscopy *in vivo*. *J. Cereb. Blood Flow Metab.* 32, 2153–2160. doi: 10.1038/jcbfm.2012.119

Merboldt, K. D., Hörstermann, D., Hänicke, W., Bruhn, H., and Frahm, J. (1993). Molecular self-diffusion of intracellular metabolites in rat brain *in vivo* investigated by localized proton NMR diffusion spectroscopy. *Magn. Reson. Med.* 29, 125–129. doi: 10.1002/mrm.1910290123

Najac, C., Branzoli, F., Ronen, I., and Valette, J. (2016). Brain intracellular metabolites are freely diffusing along cell fibers in grey and white matter, as measured by diffusion-weighted MR spectroscopy in the human brain at 7 T. *Brain Struct. Funct.* 221, 1245–1254. doi: 10.1007/s00429-014-0968-5

Najac, C., Marchadour, C., Guillermier, M., Houitte, D., Slavov, V., Brouillet, E., et al. (2014). Intracellular metabolites in the primate brain are primarily localized in long fibers rather than in cell bodies, as shown by diffusion-weighted magnetic resonance spectroscopy. *Neuroimage* 90, 374–380. doi: 10.1016/j.neuroimage.2013.12.045

Nilsson, M., Lätt, J., Ståhlberg, F., van Westen, D., and Hagslätt, H. (2012). The importance of axonal undulation in diffusion MR measurements: a Monte Carlo simulation study. *NMR Biomed.* 25, 795–805. doi: 10.1002/nbm.1795

Novikov, D. S., Jensen, J. H., Helpern, J. A., and Fieremans, E. (2014). Revealing mesoscopic structural universality with diffusion. *Proc. Natl. Acad. Sci. U.S.A.* 111, 5088–5093. doi: 10.1073/pnas.1316944111

Novikov, D. S., and Kiselev, V. G. (2011). Surface-to-volume ratio with oscillating gradients. *J. Magn. Reson.* 210, 141–145. doi: 10.1016/j.jmr.2011.02.011

Palombo, M., Ligneul, C., Hernandez-Garzon, E., and Valette, J. (2017). Can we detect the effect of spines and leaflets on the diffusion of brain intracellular metabolites? *Neuroimage*. doi: 10.1016/j.neuroimage.2017.05.003. [Epub ahead of print].

Palombo, M., Ligneul, C., Najac, C., Le Douce, J., Flament, J., Escartin, C., et al. (2016a). New paradigm to assess brain cell morphology by diffusion-weighted MR spectroscopy *in vivo*. *Proc. Natl. Acad. Sci. U.S.A.* 113, 6671–6676. doi: 10.1073/pnas.1504327113

Palombo, M., Ligneul, C., and Valette, J. (2016b). Modeling diffusion of intracellular metabolites in the mouse brain up to very high diffusion-weighting: diffusion in long fibers (almost) accounts for non-monoexponential attenuation. *Magn. Reson. Med.* 77, 343–350. doi: 10.1002/mrm.26548

Parsons, E. C., Does, M. D., and Gore, J. C. (2006). Temporal diffusion spectroscopy: theory and implementation in restricted systems using oscillating gradients. *Magn. Reson. Med.* 55, 75–84. doi: 10.1002/mrm.20732

Posse, S., Cuenod, C. A., and Le Bihan, D. (1993). Human brain: proton diffusion MR spectroscopy. *Radiology* 188, 719–725. doi: 10.1148/radiology.188.3.8351339

Santamaria, F., Wils, S., De Schutter, E., and Augustine, G. J. (2006). Anomalous diffusion in Purkinje cell dendrites caused by spines. *Neuron* 52, 635–648. doi: 10.1016/j.neuron.2006.10.025

Sibson, N. R., Mason, G. F., Shen, J., Cline, G. W., Herskovits, A. Z., Wall, J. E. M., et al. (2001). *In vivo* C-13 NMR measurement of neurotransmitter glutamate cycling, anaplerosis and TCA cycle flux in rat brain during [2-C-13]glucose infusion. *J. Neurochem.* 76, 975–989. doi: 10.1046/j.1471-4159.2001.00074.x

Simmons, M. L., Frondoza, C. G., and Coyle, J. T. (1991). Immunocytochemical localization of N-acetyl-aspartate with monoclonal antibodies. *Neuroscience* 45, 37–45. doi: 10.1016/0306-4522(91)90101-S

Stepisnik, J. (1981). Analysis of NMR self-diffusion measurements by a density-matrix calculation. *Physica B+C* 104, 350–364. doi: 10.1016/0378-4363(81)90182-0

Valette, J. (2014). Diffusion modeling in brain cell geometries parameterized according to morphometric statistics. *Proc. Intl. Soc. Mag. Reson. Med.* 22:4424.

Van, A. T., Holdsworth, S. J., and Bammer, R. (2014). *In vivo* investigation of restricted diffusion in the human brain with optimized oscillating diffusion gradient encoding. *Magn. Reson. Med.* 71, 83–94. doi: 10.1002/mrm.24632

Wick, M., Nagatomo, Y., Prielmeier, F., and Frahm, J. (1995). Alteration of intracellular metabolite diffusion in rat brain *in vivo* during ischemia and reperfusion. *Stroke* 26, 1930–1933. discussion: 1934. doi: 10.1161/01.STR.26.10.1930

Conflict of Interest Statement: The authors declare that the research was conducted in the absence of any commercial or financial relationships that could be construed as a potential conflict of interest.

The handling editor is currently editing a Research Topic with one of the authors JV, and confirms the absence of any other collaboration.

frontiers in Physics

ORIGINAL RESEARCH
published: 25 September 2018
doi: 10.3389/fphy.2018.00091

Characterization of Prostate Microstructure Using Water Diffusion and NMR Relaxation

Gregory Lemberskiy[1,2]*, *Els Fieremans*[1], *Jelle Veraart*[1], *Fang-Ming Deng*[3], *Andrew B. Rosenkrantz*[4] and *Dmitry S. Novikov*[1]

[1] Center for Biomedical Imaging, Department of Radiology, NYU School of Medicine, New York, NY, United States, [2] Sackler Institute of Graduate Biomedical Sciences, Biomedical Imaging and Technology Program, NYU School of Medicine, New York, NY, United States, [3] Department of Pathology, New York University Langone Medical Center, New York, NY, United States, [4] Department of Radiology, New York University Langone Medical Center, New York, NY, United States

For many pathologies, early structural tissue changes occur at the cellular level, on the scale of micrometers or tens of micrometers. Magnetic resonance imaging (MRI) is a powerful non-invasive imaging tool used for medical diagnosis, but its clinical hardware is incapable of reaching the cellular length scale directly. In spite of this limitation, microscopic tissue changes in pathology can potentially be captured indirectly, from macroscopic imaging characteristics, by studying water diffusion. Here we focus on water diffusion and NMR relaxation in the human prostate, a highly heterogeneous organ at the cellular level. We present a physical picture of water diffusion and NMR relaxation in the prostate tissue, that is comprised of a densely-packed cellular compartment (composed of stroma and epithelium), and a luminal compartment with almost unrestricted water diffusion. Transverse NMR relaxation is used to identify fast and slow T_2 components, corresponding to these tissue compartments, and to disentangle the luminal and cellular compartment contributions to the temporal evolution of the overall water diffusion coefficient. Diffusion in the luminal compartment falls into the short-time surface-to-volume (S/V) limit, indicating that only a small fraction of water molecules has time to encounter the luminal walls of healthy tissue; from the S/V ratio, the average lumen diameter averaged over three young healthy subjects is measured to be $217.7 \pm 188.7\,\mu$m. Conversely, the diffusion in the cellular compartment is highly restricted and anisotropic, consistent with the fibrous character of the stromal tissue. Diffusion transverse to these fibers is well described by the random permeable barrier model (RPBM), as confirmed by the dynamical exponent $\vartheta = 1/2$ for approaching the long-time limit of diffusion, and the corresponding structural exponent $p = -1$ in histology. The RPBM-derived fiber diameter and membrane permeability were $19.8 \pm 8.1\,\mu$m and $0.044 \pm 0.045\,\mu$m/ms, respectively, in agreement with known values from tissue histology and membrane biophysics. Lastly, we revisited 38 prostate cancer cases from a recently published study, and found the same dynamical exponent $\vartheta = 1/2$ of diffusion in tumors and benign regions. Our results suggest that a multi-parametric MRI acquisition combined with biophysical modeling may be a powerful non-invasive complement to prostate cancer grading, reducing the need for biopsies.

Keywords: prostate diffusion, microstructure imaging, prostate cancer, gleason score, RPBM, diffusion tensor imaging, biophysical modeling, PIRADS

OPEN ACCESS

Edited by:
Julien Valette, Commissariat à l'Energie Atomique et aux Energies Alternatives (CEA), France

Reviewed by:
Eleftheria Panagiotaki, University College London, United Kingdom
Denis Grebenkov, Centre National de la Recherche Scientifique (CNRS), France

***Correspondence:**
Gregory Lemberskiy
gregorylemberskiy@gmail.com

Specialty section:
This article was submitted to Biomedical Physics, a section of the journal Frontiers in Physics

Received: *27 December 2017*
Accepted: *26 July 2018*
Published: *25 September 2018*

Citation:
Lemberskiy G, Fieremans E, Veraart J, Deng F-M, Rosenkrantz AB and Novikov DS (2018) Characterization of Prostate Microstructure Using Water Diffusion and NMR Relaxation. Front. Phys. 6:91. doi: 10.3389/fphy.2018.00091

INTRODUCTION

Magnetic resonance imaging (MRI) research aims to identify and validate imaging biomarkers that offer insight for diagnosing diseases and monitoring their progression. This problem is difficult, because MRI hardware limitations result in images of about 1 mm resolution in all three dimensions. This resolution is too coarse to directly observe and categorize pathologies originating, primarily, at the cellular level of ∼1–100 μm. Hence, tissue characterization with MRI has generally been empirical in nature. However, recently the field of quantifying tissue microstructure with MRI has been gaining increasing attention, with the number of publications growing exponentially [1]. While not accessing the cellular-level structure directly, its overarching goal is to quantify typical microstructural tissue parameters *indirectly*, relying on biophysical modeling of the NMR signal acquired (i.e., averaged) over a macroscopic imaging voxel [2, 3].

The possibility of model-based microstructural mapping has spurred with the advent of diffusion MRI (dMRI) [4, 5], an imaging technique based on diffusion NMR [6–8], that measures the spatial Fourier transform $G_{t,q}$ of the voxel-averaged diffusion propagator $G_{t,x}$ (i.e., probability density of water molecules' displacements $x(t)$ over time t), in each voxel. By shifting the focus from nominal hardware resolution, to the effective length scale probed by the Brownian motion of spin-carrying molecules in each voxel, dMRI becomes sensitive to the microscopic tissue structure commensurate with the diffusion length (rms molecular displacement) $L(t) \sim \sqrt{D(t)\,t}$. The time-dependent diffusion coefficient $D(t) = \langle x^2(t)\rangle/2t \sim 1\ \mu\text{m}^2/\text{ms}$, or more generally, the time-dependent diffusion tensor, characterizes the rate of effective coarse-graining [3] of the tissue structure by the diffusing molecules over the diffusion time t. This time scale, and with that, the coarse-graining window $L(t)$, can be experimentally controlled within the range between a few to a few tens of microns, limited by the tissue NMR $T_1 \sim 1{,}000$ ms time scale.

The fundamental challenge lies in interpreting the measured diffusion propagator $G_{t,q}$, or its basic characteristics [e.g., the cumulants, such as the bulk diffusion coefficient $D(t)$], in the context of the complex mesh of biological tissue. In physics terms, for a given tissue, one has to identify the *relevant degrees of freedom* of its structural complexity at the scale of $L(t)$, that affect the bulk measurement the most, and thus can be quantified using biophysical modeling. Therefore, from the basic science standpoint, clinically-relevant dMRI research falls into the category of transport in classical disordered (random) media, a part of modern-day condensed matter physics. This establishes a somewhat unexpected yet exciting and fruitful connection [3, 9, 10] between the fundamental characterization of classical disordered transport, and the potentially clinically impactful applications in diagnostic radiology and in assessing treatment efficacy.

This study is focused on identifying the relevant degrees of freedom for dMRI within the prostate, which is a male organ that has highly heterogeneous tissue at multiple length scales **Figures 1A,B** [11]. While dMRI is used in clinic for prostate cancer diagnosis [12], the basic MRI-relevant characteristics of prostate microstructure have yet to be identified and validated. We will use prostate dMRI as an example to illustrate our basic physics-inspired approach for revealing and validating potential diagnostic markers of *in vivo* MRI.

To give a general sense of the relevant prostate anatomy (**Figure 1**), signal arising from any given voxel will come from a mixture of *macroscopic* stroma, epithelium, and lumen contributions, usually referred to as "compartments" [13]. Here, "macroscopic" means that their sizes exceed the available range of diffusion length scales. Yet the diffusion inside each of these compartments, at the scale $L(t)$, may be quite complex (non-Gaussian), as we will argue below. The stroma and epithelium compartments are densely packed and have comparable cellular length scales ∼10 μm, which allows us, for simplicity, to lump them into a single "cellular" compartment, whereas the glandular lumen are considerably larger and biophysically distinct—reminiscent of the "lakes" of almost unrestricted water, of ∼100 μm diameter in healthy tissue **Figure 1B** [14, 15]. (Later, we will comment on the relative roles of epithelium and stroma in the dMRI signal).

Partial-volume contributions of macroscopic compartments have been a persistent problem for model selection in dMRI. An empirical approach to intermixing compartments is by representing them with a multi-Gaussian diffusion signal expression, in which the signal is separated into components with different diffusion coefficients (or tensors), equivalent to the Laplace transform with respect to the so-called "diffusion weighting" parameter $b = q^2 t$, such that the Gaussian propagator corresponds to a monoexponential diffusion signal $S \sim e^{-bD}$. A bi-exponential signal representation, with "fast" and "slow" empirical diffusion coefficients, has been shown to fit very well to signals from fresh and fixed *ex-vivo* prostates [16], however the biophysical origin of compartment fractions and diffusivities has remained unclear.

The parameter b does not fully characterize a measurement, since, generally speaking, signal from each tissue compartment does not have to be Gaussian, in which case one needs to specify two parameters – e.g., q and t, or, as we will do here, b and t, in adherence to existing historical conventions [5]. In fact, the time dependence of the overall diffusion coefficient $D(t)$ necessarily means that at least one macroscopic tissue compartment n is characterized by time-dependent diffusion, in which case its propagator $G^{(n)}_{t,q}$ must be non-Gaussian [10], i.e., the Taylor expansion of $\ln G^{(n)}_{t,q}$ should generally have time-dependent higher-order cumulant terms $O(q^4)$, $O(q^6)$, ... Recently, we found significant time-dependence of the diffusion coefficient in benign and cancerous human prostates [17], highlighting the need to re-interpret multiexponential fits. Even at fixed t, over-interpreting the bi-exponential fit of the signal in terms of genuine Gaussian diffusion compartments has been cautioned against [18, 19].

Several studies have compared various modeling approaches side-by-side to determine the "correct" model using fit quality. Unfortunately, there is still no clear consensus on the preferred biophysical model, or even the most optimal

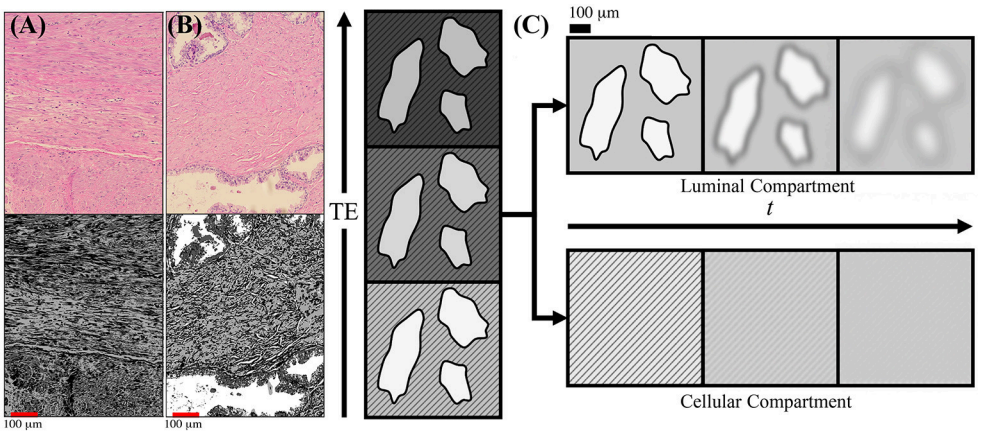

FIGURE 1 | Schematic of prostate microstructure and coarse-graining. H&E stained cross sections are shown from a radical prostatectomy **(A,B)**. To emphasize the structures and orientations, K-means clustering was applied onto the H&E images to emphasize the different intra-voxel compartrments and stromal orientations. In **(A)** we show that there is considerable structural anisotropy and local coherence in stromal cell orientation. There is an apparent directionality as certain fiber bundles of smooth muscle appear in both perpendicular and longitudinal cross sections within the a 1,000 × 784 μm^2 section. In **(B)** we show that stroma and glandular lumen can reside very close to each other, therefore the signal contribution from a voxel will be a weighted average depending on various tissue weightings. **(C)** As the echo time (T_E) increases, the cellular compartment (stripes) decays with a faster T_2, while the luminal compartment (solids) decays with a slower T_2. By modeling the T_2 weighting of each compartment, the signal weighting, W, of each tissue subtype can be determined based on the diffusion-free signal, S_0, cellular compartment fraction, f, and relaxation parameters T_1, T_2^C, and T_2^L. Given the compartment weights, the overall diffusion tensor may be subsequently separated into cellular-only and lumen-only tensors. Once tissue compartments are separated, the evolution of $D(t)$ in each tissue compartment can be interpreted through the context of the underlying microstructure. Diffusing molecules "see" the compartmental microstructure through the lens of a Gaussian filter of width $L(t) \sim \sqrt{D(t)\,t}$, which increases with t.

signal representation (i.e., a set of basis functions, cf. ref [1]). Some studies favor a mono-exponential [20, 21], others favor bi-exponential [16], while some suggest that including the empirical fourth-order cumulant (kurtosis) term in the overall signal provides the best fit [22]. Most importantly, each of these works agree that even the simplest mono-exponential representation of diffusion (at fixed t) already fits clinical data reasonably well. Putting their conclusions together, these works suggest that there may not be enough information to reliably select the adequate biophysical tissue model by studying diffusion (at fixed t) alone in clinically feasible acquisitions.

While identifying tissue compartments using diffusion is a challenge, separating compartments using transverse NMR relaxation, T_2, has been done as early as 1987 [23]. There has been a catalog of studies [23–27], which state that there exists a fast-decaying T_2 component, associated with cellular (epithelium+stromal) tissue, $T_2^C \sim 50$ ms, and a slowly-decaying T_2 component, associated with luminal tissue, $T_2^L \sim 350$ ms. Interestingly, the luminal compartment has a small volume fraction in the average MRI voxel (<10%) [13], yet due to its much longer T_2, it may notably contribute to the overall signal, as we confirm below. Meanwhile, the distinct geometry [14, 15] of cellular and luminal compartments should give rise to distinct functional forms for the time-dependent diffusion coefficients $D^C(t)$ and $D^L(t)$, respectively.

Here we introduce the following diffusion-relaxation model in the 3-dimensional parameter space: b, t, and echo time, T_E (**Figure 2**), with the signal as a sum of (generally non-Gaussian) contributions with distinct T_2 times:

$$S(b,t,T_E) = S|_{b,\,t,T_E=0} \cdot \sum_{n=C,L} f_n\, e^{-\frac{T_E}{T_2^{(n)}} - bD^{(n)}(t) + O(b^2)}. \quad (1)$$

In this work, we limit ourselves to the two major compartments, cellular = (stroma + epithelium), with volume fraction $f_C \equiv f$, and luminal, with $f_L = 1 - f$. Due to the notable difference in T_2 relaxation rates, the cellular compartment will lose its signal much faster than the luminal compartment with increasing echo time T_E, thereby creating a large dynamic range that will facilitate the separation of tissue compartments and their diffusion properties, as schematically pointed in **Figure 1C**. We will keep the b-value low, to stay in the diffusion tensor regime (effectively, factoring out the q-dependence) (see **Supplemental Information**), and vary the mixing time T_M of the stimulated echo sequence (**Figure 3**), thereby studying the dependence of diffusion tensors in the cellular and luminal compartments separately on the diffusion time t. The qualitatively distinct time-dependencies of $D^C(t)$ and $D^L(t)$ will be utilized for model selection in each compartment.

RELEVANT MODELS OF TIME-DEPENDENT DIFFUSION

Short-Time Limit: $D(t)$ as a Probe of S/V

At short diffusion times, the time-dependence of the diffusion coefficient can be described solely by the surface-to-volume

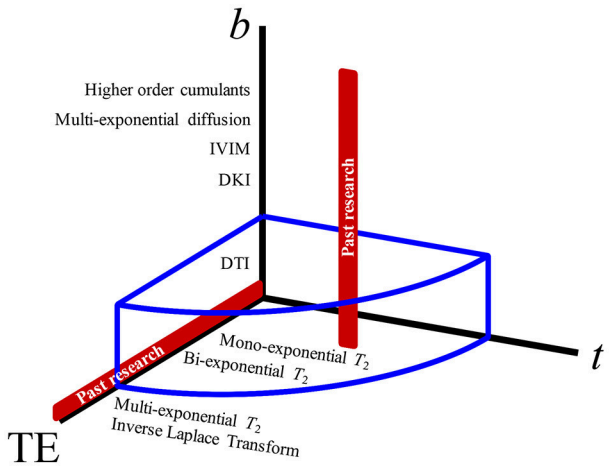

FIGURE 2 | The parameter space of MRI experiments. Varying the *b*-value (that yields, progressively, diffusion tensor imaging, diffusion kurtosis imaging, intravoxel-inherent motion, multiexponential diffusion, and other signal representations) has been the most popular approach to studying diffusion weighting (red vertical line). Diffusion time, *t*, giving measurements regarding structural disorder, and echo time, T_E, which can be used for altering the compartment weighting, have both been largely unexplored as effects on the diffusion measurements in the prostate. The blue volume surrounding the 3-axes represents the extent of parameter space covered by this study.

ratio (S/V) of the pore walls (e.g., cell membranes), and the unrestricted (free) diffusivity D_0 [28]:

$$D(t) = D_0\left(1 - \frac{4}{3d\sqrt{\pi}}\frac{S}{V}\sqrt{D_0 t}\right). \quad (2)$$

This equation assumes isotropic distribution of the restrictions to diffusion in d spatial dimensions. The advantage of this limit is that it offers a biologically relevant length scale, the inverse S/V, without too much model complexity and minimal assumptions. The disadvantage is in being sensitive only to the net amount of restrictions, rather than to their relative positions in space (i.e., structural correlations) and their permeability, as it occurs at longer times.

The range of times over which the S/V limit (2) is applicable is $t \ll l_{pore}^2/(2dD_0)$, where l_{pore} is the pore characteristic length scale; this estimate was recently validated in a phantom on the same clinical scanner used in this study [29]. Assuming that glandular lumen has $D_0 \approx 3\ \mu m^2/ms$ (free water at body temperature), and diameter $l_{pore} \sim 100\ \mu m$, the S/V limit will apply for $t \ll 500$ ms. This indicates that the S/V limit would be applicable in the healthy glandular lumen over a broad t range. However, luminal diameters do shrink with tumor grade [15, 30], which will shorten the range of t over which the S/V limit is applicable in patients. The corrections to Equation (2) due to wall curvature or permeability are beyond the scope of this work, due to signal-to-noise ratio and scan time limitations.

Long-Time Limit: *D*(*t*) as a Probe of Membrane Permeability and Structural Correlations

In contrast to the luminal compartment, the cellular compartment is densely packed and contains cells with small $\sim 10\ \mu m$ diameters, which may shrink even further with increasing tumor grade [31]. Assuming $D_0 \sim 1\ \mu m^2/ms$, locally in $d = 2$-dimensions due to fibrous geometry [13, 32] (as we will also confirm below), the range over which the S/V limit would apply is expected to be $t \leq 25$ ms. For clinically accessible t, diffusion in the cellular compartment will be acquired outside of the S/V limit. Exceeding this limit, the diffusion length becomes comparable or greater than the characteristic length scale of the tissue (cell diameter), and $D(t)$ becomes dependent on numerous tissue parameters describing both cell geometry and membrane permeability. In general, modeling diffusion in tissue geometry over a broad range of times is an unsolved problem, as it is unclear which features of tissue microarchitecture need to be included.

To identify what features of tissue complexity are most relevant for the measurement, Novikov et al. [9] showed that it is advantageous to observe time-dependent diffusion in the long time limit, approaching the bulk diffusion coefficient D_∞. Time-dependence in this limit reveals the most essential footprint of the underlying structure via the dynamical exponent ϑ in the *instantaneous* diffusion coefficient

$$D_{\text{inst}}(t) \equiv \frac{1}{2}\frac{\partial}{\partial t}\left\langle x^2(t)\right\rangle \sim D_\infty + A\cdot t^{-\vartheta},\ t\to\infty. \quad (3)$$

Here, A is the associated strength of the structural disorder, which is being effectively coarse-grained [3] by the molecules traveling over an increasing diffusion length. The exponent

$$\vartheta = (p+d)/2 \quad (4)$$

is related to the statistics of the global arrangement of tissue microstructure—in our case, of stroma and epithelium cells—via the *structural exponent* p in d spatial dimensions. The exponent p defines the structural universality class [9] of random media. Roughly speaking, the larger the exponent p, the faster the structural fluctuations decrease at large distances, and the more ordered the medium. Formally, this exponent describes the low-k behavior of the power spectrum $\Gamma(k) \sim Ak^p$ of the restrictions, corresponding to the decay of their density-density correlation function $\Gamma(\mathbf{r}) = \int \frac{d^dk}{(2\pi)^d} e^{i\mathbf{kr}}\Gamma(k)$ at large distances r. The Poissonian, and more generally, short-range disorder corresponds to $p = 0$, strong disorder to $p < 0$ (diverging fluctuations at large distances, e.g., due to spatially extended restrictions [9, 33]), and hyper-uniform disorder to $p > 0$ (variance of fluctuations within a volume growing slower than the volume [34]). The gradual coarse-graining of the structure embodied in $\Gamma(r)$ over an increasing diffusion length $L(t) \sim r$ results in the universal scaling, Equation (3). Note that the dimensionality d of the diffusion process has to be inferred from the shape of the diffusion tensor. In an isotropic case $d = 3$, whereas, for instance, for an axially symmetric diffusion tensor

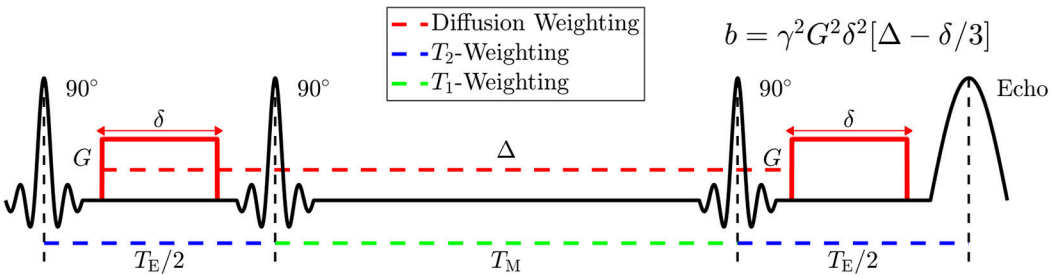

FIGURE 3 | Diagram of the Stimulated Echo Acquisition Mode (STEAM) sequence showing how to manipulate parameters of NMR relaxometry (T_2 and T_1) by varying the echo time, T_E, and the mixing time, T_M; and how to manipulate parameters of diffusion weighting by varying the applied gradient amplitude, G, the applied gradient duration, δ, and the spacing Δ between applied gradients. The diffusion time t is approximately given by Δ; the accuracy in its definition is set by the value of δ, cf. section 2.3 of Novikov et al. [3].

(e.g., in tissue fibrous geometry), $d = 2$ for the transverse and $d = 1$ for the longitudinal diffusion eigenvalues $\lambda_\perp$ and $\lambda_{||}$, correspondingly.

The universal asymptotic law (3), with the relation (4) between the structure and diffusive dynamics, is a recipe for model selection. However, dMRI measures the cumulative $D(t) = \frac{1}{t}\int_0^t D_{\text{inst}}(t')dt'$. Such temporal averaging limits the range of directly-measurable exponents (without differentiating noisy data), since the corresponding long-time tail in $D(t)$ will have the exponent $\tilde{\vartheta} = \min(\vartheta, 1)$ [9, 35]. We now outline a few relevant structural universality classes.

Structural order in any *d*, and hyperuniform disorder ($p > 0$) in $d \geq 2$ dimensions all have $\vartheta > 1$, which means that the tail in the cumulative $D(t)$ will have exponent $\tilde{\vartheta} = 1$, masking the genuine ϑ:

$$D(t) \simeq D_\infty + A \cdot t^{-1},\ t \to \infty. \quad (5)$$

Hyperuniform disorder suppresses structural fluctuations and may arise in optimal random packings [36]. In a sense, hyperuniform disorder is the closest to a perfectly periodic arrangement of the building blocks in a medium. Equation (5) tells that any such arrangement (e.g., a *periodic* lattice of barriers [37], or the "crystal lattice" of identical cells) would yield the asymptotic $\sim 1/t$ behavior in $D(t)$.

A similar-looking $1/t$ tail arises when a tissue compartment corresponds to perfectly *impermeable* cells of size $\sim \sqrt{A}$ (fully restricting cell walls), placing a hard upper bound on $\langle x^2(t)\rangle$. This is, perhaps, the simplest non-Gaussian compartment model, and it has been popular in describing dMRI signal from tumors [38–42].

Short-range disorder in 2 dimensions (e.g., transverse to aligned fibers randomly packed in a bundle) yields $\vartheta = 1$ and the corresponding $\ln(t/\delta)/t$ tail in $D(t)$, which, for the diffusion gradient pulse width $\delta > t_c$ exceeding the corresponding correlation time across the packing correlation length, yields the behavior [43]

$$D(t,\delta) \simeq D_\infty + \frac{A}{2\delta^2\left(t-\frac{\delta}{3}\right)}\left[t^2 \ln\frac{t^2-\delta^2}{t^2} + \delta^2 \ln\frac{t^2-\delta^2}{\delta^2} + 2t\delta \ln\frac{t+\delta}{t-\delta}\right],\ t > \delta, \quad (6)$$

that asymptotically becomes $A\ln(t/\delta)/t$ for $t \gg \delta$.

Extended-disorder (random membranes), e.g., random lines in $d = 2$ dimensions or randomly placed and oriented planes in $d = 3$, yields the slow power-law tail [33]

$$D(t) \simeq D_\infty + A \cdot t^{-\frac{1}{2}},\ t \to \infty. \quad (7)$$

This disorder geometry was approximately described for all t by the random permeable barrier model (RPBM) based on the real-space renormalization group approach to the diffusion equation represented as a scattering problem [33]. The RPBM was subsequently found to well describe diffusion transverse to muscle fibers ($d = 2$) [9, 44–46], where diffusion along fibers was practically unrestricted, while the transverse diffusion coefficient strongly decreased with t.

Note a subtle yet important difference between Equations (6) and (7), as applied to the $d = 2$ fiber geometry: Equation (6) applies if the fibers are randomly packed in a bundle, hindering the extra-cellular water (such as a random packing of disks in the cross-section [43]), yielding $\Gamma(k) \sim$ const for $k \to 0$, i.e., $p = 0$, while Equation (7) applies if the cell walls appear to be *locally flat* (i.e., lines in the cross-section, **Figure 4A**) and sufficiently permeable, so that the intra- and extra-cellular spaces can be considered on an equal footing. The exponent ½ arises due to the distinct spatial statistics of the restrictions, **Figure 4A**, represented by the locally flat permeable membranes (fiber walls) that extend for longer than the diffusion length, and yield the corresponding low-k divergence in $\Gamma(k) \sim k^{-1}$; the temporal scaling (7) emerges when these membranes are traversed more than once during the diffusion time t.

We have recently shown that there is a measurable effect of a time-dependent $D(t)$, which differs between benign and various stages of peripheral zone cancer [17]. This adds to a growing body of research that is interested in modeling $D(t)$ for cancer applications [42]. However, at that point we have not separated the relative compartment contributions to the overall $D(t)$. We realized that partial volume effects [47] need to be overcome, so that the microstructure of intermixing tissue can be identified. In what follows, by decomposing the dMRI signal into fast and slow T_2 compartments, model selection for $D(t)$ within cellular and luminal tissues will be performed independently, based on the above range of models of diffusion in disordered media.

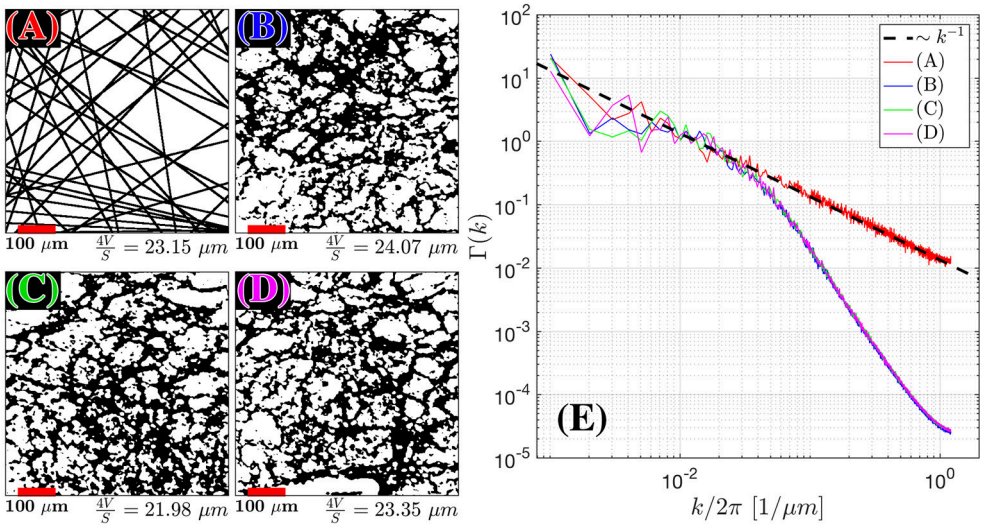

FIGURE 4 | Structural Correlation from histopathology. H&E stained samples of benign fibromuscular stroma from a radical prostatectomy were considered. In the body of the text, we found that extended disorder geometry, related to random membranes, defined the structural disorder for $D_{\perp}^{C}$. We plot 55 randomly oriented membranes in 2D **(A)** as an idealistic case for extended disorder and 3 samples **(B–D)** of segmented prostate fibromuscular stroma, which are predominantly taken through perpendicular cross sections. The segmentation was used to emphasize the cell walls as the primary sources of restriction to diffusion. The average length scale from was determined by calculating $S/V = 2l/A$ **(A)** and $S/V = l/A$ for **(B–D)**, where l is the number of voxels found at the edge of each cell, and A is the area of the sample. The number of randomly oriented barriers in **(A)** was selected to match the average fiber diameter $4V/S$ for the histological samples. For **(A–D)** the Fourier transform density autocorrelation function, $\Gamma(k)$ was determined by radially averaging over k-space and plotting 1,200 bins from the 1,440 × 1,440 pixel^2 / 590 × 590 μm^2 images **(E)**. The dashed black line represents the fit $\Gamma(k) = Ak^{-1}$.

We emphasize, that here we are performing model selection by inferring the distinct *functional form* of the measured $D(t)$, rather than relying on goodness-of-fit metrics which can be often misleading [1]. By identifying the dynamical exponent (4), or the short-time regime (2), we are, in a way, asking the tissue to reveal its type of structure (the S/V limit, or a structural universality class), instead of imposing a particular model of restricted diffusion from the outset. Identification of the disorder class will then justify searching for the most parsimonious model within that class. This logic naturally follows the fact that the structural complexity is hierarchical; its most relevant degrees of freedom should be identified first (they define the signal's overall functional form), followed by fine-tuning the remaining microscopic details, SNR permitting.

METHODS

Subjects

This study was in compliance with the Health Insurance Portability and Accountability Act guidelines and was approved by the institutional review board of New York University School of Medicine. Following written informed consent, 3 male volunteers (ages: 22, 28, 32) with no history of prostate disease were imaged on a MAGNETOM 3T Prisma system (Siemens AG, Erlangen, Germany) using the 18-channel phased array body coil.

MRI Acquisition

The major challenge in separating between the compartment diffusivities is to accurately map out the necessary parameters pertaining multi-compartment relaxation, and to measure the diffusion in a broad range of diffusion times for the model selection purpose. For these reasons, we used a stimulated echo acquisition mode (STEAM) sequence (WIP916B, Siemens), which allows us to study diffusion dependence on T_E and t simultaneously (**Figure 3**). STEAM is the preferable pulse sequence, as it is T_1-weighted and preserves more signal at long t, than the more commonly used T_2-weighted pulsed gradient spin echo (PGSE) diffusion sequence.

Diffusion weighted images (DWI) were acquired in sets of 17 non-collinear directions distributed on a sphere at $b = 0.5$ ms/μm^2 $= 500$ s/mm^2, and 2 nominally-unweighted images (which do not, technically, correspond to $b = 0$, but whose b-value is calculated within the sequence). With this orientation of gradient directions, DWI were acquired with $T_E = [52, 115, 180]$ ms and $t = [25.2, 40, 65, 105, 175, 280, 450, 740]$ ms, resulting in a total of 24 imaging series, each containing 17+2 = 19 imaging volumes. The applied gradient pulse duration, δ, was fixed to 10 ms, and the applied gradient amplitude, G, decreased with t, where the average $G(t)$ was [56.51, 43.65, 33.66, 26.21, 20.18, 15.89, 12.51, 9.74] mT/m. STEAM allows the user to modulate the mixing time (T_M), which is the spacing between the second and third RF pulses, giving rise to a variable T_1 weighting (**Figure 3**). The mixing time is also related to t, which is the spacing between the de-phasing and re-phasing diffusion gradients in the narrow-pulse limit. Here, T_M ranged from 6.38 to 719.32 ms and varied with changing T_E and t.

The order of the acquisitions was randomized to avoid any potential temperature effects and aid in image registration (see

next sub-section). Diffusion gradients were compensated to match the requested *b*-value [42, 48, 49]. As the amplitude of diffusion gradients decreased with *t*, the nominal $b = 0$ weighting increased from 3 to 102 s/mm^2. The SNR, calculated via [50], at these nominal $b = 0$ ranged from 39.0 down to 5.3, dropping with increasing T_M and T_E. The repetition time, T_R, was fixed to 5 s in order to minimize scan time, yet enabling practically full magnetization recovery. The imaging resolution was 2.5 × 2.5 × 5.0 mm^3 over a 96 × 96 × 10 grid with a bandwidth of 1,490 Hz/pixel. To minimize the echo train length, the acquisition was under-sampled using GRAPPA parallel receive with acceleration factor 2, multiband acceleration with factor 2, and 6/8 partial Fourier. Adaptive combine was used to merge images from individual receive coils with optimal phase shifts. In order to minimize geometric distortions, diffusion images were acquired axially with slices oriented parallel to the static magnetic field rather than perpendicular to the rectal wall. Distortion was further reduced through the use of the static field correction [51] as implemented by the vendor.

Image Processing

Firstly, Gibbs ringing correction [52] was applied to all dMRI images. Outlier rejection and reduction of eddy currents was then implemented for each of the 24 series separately, using FSL's *eddy* [53] tool. This tool also applied rigid registration within each diffusion tensor. A separate mutual-information rigid transformation was performed [54, 55] to align the images from each series to one another. Given the wide range of T_E and SNR, we found that mutual registration to $T_E = 180$ ms would produce inconsistent results. To resolve this, the acquisition was performed in random order. The parameters for rigid (Euler) transformation calculated from higher SNR images at either $T_E = 52$ or 115 ms were then applied to the subsequent $T_E = 180$ ms series, acquired immediately afterwards. This assumes that the volunteers remained mostly stationary for ∼3 minutes. Parametric maps of mean diffusivity *(D)* and fractional anisotropy (FA) were derived for each tensor acquisition using a weighted linear least squares fit [56, 57] using diffusion tensor imaging (DTI) estimation implemented in MATLAB. The region of interest (ROI) was drawn on a high resolution T_2-weighted image to study the peripheral zone (PZ) of the prostate (**Figure 9A**). Our volunteers were much younger than a typical prostate patient, so the size of the transition zone/central gland was much smaller than that in the clinical practice. For this reason, ROI analysis focused on PZ only.

Estimation of Compartment Weights

If there are observable compartments in T_2, they likely exist in T_1 as well. One conference abstract [58] identified a slow T_1 compartment of 2,944 ± 765 ms, which suggests that the luminal compartment is indeed nearly unbounded water. Kjaer et al. [23] have also acknowledged that a long T_1 compartment likely exists, but stated that they were unable to measure it within clinical SNR and time-constraints. Since the range of T_M in our experiment was <800 ms, we were unable to take advantage of this longer T_1 compartment to improve our modeling estimates. For this reason, we account for mono-exponential T_1 relaxation only. If we maintain a constant repetition time (T_R) and assume perfect $\pi/2$ RF pulses, the signal evolution for a STEAM acquisition *without* diffusion weighting can be written as:

$$S|_{b=0}(T_M, T_E) = S_0 e^{-T_M/T_1}\left(\underbrace{f e^{-T_E/T_2^C}}_{C} + \underbrace{(1-f)\, e^{-T_E/T_2^L}}_{L}\right). \quad (8)$$

We used weighted linear least squares [57] to estimate the unweighted $S|_{b=0}$ images. $S|_{b=0}$ values for the range of T_M and T_E were used to solve for the 5 parameters $(S_0, f, T_2^C, T_2^L, T_1)$ in Equation (8), **Figure 5**. The fit of Equation (8) to the data in each voxel was reinitialized 100 times with randomized starting values over unconstrained bounds. After rejecting the trials in which the fit results were unphysical, the median of the cluster of estimated parameters with the highest prevalence was selected as the final result.

Subsequently, the relative compartment weights for each T_M and T_E can be determined [with *C* and *L* from Equation (8)]:

$$W^C \equiv W(T_E) = \frac{C(T_E)}{C(T_E) + L(T_E)},\ W^L = 1 - W. \quad (9)$$

The cumulant expansion [59] of the signal, Equation (1), yields

$$D(t, T_E) = W^C(T_E) \cdot D^C(t) + W^L(T_E) \cdot D^L(t). \quad (10)$$

For a number *N* of distinct T_E measurements, Equation (10) reads

$$\begin{bmatrix} D(t, T_{E_1}) \\ D(t, T_{E_2}) \\ \vdots \\ D(t, T_{E_N}) \end{bmatrix} = \mathbf{W}\begin{pmatrix} D^C(t) \\ D^L(t) \end{pmatrix},\ \mathbf{W} = \begin{bmatrix} W^C(T_{E_1}) & W^L(T_{E_1}) \\ W^C(T_{E_2}) & W^L(T_{E_2}) \\ \vdots & \vdots \\ W^C(T_{E_N}) & W^L(T_{E_N}) \end{bmatrix}.$$

Using the fact that the weights depend on T_E but not on *t*, while the compartment diffusivities (in any given diffusion direction) depend on *t* but not on T_E, we determine $D^C(t)$ and $D^L(t)$ (in any given direction) separately for each *t* using matrix pseudo-inversion $\mathbf{W}^+ = (\mathbf{W}'\mathbf{W})^{-1}\mathbf{W}'$, as

$$\begin{pmatrix} D^C(t) \\ D^L(t) \end{pmatrix} = \mathbf{W}^+ \begin{bmatrix} D(t, T_{E_1}) \\ D(t, T_{E_2}) \\ \vdots \\ D(t, T_{E_N}) \end{bmatrix}. \quad (11)$$

This is schematically illustrated in **Figure 1**. In our case, the number of different T_E measurements was $N = 3$.

Compartment Tensor Eigenvalues and Fiber Tracking

Each set of compartment directional diffusivities [cf. Equation (11)] was processed using standard DTI methodology [5] with weights of Veraart et al. [57] to generate the diffusion tensors, the

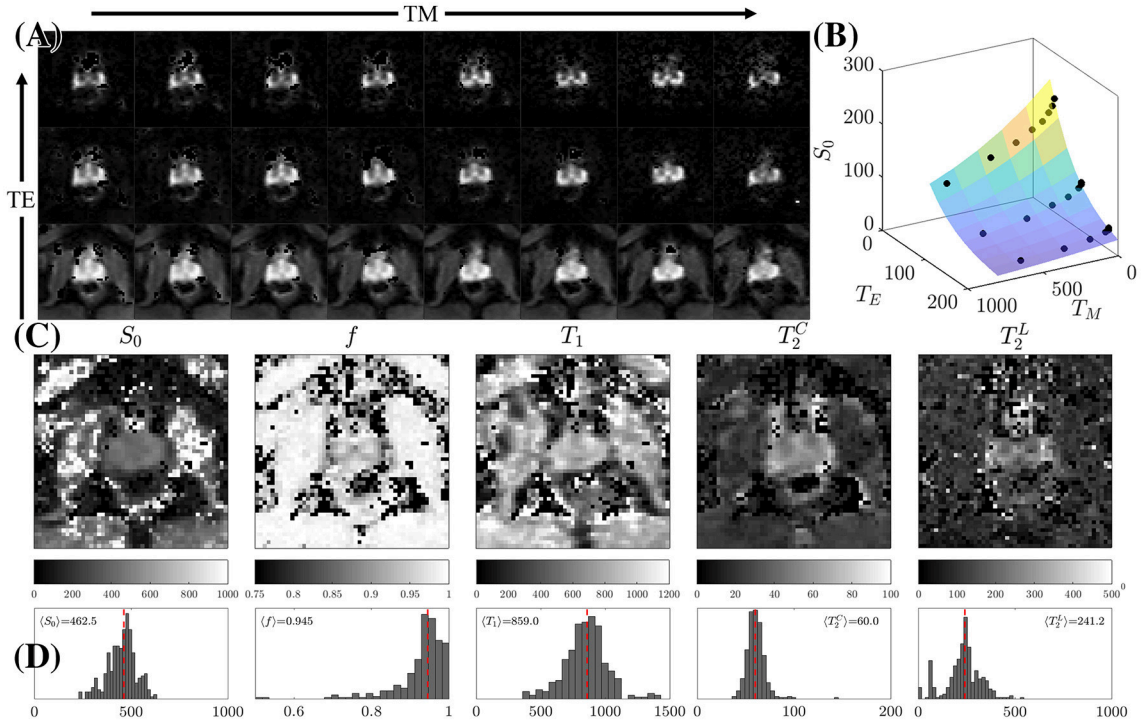

FIGURE 5 | STEAM Relaxometry. **(A)** Echo time (T_E) and mixing time (T_M) dependence of the non-diffusion-weighted dMRI signal, $S|_{b=0}$, demonstrating the suppression of the majority of tissues at long T_E. **(B)** Fitting Equation (8) to $S|_{b=0}$ after averaging over the peripheral zone (PZ). **(C)** Parametric maps of the 5 fitted parameters: the proton density S_0, overall T_1, cellular compartment fraction, f, fast (cellular) T_2^C, and slow (luminal) T_2^L. **(D)** Histograms displaying the distribution of relaxation parameters on all 3 volunteers within PZ only. The dashed line is the mean parameter derived from $\langle S|_{b=0}\rangle$ across all volunteers.

TABLE 1 | The mean and standard deviation over a PZ ROI is shown for the relaxation parameters derived from $S|_{b=0}$.

Parameters	W(T_E)	f	T_2^c[ms]	T_2^L[ms]	T_1[ms]	R^2
Subject 1 (22y/o)	[0.82, 0.66, 0.49] ± [0.11, 0.14, 0.18]	0.91 ± 0.09	62.20 ± 14.46	269.95 ± 93.03	1,014.70 ± 292.70	0.933 ± 0.064
Subject 2 (28y/o)	[0.91, 0.82, 0.69] ± [0.09, 0.14, 0.20]	0.95 ± 0.06	62.75 ± 6.66	244.87 ± 88.95	857.97 ± 154.38	0.972 ± 0.037
Subject 3 (32y/o)	[0.91, 0.82, 0.66] ± [0.05, 0.12, 0.21]	0.96 ± 0.03	55.65 ± 6.95	226.45 ± 85.94	824.02 ± 117.88	0.942 ± 0.038

associated eigenvectors $(\varepsilon_1, \varepsilon_2, \varepsilon_3)$, eigenvalues $(\lambda_1, \lambda_2, \lambda_3)$, and fractional anisotropy (FA), for each compartment, over each t, **Figure 6**. Eigenvalues for each t were averaged to produce mean diffusivity, $\overline{D}(t)$.

FA(t) typically increases with t [17, 60], implying that the anisotropy of the diffusion tensor becomes more apparent at longer diffusion times, driven by the fact that the differences between the physics of diffusion in different directions become more apparent with coarse-graining over larger distances.

Orientation in each eigenvector, on the other hand, will be independent of t, as it is produced by the same underlying tissue anisotropy. Given this orientation redundancy, an *averaged* orientation of the i-th eigenvector can be derived from the mean dyadic tensor computed across t [61]:

$$\left\langle \varepsilon_i^t \varepsilon_i^{tT} \right\rangle = \frac{1}{N_t} \sum_{t=1}^{N_t} \varepsilon_i^t \varepsilon_i^{tT} \tag{12}$$

for each of principal directions i (no summation over i is implied). The principal eigenvector associated with the dyadic tensor serves as the tissue orientation averaged over all t, where $N_t = 8$. The orientation and anisotropy is then visualized by creating directionally-encoded color FA (DEC-FA) maps, in which the median FA(t) is multiplied by the principal eigenvector of $\left\langle \varepsilon_1^t \varepsilon_1^{tT} \right\rangle$.

The principal eigenvectors from $\left\langle \varepsilon_1^t \varepsilon_1^{tT} \right\rangle$, $\left\langle \varepsilon_2^t \varepsilon_2^{tT} \right\rangle$, and $\left\langle \varepsilon_3^t \varepsilon_3^{tT} \right\rangle$ for each compartment and the eigenvalues at $t = 105$ ms were used to reconstruct the corresponding diffusion-weighted images. They were subsequently used as input to perform fiber tractography in *mrtrix3.0* using probabilistic streamline tractography. The fibers from the cellular compartment represent smooth muscle stroma, for which the structural anisotropy is clear on histology (**Figure 1A**). At each voxel, residual bootstrap was performed to obtain a unique realization of the dMRI data. The data was then resampled via trilinear interpolation at each streamline step. The diffusion tensor representation was then applied and

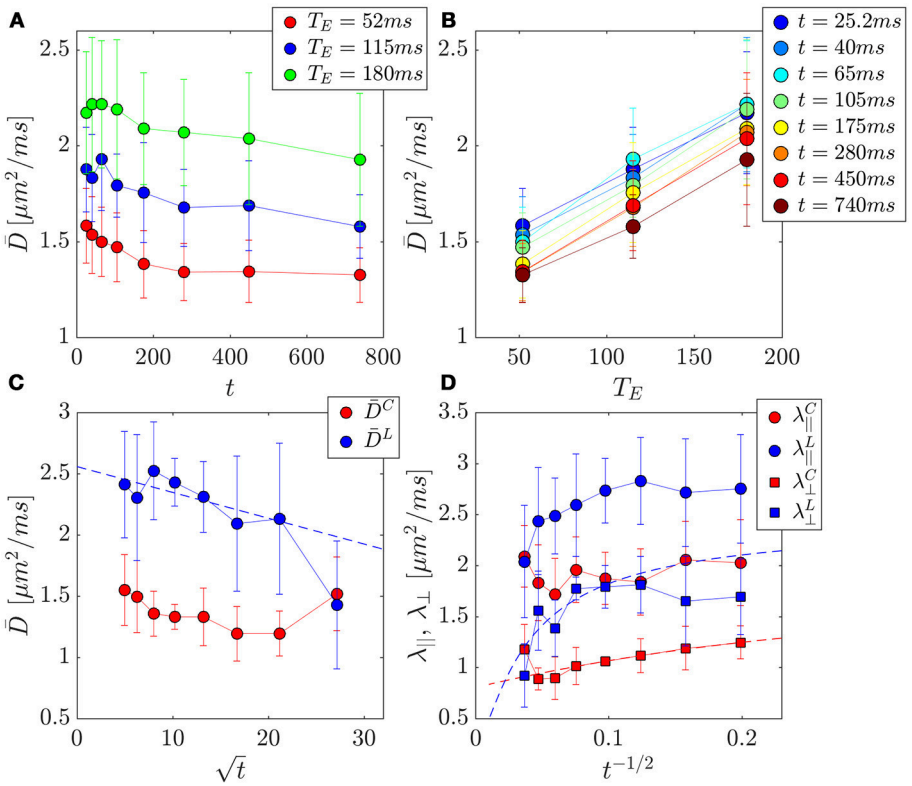

FIGURE 6 | PZ ROI separation of prostate tissue diffusivities **(A,B)** into compartment contributions **(C,D)** in 3 healthy volunteers. Error bars indicate variance between subjects. **(A)** The change in the mean diffusivity, D, with t was as much as ∼16% for a given T_E. **(B)** Replotting D as function of T_E for a given t, reveals a larger change of ∼59% over this parameter. **(C)** Mean diffusivities from the cellular and luminal compartments plotted against $\sqrt{t}$, where a linear dependence be the hallmark of the short-time S/V limit. **(D)** Axial and radial compartment diffusivities, $\lambda_{||}$, $\lambda_{\perp}$ plotted against $t^{-1/2}$, where a linear dependence of $\lambda_{\perp}$ would indicate extended disorder universality class of random membranes, and justify the usage of the RPBM for calculating length scales and permeability.

streamlines were drawn following the orientation of the principal eigenvector.

Revisiting Clinical Data From 38 Subjects, Lemberskiy et al. [17]

In addition to the newly acquired data from 3 normal volunteers, we also revisited the dataset recently published [17], with the purpose of determining the disorder class in regions of variable Gleason score. This set of dMRI was not acquired with multiple T_E, thus it cannot be used to assess cellular and luminal diffusivities separately. Instead, relaxation parameters derived from each of the 3 volunteer subjects were used to determine the signal weighting $W = W^C$ at the $T_E = 40.4$ms of the patient data: [0.862, 0.916, 0.927]. The prostate increases in size with age, largely relating to expansion of the stroma and epithelium [62]. Given a median age in Lemberskiy et al. [17] of 64 years, we assume that the patient data was weighted more heavily by the cellular compartment ($\sim W \geq 0.927$, fast T_2, large f), with approximately less than 0.07 of the signal represented by the luminal compartment. Additionally, the luminal compartment shrinks as prostate cancer progresses [63], therefore prostate cancer ROIs are expected to have an even greater cellular compartment fraction. For these reasons, we treat $D(t)$ from the patient cohort as samples of the cellular compartment.

Determination of the Dynamical Exponent From Diffusion

The compartmental diffusion coefficients, $D^C(t)$, and $D^L(t)$, were compared against the short-time S/V limit, Equation (2), and the associated power law tail of the long-time limit for ordered or hyperuniform restrictions, Equation (5), short-range disorder in dimension $d = 2$, Equation (6), and extended disorder, Equation (7). The most appropriate disorder geometry and its corresponding tissue model was selected using Pearson correlation, ρ, with the corresponding power-law tail $t^{-\tilde{\vartheta}}$, as an objective goodness-of-fit criterion. In addition, systematic features in the residuals were examined, **Figure 7**.

Given the anisotropy and fiber-like geometry of the stromal contribution to the cellular compartment (**Figures 8A**, **9B**), the long-time models were evaluated in $d = 2$ dimensions, perpendicular to the principal axis of diffusion, using the overall $\lambda_{\perp}(t, T_E)$, and the derived $\lambda_{\perp}^C(t)$ and $\lambda_{\perp}^L(t)$, from the compartment diffusion tensors. Conversely, given the isotropic characteristics of the luminal compartment **(Figure 8A)**, the

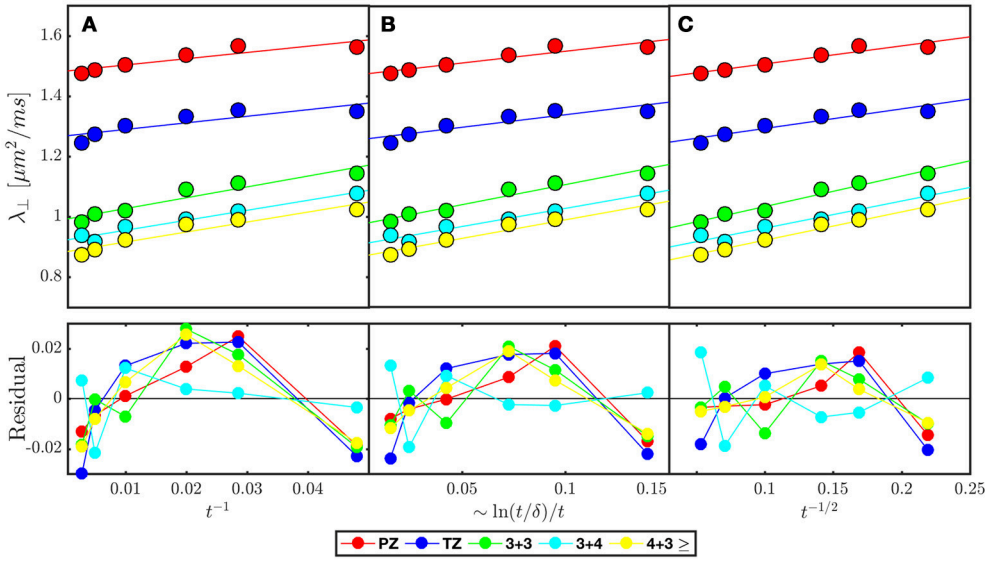

FIGURE 7 | Model selection in prostate cancer of various Gleason Scores based on disorder class from ROI averaged across 38 patients published in Lemberskiy et al. [17] Radial diffusivity ($\lambda_\perp$) is fitted (solid line over each ROI) by the associated power law tail for **(A)** ordered or hyper-uniform restrictions Equation (5), **(B)** short-range disorder in 2-dimensions Equation (6), and **(C)** extended-range disorder Equation (7). The residual is included to emphasize systematic differences between the tested disorder classes. $\lambda_\perp$ and the residual is plotted against the corresponding power laws of t, in which a linear dependence would indicate stronger association with the given disorder class (**Table 2**).

TABLE 2 | Pearson correlation coefficient, ρ, is used as a proxy for model selection at various echo time (T_E) and at separated cellular/luminal diffusion tensors.

(A) Pearson correlation (ρ) on volunteers	**T_E = 52ms**	**T_E = 115ms**	**T_E = 180ms**	**Cellular**	**Luminal**
$\overline{D}$ (t) vs. Equation (2)	0.912	**0.932**	**0.957**	0.9476	**0.9160**
$\lambda_\perp$ (t) vs. Equation (5)	0.925	0.703	0.617	0.9192	0.1796
$\lambda_\perp$ (t) vs. Equation (6)	0.955	0.765	0.693	0.9458	0.2315
$\lambda_\perp$ (t) vs. Equation (7)	**0.972**	0.817	0.757	**0.9634**	0.2794
(B) Pearson correlation (ρ) on patients from Lemberskiy et al. [17]	**PZ**	**TZ**	**3+3**	**3+4**	**≥4+3**
$\bar{D}$ (t) vs. Equation (2)	0.911	**0.983**	0.902	0.771	0.855
$\lambda_\perp$ (t) vs. Equation (5)	0.826	0.730	0.912	0.959	0.910
$\lambda_\perp$ (t) vs. Equation (6)	0.886	0.809	0.952	**0.961**	0.956
$\lambda_\perp$ (t) vs. Equation (7)	**0.921**	0.868	**0.971**	0.948	**0.982**

Averaged mean diffusivity (D) or radial diffusivity ($\lambda_\perp$) across (A) volunteer peripheral zone (PZ) and (B) patient ROIs: PZ, transition zone (TZ), low grade PZ (3+3), intermediate grade PZ (3+4), and high grade PZ (≥4+3) were compared against short-time Equation (2) S/V limit $t \to 0$ and long-time Equation (5–7) limit (t^{-1}, $\sim log(t/\delta)/t$, $t^{-1/2}$) models. The bolded ρ in each column displays the highest correlation with the ROI.

short-time behavior was evaluated over the mean diffusivity: the measured $D(t, T_E)$, and the derived $\overline{D}^C(t)$, and $\overline{D}^L(t)$. For the volunteer data, SNR became an issue for $D^{(n)}$ ($t = 480, 740$ ms) at SNR < 10, as evident on both ROI analysis, **Figures 6C,D**, and parametric maps, **Figure 8I**. The last two points were excluded from studying correlations between $D^{(n)}(t)$ and $t^{-\tilde{\vartheta}}$.

For the patient data from Lemberskiy et al. [17], the diffusion tensor eigenvalues were averaged over 5 ROIs and over the cohorts taken from the set of 38 subjects: peripheral zone (PZ), transition zone (TZ), low grade PZ (3+3), intermediate grade PZ (3+4), and high grade PZ (≥4+3) tumors. The power-law tails corresponding to hyper-uniform (Equation 5), short-range (Equation 6), and extended (Equation 7) disorder classes in $d = 2$ dimensions were compared with the ROI-averaged data. Linear evolution of $\lambda_\perp(t)$ was plotted against the power-law scaling, $t^{-\tilde{\vartheta}}$, for each disorder class, and the Pearson correlation values as well as qualitative inspection of fit residuals were used to identify the most appropriate disorder geometry among the long-time models.

Parameter Estimation for Tissue Compartments (Healthy Controls)

As a result of model selection (see section Results), time-dependent diffusion was modeled within the PZ ROI of each

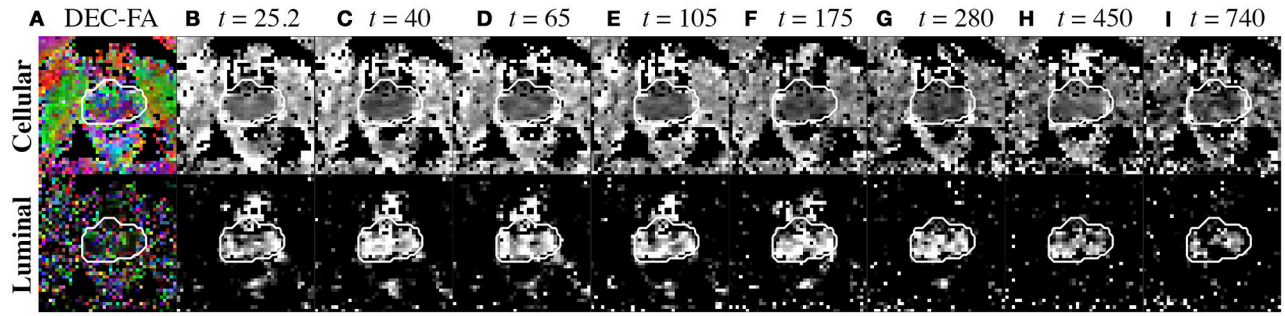

FIGURE 8 | Compartment parameters derived from the diffusion tensor. **(A)** Cellular and luminal directionally-encoded color FA (DEC-FA) were derived from principle eigenvalues of the mean dyadic tensor over time and the median FA(t). **(B–I)** Mean diffusion over diffusion time, $D(t)$, is shown for both cellular and luminal compartments. The whole prostate ROI was drawn from the image at $t = 25.2$ ms and overlaid onto all parameter maps with a white outline to highlight any motion.

subject using the RPBM in the cellular compartment and the S/V limit in the luminal compartment.

Luminal Compartment

$D(t)$ within the luminal compartment was evaluated using the S/V limit, Equation (2). Lumen diameters were estimated from $a^L = 6V/S$, which would be the length of one side on a 3-dimensional cube with given S/V. Alternatively, one can consider modeling a^L via a 3-dimensional sphere, which would result in a factor of 2 difference in the definition of luminal diameters; given the irregular shape of the lumen, the identification of the precise pre-fractor in front of V/S is beyond the scope of this work. We also estimate $a^L|_{D_0=3}$ with a fixed $D_0^L = 3.0\ \mu\text{m}^2/\text{ms}$, which follows from the model assumption that the glandular lumen are lakes of largely unrestricted restricted water, where $t \to 0$ would give the free water diffusion coefficient at body temperature [64].

Cellular Compartment

The dynamical exponent analysis (see section Results) indicated the dominance of the extended disorder geometry in 2 dimensions (**Figure 7**, **Table 2**). This suggests that the RPBM utilized previously for studying muscle fiber diameter and membrane permeability [9, 33, 44–46] can be applied to study the cellular compartment using $\lambda_\perp^C(t)$.

The RPBM depends on 3 parameters: the free-diffusivity D_0, the S/V ratio of all membranes, and the membrane permeability κ. The RPBM result for $D(t)$ in $d = 2$ dimensions is given in terms of D_0 and the two auxiliary parameters: the effective "volume fraction" $\zeta = (S/V) \cdot (D_0/4\kappa)$ of the membranes [describing the net effect of their hindrance relative to D_0, as $D_\infty = D_0/(1 + \zeta)$], and the time-scale associated with a single membrane, $\tau = D_0/(2\kappa)^2$ [33]; see Fieremans et al. [45] for the details of fitting and practical implementation of RPBM. For improved model precision, $D_0 \equiv D_0^C$ here was fixed to $\left\langle \lambda_{||}^C(t > 100\text{ ms}) \right\rangle$, **Figure 9C**. These model parameters are then used to calculate cellular (fiber) diameter, which can be approximately estimated as $a^C = 4/(S/V)$, which yields $a^C = 2\sqrt{D_0\tau}/\zeta$; and fiber membrane permeability $\kappa^C = D_0/(2\sqrt{D_0\tau})$.

The parameters from the RPBM: D_0^C, a^C, and, κ^C; and from the S/V limit: D_0^L, and a^L, were estimated (i) by applying the model to every voxel separately, and (ii) averaging the corresponding DTI eigenvalues across all PZ voxels and estimating model parameters from this average.

Determination of Structural Exponent and Fiber Diameter From Histopathology

For an independent validation of the prevailing disorder geometry, 590 × 590 μm samples with 1,440 × 1,440 pixels of benign stromal tissue in cross-section were selected by a board certified pathologist. These samples were obtained from radical prostatectomy of a 72 y/o patient with Gleason Score 4+3, which were stained with Hematoxylin and eosin (H&E). These samples were evaluated using the power spectrum approach [9, 43], determining the power-law behavior $\Gamma(k)\big|_{k\to 0} \sim Ak^p$ of the power spectrum at low wave-vectors k=|**k**|, by calculating the 2-dimensional $\Gamma(\mathbf{k}) = \rho(-\mathbf{k})\rho(\mathbf{k})/V$, where $\rho(\mathbf{k})$ is the Fourier transform of the intensity of restrictions in the histological image (**Figures 4B–D**), and subsequent binning of $\Gamma(\mathbf{k})$ over 1,200 concentric shells (bins), parametrized by the shell radius k. The low-k behavior was then characterized by a structural exponent p, which can take a discrete set of values (cf. text after Equation 4).

From the H&E-stained histology image we needed to produce the contrast that depicts fiber walls in the cross-section, **Figure 4**. The domains with fiber bundles transverse to the histology slice were identified within a large field of view that contained many fiber orientations; these fragments of the large image were subsequently processed to emphasize the cell walls, as we now describe.

First, the red channel was isolated and filtered by a Gaussian filter with a smoothing kernel of $\sigma = 5$ pixels. The low pass filter removed salt-and-pepper spatially-uncorrelated noise that would otherwise interfere with segmentation in the subsequent steps, but did not have an impact on the low-k (large-distance) behavior which we were after. Second, K-means clustering in MATLAB was performed to isolate the three predominant clusters: extracellular space, intracellular space, and cellular nuclei. The masks of cellular nuclei and intracellular space were then combined; the remaining space was deemed mostly related to the fiber membranes (i.e., everything but cells and their organelles). The resulting membrane mask was used to determine

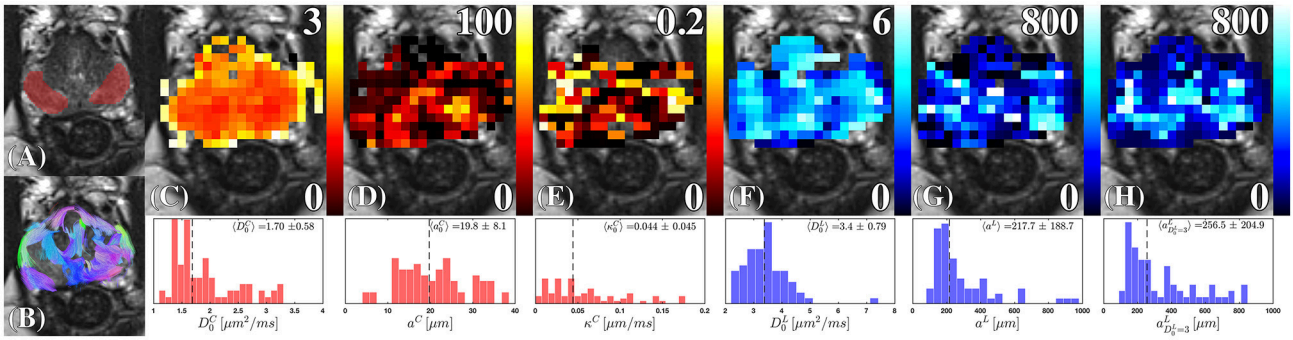

FIGURE 9 | Cellular and luminal parameters derived from $D(t)$. **(A)** The peripheral zone ROI, is overlaid onto a high-resolution T_2-weighted image. **(B)** The probabilistic fiber tracks, derived from the cellular compartment, are color coded by their terminal endpoints. These tracks were derived from a dyadic tensor across all diffusion times. **(C)** Cellular diffusivity, D_0^C, **(D)** cellular fiber diameter, a^C, and **(E)** cellular membrane permeability, κ^C, were derived from the RPBM applied to the cellular diffusion tensor. The **(F)** luminal diffusivity, D_0^L, **(G)** luminal diameter, a^L, and **(H)** the luminal diameter, $a^L_{D_0^L=3}$, were derived by applying Equation (2) to the luminal diffusion tensor. The corresponding histograms under each parameter map, show the range and median (dashed line) of the modeled parameter under the ROI **(A)** combining estimates obtained from all volunteers.

the power spectrum $\Gamma(\mathbf{k})$ as a function of the two-dimensional Fourier wave vector k. Last, the histological length scale was determined by calculating $a_{\text{hist}} = 4V/S$, where $S/V = l/A$. The area, A, was determined by the total area of the membrane mask image, and the length, l, was determined by finding the total number of voxels outlining each cell from the membrane mask, i.e., counting both faces of each membrane. In the case of the simulated image with parallel lines, l was multiplied by 2 to account for the surface on both sides of the unit-thickness membrane, **Figure 4A**. With this definition of S/V, conventional in the field of porous media, the length scale a_{hist} would correspond to the size of a square if the membranes were to be arranged in a perfect square lattice (a checkerboard) within the fiber cross-section.

Determination of the Luminal Fraction f_L and the Luminal Diameter a^L From Histology

Two larger samples taken again from the radical prostatectomy of the 72 y/o subject (**Figures 10A,B**) of benign peripheral zone were selected containing 1,000 × 1,400 pixels over a field of view of 2.4 × 3.4 mm^2. The lumen were segmented using K-means clustering with the same approach described in the previous subsection. The luminal mask was used to determine the lumen *area* fraction, $f_{L,A}$, over 200 × 200 non-overlapping pixel segments. In order to compare our results with MRI, we assumed cubic-shaped lumen and estimated the corresponding luminal *volume* fraction and the cell volume fraction:

$$f_{L,\text{hist}} = f_{L,A}^{3/2}; \qquad f_{\text{hist}} = 1 - f_{L,\text{hist}}. \tag{13}$$

We note that for lumen of different shape, the right-hand side of the first formula in Equation (13) would have a non-universal coefficient ∼1. Therefore, our estimates are to be treated as order-of-magnitude. However, the power law exponent 3/2 in the above equation is universal, and will prove to be quite important to match MRI with histology.

To determine the luminal diameter, a^L_{hist}, from the histology, we again, for simplicity and consistency, assume the cubic-shaped lumen of size a^L_{hist}, for which case the perimeter-to-area ratio $l/A = 4/a^L_{\text{hist}}$, or, equivalently, the 3-dimensional $S/V = \frac{3}{2}l/A$. Hence, we estimate $a^L_{\text{hist}} = 6V/S$ within each histology segment, and compare our distributions with MRI-derived metrics. We can equivalently view this comparison as that between the 3-dimensional S/V ratios from MRI and from histology (re-calculated from the 2-dimensional slices).

RESULTS

Relative Contributions of Prostate Compartments

Increasing T_E led to suppression of much of the surrounding pelvic signal as shown on $S|_{b=0}(T_M, T_E)$. Surrounding tissues which are largely composed of muscle or collagen are completely dark at $T_E = 180$ ms (**Figure 5A**). Unlike the surrounding tissues, the prostate retains its signal, particularly around PZ. Fitting Equation (8) to $S|_{b=0}(T_M, T_E)$ reveals a non-linear surface, dependent on compartment fractions and NMR relaxation times (**Figure 5B**). On average, fit $R^2 > 0.92$ for each subject; however, as with previous studies [23–27], our dynamic range and SNR limitations led toward larger variance on estimated T_2^L (**Table 1**, **Figures 5C,D**). The range of parameters derived from Equation (8) indicate that the signal at each T_E are weighted by the cellular compartment differently, W(T_E=52)∼0.9, whereas W(T_E=180)∼0.6. Additionally, model fitting suggests that the volume fraction of the cellular compartment, f, increases with age as evidenced by the $f = [0.91, 0.95, 0.96]$, which confirms observations from histopathology [9].

We found a remarkably strong agreement between MRI and histology-derived f (**Figure 10D**), where Equation (13) was used

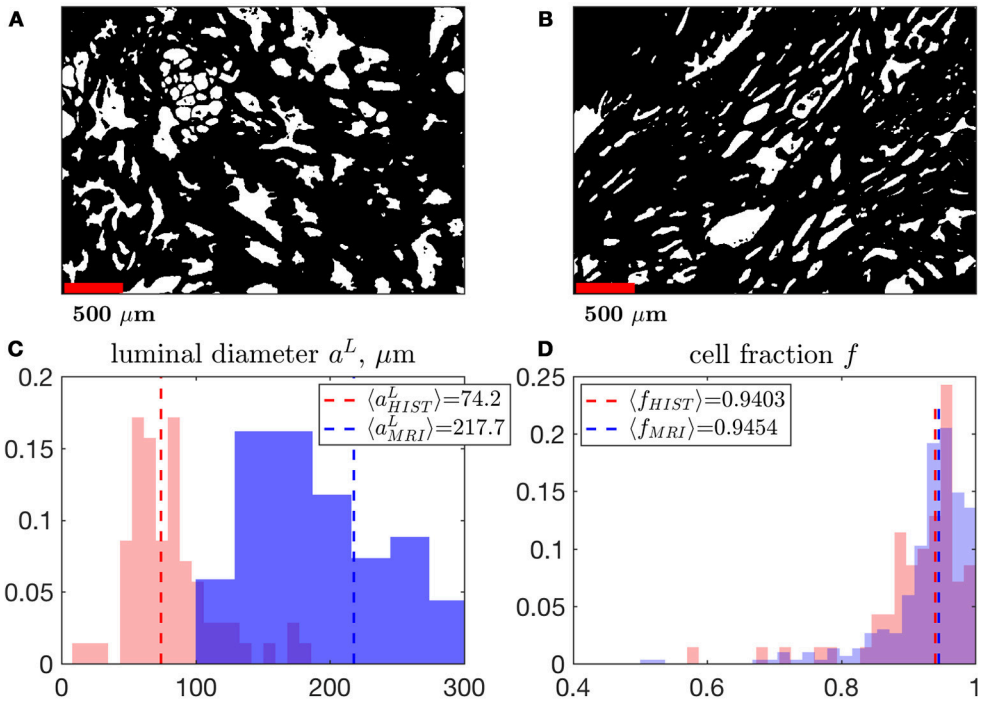

FIGURE 10 | A comparison of MRI- and histology-derived cellular fraction, f, and luminal diameter, a^L. **(A,B)** Two samples of benign peripheral zone containing 1,000 × 1,400 pixels over a field of view of 2.4 × 3.4 mm^2 were segmented using K-means clustering. 200 × 200 non-overlapping pixel segments were sampled from these masks in order to determine the volume fraction, Equation (13), and surface-to-volume ratio, $S/V = \frac{3}{2}I/A$, which was then used to approximate $a^L_{hist} = 6V/S$. The power-law exponent 3/2 was used to convert the 2-dimensional properties of histology into 3-dimensional units (in order to match the MRI results). This conversion approximately assumes a 3-dimensional cubic geometry within the luminal compartment (see section Methods). We display histograms the median of each distribution comparing a^L **(C)** and f **(D)**, derived from MRI and histology. Note that the histograms for MRI results are identical to distributions shown in **Figure 5C**, for f_{MRI}, **Figure 9G**, for a^L_{MRI}.

to calculate the histological counterpart. The difference between the medians of the MRI distribution across voxels, and histology distribution across histology segments is 0.5%. Such degree of the quantitative agreement may be accidental because of the ∼1 coefficient in Equation (13) for non-cubic glands, as well as because of comparing young healthy controls (MRI) with radical prostatectomy (benign area, histology). However, the order-of-magnitude correspondence between MRI and histology is reassuring.

Dependence of the Overall $D(t)$ on T_E

Mean diffusivity D consistently increased with T_E **(Figures 6A,B)**, revealing the competing effect of cellular and luminal compartment weighting on the measured diffusion signal. The difference between $D(t)$ *at* $T_E = 52$ ms and $T_E = 180$ ms appears to grow over the first six time points (25.2–280 ms) ($\rho = 0.89, p = 0.016$), with $\overline{D}(t = 25.2\,\text{ms})$ increasing by 34% and $\overline{D}(t = 280\,\text{ms})$ increasing by 59%. However, it begins to drop at the latest t, ($t = 450$ ms, 51%) and ($t = 740$ ms, 45%). This finding indicates that the degree of separation between compartments is also confounded by diffusion time-dependence.

Structural Universality Class and Model Selection From Diffusion Measurements

First, we consider the time-dependence of the overall $D(t)$. The volunteer data at each T_E was used to determine the most appropriate choice of tissue specific $D(t)$ model (**Table 2**). Linear correlation of mean diffusivity $\overline{D}(t)$ with various models is chosen to be the criterion for evaluating the changing functional form of $\overline{D}(t)$ with T_E. At the shortest T_E, all models representing the long-time limit, Equations (5–7), ($\rho > 0.93$) describe $D(t)$ better than the S/V limit, Equation (2) ($\rho = 0.92$). Overall, the model with $\vartheta = 1/2$, Equation (7), had the greatest correlation with the overall radial diffusivity $\lambda_\perp(t)$ at $T_E = 52$ ms. At longer T_E, the correlation with the S/V limit continued to increase: $\rho(T_E = 115) = 0.93$, $\rho(T_E = 180) = 0.96$; whereas the correlation with long-time limit continued to drop precipitously: $\rho\,(T_E = 115) \sim 0.7$, $\rho\,(T_E = 180) \sim 0.6$. To summarize, shorter T_E is associated with diffusion through extended disorder, Equation (7), whereas longer T_E is associated with the short-time S/V limit, Equation (2).

Clinical data from Lemberskiy et al. [17] was acquired with low $T_E = 40.4$ ms, suggesting $W{=}W_c \geq 0.927$. For this reason, the diffusion-weighted signal was dominated by the cellular

compartment (**Table 2**). Given this context, the power law scaling of the radial diffusivity $\lambda_\perp(t)$ can be used to determine the most appropriate tissue model for (stroma+epithelium). We find that the power-law approach of $\lambda_\perp(t)$ in nearly all ROIs was described best by the dynamical exponent $\vartheta = 1/2$, Equation (7), again indicating the extended disorder (**Figure 7**), with the exception of $\overline{D}(t)$ in the Gleason-score 3+4 ROIs, which were best described by Equation (6). Given the overall agreement of benign and malignant PZ with Equation (7), it seems appropriate to use the RPBM to study $\lambda_\perp(t)$ in the cellular compartment.

As for TZ, although there is a preference for Equation (7) in the ROI pertaining to TZ, it is not well described by any of the established disorder classes: $R^2 = [0.73, 0.81, 0.87]$, for Equations (5–7), respectively. If considered as a long-time limit, the corresponding ϑ appears to be closer to 0 than to 1/2, indicating that $\overline{D}(t)$ in TZ is either (i) highly confounded by partial volume, or (ii) far from the long-time limit. Alternatively, comparing $D(t)$ to the short-time S/V limit, Equation (2), revealed remarkably strong correlation with the model in TZ ($\rho = 0.98$).

For the volunteer data, $D_\perp^C(t)$ and $D_\perp^L(t)$ (**Figures 6C,D**, **8B–I**) were best described by extended disorder, Equation (7) ($\rho = 0.963$), and the S/V limit, Equation (2) ($\rho = 0.916$), respectively. This is consistent with the above observation that shorter T_E is associated with extended disorder (where $D^C(t)$ dominates), while longer T_E is associated with the S/V limit, where $D^L(t)$ is dominant. Following the conclusion of extended disorder defining the cellular compartment, we find that RPBM had better correlation with the cellular $\lambda_\perp(t)$ ($\rho = 0.986$) than with the luminal $\lambda_\perp(t)$ ($\rho = 0.551$) (**Figure 6D**).

Quite remarkably, the $1/t$ scaling, Equation (5), a hallmark of either ordered/hyperuniform restrictions, or fully confined water pools (e.g., impermeable cells), never gives the best fit. Moreover, the data residuals (**Figure 7B**) show temporal structure, which also disfavors this scaling, and with that, the assumption of assigning compartment non-Gaussianity (i.e., time-dependence of diffusion) to fully restricted pore(s) in VERDICT [38] and RSI [39, 65] models. This means that randomly-placed, *permeable* and extended membranes, **Figure 4A,** rather than the fully restricted compartments, are most relevant for explaining the diffusion time dependence in the bulk prostate tissue (excluding lumen), and therefore are also key for biophysical modeling of non-Gaussian diffusion in its microstructure.

The DEC-FA based on the calculated diffusion tensor in each compartment provides a measurement of compartment anisotropy (**Figure 8A**). The cellular compartment displays highly oriented structure, with large regions within PZ colored in purple, which would be characterized by a mixture of blue (in-plane/out-plane) and green (up-down) orientation (**Figure 9B**). The urethra, which is at the center of the prostate, is entirely colored in blue (in-plane/out-plane orientation). In contrast, it is difficult to identify any meaningful structures from the DEC-FA of the luminal compartment, as both FA and principal eigenvector ε_1 are dominated by noise (**Figure 8A**).

Structural Universality Class From Histology

The power spectra for the restrictions in all of the histological samples in the cellular compartment converged toward $\Gamma \sim k^p$ with exponent $p = -1$, where the measured p across each sample was found to be—[1.00, 1.17, 1.01 ± 0.17, 0.14, 0.13] (**Figures 4B–D**), indicating that the structure belongs to the extended-disorder structural universality class. This is consistent with the low-frequency/long diffusion time dependence in the stromal cross section being well described by randomly oriented barriers (RPBM), a representative of this universality class.

Between the 3 cases shown in this publication, the scale beyond which random barriers become a dominant tissue feature occur at $k = 1/a_{\text{hist}} = 1/23.13 \pm 1/1.06\,\mu m^{-1}$. At the smallest k (corresponding to distances of the order of the histology cut-out), statistical fluctuations between the samples are large, and the power-law scaling becomes noisy.

The dynamical exponent $\vartheta = 1/2$ identified above in $\lambda_\perp(t)$ for the cellular compartment, and the structural exponent $p = -1$ in $d = 2$ dimensions, are in agreement with the relation (4).

Cellular and Luminal Parameters From the Compartmental $D(t)$

Luminal Compartment

Fitting of D_0^L (**Figure 9F**), we find its values sometimes greater than 3 $\mu m^2/ms$. In the **Supplementary Information** we show that this is consistent with the noise propagation at the relevant SNR. As the mean of the distribution of D_0^L is quite close to water diffusion coefficient at the body temperature, this result reinforces our initial assumption that the luminal compartment is composed of "lakes" of practically unrestricted water. The range of luminal diameters, a^L, and $a^L|_{D_0=3}$ (**Figures 9G,H**), overlap with the range of observed diameters anticipated from histology 300 ± 120 μm [14, 15, 30]. However, the lumen diameter of our healthy controls exceeds that obtained from histology of radical prostatectomy, $a^L_{MRI} > a^L_{\text{hist}}$, **Figure 10C**, with 65.9% difference between the means of each distribution; this is consistent with the glandular shrinkage with age. Fixing $D_0^L = 3\ \mu m^2/ms$ does improve the precision of $a^L|_{D_0=3}$ over a^L (**Figure 9H**, **Supplementary Figure S4**). Overall, the spread in the model parameter estimates seem to come mostly from the noise rather than from the biological variability (see **Supplementary Information**).

Cellular Compartment

Diffusion through the cellular compartment reveals restriction sizes of $a^C = 19.79 \pm 8.09\ \mu m$ from diffusion MRI, indicating a near perfect match with histology reported from $\Gamma(k)\big|_{k\to 0}$. Although the striking similarity in diameters may to some degree be a coincidence, our findings indicate that cellular diameters measured with diffusion were consistent with the length scales anticipated from the tissue (**Figure 4**). Moreover, a^C varies over the prostate, where the largest fibers appeared closer toward the peripheral zone (**Figure 9D**). The distribution of cellular permeability (**Figure 9E**) was close to the permeability of the red blood cell membrane—perhaps, the most studied permeable

biological membrane, with permeability between 0.02 and 0.09 μm/ms [66, 67]. On the other hand, voxel-wise and ROI averaged κ^C demonstrated substantial similarity, indicating that the range of possible permeability is much smaller than the range of possible fiber diameters.

DISCUSSION

Specificity Toward Microstructure Arising From Dependence on Both *t* and T_E

This study emphasizes the importance of compartment weighting on modeling prostate diffusion. Although time-dependence is apparent at individual T_E, the functional form of $D(t)$ for different T_E reflects a different mixture of tissue microstructure (**Table 2**). This relative compartment weighting implies that the selection of the most appropriate tissue model is confounded by T_E. Partial volume between cellular and luminal compartments must be resolved, before modeling $D(t)$ could reflect tissue specific length scales. For example, when applying RPBM or S/V limit models to the overall $D(t)$, the calculated length scale, $a = 4/(S/V)$, increased with T_E. Using compartment weighting to decompose the diffusion representation into cellular and luminal tensors reveals a unique contrast as well; the maps of $\overline{D}^C$ appear smooth, whereas the $\overline{D}^L$ has higher diffusivity localized around PZ, a region that is dense with glandular lumen (**Figure 8**).

We emphasize that it is the t-dependence, in combination with T_E, that helped us identify the relevant microstructural degrees of freedom, as the time dependence provides the sensitivity to the cellular-level length scale and the spatial correlations of the restrictions. Without investigating $D(t)$, one could only argue that there are 2 compartments with different T_2, and that this has an impact on the diffusivity (**Figures 6A,B**). Having identified the relevant degrees of freedom for the compartmental $D(t)$, we apply specific models to obtain corresponding length scales and membrane permeability. Good agreement with existing histopathology [14, 15, 30] for the luminal sizes ($300 \pm 120\,\mu$m) and myofiber diameters ($19.81 \pm 1.18\,\mu$m, as well as with previous measurements of T_2 volume fractions ($f_{\text{fast}} > 0.8$ and $f_{\text{slow}} < 0.2$) [13, 26], points at strong associations of compartment-specific properties with non-invasive MRI parameters.

Due to the large differences between cellular and lumen T_2 values, this study focused on separation of only these tissue compartments. In principle, the "cellular" compartment which had volume fractions >0.9 was a combination of all non-luminal tissue subtypes. Since our acquisition had merely 3 T_E values, modeling more than 2 compartments would be a challenge. Researchers have shown considerable interest in studying epithelium and stroma separately [13, 15, 30, 63, 68]. If this experiment were revisited with a denser sampling of T_E, the "cellular" compartment would be expected to split into more granular components, such as epithelium and stroma, with potentially different microstructural degrees of freedom.

RPBM v. Fully Restricted Compartment (RSI, VERDICT)

Model selection based solely on the goodness of fit is unreliable [1]. Given how "remarkably unremarkable" [69, 70] the dMRI signal is, model selection is always a challenge. Here, we tried to reveal subtle signatures of distinct classes of structural complexity, by choosing between them on an equal footing, rather than pre-conditioning ourselves toward a particular model. For Equations (5–7), the goodness of fit at low T_E or in the cellular compartment were all consistently strong, $\rho > 0.9$. If this work were dedicated to an individual model, the strong correlation would likely give a false sense of security about that model's success.

The previous modeling assumption of diffusion being fully restricted by impermeable barriers is a common one in the prostate [38, 39, 65], perhaps, because this is the easiest "nontrivial" model of diffusion, for which exact solutions for simple geometries (e.g., a spherical pore) have been derived decades ago [71, 72]. However, a fully restricted compartment's asymptotic $D(t)$ behavior, Equation (5), is not preferred by the goodness-of-fit (neither in volunteers nor in the clinical population), and, more importantly, shows *systematic* temporal structure in the fit residuals, **Figure 7**. Based on our accumulated body of evidence, we conclude that the cellular compartment's time dependence is dominated by the extended disorder universality class, Equation (7).

Strictly speaking, the biophysical assumptions of, on the one hand, the RPBM, and on the other hand, an impermeable compartment at the heart of RSI and VERDICT, are mutually exclusive. If the extended disorder and the functional form of Equation (7) is indeed a correct assumption, fitting a model based on the asymptotic behavior of Equation (5) (e.g., for a fixed t by varying b) will yield biased results; moreover, because of a qualitatively different functional form, the fit results for VERDICT and RSI will depend on the chosen range of t and b, reflecting the acquisition/modeling variability challenge discussed by Novikov et al. [1]. The corresponding estimated "compartment sizes," technically speaking, will lose their meaning.

Because we lumped fibromuscular stroma and epithelium into a single cellular compartment, in principle there could be a competition between different power law tails from different compartments. If, for instance, the epithelium compartment is described by approximately impermeable cells (VERDICT/RSI holds there), it will be practically impossible to distinguish its role in the overall "cellular" diffusivity time dependence as it will be asymptotically dominated by the smallest exponent $\vartheta = 1/2$,

$$c_{1/2}\, t^{-\frac{1}{2}} + c_1\, t^{-1} \sim c_{1/2}\, t^{-\frac{1}{2}},\ t \to \infty,$$

which will overshadow the effect of other compartments. To understand whether the fully restricted compartment can play a non-negligible role, one should repeat our analysis but with $N = 3$ compartments, provided that the separation between epithelium and stroma via their T_2 values is practically achievable, and investigate the dynamical exponent of the epithelium separately.

The dynamical exponent ½ reveals the extended nature of the restrictions and their permeability as relevant degrees of freedom for diffusion in this tissue. Furthermore, we find that the cellular compartment falls into the same disorder structural universality class as skeletal muscle. If restrictions in the cellular compartment are largely dominated by *fibromuscular stroma (smooth muscle)*, as shown by Bourne et al. [13], then the strong agreement with Equation (7), which also best describes skeletal muscle [9, 44–46], should be anticipated. Based on our permeability estimates, the effective membrane hindrance parameter $\zeta \sim 2.14 \pm 1.77$ is not very large, indicating that the membranes are quite leaky, which a posteriori also justifies neglecting the distinction between intra- and extra-cellular space in the RPBM. Lastly, the average standard deviation in D_∞ across all measurements was $\sim$0.03 μm^2/ms, indicating that this is a highly robust parameter. These consistent findings of a *finite* D_∞ are also incompatible [1] with the pictures of stretched-exponential diffusion signal, and anomalous diffusion in prostate [73].

Correlating MRI With Histology

In 2012, Bourne et al. [13] presented work that quantified microscopic diffusion compartmentation using high resolution MRI on a 16.4 T magnet, with 40 μm isotropic voxels. The study stated that benign prostate had an extremely small luminal compartment, with fraction of about 0.03, and a massive cellular compartment, with fraction of about 0.97. Remarkably, our estimates (**Figure 10**) are very close to these values. This agreement can be expected, since the experiment of Bourne et al. was directly resolving the three-dimensional volume fractions of sufficiently large glands. Other publications [27, 63, 74] correlate histology with MRI findings, which is a challenging task as histological images are in 2 dimensions whereas MRI measurements are in 3 dimensions. Sabouri et al. [27] discussed this challenge and suggests that this difference contributes to as much as 33% of the mismatch between histology and MRI. To our knowledge it is for this reason, that no previous MRI publication has been able to reproduce the volume fractions obtained from Bourne et al. [13]. In our work, the median *area* fraction was $f_{L,A} = 0.153 \pm 0.119$; however the corresponding median *volume* fraction estimated via Equation (13) was $f_{L,Hist} = 0.059 \pm 0.734$. This conversion from 2d to 3d makes the agreement between Bourne et al. [13] and the results of our histology and MRI experiment very close (**Figure 10**). We anticipate that this assumption would break down as the isotropic 3d geometry of the luminal compartment may gradually change with the progression of prostate cancer. The mismatch between histology and MRI for a^L could suggest that the S/V greatly changes with age and/or noise propagation and modeling considerations should be refined in future work (we note, however, that MRI was performed on healthy controls, while histology was obtained from the benign area of the radical prostatectomy in a 72 yo patient). Measurements sampling multiple slices or more sophisticated modeling approaches should be considered for future histological comparisons with MRI.

Effect of Intra-Compartmental Non-Gaussian Diffusion

Previous studies have invoked the concept of multiple compartments, by empirically separating fast/slow diffusing water "pools" from an individual voxel [75, 76]. However, the estimation of the compartment fractions can be easily biased via higher-order terms in b from an *individual* compartment [10, 18]. Fast diffusivity derived from the bi-exponential model represents well over 40% of the signal in the prostate [16, 22]. Given that the expected luminal volume fraction is $\sim$5%, it is clear that compartment fractions derived from the bi-exponential model cannot be easily linked toward major tissue compartments: stroma, epithelium, and lumen. A likely reason for why the bi-exponential model does not reflect any meaningful familiar tissue properties is that for the prostate in particular, the assumption of Gaussian compartments was in-validated by the observation of a time-dependent $D(t)$ [17, 60]. Fortunately, separating compartments via T_2 relaxation is "orthogonal" (**Figure 2**) to diffusion acquisition parameters b and t. This implies that our approach, Equation (1), can be extended further to include higher order diffusion metrics, such as kurtosis, in *each* compartment, by relying on the distinct T_2 relaxation properties.

Chatterjee et al. [74] modeled diffusion and T_2 relaxometry together, albeit assigning purely *Gaussian* diffusion to each of the distinct compartments. In particular, a compartment with high diffusivity and long T_2 was also assigned to the lumen. However, the 3d volume fractions estimated in that paper from MRI were nearly in a 1:1 agreement with the 2d *area* fractions from histology. While these results were presented as a validation of the model, as we already mentioned above, the 3d *volume* fractions [13] have been shown to be significantly different from those measured from 2d histology [27]; in other words, a correct model should provide the lumen fraction that is notably below the histological area fraction. Hence, we suggest that the volume fractions estimated in Chatterjee et al. [74] are notably biased by the non-negligible effect of time-dependent diffusion resulting in the non-Gaussianity of the diffusion propagator at higher-b values employed in the multi-exponential dMRI fit. This strong effect of higher-order terms in b in each compartment has been precisely the reason to leave them out in this work, and to rather remain at the level of DTI.

Our multi-parametric acquisition revealed T_E as a meaningful filter to separate cellular and luminal diffusivity. T_E compartment weighting affecting ADC measurements in the prostate has been shown previously [77]; however, the connection to the bi-exponential T_2 was not established in that publication. A recent study explored the effect of T_E and t on the prostate diffusion signal *ex-vivo* [60], by varying both T_E and t simultaneously. The effect of T_E dependence was minimal on that dataset as the monotonically decreasing diffusion coefficient began to increase only at the longest t and T_E. Outside of prostate applications, the value of varying T_E to study diffusion to stabilize model fitting was recently demonstrated in the brain [78, 79].

Given the appropriate range of T_E, estimating the NMR relaxation times via $S|_{b=0}(T_M, T_E)$ was fairly simple, i.e., we did not need to employ constraints or priors to produce robust

estimates of f, T_2^C, T_2^L. The fitting was simple mainly due to the large separation of compartmental T_2 values. However, it is well established that T_2 becomes shorter with increasing field strength [80]. By extension, this will have an impact on diffusion measurements: the diffusion coefficient in the brain between 1.5 and 3T systems has been reported to have a variance of ∼7% [81].

Compartmental Anisotropy

Since the cellular compartment was found to be within the long-time limit, it is possible to derive a meaningful interpretation of the diffusion tensor orientation. Fiber tracking could be performed on this compartment to characterize tissue anisotropy in 3-dimensions. Many areas do not display any track information, which could mean that (1) the fiber orientation was incoherent, as an example, **Figure 1A** shows a histological cross section with axial and perpendicular stromal cross-sections, or (2) the dataset was unable to resolve meaningful tracts. This could be expected as prostate imaging is vulnerable to motion and distortion artifacts. While the rigid motion correction and the Siemens static distortion correction [51] have been very useful for the experiment, the image quality is still imperfect (**Figures 8B–I**). For this reason, the only fiber tracks shown are the ones that were generated with high confidence. The luminal compartment is far from the long-time limit, and thus no consistent orientation information is apparent (**Figure 8A**). This finding serves as additional confirmation that the luminal compartment for our volunteer data is indeed within the S/V limit. Note that lumen may as well be anisotropic (at sufficiently large length scales), but our acquisition would only become sensitive to this anisotropy at prohibitively long t in healthy subjects. The applicability of the S/V limit to the lumen compartment is expected to change in patient populations as glandular lumen shrinks with increasing tumor grade [15, 82]. At higher tumor grade, characterization of orientation dependence in both the cellular and gland compartments may become feasible.

Perfusion/IVIM as a Possible Confounding Factor

At low b-values, the signal dependence on b is sensitive to incoherent or multi-directional flow, attributed to a vascular compartment. Perfusion has been studied in the context of prostate cancer through the intra-vascular incoherent motion (IVIM) [20, 83], e.g., incorporated in the VERDICT parameter estimation scheme [20, 38]. However, in a recent paper, Merisaari et al. [20] performed a diffusion acquisition that has been optimized for measuring perfusion: $b = 0, 2, 4, 6, 9, 12, 14, 18, 23, 28, 50, 100, 300, 500$ s/mm^2. After comparing multiple models using Akaike Information Criterion, the mono-exponential model prevailed as the best representation of diffusion in the prostate over $b = 0$–500 s/mm^2 (same range as our study). Remarkably, an acquisition with 14 b-values in the optimal range was insufficient for IVIM parameters to outperform the mono-exponential diffusion. Given this finding, we doubt that perfusion would bias our results in any meaningful capacity.

As a counter-argument, one may point toward the ∼10% vascular fraction, f_{vasc}, estimated by the VERDICT model [84]. Let us now argue that this apparent vascular compartment (characterized by high diffusivity) could rather be assigned to the luminal water. For that, we recall that VERDICT models the IVIM compartment not by the signal's phase $e^{i\mathbf{q}\mathbf{v}t}$ averaged over the directions of flow velocity $\mathbf{v}$, but rather via a collection of "sticks" (i.e., cylinders with zero radius) in direction $\mathbf{n}$ with longitudinal effective diffusion coefficient P. For the prostate, the sticks are considered to be uniformly oriented within a voxel, such that a signal in the gradient direction $\mathbf{g}$ averaged over sticks' orientations

$$S_{\text{vasc}}(b,\mathbf{g}) = \langle e^{-bP(\mathbf{gn})^2}\rangle_{\mathbf{n}} = 1 - \frac{bP}{3} + O\left(b^2\right) = e^{-bD^* + O(b^2)},$$
$$D^* = \frac{P}{3}$$

looks like an isotropic diffusion signal with an effective diffusion coefficient $D^* = P\langle\cos^2\theta\rangle = P/3$. To improve the precision for the prostate, the intrinsic diffusivity of the vascular compartment was fixed to $P = 8$ μm^2/ms [84]; the values for P were previously estimated to range between 7 and 12 μm^2/ms [38]. Hence, the effective diffusivity value for the vascular VERDICT compartment is $D^* = \frac{8}{3}$ μm^2/ms. Remarkably, D^* and f_{vasc} from VERDICT are quite similar to our $\overline{D}^L$ (free water value) and f^L. Hence, VERDICT seems to be attributing the luminal contribution to the vascular compartment. If this is the case, VERDICT's f_{vasc} encapsulates both vascular and luminal contributions. Since luminal fraction [27] is much larger than the vascular fraction [85], then $f_{\text{vasc}} \approx f_L$, especially in the view of the shorter T_2 of the blood than of the luminal water (T_2 ≈180 ms for the oxygenated blood at 3T and even shorter for the deoxygenated blood [86, 87]). This suggests that the luminal contribution should dominate the vascular one in the high-diffusivity compartment.

Localization Regime as a Possible Future Avenue for Model Validation and Parameter Estimation

Since the diffusion gradient G was not fixed with t, the diffusion weighting could be confounded by spatially variable spin dephasing (with the signal suppressed less next to, e.g., lumen walls), which is an interesting albeit orthogonal avenue of microstructure investigation [88–90]. In the case of luminal diffusivities, $D = 3$ μm^2/ms, the localization length in our experiment increased together with t, because of the decreasing gradient: $L_G = (D/\gamma G)^{1/3} = [5.83, 6.36, 6.93, 7.54, 8.22, 8.90, 9.64, 10.48]$ μm; the diffusion length $L_D = \sqrt{D\delta} = 4.47$ μm was fixed. This indicates that our experiment was always performed in the "free-diffusion" regime [91] ($L_G > L_D$), where the "localization regime" near the walls has a relatively weak contribution toward echo decay. However, we emphasize that L_G and L_D are fairly close to each other; therefore, we in principle can have the choice of selecting for the free diffusion regime or the localization regime. In practice, the localization regime could be probed by varying G while setting

$\delta \sim t$, or by varying δ, with relatively high G, such that $L_D > L_G$.

Limitations

The study had some notable limitations that should be addressed in future research. From a theoretical perspective, we did not investigate diffusion kurtosis or higher-order terms in q-space. For a finite b, this may cause potential bias for estimated D^C and D^L (see **Supplementary Information**). **Supplementary Figure S3** shows that higher-order terms may affect diffusion estimates, but does not alter the functional form of $D(t)$ or the conclusions regarding model selection (**Supplementary Table S2**). This modeling limitation will be revisited in later works.

This volunteer data experiments employed only 3 T_E values. More T_E values potentially would enable to become sensitive to different compartments of the bulk tissue (such as stroma vs. epithelium), and produce more precise measurements, which will be investigated in future work. The patient data was not acquired with multiple T_E; for this reason, model selection on $D(t)$ was confounded by the luminal compartment. However, since the clinical dataset was acquired with smaller T_E, coupled with the fact that the luminal compartment shrinks with age, we made the assumption that the signal contribution from lumen did not impact model selection too much.

Due to the acquisition length, nearly 1 h, the volunteer could move a great deal. We were able to address most of the motion using rigid registration, but there is still room for improvement as registration was impacted by SNR limitations, particularly at long T_M and T_E. Alternative coil designs and removing noise through data redundancy [50, 92] may alleviate concerns regarding SNR. As for the scan time, many cutting edge acceleration techniques such as parallel imaging and multiband, were already used in this experiment. Reducing the acquisition time any further would require a novel acquisition approach, similar to Sabouri et al. [26].

Finally, our histological validation had the following confounds. Although a histological image is two dimensional, a 1:1 cross section of fibromuscular stroma representing 2-dimensional diffusion may be difficult to find. Even in the samples that were selected, there is inevitably some degree of orientation dispersion that confounds $\Gamma(k)$. Lastly, the H&E is not a faithful representation of restrictions to water diffusion. For example, heavily stained structures such as cellular nuclei are prominent on H&E, but are unlikely to be the primary sources of restriction to $D_\perp(t)$. The histological images had to be segmented to emphasize the borders of the cell walls, providing a more faithful representation of tissue diffusion. Nonetheless, we were reassured that the length scale beyond which the $1/k$ scaling is valid, estimated to be about 20 μm from histology, **Figures 4A–D**, is quite close to the length scale estimated from applying the RPBM onto $D_\perp^C(t)$, $a^C \sim 20\,\mu m$.

Clinical Implications

According to the National Cancer Institute, roughly 11.6% of men will be diagnosed with prostate cancer (PC) within their lifetime. It is the second most common cancer among men in the United States and represents nearly 9.6% of all new cancers [93]. An estimated 26,730 individuals will die from PC in 2017; however, this represents less than 1% of the 3,085,209 individuals living with PC.

Given the indolent nature of most cases, it is valuable to be able to properly identify tumor grade before pursuing radical prostatectomy (RP). While RP entails complete surgical removal of the prostate and is effective for preventing disease progression in patients with high-grade disease, the operation is associated with considerable morbidity including erectile dysfunction and incontinence [94]. In order to maintain quality of life, there is increasing use of active surveillance (AS) for managing patients with low-risk PC. Traditionally, AS involves serial biopsies and measurements of serum prostate specific antigen (PSA), with any evidence of PC progression on such testing resulting in RP [95, 96]. The biopsy specimens are interpreted using the Gleason Score, which remains the gold standard for PC grading [97–100]. However, a primary challenge relates to incomplete sampling during biopsy [101–104], such that there may be a lack of confidence in low-risk biopsy results.

Diffusion MRI is actively used as a biomarker aiding in AS [12]. The sequence has a key role in identifying regions suspicious for clinically significant PC that can be confirmed via targeted biopsy. The so-called apparent diffusion coefficient (ADC) is utilized through a single b, t, and T_E measurement. Much of the imaging and clinical community interprets ADC as a biomarker of "cellularity." This association with cellularity relied on studies observing a strong correlation between cell density and ADC [105–107]. A more recent study recognized that the representation described earlier is insufficient and that changes in epithelium, stroma, and lumen *volume fractions* correlate more strongly with prostate ADC values than the cellularity [63]. This study offered histological validation that diffusion MRI is actually more sensitive to changes in prostate tissue microstructure rather than to changes in cell density. Our study builds upon this observed correlation with prostate tissue microstructure by modeling individual features that make up the prostate signal, rather than a vague concept of an aggregate cellularity. Our work suggests that the dMRI signal is specific to the individual underlying microarchitecture of distinct tissue types.

It has not escaped our notice that specific microstructural degrees of freedom, such as compartment fractions, luminal diameter, fiber diameter, and cell membrane permeability, identified by our physics-inspired model selection strategy, may serve as a foundation for objective cellular-level assessment of tumor grade and of treatment efficacy. Furthermore, our acquisition and parameter estimation is quite modest from a hardware perspective. For example, our choice of b does not require high imaging gradients, which implies that this approach can be easily ported toward lower-end scanners. Though we employed DTI for our images, our acquisition and modeling approach may be further simplified: e.g., if clinicians are mainly interested in lumen diameters, the acquisition may be accelerated even further by only studying

the isotropic mean diffusion coefficient $\overline{D}(t)$ derived from 3 orthogonal directions, without the need to estimate the full tensor.

CONCLUSIONS

This study identified basic building blocks for a physical picture of water diffusion in prostate tissue microstructure, relevant for *in vivo* diffusion MRI measurements in humans. We showed that both diffusion and transverse NMR relaxation is comprised of at least two biophysically distinct contributions, which we attribute to glandular lumen (long T_2 and fast diffusion), and tissue, such as stroma, with short T_2 and heavily restricted anisotropic diffusion. In both compartments, the diffusion is time-dependent, and therefore, non-Gaussian. For the luminal compartment, diffusion appears to be in the short-time S/V limit, affected by the initial restrictions by lumen walls; the corresponding time-dependent diffusion coefficient yields typical prostate lumen diameters. In the tissue compartment, diffusion is anisotropic, with the transverse diffusivity strongly decreasing with diffusion time. Its dynamical exponent reveals that the restrictions are permeable, and fall into the universality class of random permeable barriers in two spatial dimensions, most likely corresponding to the stroma fiber walls in cross-section. Applying the RPBM, we derive the fiber diameter and membrane permeability, which have good agreement with histopathology from literature and from our quantification of radical prostatectomy specimen. Our approach offers a number of objective cellular-level tissue structure parameters as candidate markers for the non-invasive diagnosis and staging of prostate cancer with MRI.

AUTHOR CONTRIBUTIONS

GL and DN developed theory. GL and EF planned experiments. GL, DN, EF, and JV developed the parameter estimation approach. GL performed the experiments and analyzed data. AR identified zones and grades for prostate cancer lesions on MRI. FMD provided histology and identified relevant prostate regions. GL and DN wrote the manuscript. DN and EF supervised the project. All authors discussed the results, implications, and commented on the manuscript at all stages.

ACKNOWLEDGMENTS

This research was supported in part by the Center of Advanced Imaging Innovation and Research (CAI2R, www.cai2r.net), a NIBIB Biomedical Technology Research Center: P41 EB017183. JV is a postdoctoral fellow of the Research Foundation - Flanders (FWO; grant number 12S1615N).

SUPPLEMENTARY MATERIAL

The Supplementary Material for this article can be found online at: https://www.frontiersin.org/articles/10.3389/fphy.2018.00091/full#supplementary-material

REFERENCES

1. Novikov DS, Kiselev VG, Jespersen SN. On modeling. *Magn Reson Med.* (2018) **79**:3172–93. doi: 10.1002/mrm.27101
2. Kiselev VG. Fundamentals of diffusion MRI physics. *NMR Biomed.* (2017) **30**:e3602. doi: 10.1002/nbm.3602
3. Novikov DS, Fieremans E, Jespersen SN, Kiselev VG. Quantifying brain microstructure with diffusion MRI: Theory and parameter estimation. *NMR Biomed.* (2018) doi: 10.1002/nbm.3998
4. Le Bihan D, Breton E, Lallemand D, Grenier P, Cabanis E, Laval-Jeantet M. MR imaging of intravoxel incoherent motions: application to diffusion and perfusion in neurologic disorders. *Radiology* (1986) **161**:401–7. doi: 10.1148/radiology.161.2.3763909
5. Jones DK. *Diffusion MRI: Theory, Methods, and Application*. Oxford, NY: Oxford University Press (2010).
6. Hahn EL. Spin echoes. *Phys Rev.* (1950) **80**:580–94. doi: 10.1103/PhysRev.80.580
7. Stejskal EO, Tanner JE. Spin diffusion measurements: spin echoes in the presence of a time-dependent field gradient. *J Chem Phys.* (1965) **42**:288.
8. Callaghan PT. *Principles of Nuclear Magnetic Resonance Microscopy*. Oxford: Clarendon Press (1991).
9. Novikov DS, Jensen JH, Helpern JA, Fieremans E. Revealing mesoscopic structural universality with diffusion. *Proc Natl Acad Sci USA*. (2014) **111**:5088–93. doi: 10.1073/pnas.1316944111
10. Novikov DS, Kiselev VG. Effective medium theory of a diffusion-weighted signal. *NMR Biomed*. (2010) **23**:682–97. doi: 10.1002/nbm.1584
11. Bourne R, Panagiotaki E. Limitations and prospects for diffusion-weighted MRI of the prostate. *Diagnostics* (2016) **6**:E21. doi: 10.3390/diagnostics6020021
12. Radiology ACo. *MR Prostate Imaging Reporting and Data System version 2.0*. Available online at: http://www.acr.org/Quality-Safety/Resources/PIRADS/ (Accessed December 2015).
13. Bourne RM, Kurniawan N, Cowin G, Stait-Gardner T, Sved P, Watson G, et al. Microscopic diffusivity compartmentation in formalin-fixed prostate tissue. *Magn Reson Med.* (2012) **68**:614–20. doi: 10.1002/mrm.23244
14. Gorelick L, Veksler O, Gaed M, Gomez JA, Moussa M, Bauman G, et al. Prostate histopathology: learning tissue component histograms for cancer detection and classification. *IEEE Trans Med Imaging* (2013) **32**:1804–18. doi: 10.1109/TMI.2013.2265334
15. Gilani N, Malcolm P, Johnson G. A monte carlo study of restricted diffusion: Implications for diffusion MRI of prostate cancer. *Magn Reson Med.* (2017) **77**:1671–7. doi: 10.1002/mrm.26230
16. Bourne RM, Panagiotaki E, Bongers A, Sved P, Watson G, Alexander DC. Information theoretic ranking of four models of diffusion attenuation in fresh and fixed prostate tissue *ex vivo*. *Magn Reson Med.* (2014) **72**:1418–26. doi: 10.1002/mrm.25032
17. Lemberskiy G, Rosenkrantz AB, Veraart J, Taneja SS, Novikov DS, Fieremans E. Time-dependent diffusion in prostate cancer. *Invest Radiol.* 2017. **52**:405–11. doi: 10.1097/RLI.0000000000000356
18. Kiselev VG, Il'yasov KA. Is the "biexponential diffusion" biexponential? *Magn Reson Med.* (2007) **57**:464–9. doi: 10.1002/mrm.21164
19. Grebenkov DS. Use, misuse, and abuse of apparent diffusion coefficients. *Concepts Magn Reson Part A* (2010) **36A:**24–35. doi: 10.1002/cmr.a.20152
20. Merisaari H, Movahedi P, Perez IM, Toivonen J, Pesola M, Taimen P, et al. Fitting methods for intravoxel incoherent motion imaging of prostate cancer on region of interest level: Repeatability and gleason score prediction. *Magn Reson Med.* (2017) **77**:1249–64. doi: 10.1002/mrm.26169

21. Quentin M, Blondin D, Klasen J, Lanzman RS, Miese FR, Arsov C, et al. Comparison of different mathematical models of diffusion-weighted prostate MR imaging. *Magn Reson Imaging* (2012) **30**:1468–74. doi: 10.1016/j.mri.2012.04.025
22. Jambor I, Merisaari H, Taimen P, Bostrom P, Minn H, Pesola M, et al. Evaluation of different mathematical models for diffusion-weighted imaging of normal prostate and prostate cancer using high b-values: a repeatability study. *Magn Reson Med.* (2015) **73**:1988–98. doi: 10.1002/mrm.25323
23. Kjaer L, Thomsen C, Iversen P, Henriksen O. *In vivo* estimation of relaxation processes in benign hyperplasia and carcinoma of the prostate gland by magnetic resonance imaging. *Magn Reson Imaging* (1987) **5**:23–30. doi: 10.1016/0730-725X(87)90480-2
24. Storas TH, Gjesdal KI, Gadmar OB, Geitung JT, Klow NE. Prostate magnetic resonance imaging: multiexponential T2 decay in prostate tissue. *J Magn Reson Imaging* (2008) **28**:1166–72. doi: 10.1002/jmri.21534
25. Gilani N, Rosenkrantz AB, Malcolm P, Johnson G. Minimization of errors in biexponential T2 measurements of the prostate. *J Magn Reson Imaging* (2015) **42**:1072–7. doi: 10.1002/jmri.24870
26. Sabouri S, Chang SD, Savdie R, Zhang J, Jones EC, Goldenberg SL, et al. Luminal water imaging: a new mr imaging T2 mapping technique for prostate cancer diagnosis. *Radiology* (2017) **284**:451–9. doi: 10.1148/radiol.2017161687
27. Sabouri S, Fazli L, Chang SD, Savdie R, Jones EC, Goldenberg SL, et al. MR measurement of luminal water in prostate gland: quantitative correlation between MRI and histology. *J Magn Reson Imaging* (2017). **46**:861–9. doi: 10.1002/jmri.25624
28. Mitra PP, Sen PN, Schwartz LM. Short-time behavior of the diffusion coefficient as a geometrical probe of porous media. *Phys Rev B* (1993) **47**:8565–74. doi: 10.1103/PhysRevB.47.8565
29. Lemberskiy G, Baete SH, Cloos MA, Novikov DS, Fieremans E. Validation of surface-to-volume ratio measurements derived from oscillating gradient spin echo on a clinical scanner using anisotropic fiber phantoms. *NMR Biomed.* (2017) **30**:e3612. doi: 10.1002/nbm.3708
30. Gilani N, Malcolm P, Johnson G. A model describing diffusion in prostate cancer. *Magn Reson Med.* (2017) **78**:316–26. doi: 10.1002/mrm.26340
31. Delahunt B, Grignon DJ, Samaratunga H, Srigley JR, Leite KR, Kristiansen G, et al. Prostate cancer grading: a decade after the 2005 modified gleason grading system. *Arch Pathol Lab Med.* (2017) **141**:182–3. doi: 10.5858/arpa.2016-0300-LE
32. Bourne RM, Bongers A, Chatterjee A, Sved P, Watson G. Diffusion anisotropy in fresh and fixed prostate tissue *ex vivo*. *Magn Reson Med.* (2016) **76**:626–34. doi: 10.1002/mrm.25908
33. Novikov DS, Fieremans E, Jensen JH, Helpern JA. Random walk with barriers. *Nat Phys.* (2011) **7**:508–14. doi: 10.1038/nphys1936
34. Torquato S. Hyperuniformity and its generalizations. *Phys Rev E* (2016) **94:**022122. doi: 10.1103/PhysRevE.94.022122
35. Papaioannou A, Novikov DS, Fieremans E, Boutis GS. Observation of structural universality in disordered systems using bulk diffusion measurement. *Phys Rev E* (2017) **96**:61101. doi: 10.1103/PhysRevE.96.061101
36. Skoge M, Donev A, Stillinger FH, Torquato S. Packing hyperspheres in high-dimensional Euclidean spaces. *Phys Rev E Stat Nonlin Soft Matter Phys.* (2006) 74:041127. doi: 10.1103/PhysRevE.74.041127
37. Tanner JE. Self diffusion of water in frog muscle. *Biophys J.* (1979) **28**:107–16. doi: 10.1016/S0006-3495(79)85162-0
38. Panagiotaki E, Walker-Samuel S, Siow B, Johnson SP, Rajkumar V, Pedley RB, et al. Noninvasive quantification of solid tumor microstructure using VERDICT MRI. *Cancer Res.* (2014) **74**:1902–12. doi: 10.1158/0008-5472.CAN-13-2511
39. Rakow-Penner RA, White NS, Parsons JK, Choi HW, Liss MA, Kuperman JM, et al. Novel technique for characterizing prostate cancer utilizing MRI restriction spectrum imaging: proof of principle and initial clinical experience with extraprostatic extension. *Prostate Cancer Prostatic Dis.* (2015) **18**:81–5. doi: 10.1038/pcan.2014.50
40. Reynaud O, Winters KV, Hoang DM, Wadghiri YZ, Novikov DS, Kim SG. Pulsed and oscillating gradient MRI for assessment of cell size and extracellular space (POMACE) in mouse gliomas. *NMR Biomed.* (2016) **29**:1350–63. doi: 10.1002/nbm.3577
41. Jiang X, Li H, Xie J, McKinley ET, Zhao P, Gore JC, et al. *In vivo* imaging of cancer cell size and cellularity using temporal diffusion spectroscopy. *Magn Reson Med.* (2017) **78**:156–64. doi: 10.1002/mrm.26356
42. Reynaud O. Time-dependent diffusion MRI in cancer: tissue modeling and applications. *Front Phys.* (2017) **5**:58. doi: 10.3389/fphy.2017.00058
43. Burcaw LM, Fieremans E, Novikov DS. Mesoscopic structure of neuronal tracts from time-dependent diffusion. *Neuroimage* (2015) **114**:18–37. doi: 10.1016/j.neuroimage.2015.03.061
44. Sigmund EE, Novikov DS, Sui D, Ukpebor O, Baete S, Babb JS, et al. Time-dependent diffusion in skeletal muscle with the random permeable barrier model (RPBM): application to normal controls and chronic exertional compartment syndrome patients. *NMR Biomed.* (2014) **27**:519–28. doi: 10.1002/nbm.3087
45. Fieremans E, Lemberskiy G, Veraart J, Sigmund EE, Gyftopoulos S, Novikov DS. *In vivo* measurement of membrane permeability and myofiber size in human muscle using time-dependent diffusion tensor imaging and the random permeable barrier model. *NMR Biomed.* (2017) **30**:e3612. doi: 10.1002/nbm.3612
46. Winters KV, Reynaud O, Novikov DS, Fieremans E, Kim SG. Quantifying myofiber integrity using diffusion MRI and random permeable barrier modeling in skeletal muscle growth and Duchenne muscular dystrophy model in mice. *Magn Reson Med.* (2018) 1–15. doi: 10.1002/mrm.27188
47. Langer DL, van der Kwast TH, Evans AJ, Sun L, Yaffe MJ, Trachtenberg J, Haider MA. Intermixed normal tissue within prostate cancer: effect on MR imaging measurements of apparent diffusion coefficient and T2–sparse versus dense cancers. *Radiology* (2008) **249**:900–8. doi: 10.1148/radiol.2493080236
48. Fieremans E, Burcaw LM, Lee HH, Lemberskiy G, Veraart J, Novikov DS. *In vivo* observation and biophysical interpretation of time-dependent diffusion in human white matter. *Neuroimage* (2016) **129**:414–27. doi: 10.1016/j.neuroimage.2016.01.018
49. Lundell H, Alexander DC, Dyrby TB. High angular resolution diffusion imaging with stimulated echoes: compensation and correction in experiment design and analysis. *NMR Biomed.* (2014) **27**:918–25. doi: 10.1002/nbm.3137
50. Veraart J, Fieremans E, Novikov DS. Diffusion MRI noise mapping using random matrix theory. *Magn Reson Med.* (2016) **76**:1582–93. doi: 10.1002/mrm.26059
51. Jezzard P, Balaban RS. Correction for geometric distortion in echo planar images from B0 field variations. *Magn Reson Med.* (1995) **34**:65–73. doi: 10.1002/mrm.1910340111
52. Kellner E, Dhital B, Kiselev VG, Reisert M. Gibbs-ringing artifact removal based on local subvoxel-shifts. *Magn Reson Med.* (2016) **76**:1574–81. doi: 10.1002/mrm.26054
53. Andersson JL, Sotiropoulos SN. An integrated approach to correction for off-resonance effects and subject movement in diffusion MR imaging. *Neuroimage* (2016) **125**:1063–78. doi: 10.1016/j.neuroimage.2015.10.019
54. Klein S, Staring M, Murphy K, Viergever MA, Pluim JP. Elastix: a toolbox for intensity-based medical image registration. *IEEE Trans Med Imaging* (2010) **29**:196–205. doi: 10.1109/TMI.2009.2035616
55. Shamonin DP, Bron EE, Lelieveldt BP, Smits M, Klein S, Staring M. Alzheimer's Disease neuroimaging i. fast parallel image registration on CPU and GPU for diagnostic classification of Alzheimer's disease. *Front Neuroinform.* (2013) **7**:50. doi: 10.3389/fninf.2013.00050
56. Salvador R, Pena A, Menon DK, Carpenter TA, Pickard JD, Bullmore ET. Formal characterization and extension of the linearized diffusion tensor model. Hum Brain Mapp (2005) **24**:144–55. doi: 10.1002/hbm.20076
57. Veraart J, Sijbers J, Sunaert S, Leemans A, Jeurissen B. Weighted linear least squares estimation of diffusion MRI parameters: strengths, limitations, and pitfalls. *Neuroimage* (2013) **81**:335–46. doi: 10.1016/j.neuroimage.2013.05.028
58. Storaas T, Gjesdal KI. (2012). Assessment of biexponential T1 decay in prostate tissue. In: *ISMRM 20th Scientific Meeting & Exhibition*. Melbourne, VIC Australia (2012).
59. Kiselev VG. The cumulant expansion: an overarching mathematical framework for understanding diffusion NMR. In: *Diffusion MRI: Theory, Methods, and Applications*. Oxford, UK: Oxford University Press (2010). p. 152–68. Available online at: http://oxfordmedicine.com/view/10.1093/med/9780195369779.001.0001/med-9780195369779-chapter-010

60. Bourne R, Liang S, Panagiotaki E, Bongers A, Sved P, Watson G. Measurement and modeling of diffusion time dependence of apparent diffusion coefficient and fractional anisotropy in prostate tissue *ex vivo*. *NMR Biomed.* (2017) **30**:e3751. doi: 10.1002/nbm.3751
61. Jones DK. Determining and visualizing uncertainty in estimates of fiber orientation from diffusion tensor MRI. *Magn Reson Med*. (2003) **49**:7–12. doi: 10.1002/mrm.10331
62. Williams AM, Simon I, Landis PK, Moser C, Christens-Barry W, Carter HB, et al. Prostatic growth rate determined from MRI data: age-related longitudinal changes. *J Androl.* (1999) **20**:474–80. doi: 10.1097/00005392-199904020-00155
63. Chatterjee A, Watson G, Myint E, Sved P, McEntee M, Bourne R. Changes in epithelium, stroma, and lumen space correlate more strongly with gleason pattern and are stronger predictors of prostate ADC changes than cellularity metrics. *Radiology* (2015) **277**:751–62. doi: 10.1148/radiol.2015142414
64. Holz M, Heil SR, Sacco A. Temperature-dependent self-diffusion coefficients of water and six selected molecular liquids for calibration in accurate 1H NMR PFG measurements. *Phys Chem Chem Phys.* (2000) **2**:4740–2. doi: 10.1039/b005319h
65. Brunsing RL, Schenker-Ahmed NM, White NS, Parsons JK, Kane C, Kuperman J, et al. Restriction spectrum imaging: an evolving imaging biomarker in prostate MRI. *J Magn Reson Imaging* (2017) **45**:323–36. doi: 10.1002/jmri.25419
66. Benga G, Pop VI, Popescu O, Borza V. On measuring the diffusional water permeability of human red blood cells and ghosts by nuclear magnetic resonance. *J Biochem Biophys Methods* (1990) **21**:87–102. doi: 10.1016/0165-022X(90)90057-J
67. Herbst MD, Goldstein JH. A review of water diffusion measurement by NMR in human red blood cells. *Am J Physiol.* (1989) 256(5 Pt 1):C1097–104.
68. Gilani N, Malcolm P, Johnson G. An improved model for prostate diffusion incorporating the results of Monte Carlo simulations of diffusion in the cellular compartment. *NMR Biomed.* (2017) **30**:e3782. doi: 10.1002/nbm.3782
69. Ackerman JJ, Neil JJ. The use of MR-detectable reporter molecules and ions to evaluate diffusion in normal and ischemic brain. *NMR Biomed.* (2010) **23**:725–33. doi: 10.1002/nbm.1530
70. Yablonskiy DA, Sukstanskii AL. Theoretical models of the diffusion weighted MR signal. *NMR Biomed*. (2010) **23**:661–81. doi: 10.1002/nbm.1520
71. Stepišnik J. Time-dependent self-diffusion by NMR spin-echo. *Phys B* (1993) **183**:343–50.
72. Murday JS, Cotts RM. Self-diffusion coefficient of liquid lithium. *J Chem Phys.* (1968) **48**:4938–45. doi: 10.1063/1.1668160
73. Mazaheri Y, Afaq A, Rowe DB, Lu Y, Shukla-Dave A, Grover J. Diffusion-weighted magnetic resonance imaging of the prostate: improved robustness with stretched exponential modeling. *J Comput Assist Tomogr.* (2012) **36**:695–703. doi: 10.1097/RCT.0b013e31826bdbbd
74. Chatterjee A, Bourne RM, Wang S, Devaraj A, Gallan AJ, Antic T, et al. Diagnosis of prostate cancer with noninvasive estimation of prostate tissue composition by using hybrid multidimensional MR imaging: a feasibility study. *Radiology* (2018) **287**:864–73. doi: 10.1148/radiol.2018171130
75. White NS, Leergaard TB, D'Arceuil H, Bjaalie JG, Dale AM. Probing tissue microstructure with restriction spectrum imaging: Histological and theoretical validation. *Hum Brain Mapp*. (2013) **34**:327–46. doi: 10.1002/hbm.21454
76. Clark CA, Le Bihan D. Water diffusion compartmentation and anisotropy at high b values in the human brain. *Magn Reson Med.* (2000) **44**:852–9. doi: 10.1002/1522-2594(200012)44:6<852::AID-MRM5>3.0.CO;2-A
77. Wang S, Peng Y, Medved M, Yousuf AN, Ivancevic MK, Karademir I, et al. Hybrid multidimensional T(2) and diffusion-weighted MRI for prostate cancer detection. *J Magn Reson Imaging* (2014) **39**:781–8. doi: 10.1002/jmri.24212
78. Veraart J, Novikov DS, Fieremans E. TE dependent Diffusion Imaging (TEdDI) distinguishes between compartmental T2 relaxation times. *Neuroimage* (2017). doi: 10.1016/j.neuroimage.2017.09.030
79. Ferizi U, Scherrer B, Schneider T, Alipoor M, Eufracio O, Fick RHJ, et al. Diffusion MRI microstructure models with *in vivo* human brain Connectome data: results from a multi-group comparison. *NMR Biomed.* (2017) **30**:e3734. doi: 10.1002/nbm.3734
80. Crooks LE, Arakawa M, Hoenninger J, McCarten B, Watts J, Kaufman L. Magnetic resonance imaging: effects of magnetic field strength. *Radiology* (1984) **151**:127–33. doi: 10.1148/radiology.151.1.6701302
81. Qin W, Yu CS, Zhang F, Du XY, Jiang H, Yan YX, et al. Effects of echo time on diffusion quantification of brain white matter at 1.5 T and 3.0 T. *Magn Reson Med.* (2009) **61**:755–60. doi: 10.1002/mrm.21920
82. Gordetsky J, Epstein J. Grading of prostatic adenocarcinoma: current state and prognostic implications. *Diagn Pathol.* (2016) **11**:25. doi: 10.1186/s13000-016-0478-2
83. Pang Y, Turkbey B, Bernardo M, Kruecker J, Kadoury S, Merino MJ, et al. Intravoxel incoherent motion MR imaging for prostate cancer: an evaluation of perfusion fraction and diffusion coefficient derived from different b-value combinations. *Magn Reson Med.* (2013) **69**:553–62. doi: 10.1002/mrm.24277
84. Panagiotaki E, Chan RW, Dikaios N, Ahmed HU, O'Callaghan J, Freeman A, et al. Microstructural characterization of normal and malignant human prostate tissue with vascular, extracellular, and restricted diffusion for cytometry in tumours magnetic resonance imaging. *Invest Radiol.* (2015) **50**:218–27. doi: 10.1097/RLI.0000000000000115
85. Bonet-Carne E, Tariq M, Pye H, Appayya M, Haider A, Bayley C, et al. Histological Validation of *in-vivo* VERDICT MRI for Prostate using 3D Personalised Moulds. In: *(Proceedings) ISMRM 2018, International Society for Magnetic Resonance in Medicine,* Paris (2018). p. 16–21.
86. Spees William M, Yablonskiy Dmitriy A, Oswood Mark C, Ackerman Joseph JH. Water proton MR properties of human blood at 1.5 Tesla: Magnetic susceptibility, T1, T2, T, and non-Lorentzian signal behavior. *Magn Reson Med.* (2001) **45**:533–42. doi: 10.1002/mrm.1072
87. Chen Jean J, Pike GB. Human whole blood T2 relaxometry at 3 Tesla. *Magn Reson Med.* (2009) **61**:249–54. doi: 10.1002/mrm.21858
88. Stoller SD, Happer W, Dyson FJ. Transverse spin relaxation in inhomogeneous magnetic fields. *Phys Rev A* (1991) **44**:7459–77. doi: 10.1103/PhysRevA.44.7459
89. Axelrod S, Sen PN. Nuclear magnetic resonance spin echoes for restricted diffusion in an inhomogeneous field: methods and asymptotic regimes. *J Chem Phys.* (2001) **114**:6878–95. doi: 10.1063/1.1356010
90. Grebenkov DS. NMR survey of reflected Brownian motion. *Rev Mod Phys.* (2007) **79**:1077–137. doi: 10.1103/RevModPhys.79.1077
91. Hurlimann MD, Helmer KG, Deswiet TM, Sen PN. Spin echoes in a constant gradient and in the presence of simple restriction. *J Magn Reson A* (1995) **113**:260–4. doi: 10.1006/jmra.1995.1091
92. Veraart J, Novikov DS, Christiaens D, Ades-Aron B, Sijbers J, Fieremans E. Denoising of diffusion MRI using random matrix theory. *Neuroimage* (2016) **142**:394–406. doi: 10.1016/j.neuroimage.2016.08.016
93. Howlader N, Noone A, Krapcho M, Miller D, Bishop K, Kosary C, et al. *SEER Cancer Statistics Review, 1975-2014*. Bethesda, MD: National Cancer Institute. Available online at: https://seer.cancer.gov/csr/1975_2014/, based on November 2016 SEER data submission, posted to the SEER web site, April 2017.
94. Hugosson J, Stranne J, Carlsson SV. Radical retropubic prostatectomy: a review of outcomes and side-effects. *Acta Oncol.* (2011) **50**(Supp1.):92–7. doi: 10.3109/0284186X.2010.535848
95. Klotz L. Active surveillance for prostate cancer: a review. *Curr Urol Rep.* (2010) **11**:165–71. doi: 10.1007/s11934-010-0110-z
96. Klotz L, Zhang L, Lam A, Nam R, Mamedov A, Loblaw A. Clinical results of long-term follow-up of a large, active surveillance cohort with localized prostate cancer. *J Clin Oncol.* (2010) **28**:126–31. doi: 10.1200/JCO.2009.24.2180
97. Epstein JI, Allsbrook WC Jr, Amin MB, Egevad LL. The 2005 International Society of Urological Pathology (ISUP) Consensus Conference on Gleason Grading of Prostatic Carcinoma. *Am J Surg Pathol.* (2005) **29**:1228–42. doi: 10.1097/01.pas.0000173646.99337.b1
98. Epstein JI. What's new in prostate cancer disease assessment in 2006? *Curr Opin Urol.* (2006) **16**:146–51. doi: 10.1097/01.mou.0000193389.31727.9b
99. Kattan MW, Eastham JA, Stapleton AM, Wheeler TM, Scardino PT. A preoperative nomogram for disease recurrence following radical prostatectomy for prostate cancer. *J Natl Cancer Inst*. (1998) **90**:766–71. doi: 10.1093/jnci/90.10.766

100. Kattan MW, Wheeler TM, Scardino PT. Postoperative nomogram for disease recurrence after radical prostatectomy for prostate cancer. *J Clin Oncol.* (1999) **17**:1499–507. doi: 10.1200/JCO.1999.17.5.1499
101. Fine SW, Epstein JI. A contemporary study correlating prostate needle biopsy and radical prostatectomy Gleason score. *J Urol*. (2008) **179**:1335–8. doi: 10.1016/j.juro.2007.11.057
102. Mufarrij P, Sankin A, Godoy G, Lepor H. Pathologic outcomes of candidates for active surveillance undergoing radical prostatectomy. *Urology* (2010) **76**:689–92. doi: 10.1016/j.urology.2009.12.075
103. Boccon-Gibod LM, Dumonceau O, Toublanc M, Ravery V, Boccon-Gibod LA. Micro-focal prostate cancer: a comparison of biopsy and radical prostatectomy specimen features. *Eur Urol*. (2005) **48**:895–9. doi: 10.1016/j.eururo.2005.04.033
104. Anast JW, Andriole GL, Bismar TA, Yan Y, Humphrey PA. Relating biopsy and clinical variables to radical prostatectomy findings: can insignificant and advanced prostate cancer be predicted in a screening population? *Urology* (2004) **64**:544–50. doi: 10.1038/aja.2011.140
105. Gibbs P, Liney GP, Pickles MD, Zelhof B, Rodrigues G, Turnbull LW. Correlation of ADC and T2 measurements with cell density in prostate cancer at 3.0 Tesla. *Invest Radiol*. (2009) **44**:572–6. doi: 10.1097/RLI.0b013e3181b4c10e
106. Zelhof B, Pickles M, Liney G, Gibbs P, Rodrigues G, Kraus S, et al. Correlation of diffusion-weighted magnetic resonance data with cellularity in prostate cancer. *BJU Int*. (2009) **103**:883–8. doi: 10.1111/j.1464-410X.2008.08130.x
107. Surov A, Meyer HJ, Wienke A. Correlation between apparent diffusion coefficient (ADC) and cellularity is different in several tumors: a meta-analysis. *Oncotarget* (2017) **8**:59492–99. doi: 10.18632/oncotarget.17752

Conflict of Interest Statement: GL, EF and DN disclose intellectual property rights related to a pending patent. JV, FMD and ABR declare that the research was conducted in the absence of any commercial or financial relationships that could be construed as a potential conflict of interest.

frontiers in Physics

REVIEW
published: 15 September 2017
doi: 10.3389/fphy.2017.00040

Recent Developments in Fast Kurtosis Imaging

Brian Hansen[1]* *and Sune N. Jespersen*[1, 2]*

[1] Center of Functionally Integrative Neuroscience and MINDLab, Department of Clinical Medicine, Aarhus University, Aarhus, Denmark, [2] Department of Physics and Astronomy, Aarhus University, Aarhus, Denmark

Diffusion kurtosis imaging (DKI) is an extension of the popular diffusion tensor imaging (DTI) technique. DKI takes into account leading deviations from Gaussian diffusion stemming from a number of effects related to the microarchitecture and compartmentalization in biological tissues. DKI therefore offers increased sensitivity to subtle microstructural alterations over conventional diffusion imaging such as DTI, as has been demonstrated in numerous reports. For this reason, interest in routine clinical application of DKI is growing rapidly. In an effort to facilitate more widespread use of DKI, recent work by our group has focused on developing experimentally fast and robust estimates of DKI metrics. A significant increase in speed is made possible by a reduction in data demand achieved through rigorous analysis of the relation between the DKI signal and the kurtosis tensor based metrics. The fast DKI methods therefore need only 13 or 19 images for DKI parameter estimation compared to more than 60 for the most modest DKI protocols applied today. Closed form solutions also ensure rapid calculation of most DKI metrics. Some parameters can even be reconstructed in real time, which may be valuable in the clinic. The fast techniques are based on conventional diffusion sequences and are therefore easily implemented on almost any clinical system, in contrast to a range of other recently proposed advanced diffusion techniques. In addition to its general applicability, this also ensures that any acceleration achieved in conventional DKI through sequence or hardware optimization will also translate directly to fast DKI acquisitions. In this review, we recapitulate the theoretical basis for the fast kurtosis techniques and their relation to conventional DKI. We then discuss the currently available variants of the fast kurtosis techniques, their strengths and weaknesses, as well as their respective realms of application. These range from whole body applications to methods mostly suited for spinal cord or peripheral nerve, and analysis specific to brain white matter. Having covered these technical aspects, we proceed to review the fast kurtosis literature including validation studies, organ specific optimization studies and results from clinical applications.

Keywords: MRI, diffusion, kurtosis, higher-order tensors, orientational sampling, WMTI

OPEN ACCESS

Edited by:
Federico Giove,
Centro Fermi, Italy

Reviewed by:
Lipeng Ning,
Brigham and Women's Hospital, United States
Marco Palombo,
University College London, United Kingdom

***Correspondence:**
Brian Hansen
brian@cfin.au.dk
Sune N. Jespersen
sune@cfin.au.dk

Specialty section:
This article was submitted to Biomedical Physics, a section of the journal Frontiers in Physics

Received: *12 July 2017*
Accepted: *30 August 2017*
Published: *15 September 2017*

Citation:
Hansen B and Jespersen SN (2017) Recent Developments in Fast Kurtosis Imaging. Front. Phys. 5:40. doi: 10.3389/fphy.2017.00040

INTRODUCTION

Microstructural sensitivity in MRI is most often obtained by sensitizing the signal to the diffusion of water. In combination with modeling, such data can yield specific microstructural markers, but the data required to support such modeling is often prohibitive in particular in a clinical context. A less data intense strategy to obtain microstructural sensitivity in diffusion MRI (dMRI) is the diffusion kurtosis imaging (DKI) framework [1] which quantifies the leading deviation from Gaussian diffusion in each image point. This deviation arises from the influence of tissue microstructure on the water diffusion profile and is easily visualized by plotting the log signal as function of b-value. This is done in **Figure 1** using data acquired along one direction in a white matter region in normal human brain (circles). Here the familiar log-linear signal decay is seen up to $b \approx 1$ ms/μm^2, below which a diffusion tensor fit (solid red line) approximates the signal very well. Extrapolation of this fit beyond $b \approx 1$ ms/μm^2 (dashed red line), however, clearly does not match the observed signal. Conversely, the DKI fit (solid green line) is seen to approximate the measured signal over the entire b-value range shown, although it will diverge at sufficiently high b-values. DKI thus allows quantification of the deviation from log-linear signal decay caused by tissue microarchitecture and compartmentalization. This deviation thereby indirectly provides information about these tissue properties.

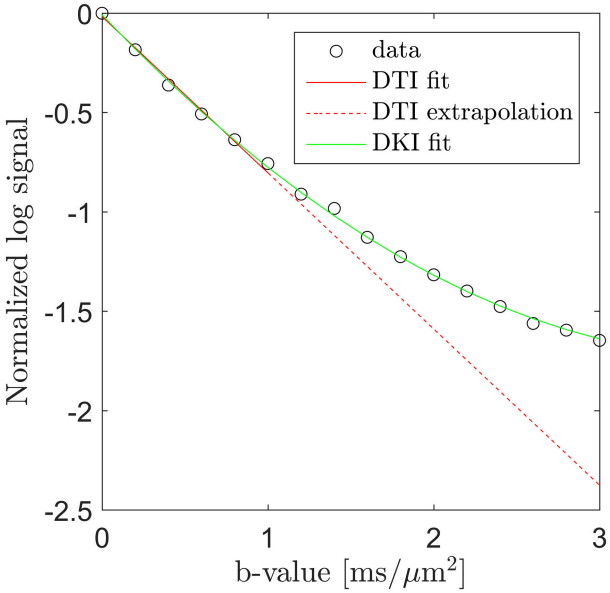

FIGURE 1 | Diffusion MRI data (circles) from a white matter region in human brain acquired along one direction over the b-value range from 0 to 3 ms/μm^2. Fits obtained with DTI (solid red line, $b = 0$–1 ms/μm^2) and DKI (green line, all b-values) are shown. The signal deviation from the DTI signal prediction is illustrated by extrapolating the DTI fit (the dashed red line) into the DKI regime ($b > 1$ ms/μm^2). Conversely, the DKI fit is seen to approximate the signal very well.

Compared to most other advanced dMRI techniques, DKI is easily implemented. For this reason, and because of its increased sensitivity to tissue microstructure compared to diffusion tensor imaging (DTI), DKI has grown to be a popular dMRI method. Nevertheless, DKI is not experimentally inexpensive, as typical protocols consist of a few unweighted images for normalization and two 30-direction shells at two non-zero b-values (typically 1.0 ms/μm^2 and 2.0–2.5 ms/μm^2) thus totaling 60–70 images [2]. This is current standard, although more data intense protocols are not uncommon [3]. While most DKI protocols are too lengthy for everyday clinical use, high quality data can be acquired in a time frame considered reasonable for many clinical and preclinical studies. Even so, the time required for post-processing of DKI is significant, and both acquisition time and data processing time limit its clinical application, especially in patients with time sensitive ailments (e.g., stroke or trauma), or patients with difficulties lying still, e.g., children.

The DKI method yields a wealth of parameters that can be mapped on a voxel by voxel basis. Several of these DKI metrics have been shown to detect subtle changes in brain tissue structure. To briefly summarize, studies have shown DKI to have potential in diagnostics of a number of diseases such as stroke [4, 5], Alzheimer's disease [6], multiple sclerosis [7], gliomas [8, 9], and head trauma [10–12] (see also the review of this area in Ostergaard et al. [13]). DKI is not only of clinical interest but is also a valuable tool in basic neuroscience, and the method has for example been employed in studies of natural alteration of brain microstructure e.g., in the context of development and aging [14, 15].

DKI is sensitive to microstructure generally, and therefore in brain it can be used to study both gray matter (GM) and white matter (WM). However, in WM, DKI can be combined with modeling to obtain some of the biophysical specificity of more advanced dMRI modeling frameworks. One important example of this is the white matter tract integrity (WMTI) technique [2] which on the basis of a DKI data set provides detailed information about microstructure of highly aligned fiber bundles, such as intra- and extra-axonal diffusivities, axonal water fraction (AWF), and the tortuosity, α, of the extra-axonal space.

Like DKI, WMTI has also been used to study the brain in a wide range of contexts: normal brain development and aging [16, 17], Alzheimer's disease [18, 19], mild head trauma [20], multiple sclerosis [21], autism [22], and stroke [4]. Validation studies comparing WMTI indices to histology and electron microscopy [23–26] have largely confirmed the ability of WMTI to detect microstructural changes in WM. While other frameworks for DKI-based estimation of tissue model parameters have been proposed [27, 28], a recent comparative study showed WMTI to be the most widely applicable [27].

While WMTI was developed specifically for analysis of WM, the DKI framework itself is almost without assumptions and its applications are therefore not limited to brain imaging. Consequently, interest in DKI for body imaging is growing [29] with demonstrated applications in imaging of liver [30, 31], kidney [32, 33], and prostate [34–36].

This short survey of the DKI literature documents the high potential of DKI as a method to obtain sensitive markers suitable for basic research (e.g., for the study of brain plasticity), diagnostics and treatment monitoring. However, widespread

clinical application of DKI and WMTI has yet to emerge. Two major limitations that are most likely responsible for DKI not being routinely used in the clinic have already been identified: acquisition time and post-processing time. Lowering both of these barriers has therefore been an important goal as methods for fast DKI and WMTI would not only increase the clinical applicability of DKI and WMTI, but also make possible more widespread, routine exploration of DKI metrics by allowing inclusion of DKI, at little additional cost, as a component of any protocol for imaging of the brain or other organs. Furthermore, such methods would facilitate high resolution preclinical studies for characterization of animal models of disease or for validation studies.

Here we review recent developments enabling fast kurtosis imaging based on small data sets (13 or 19 images) and with near-instant post-processing [37–42]. The review is structured such that first the theoretical foundation of DKI and WMTI is recapitulated briefly. For a more in-depth review of conventional DKI we refer to Jensen and Helpern [43], Wu and Cheung [44]. On this basis we then introduce the rapidly obtainable DKI metrics used in fast kurtosis and discuss their relation to conventional DKI definitions. Since a few variants of fast kurtosis have been introduced we cover all of them and their various area of application. Having covered the methodological background we review the literature of fast DKI application studies and discuss current efforts for method refinement and potential future applications. All data shown was reused from the cited papers from our group. The presented non-human data was acquired at 9.4T (except from **Figure 8**, acquired at 16.4T) while human brain data was acquired in normal volunteers at 3T. We refer to the original publications for details on data acquisition and analysis.

DIFFUSION KURTOSIS IMAGING VARIANTS

Conventional DKI

The standard expression for the DKI signal is [1]:

$$\begin{aligned}\log S(b,\hat{n})/S_0 &= -bn_in_jD_{ij} + \frac{1}{6}b^2\overline{D}^2n_in_jn_kn_lW_{ijkl} + O(b^3)\\ &= -bD(\hat{n}) + \frac{1}{6}b^2\overline{D}^2W(\hat{n}) + O(b^3)\\ &= -bD(\hat{n}) + \frac{1}{6}b^2D(\hat{n})^2K(\hat{n}) + O(b^3)\end{aligned} \quad (2.1.1)$$

Here $S_0 = S(b = 0)$ is the unweighted signal used for normalization and b is the diffusion weighting applied along a direction $\hat{n} = (n_x, n_y, n_z)$. The normalized signal is denoted S from here on. Throughout, subscripts label Cartesian components (e.g., $i = x,y,z$) and summation over repeated indices is assumed. D is the diffusion tensor [45], and the kurtosis tensor W and the apparent excess kurtosis $K(\hat{n})$ are defined as in Jensen et al. [1]. Overbar denotes mean value over diffusion directions, i.e., $\overline{D} = \mathrm{Tr(D)}/3$ is the mean diffusivity (Tr is the trace).

In the DKI analysis, the tensors D and W are estimated by fitting Equation (2.1.1) to data acquired as described above (with b-values sufficiently low so that the $O(b^3)$ terms can be neglected and satisfying $b \leq 3/D(\hat{n})K(\hat{n})$ [46] so that the DKI signal model Equation (2.1.1) does not diverge). From these tensors, a wealth of metrics is available. For the diffusion tensor, the most important metrics are $\overline{D}$, fractional anisotropy (FA) and radial and axial diffusivities. To obtain these, the diffusion tensor is diagonalized to yield three pairs of eigenvectors $\hat{v}_i$ and eigenvalues λ_i ($i = 1,2,3$). The eigenvalues (diffusivities) are sorted by size so that the primary eigenvector ($\hat{v}_1$) indicates the direction of highest diffusivity (λ_1), etc. The axial diffusivity is then $D_{||} = \lambda_1$ and radial diffusivity is $D_\perp = (\lambda_2 + \lambda_3)/2$. The anisotropy of D is summarized by the FA due to Basser and Pierpaoli [47]:

$$\begin{aligned}FA &= \sqrt{\frac{3}{2}}\frac{\sqrt{\left(\lambda_1-\overline{D}\right)^2+\left(\lambda_2-\overline{D}\right)^2+\left(\lambda_3-\overline{D}\right)^2}}{\sqrt{\lambda_1^2+\lambda_2^2+\lambda_3^2}}\\ &= \sqrt{\frac{3}{2}}\frac{\left\|\mathrm{D}-\overline{D}\mathbb{I}\right\|}{\|\mathrm{D}\|},\end{aligned} \quad (2.1.2)$$

where the double vertical bars $\|\cdot\|$ denote the Frobenius norm and $\mathbb{I}$ is the rank-2 identity matrix. From the kurtosis tensor, summary metrics can also be derived, the most important parameter being the mean kurtosis (MK, $\overline{K}$) [1]:

$$\overline{K} = \frac{1}{4\pi}\int_{S_2}K(\hat{n})d\hat{n} = \frac{1}{4\pi}\int_{S_2}W(\hat{n})\frac{\overline{D}^2}{D(\hat{n})^2}d\hat{n} \quad (2.1.3)$$

Other meaningful parameters can be extracted from the kurtosis tensor. Similar to the directional diffusivities, the kurtoses observed along (||) and orthogonal ($\perp$) to the primary eigenvector direction have been introduced [3, 43, 48, 49]:

$$\begin{aligned}K_{||} &= K(\hat{v}_1)\\ K_\perp &\equiv \frac{1}{2\pi}\int_{S_2}d\hat{n}\,\delta(\hat{n}\cdot\hat{v}_1)K(\hat{n})\\ &= \frac{1}{2\pi}\int_0^{2\pi}d\varphi K(\hat{v}_2\cos\varphi + \hat{v}_3\sin\varphi)\end{aligned} \quad (2.1.4)$$

where S_2 is the sphere. These are known respectively as (conventional) radial and axial kurtosis. Note that in contrast to their diffusion tensor counterparts, they are not strictly rotationally invariant. The reason for this behavior is that in orthogonal fiber bundle crossings the diffusion eigenvalues may be degenerate (i.e., for such a 3D fiber arrangement there is no primary fiber direction and the diffusion tensor is isotropic) while the apparent kurtosis can differ among the fiber directions due to microstructural differences in the bundles [42]. Consequently, in this thought-experiment noise will determine which eigenvector will be deemed the primary direction thus causing the estimated directional kurtosis values to vary between measurements. While such fiber configurations are most likely rare this property should nevertheless be kept in mind when employing directional kurtosis metrics. Other definitions have been proposed and the fast DKI counterparts rely on other definitions than those presented in Equations (2.1.3) and (2.1.4). These will be discussed

in Sections "Fast estimation of mean diffusivity and mean kurtosis", "Fast kurtosis estimation with increased experimental robustness" and, "Axisymmetric DKI".

In addition to the raw tensor metrics, D and W can also provide metrics of white matter tract integrity (WMTI) based on modeling described in Fieremans et al. [2]. The assumptions and modeling choices that make estimation of these WM metrics possible are covered in the following section.

White Matter Tract Integrity from DKI

WMTI uses the estimated tensors D and W to estimate the (MR detectable) axonal water fraction, and several compartmental diffusivities. This analysis exploits the relation between the tensors D and W and the WMTI parameters found by the cumulant expansion of the expression for the dMRI signal from a two-compartment system consisting of the extra-axonal space (EAS) and an intra-axonal space (IAS) described as sticks with an effective radius of zero, which is valid for the gradients employed in acquiring typical clinical diffusion data. Diffusion in both the EAS and the IAS is approximated with anisotropic Gaussian diffusion, and because of the latter, the analysis is restricted to areas of highly aligned WM. Water exchange is assumed to be negligible over the experimental time window, and myelin water is assumed not to contribute because of its large value of TE/T2. A limited amount of dispersion of axons within the WM bundle does not violate the Gaussian intra-axonal assumption, but implies that the intra-axonal diffusion tensor has three non-vanishing eigenvalues [2]. With these assumptions, the signal expression for this two-compartment system becomes:

$$S(b,\hat{n}) = f\exp(-b\hat{n}^T \mathrm{D}_a \hat{n}) + (1-f)\exp(-b\hat{n}^T \mathrm{D}_e \hat{n}) \quad (2.2.1)$$

where f is the axonal water fraction (AWF from here on), D_a and D_e are the diffusion tensors belonging to the IAS and EAS respectively. The form of these tensors is:

$$\mathrm{D}_a = \begin{bmatrix} D_{a3} & 0 & 0 \\ 0 & D_{a2} & 0 \\ 0 & 0 & D_{a1} \end{bmatrix}, \qquad \mathrm{D}_e = \begin{bmatrix} D_{e3} & 0 & 0 \\ 0 & D_{e2} & 0 \\ 0 & 0 & D_{e1} \end{bmatrix} \quad (2.2.2)$$

where subscript numbers label the eigenvalues by magnitude in descending order, implying that here the primary direction is $\hat{z}$. From the cumulant expansion of this model, the measured diffusion and kurtosis tensors D and W can be expressed in terms of the model parameters. In this manner, the otherwise unspecific DKI parameters yield approximations for specific biophysical parameters: the AWF, IAS diffusivity ($D_a = \mathrm{Tr}(\mathrm{D}_a)$), parallel and radial EAS diffusivities ($D_{e,||} = D_{e,1}$ and $D_{e,\perp} = (D_{e2} + D_{e3})/2$), and the EAS tortuosity ($\alpha = D_{e,||}/D_{e,\perp}$). Notably, the estimates are only approximate, as the diffusion and kurtosis tensors in principle do not supply sufficient information to estimate all diffusivities and the axonal volume fraction because of the confounding factors of axonal dispersion [50]. Additionally, kurtosis based estimation of compartmental diffusivities yields two solutions. This arises because the kurtosis is related to the variance ("mean of square minus square of mean") over diffusivities [43] causing the square root to enter the analysis.

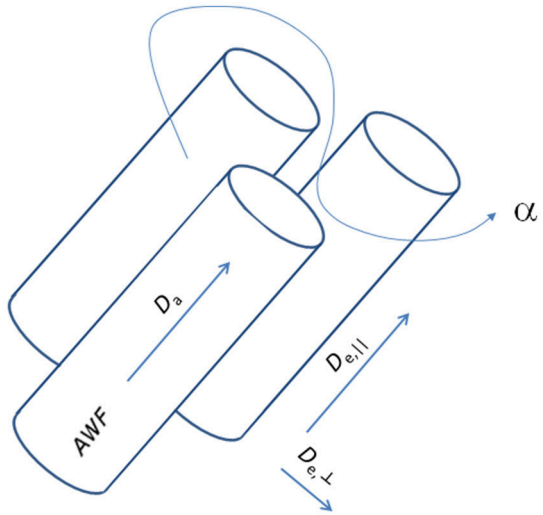

FIGURE 2 | Schematic representation of a white matter fiber bundle and its biophysical properties accessible with the WMTI analysis framework.

For this reason, WMTI furthermore relies on the assumption that intra-axonal diffusivity D_{a1} is smaller than extra-axonal diffusivity D_{e1} as argued in Fieremans et al. [2]. **Figure 2** shows a schematic of this representation of a WM bundle and the biophysical properties that may be estimated from WMTI analysis. For further details on derivations and modeling assumptions, the reader is referred to the original WMTI papers [2, 51].

Fast Estimation of Mean Diffusivity and Mean Kurtosis

The ability to rapidly estimate mean diffusivity and mean kurtosis from only 13 images was presented in Hansen et al. [39, 40]. In order to achieve this, a mean kurtosis definition was introduced ($\overline{W}$) which differs from the definition in Equation (2.1.3), namely:

$$\begin{aligned} \overline{W} &= \frac{1}{4\pi}\int_{S_2} d\hat{n}\, W(\hat{n}) \\ &= \frac{1}{5}\mathrm{Tr}(\mathrm{W}) \\ &= \frac{1}{5}(W_{xxxx} + W_{yyyy} + W_{zzzz} + 2W_{xxyy} + 2W_{xxzz} + 2W_{yyzz}) \end{aligned} \quad (2.3.1)$$

This definition differs from the conventional MK definition in Equation (2.1.3) in that it is based on the spherical average of the apparent tensor kurtosis $W(\hat{n})$:

$$W(\hat{n}) = K(\hat{n})\frac{D(\hat{n})^2}{\overline{D}^2}, \quad (2.3.2)$$

instead of $K(\hat{n})$. For this reason we also refer to $\overline{W}$ as the mean of the kurtosis tensor (MKT). This definition is compactly written

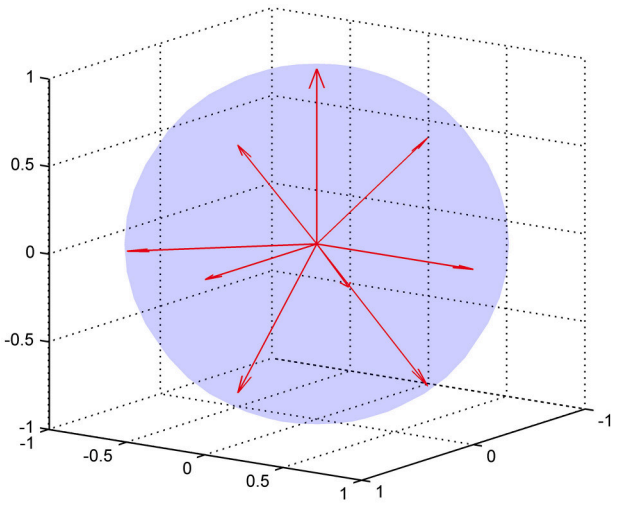

FIGURE 3 | The nine encoding directions required for fast DKI illustrated as unit vectors. The directions are listed explicitly in **Table 1**.

as one fifth of the trace (Tr) of the kurtosis tensor W. The factor of one fifth stems from the spherical average [52]:

$$\frac{1}{4\pi}\int_{S_2} d\hat{n}\, n_i n_j n_k n_l = \frac{1}{15}(\delta_{ij}\delta_{kl}+\delta_{ik}\delta_{jl}+\delta_{il}\delta_{jk}) \equiv \frac{1}{5}\mathbb{I}_{ijkl} \tag{2.3.3}$$

where $\mathbb{I}$ is the fully symmetric isotropic rank 4 tensor [53]. Hence, $\overline{W}$ represents the isotropic part of the kurtosis tensor [39]. The advantage of this mean kurtosis definition is apparent from the last line in Equation (2.3.1) which states that $\overline{W}$ is proportional to a linear combination of six tensor elements, and this linear combination can be obtained from measurements without fitting to the data. For the measurements, the "pure" tensor elements (W_{iiii}) can be probed directly, whereas the mixed elements (W_{iijj}, $i \neq j$) requires the combination of two directions for each to cancel cross terms, see Hansen et al. [39] for details. Therefore, a total of nine directions is needed to calculate $\overline{W}$. These directions are illustrated in **Figure 3**, where it is readily seen that this encoding scheme does not sample the sphere very efficiently; the high estimation quality obtained with this scheme rests entirely on the relations introduced shortly. The directions are also listed in **Table 1** which also defines the notation used in the following equations.

For data acquired along these directions (i = 1,2,3) the following holds [39]:

$$\frac{1}{15}\left(\sum_{i=1}^{3}\log S(b,\hat{n}^{(i)})+2\sum_{i=1}^{3}\log S(b,\hat{n}^{(i+)})+2\sum_{i=1}^{3}\log S(b,\hat{n}^{(i-)})\right) = -b\overline{D}+\frac{1}{6}b^2\overline{D}^2\overline{W} \tag{2.3.4}$$

With an independent estimate of $\overline{D}$, Equation (2.3.4) allows estimation of $\overline{W}$ without data fitting, thus eliminating both the time consuming post-processing and the pitfalls associated with it [54–56]. The mean diffusivity $\overline{D}$ can be estimated from data acquired along three orthogonal directions at a single b-value (and $b = 0$), but is improved by taking into account the kurtosis term in the analysis [57], which can be done if the 3 directions are acquired also at a second higher b-value shell. In this manner a closed form solution for $\overline{D}$ [58] is obtained taking into account the directional kurtosis for high fidelity estimation [57]. The strategy proposed in Hansen et al. [39] thus implements the estimation of $\overline{D}$ based on data acquired at an intermediate b-value along the three main directions, $\hat{n}^{(1)}$, $\hat{n}^{(2)}$ and $\hat{n}^{(3)}$, which are already contained in the nine directions in **Table 1**. Thus, the "1-3-9 approach" for fast estimation of $\overline{D}$ and $\overline{W}$ is to acquire one b=0 image, 3 images at b_1 =1.0 ms/ μm^2 along the x,y,z directions ($\hat{n}^{(i)}$, i = 1,2,3), and nine images acquired at b_2 = 2.5 ms/μm^2 along the directions listed in **Table 1**.

TABLE 1 | The nine directions in the compact notation (leftmost column) used in the manuscript and stated as normalized vectors.

Direction	*x*-component	*y*-component	*z*-component
$\hat{n}^{(1)}$	1	0	0
$\hat{n}^{(1+)}$	0	$1/\sqrt{2}$	$1/\sqrt{2}$
$\hat{n}^{(1-)}$	0	$1/\sqrt{2}$	$-1/\sqrt{2}$
$\hat{n}^{(2)}$	0	1	0
$\hat{n}^{(2+)}$	$1/\sqrt{2}$	0	$1/\sqrt{2}$
$\hat{n}^{(2-)}$	$1/\sqrt{2}$	0	$-1/\sqrt{2}$
$\hat{n}^{(3)}$	0	0	1
$\hat{n}^{(3+)}$	$1/\sqrt{2}$	$1/\sqrt{2}$	0
$\hat{n}^{(3-)}$	$1/\sqrt{2}$	$-1/\sqrt{2}$	0

The scaling factor of $D(\hat{n})^2/\overline{D}^2$ in Equation (2.3.2) generally depends on direction and as such will affect the spherical average so that $\overline{K} = \overline{W}$ only for isotropic systems. From the definitions therefore, $\overline{K}$ and $\overline{W}$ are expected to deviate the most in highly anisotropic tissue. It is natural therefore to evaluate whether the rapidly obtainable tensor based mean kurtosis ($\overline{W}$) offers similar contrast to the conventional MK. This is illustrated in **Figure 4** which shows typical DTI and DKI parameters mapped in fixed rat brain at an in-plane resolution of 100 μm x 100 μm to allow contrast comparison in specific brain regions such as the subfields of the hippocampus. Overall, the parameters can be seen to provide vastly different contrast, except for $\overline{K}$ and $\overline{W}$ which are seen to be almost indistinguishable although a few blank pixels are seen in the $\overline{W}$ map due to noise (see also comments on preprocessing below). The level of agreement between $\overline{K}$ and $\overline{W}$ presented in **Figure 4** has been quantified (linear correlations exceed 0.9 in most cases but will depend on the data foundation) and demonstrated in both fixed and live brain in a number of studies [59–61] and also in fixed kidney [62]. In the diseased brain, the 1-3-9 method has been validated in an animal model of stroke [63, 64] and was found to yield diffusion and kurtosis lesions in good agreement with conventional DKI. Similarly, strong correlations between the diffusion-kurtosis stroke lesion mismatch obtained from 1-3-9 and conventional DKI was shown

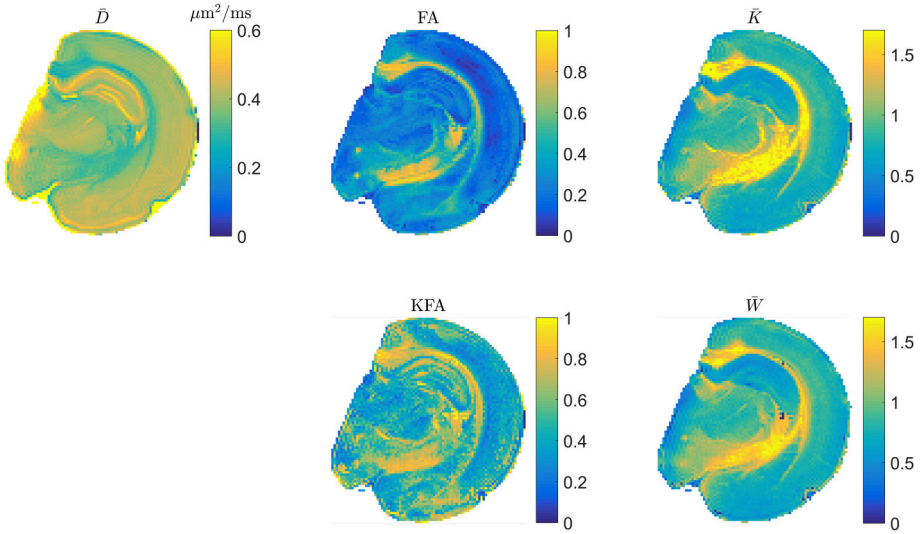

FIGURE 4 | Example maps of typical DTI and DKI parameters in fixed rat brain. The two mean kurtosis definitions are shown and seen to provide similar contrast. Figure adapted from Hansen and Jespersen [37] with permission.

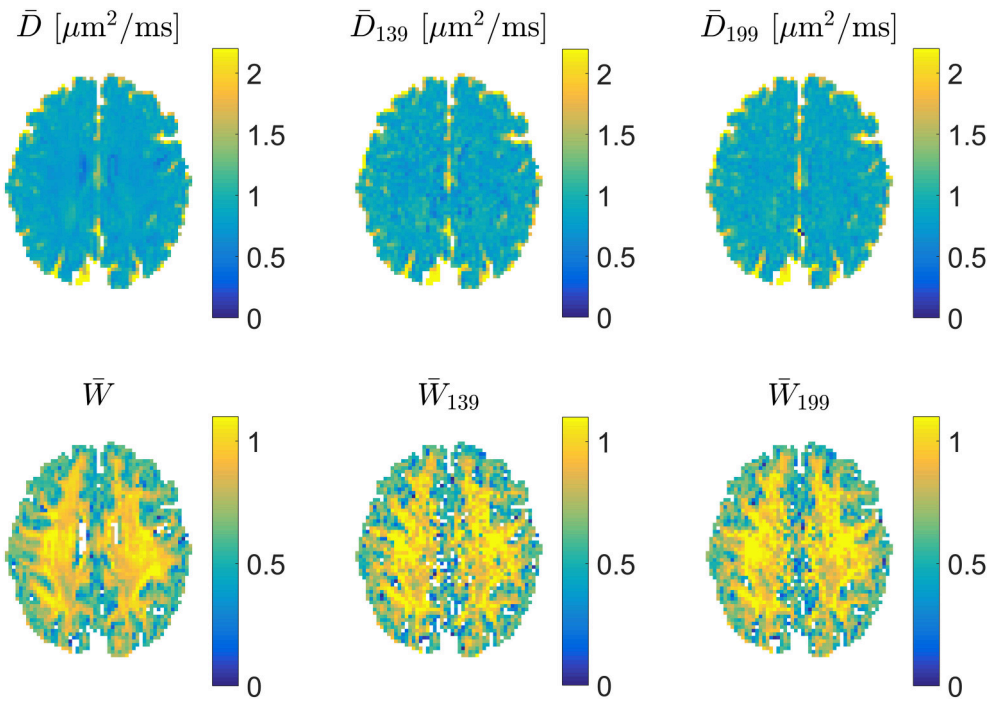

FIGURE 5 | Examples of estimates of mean diffusivity **(Top)** and $\overline{W}$ **(Bottom)**. In each row estimates were obtained (left to right) from a large DKI data set, a 1-3-9 acquisition, and a 1-9-9 data set. Figure adapted from Hansen et al. [41] with permission.

[63]. Additionally, $\overline{W}$ was found to be the most sensitive parameter for revealing acute ischemic injury in an analysis also including axial and radial kurtosis [64]. This is important because $\overline{W}$ can be reconstructed almost instantly once acquisition is complete, making this most sensitive parameter immediately available e.g., for clinical decision making. In the same study [64], the contrast to noise ratio (CNR) of $\overline{W}$ estimated from fast DKI was found to be significantly higher than for conventional DKI. Importantly, the fast DKI CNR efficiency (CNR per unit scan time) was shown to be twice that of conventional DKI. The authors conclude that the fast kurtosis method captures heterogeneous diffusion and kurtosis lesions in acute ischemic

stroke, and thus is suitable for translational applications. The rapidly obtainable $\overline{W}$ is therefore by now established as a biomarker offering the same information as the conventional $\overline{K}$ in normal tissue and stroked brain. Strictly speaking, the methods await similar validation in other pathologies but $\overline{W}$ is now recognized as an independent marker and not merely a rapidly obtainable surrogate for $\overline{K}$. Recent clinical studies have employed the 1-3-9 method for glioma grading [65], for studying the effect of crack cocaine addiction [66], and in mild traumatic brain injury patients [12]. Preliminary results in stroke patients was presented in Li et al. [67] obtained using a combination of the 1-3-9 technique and the simultaneous multislice imaging (SMS) technique [68].

Fast Kurtosis Estimation with Increased Experimental Robustness

The 1-3-9 method relies heavily on the nine direction scheme being precisely met. Encoding may, however, be imperfect causing deviations from the encoding scheme required for Equation (2.3.4) to hold. Such encoding errors may have a number of causes such as gradient non-linearities, eddy currents, contributions from gradient cross-terms and coregistration due to subject movement. While not explored initially, subsequent analysis of these effects showed the 1-3-9 scheme to be quite sensitive to severe encoding deviations. A simple remedy was demonstrated in Hansen et al. [41] where the 1-3-9 scheme was extended so that all of the nine directions in **Table 1** are acquired at the two non-zero b-values, b_1 and b_2. This so-called 1-9-9 version of fast DKI achieves increased experimental robustness by forming Equation (2.3.4) at two distinct b-values, b_1 and b_2:

$$\begin{aligned} A_1 \equiv \frac{1}{15}\left(\sum_{i=1}^{3}\log S(b_1,\hat{n}^{(i)}) + 2\sum_{i=1}^{3}\log S(b_1,\hat{n}^{(i+)})\right. \\ \left. + 2\sum_{i=1}^{3}\log S(b_1,\hat{n}^{(i-)})\right) = -b_1\overline{D} + \frac{1}{6}b_1^2\overline{D}^2\overline{W} \\ A_2 \equiv \frac{1}{15}\left(\sum_{i=1}^{3}\log S(b_2,\hat{n}^{(i)}) + 2\sum_{i=1}^{3}\log S(b_2,\hat{n}^{(i+)})\right. \\ \left. + 2\sum_{i=1}^{3}\log S(b_2,\hat{n}^{(i-)})\right) = -b_2\overline{D} + \frac{1}{6}b_2^2\overline{D}^2\overline{W} \end{aligned} \quad (2.3.5)$$

producing a set of two equations with two unknowns, $\overline{D}$ and $\overline{W}$, for which closed for solutions are readily obtained so that the 1-9-9 estimate for $\overline{D}$ is:

$$\overline{D}_{199} = \left(b_1^2A_2 - b_2^2A_1\right)/\left(b_1b_2^2 - b_1^2b_2\right) \quad (2.3.6)$$

and for $\overline{W}$:

$$\overline{W}_{199} = 6b_1b_2\left(A_1b_2 - A_2b_1\right)\left(b_1 - b_2\right)/\left(A_1b_2^2 - A_2b_1^2\right)^2 \quad (2.3.7)$$

For precise encoding, i.e., when effective b-values are constant among directions on each encoding shell and encoding directions follow the prescribed directions, the 1-3-9 and 1-9-9 schemes produce very similar appearing maps as shown in **Figure 5**, where estimates of $\overline{D}$ and $\overline{W}$ from a full DKI data set can be compared to estimates obtained with 1-3-9 and 1-9-9 in the same normal human brain. The effect of the 1-9-9 method's increased data foundation is apparent when comparing the schemes' robustness to experimental imperfections: numerical analysis reveals that the 1-9-9 scheme has precision similar to nonlinear least squares (NLS) fitting to large data sets, vastly outperforming the 1-3-9 scheme [41]. The effects of imperfect encoding was also addressed in a series of simulations showing that the 1-9-9 estimation quality (evaluated as the %-error compared to the ground truth value) remains below 10% even when b-values vary by as much as 10% among directions and the within-shell encoding directions deviate up to 10° from the prescribed directions. For the 1-3-9 scheme, these conditions cause estimates to deviate on the order of 15%. These results indicate that the 1-9-9 method is robust to most real-world encoding imperfections and even to effects from subject movement, where coregistration will cause b-matrices to require rotation. Nevertheless, a post-hoc correction scheme was also proposed and demonstrated to repair effects of even severe encoding faults [41].

Recommended b-values for both the 1-3-9 and 1-9-9 schemes are $b_1 \approx 1$ ms/μm^2 and $b_2 \approx 2.5$ ms/μm^2, but the experimental and numerical b-value optimization in Hansen et al. [41] showed that precise matching to these two b-values was not critical. These values are achievable on most if not all gradient systems while also keeping the echo time sufficiently short to retain good SNR even at b_2. The analysis in Hansen et al. [41] showed that the recommended b-values are (perhaps surprisingly) suitable for both *in vivo* (37°C) and *ex vivo* (21°C) work. These b-values were used with the 1-9-9 method in an animal model of stroke, where a relaxation-based normalization method was introduced to enable automatic segmentation of kurtosis lesions [69]. Nevertheless, optimal b-values may vary between brain regions, and example data sets for region specific b-value optimization are freely available as described in Hansen et al. [70].

Increasing the number of data points from 13 (1-3-9) to 19 (1-9-9) also makes possible estimation of the full diffusion tensor (with fitting) from which all DTI metrics can then be calculated. As a rapid alternative, FA estimation from 1-9-9 data was also proposed based on the variance (var) of $D(\hat{n})$ over the 9 sampling directions (the expression is exactly FA for complete sampling of the sphere):

$$FA_{199} = \sqrt{\frac{3}{2}\frac{\mathrm{var}(D(\hat{n}))}{\mathrm{var}(D(\hat{n})) + 6/15\overline{D}^2}} \quad (2.3.8)$$

Here the $D\left(\hat{n}\right)$ values over the nine directions are calculated using both non-zero b-values as in Jensen et al. [58] so that the directional kurtosis is included to improve estimation [57]. FA maps obtained in this manner were found to correlate strongly (average correlation was 0.77 ± 0.04 across three subjects) with ground truth FA from a large data set. Code enabling automatic parameter map calculation from 1-3-9 and 1-9-9 data during image reconstruction on Siemens systems is available as described in Hansen et al. [41]. The data examples shown in **Figures 4**, **5** were produced from non-preprocessed data and so

the maps in **Figure 5** illustrate the map quality one might expect to achieve with online parameter calculation. For offline dMRI data preprocessing and analysis (including DKI and WMTI) a number of toolboxes are available e.g., Diffusion Kurtosis Estimator (DKE: http://academicdepartments.musc.edu/cbi/dki/dke.html), the Dipy library in python [71] (http://nipy.org/dipy/), MRTrix (http://www.mrtrix.org), some of which also include estimation of $\overline{W}$ and kurtosis fractional anisotropy (KFA, see Equation (2.5.5) and the related text).

Recent work on efficient experimental designs for estimating the isotropic part of higher-order tensors [72], suggests that the 9 directions of the 1-3-9 and 1-9-9 designs can be reduced to 7 for an even more economical version of fast mean kurtosis imaging.

Axisymmetric DKI

As mentioned in the introduction, DKI parameters other than mean kurtosis are available, e.g., the kurtosis along the primary eigenvector (axial kurtosis) and perpendicular to it (radial kurtosis). Furthermore, modeling based WM characterization such as WMTI provides other valuable markers, but requires knowledge of the full diffusion and kurtosis tensors. It is therefore desirable to be able to estimate these valuable markers from fast protocols. Since the number of free parameters in the conventional DKI signal equation amounts to 22 (Equation 2.1.1), the 1-9-9 protocol does not provide enough data points to support estimation of D and W from fitting. For estimation of D and W from reduced data sets (say a 1-9-9 acquisition, but in principle it could be other low angular resolution DKI acquisitions), a substantial reduction of parameters in the DKI signal expression would be needed. An effective strategy to achieve such a reduction was proposed in Hansen et al. [42], and builds on the observation that if the system is assumed to possess axial symmetry, the apparent kurtosis $W(\hat{n})$ can be expressed by only three independent parameters: letting $\hat{z}$ be parallel to the symmetry axis, $W(\hat{n})$ is characterized by $\overline{W}$, $W_{||} = W(\hat{z})$ (axial kurtosis), and $W_\perp$ (radial kurtosis). Stated in terms of the diffusion tensor eigenvectors ($\hat{v}_1$, $\hat{v}_2$, $\hat{v}_3$ in decreasing order of the eigenvalues as above), the tensor-based directional kurtosis parameters are defined to be:

$$\begin{aligned} W_\perp &\equiv \frac{1}{2\pi}\int_{S_2} d\hat{n}\,\delta(\hat{n}\cdot\hat{v}_1)W(\hat{n}) = \frac{1}{4}\Big(W(\hat{v}_2)+W(\hat{v}_3) \\ &\quad + W\left((\hat{v}_2+\hat{v}_3)/\sqrt{2}\right)+W\left((\hat{v}_2-\hat{v}_3)/\sqrt{2}\right)\Big) \\ W_{||} &= W(\hat{v}_1) \end{aligned} \tag{2.5.1}$$

Comparing these definitions to the conventional directional kurtosis parameter definitions in Equation (2.1.4) shows $K_{||} = \left(\overline{D}^2/\lambda_1^2\right) W_{||}$ so that only for isotropic media $K_{||} = W_{||}$. Rescaling of the axial and radial tensor kurtosis is convenient and causes the axial kurtosis definitions to become identical but radial kurtosis as defined in Equation (2.5.1) is in general different from the convention in Equation (2.1.4), unless there is axial symmetry [42].

The assumption of axial symmetry requires the axis of symmetry to be specified with respect to the lab frame, which adds two angles, resulting in a total of only 5 parameters needed to fully describe an axisymmetric kurtosis tensor. Under axisymmetry, D and W share their symmetry axis so that D only adds two parameters. Finally, signal normalization adds one parameter, producing a total of eight free parameters for axisymmetric DKI [42]. Even in regions where axial symmetry is unlikely to hold in reality, the simplified DKI signal expression thus obtained yields reliable estimates of mean and directional kurtosis and diffusion metrics [42]. Not only does this open the possibility of estimation of all DTI and DKI metrics from small DKI data sets such as those acquired with the 1-9-9 scheme, the axisymmetric DKI framework also allows direct (no fitting) estimation of tensor-based directional kurtosis parameters in regions with a well-defined axis of symmetry (i.e., known pricipal axis) such as large peripheral nerves and spinal cord. This is readily seen in Equation (2.5.1) for $W_{||} = W(\hat{z})$ and from the rightmost expression for $W_\perp$. Software for axisymmetric DKI analysis is freely available on our group homepage: http://cfin.au.dk/cfinmindlab-labs-research-groups/neurophysics/software.

Fast Estimation of White Matter Biomarkers Using Axisymmetic DKI

Axisymmetric DKI makes it possible to estimate D and W from small data sets. A natural next step is to use this framework to provide a fast variant of the technique for assessment of WM tract integrity metrics (WMTI) proposed in Fieremans et al. [2, 51]. In its original form, WMTI adds an analysis step so that in addition to the data acquisition and data processing related to conventional DKI, WMTI also requires a rather time-consuming pixel-by-pixel estimation procedure including numerical optimization. With the assumption of axial symmetry and fully aligned axons, both the data requirement and computational load can be reduced significantly. This is achieved by establishing closed form solutions for all WMTI parameters based on the axisymmetric DKI parameters directly. In this manner, only one optimization procedure is needed for the WMTI analysis, the initial fitting to Equation (2.1.1) or its axisymmetric counterpart. The expressions for the biophysical parameters that describe the axonal system are obtained from this relationship for 2-compartment Gaussian systems [43]:

$$\begin{aligned} D(\hat{n}) &= fD_a(\hat{n}) + (1-f)D_e(\hat{n}) \\ W(\hat{n})\overline{D}^2 &= 3f(1-f)(D_a(\hat{n}) - D_e(\hat{n}))^2 \end{aligned} \tag{2.5.2}$$

When evaluated along the radial and axial directions and with averaging over all directions, these general expressions yield directional diffusivities and kurtoses from which expressions for $AWF = f$, D_a, $D_{e,\perp}$, and $D_{e,||}$ can be derived [38]:

$$\begin{aligned} D_\perp &= (1-f)D_{e,\perp} && \text{(a)} \\ D_{||} &= fD_a + (1-f)D_{e,||} && \text{(b)} \\ W_\perp\overline{D}^2 &= 3f(1-f){D_{e,\perp}}^2 && \text{(c)} \\ W_{||}\overline{D}^2 &= 3f(1-f)(D_a - D_{e,||})^2 && \text{(d)} \\ \overline{WD}^2 &= 3f(1-f)\Big[{D_{e,\perp}}^2 + \frac{1}{15}(D_{e,||} - D_a - D_{e,\perp})\big(7D_{e,\perp} \\ &\quad + 3(D_{e,||} - D_a)\big)\Big] && \text{(e)} \end{aligned} \tag{2.5.3}$$

where it was used that $D_{a\perp} = 0$ for parallel sticks. It is readily seen that the left-hand sides of Equation (2.5.3) can be determined using parameters obtained directly from an axially symmetric DKI fit as well as from a general DKI fit.

Of the five equations in Equation (2.5.3), only 4 of the equations are actually independent (i.e., they have only four unknowns due to the assumption of parallel axons with radius zero), so that one equation can be omitted. In Hansen et al. [42] $\overline{W}$ was found to be more robustly estimated from 1-9-9 than $W_{||}$. We therefore advice to omit Equation (2.5.3d) which contains the slightly noisier $W_{||}$. In this way, closed form expressions for the WMTI parameters can be established based on Equations (2.5.3a,b,c,e):

$$f = AWF = \left(1 + 3D_{\perp}^2 / W_{\perp}\bar{D}^2\right)^{-1} \quad \text{(a)}$$

$$D_{e,\perp} = D_{\perp} / \left(1 - f\right) \quad \text{(b)}$$

$$D_{e,||} = D_{||} - \frac{2}{3}\frac{f}{1-f}\left(D_{\perp} \pm \sqrt{\frac{15\left(1-f\right)}{4f}\bar{D}^2\bar{W} - 5D_{\perp}^2}\right) \quad \text{(c)}$$

$$D_a = D_{||} - \frac{2}{3}\left(D_{\perp} \mp \sqrt{\frac{15\left(1-f\right)}{4f}\bar{D}^2\bar{W} - 5D_{\perp}^2}\right) \quad \text{(d)}$$

$$\alpha = D_{e,||} / D_{e,\perp} \quad \text{(e)} \quad (2.5.4)$$

These expressions clearly show the existence of a sign ambiguity which affects the estimates of $D_{e,||}$ (and consequently α) and D_a [2]. Determining which of these two "branches" yields physically correct parameter estimates has been subject of some debate [38, 73, 74] and is not yet fully resolved. In Hansen et al. [38] affected parameters are reported for both branches. The solutions for the two branches are much more obvious than in conventional WMTI, where the sign choice is only known to be stable over diffusion encoding directions for the branch defined by $D_a \leq D_{e,||}$ [2]. WMTI analysis based on modest data makes it feasible to experimentally investigate the unresolved branch duality—e.g., using data acquisitions employing varying diffusion times as in Jespersen et al. [73] which would have been prohibitively time consuming with conventional WMTI. Similarly, the increase in acquisition speed facilitates high resolution data acquisitions for validation purposes or for *in vivo* applications. High resolution *in vivo* WMTI based on the 1-9-9 fast DKI protocol is demonstrated in **Figure 6** using one of four rats analyzed in Hansen et al. [38]. The advantage of the fast WMTI techniques is evident as the low data requirement allows whole brain coverage at an isotropic resolution of 300 μm to be acquired in 1 h. For *ex vivo* studies, e.g., for validation studies with subsequent histological analysis, the fast axisymmetric WMTI method enables studies at even higher resolution with high SNR with substantially shorter acquisition times than required for conventional WMTI.

When abandoning the assumption of fully parallel axons, the relationships between the measured diffusion and kurtosis metrics and the microstructural parameters will also involve parameters characterizing the orientation distribution of the axons (fODF) [75]. For axially symmetric systems specifically, these are p_2 and p_4, the two lowest nontrivial Legendre expansion coefficients of the fODF [73]. Hence in general, there are more unknowns than equations. However, if a one parameter fODF, such as the Watson distribution, can be assumed, p_2 and p_4 become interdependent and the number of unknowns equals the number of equations, facilitating fast axisymmetric WMTI in the presence of dispersion [73]. **Figure 7A** (upper row) shows estimates of the time-dependent dispersion [Watson concentration parameter κ (kappa)] of both branches (labeled + and −, shown on the left and right, respectively) measured using such an approach with data acquired from a stimulated echo diffusion-weighted sequence in four regions of interest (ROIs) in in pig spinal cord white matter. The data is from Jespersen et al. [73] with ROI labels matching that work. **Figure 7B** (lower row) plots time dependence of intra-axonal diffusivity of both branches (again + branch on the left and − branch on the right). As argued in Jespersen et al. [73], these results indicate the most likely choice to be the plus branch $D_a > D_{e,||}$ for this data set. In this manner, the framework allows analysis of time dependence of microstructural parameters in both branches in white matter providing further insight into the branch choice.

Other metrics suitable for WM characterization are available from DKI, e.g., the kurtosis fractional anisotropy (KFA) introduced in Hansen et al. [39] and Jespersen [76] in complete analogy to FA (Equation 2.1.2):

$$KFA = \frac{\left\| \mathrm{W} - \overline{W}\mathbb{I} \right\|}{\left\| \mathrm{W} \right\|} \quad (2.5.5)$$

where double bars $\|\cdot\|$ signify the Frobenius norm of the tensor and $\mathbb{I}$ is the fully symmetric isotropic tensor. This metric describes the ratio of the size of the anisotropic part of W to the Frobenius norm of the full W and thus assumes values in the range 0–1 without the need for rescaling to this range as done for FA (Equation 2.1.2). KFA can be estimated in any region but is likely to be of most interest in anisotropic tissues and in regions where more than one dominant fiber orientation exists. KFA was investigated using simulations and human brain data in Hansen and Jespersen [37] and Glenn et al. [61] and found to provide contrast in regions where complex WM fiber composition causes the FA to vanish, manifesting as dark bands in the FA maps in **Figure 8**. This is because D cannot resolve more than one primary direction and is related to the well-known crossing fiber problem in DTI. Since KFA does not vanish when 2 or 3 fiber bundles cross, KFA may aid in identifying regions where low FA is due to fiber complexity. The maps from normal human brain shown in **Figure 8** allow comparison of FA and KFA contrast in three consecutive slices. Evidently, KFA provides a different contrast than FA. Such additional information from W may be used to increase the robustness of diffusion tensor tractography in complex fiber arrangements. In Hansen and Jespersen [37] KFA was explored further using data from various model systems and KFA estimation by proxy was tested. With sufficient SNR, the proxy was found to agree very well with true KFA even for estimates based on a 1-9-9 data set. However, the SNR required (>100) for this strategy is unrealistic for practical purposes. A strategy for KFA estimation from small data sets based on an

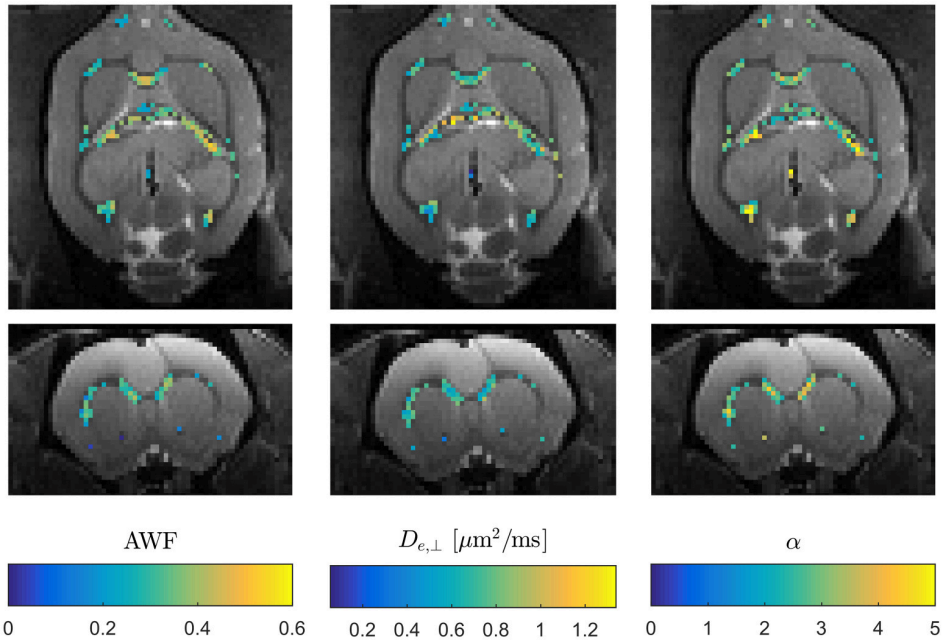

FIGURE 6 | Example of three WMTI parameters mapped in an *in vivo* rat brain using axisymmetric WMTI analysis of a 1-9-9 data set. Parameters are shown mapped onto $b = 0$ data in two orthogonal slice orientations. Data was acquired at 300 μm isotropic resolution.

axisymmetric W was evaluated in Hansen et al. [38], but here KFA contrast deteriorates due to the symmetry imposed on W. At present, therefore, KFA can only be reliably estimated based on conventional DKI acquisitions and post-processing yielding the full W tensor with no symmetry constraints.

Summary of Parameter Definitions

In addition to allowing fast estimation, the tensor-based kurtosis metrics covered above also bring DKI metrics onto a form more analogous to their DTI counterparts. This feature is evident in **Table 2** which summarizes the definitions for each of the corresponding parameters derived from D and W. Note that the different ranks of D and W cause some definitions to differ by a scaling factor, nevertheless the analogy is obvious in most cases with the notable exception being radial kurtosis in the principal diffusion tensor frame, which cannot be formed from the two non-primary axis directions alone but also contains a crossterm (W_{xxyy}). For completeness, we also note that other mean kurtosis definitions than those shown in **Table 2** have been proposed such as the generalized kurtosis (GK) and the generalized kurtosis of the norm (GKN) [77] which reflect the kurtosis of the diffusion propagator obtained from q-space data based on concepts from multivariate statistics [78].

FUTURE DIRECTIONS FOR THE FAST KURTOSIS TECHNIQUES

Imaging of tissue microstructure has been a strong motivation for diffusion MRI research since the technique was introduced. Since then, studies aimed at improving our ability to image tissue microstructure have focused on understanding cellular-level diffusion properties by MR microscopy in an effort to inform modeling [79–85], and modeling aimed at extracting specific cytoarchitectural measures [86, 87]. A common limitation of these methods is the requirement for strong gradients. In contrast, DKI yields valuable reporters of tissue microstructure (although most frequently unspecific) while remaining feasible on clinical systems, even those with modest gradient capability. However, acquisition and post-processing time are often limiting factors for clinical imaging and therefore may impede routine clinical application of DKI. Therefore, rapid DKI acquisitions with fast post-processing are important for further clinical adaptation of DKI. Preclinically, the mentioned time constraints are perhaps not as severe. However, the low data requirement of the 1-3-9/1-9-9 protocols enables higher spatial resolution or higher SNR in the same (or less) scan time as conventional DKI acquisitions, which is certainly a significant benefit for all areas of DKI related research. Furthermore, fast DKI may become increasingly valuable in preclinical studies as imaging of awake animals becomes more widely used to avoid physiological perturbations caused by either inhaled or injected anesthesia [88, 89]. Here, methods with modest data demand are preferable to reduce animal stress and to afford data acquisition with gating or even reacquisition if data is affected by movement.

Despite its sensitivity, DKI is microstructurally unspecific, causing studies with comparison of DKI metrics to histology to be needed to understand how disease related microstructural alterations are reflected in DKI (regardless of metric definitions and acquisition methods). Such studies have been carried out for experimental stroke [5, 90], stress and depression [60, 91], and kidney fibrosis [62] to name a few. Furthermore, studies have been performed to elucidate the relation between DKI metrics

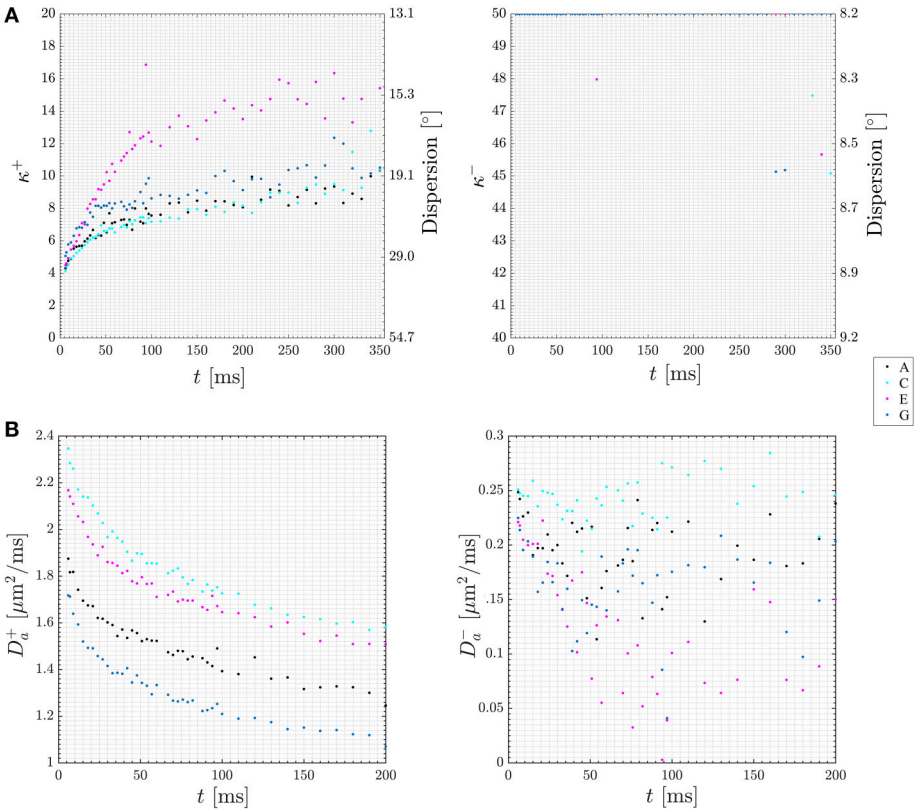

FIGURE 7 | Plots of diffusion time dependence for dispersion **(A)** and intra-axonal diffusivity (D_a, **B**) in both of the two WMTI solution branches (labeled + and −). Data points are color coded to four ROIs in the pig spinal cord used for this experiment. The ROIs are labeled A, C, E, G in keeping with Jespersen et al. [73] where the data was first presented. Figure adapted from Jespersen et al. [73] with permission.

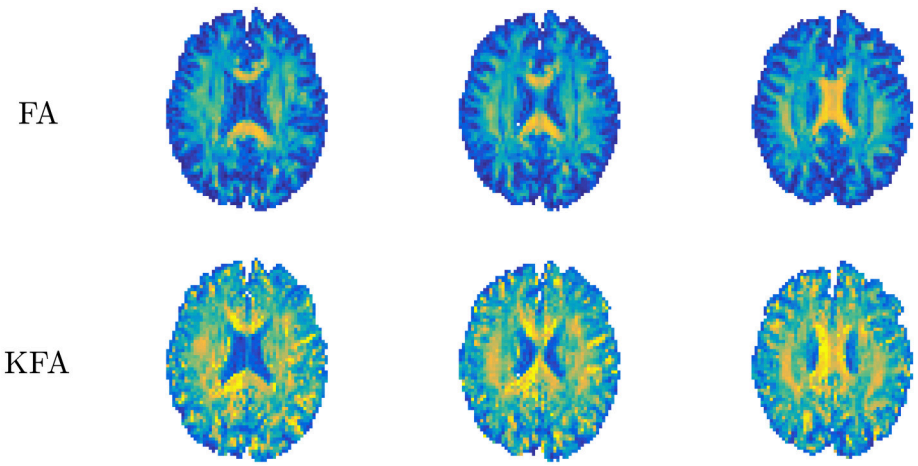

FIGURE 8 | Comparison of diffusion tensor derived fractional anisotropy (FA, upper row) and kurtosis fractional anisotropy (KFA). Contrast differences are evident with FA being uninformative in certain white matter regions (dark bands). Conversely, KFA remains informative in these regions. Figure adapted from Hansen and Jespersen [37] with permission.

and tissue magnetic susceptibility [92, 93] with results suggesting a susceptibility contribution in DKI metrics warranting further investigation. Similarly, studies have been performed to optimize diffusion sampling schemes for DKI [3] and to assess the DKI metric reproducibility across field strengths [94]. Field strength dependence was found to be most pronounced for KFA which

TABLE 2 | Summary of the fast kurtosis metrics definitions and their DTI counterparts.

	Diffusion tensor	**Kurtosis tensor**
Mean	$\overline{D} = \frac{\mathrm{Tr(D)}}{3}$	$\overline{W} = \frac{\mathrm{Tr(W)}}{5}$
Anisotropy	$FA = \sqrt{\frac{3}{2}} \frac{\left\|\mathrm{D} - \overline{D}\mathbb{I}\right\|}{\|\mathrm{D}\|}$	$KFA = \frac{\left\|\mathrm{W} - \overline{W}\mathbb{I}\right\|}{\|\mathrm{W}\|}$
Axial/longitudinal	$D_{\|\|} = D(\hat{v}_1) = \lambda_1$	$W_{\|\|} = W(\hat{v}_1) = W_{zzzz}$ (*)
Radial/orthogonal	$D_\perp = \frac{1}{2\pi} \int_{S_2} d\hat{n}\, D(\hat{n}) \delta(\hat{n} \cdot \hat{v}_1) = (\lambda_2 + \lambda_3)/2$ $= \frac{1}{2}(D_{xx} + D_{yy})$ (*)	$W_\perp \equiv \frac{1}{2\pi} \int_{S_2} d\hat{n}\, \delta(\hat{n} \cdot \hat{v}_1) W(\hat{n})$ $= \frac{3}{8}(W_{xxxx} + W_{yyyy} + 2W_{xxyy})$ (*)

Note the convenient similarity in these DTI and DKI metric definitions. (*), The latter identity holds in the frame with $\hat{z} = \hat{v}_1$.

is known to be more SNR dependent than the remaining DKI metrics [37, 61]. In validation studies, high resolution is often desirable in order to identify specific regions or sub-regions, since varying response is sometimes seen in sub-regions as for example in the hippocampus in relation to stress [60, 95]. In such cases, the fast DKI methods are convenient to ensure reasonable scan time for high resolution data acquisitions.

The fast kurtosis methods are already used for imaging of experimental stroke [63, 64] and with the developments in Hansen et al. [38, 42], axial and radial kurtosis can also be investigated from fast DKI data along with WMTI parameters, e.g., for detection of axonal beading [96]. Fast kurtosis imaging is also convenient for studies of the diffusion time dependence of DKI and WMTI parameters. Such experiments are expected to provide a deeper understanding of the WMTI branch ambiguity explored in Hansen et al. [38] by making use of the theoretically expected diffusion time dependence [73].

An intriguing prospect of the fast DKI methods is the combination with SNR-efficient, rapid imaging techniques such as simultaneous multislice imaging (SMS) [68]. Combined with slice dithered enhanced resolution (gSlider), SMS can in principle be used to acquire diffusion MRI with sub-millimeter resolution on clinical systems, although so far demonstrations have used non-standard, high-performance gradient sets [97]. The combination of these fast imaging techniques and fast kurtosis methods would make it feasible to acquire high resolution DKI and WMTI data sets in clinically feasible acquisition times and might even be used for acquisition of time series data so that 1-9-9 data sets can be acquired with high (sub-minute) sliding window temporal resolution. Such data sets may then form the basis for analysis with the presented techniques, yielding time series data of DKI metrics (e.g., mean, radial and axial kurtosis for use in the study of GM plasticity [98]) and WM biomarkers for high sensitivity studies of WM plasticity [99, 100]. Other future applications might include combination of the 1-9-9 framework with diffusion weighted spectroscopy. With such data sets from cell-specific reporter molecules, such as NAA for neurons or myo-inositol for glia, the intra-cellular environment could be selectively probed to non-invasively assess cellular mechanisms in a number of neurological diseases, e.g., stroke as done in Shemesh et al. [101].

In conclusion, DKI is a non-invasive imaging technique with high sensitivity to microstructural alterations in biological tissue and has demonstrated value in a number of neuroscientific and clinical contexts. Methods now exist which enable rapid estimation of the full range of DKI parameters facilitating routine clinical use of DKI and WMTI.

AUTHOR CONTRIBUTIONS

BH and SNJ developed fast kurtosis methods, BH wrote the paper, BH and SNJ edited the paper.

FUNDING

The authors were supported by the Danish Ministry of Science, Technology and Innovation's University Investment Grant (MINDLab, Grant no. 0601-01354B). The authors acknowledge support from NIH 1R01EB012874-01 (BH), Lundbeck Foundation R83-A7548 (SNJ) and the Augustinus Foundation (BH). The 9.4T lab was funded by the Danish Research Council's Infrastructure program, the Velux Foundations, and the Department of Clinical Medicine, AU. The 3T Magnetom Tim Trio was funded by a grant from the Danish Agency for Science, Technology and Innovation.

ACKNOWLEDGMENTS

The authors are grateful for assistance and input from all our coauthors in the development of the fast kurtosis techniques. Reviewers also provided valuable suggestions in the publication process of all studies.

REFERENCES

1. Jensen JH, Helpern JA, Ramani A, Lu H, Kaczynski K. Diffusional kurtosis imaging: the quantification of non-gaussian water diffusion by means of magnetic resonance imaging. *Magn Reson Med.* (2005) **53**:1432–40. doi: 10.1002/mrm.20508
2. Fieremans E, Jensen JH, Helpern JA. White matter characterization with diffusional kurtosis imaging. *Neuroimage* (2011) **58**:177–88. doi: 10.1016/j.neuroimage.2011.06.006
3. Poot DH, den Dekker AJ, Achten E, Verhoye M, Sijbers J. Optimal experimental design for diffusion kurtosis imaging. *IEEE Trans Med Imaging.* (2010) **29**:819–29. doi: 10.1109/TMI.2009.2037915

4. Hui ES, Fieremans E, Jensen JH, Tabesh A, Feng W, Bonilha L, et al. Stroke assessment with diffusional kurtosis imaging. *Stroke* (2012) **43**:2968–73. doi: 10.1161/STROKEAHA.112.657742
5. Weber RA, Hui ES, Jensen JH, Nie X, Falangola MF, Helpern JA, et al. Diffusional kurtosis and diffusion tensor imaging reveal different time-sensitive stroke-induced microstructural changes. *Stroke* (2015) **46**:545–50. doi: 10.1161/STROKEAHA.114.006782
6. Falangola MF, Jensen JH, Tabesh A, Hu C, Deardorff RL, Babb JS, et al. Non-Gaussian diffusion MRI assessment of brain microstructure in mild cognitive impairment and Alzheimer's disease. *Magn Reson Imaging*. (2013) **31**:840–6. doi: 10.1016/j.mri.2013.02.008
7. Inglese M, Bester M. Diffusion imaging in multiple sclerosis: research and clinical implications. *NMR Biomed*. (2010) **23**:865–72. doi: 10.1002/nbm.1515
8. Van Cauter S, Veraart J, Sijbers J, Peeters RR, Himmelreich U, De Keyzer F, et al. Gliomas: diffusion kurtosis MR imaging in grading. *Radiology* (2012) **263**:492–501. doi: 10.1148/radiol.12110927
9. Bai Y, Lin Y, Tian J, Shi D, Cheng J, Haacke EM, et al. Grading of Gliomas by Using Monoexponential, Biexponential, and Stretched Exponential Diffusion-weighted MR Imaging and Diffusion Kurtosis MR Imaging. *Radiology* (2016) **278**:496–504. doi: 10.1148/radiol.2015142173
10. Grossman EJ, Ge Y, Jensen JH, Babb JS, Miles L, Reaume J, et al. Thalamus and cognitive impairment in mild traumatic brain injury: a diffusional kurtosis imaging study. *J Neurotrauma*. (2012) **29**:2318–27. doi: 10.1089/neu.2011.1763
11. Grossman EJ, Jensen JH, Babb JS, Chen Q, Tabesh A, Fieremans E, et al. Cognitive impairment in mild traumatic brain injury: a longitudinal diffusional kurtosis and perfusion imaging study. *AJNR Am J Neuroradiol*. (2013) **34**:951–7. doi: 10.3174/ajnr.A3358
12. Næss-Schmidt E, Blicher JU, Eskildsen SF, Tietze A, Østergaard L, Stubbs P, et al. Microstructural changes in the thalamus after mild traumatic brain injury – a longitudinal diffusion and mean kurtosis tensor MRI study. *Brain Injury*. (2016) **31**:230–6. doi: 10.1080/02699052.2016.1229034
13. Ostergaard L, Engedal TS, Aamand R, Mikkelsen R, Iversen NK, Anzabi M, et al. Capillary transit time heterogeneity and flow-metabolism coupling after traumatic brain injury. *J Cereb Blood Flow Metab*. (2014) **34**:1585–98. doi: 10.1038/jcbfm.2014.131
14. Falangola MF, Jensen JH, Babb JS, Hu C, Castellanos FX, Di Martino A, et al. Age-related non-Gaussian diffusion patterns in the prefrontal brain. *J Magn Reson Imaging* (2008) **28**:1345–50. doi: 10.1002/jmri.21604
15. Paydar A, Fieremans E, Nwankwo JI, Lazar M, Sheth HD, Adisetiyo V, et al. Diffusional kurtosis imaging of the developing brain. *AJNR Am J Neuroradiol*. (2014) **35**:808–14. doi: 10.3174/ajnr.A3764
16. Gong NJ, Wong CS, Chan CC, Leung LM, Chu YC. Aging in deep gray matter and white matter revealed by diffusional kurtosis imaging. *Neurobiol Aging*. (2014) **35**:2203–16. doi: 10.1016/j.neurobiolaging.2014.03.011
17. Jelescu IO, Veraart J, Adisetiyo V, Milla SS, Novikov DS, Fieremans E. One diffusion acquisition and different white matter models: how does microstructure change in human early development based on WMTI and NODDI? *NeuroImage* (2015) **107**:242–56. doi: 10.1016/j.neuroimage.2014.12.009
18. Fieremans E, Benitez A, Jensen JH, Falangola MF, Tabesh A, Deardorff RL, et al. Novel white matter tract integrity metrics sensitive to Alzheimer disease progression. *AJNR Am J Neuroradiol*. (2013) **34**:2105–12. doi: 10.3174/ajnr.A3553
19. Benitez A, Fieremans E, Jensen JH, Falangola MF, Tabesh A, Ferris SH, et al. White matter tract integrity metrics reflect the vulnerability of late-myelinating tracts in Alzheimer's disease. *Neuroimage Clin*. (2014) **4**:64–71. doi: 10.1016/j.nicl.2013.11.001
20. Davenport EM, Apkarian K, Whitlow CT, Urban JE, Jensen JH, Szuch E, et al. Abnormalities in Diffusional Kurtosis Metrics Related to Head Impact Exposure in a Season of High School Varsity Football. *J Neurotrauma*. (2016) **33**:2133–46. doi: 10.1089/neu.2015.4267
21. de Kouchkovsky I, Fieremans E, Fleysher L, Herbert J, Grossman RI, Inglese M. Quantification of normal-appearing white matter tract integrity in multiple sclerosis: a diffusion kurtosis imaging study. *J Neurol*. (2016) **263**:1146–55. doi: 10.1007/s00415-016-8118-z
22. Lazar M, Miles LM, Babb JS, Donaldson JB. Axonal deficits in young adults with High Functioning Autism and their impact on processing speed. *Neuroimage Clin*. (2014) **4**:417–25. doi: 10.1016/j.nicl.2014.01.014
23. Guglielmetti C, Veraart J, Roelant E, Mai Z, Daans J, Van Audekerke J, et al. Diffusion kurtosis imaging probes cortical alterations and white matter pathology following cuprizone induced demyelination and spontaneous remyelination. *Neuroimage* (2016) **125**:363–77. doi: 10.1016/j.neuroimage.2015.10.052
24. Jelescu IO, Zurek M, Winters KV, Veraart J, Rajaratnam A, Kim NS, et al. *In vivo* quantification of demyelination and recovery using compartment-specific diffusion MRI metrics validated by electron microscopy. *Neuroimage* (2016) **132**:104–14. doi: 10.1016/j.neuroimage.2016.02.004
25. Falangola MF, Guilfoyle DN, Tabesh A, Hui ES, Nie X, Jensen JH, et al. Histological correlation of diffusional kurtosis and white matter modeling metrics in cuprizone-induced corpus callosum demyelination. *NMR Biomed*. (2014) **27**:948–57. doi: 10.1002/nbm.3140
26. Kelm ND, West KL, Carson RP, Gochberg DF, Ess KC, Does MD. Evaluation of diffusion kurtosis imaging in *ex vivo* hypomyelinated mouse brains. *Neuroimage* (2016) **124**(Pt A):612–26. doi: 10.1016/j.neuroimage.2015.09.028
27. Jensen JH, McKinnon ET, Russell Glenn G, Helpern JA. Evaluating kurtosis-based diffusion MRI tissue models for white matter with fiber ball imaging. *NMR Biomed*. (2017) **30**:e3689. doi: 10.1002/nbm.3689
28. Hui ES, Russell Glenn G, Helpern JA, Jensen JH. Kurtosis analysis of neural diffusion organization. *Neuroimage* (2015) **106**:391–403. doi: 10.1016/j.neuroimage.2014.11.015
29. Rosenkrantz AB, Padhani AR, Chenevert TL, Koh DM, De Keyzer F, Taouli B, et al. Body diffusion kurtosis imaging: Basic principles, applications, and considerations for clinical practice. *J Magn Reson Imaging*. (2015) **42**:1190–202. doi: 10.1002/jmri.24985
30. Sheng RF, Wang HQ, Yang L, Jin KP, Xie YH, Chen CZ, et al. Diffusion kurtosis imaging and diffusion-weighted imaging in assessment of liver fibrosis stage and necroinflammatory activity. *Abdom Radiol (NY)*. (2017) **42**:1176–82. doi: 10.1007/s00261-016-0984-4
31. Budjan J, Sauter EA, Zoellner FG, Lemke A, Wambsganss J, Schoenberg SO, et al. Diffusion kurtosis imaging of the liver at 3 Tesla: *in vivo* comparison to standard diffusion-weighted imaging. *Acta Radiol*. (2017). doi: 10.1177/0284185117706608. [Epub ahead of print].
32. Pentang G, Lanzman RS, Heusch P, Muller-Lutz A, Blondin D, Antoch G, et al. Diffusion kurtosis imaging of the human kidney: a feasibility study. *Magn Reson Imaging* (2014) **32**:413–20. doi: 10.1016/j.mri.2014.01.006
33. Huang Y, Chen X, Zhang Z, Yan L, Pan D, Liang C, et al. MRI quantification of non-Gaussian water diffusion in normal human kidney: a diffusional kurtosis imaging study. *NMR Biomed*. (2015) **28**:154–61. doi: 10.1002/nbm.3235
34. Suo S, Chen X, Wu L, Zhang X, Yao Q, Fan Y, et al. Non-Gaussian water diffusion kurtosis imaging of prostate cancer. *Magn Reson Imaging* (2014) **32**:421–7. doi: 10.1016/j.mri.2014.01.015
35. Tamura C, Shinmoto H, Soga S, Okamura T, Sato H, Okuaki T, et al. Diffusion kurtosis imaging study of prostate cancer: preliminary findings. *J Magn Reson Imaging* (2014) **40**:723–9. doi: 10.1002/jmri.24379
36. Roethke MC, Kuder TA, Kuru TH, Fenchel M, Hadaschik BA, Laun FB, et al. Evaluation of Diffusion Kurtosis Imaging Versus Standard Diffusion Imaging for Detection and Grading of Peripheral Zone Prostate Cancer. *Invest Radiol*. (2015) **50**:483–9. doi: 10.1097/RLI.0000000000000155
37. Hansen B, Jespersen SN. Kurtosis fractional anisotropy, its contrast and estimation by proxy. *Sci Rep*. (2016) **6**:23999. doi: 10.1038/srep23999
38. Hansen B, Khan AR, Shemesh N, Lund TE, Sangill R, Eskildsen SF, et al. White matter biomarkers from fast protocols using axially symmetric diffusion kurtosis imaging. *NMR Biomed*. (2017) **30**:e3741. doi: 10.1002/nbm.3741
39. Hansen B, Lund TE, Sangill R, Jespersen SN. Experimentally and computationally fast method for estimation of a mean kurtosis. *Magn Reson Med*. (2013) **69**:1754–60. doi: 10.1002/mrm.24743
40. Hansen B, Lund TE, Sangill R, Jespersen SN. Erratum: Hansen, Lund, Sangill, and Jespersen. Experimentally and Computationally Fast Method for Estimation of a Mean Kurtosis. *Magn Reson Med*. (2013) **69**:1754–60. *Magn Reson Med*. (2014) **71**:2250. doi: 10.1002/mrm.25090

41. Hansen B, Lund TE, Sangill R, Stubbe E, Finsterbusch J, Jespersen SN. Experimental considerations for fast kurtosis imaging. *Magn Reson Med.* (2015) **76**:1455–68. doi: 10.1002/mrm.26055
42. Hansen B, Shemesh N, Jespersen SN. Fast imaging of mean, axial and radial diffusion kurtosis. *NeuroImage* (2016) **142**:381–93. doi: 10.1016/j.neuroimage.2016.08.022
43. Jensen JH, Helpern JA. MRI quantification of non-Gaussian water diffusion by kurtosis analysis. *NMR Biomed.* (2010) **23**:698–710. doi: 10.1002/nbm.1518
44. Wu EX, Cheung MM. MR diffusion kurtosis imaging for neural tissue characterization. *Nmr Biomed.* (2010) **23**:836–48. doi: 10.1002/nbm.1506
45. Basser PJ, Mattiello J, LeBihan D. Estimation of the effective self-diffusion tensor from the NMR spin echo. *J Magn Reson B.* (1994) **103**:247–54. doi: 10.1006/jmrb.1994.1037
46. Lazar M, Jensen JH, Xuan L, Helpern JA. Estimation of the Orientation Distribution Function from diffusional kurtosis imaging. *Magn Reson Med.* (2008) **60**:774–81. doi: 10.1002/mrm.21725
47. Basser PJ, Pierpaoli C. Microstructural and physiological features of tissues elucidated by quantitative-diffusion-tensor MRI. *J Magn Reson B.* (1996) **111**:209–19. doi: 10.1006/jmrb.1996.0086
48. Hui ES, Cheung MM, Qi LQ, Wu EX. Advanced MR Diffusion characterization of neural tissue using directional diffusion kurtosis analysis. *IEEE Eng Med Bio.* (2008) **2008**:3941–4. doi: 10.1109/IEMBS.2008.4650072
49. Hui ES, Cheung MM, Qi LQ, Wu EX. Towards better MR characterization of neural tissues using directional diffusion kurtosis analysis. *Neuroimage* (2008) **42**:122–34. doi: 10.1016/j.neuroimage.2008.04.237
50. Novikov DS, Veraart J, Jelescu IO, Fieremans E. Mapping orientational and microstructural metrics of neuronal integrity with *in vivo* diffusion MRI. ArXiv preprint. (2016) arXiv:1609.09144v1 [physics.bio-ph]
51. Fieremans E, Novikov DS, Jensen JH, Helpern JA. Monte Carlo study of a two-compartment exchange model of diffusion. *NMR Biomed.* (2010) **23**:711–24. doi: 10.1002/nbm.1577
52. Moakher M. Fourth-order cartesian tensors: Old and new facts, notions and applications. *Q J Mech Appl Math.* (2008) **61**:181–203. doi: 10.1093/qjmam/hbm027
53. Jeffreys H. Isotropic Tensors. *P Camb Philos Soc.* (1973) **73**:173–6.
54. Chuhutin A, Khan AR, Hansen B, Jespersen SN. *The Mean Kurtosis Evaluation Measurements Show a Considerable Disparity from the Analytically Evaluated Ones for a Clinically Used Range of B-Values*. Toronto, ON: Proceedings of the ISMRM (2015).
55. Chuhutin A, Shemesh N, Hansen B, Jespersen SN, editors. *The Importance of B-Values Selection and the Precision of Diffusion Kurtosis Estimation by the Conventional Schemes*. Singapore: ISMRM 2016 (2016).
56. Chuhutin A, Hansen B, Jespersen SN. Precision and accuracy of diffusion kurtosis estimation and the influence of b-value selection. *NMR Biomed.* (2017). doi: 10.1002/nbm.3777. [Epub ahead of print].
57. Veraart J, Poot DHJ, Van Hecke W, Blockx I, Van der Linden A, Verhoye M, et al. More Accurate Estimation of Diffusion Tensor Parameters Using Diffusion Kurtosis Imaging. *Magn Reson Med.* (2011) **65**:138–45. doi: 10.1002/mrm.22603
58. Jensen JH, Hu C, Helpern JA, editors. Rapid data acquisition and postprocessing for diffusional kurtosis imaging. In: *Proceedings of the 17th Annual Meeting of ISMRM*. Honolulu, Hawaii (2009).
59. Hansen MB, Jespersen SN, Leigland LA, Kroenke CD. Using diffusion anisotropy to characterize neuronal morphology in gray matter: the orientation distribution of axons and dendrites in the NeuroMorpho.org database. *Front Integr Neurosci.* (2013) **7**:31. doi: 10.3389/fnint.2013.00031
60. Khan AR, Chuhutin A, Wiborg O, Kroenke CD, Nyengaard JR, Hansen B, et al. Biophysical modeling of high field diffusion MRI demonstrates microstructural aberration in chronic mild stress rat brain. *Neuroimage* (2016) **142**:421–30. doi: 10.1016/j.neuroimage.2016.07.001
61. Glenn GR, Helpern JA, Tabesh A, Jensen JH. Quantitative assessment of diffusional kurtosis anisotropy. *NMR Biomed.* (2015) **28**:448–59. doi: 10.1002/nbm.3271
62. Kjolby BF, Khan AR, Chuhutin A, Pedersen L, Jensen JB, Jakobsen S, et al. Fast diffusion kurtosis imaging of fibrotic mouse kidneys. *NMR Biomed.* (2016) **29**:1709–19. doi: 10.1002/nbm.3623
63. Sun PZ, Wang Y, Mandeville E, Chan ST, Lo EH, Ji XM. Validation of fast diffusion kurtosis MRI for imaging acute ischemia in a rodent model of stroke. *Nmr Biomed.* (2014) **27**:1413–8. doi: 10.1002/nbm.3188
64. Wu Y, Kim J, Chan ST, Zhou IY, Guo Y, Igarashi T, et al. Comparison of image sensitivity between conventional tensor-based and fast diffusion kurtosis imaging protocols in a rodent model of acute ischemic stroke. *NMR Biomed.* (2016) **29**:625–30. doi: 10.1002/nbm.3506
65. Tietze A, Hansen MB, Ostergaard L, Jespersen SN, Sangill R, Lund TE, et al. Mean Diffusional Kurtosis in Patients with Glioma: Initial Results with a Fast Imaging Method in a Clinical Setting. *AJNR Am J Neuroradiol.* (2015) **36**:1472–8. doi: 10.3174/ajnr.A4311
66. Garza-Villarreal EA, Chakravarty MM, Hansen B, Eskildsen SF, Devenyi GA, Castillo-Padilla D, et al. The effect of crack cocaine addiction and age on the microstructure and morphology of the human striatum and thalamus using shape analysis and fast diffusion kurtosis imaging. *Transl Psychiat.* (2017) **7**:e1122. doi: 10.1038/tp.2017.92
67. Li C, Qian T, Kim J, Sun PZ, Lu J, Li K. Evaluation of acute cerebral infarction Using a fast kurtosis diffusion imaging protocol. *Proc. Intl. Soc. Mag. Reson. Med.* (2016) **24**:3493.
68. Feinberg DA, Setsompop K. Ultra-fast MRI of the human brain with simultaneous multi-slice imaging. *J Magn Reson.* (2013) **229**:90–100. doi: 10.1016/j.jmr.2013.02.002
69. Zhou IY, Guo Y, Igarashi T, Wang Y, Mandeville E, Chan ST, et al. Fast diffusion kurtosis imaging (DKI) with Inherent COrrelation-based Normalization (ICON) enhances automatic segmentation of heterogeneous diffusion MRI lesion in acute stroke. *NMR Biomed.* (2016) **29**:1670–7. doi: 10.1002/nbm.3617
70. Hansen B, Jespersen SN. Data for evaluation of fast kurtosis strategies, b-value optimization and exploration of diffusion MRI contrast. *Sci Data.* (2016) **3**:160072. doi: 10.1038/sdata.2016.72
71. Garyfallidis E, Brett M, Amirbekian B, Rokem A, van der Walt S, Descoteaux M, et al. Dipy, a library for the analysis of diffusion MRI data. *Front Neuroinform.* (2014) **8**:8. doi: 10.3389/fninf.2014.00008
72. Avram AV, Sarlls JE, Hutchinson E, Basser PJ. Efficient experimental designs for isotropic generalized diffusion tensor MRI (IGDTI). *Magn Reson Med.* (2017). doi: 10.1002/mrm.26656
73. Jespersen SN, Olesen JL, Hansen B, Shemesh N. Diffusion time dependence of microstructural parameters in fixed spinal cord. *Neuroimage* (2017). doi: 10.1016/j.neuroimage.2017.08.039. [Epub ahead of print].
74. Jelescu IO, Veraart J, Fieremans E, Novikov DS. Degeneracy in model parameter estimation for multi-compartmental diffusion in neuronal tissue. *NMR Biomed.* (2016) **29**:33–47. doi: 10.1002/nbm.3450
75. Jespersen SN, Leigland LA, Cornea A, Kroenke CD. Determination of axonal and dendritic orientation distributions within the developing cerebral cortex by diffusion tensor imaging. *IEEE Trans Med Imaging.* (2012) **31**:16–32. doi: 10.1109/TMI.2011.2162099
76. Jespersen SN. Equivalence of double and single wave vector diffusion contrast at low diffusion weighting. *NMR Biomed.* (2012) **25**:813–8. doi: 10.1002/nbm.1808
77. Ning L, Westin CF, Rathi Y. Estimating diffusion propagator and its moments using directional radial basis functions. *IEEE Trans Med Imaging.* (2015) **34**:2058–78. doi: 10.1109/TMI.2015.2418674
78. Mardia KV. Measures of Multivariate Skewness and Kurtosis with Applications. *Biometrika* (1970) **57**:519–30. doi: 10.1093/biomet/57.3.519
79. Grant SC, Buckley DL, Gibbs S, Webb AG, Blackband SJ. MR microscopy of multicomponent diffusion in single neurons. *Magn Reson Med.* (2001) **46**:1107–12. doi: 10.1002/mrm.1306
80. Flint JJ, Lee CH, Hansen B, Fey M, Schmidig D, Bui JD, et al. Magnetic resonance microscopy of mammalian neurons. *Neuroimage* (2009) **46**:1037–40. doi: 10.1016/j.neuroimage.2009.03.009
81. Flint JJ, Hansen B, Fey M, Schmidig D, King MA, Vestergaard-Poulsen P, et al. Cellular-level diffusion tensor microscopy and fiber tracking in mammalian nervous tissue with direct histological correlation. *Neuroimage* (2010) **52**:556–61. doi: 10.1016/j.neuroimage.2010.04.031
82. Hansen B, Flint JJ, Heon-Lee C, Fey M, Vincent F, King MA, et al. Diffusion tensor microscopy in human nervous tissue with quantitative correlation based on direct histological comparison. *Neuroimage* (2011) **57**:1458–65. doi: 10.1016/j.neuroimage.2011.04.052

83. Flint JJ, Hansen B, Portnoy S, Lee CH, King MA, Fey M, et al. Magnetic resonance microscopy of human and porcine neurons and cellular processes. *Neuroimage* (2012) **60**:1404–11. doi: 10.1016/j.neuroimage.2012.01.050
84. Lee CH, Flint JJ, Hansen B, Blackband SJ. Investigation of the subcellular architecture of L7 neurons of Aplysia californica using magnetic resonance microscopy (MRM) at 7.8 microns. *Sci Rep.* (2015) **5**:11147. doi: 10.1038/srep11147
85. Flint JJ, Hansen B, Blackband SJ. Diffusion tensor microscopy data (15.6 μm in-plane) of white matter tracts in the human, pig, and rat spinal cord with corresponding tissue histology. *Data Brief.* (2016) **9**:271–4. doi: 10.1016/j.dib.2016.08.020
86. Jespersen SN, Kroenke CD, Ostergaard L, Ackerman JJ, Yablonskiy DA. Modeling dendrite density from magnetic resonance diffusion measurements. *Neuroimage* (2007) **34**:1473–86. doi: 10.1016/j.neuroimage.2006.10.037
87. Jespersen SN, Bjarkam CR, Nyengaard JR, Chakravarty MM, Hansen B, Vosegaard T, et al. Neurite density from magnetic resonance diffusion measurements at ultrahigh field: comparison with light microscopy and electron microscopy. *Neuroimage* (2010) **49**:205–16. doi: 10.1016/j.neuroimage.2009.08.053
88. Ferris CF, Smerkers B, Kulkarni P, Caffrey M, Afacan O, Toddes S, et al. Functional magnetic resonance imaging in awake animals. *Rev Neurosci.* (2011) **22**:665–74. doi: 10.1515/RNS.2011.050
89. Yoshida K, Mimura Y, Ishihara R, Nishida H, Komaki Y, Minakuchi T, et al. Physiological effects of a habituation procedure for functional MRI in awake mice using a cryogenic radiofrequency probe. *J Neurosci Meth.* (2016) **274**:38–48. doi: 10.1016/j.jneumeth.2016.09.013
90. Weber RA, Chan CH, Nie X, Maggioncalda E, Valiulis G, Lauer A, et al. Sensitivity of diffusion MRI to perilesional reactive astrogliosis in focal ischemia. *NMR Biomed.* (2017) **30**:e3717. doi: 10.1002/nbm.3717
91. Khan AR, Chuhutin A, Wiborg O, Kroenke CD, Nyengaard JR, Hansen B, et al. Summary of high field diffusion MRI and microscopy data demonstrate microstructural aberration in chronic mild stress rat brain. *Data Brief.* (2016) **8**:934–7. doi: 10.1016/j.dib.2016.06.061
92. Palombo M, Gentili S, Bozzali M, Macaluso E, Capuani S. New insight into the contrast in diffusional kurtosis images: does it depend on magnetic susceptibility? *Magn Reson Med.* (2015) **73**:2015–24. doi: 10.1002/mrm.25308
93. Farrher E, Lindemeyer J, Grinberg F, Oros-Peusquens AM, Shah NJ. Concerning the matching of magnetic susceptibility differences for the compensation of background gradients in anisotropic diffusion fibre phantoms. *PLoS ONE* (2017) **12**:e0176192. doi: 10.1371/journal.pone.0176192
94. Shaw CB, Jensen JH, Deardorff RL, Spampinato MV, Helpern JA. Comparison of Diffusion Metrics Obtained at 1.5T and 3T in Human Brain With Diffusional Kurtosis Imaging. *J Magn Reson Imag* (2017) **45**:673–80. doi: 10.1002/jmri.25380
95. Vestergaard-Poulsen P, Wegener G, Hansen B, Bjarkam CR, Blackband SJ, Nielsen NC, et al. Diffusion-weighted MRI and quantitative biophysical modeling of hippocampal neurite loss in chronic stress. *PLoS ONE* (2011) **6**:e20653. doi: 10.1371/journal.pone.0020653
96. Budde MD, Frank JA. Neurite beading is sufficient to decrease the apparent diffusion coefficient after ischemic stroke. *Proc Natl Acad Sci U S A.* (2010) **107**:14472–7. doi: 10.1073/pnas.1004841107
97. Setsompop K, Fan Q, Stockmann J, Bilgic B, Huang S, Cauley SF, et al. High-resolution *in vivo* diffusion imaging of the human brain with generalized slice dithered enhanced resolution: Simultaneous multislice (gSlider-SMS). *Magn Reson Med.* (2017). doi: 10.1002/mrm.26653. [Epub ahead of print].
98. Sagi Y, Tavor I, Hofstetter S, Tzur-Moryosef S, Blumenfeld-Katzir T, Assaf Y. Learning in the Fast Lane: New Insights into Neuroplasticity. *Neuron* (2012) **73**:1195–203. doi: 10.1016/j.neuron.2012.01.025
99. Hofstetter S, Tavor I, Tzur Moryosef S, Assaf Y. Short-term learning induces white matter plasticity in the fornix. *J Neurosci.* (2013) **33**:12844–50. doi: 10.1523/JNEUROSCI.4520-12.2013
100. Metzler-Baddeley C, Foley S, de Santis S, Charron C, Hampshire A, Caeyenberghs K, et al. Dynamics of white matter plasticity underlying working memory training: multimodal evidence from diffusion MRI and T2 relaxometry. *J Cogn Neurosci.* (2017) **29**:1509–20. doi: 10.1162/jocn_a_01127
101. Shemesh N, Rosenberg JT, Dumez JN, Muniz JA, Grant SC, Frydman L. Metabolic properties in stroked rats revealed by relaxation-enhanced magnetic resonance spectroscopy at ultrahigh fields. *Nat Commun.* (2014) **5**:4958. doi: 10.1038/ncomms5958

Conflict of Interest Statement: The authors declare that the research was conducted in the absence of any commercial or financial relationships that could be construed as a potential conflict of interest.

frontiers in Physics

REVIEW
published: 28 November 2017
doi: 10.3389/fphy.2017.00061

Design and Validation of Diffusion MRI Models of White Matter

Ileana O. Jelescu[1]* *and Matthew D. Budde*[2]*

[1] Centre d'Imagerie Biomédicale, École Polytechnique Fédérale de Lausanne, Lausanne, Switzerland, [2] Department of Neurosurgery, Zablocki VA Medical Center, Medical College Wisconsin, Milwaukee, WI, United States

Diffusion MRI is arguably the method of choice for characterizing white matter microstructure *in vivo*. Over the typical duration of diffusion encoding, the displacement of water molecules is conveniently on a length scale similar to that of the underlying cellular structures. Moreover, water molecules in white matter are largely compartmentalized which enables biologically-inspired compartmental diffusion models to characterize and quantify the true biological microstructure. A plethora of white matter models have been proposed. However, overparameterization and mathematical fitting complications encourage the introduction of simplifying assumptions that vary between different approaches. These choices impact the quantitative estimation of model parameters with potential detriments to their biological accuracy and promised specificity. First, we review biophysical white matter models in use and recapitulate their underlying assumptions and realms of applicability. Second, we present up-to-date efforts to validate parameters estimated from biophysical models. Simulations and dedicated phantoms are useful in assessing the performance of models when the ground truth is known. However, the biggest challenge remains the validation of the "biological accuracy" of estimated parameters. Complementary techniques such as microscopy of fixed tissue specimens have facilitated direct comparisons of estimates of white matter fiber orientation and densities. However, validation of compartmental diffusivities remains challenging, and complementary MRI-based techniques such as alternative diffusion encodings, compartment-specific contrast agents and metabolites have been used to validate diffusion models. Finally, white matter injury and disease pose additional challenges to modeling, which are also discussed. This review aims to provide an overview of the current state of models and their validation and to stimulate further research in the field to solve the remaining open questions and converge toward consensus.

Keywords: diffusion MRI, white matter, modeling, microstructure, tissue compartments

OPEN ACCESS

Edited by:
Julien Valette, Commissariat à l'Energie Atomique et aux Energies Alternatives (CEA), France

Reviewed by:
Valerij G. Kiselev, Universitätsklinikum Freiburg, Germany
Silvia Capuani, Consiglio Nazionale Delle Ricerche (CNR), Italy

***Correspondence:**
Ileana O. Jelescu
ileana.jelescu@epfl.ch
Matthew D. Budde
mdbudde@mcw.edu

Specialty section:
This article was submitted to Biomedical Physics, a section of the journal Frontiers in Physics

Received: *28 September 2017*
Accepted: *10 November 2017*
Published: *28 November 2017*

Citation:
Jelescu IO and Budde MD (2017) Design and Validation of Diffusion MRI Models of White Matter. Front. Phys. 5:61. doi: 10.3389/fphy.2017.00061

Diffusion weighted MRI (DWI) is unique in its ability to detect brain microstructure non-invasively. Characterization of white matter microstructure using DWI has shown high sensitivity to changes associated with normal brain development and aging and to the wide array of neurological diseases, injuries, and potential treatments. DWI is an excellent probe of microstructure, whose characteristic features are on the same length scale as the micrometer-scale displacement of water molecules. However, it remains an **indirect** probe, because extracting quantitative metrics that characterize the underlying tissue microstructure requires modeling of the DWI signal. Decisions regarding model choice and fitting procedures have considerable influence on the accuracy, reliability, and validity of the extracted metrics.

This review first presents an overview of current white matter models "in circulation" and exposes their common features and individual limitations (Part 1), noting that the discussion is restricted to long-time limit diffusion models, where axons are modeled as sticks. Next, efforts to validate models in the normal white matter using complementary techniques are discussed (Part 2), followed by a brief discussion of the additional challenges related to modeling of the diseased tissue (Part 3). Future directions of research are highlighted at every step.

MODELS

Two complementary approaches have emerged for extracting information about the tissue microstructure from the diffusion signal: signal representations and tissue models.

Signal representations—sometimes also referred to as "statistical models"—aim at empirically describing the diffusion signal behavior in a given voxel without assumptions about the underlying tissue. Thus, they are applicable to any tissue type, healthy or diseased, but the estimated parameters lack specificity and remain an indirect characterization of microstructure.

Tissue models, on the other hand, assume a given (schematic) geometry—a "picture" of the underlying tissue [1]. The analytical expression of the diffusion signal in the chosen environment is fit to the diffusion data, which allows the estimation of the relevant parameters of the microstructure. Tissue models can potentially provide greater specificity and interpretation of biologically-relevant parameters, but only if the assumption is met that the chosen model accurately captures all of the relevant features of the tissue, i.e., all those that effectively and substantially impact the diffusion signal in a given acquisition range.

In this section, we will first briefly review examples of signal representations, in order to reinforce the distinction with modeling. We will then review major biophysical models of white matter, with clear identification of their main assumptions and estimated parameters.

Signal Representations

The most widespread signal representation is the cumulant expansion [2–4], which relies on an expansion of the logarithm of the signal in polynomials up to a given order in b—i.e., a Taylor series:

$$\ln\left(\frac{S}{S_0}\right) = -bD + \frac{1}{6}\left(bD\right)^2 K + \ldots \quad (1)$$

where D is the diffusion coefficient and K the kurtosis. Or, in tensor form:

$$\ln\left(\frac{S}{S_0}\right) = -b\sum_{i,j=1}^{3} g_i g_j D_{ij} + \frac{1}{6}\left(b\bar{D}\right)^2 \sum_{i,j,k,l=1}^{3} g_i g_j g_k g_l W_{ijkl} + \ldots (2)$$

where $\boldsymbol{D}$ is the rank-2 diffusion tensor, $\boldsymbol{W}$ is the rank-4 kurtosis tensor, $\overline{D}$ is the mean diffusivity and $\boldsymbol{g}$ is the direction of the applied diffusion weighting.

Diffusion tensor imaging (DTI) is thus an expansion up to the first order in b, valid for low diffusion weighting ($b \ll 1/(DK)$) [5]. It is important to stress that DTI does not assume that the tissue is a Gaussian medium ($K = 0$)—which is reputedly not true for biological tissue, but rather that it is indistinguishable from a Gaussian medium when $b \ll 1/(DK)$.

Naturally, going beyond this low b-value regime and estimating the kurtosis of the diffusion probability distribution function—i.e., by how much it deviates from a Gaussian distribution—provides information about tissue complexity that is complementary to DTI metrics [2].

In order to estimate the six independent components of the diffusion tensor, the minimal required data is one $b = 0$ (unweighted) image and six non collinear directions on a single diffusion weighting, or "shell." The additional estimation of the 15 independent components of the kurtosis tensor requires a minimal acquisition of one $b = 0$ image and 21 measurements distributed over 2 shells. The choice of the shell b-values is a trade-off between accuracy—they should be as low as possible, since the Taylor expansion is valid for $bD \to 0$ — and precision—they should be as high as admittedly possible to limit the impact of noise [6]. This trade-off value is typically around $b = 1$ ms/μm^2 for DTI and $b = 2$ ms/μm^2 for DKI, *in vivo*. Largely improved algorithms for unbiased estimation of the diffusion and kurtosis tensors have been developed [7]. It is also noteworthy that fitting the kurtosis tensor greatly improves the accuracy of the diffusion tensor estimation [8]. Extending the series to the sixth order cumulant (in b^3) increases the accuracy of the kurtosis estimation, albeit with a penalty on precision [9].

Since no assumption is made about the tissue structure, metrics derived from the diffusion tensor, such as mean diffusivity and fractional anisotropy are used extensively for brain and body tissue characterization in a wide variety of conditions [10, 11]. DKI metrics, such as mean kurtosis, are also increasingly used as complementary biomarkers to DTI metrics in a large panel of applications [12–17]. With acquisition acceleration options available on most clinical scanners, and new reduced acquisition schemes [18, 19], DKI is expected to become more and more widespread.

Other signal representations than the cumulant expansion are of course possible. Yablonskiy et al. [20] proposed to introduce a distribution of diffusion coefficients $\rho(D)$ in the tissue, which can theoretically be estimated by inverse Laplace transform:

$$\frac{S}{S_0} = \int_0^\infty \rho(D) e^{-bD} dD \quad (3)$$

However, because the inverse Laplace transform is a mathematically ill-posed problem, in practice some functional form is assumed for $\rho(D)$ and its characteristic parameters estimated [20, 21]. Moreover, the estimated distribution does not mirror the actual distribution of diffusion coefficients in the tissue unless the measurement is performed in a very strong diffusion weighting regime ($ql_c \gg 1$, where q is the amount of spatial phase-warping introduced and l_c is the diffusion distance) [9, 22]. Thus, this approach remains an empirical description of

the diffusion-weighted signal and falls in the category of signal representations rather than biophysical models.

The departure from Gaussianity can also be captured empirically as a "stretched exponential" expression of the diffusion signal [23]:

$$\frac{S}{S_0} = \exp\left(-\left(b \cdot \mathrm{ADC}\right)^{\alpha}\right) \tag{4}$$

The stretched exponential function has later been associated with the theory of anomalous diffusion, which represents a departure from Brownian motion ($\langle x^2 \rangle \propto t$), by several groups [24–26]. A comprehensive discussion on the implications of such a theory for biological tissue can be found in Kiselev [9] and Novikov et al. [1]. Although devoid of biophysical meaning, the stretching parameter α is largely used in the literature for tumor delineation and characterization [27–30].

Another example of signal representation is the expansion of the diffusion signal using harmonic oscillator basis functions (Hermite polynomials), as proposed by Özarslan et al. [31], a method dubbed mean apparent propagator (MAP-MRI). In addition to the reconstruction of a diffusion tensor, the method allows the estimation of the return-to-origin probability, which is sensitive to compartment sizes, and of non-Gaussianity indices, indicative of tissue complexity. The data required for MAP-MRI can be acquired in under 10 min on a clinical scanner [32].

Biophysical Models of White Matter

The first attempts at modeling the diffusion signal as multi-compartmental can be attributed to Latour et al. [33] in red blood cells and Szafer et al. [34] who modeled "tissue" as cuboids on a regular lattice, surrounded by extracellular medium. Building on their work, Stanisz et al. [35] proposed the first white matter model based on electron micrographs of bovine optic nerve. In their model, axons were represented as prolate ellipsoids and glial soma as spheres, the extracellular space constituting the third compartment. The model also accounted for membrane permeability of axons and glial cells. The authors noted that the nine-parameter model required a wide range of diffusion times and gradient strengths, and that even with extensive data, the goodness of fit remained unsatisfactory. They also underlined that releasing some of the assumptions and increasing the number of parameters would make the fit unstable. Twenty years later, those insights are still very much topical.

At long diffusion times, the diffusion distance across the axon becomes constant (it is limited by the axon diameter) and the diffusivity tends to zero: axons can thus be modeled as infinitely long "sticks" (cylinders with zero radius). The first group to introduce the stick geometry was Behrens et al. [36] and assumed that water in and around the axons similarly diffused only in the fiber direction with a second compartment of free, isotropically diffusing water. Shortly after, Kroenke et al. [37] used a biophysical model of isotropically oriented sticks to characterize the diffusion of N-acetyl aspartate (NAA) in the neurites. A similar description to Behrens' of two compartments was later adopted by Jespersen et al. [38], who also formulated for the first time the clear goal of estimating dendrite density—i.e., a specific biomarker of the microstructure—*in vivo*, using diffusion MRI modeling.

Building on these initial works, most white matter models "in use" today rely on the same common picture: water signal is assumed to originate from two or three non-exchanging compartments, each weighted by their relative volume fractions (**Figure 1**).

The first compartment is the collection of axons, which are modeled as infinitely long sticks, and whose collective orientations are characterized by some orientation distribution function (ODF). Water diffusivity inside each axon is $D_{a,\parallel}$ along the axon and zero perpendicular to it. The parametrization of the ODF varies between models.

The second compartment is the extra-axonal space which, by exclusion, includes features not explicitly ascribed to the axonal space, including extracellular water, cell somas, and glial cells, all assumed to be in fast exchange. This compartment is modeled as Gaussian anisotropic, with axial and radial diffusivities $D_{e,\parallel}$

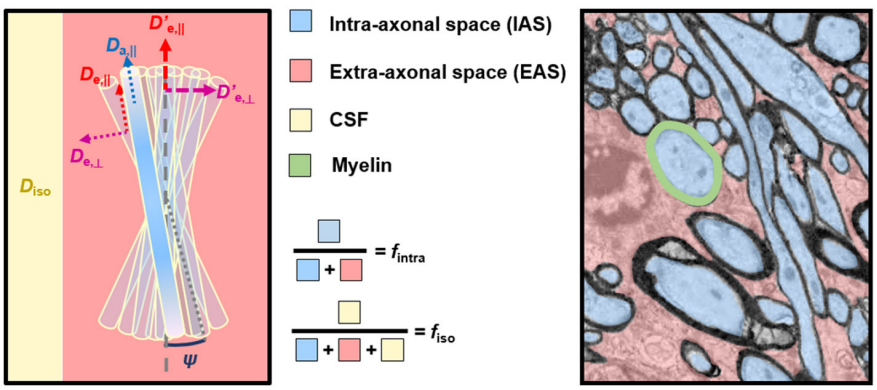

FIGURE 1 | Correspondence between model compartments **(Left)** and tissue components **(Right)**. **(Left)** Schematic of a typical three-compartment model with relevant parameters. $D_{e,\parallel}$ and $D_{e,\perp}$ are local extra-axonal diffusivities, and $D'_{e,\parallel}$ and $D'_{e,\perp}$, are apparent extra-axonal diffusivities, depending how the model defines them. **(Right)** Cross-sectional electron microscopy image of a white matter bundle. Adapted from Mikula and Denk [39] with permission. While myelin is present in WM, it is absent from DWI models due to its short T_2.

and $D_{e,\perp}$, respectively. These extra-axonal diffusivities are either defined locally in proximity of a coherent axon sub-bundle with the resulting signal response convolved with the ODF, or as apparent extra-axonal diffusivities over the entire voxel (indicated with a "prime" symbol in **Figure 1** and hereafter, for disambiguation).

The third compartment, if included, is modeled as Gaussian isotropic, with a diffusivity D_{iso}. If it represents freely diffusing water such as cerebrospinal fluid (CSF), D_{iso} (D_{free}) is set to 3 μm^2/ms *in vivo*. If it represents water with a negligible diffusivity in all directions, often referred to as "still water," and non-exchanging with the extracellular space, $D_{iso} = 0$. The parametrization, constraints, and nomenclature of D_{iso} vary between models.

Modeling necessarily comes with a level of simplification, since the entire biological complexity certainly cannot be rendered. The most difficult part of the modeling task is perhaps figuring out which features of the microstructure are relevant to the voxel-averaged diffusion signal and should be represented in the model, and which ones can be omitted without violating assumptions or accuracy. For a more detailed discussion on coarse-graining and effective medium theory, we direct the reader to a very comprehensive review by Novikov et al. [1].

In what follows, we will briefly review the main white matter models that have, for the most part, emerged in the last decade and that share the common features outlined above. While many different diffusion models and corresponding applications have been proposed, this review will only focus on models of tissue microstructure pertaining to the brain and spinal cord and in the long-time limit where axons are modeled as sticks. We also neglect potential measures of permeability between compartments, though they could have substantial impact on modeling, especially in the case of pathologies [40].

NODDI

The tissue model in Neurite Orientation Dispersion and Density Imaging (NODDI) matches exactly the cartoon in **Figure 1** [41]. It is a three-compartment model fully described by seven parameters: two volume fractions (f_{intra} and f_{iso}), four diffusivities ($D_{a,\parallel}$, $D_{e,\parallel}$, $D_{e,\perp}$, and D_{iso}) and the orientation dispersion, modeled by a Watson distribution of concentration parameter κ. The latter can be related to the angular spread via

$$\left\langle (\cos\psi)^2 \right\rangle = -\frac{1}{2\kappa} + \frac{1}{\sqrt{\pi}e^{-\kappa}\,\mathrm{erfi}(\sqrt{\kappa})\sqrt{\kappa}}.$$

where ψ is the angle between an axon and the main diffusion orientation in the voxel. In order to stabilize the fitting procedure, NODDI constrains all diffusivity values, effectively leaving only the two volume fractions and the orientation dispersion to be estimated, i.e., the underlying geometry. The model assumptions are as follows:

$$D_{a,\parallel} = D_{e,\parallel} = 1.7\ \mu m^2/\mathrm{ms} \quad (5)$$

$$D_{e,\perp} = (1 - f_{intra}) \cdot D_{e,\parallel} \quad (6)$$

$$D_{iso} = 3\ \mu m^2/\mathrm{ms} \quad (7)$$

The popularity of NODDI is indisputable, with applications to a very large panel of brain alterations and pathologies [42–48]. However, there are important assumptions within NODDI related to its design that have strong implications to its specificity.

NODDI imposes assumptions on the intrinsic diffusivities to the point of fixing $D_{a,\parallel}$ and $D_{e,\parallel}$ to the same predetermined value for all tissues (Equation 5). First, any deviation from these fixed values can bias the remaining parameters and they will lose their desired specificity. Substantial changes in diffusivity, such as that occurring in cerebral ischemia, for example, will impart a false change in orientation dispersion, neurite density, or CSF partial volume that does not accurately capture the underlying tissue pathology—as will be discussed in more detail in the third part of this review. The decision to fix the axial intra- and extra-axonal diffusivities equal to one another is another assumption that can lead to unpredictable effects. Recent work has shown that fixing $D_{a,\parallel} = D_{e,\parallel}$ masks a fundamental property of multi-compartment models, namely the multiplicity of mathematical solutions [49, 50]. Indeed, it has been shown that, if all parameters in the fitting procedure are released, namely f_{intra}, $D_{a,\parallel}$, $D_{e,\parallel}$, $D_{e,\perp}$, and κ (ignoring the CSF compartment), there are two distinct solutions to the parameter estimation problem, both within biologically plausible ranges (**Figure 2**). The two solutions of a two-compartment model can roughly be described as one where $D_{a,\parallel} < D_{e,\parallel}$, and another where $D_{a,\parallel} > D_{e,\parallel}$. Establishing which inequality is biologically valid is an active field of research, with most studies pointing toward $D_{a,\parallel} > D_{e,\parallel}$. This will be covered in detail in the second part of the review. Finally, the tortuosity approximation that relates $D_{e,\parallel}$ and $D_{e,\perp}$ (Equation 6) has been shown not to hold for tight packings of axons [51].

WMTI

White Matter Tract Integrity (WMTI) is a two-compartment model of sticks embedded in a Gaussian anisotropic extra-axonal medium [52]. The tissue can be described as a combination of two Gaussian compartments (intra- and extra-axonal) each characterized by a tensor ($\hat{D}_a$ and $\hat{D}_e{}'$) which can be directly derived from the overall diffusion and kurtosis tensors $\hat{D}$ and $\hat{K}$ [53]. In any direction j,

$$D_j = f_{intra} D_{a,j} + (1 - f_{intra}) D'_{e,j} \quad (8)$$

$$K_j = 3 f_{intra} \cdot (1 - f_{intra}) \frac{\left(D'_{e,j} - D_{a,j}\right)^2}{D_j^2} \quad (9)$$

This approach by-passes inherent limitations associated with non-linear fitting (local minima and long computation time): the linear estimation of the diffusion and kurtosis tensors is followed by a direct derivation of the WMTI model parameters. The quadratic expression in Equation (9) demonstrates, as previously mentioned, that for a two-compartment model, there are two mathematical solutions, where either $D_{a,\parallel} < D_{e,\parallel}$, or $D_{a,\parallel} > D_{e,\parallel}$. Establishing which inequality is biologically valid is an active field of research, which will be covered in detail in the second part of the review.

In WMTI, the authors had chosen the inequality $D_{a,\parallel} < D_{e,\parallel}$ to solve the system (which is the opposite of the inequality that

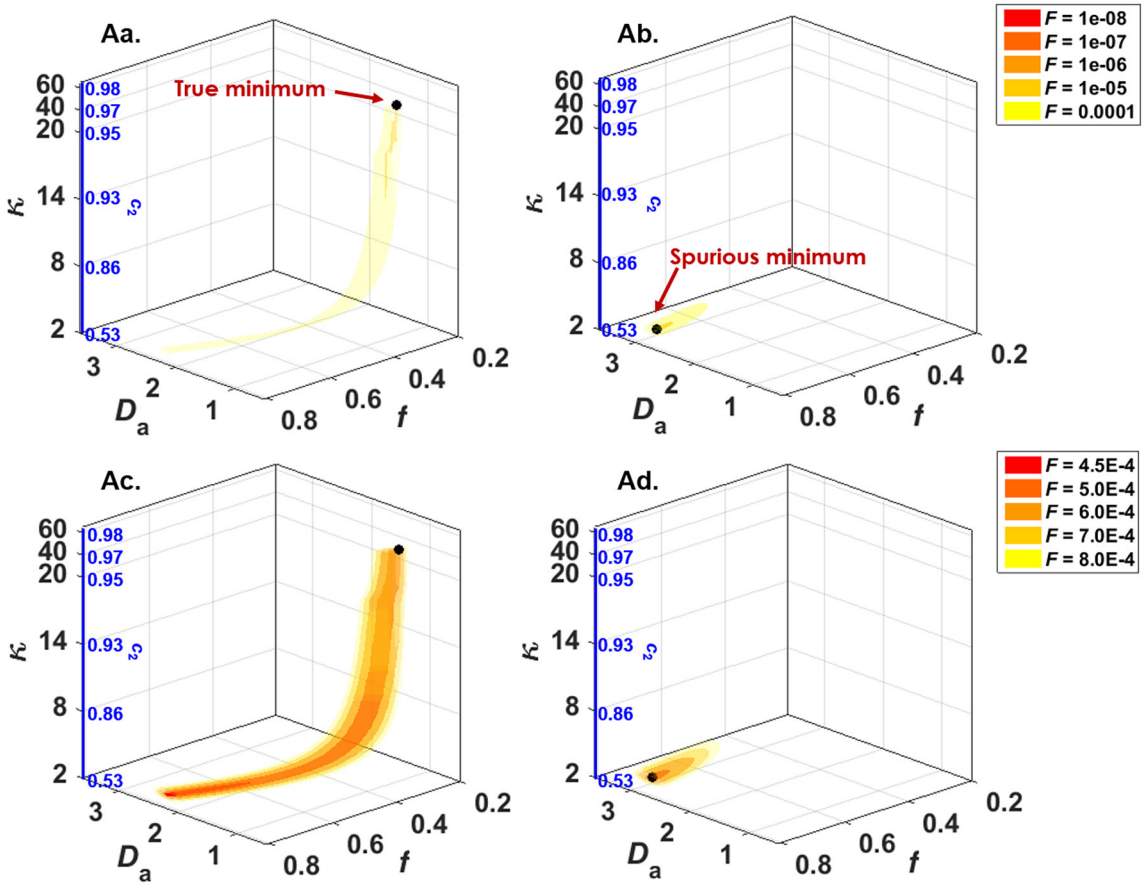

FIGURE 2 | NODDIDA optimization landscape reveals the existence, in the full 5-parameter space, of two disconnected minima, each surrounded by a pipe-like ensemble of low objective function values. Shown are 3D isosurfaces of the objective function $F(f, D_{a,\parallel}, \kappa)$. **(Aa)** F calculated with $(D_{e,\parallel}; D_{e,\perp}) = (2.10; 0.74)$ and SNR $= \infty$, thus containing the true global minimum. **(Ab)** F calculated with $(D_{e,\parallel}; D_{e,\perp}) = (0.32; 0.85)$ and SNR $= \infty$, thus containing the second local minimum of the 5D minimization problem. **(Ac)** The same as **(Aa)**, but SNR = 50. **(Ad)** The same as **(Ab)**, but SNR = 50. The theoretical minimum of F along each pipe is identified by a black bullet. Noise can displace the effective minimum along the pipe very far from the true one (see **Ac**). Figure taken from Jelescu et al. [49], with permission.

seems to hold from recent work), hence:

$$f_{\text{intra}} = \frac{K_{\max}}{K_{\max} + 3} \tag{10}$$

$$D'_{\text{e,j}} = D_{\text{j}} \left[1 + \sqrt{\frac{K_j \cdot f_{\text{intra}}}{3(1 - f_{\text{intra}})}} \right] \tag{11}$$

$$D_{\text{a,j}} = D_{\text{j}} \left[1 - \sqrt{\frac{K_{\text{j}}(1 - f_{\text{intra}})}{3 f_{\text{intra}}}} \right] \tag{12}$$

WMTI has been used in studies of a large variety of conditions, with substantial validation efforts using animal models of altered myelin [12, 13, 54–58].

In WMTI, the collection of axons is modeled as a Gaussian compartment, which is an assumption that only holds if the axons are highly aligned in a single bundle. Fieremans and colleagues estimated a maximum orientation dispersion of 30° for this approximation to hold, in the case of coplanar dispersion only. The validity of the approximation for three-dimensional dispersion has not been evaluated. Thus, while WMTI captures changes in diffusivities, it is best applied to regions of highly aligned single fiber bundles as per the recommendations. A more recent approach consists in deriving the WMTI equations assuming a Watson distribution of axons, like in NODDI, thus alleviating one of the strongest assumptions of WMTI [59]. The authors then further use time dependent functional forms of model parameters to evaluate which of the two possible solutions is the biologically valid one.

Another limitation is that since WMTI is based on the kurtosis model, it is restricted to the low b-value regime which could lead to some bias, although this may also be advantageous for compatibility with clinical hardware systems.

Rotationally Invariant Features: LEMONADE & co.

In a two-compartment model, estimating compartment diffusivities and orientation dispersion of axons simultaneously is problematic and prone to bias, hence requiring fixed parameter assumptions (NODDI) or limitations to coherent fibers only (WMTI). Loosening these constraints to achieve

greater specificity comes at the expense of a larger number of parameters to be estimated in the model, which is problematic for non-linear fitting. In particular, allowing for a complex ODF quickly increases the number of parameters. NODDI for example also has a declination that uses a Bingham rather than Watson distribution (2 free parameters) [60]. Jespersen and colleagues modeled the ODF using a spherical harmonic expansion up to $L = 2$ (5 free parameters) [38] and later $L = 4$ (14 free parameters) [61].

For the purpose of extracting a reliable ODF for tractography, several groups had modeled the diffusion signal as a convolution between the response of a perfectly aligned fascicle (axons and their immediate extra-axonal space) pointing in direction **n**, and the fiber ODF $P(\mathbf{n})$ [62–64]:

$$S_{\mathbf{g}}(b) = S(0) \cdot \int_{|\mathbf{n}|=1} \mathcal{K}(b, \mathbf{g}\cdot\mathbf{n})\, \mathcal{P}(\mathbf{n})\, d\mathbf{n} \tag{13}$$

Equation 13 factorizes in the spherical harmonics basis, thus separating the estimation of the scalar parameters of the kernel K from that of the ODF parameters. Recently, Novikov et al. [50] and Reisert et al. [65] have exploited this property to estimate the scalar parameters of a two-compartment kernel separately from the ODF:

$$\begin{aligned}\mathcal{K}(b, \mathbf{g}\cdot\mathbf{n}) = {} & f_{\text{intra}} e^{-bD_{a,\parallel}(\mathbf{g}\cdot\mathbf{n})^2} \\ & + (1 - f_{\text{intra}}) e^{-bD_{e,\parallel}(\mathbf{g}\cdot\mathbf{n})^2 - bD_{e,\perp}(1-(\mathbf{g}\cdot\mathbf{n})^2)}\end{aligned} \tag{14}$$

The approach of Novikov et al. [50] can be decomposed into two steps. The first step relies on solving an algebraic system of equations which relates the kernel parameters to the signal moments. More specifically, using "low b-value" data (e.g., $b_{\max} = 2.5$ ms/μm^2), the scalar parameters and a few basis-independent ODF parameters p_l can be directly derived from the first moments of the diffusion signal (up to 6th order) in a similar fashion to which WMTI uses direct relationships between model parameters and cumulants up to the 4th order. This method was dubbed LEMONADE (Linearly Estimated Moments provide Orientations of Neurites And their Diffusivities Exactly), and requires diffusion data distributed over 3 non-zero b shells. Circumventing issues related to non-linear fitting, LEMONADE provides estimates for f_{intra}, $D_{\text{a},\parallel}$, $D_{\text{e},\parallel}$, $D_{\text{e},\perp}$, and $p_2 = \frac{3\langle(\cos\psi)^2\rangle - 1}{2}$, which gives an estimate of the orientation dispersion in a similar way to κ from the Watson distribution. The spherical harmonic expansion of the ODF can then be fully reconstructed up to $L = 6$. In a second step, all available data (including high b-values) can be exploited to minimize the rotationally invariant (RotInv) energy function of the system, using the LEMONADE estimates as initialization values. In other words, the projections of the scalar kernel onto Legendre polynomials, weighted by rotational invariants of the ODF, are fitted to rotational invariants of the spherical harmonics decomposition of the signal, in a least-squares sense.

LEMONADE provides further evidence for the existence of two mathematical solutions to the two-compartment model and that, in principle, the degeneracy can be lifted with robust measurements up the 3rd order in b. In practice, solution selection based on noisy data remains challenging and should be validated independently.

The approach of Reisert et al. [65] relies on machine learning to estimate the model parameters. A choice of plausible parameter values is made using insight from isotropic diffusion weighting results, as will be discussed in Validating Microstructural Features. This method also allows renouncing to the determination of specific parameters of the model when data proves insufficient.

The remaining assumptions behind these two methods are: the existence of only two compartments (intra- and extra-axonal), the consistency of kernel parameters across all fascicles in the voxel (e.g., all axons in the voxel have the same diffusivity $D_{\text{a},\parallel}$), and axial symmetry of the elementary fiber response (kernel).

By contrast to these two approaches, the method described by Kaden et al. [66] based on the spherical mean technique is similar in spirit, in the sense that it factors out the fiber ODF, but it only exploits the lowest order rotational invariant and the estimation of the scalar kernel is constrained by $D_{\text{a},\parallel} = D_{\text{e},\parallel}$ and by the tortuosity approximation for the extra-axonal space (Equation 6).

DBSI

Another model was proposed with the intent of covering regions of multiple fiber crossings; this model is DBSI (Diffusion Basis Spectrum Imaging) [67], and its general formulation is the following:

$$\begin{aligned}S_{\mathbf{g}}(b) = {} & \sum_{i=1}^{N_{\text{Aniso}}} f_i \cdot e^{-bD_{\parallel,\text{i}}(\mathbf{g}\cdot\mathbf{n_i})^2 - bD_{\perp,\text{i}}(1-(\mathbf{g}\cdot\mathbf{n_i})^2)} \\ & + \int_{\alpha}^{\beta} f(D) e^{-bD} dD\end{aligned} \tag{15}$$

where the tissue is described as a collection of N_{Aniso} axially symmetric anisotropic tensors (each with unknown fraction f_{i}, axial and radial diffusivities $D_{\parallel,\text{i}}$ and $D_{\perp,\text{i}}$ and orientation $\mathbf{n}_{\text{i}}$) and a continuous spectrum $f(D)$ of isotropic diffusion tensors. The anisotropic tensors represent water inside and just outside myelinated and unmyelinated axons of varied directions, while the continuum of isotropic tensors represents water in cells, sub-cellular structures, and edematous water.

The DBSI fitting procedure is complex and details can be found in Wang et al. [67]. Briefly, it is a two-step process where first the number of anisotropic tensors and their principal orientations are estimated. These parameters are then fixed in the second step of the procedure, which aims at estimating f_{i}, $D_{\parallel,\text{i}}$, and $D_{\perp,\text{i}}$ for each anisotropic tensor, as well as f(D). This is achieved by optimizing f_{i} and f(D) for recursively chosen combinations of $D_{\parallel,\text{i}}$ and $D_{\perp,\text{i}}$ and finally selecting the combination providing a global minimum.

DBSI has been applied to a variety of pathologies [68–72], but has not been extensively validated outside of the originating group. Given the unfavorable fitting landscape in a comparatively much simpler model such as NODDIDA [49], especially in the presence of limited signal-to-noise ratio (SNR) (**Figure 2**), the reliability of DBSI model estimates remains to be clarified.

Moreover, the biophysical interpretation of the continuous distribution of diffusion coefficients $f(D)$ is also problematic, as explained in connection with Equation (3).

Hybrid Models

Hybrid models are based on a combination of biophysical modeling and signal representations.

Free Water Elimination (FWE)

The motivation of the free water elimination technique is to separate CSF contamination from "brain tissue" diffusion properties. The overall signal is separated into an isotropic component of free diffusion (D_{free}) and a single diffusion tensor representing the rest of the tissue signal (D_{tissue}). This approach was first proposed by Pierpaoli and Jones [73] using a comprehensive q-space acquisition (107 directions over 8 shells, $b_{\max} = 1.2$ ms/μm^2). Its potential advantages are the extraction of a free water map (as a new biomarker), improved tissue tensor estimation, and benefits for fiber tracking. The direct correspondence between "free water" and CSF is however not straightforward.

Its application was further extended to single-shell DTI data by Pasternak et al. [74]. Naturally, estimating a system which includes a tensor and an isotropic compartment from single-shell data is an underdetermined problem. To circumvent this issue, Pasternak and colleagues initially imposed additional constraints: spatial regularization and tighter upper and lower bounds on the tissue volume fraction, dependent on tissue diffusivities. This constrained implementation has been applied to a variety of conditions [75–78].

While the intention of making the method applicable to the most widespread acquisition scheme (i.e., single shell) is understandable, the ill-posed nature of the mathematical problem and the issue of constraints has been recognized by the authors, who proposed incorporation of an additional low b-value shell for accuracy and stability [79]. The initial, more conventional, multi-shell approach proposed by Pierpaoli and Jones has also been reintroduced in parallel by Hoy et al. [80]. The latter work included simulations showing that in the absence of a CSF compartment, fitting the FWE model indeed overestimated tissue FA. Later work by the same group compared the FWE technique to the more standard FLAIR-DTI approach where the CSF signal was directly suppressed at the acquisition stage [81, 82]. They reported similar performance between the two techniques in WM tracts where CSF contamination was expected to be high (i.e., fornix and corpus callosum), but unlike FLAIR-DTI, the FWE technique resulted in greater FA and reduced diffusivity measures even in tissues without CSF partial volume effects (e.g., cingulum). The proposed explanation that the "free water" signal arises from the extracellular space [79] highlights the complications of assigning a single tensor to a "tissue" compartment which is known to exhibit non-Gaussian behavior.

DIAMOND

A new hybrid model, termed DIAMOND (DIstribution of 3D Anisotropic MicrOstructural eNvironments in Diffusion-compartment imaging) [83] has recently been proposed. It expands on the concept of distribution of diffusion coefficients introduced by Yablonskiy et al. [20], by accounting for several discrete compartments (biophysical modeling), each withholding a continuous distribution of diffusion tensors (statistical modeling). In mathematical terms:

$$S_{\mathbf{g}}(b) = S_0 \sum_{i=1}^{N_p} f_i \cdot \int_{\mathbf{D}\in Sym^+(3)} P_{\kappa_i,\Sigma_i}(\mathbf{D})\, e^{-b\mathbf{g}^T\mathbf{D}\mathbf{g}} d\mathbf{D} \qquad (16)$$

where N_{p} is the number of compartments (or spin populations), each with its associated volume fraction, and $P_{\kappa_i,\Sigma_i}(\mathbf{D})$ is the distribution of diffusion tensors within the compartment, chosen to be a multi-variate Gamma distribution of shape parameter κ and scale parameter Σ. The diffusion tensors are symmetric positive definite matrices [Sym$^+$(3)].

Starting from the generic expression in Equation (16), three types of particular compartments are considered and their presence in each voxel is evaluated using model selection techniques. The three types of compartments are free isotropic (attributed to CSF), restricted isotropic (attributed to water in glial cells) and water in and around white matter fascicles.

In practice, DIAMOND uses an iterative approach in defining the number of compartments in each voxel. The optimization begins with a freely-diffusing compartment and zero fascicles, and the number of fascicles is gradually increased up to three—the higher complexity is retained only if the general error of the model is significantly reduced compared to the previous simpler model. Spatial regularization of voxel parameters is also used. While the goodness of fit has been extensively used in the past to choose which model is most appropriate for describing the data [84, 85], recent insights into the topology of the fitting landscape for a two-compartment model (**Figure 2**) advises against relying solely on such metrics for model selection [49, 50].

As an extension of the concept of continuous distribution of diffusion coefficients (Equation 3), DIAMOND also inherits from its associated issues, discussed in the section on Signal Representations.

Microstructure metrics estimated using DIAMOND will need to be subjected to substantial validation studies in the near future. Recent work on traumatic brain injury in the mouse suggests that DIAMOND, as any higher order model, is more sensitive than DTI in detecting differences, but a more thorough validation of specificity against histology remains to be performed [86].

Summary

Main approaches for deriving quantities from the diffusion weighted signal include signal representations (also known as statistical models), biophysical models of white matter, and hybrid models that contain features of both approaches. **Table 1** summarizes the properties of each of these approaches. Essentially, single-shell diffusion MRI data only enables the estimation of a single diffusion tensor for the voxel, i.e., DTI. Any other more complex analysis that accounts for non-Gaussian diffusion effects in the tissue requires at least two non-zero b-shells, each with sampling along a minimum number of directions.

Biophysical models come with the promise of characterizing tissue microstructure with improved specificity. However, their intrinsic assumptions have the potential to introduce bias.

TABLE 1 | Summary of method characteristics.

	Method	Minimum/typical data requirements	Estimated metrics	Assumptions/constraints
Statistical models	DTI	1 $b = 0$; 6 $b = 1$	Diffusion tensor (and derived FA, MD, AD, RD)	None
	DKI	1 $b = 0$; 6 $b = 1$; 15 $b = 2$	Same as DTI + kurtosis tensor (and derived MK, AK, RK)	None
Biophysical models	NODDI	1 $b = 0$; 30 $b = 0.7$; 60 $b = 2$	f_{intra}, f_{iso}, κ	$D_{a,\parallel} = D_{e,\parallel} = 1.7$ $D_{e,\perp} = (1- f_{intra})D_{e,\parallel}$ $D_{iso} = 3$
	WMTI	1 $b = 0$; 6 $b = 1$; 15 $b = 2$	f_{intra}, $D_{a,\parallel}$, $D_{e,\parallel}$, $D_{e,\perp}$	Limited dispersion $f_{iso} = 0$ $D_{a,\parallel} \leq D_{e,\parallel}$
	LEMONADE / RotInv	1 $b = 0$; minimum 3 non-zero shells with e.g., 64 dirs per shell	f_{intra}, $D_{a,\parallel}$, $D_{e,\parallel}$, $D_{e,\perp}$ SH up to 6th order for ODF	$f_{iso} = 0$
	Reisert et al. [65]	2 non-zero shells or uniform filling of q-space	f_{intra}, f_{iso}, $D_{a,\parallel}$, $D_{e,\parallel}$, $D_{e,\perp}$	Some parameters will not be estimated if insufficient data
	DBSI	99 directions over 9 b-shells, $b_{max} = 1$	Number of anisotropic tensors N and their respective f_i, $\lambda_{\parallel,i}$ and $\lambda_{\perp,i}$, + isotropic tensor distribution f(D)	Two-step fitting process, with some parameters temporarily fixed
Hybrid models	FWE	1 $b = 0$; 32 $b = 0.5$; 32 $b = 1.5$	f_{iso} + tissue diffusion tensor	$D_{iso} = 3$ Tissue described by a tensor
	DIAMOND	"CUSP90": 12 $b = 0$; 6 $b = 0.4$; 6 $b = 0.6$; 6 $b = 0.8$; 30 $b = 1$ + 30 directions on a cube ($1 \leq b \leq 3$)	f_{iso}, number of fascicles (up to 3) and their respective f_i, κ_i and Σ_i	Iterative fitting for number of compartments; Spatial regularization; mv-Γ distribution of tensors within compartment

b-values are in ms/μm^2 and diffusivities in μm^2/ms.

Nearly all models outperform DTI in capturing tissue diffusion properties, but this is a very low benchmark. Biophysical models need to be increasingly compared to one another, and to higher order signal representations such as DKI, to understand convergent model properties likely to be successful in broad applications [57, 65, 87, 88]. Their reliability in the case of pathological tissue also needs thorough investigation.

VALIDATING DIFFUSION MODELS

Most biophysical diffusion models share at least partial similarity with one another with respect to their common geometry, as represented in **Figure 1**. This section will review validation efforts for each of the model features (compartment volume fractions, axon orientation dispersion, and compartment diffusivities). While many validation studies have been performed for DTI, the goal is to emphasize results in the context of biophysical models and how well their derived parameters reflect the true biology of interest. The first two sub-sections focus on method validation using either computer simulations or phantoms, while the following ones discuss the validation of quantitative estimates for each microstructural feature of white matter.

Computational Simulations

Simulating the random walk of diffusing spins within simple or complex environments is often the first step to establish a connection between derived estimates of physical features and their ground truth values. Simulations have been used where analytic solutions are difficult or impossible, and their use is so common that it is impossible to list them here. Notable examples are those that have also released accompanying software packages [89–92]. Synthetic geometries, which are typically composed of cylindrical axons, have been used to model the effects of axon diameter, packing, volume fractions, permeability, and other features that can be easily modulated synthetically, and these have in turn been performed under many different simulated experimental conditions such as modulation of diffusion times, gradient waveform shapes, signal to noise ratios, and other features that would be difficult or time-consuming to perform experimentally. As the diffusion models have evolved to include more complex features such as bending, crossing, and asymmetric fiber orientations, simulations have followed suit and implemented similar physical features. In addition to purely fiber models, other notable examples include complex axonal geometries to demonstrate the effects of swelling [93], beading [94], undulation [95], and other features. Geometrical substrates derived from tissue specimens [96] have been also demonstrated recently, although these remain challenging due to the difficulties in obtaining high-resolution, 3D images of tissues and their subsequent conversion to physical substrates. As 3D microscopy and connectomic techniques push for high resolution and large-scale imaging of brain tissues at microscopic resolutions, parallel advances in relating diffusion indices with more realistic models will likely follow. Importantly, the fidelity of the simulation geometry to the true underlying biology is a major concern. To the extent possible, these should encompass realistic and accurate distributions of axon diameters consistent with histological reports, random packing as opposed to a regular

lattice, and other physical features that have been validated in tissue preparations. Although geometrical models are simplistic, simulations ensure that the estimated parameters are at least accurate and precise with respect to known ground truth features, and if this criteria is not met, acceptable performance in real tissues is likely compromised.

Phantoms

Ground truth hardware phantoms have been developed to estimate relevant parameters and calibrate multi-center studies. Ideally, phantoms mimicking WM structure possess certain desirable qualities most notably being tubular hollow structures with diameters approximating those of axons. Another desirable feature is to organize axon-like structures in different configurations that mimic complex features such as dispersed and crossing fibers. Intrinsic diffusivity of the filling material may also be considered, as well as magnetic susceptibility of the scaffolding material. Vegetables with tubular structures or domains, such as celery, asparagus, and chives, have been routinely used to demonstrate the effects of anisotropic diffusion, but these substances are clearly not amenable to long-term or cross-center studies, and phantoms with high consistency and longevity were sought. Most hardware phantoms have so far been developed for the purpose of optimizing DTI acquisitions or validating tractography rather than microstructure models. Textile fiber phantoms were developed with the scope of easily mimicking bending or dispersed fibers but their diameters typically far exceed the range of axons and they are of course not hollow [97]. Microcapillaries have the advantage of producing both an intra-axonal and an extra-axonal space to be filled [98–100], and most recent designs display somewhat more realistic diameters between 9 and 20 microns [101]. However, while crossing bundles can be designed, within each bundle the capillaries are highly aligned, which is a limitation for modeling true white matter.

Two types of phantoms have so far been developed for the purpose of validating higher order diffusion models. Fieremans et al. proposed a phantom of tightly packed solid fibers of Dyneema and compared the measured signal to simulations for diffusion, kurtosis and time dependence [102–104]. While it used reasonable diameters (20 μm) the drawback was that it only modeled the extra-axonal space. Better magnetic susceptibility matching between water and the Dyneema material can be achieved using magnesium chloride [105]. A complementary phantom design of the intra-axonal space has recently been proposed using co-electrospun fibers that produce a hollow honeycomb-like arrangement and a distribution of diameters of about 9.5 μm [106]. The ideal phantom for diffusion microstructure model validation would mimic both intra- and extra-axonal water with diameters matching those of white matter axons, randomly packed to appropriate volume fractions, and orientation dispersion. Clearly, it is challenging to meet all of these conditions simultaneously.

The advantages of phantoms are well recognized and aim to be standardized instruments for calibration of MRI experiments and assessments of multi-site variability. The disadvantages include sophisticated chemistry, limited availability to materials and specialized equipment, and non-standardization. Despite these current limitations, the role of consistent and widely-accepted phantoms has been well-recognized [107]. With the push for reproducibility and precision medicine, physical phantoms will continue to emerge as a solution to multi-center and multi-vendor diffusion MRI data acquisition and modeling.

Validating Microstructural Features

Fiber Orientation and Dispersion

Diffusion MRI and its associated models offer the unique ability to track fiber pathways non-invasively. Diffusion tractography has been widely used in research settings to probe structural connectivity in health and disease and has seen success in clinical scenarios. Most notably, tractography has been used to identify fiber pathways during tumor resection [108] or other neurosurgical applications [109]. Tractography is based on the coherence in fiber orientation between adjacent voxels and is therefore fundamentally based on the accuracy of the estimated fiber orientation within each voxel. Validation efforts to demonstrate the accuracy of diffusion MRI have typically focused on applications to tractography, but these findings are also pertinent to microstructural modeling to derive local (i.e., voxel level) estimates of fiber orientations and dispersion. While the diffusion tensor models a single fiber orientation within each voxel, several methods have been developed to provide

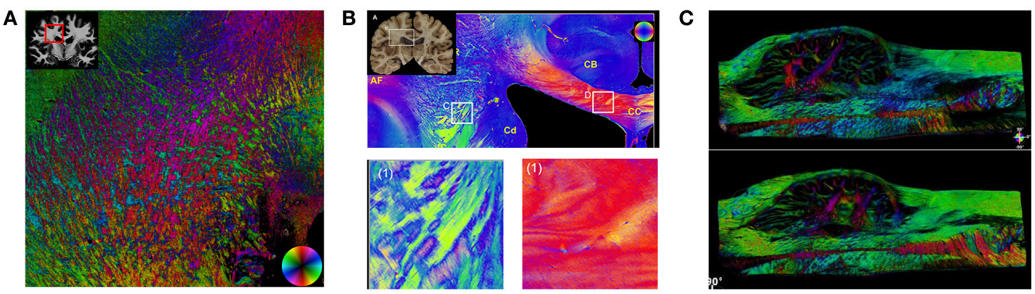

FIGURE 3 | Fiber Orientation Measurements in Fixed Tissues. Examples of fiber orientation measurements in human brain specimens. Structure tensor analysis **(A)** uses a digital texture analysis method to detect fiber orientations in stained sections imaged with bright-field or fluorescence microscopy. Both polarized light imaging **(B)** and polarization-sensitive optical coherence tomography **(C)** exploit the intrinsic birefringence of myelin to obtain fiber orientations. Sections in **(A)** [114] and **(B)** [115] (reproduced under the Creative Commons Attribution License) are from the human brain white matter, and **(C)** [116] from the human medulla oblongata (with permission).

a comprehensive estimate of the number and distribution of fiber orientations within each voxel [64, 110], each with their own implications for tractography. Although, they have potential applications to tractography [111–113], diffusion MRI microstructural models aim to estimate intra-voxel orientation dispersion as its own unique feature to reveal interesting characteristics of the healthy, developing, or diseased brain.

Validating the intravoxel fiber dispersion, or ODF, is typically accomplished through imaging of the tissues using light microscopy or similar modalities and deriving quantities reflecting the neurite orientations (**Figure 3**). Thus, there is a more direct relationship between diffusion MRI quantities and those measured from histological samples than for volume fractions (see following section) because fiber orientations are largely unaffected by fixation and can be reliably measured in tissues with relative ease. Among the first examples to conduct direct validation studies, manual segmentation of axons in stained tissue white matter sections were compared to DTI and Diffusion Spectrum Imaging (DSI) estimates [117]. A variety of automated image processing techniques have been used to derive the angular orientation profiles of stained tissues, permitting large-scale automated analysis of tissue specimens [118–127]. These methods generally fall into classes of algorithms that use pattern-matching, Fourier analysis, or edge detection. Pattern matching attempts to identify discrete fibers within the image to build a full distribution of fiber dispersion. On the other hand, Fourier analysis and structure tensor analysis instead use the texture of the images to derive angular profiles of edges or spectral content. Structure tensor analysis has been particularly attractive since its interpretation is analogous to the diffusion tensor. Typically, the histological specimens were limited by two-dimensional samples, but the structure tensor analysis has also been extended to 3D sections using confocal imaging [128, 129]. Collectively, the results from these studies all demonstrate a consistent and expected finding that while DTI fails to capture the full complexity of the underlying fiber orientation distributions, diffusion models that include dispersion as a feature better reflect the underlying structures. However, most studies thus far have validated orientation in tractography-driven approaches that focus solely on retrieving orientation without regard for diffusivities and volume fractions and do not fall into the category of microstructure models.

Stained histological sections for validation have several disadvantages and potential complications and confounds. Tissue processing and cutting can lead to distortion or artifacts, and histological staining may also be complicated by staining irregularity or artifacts. Moreover, sectioning, staining, and imaging large volumes at high magnification is very time consuming [130]. Although the brains and spinal cords of small animals can be captured with most laboratory microscopes, imaging large-scale tissues at high resolution such as human brain slices may require custom equipment and high-performance computing. Advances in large-scale microscopic imaging of fixed tissues have circumvented some of the issues with traditional sectioning and staining by using blockface imaging and intrinsic contrasts. Myelin exhibits the property of birefringence [131] which permits imaging of fiber architecture in fixed but unstained tissue sections. Somewhat analogous to diffusion encoding, rotating the polarization angle along different directions enables the estimation of fiber orientations in both 2D and 3D to examine human brain sections in their entirety [115, 132, 133]. Blockface microscopy, which consists of repeated imaging of the exposed surface of a tissue cut using serial sectioning, has also emerged as a powerful tool for large-scale imaging. Notably, compared to traditional sectioning, blockface imaging reduces distortions and the full process can be automated [116, 134, 135]. Modalities such as two-photon microscopy [136] or optical coherence tomography [137, 138] also image up to tens of microns below the surface and can provide contiguous 3D images of large tissue. Many of the whole-specimen imaging techniques developed for local neuron connectomic studies [139–141] have demonstrated utility when coupled with diffusion MRI [142].

Direct histological examination with microscopy has consistently demonstrated that white matter tracts are not strictly composed of uniform bundles. Even in the corpus callosum, an intravoxel dispersion of ∼18–20 degrees is consistently evident from rodent [117], and human samples [118, 143]. In the gray matter, Jespersen et al. demonstrated strong agreement between the estimated neurite orientation distributions and histological staining [144].

Volume Fractions or Neurite Density

The ability of diffusion MRI to monitor axon content in the brain and spinal cord has demonstrated wide ranging utility in a variety of applications across normal development, aging, injury, and disease. Unlike fiber orientation, which is generally preserved in fixed tissues, the relative volume fractions are perturbed during fixation and processing which has made non-MR measurements somewhat biased and inconsistent. It is important to first distinguish the true physical cellular fractions obtained from microscopy or other non-MRI methods from those reported from diffusion MRI models. In the brain, the extracellular volume fraction is typically around 20% [145], but traditional tissue fixation and processing artificially reduces this to ∼2–5% [146]. In white matter, the axoplasm constitutes ∼25–30% of the physical space in white matter tissues [147], myelin constitutes ∼20–30% [147, 148], and glial cell bodies and processes constitute ∼30–40% [147]. Recent extracellular space-preserving methods of fixation support the approximation of 15–20% extracellular space [149] and indicate that axonal volumes are relatively unaffected by the method of fixation [150]. In typical diffusion MRI experiments, the signal from water associated with myelin has a negligible contribution to the overall signal due to its short T_2 and is therefore routinely ignored in diffusion models. Diffusion MRI measures of compartment signal fractions are commonly referred to as neurite density or axonal volume fraction. Since density implies axonal counts and axonal volume fraction is ambiguous due to the myelin volume fraction, the term axonal water fraction (AWF) is a more precise terminology. Thus, derived from physical measurements alone, the AWF in healthy WM should be ∼33% [147, 148]. However, to further complicate things, the relative fractions of the remaining

"MR-visible" compartments are also weighted by their respective T_2's.

Several studies have compared MR-derived axon water fractions with direct histologic preparations of the same samples. Estimates of the intra-axonal volume fractions from DWI models consistently emerge around 40–60% [38, 151], which is generally in line with histologic estimates although slightly higher than estimated from microscopy [152]. Jespersen et al. demonstrated agreement between neurite density estimates from DWI and quantitative microscopy, notably using both *ex vivo* DWI and histology [38, 61], and others have shown similarly strong relationships [153], although lower fractions have been noted in some samples [154]. Correlations (or absence thereof) between diffusion-derived and electron microscopy (EM)-derived metrics have also helped further establish the selective sensitivity of biomarkers derived from diffusion modeling to different features. For example, using WMTI, AWF has been shown to correlate with axon volume fraction but not with the *g*-ratio derived from EM, while $D_{e,\perp}$ correlated with the *g*-ratio but not the with axon volume fraction [56]. Measures of AWF have also been combined with MRI measures of myelin content to estimate myelin g-ratio *in vivo*, which compared favorably to that derived from EM [155, 156]. However, a strong correlation is not necessarily proof of parameter specificity. Notably, axon fractions derived from microscopy typically correlate very strongly with radial diffusivity (RD) derived from the diffusion tensor [61].

Compartment-Specific Diffusivities

Diffusivities of the various modeled cellular compartments are both critical features that form the basis for diffusion models, and have been arguably the most difficult to validate. Alternative methods to NMR for measuring the self-diffusion coefficient of water are not available, and NMR-based measurements include signals from all compartments. In order to circumvent this issue and gain information about compartment-specific diffusivities, alternative approaches have been proposed: the use of model systems, endogenous compartment-specific metabolites, exogenous compartment-specific probes and tracers, signal suppression in a given compartment, exploiting alternative encoding methods, analyzing time-dependent properties, and combining diffusion methods with other contrasts (T_2). Early studies examined compartment-specific diffusivities to glean insight into the nature of diffusion in the nervous system, with a particular focus on the biophysical basis of changes in cerebral ischemia. More recently, as highlighted in Part 1, a two-compartment model of diffusion shows a degeneracy that only an independent determination of compartment diffusivities can lift.

Model systems using invertebrates with large axons were first used to identify the source of anisotropy in the nervous system [157], demonstrating that biological membranes were the primary determinants of diffusion restriction/hindrance. These studies measured the intrinsic intra-axonal diffusivity, demonstrating it was ∼70–80% that of pure water [158, 159]. Hence, these studies set the stage showing that intra-axonal diffusion was largely unrestricted along the axon, and the axonal membrane serves as a considerable barrier to diffusion perpendicular to the fibers.

Endogenous MRI-detectable tracers to assess diffusion primarily include metabolites detected through proton magnetic resonance spectroscopy (MRS). These include NAA, creatine, choline, and myo-inositol. NAA is a neuronal-specific metabolite and a surrogate marker of the intra-axonal space in white matter. Although, the neuronal specificity of NAA has recently been called into question since it was found to be also localized in myelin [160], the influence of myelin-associated NAA on the MR signal remains unclear and diffusion of NAA has so far been used to probe intra-axonal diffusion. Kroenke et al. [37] performed diffusion-weighted MRS in the human corpus callosum and rat brain, demonstrating that *in vivo* the $D_{a,\parallel}$ of NAA was ∼50% (0.36 μm^2/ms) of that of an aqueous solution and $D_{a,\perp}$ was effectively zero. Similar results were shown for NAA in the human brain and in a peripheral nerve preparation [161, 162]. Ronen et al. [143], accounting for both the macro- and microscopic curvature of the human corpus callosum, measured a slightly larger $D_{a,\parallel}$ (0.51 μm^2/ms) putting it in the range of 60–70% of aqueous NAA. Palombo et al. [163] have also demonstrated diffusion of NAA and other metabolites can be modeled as occurring in long, cylindrical fibers, having a $D_{a,\parallel}$ of 0.33 μm^2/ms. The diffusion weighted signals of other metabolites were also fit well by assuming long cylindrical processes [163–165]. Since metabolites have differences in molecular size, affinity to charged surfaces, and potential ambiguity in compartment selectivity, the intra-axonal diffusivity of water cannot be unequivocally extrapolated from metabolite diffusivities. However, these studies and those in experimental preparations are consistent with the intra-axonal water diffusivity being 60–80% of its temperature-matched aqueous diffusivity.

Exogenous MRI-detectable tracers, most notably injectable agents used in animal models, have also been used to probe the diffusivity of specific environments. Non-proton probes have been used to selectively probe either the extracellular space (sodium-based [166]), the intracellular space (cesium-based [167]) or each of them separately (fluorine-based [168]). The diffusivity of extracellular proton-based agents such as mannitol, phenylphosphonate, and polyethylene glycols has also been investigated using diffusion spectroscopy [169]. Often though, the compartment specificity is not perfect and transmembrane exchange is a complicating factor [170]. Nonetheless, using these approaches, it has been suggested that the diffusivities in the intra- and extracellular environments for molecules of these sizes are approximately similar to one another. It should be noted though that these measurements were typically limited to the apparent diffusion coefficient (ADC) in rat gray matter, and should rather be interpreted as: the traces of the diffusion tensors in the intra- and extracellular environments are approximately similar to one another.

Compartment selectivity can be also achieved by suppressing the extracellular water signal using exogenous tracers. Intracerebroventricular infusion of a gadolinium-based contrast agent causes the T_2 of the extracellular space to decrease,

effectively suppressing its contribution during signal acquisition. Following measurements in the rat gray matter, Silva et al. reported similar ADCs with and without the suppression, which supports the idea of comparable diffusion traces in the intra- and extracellular environments for water molecules as well [171]. Recently, this experiment was replicated in the rat corpus callosum in a direction-specific manner and concluded that $D_{a,\parallel} \geq D_{e,\parallel}$ [172].

Non contrast-based alternatives using non-conventional diffusion encoding have also provided insight into how axial compartment diffusivities compare. A double diffusion encoding (DDE) sequence was recently used to exploit $D_{a,\perp} = 0$ and suppress the extra-axonal signal using a strong initial diffusion gradient perpendicular to the spinal cord, with the results suggesting $D_{a,\parallel} \approx D_{e,\parallel}$ [173]. Isotropic diffusion weighting has been used by two independent groups to show that isotropic kurtosis is negligible in most brain structures, including white matter tracts [174, 175], whereby the traces of the intra- and extra-axonal compartments were similar. This recurrent observation implied the $D_{a,\parallel} \geq D_{e,\parallel}$ solution of the two-compartment model was valid. Most recently, Jespersen et al. have shown also that the time-dependence for compartment-specific diffusivities in a Watson-WMTI model is physically acceptable only for $D_{a,\parallel} \geq D_{e,\parallel}$, albeit in fixed rat spinal cord [59]. The inclusion of compartment T_2's in the LEMONADE model also suggested likewise [176]. Thus, evidence from a variety of experiments has generally favored $D_{a,\parallel} \geq D_{e,\parallel}$, although true independent validation is still lacking.

Validation of Model Parameter Choices

The choice and accuracy of diffusion model parameters can be gleaned from these validation studies. The first observation is that, for clinical diffusion times, the long-time limit applies and intra-axonal diffusion perpendicular to a single fiber ($D_{a,\perp}$) is effectively zero: thus the "stick" model of axons is generally appropriate for axon diameters in the central nervous system, as has also been demonstrated recently [177]. Second, under this stick model assumption, the orientations of fibers examined histologically are reasonably well-approximated by diffusion models that account for dispersion or crossing-fibers, but it should be noted that most of these studies have not jointly considered dispersion along with simultaneous estimates of other microstructural properties. Third, the intra-axonal parallel diffusivity ($D_{a,\parallel}$) is ∼60–80% of the temperature-matched aqueous solution of the same molecule (D_{free}). Fourth, in the healthy white matter, the intra-axonal parallel diffusivity $D_{a,\parallel}$ is likely faster than the extra-axonal diffusivity $D_{e,\parallel}$, although not substantially.

PARAMETER CHOICE IN THE INJURED AND DISEASED WHITE MATTER

In the healthy white matter, diffusion models have converged to a relatively uniform set of parameters as described previously, which has been proposed as the universal model of white matter diffusion. To avoid model overfitting, each of the biophysical model variants neglects, constrains, or holds fixed certain parameters while leaving others free to fit to the data. Importantly, while these constraints have nuanced effects in the healthy brain and spinal cord, there is still considerable disparity and disagreement about the necessary and relevant model parameters in the injured or diseased brain. A complication arises in which the pathologies of different injuries or diseases may be different from one another and are likely to evolve over time and therefore, since there is no consistent pathology, there is unlikely to be a diffusion model that universally captures it. Moreover, while a specific pathology can lead to predictable diffusion MRI outcomes, many different pathologies can lead to the same diffusion behavior. Furthermore, single pathologies rarely occur in isolation. While the diffusion model parameters themselves are independent, there are often strong correlations between pairs of diffusion parameters and specific pathological features.

Diffusion MRI has been applied to nearly every brain and spinal cord disease or injury. DTI represents the overwhelming majority of studies related to validation, yet many investigators have conducted comprehensive studies to relate biophysical model parameters with the gold-standard techniques. While a comprehensive review of all of the different disease and injury categories is beyond the scope here, highlighting specific examples will shed light on the issues.

Cerebral Ischemia

The most common clinically useful application of diffusion MRI is in the detection of acute cerebral ischemia [178, 179]. Within minutes of the onset, diffusion within the infarct is decreased by approximately one half. Although the precise mechanism has been debated, it is closely related to the loss of membrane polarization, ion imbalance, and cell swelling characteristic of acute ischemia [180]. Compartment-specific tracer studies have indicated that the intracellular and extracellular compartments exhibit similar decreases in diffusion [168, 171], while others have shown that intracellular diffusivity decreases substantially while the extracellular diffusivity experiences a somewhat lesser decrease [167]. The extracellular decrease is consistent with a reduction in the extracellular space and increase in tortuosity that leads to decreased diffusivity in that compartment [33], while the intracellular decrease is consistent with neurite beading [94, 181]. Oscillating gradient measurements in the rat brain have demonstrated that restrictions caused by ischemia occur on the scale of several microns typical of cell sizes [182]. The reduced diffusion in stroke can also relate to a larger fraction of highly restricted diffusion [183, 184] which may be compatible with a still water compartment ($D_{iso} = 0$). Clearly, as the injured tissue degenerates, multiple coincident pathologies exist and the interpretation of diffusion MRI changes becomes increasingly more complex. For example, both NODDI and WMTI have been applied to acute human stroke, with contrasting results. WMTI demonstrated a large reduction in $D_{a,\parallel}$ in coherent fiber pathways, with lesser reductions in $D_{e,\parallel}$ (under the assumption $D_{a,\parallel} < D_{e,\parallel}$) consistent with neurite beading hypothesis [13]. On the other hand, NODDI applied to human stroke demonstrated

pronounced increases in the estimated orientation dispersion [42]. Although these differences may be related to the time after onset, animal models reveal almost no changes to neurite organization in the acute aftermath [185]. Thus, the model assumptions of NODDI of fixed diffusivities appear to cause misleading interpretations when those assumptions are strongly violated.

Demyelination and Myelin Disorders

Demyelination and other myelin disorders, despite having hallmark pathologies of myelin loss, degeneration, or dysfunction, also typically exhibit multiple overlapping pathologies. Particularly in the acute inflammatory phases of the disease or model, myelin pathologies are accompanied by microglia and astrocyte activation and proliferation [186], and axonal injury is also prominent in some models of multiple sclerosis or optic neuritis [187]. Thus, multiple confounding pathologies present significant challenges of both specificity and sensitivity in relation to diffusion models. A chemical model of demyelination induced through cuprizone toxicity has been used by many groups to validate diffusion and other MRI markers related to specific pathologies. Using the WMTI framework, Guglielmetti et al. [12] demonstrated a prominent reduction in $D_{a,\parallel}$ during the acute inflammatory phase, while a reduced AWF was observed throughout the remyelination and recovery period. Jelescu et al. [56] showed that the axonal fraction assessed with electron microscopy correlated with AWF derived from WMTI, while the g-ratio correlated with $D_{e,\perp}$. In a model of hypomyelination, Kelm et al. [58] demonstrated strong correlations between axonal fractions obtained from histology and MRI, again using WMTI, but no significant correlations between other WMTI parameters and histology measures were found. Using the DBSI framework, Wang et al. [67] demonstrated strong correlations between axial diffusivity (a DBSI parameter related to $D_{a,\parallel}$) and axon integrity, radial diffusivity (a parameter related to $D_{e,\perp}$), and myelinated axons, and cell ratio (a parameter related to D_{iso}) and histological cell counts, with similar findings reported in the experimental autoimmune encephalomyelitis [72] and optic neuritis [68] animal models. However, most disease models examined previously with DTI [188, 189] demonstrated strong associations between many of the microscopy measures and quantitative diffusion MRI measures, thus strong correlations are not an indicator of specificity. These studies highlight the challenges of diffusion MRI-based biomarkers since many different pathologies can give rise to similar diffusion signatures and separate pathologies rarely occur in isolation from one another. Moreover, it is worth reiterating that diffusion is an indirect marker of the entire water content of the voxel, and while high specificity is desired, the reliability, sensitivity, and clinical usefulness of these techniques will also be paramount.

SUMMARY

Diffusion MRI is uniquely sensitive to microscopic tissue features that are nearly impossible to achieve through other means. However, diffusion MRI is intrinsically limited since it is an indirect measure of tissue microstructure and relies on inferences from models and estimation of relevant parameters. A plethora of approaches have emerged. The biologically-inspired models have many similarities although each has different inherent assumptions and algorithms. Consequently, validating diffusion models and derived parameters is necessary to demonstrate accuracy, and has relied on various approaches. Simulations and phantoms have a role in demonstrating the accuracy and precision to a known ground truth and can identify sources of error and effects of violating the underlying assumptions. The predominant approach to validate diffusion MRI models is optical imaging of fixed tissue specimens since it offers a direct assessment of the physical features of the tissues and their true biological complexity. An increasing body of literature has demonstrated that diffusion models which account for intra-voxel fiber dispersion are generally good approximations to the underlying white matter fiber organization. Estimates of axonal volume fraction with diffusion MRI are also approximately consistent with histological measurements when accounting for potential bias of fixation and tissue processing. The intrinsic diffusivities of the intra- and extra-axonal compartments are more challenging to validate independently since they can only be measured using NMR itself, and alternative diffusion encodings seem promising in providing the sought validation. In the injured and diseased white matter, considerable ambiguity still exists in the choice of model parameters along with their imposed constraints. Critically, the range of possible pathologies is likely to be too complex to be accurately captured with a single universal model and avoid over-fitting. Validation studies will be important to establish disease and pathology specific applications. Ultimately, the goal of diffusion MRI modeling is to provide a clinically meaningful insight for diagnosis and treatment efficacy.

AUTHOR CONTRIBUTIONS

All authors listed have made a substantial, direct, and intellectual contribution to the work, and approved it for publication.

FUNDING

IJ acknowledges support from the Centre d'Imagerie Biomédicale (CIBM) of the University of Lausanne (UNIL), the Swiss Federal Institute of Technology Lausanne (EPFL), the University of Geneva (UniGe), the Centre Hospitalier Universitaire Vaudois (CHUV), the Hôpitaux Universitaires de Genève (HUG) and the Leenaards and the Jeantet Foundations. MDB acknowledges support from the Craig H. Neilsen Foundation (297024), the US Department of Veterans Affairs Rehabilitation Research and Development Service (Merit Review Award I01 RX001497), and the Bryon Riesch Paralysis Foundation.

REFERENCES

1. Novikov DS, Jespersen SN, Kiselev VG, Fieremans E. Quantifying brain microstructure with diffusion MRI: Theory and parameter estimation. *arXiv:1612.02059 [physics.bio-ph]* (2016a).
2. Jensen JH, Helpern JA, Ramani A, Lu H, Kaczynski K. Diffusional kurtosis imaging: the quantification of non-gaussian water diffusion by means of magnetic resonance imaging. *Magn Reson Med.* (2005) **53**:1432–40. doi: 10.1002/mrm.20508
3. Kiselev VG. The cumulant expansion: an overarching mathematical framework for understanding diffusion NMR. In: Jones, DK, editor. *Diffusion MRI: Theory, Methods, and Applications*. Oxford: Oxford University Press (2010), p. 152–68.
4. Van Kampen NG. *Stochastic Processes in Physics and Chemistry*. 3rd edn. North Holland, North Holland (2007).
5. Basser PJ, Mattiello J, LeBihan D. Estimation of the effective self-diffusion tensor from the NMR spin echo. *J Magn Reson B.* (1994) **103**:247–54. doi: 10.1006/jmrb.1994.1037
6. Jones DK. Precision and accuracy in diffusion tensor magnetic resonance imaging. *Top Magn Reson Imaging* (2010) **21**:87–99. doi: 10.1097/RMR.0b013e31821e56ac
7. Veraart J, Sijbers J, Sunaert S, Leemans A, Jeurissen B. Weighted linear least squares estimation of diffusion MRI parameters: strengths, limitations, and pitfalls. *Neuroimage* (2013) **81**:335–46. doi: 10.1016/j.neuroimage.2013.05.028
8. Veraart J, Poot DH, Van Hecke W, Blockx I, Van der Linden A, Verhoye M, et al. More accurate estimation of diffusion tensor parameters using diffusion Kurtosis imaging. *Magn Reson Med.* (2011) **65**:138–45. doi: 10.1002/mrm.22603
9. Kiselev VG. Fundamentals of diffusion MRI physics. *NMR Biomed.* (2017) **30**:e3602. doi: 10.1002/nbm.3602
10. Mori S (editor). Chapter 11: Application studies. In: *Introduction to Diffusion Tensor Imaging*. Amsterdam: Elsevier Science B.V (2007), p. 149–61.
11. Van Hecke W, Emsell L, Sunaert S. *Diffusion Tensor Imaging - A Practical Handbook*. 1st ed. New York, NY: Springer-Verlag (2016).
12. Guglielmetti C, Veraart J, Roelant E, Mai Z, Daans J, Van Audekerke J, et al. Diffusion kurtosis imaging probes cortical alterations and white matter pathology following cuprizone induced demyelination and spontaneous remyelination. *Neuroimage* (2016) **125**:363–77. doi: 10.1016/j.neuroimage.2015.10.052
13. Hui ES, Fieremans E, Jensen JH, Tabesh A, Feng W, Bonilha L, et al. Stroke assessment with diffusional kurtosis imaging. *Stroke* (2012) **43**:2968–73. doi: 10.1161/STROKEAHA.112.657742
14. Jensen JH, Helpern JA. MRI quantification of non-Gaussian water diffusion by kurtosis analysis. *NMR Biomed.* (2010) **23**:698–710. doi: 10.1002/nbm.1518
15. Kochunov P, Rowland LM, Fieremans E, Veraart J, Jahanshad N, Eskandar G, et al. Diffusion-weighted imaging uncovers likely sources of processing-speed deficits in schizophrenia. *Proc Natl Acad Sci USA.* (2016) **113**:13504–9. doi: 10.1073/pnas.1608246113
16. Paydar A, Fieremans E, Nwankwo JI, Lazar M, Sheth HD, Adisetiyo V, et al. Diffusional kurtosis imaging of the developing brain. *AJNR Am J Neuroradiol.* (2014) **35**:808–14. doi: 10.3174/ajnr.A3764
17. Rosenkrantz AB, Padhani AR, Chenevert TL, Koh DM, De Keyzer F, Taouli B, et al. Body diffusion kurtosis imaging: basic principles, applications, and considerations for clinical practice. *J Magn Reson Imaging* (2015) **42**:1190–1202. doi: 10.1002/jmri.24985
18. Hansen B, Lund TE, Sangill R, Jespersen SN. Experimentally and computationally fast method for estimation of a mean kurtosis. *Magn Reson Med.* (2013) **69**:1754–60. doi: 10.1002/mrm.24743
19. Hansen B, Shemesh N, Jespersen SN. Fast imaging of mean, axial and radial diffusion kurtosis. *Neuroimage* (2016) **142**:381–93. doi: 10.1016/j.neuroimage.2016.08.022
20. Yablonskiy DA, Bretthorst GL, Ackerman JJ. Statistical model for diffusion attenuated MR signal. *Magn Reson Med.* (2003) **50**, 664–9. doi: 10.1002/mrm.10578
21. Grinberg F, Farrher E, Ciobanu L, Geffroy F, Le Bihan D, Shah NJ. Non-Gaussian diffusion imaging for enhanced contrast of brain tissue affected by ischemic stroke. *PLoS ONE* (2014) **9**:e89225. doi: 10.1371/journal.pone.0089225
22. Novikov DS, Kiselev VG. Effective medium theory of a diffusion-weighted signal. *NMR Biomed.* (2010) **23**:682–97. doi: 10.1002/nbm.1584
23. Bennett KM, Schmainda KM, Bennett RT, Rowe DB, Lu H, Hyde JS. Characterization of continuously distributed cortical water diffusion rates with a stretched-exponential model. *Magn Reson Med.* (2003) **50**:727–34. doi: 10.1002/mrm.10581
24. Ingo C, Magin RL, Colon-Perez L, Triplett W, Mareci TH. On random walks and entropy in diffusion-weighted magnetic resonance imaging studies of neural tissue. *Magn Reson Med.* (2014) **71**:617–27. doi: 10.1002/mrm.24706
25. Palombo M, Gabrielli A, De Santis S, Cametti C, Ruocco G, Capuani S. Spatio-temporal anomalous diffusion in heterogeneous media by nuclear magnetic resonance. *J Chem Phys.* (2011) **135**:034504. doi: 10.1063/1.3610367
26. Zhou XJ, Gao Q, Abdullah O, Magin RL. Studies of anomalous diffusion in the human brain using fractional order calculus. *Magn Reson Med.* (2010) **63**:562–9. doi: 10.1002/mrm.22285
27. Bai Y, Lin Y, Tian J, Shi D, Cheng J, Haacke EM, et al. Grading of gliomas by using monoexponential, biexponential, and stretched exponential diffusion-weighted MR imaging and diffusion kurtosis MR imaging. *Radiology* (2016) **278**:496–504. doi: 10.1148/radiol.2015142173
28. Lai V, Lee VH, Lam KO, Sze HC, Chan Q, Khong PL. Intravoxel water diffusion heterogeneity MR imaging of nasopharyngeal carcinoma using stretched exponential diffusion model. *Eur Radiol.* (2015) **25**:1708–13. doi: 10.1007/s00330-014-3535-9
29. Liu X, Zhou L, Peng W, Wang H, Zhang Y. Comparison of stretched-Exponential and monoexponential model diffusion-Weighted imaging in prostate cancer and normal tissues. *J Magn Reson Imaging* (2015) **42**:1078–85. doi: 10.1002/jmri.24872
30. Mazaheri Y, Afaq A, Rowe DB, Lu Y, Shukla-Dave A, Grover J. Diffusion-weighted magnetic resonance imaging of the prostate: improved robustness with stretched exponential modeling. *J Comput Assist Tomogr.* (2012) **36**:695–703. doi: 10.1097/RCT.0b013e31826bdbbd
31. Özarslan E, Koay CG, Shepherd TM, Komlosh ME, Irfanoglu MO, Pierpaoli C, et al. Mean apparent propagator (MAP) MRI: a novel diffusion imaging method for mapping tissue microstructure. *Neuroimage* (2013) **78**:16–32. doi: 10.1016/j.neuroimage.2013.04.016
32. Avram AV, Sarlls JE, Barnett AS, Ozarslan E, Thomas C, Irfanoglu MO, et al. Clinical feasibility of using mean apparent propagator (MAP) MRI to characterize brain tissue microstructure. *Neuroimage* (2016) **127**:422–34. doi: 10.1016/j.neuroimage.2015.11.027
33. Latour LL, Svoboda K, Mitra PP, Sotak CH. Time-dependent diffusion of water in a biological model system. *Proc Natl Acad Sci USA.* (1994) **91**:1229–33. doi: 10.1073/pnas.91.4.1229
34. Szafer A, Zhong J, Gore JC. Theoretical model for water diffusion in tissues. *Magn Reson Med.* (1995) **33**:697–712. doi: 10.1002/mrm.1910330516
35. Stanisz GJ, Szafer A, Wright GA, Henkelman RM. An analytical model of restricted diffusion in bovine optic nerve. *Magn Reson Med.* (1997) **37**:103–11. doi: 10.1002/mrm.1910370115
36. Behrens TE, Woolrich MW, Jenkinson M, Johansen-Berg H, Nunes RG, Clare S, et al. Characterization and propagation of uncertainty in diffusion-weighted MR imaging. *Magn Reson Med.* (2003) **50**:1077–88. doi: 10.1002/mrm.10609
37. Kroenke CD, Ackerman JJ, Yablonskiy DA. On the nature of the NAA diffusion attenuated MR signal in the central nervous system. *Magn Reson Med.* (2004) **52**:1052–59. doi: 10.1002/mrm.20260
38. Jespersen SN, Kroenke CD, Ostergaard L, Ackerman JJ, Yablonskiy DA. Modeling dendrite density from magnetic resonance diffusion measurements. *Neuroimage* (2007) **34**:1473–86. doi: 10.1016/j.neuroimage.2006.10.037
39. Mikula S, Denk W. High-resolution whole-brain staining for electron microscopic circuit reconstruction. *Nat Methods* (2015) **12**:541–6. doi: 10.1038/nmeth.3361
40. Lampinen B, Szczepankiewicz F, van Westen D, Englund E, Sundgren PC, Lätt J, et al. Optimal experimental design for filter exchange imaging: apparent exchange rate measurements in the healthy brain and in intracranial tumors. *Magn Reson Med.* (2017) **77**:1104–14. doi: 10.1002/mrm.26195
41. Zhang H, Schneider T, Wheeler-Kingshott CA, Alexander DC. NODDI: practical *in vivo* neurite orientation dispersion and density imaging of the human brain. *Neuroimage* (2012) **61**:1000–16. doi: 10.1016/j.neuroimage.2012.03.072

42. Adluru G, Gur Y, Anderson JS, Richards LG, Adluru N, DiBella EV. Assessment of white matter microstructure in stroke patients using NODDI. *Conf Proc IEEE Eng Med Biol Soc.* (2014) **2014**:742–5. doi: 10.1109/EMBC.2014.6943697
43. Churchill NW, Caverzasi E, Graham SJ, Hutchison MG, Schweizer TA. White matter microstructure in athletes with a history of concussion: comparing diffusion tensor imaging (DTI) and neurite orientation dispersion and density imaging (NODDI). *Hum Brain Mapp.* (2017) **38**:4201–11. doi: 10.1002/hbm.23658
44. Kunz N, Zhang H, Vasung L, O'Brien KR, Assaf Y, Lazeyras F, et al. Assessing white matter microstructure of the newborn with multi-shell diffusion MRI and biophysical compartment models. *Neuroimage* (2014) **96**, 288–99. doi: 10.1016/j.neuroimage.2014.03.057
45. Okita G, Ohba T, Takamura T, Ebata S, Ueda R, Onishi H, et al. Application of neurite orientation dispersion and density imaging or diffusion tensor imaging to quantify the severity of cervical spondylotic myelopathy and assess postoperative neurological recovery. *Spine J.* (2017). doi: 10.1016/j.spinee.2017.07.007. [Epub ahead of print].
46. Schneider T, Brownlee W, Zhang H, Ciccarelli O, Miller DH, Wheeler-Kingshott CG. Sensitivity of multi-shell NODDI to multiple sclerosis white matter changes: a pilot study. *Funct Neurol.* (2017) **32**:97–101. doi: 10.11138/FNeur/2017.32.2.097
47. Slattery CF, Zhang J, Paterson RW, Foulkes AJM, Carton, A, Macpherson, K, et al. ApoE influences regional white-matter axonal density loss in Alzheimer's disease. *Neurobiol Aging* (2017) **57**:8–17. doi: 10.1016/j.neurobiolaging.2017.04.021
48. Wen Q, Kelley DA, Banerjee S, Lupo JM, Chang SM, Xu D, et al. Clinically feasible NODDI characterization of glioma using multiband EPI at 7 T. *Neuroimage Clin.* (2015) **9**:291–9. doi: 10.1016/j.nicl.2015.08.017
49. Jelescu IO, Veraart J, Fieremans E, Novikov DS. Degeneracy in model parameter estimation for multi-compartmental diffusion in neuronal tissue. *NMR Biomed.* (2016a) **29**, 33–47. doi: 10.1002/nbm.3450
50. Novikov DS, Veraart J, Jelescu IO, Fieremans E. Mapping orientational and microstructural metrics of neuronal integrity with *in vivo* diffusion MRI. *arXiv:1609.09144* (2016b).
51. Novikov DS, Fieremans E. Relating extracellular diffusivity to cell size distribution and packing density as applied to white matter. In: *Proc Intl Soc Mag Reson Med*. Melbourne, VIC (2012). p. 1829.
52. Fieremans E, Jensen JH, Helpern JA. White matter characterization with diffusional kurtosis imaging. *Neuroimage* (2011) **58**:177–88. doi: 10.1016/j.neuroimage.2011.06.006
53. Fieremans E, Novikov DS, Jensen JH, Helpern JA. Monte Carlo study of a two-compartment exchange model of diffusion. *NMR Biomed.* (2010) **23**:711–24. doi: 10.1002/nbm.1577
54. Benitez A, Fieremans E, Jensen JH, Falangola MF, Tabesh A, Ferris SH, et al. White matter tract integrity metrics reflect the vulnerability of late-myelinating tracts in Alzheimer's disease. *Neuroimage Clin.* (2013) **4**:64–71. doi: 10.1016/j.nicl.2013.11.001
55. de Kouchkovsky I, Fieremans E, Fleysher L, Herbert J, Grossman RI, Inglese M. Quantification of normal-appearing white matter tract integrity in multiple sclerosis: a diffusion kurtosis imaging study. *J Neurol.* (2016) **263**:1146–55. doi: 10.1007/s00415-016-8118-z
56. Jelescu IO, Zurek M, Winters KV, Veraart J, Rajaratnam A, Kim NS, et al. *In vivo* quantification of demyelination and recovery using compartment-specific diffusion MRI metrics validated by electron microscopy. *Neuroimage* (2016b) **132**:104–14. doi: 10.1016/j.neuroimage.2016.02.004
57. Kamiya K, Hori M, Irie R, Miyajima M, Nakajima M, Kamagata K, et al. Diffusion imaging of reversible and irreversible microstructural changes within the corticospinal tract in idiopathic normal pressure hydrocephalus. *Neuroimage Clin.* (2017) **14**:663–71. doi: 10.1016/j.nicl.2017.03.003
58. Kelm ND, West KL, Carson RP, Gochberg DF, Ess KC, Does MD. Evaluation of diffusion kurtosis imaging in *ex vivo* hypomyelinated mouse brains. *Neuroimage* (2016) **124**:612–26. doi: 10.1016/j.neuroimage.2015.09.028
59. Jespersen SN, Olesen JL, Hansen B, Shemesh N. Diffusion time dependence of microstructural parameters in fixed spinal cord. *Neuroimage* (2017). doi: 10.1016/j.neuroimage.2017.08.039. [Epub ahead of print].
60. Tariq M, Schneider T, Alexander DC, Gandini Wheeler-Kingshott CA, Zhang H. Bingham-NODDI: mapping anisotropic orientation dispersion of neurites using diffusion MRI. *Neuroimage* (2016) 133, 207–23. doi: 10.1016/j.neuroimage.2016.01.046
61. Jespersen SN, Bjarkam CR, Nyengaard JR, Chakravarty MM, Hansen B, Vosegaard T, et al. Neurite density from magnetic resonance diffusion measurements at ultrahigh field: comparison with light microscopy and electron microscopy. *Neuroimage* (2010) **49**:205–16. doi: 10.1016/j.neuroimage.2009.08.053
62. Anderson AW. Measurement of fiber orientation distributions using high angular resolution diffusion imaging. *Magn Reson Med.* (2005) **54**:1194–206. doi: 10.1002/mrm.20667
63. Dell'Acqua F, Rizzo G, Scifo P, Clarke RA, Scotti G, Fazio F. A model-based deconvolution approach to solve fiber crossing in diffusion-weighted MR imaging. *IEEE Trans Biomed Eng.* (2007) **54**:462–72. doi: 10.1109/TBME.2006.888830
64. Tournier JD, Calamante F, Gadian DG, Connelly A. Direct estimation of the fiber orientation density function from diffusion-weighted MRI data using spherical deconvolution. *Neuroimage* (2004) **23**:1176–85. doi: 10.1016/j.neuroimage.2004.07.037
65. Reisert M, Kellner E, Dhital B, Hennig J, Kiselev VG. Disentangling micro from mesostructure by diffusion MRI: a Bayesian approach. *Neuroimage* (2017) **147**:964–75. doi: 10.1016/j.neuroimage.2016.09.058
66. Kaden E, Kelm ND, Carson RP, Does MD, Alexander DC. Multi-compartment microscopic diffusion imaging. *Neuroimage* (2016) **139**:346–59. doi: 10.1016/j.neuroimage.2016.06.002
67. Wang Y, Wang Q, Haldar JP, Yeh FC, Xie M, Sun P, et al. Quantification of increased cellularity during inflammatory demyelination. *Brain* (2011) **134**:3590–601. doi: 10.1093/brain/awr307
68. Chiang CW, Wang Y, Sun P, Lin TH, Trinkaus K, Cross AH, et al. Quantifying white matter tract diffusion parameters in the presence of increased extra-fiber cellularity and vasogenic edema. *Neuroimage* (2014) **101**:310–9. doi: 10.1016/j.neuroimage.2014.06.064
69. Lin TH, Chiang CW, Perez-Torres CJ, Sun P, Wallendorf M, Schmidt RE, et al. Diffusion MRI quantifies early axonal loss in the presence of nerve swelling. *J Neuroinflammation* (2017) **14**:78. doi: 10.1186/s12974-017-0852-3
70. Murphy RK, Sun P, Xu J, Wang Y, Sullivan S, Gamble P, et al. Magnetic resonance imaging biomarker of axon loss reflects cervical spondylotic myelopathy severity. *Spine* (2016) **41**:751–6. doi: 10.1097/BRS.0000000000001337
71. Sun P, Murphy RK, Gamble P, George A, Song SK, Ray WZ. Diffusion assessment of cortical changes, induced by traumatic spinal cord injury. *Brain Sci*. (2017) **7**:E21. doi: 10.3390/brainsci7020021
72. Wang X, Cusick MF, Wang Y, Sun P, Libbey JE, Trinkaus K, et al. Diffusion basis spectrum imaging detects and distinguishes coexisting subclinical inflammation, demyelination and axonal injury in experimental autoimmune encephalomyelitis mice. *NMR Biomed.* (2014c) **27**:843–52. doi: 10.1002/nbm.3129
73. Pierpaoli C, Jones DK. Removing CSF contamination in brain DT-MRIs by using a two-compartment tensor model. In: *Proc Intl Soc Mag Reson Med*. Kyoto (2004). p. 1215.
74. Pasternak O, Sochen N, Gur Y, Intrator N, Assaf Y. Free water elimination and mapping from diffusion MRI. *Magn Reson Med.* (2009) **62**:717–30. doi: 10.1002/mrm.22055
75. Albi A, Pasternak O, Minati L, Marizzoni M, Bartres-Faz D, Bargallo N, et al. Free water elimination improves test-retest reproducibility of diffusion tensor imaging indices in the brain: a longitudinal multisite study of healthy elderly subjects. *Hum Brain Mapp*. (2017) **38**:12–26. doi: 10.1002/hbm.23350
76. Bergamino M, Pasternak O, Farmer M, Shenton ME, Hamilton JP. Applying a free-water correction to diffusion imaging data uncovers stress-related neural pathology in depression. *Neuroimage Clin.* (2016) **10**:336–42. doi: 10.1016/j.nicl.2015.11.020
77. Oestreich LK, Pasternak O, Shenton ME, Kubicki M, Gong X, McCarthy-Jones S, et al. Abnormal white matter microstructure and increased extracellular free-water in the cingulum bundle associated with delusions in chronic schizophrenia. *Neuroimage Clin.* (2016) **12**:405–14. doi: 10.1016/j.nicl.2016.08.004
78. Ofori E, Pasternak O, Planetta PJ, Li H, Burciu RG, Snyder AF, et al. Longitudinal changes in free-water within the substantia nigra of Parkinson's disease. *Brain* (2015) **138**:2322–31. doi: 10.1093/brain/awv136

79. Pasternak O, Shenton ME, Westin CF. Estimation of extracellular volume from regularized multi-shell diffusion MRI. *Med Image Comput Comp Assist Interv.* (2012) **15**:305–12. doi: 10.1007/978-3-642-33418-4_38
80. Hoy AR, Koay CG, Kecskemeti SR, Alexander AL. Optimization of a free water elimination two-compartment model for diffusion tensor imaging. *Neuroimage* (2014) **103**:323–33. doi: 10.1016/j.neuroimage.2014.09.053
81. Chou MC, Lin YR, Huang TY, Wang CY, Chung HW, Juan CJ, et al. FLAIR diffusion-tensor MR tractography: comparison of fiber tracking with conventional imaging. *AJNR Am J Neuroradiol.* (2005) **26**:591–7.
82. Hoy AR, Kecskemeti SR, Alexander AL. Free water elimination diffusion tractography: a comparison with conventional and fluid-attenuated inversion recovery, diffusion tensor imaging acquisitions. *J Magn Reson Imaging* (2015) **42**:1572–81. doi: 10.1002/jmri.24925
83. Scherrer B, Schwartzman A, Taquet M, Sahin M, Prabhu SP, Warfield SK. Characterizing brain tissue by assessment of the distribution of anisotropic microstructural environments in diffusion-compartment imaging (DIAMOND). *Magn Reson Med.* (2016) **76**:963–77. doi: 10.1002/mrm.25912
84. Ferizi U, Schneider T, Panagiotaki E, Nedjati-Gilani G, Zhang H, Wheeler-Kingshott CA, et al. A ranking of diffusion MRI compartment models with *in vivo* human brain data. *Magn Reson Med.* (2014) **72**:1785–92. doi: 10.1002/mrm.25080
85. Panagiotaki E, Schneider T, Siow B, Hall MG, Lythgoe MF, Alexander DC. Compartment models of the diffusion MR signal in brain white matter: a taxonomy and comparison. *Neuroimage* (2012) **59**, 2241–54. doi: 10.1016/j.neuroimage.2011.09.081
86. Scherrer B, Qiu J, Hashim J, Afacan O, Wu Y, Marcotrigiano M, et al. Diffusion compartment imaging reveals microstructural injuries in a mouse model of mild traumatic brain injury. In: *Proc Intl Soc Mag Reson Med.* Honolulu, HI (2017). p. 286.
87. Jelescu IO, Veraart J, Adisetiyo V, Milla SS, Novikov DS, Fieremans E. One diffusion acquisition and different white matter models: how does microstructure change in human early development based on WMTI and NODDI? *Neuroimage* (2015) **107**:242–56. doi: 10.1016/j.neuroimage.2014.12.009
88. Wang S, Peterson DJ, Wang Y, Wang Q, Grabowski TJ, Li W, et al. Empirical comparison of diffusion kurtosis imaging and diffusion basis spectrum imaging using the same acquisition in healthy young adults. *Front Neurol.* (2017) 8:118. doi: 10.3389/fneur.2017.00118
89. Balls GT, Frank LR. A simulation environment for diffusion weighted MR experiments in complex media. *Magn Reson Med.* (2009) **62**, 771–8. doi: 10.1002/mrm.22033
90. Hall MG, Alexander DC. Convergence and parameter choice for Monte-Carlo simulations of diffusion MRI. *IEEE Trans Med Imaging* (2009) **28**:1354–64. doi: 10.1109/TMI.2009.2015756
91. Mingasson T, Duval T, Stikov N, Cohen-Adad J. AxonPacking: an open-source software to simulate arrangements of axons in white matter. *Front. Neuroinform.* (2017) 11:5. doi: 10.3389/fninf.2017.00005
92. Yeh CH, Schmitt B, Le Bihan D, Li-Schlittgen JR, Lin CP, Poupon C. Diffusion microscopist simulator: a general Monte Carlo simulation system for diffusion magnetic resonance imaging. *PLoS ONE* (2013) **8**:e76626. doi: 10.1371/journal.pone.0076626
93. Landman BA, Farrell JA, Smith SA, Reich DS, Calabresi PA, van Zijl PC. Complex geometric models of diffusion and relaxation in healthy and damaged white matter. *NMR Biomed.* (2010) **23**:152–62. doi: 10.1002/nbm.1437
94. Budde MD, Frank JA. Neurite beading is sufficient to decrease the apparent diffusion coefficient after ischemic stroke. *Proc Natl Acad Sci USA.* (2010) **107**:14472–7. doi: 10.1073/pnas.1004841107
95. Nilsson M, Latt J, Stahlberg F, van Westen D, Hagslatt H. The importance of axonal undulation in diffusion MR measurements: a Monte Carlo simulation study. *NMR Biomed.* (2012) **25**:795–805. doi: 10.1002/nbm.1795
96. Panagiotaki E, Hall MG, Zhang H, Siow B, Lythgoe MF, Alexander DC. High-fidelity meshes from tissue samples for diffusion MRI simulations. *Med. Image Comput. Comp. Assist. Interv.* (2010) **13**(Pt 2):404–11. doi: 10.1007/978-3-642-15745-5_50
97. Perrin M, Poupon C, Rieul B, Leroux P, Constantinesco A, Mangin JF, et al. Validation of q-ball imaging with a diffusion fibre-crossing phantom on a clinical scanner. *Philos Trans R Soc Lond B Biol Sci.* (2005) **360**:881–91. doi: 10.1098/rstb.2005.1650
98. Kim SJ, Choi CG, Kim JK, Yun SC, Jahng GH, Jeong HK, et al. Effects of MR parameter changes on the quantification of diffusion anisotropy and apparent diffusion coefficient in diffusion tensor imaging: evaluation using a diffusional anisotropic phantom. *Korean J Radiol.* (2015) **16**:297–303. doi: 10.3348/kjr.2015.16.2.297
99. Oida T, Nagahara S, Kobayashi T. Acquisition parameters for diffusion tensor imaging to emphasize fractional anisotropy: phantom study. *Magn Reson Med Sci.* (2011) **10**:121–128. doi: 10.2463/mrms.10.121
100. Tournier JD, Yeh CH, Calamante F, Cho KH, Connelly A, Lin CP. Resolving crossing fibres using constrained spherical deconvolution: validation using diffusion-weighted imaging phantom data. *Neuroimage* (2008) **42**:617–25. doi: 10.1016/j.neuroimage.2008.05.002
101. Komlosh ME, Benjamini D, Barnett AS, Schram V, Horkay F, Avram AV, et al. Anisotropic phantom to calibrate high-q diffusion MRI methods. *J Magn Reson.* (2017) **275**:19–28. doi: 10.1016/j.jmr.2016.11.017
102. Burcaw LM, Fieremans E, Novikov DS. Mesoscopic structure of neuronal tracts from time-dependent diffusion. *Neuroimage* (2015) **114**:18–37. doi: 10.1016/j.neuroimage.2015.03.061
103. Fieremans E, De Deene Y, Delputte S, Ozdemir MS, Achten E, Lemahieu I. The design of anisotropic diffusion phantoms for the validation of diffusion weighted magnetic resonance imaging. *Phys Med Biol.* (2008a) **53**:5405–19. doi: 10.1088/0031-9155/53/19/009
104. Fieremans E, De Deene Y, Delputte S, Özdemir MS, D'Asseler Y, Vlassenbroeck J, et al. Simulation and experimental verification of the diffusion in an anisotropic fiber phantom. *J. Magn Reson.* (2008b) **190**:189–99. doi: 10.1016/j.jmr.2007.10.014
105. Farrher E, Lindemeyer J, Grinberg F, Oros-Peusquens A.-M, Shah, NJ. Concerning the matching of magnetic susceptibility differences for the compensation of background gradients in anisotropic diffusion fibre phantoms. *PLoS ONE* (2017) **12**:e0176192. doi: 10.1371/journal.pone.0176192
106. Hubbard PL, Zhou FL, Eichhorn SJ, Parker GJ. Biomimetic phantom for the validation of diffusion magnetic resonance imaging. *Magn Reson Med* (2015) **73**:299–305. doi: 10.1002/mrm.25107
107. Palacios EM, Martin AJ, Boss MA, Ezekiel F, Chang YS, Yuh EL, et al. Toward precision and reproducibility of diffusion tensor imaging: a multicenter diffusion phantom and traveling volunteer study. *AJNR Am J Neuroradiol.* (2017) **38**:537–45. doi: 10.3174/ajnr.A5025
108. Nimsky C, Ganslandt O, Hastreiter P, Wang R, Benner T, Sorensen AG, et al. Preoperative and intraoperative diffusion tensor imaging-based fiber tracking in glioma surgery. *Neurosurgery* (2005) **56**:130–7; discussion: 138. doi: 10.1227/01.NEU.0000144842.18771.30
109. Johansen-Berg H, Behrens TE. Just pretty pictures? What diffusion tractography can add in clinical neuroscience. *Curr Opin Neurol.* (2006) **19**:379–385. doi: 10.1097/01.wco.0000236618.82086.01
110. Tuch DS, Reese TG, Wiegell MR, Wedeen VJ. Diffusion MRI of complex neural architecture. *Neuron* (2003) **40**:885–95. doi: 10.1016/S0896-6273(03)00758-X
111. Christiaens D, Reisert M, Dhollander T, Sunaert S, Suetens P, Maes F. Global tractography of multi-shell diffusion-weighted imaging data using a multi-tissue model. *Neuroimage* (2015) **123**:89–101. doi: 10.1016/j.neuroimage.2015.08.008
112. Daducci A, Dal Palu A, Descoteaux M, Thiran JP. Microstructure informed tractography: pitfalls and open challenges. *Front Neurosci* (2016) **10**:247. doi: 10.3389/fnins.2016.00247
113. Reisert M, Kiselev VG, Dihtal B, Kellner E, Novikov DS. MesoFT: unifying diffusion modelling and fiber tracking. *Med Image Comput Comp Assist Interv.* (2014) **17**:201–8. doi: 10.1007/978-3-319-10443-0_26
114. Budde MD, Annese J. Quantification of anisotropy and fiber orientation in human brain histological sections. *Front Integr Neurosci.* (2013a) **7**:3. doi: 10.3389/fnint.2013.00003
115. Axer M, Strohmer S, Gräßel D, Bücker O, Dohmen M, Reckfort J, et al. Estimating fiber orientation distribution functions in 3D-Polarized Light Imaging. *Front. Neuroanat.* (2016) **10**:40. doi: 10.3389/fnana.2016.00040
116. Wang H, Zhu J, Reuter M, Vinke LN, Yendiki A, Boas DA, et al. Cross-validation of serial optical coherence scanning and diffusion tensor imaging: a study on neural fiber maps in human medulla oblongata. *Neuroimage* (2014b) **100**:395–404. doi: 10.1016/j.neuroimage.2014.06.032
117. Leergaard TB, White NS, de Crespigny A, Bolstad I, D'Arceuil H, Bjaalie JG, et al. Quantitative histological validation of diffusion MRI fiber

orientation distributions in the rat brain. *PLoS ONE* (2010) **5**:e8595. doi: 10.1371/journal.pone.0008595
118. Budde MD, Annese J. Quantifying anisotropy and fiber orientation in human brain histological sections. *Front Integr Neurosci.* (2013b) **7**:3. doi: 10.3389/fnint.2013.00003
119. Budde MD, Frank JA. Examining brain microstructure using structure tensor analysis of histological sections. *Neuroimage* (2012) **63**:1–10. doi: 10.1016/j.neuroimage.2012.06.042
120. Choe AS, Stepniewska I, Colvin DC, Ding Z, Anderson AW. Validation of diffusion tensor MRI in the central nervous system using light microscopy: quantitative comparison of fiber properties. *NMR Biomed.* (2012) **25**:900–8. doi: 10.1002/nbm.1810
121. Gangolli M, Holleran L, Hee Kim J, Stein TD, Alvarez V, McKee AC, et al. Quantitative validation of a nonlinear histology-MRI coregistration method using generalized Q-sampling imaging in complex human cortical white matter. *Neuroimage* (2017) **153**:152–67. doi: 10.1016/j.neuroimage.2017.03.059
122. Grussu F, Schneider T, Yates RL, Zhang H, Wheeler-Kingshott CAMG, DeLuca GC, et al. A framework for optimal whole-sample histological quantification of neurite orientation dispersion in the human spinal cord. *J. Neurosci. Methods* (2016) **273**:20–32. doi: 10.1016/j.jneumeth.2016.08.002
123. Hansen B, Flint JJ, Heon-Lee C, Fey M, Vincent F, King MA, et al. Diffusion tensor microscopy in human nervous tissue with quantitative correlation based on direct histological comparison. *Neuroimage* (2011) **57**:1458–65. doi: 10.1016/j.neuroimage.2011.04.052
124. Mitter C, Jakab A, Brugger PC, Ricken G, Gruber GM, Bettelheim D, et al. Validation of in utero tractography of human fetal commissural and internal capsule fibers with histological structure tensor analysis. *Front. Neuroanat.* (2015) **9**:164. doi: 10.3389/fnana.2015.00164
125. Mollink J, Kleinnijenhuis M, Cappellen van Walsum AMV, Sotiropoulos SN, Cottaar M, Mirfin C, et al. Evaluating fibre orientation dispersion in white matter: comparison of diffusion MRI, histology and polarized light imaging. *Neuroimage* (2017) **157**:561–74. doi: 10.1016/j.neuroimage.2017.06.001
126. Nazaran A, Wisco JJ, Hageman N, Schettler SP, Wong A, Vinters HV, et al. Methodology for computing white matter nerve fiber orientation in human histological slices. *J Neurosci Methods* (2016) **261**:75–84. doi: 10.1016/j.jneumeth.2015.11.023
127. Seehaus A, Roebroeck A, Bastiani M, Fonseca L, Bratzke H, Lori N, et al. Histological validation of high-resolution DTI in human post mortem tissue. *Front Neuroanat.* (2015) **9**:98. doi: 10.3389/fnana.2015.00098
128. Khan AR, Cornea A, Leigland LA, Kohama SG, Jespersen SN, Kroenke CD. 3D structure tensor analysis of light microscopy data for validating diffusion MRI. *Neuroimage* (2015) **111**:192–203. doi: 10.1016/j.neuroimage.2015.01.061
129. Schilling K, Janve V, Gao Y, Stepniewska I, Landman BA, Anderson AW. Comparison of 3D orientation distribution functions measured with confocal microscopy and diffusion MRI. *Neuroimage* (2016) **129**:185–97. doi: 10.1016/j.neuroimage.2016.01.022
130. Annese J. The importance of combining MRI and large-scale digital histology in neuroimaging studies of brain connectivity and disease. *Front Neuroinform.* (2012) **6**:13. doi: 10.3389/fninf.2012.00013
131. de Campos Vidal B, Mello ML, Caseiro-Filho AC, Godo C. Anisotropic properties of the myelin sheath. *Acta Histochem.* (1980) **66**:32–9. doi: 10.1016/S0065-1281(80)80079-1
132. Axer H, Beck S, Axer M, Schuchardt F, Heepe J, Flucken A, et al. Microstructural analysis of human white matter architecture using polarized light imaging: Views from neuroanatomy. *Front Neuroinform.* (2011a) **5**:28. doi: 10.3389/fninf.2011.00028
133. Axer M, Amunts K, Grässel D, Palm C, Dammers J, Axer H, et al. A novel approach to the human connectome: ultra-high resolution mapping of fiber tracts in the brain. *Neuroimage* (2011b) **54**:1091–101. doi: 10.1016/j.neuroimage.2010.08.075
134. Wang H, Lenglet C, Akkin T. Structure tensor analysis of serial optical coherence scanner images for mapping fiber orientations and tractography in the brain. *J Biomed Optics* (2015) **20**:036003. doi: 10.1117/1.JBO.20.3.036003
135. Wang H, Zhu J, Akkin T. Serial optical coherence scanner for large-scale brain imaging at microscopic resolution. *Neuroimage* (2014a) **84**:1007–1017. doi: 10.1016/j.neuroimage.2013.09.063
136. Oh SW, Harris JA, Ng L, Winslow B, Cain N, Mihalas S, et al. A mesoscale connectome of the mouse brain. *Nature* (2014) **508**:207–14. doi: 10.1038/nature13186
137. Magnain C, Augustinack JC, Reuter M, Wachinger C, Frosch MP, Ragan T, et al. Blockface histology with optical coherence tomography: a comparison with Nissl staining. *Neuroimage* (2014) **84**:524–33. doi: 10.1016/j.neuroimage.2013.08.072
138. Srinivasan VJ, Radhakrishnan H, Jiang JY, Barry S, Cable AE. Optical coherence microscopy for deep tissue imaging of the cerebral cortex with intrinsic contrast. *Opt Express* (2012) **20**:2220–39. doi: 10.1364/OE.20.002220
139. Denk W, Horstmann H. Serial block-face scanning electron microscopy to reconstruct three-dimensional tissue nanostructure. *PLoS Biol.* (2004) **2**:e329. doi: 10.1371/journal.pbio.0020329
140. Dodt HU, Leischner U, Schierloh A, Jährling N, Mauch CP, Deininger K, et al. Ultramicroscopy: three-dimensional visualization of neuronal networks in the whole mouse brain. *Nat Methods* (2007) **4**:331–6. doi: 10.1038/nmeth1036
141. Mikula S, Binding J, Denk W. Staining and embedding the whole mouse brain for electron microscopy. *Nat Methods* (2012) **9**:1198–201. doi: 10.1038/nmeth.2213
142. Chang EH, Argyelan M, Aggarwal M, Chandon T. SS, Karlsgodt KH, Mori S, et al. The role of myelination in measures of white matter integrity: combination of diffusion tensor imaging and two-photon microscopy of CLARITY intact brains. *Neuroimage* (2017) **147**:119–24. doi: 10.1016/j.neuroimage.2016.11.068
143. Ronen I, Budde M, Ercan E, Annese J, Techawiboonwong A, Webb A. Microstructural organization of axons in the human corpus callosum quantified by diffusion-weighted magnetic resonance spectroscopy of N-acetylaspartate and post-mortem histology. *Brain Struct Funct.* (2014) **219**:1773–85. doi: 10.1007/s00429-013-0600-0
144. Jespersen SN, Leigland LA, Cornea A, Kroenke CD. Determination of axonal and dendritic orientation distributions within the developing cerebral cortex by diffusion tensor imaging. *IEEE Trans Med Imaging* (2012) **31**:16–32. doi: 10.1109/TMI.2011.2162099
145. Sykova E, Nicholson C. Diffusion in brain extracellular space. *Physiol Rev.* (2008) **88**:1277–340. doi: 10.1152/physrev.00027.2007
146. Cragg B. Preservation of extracellular space during fixation of the brain for electron microscopy. *Tissue Cell* (1980) **12**:63–72. doi: 10.1016/0040-8166(80)90052-X
147. Perge JA, Koch K, Miller R, Sterling P, Balasubramanian V. How the optic nerve allocates space, energy capacity, and information. *J Neurosci.* (2009) **29**:7917–28. doi: 10.1523/JNEUROSCI.5200-08.2009
148. Ong HH, Wright AC, Wehrli SL, Souza A, Schwartz ED, Hwang SN, et al. Indirect measurement of regional axon diameter in excised mouse spinal cord with q-space imaging: simulation and experimental studies. *Neuroimage* (2008) **40**:1619–32. doi: 10.1016/j.neuroimage.2008.01.017
149. Pallotto M, Watkins PV, Fubara B, Singer JH, Briggman KL. Extracellular space preservation aids the connectomic analysis of neural circuits. *Elife* (2015) **4**:e08206. doi: 10.7554/eLife.08206
150. Korogod N, Petersen CC, Knott GW. Ultrastructural analysis of adult mouse neocortex comparing aldehyde perfusion with cryo fixation. *Elife* (2015) **4**:e05793. doi: 10.7554/eLife.05793
151. Grussu F, Schneider T, Zhang H, Alexander DC, Wheeler-Kingshott CA. Neurite orientation dispersion and density imaging of the healthy cervical spinal cord *in vivo*. *Neuroimage* (2015) **111**:590–601. doi: 10.1016/j.neuroimage.2015.01.045
152. Chklovskii DB, Schikorski T, Stevens CF. Wiring optimization in cortical circuits. *Neuron* (2002) **34**:341–7. doi: 10.1016/S0896-6273(02)00679-7
153. Sepehrband F, Clark KA, Ullmann JF, Kurniawan ND, Leanage G, Reutens DC, et al. Brain tissue compartment density estimated using diffusion-weighted MRI yields tissue parameters consistent with histology. *Hum Brain Mapp.* (2015) **36**:3687–702. doi: 10.1002/hbm.22872
154. Golabchi FN, Brooks DH, Hoge WS, De Girolami U, Maier SE. Pixel-based comparison of spinal cord MR diffusion anisotropy with axon packing parameters. *Magn Reson Med.* (2010) **63**:1510–9. doi: 10.1002/mrm.22337
155. Duval T, Le Vy S, Stikov N, Campbell J, Mezer A, Witzel T, et al. g-Ratio weighted imaging of the human spinal cord *in vivo*. *Neuroimage* (2017) **145**:11–23. doi: 10.1016/j.neuroimage.2016.09.018

156. Stikov N, Campbell JS, Stroh T, Lavelee M, Frey S, Novek J, et al. *In vivo* histology of the myelin g-ratio with magnetic resonance imaging. *Neuroimage* (2015) **118**:397–405. doi: 10.1016/j.neuroimage.2015.05.023
157. Beaulieu C. The basis of anisotropic water diffusion in the nervous system - a technical review. *NMR Biomed.* (2002) **15**:435–55. doi: 10.1002/nbm.782
158. Takahashi M, Hackney DB, Zhang G, Wehrli SL, Wright AC, O'Brien WT, et al. Magnetic resonance microimaging of intraaxonal water diffusion in live excised lamprey spinal cord. *Proc Natl Acad Sci USA.* (2002) **99**:16192–6. doi: 10.1073/pnas.252249999
159. Beaulieu C, Allen PS. Water diffusion in the giant axon of the squid: implications for diffusion-weighted MRI of the nervous system. *Magn Reson Med.* (1994) **32**:579–83. doi: 10.1002/mrm.1910320506
160. Nordengen K, Heuser C, Rinholm JE, Matalon R, Gundersen V. Localisation of N-acetylaspartate in oligodendrocytes/myelin. *Brain Struct Funct.* (2015) **220**:899–917. doi: 10.1007/s00429-013-0691-7
161. Ellegood J, Hanstock CC, Beaulieu C. Diffusion tensor spectroscopy (DTS) of human brain. *Magn Reson Med.* (2006) **55**:1–8. doi: 10.1002/mrm.20777
162. Ellegood J, McKay RT, Hanstock CC, Beaulieu C. Anisotropic diffusion of metabolites in peripheral nerve using diffusion weighted magnetic resonance spectroscopy at ultra-high field. *J Magn Reson.* (2007) **184**:20–28. doi: 10.1016/j.jmr.2006.09.008
163. Palombo M, Ligneul C, Valette J. Modeling diffusion of intracellular metabolites in the mouse brain up to very high diffusion-weighting: diffusion in long fibers (almost) accounts for non-monoexponential attenuation. *Magn Reson Med.* (2017) **77**:343–50. doi: 10.1002/mrm.26548
164. Najac C, Branzoli F, Ronen I, Valette J. Brain intracellular metabolites are freely diffusing along cell fibers in grey and white matter, as measured by diffusion-weighted MR spectroscopy in the human brain at 7 T. *Brain Struct Funct.* (2016) **221**:1245–1254. doi: 10.1007/s00429-014-0968-5
165. Najac C, Marchadour C, Guillermier M, Houitte D, Slavov V, Brouillet E, et al. Intracellular metabolites in the primate brain are primarily localized in long fibers rather than in cell bodies, as shown by diffusion-weighted magnetic resonance spectroscopy. *Neuroimage* (2014) **90**:374–380. doi: 10.1016/j.neuroimage.2013.12.045
166. Goodman JA, Kroenke CD, Bretthorst GL, Ackerman JJ, Neil JJ. Sodium ion apparent diffusion coefficient in living rat brain. *Magn Reson Med.* (2005) **53**:1040–1045. doi: 10.1002/mrm.20444
167. Goodman JA, Ackerman JJ, Neil JJ. Cs + ADC in rat brain decreases markedly at death. *Magn Reson Med.* (2008) **59**:65–72. doi: 10.1002/mrm.21418
168. Duong TQ, Ackerman JJ, Ying HS, Neil JJ. Evaluation of extra- and intracellular apparent diffusion in normal and globally ischemic rat brain via 19F NMR. *Magn Reson Med.* (1998) **40**:1–13. doi: 10.1002/mrm.1910400102
169. Duong TQ, Sehy JV, Yablonskiy DA, Snider BJ, Ackerman JJ, Neil JJ. Extracellular apparent diffusion in rat brain. *Magn Reson Med.* (2001) **45**:801–10. doi: 10.1002/mrm.1108
170. Ackerman JJ, Neil JJ. The use of MR-detectable reporter molecules and ions to evaluate diffusion in normal and ischemic brain. *NMR Biomed.* (2010) **23**:725–33. doi: 10.1002/nbm.1530
171. Silva MD, Omae T, Helmer KG, Li F, Fisher M, Sotak CH. Separating changes in the intra- and extracellular water apparent diffusion coefficient following focal cerebral ischemia in the rat brain. *Magn Reson Med.* (2002) **48**:826–37. doi: 10.1002/mrm.10296
172. Jelescu IO, Kunz N, Da Silva AR, Gruetter R. Intra- and extra-axonal axial diffusivities in the white matter: which one is faster? In: *Proc. Intl. Soc. Mag. Reson Med.* Honolulu, HI (2017). p. 281.
173. Skinner NP, Kurpad SN, Schmit BD, Tugan Muftuler L, Budde MD. Rapid *in vivo* detection of rat spinal cord injury with double-diffusion-encoded magnetic resonance spectroscopy. *Magn Reson Med.* (2017) **77**:1639–49. doi: 10.1002/mrm.26243
174. Dhital B, Kellner E, Reisert M, Kiselev VG. Isotropic diffusion weighting provides insight on diffusion compartments in human brain white matter *in vivo*. In: *Proc Intl Soc Mag Reson Med.* Toronto, ON (2015). p. 2788.
175. Szczepankiewicz F, Lasic S, van Westen D, Sundgren PC, Englund E, Westin CF, et al. Quantification of microscopic diffusion anisotropy disentangles effects of orientation dispersion from microstructure: applications in healthy volunteers and in brain tumors. *Neuroimage* (2015) **104**:241–52. doi: 10.1016/j.neuroimage.2014.09.057
176. Veraart J, Novikov DS, Fieremans E. TE dependent Diffusion Imaging (TEdDI) distinguishes between compartmental T2 relaxation times. *Neuroimage* (2017). doi: 10.1016/j.neuroimage.2017.09.030. [Epub ahead of print].
177. Veraart J, Fieremans E, Novikov DS. Universal power-law scaling of water diffusion in human brain defines what we see with MRI. *arXiv:1609.09145 [physics.bio-ph]* (2016).
178. Le Bihan D, Johansen-Berg H. Diffusion MRI at 25: exploring brain tissue structure and function. *Neuroimage* (2012) **61**:324–41. doi: 10.1016/j.neuroimage.2011.11.006
179. Moseley ME, Cohen Y, Mintorovitch J, Chileuitt L, Shimizu H, Kucharczyk J, et al. Early detection of regional cerebral ischemia in cats: comparison of diffusion- and T2-weighted MRI and spectroscopy. *Magn Reson Med.* (1990) **14**:330–46. doi: 10.1002/mrm.1910140218
180. Benveniste H, Hedlund LW, Johnson GA. Mechanism of detection of acute cerebral ischemia in rats by diffusion-weighted magnetic resonance microscopy. *Stroke* (1992) **23**:746–54. doi: 10.1161/01.STR.23.5.746
181. Baron CA, Kate M, Gioia L, Butcher K, Emery D, Budde M, et al. Reduction of diffusion-weighted imaging contrast of acute ischemic stroke at short diffusion times. *Stroke* (2015) **46**:2136–41. doi: 10.1161/STROKEAHA.115.008815
182. Does MD, Parsons EC, Gore JC. Oscillating gradient measurements of water diffusion in normal and globally ischemic rat brain. *Magn Reson Med.* (2003) **49**:206–215. doi: 10.1002/mrm.10385
183. Brugieres P, Thomas P, Maraval A, Hosseini H, Combes C, Chafiq A, et al. Water diffusion compartmentation at high b values in ischemic human brain. *AJNR Am J Neuroradiol.* (2004) **25**, 692–8.
184. Niendorf T, Dijkhuizen RM, Norris DG, van Lookeren Campagne M, Nicolay K. Biexponential diffusion attenuation in various states of brain tissue: implications for diffusion-weighted imaging. *Magn Reson Med.* (1996) **36**:847–57. doi: 10.1002/mrm.1910360607
185. Li P, Murphy TH. Two-photon imaging during prolonged middle cerebral artery occlusion in mice reveals recovery of dendritic structure after reperfusion. *J Neurosci.* (2008) **28**:11970–9. doi: 10.1523/JNEUROSCI.3724-08.2008
186. Lucchinetti C, Bruck W, Parisi J, Scheithauer B, Rodriguez M, Lassmann H. Heterogeneity of multiple sclerosis lesions: implications for the pathogenesis of demyelination. *Ann Neurol.* (2000) **47**:707–17. doi: 10.1002/1531-8249(200006)47:6<707::AID-ANA3>3.0.CO;2-Q
187. Trapp BD, Peterson J, Ransohoff RM, Rudick R, Mork S, Bo L. Axonal transection in the lesions of multiple sclerosis. *N Engl J Med.* (1998) **338**:278–85. doi: 10.1056/NEJM199801293380502
188. Budde MD, Xie M, Cross AH, Song SK. Axial diffusivity is the primary correlate of axonal injury in the experimental autoimmune encephalomyelitis spinal cord: a quantitative pixelwise analysis. *J Neurosci.* (2009) **29**:2805–13. doi: 10.1523/JNEUROSCI.4605-08.2009
189. Thiessen JD, Zhang Y, Zhang H, Wang L, Buist R, Del Bigio MR, et al. Quantitative MRI and ultrastructural examination of the cuprizone mouse model of demyelination. *NMR Biomed.* (2013) **26**:1562–81. doi: 10.1002/nbm.2992

Conflict of Interest Statement: IJ is a co-inventor on U.S. Patent Application No. 15/156250, pending. "System, method and computer-accessible medium for determining brain microstructure parameters from diffusion magnetic resonance."

The other author declares that the research was conducted in the absence of any commercial or financial relationships that could be construed as a potential conflict of interest.

frontiers in Neuroscience

TECHNOLOGY REPORT
published: 26 February 2018
doi: 10.3389/fnins.2018.00102

A Modified Tri-Exponential Model for Multi-*b*-value Diffusion-Weighted Imaging: A Method to Detect the Strictly Diffusion-Limited Compartment in Brain

Qiang Zeng[1], *Feina Shi*[2], *Jianmin Zhang*[1], *Chenhan Ling*[1], *Fei Dong*[3] *and Biao Jiang*[3]*

[1] Department of Neurosurgery, Second Affiliated Hospital of Zhejiang University School of Medicine, Hangzhou, China,
[2] Department of Neurology, Second Affiliated Hospital of Zhejiang University School of Medicine, Hangzhou, China,
[3] Department of Radiology, Second Affiliated Hospital of Zhejiang University School of Medicine, Hangzhou, China

Purpose: To present a new modified tri-exponential model for diffusion-weighted imaging (DWI) to detect the strictly diffusion-limited compartment, and to compare it with the conventional bi- and tri-exponential models.

Methods: Multi-*b*-value diffusion-weighted imaging (DWI) with 17 *b*-values up to 8,000 s/mm^2 were performed on six volunteers. The corrected Akaike information criterions (AICc) and squared predicted errors (SPE) were calculated to compare these three models.

Results: The mean f_0 values were ranging 11.9–18.7% in white matter ROIs and 1.2–2.7% in gray matter ROIs. In all white matter ROIs: the AICcs of the modified tri-exponential model were the lowest ($p < 0.05$ for five ROIs), indicating the new model has the best fit among these models; the SPEs of the bi-exponential model were the highest ($p < 0.05$), suggesting the bi-exponential model is unable to predict the signal intensity at ultra-high *b*-value. The mean $ADC_{very-slow}$ values were extremely low in white matter (1–7 $\times$ 10^{-6} mm^2/s), but not in gray matter (251–445 $\times$ 10^{-6} mm^2/s), indicating that the conventional tri-exponential model fails to represent a special compartment.

Conclusions: The strictly diffusion-limited compartment may be an important component in white matter. The new model fits better than the other two models, and may provide additional information.

Keywords: diffusion magnetic resonance imaging, brain, white matter, computer-assisted image processing, theoretical models

OPEN ACCESS

Edited by:
Sune Nørhøj Jespersen, Aarhus University, Denmark

Reviewed by:
Chantal M. W. Tax, Cardiff University, United Kingdom
Lipeng Ning, Brigham and Women's Hospital, United States

***Correspondence:**
Biao Jiang
jiangbiao@zju.edu.cn

Specialty section:
This article was submitted to Brain Imaging Methods, a section of the journal Frontiers in Neuroscience

Received: *07 November 2017*
Accepted: *12 February 2018*
Published: *26 February 2018*

Citation:
Zeng Q, Shi F, Zhang J, Ling C, Dong F and Jiang B (2018) A Modified Tri-Exponential Model for Multi-b-value Diffusion-Weighted Imaging: A Method to Detect the Strictly Diffusion-Limited Compartment in Brain. Front. Neurosci. 12:102. doi: 10.3389/fnins.2018.00102

INTRODUCTION

Diffusion-weighted imaging (DWI) is the only noninvasive method for detecting the diffusion motion of water molecules in tissues. Currently, in clinical practice, apparent diffusion coefficient (ADC) maps are typically calculated with the mono-exponential model. However, it has been well established that the attenuation of the DWI signal does not follow the mono-exponential model in many tissues (Clark and Le Bihan, 2000; Koh et al., 2011). It is believed that more than one proton pool exists inside each voxel (Bennett et al., 2003, 2006). Therefore, many models have been developed in order to accurately reflect the diffusion motion of water molecules *in vivo* (Le Bihan et al., 1988; Bennett et al., 2003; Jensen et al., 2005), such as the bi-exponential model.

However, the bi-exponential model is being challenged for the heterogeneity of its results across studies and its lack of reproducibility (Müller et al., 1998; Grant et al., 2001; Schwarcz et al., 2004; Koh et al., 2011; Steier et al., 2012; Hu et al., 2014; Lin et al., 2015). This model is considered oversimplified (Bisdas et al., 2013), and some researchers even speculate that there are continuous distributions of diffusion coefficients inside each voxel (Bennett et al., 2003, 2006). Recent studies have demonstrated that the three-pool model can perform a better fitting and may provide more detailed information than the bi-exponential model in many tissues (Hayashi et al., 2013, 2014; Cercueil et al., 2015; Ohno et al., 2016; Ueda et al., 2016; van Baalen et al., 2017). However, it is well known that a highly parameterized model can always fit a given data set better than a model with fewer parameters. Whether or not a model can provide more information should be well verified to avoid over-fitting.

Recently, ultra-high *b*-value DWI has been studied more frequently in recent years because of the popularization of 3.0-Tesla MR systems (Ling et al., 2015; Hu et al., 2017). Several studies using DWI with ultra-high *b*-value have found that the signal curves of DWI decrease very slowly and tend to be stability at ultra-high *b*-values in some tissues (Grant et al., 2001; Ling et al., 2015). This phenomenon can be hardly explained by the existing models. Many studies have suggested the existence of the strictly diffusion-limited compartment with extremely low ADC in tissues and even cells (Niendorf et al., 1996; Grant et al., 2001; Sen and Basser, 2005; Baxter and Frank, 2013; Ling et al., 2015). The ADC of water molecules, which are strictly limited in microstructures with extremely small space (such as intracellular organelles), might be extremely low. Because of the very low signal attenuation of this compartment at normal *b*-values, the ADC of this compartment can be set as zero mathematically. Accordingly, by setting one ADC value of the conventional tri-exponential model as zero, we developed a new modified tri-exponential model.

The purpose of this study was to present the new modified tri-exponential model to detect the strictly diffusion-limited compartment, and to compare it with the conventional bi- and tri-exponential models. Previously, stationary water molecules have been suspected to be exist in white matter (Alexander et al., 2010), and three compartment models with a "dot" compartment (zero radius sphere) have been found to produce a better fitting for diffusion MRI in white matter (Ferizi et al., 2014). Accordingly, we hypothesized that the modified tri-exponential model with a "zero-ADC" compartment might also produce a better fitting for DWI in white matter. Hence, we performed this preliminary study in brain. To indicate the existence of the strictly diffusion-limited compartment, a multi-*b*-value DWI sequence with *b*-values range from 0 to 8,000 s/mm^2 was used in this study.

MATERIALS AND METHODS

Participants

This study was approved by the institutional review board at the Second Affiliated Hospital of Zhejiang University. Six young healthy volunteers (four males and two females, age range 24–27 years) were enrolled in this study, without any previous history of central nervous system diseases. Written informed consents were obtained from all participants. This study was conducted according to the principles expressed in the Declaration of Helsinki.

DWI Parameters

The volunteers were imaged on a 3.0-Tesla MR system (Discovery MR750, GE Healthcare Systems, Milwaukee, WI) with a gradient strength of 50 mT/m using an eight-channel high-resolution receiver head coil. A single-shot echo planer imaging sequence was used for the imaging with the following parameters: number of sections, 24; section thickness, 4 mm; field of view, 240 × 240 mm; matrix, 256 × 256; in-plane resolution, 0.94 × 0.94 mm; repetition time/echo time, 3,000/107.7 ms; phase FOV, 1.00; flip angle, 90; and pixel bandwidth, 1953.1 Hz/pixel. The sequence was performed with 17 *b*-values (0, 10, 20, 30, 50, 70, 100, 150, 200, 300, 500, 700, 1,000, 2,000, 3,000, 5,000, and 8,000 s/mm^2) in three orthogonal directions, and the signals were averaged over three directions by the imaging system automatically. The numbers of scan averages (NSAs) for $b = 0$ to 8,000 s/mm2 were 1, 3, 3, 3, 3, 3, 3, 3, 3, 3, 3, 5, 5, 5, 5, 9, and 12, respectively. Magnitude reconstruction was applied by the imaging system automatically. The total scan time was 21 min 30 s.

Models

The potential biological interpretations for the three compartments of the modified tri-exponential model are shown in **Figure 1A**. The strictly diffusion-limited compartment is suspected to represent water molecules strictly limited in microstructures with extremely small space, such as intracellular organelles. The signal attenuation curves for three different ADC values are shown in **Figure 1B**. For normal ADC values, the remaining signal ratio will be very low at $b = 8{,}000$ s/mm^2 (1.8% for ADC = 500 mm^2/s and 0.0% for ADC = 2,000 mm^2/s). However, the signal ratio will still remain high at $b = 8{,}000$ s/mm^2 for an extremely low ADC value (92.3% for ADC = 10 mm^2/s).

The signal attenuation of the bi-exponential model, the conventional tri-exponential model and the modified tri-exponential model as a function of *b* is expressed by Equations (1–3), respectively.

$$\frac{S}{S_0} = f_{slow} * e^{-ADC_{slow} * b} + f_{fast} * e^{-ADC_{fast} * b},\ f_{slow} + f_{fast} = 1 \quad (1)$$

$$\frac{S}{S_0} = f_{very-slow} * e^{-ADC_{very-slow} * b} + f_{slow} * e^{-ADC_{slow} * b} + f_{fast} * e^{-ADC_{fast} * b},\ f_{very-slow} + f_{slow} + f_{fast} = 1 \quad (2)$$

$$\frac{S}{S_0} = f_0 + f_{slow} * e^{-ADC_{slow} * b} + f_{fast} * e^{-ADC_{fast} * b},\ f_0 + f_{slow} + f_{fast} = 1 \quad (3)$$

In these equations, S represents the signal intensity at corresponding b, and S_0 represents the signal intensity at $b = 0$ s/mm^2. The $f_{very-slow}$, f_{slow}, and f_{fast}, respectively represent

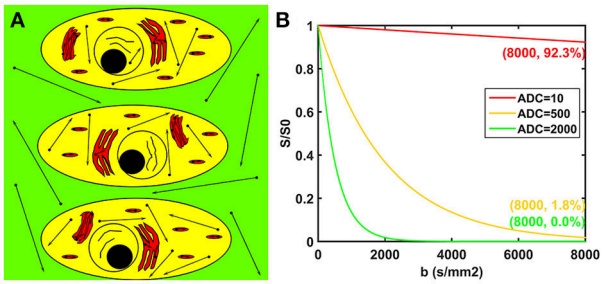

FIGURE 1 | Potential biological interpretations for the three compartments of the modified tri-exponential model **(A)**. The red regions represent the strictly diffusion-limited compartment, the yellow regions represent the slow diffusion compartment, and the green regions represent the fast diffusion compartment. Signal attenuation curves of three ADC values **(B)**. The unit of the ADC values was mm^2/s.

the fractions of corresponding diffusion compartments, with corresponding ADC marked as $ADC_{very-slow}$, ADC_{slow}, and ADC_{fast}. The f_0 represents the fraction of the strictly diffusion-limited compartment.

Model Ranking

For model selection, the small-sample corrected Akaike information criterion (AICc) has been widely used in previous studies (Bourne et al., 2014; Jambor et al., 2015). The akaike information criterion (AIC) was first proposed by Akaike for determining the best model among models and avoiding over-fitting (Akaike, 1974). Hurvich and Tsai improved this method and proposed AICc to compensate for the number of data points, and this improved method has been tested valuable in small samples (Hurvich and Tsai, 1989). The equation for calculating the AICc is as listed below:

$$AICc = 2 * k + N * \ln\left(\frac{RSS}{N}\right) + \frac{2 * k * (k+1)}{N-k-1} \quad (4)$$

where k is the number of free parameters of models, N is the number of points used for fitting, and RSS is the RSS from fitting (Hurvich and Tsai, 1989; Jambor et al., 2015).

Besides, we also compared the models with a leave-one-out test, in order to confirm that the models were correctly ranked by the AICc (Bourne et al., 2014). The predicted residual sum of squares (PRESS) is an index of this method first proposed by Allen for model selection (Allen, 1974).

Image Processing and Analysis

The DWI images were realigned by using SPM12 (available at: www.fil.ion.ucl.ac.uk/spm). Then, these images were analyzed by using programs written in MatLab (MatLab 2009b; MathWorks, Natick, MA). The conventional bi- and tri-exponential models and the modified tri-exponential model were all used for curve fitting.

Curve fittings of these three models were performed using DWI maps obtained with the first 16 b-values (excluding b = 8,000 s/mm^2), and were implemented voxel-by-voxel using the steepest descent algorithm (Lenglet et al., 2009). Signal values were all normalized to corresponding signal value S_0 prior to model fitting. The initial values of parameters were set empirically. For these three models, the initial value of f_{slow} was set to 0.50, with ADC_{slow} set to 600×10^{-6} mm^2/s and ADC_{fast} set to $2{,}000 \times 10^{-6}$ mm^2/s. For the modified tri-exponential model, the initial value of f_0 was set to 0.10, while for the conventional tri-exponential model, the initial value of $f_{very-slow}$ was set to 0.10, with $ADC_{very-slow}$ set to 100×10^{-6} mm^2/s. The detail description of the programmed algorithm of model fit is shown in Supplement Figure S1. Thus, the parametric maps and the maps of residual sums of squares (RSS) were derived. Subsequently, the AICc maps of these three models were calculated from the RSS maps. Besides, the PRESS maps were also obtained.

After the curve fitting, the signal intensities at b = 8,000 s/mm^2 were predicted, and the error of the prediction was squared to form the squared prediction error (SPE) by Equation (5). Thus, the SPE maps were derived. The SPE was a new index presented in the current study to evaluate the ability of models in predicting DWI signals at ultra-high b-values.

$$SPE = (S_m - S_p)^2 \quad (5)$$

where S_m and S_p represent the measured signal intensity and the predicted signal intensity at $b = 8{,}000$ s/mm^2, respectively.

The regions of interest (ROIs) were drawn by an experienced neuroradiologist. Each ROI was drawn to include corresponding zones as much as possible at one section. Two ROIs were drawn in the cingulate gyrus and supramarginal gyrus, representing gray matter. Six ROIs were drawn in the genu of the corpus callosum, splenium of the corpus callosum, posterior limbs of the internal capsule, centrum semiovale, forceps minor and forceps major, representing white matter. Average values of the parameters and indexes were calculated within each ROI. Besides, the signal-to-noise ratios (SNR) of DWI maps were determined by using a "difference method," which is based on the evaluation of a difference image of two repeated acquisitions on a single volunteer (Dietrich et al., 2007). ROIs were placed on centrum semiovale and cingulate gyrus, representing for white matter and gray matter, respectively.

In addition, we also performed a stability experiment to investigate the fitting stability of the modified tri-exponential model toward initial conditions. We set random values between 0.05 and 0.10 to initial f_0 values, random values between 0.50 and 0.60 to initial f_{slow} values, random values between 500 and 800 mm^2/s to initial ADC_{slow} values and random values between 1,900 and 2,200 mm^2/s to initial ADC_{fast} values. Thus, we totally generated 20 random initial value sets for the modified tri-exponential model. For each initial value set, curve fitting of the modified tri-exponential model was performed, and the mean values of the parameters were calculated over the ROI on the genu of the corpus callosum (CCG) for one volunteer.

Statistical Analysis

All statistical analyses were performed using SPSS version 22 (SPSS Inc, Chicago, IL, USA). The median values and quartile ranges of the RSS, SPE, and AICc were calculated. Wilcoxon

signed-rank test were used to compare these three indexes between any pair of the models. A value of $p < 0.05$ was regarded as statistically significant.

RESULTS

The mean DWI signal intensity over an ROI decayed much more slowly in white matter than in gray matter, shown in **Figure 2**. In particular, the remaining signal intensity ratio at $b = 8{,}000$ s/mm^2 was as high as 18.7% in the white matter ROI, while only 2.4% in the gray matter ROI. In white matter, the SNRs of the DWI image at $b = 0$, 5,000, and 8,000 s/mm^2 were 28.2, 27.8, and 23.7, respectively. In gray matter, those were 31.2, 9.8, and 6.5, respectively. For the modified tri-exponential model, the stability experiment showed that the distributions (mean $\pm$ *SD*) of the mean f_0, f_{slow}, f_{fast}, ADC_{slow}, and ADC_{fast} values on CCG over the initial value sets were 18.2 $\pm$ 0.6, 58.4 $\pm$ 1.2, 23.6 $\pm$ 1.2%, 816 $\pm$ 7 and 4,525 $\pm$ 88 mm^2/s, respectively.

For the white matter ROIs, the RSSs of the modified tri-exponential model were lower than those of the other two models ($p < 0.05$). Besides, the RSSs of the conventional tri-exponential model were lower than those of the bi-exponential model ($p < 0.05$), shown in **Table 1**. For the gray matter ROIs, the RSSs of the conventional tri-exponential model were lower than those of the other two models, and there were no significant differences in RSSs between the modified tri-exponential model and the bi-exponential model.

The AICcs of the conventional tri-exponential model were significantly larger than those of the other two models in all ROIs ($p < 0.05$), shown in **Table 2**. The AICcs of the modified tri-exponential model were lower than those of the bi-exponential model in the white matter ROIs ($p < 0.05$, except for the genu of the corpus callosum), while were higher than those of the bi-exponential model in the gray matter ROIs ($p < 0.05$).

The PRESSs of the modified tri-exponential model were significantly lower than those of the other two models in all white matter ROIs ($p < 0.05$), while those of the conventional tri-exponential model were significantly lower than those of the other two models in two gray matter ROIs ($p < 05$), shown in **Table 3**.

The bi-exponential model was unable to predict the DWI signal at $b = 8{,}000$ s/mm^2 as accurately as the other two models, shown in **Figure 3**. The SPEs of the bi-exponential model were significantly higher than those of the other two models in all white matter ROIs ($p < 0.05$), shown in **Table 4**.

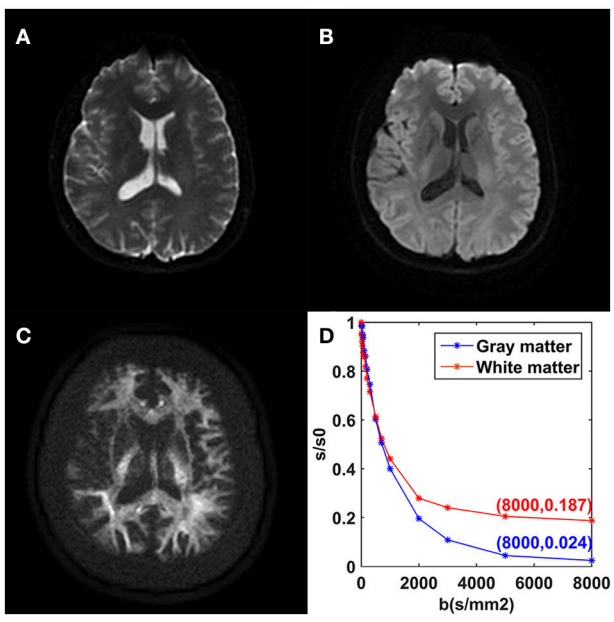

FIGURE 2 | DWI images achieved with $b = 0$ **(A)**, $b = 1{,}000$ **(B)**, and $b = 8{,}000$ s/mm^2 **(C)** from one volunteer. Plots of the average signal-intensity decay of two ROIs as a function of b **(D)**. CG, cingulate gyrus; CCg, genu of the corpus callosum.

TABLE 1 | Residual sums of squares (RSSs) of the bi-exponential, conventional tri-exponential, and modified tri-exponential models in ROIs.

ROI	Bi-exponential ($\times 10^{-4}$)	Conventional tri-exponential ($\times 10^{-4}$)	Modified tri-exponential ($\times 10^{-4}$)
CCg	194 (135, 214)	136 (122, 175)*	126 (110, 159)*#
CCs	121 (106, 159)	94 (82, 134)*	85 (78, 129)*#
ICp	61 (45, 72)	47 (34, 59)*	44 (29, 51)*#
CS	64 (58, 86)	50 (44, 70)*	44 (38, 66)*#
Fmi	80 (71, 107)	65 (53, 88)*	62 (43, 80)*#
Fmj	64 (54, 93)	52 (41, 70)*	45 (38, 60)*#
CG	187 (88, 291)	178 (82, 278)*	189 (90, 314)#
SpG	101 (69, 147)	93 (62, 142)*	96 (71, 151)#

*CCg, genu of the corpus callosum; CCs, splenium of the corpus callosum; ICp, posterior limbs of the internal capsule; CS, centrum semiovale; Fmi, forceps minor; Fmj, forceps major; CG, cingulate gyrus; SpG, supramarginal gyrus. Data expressed as median (Q1, Q3). *p < 0.05, vs. the bi-exponential model; #p < 0.05, vs. the conventional tri-exponential model.*

TABLE 2 | Small-sample corrected Akaike information criterions (AICcs) of the bi-exponential, conventional tri-exponential and modified tri-exponential models in ROIs.

ROI	Bi-exponential	Conventional tri-exponential	Modified tri-exponential
CCg	−102 (−106, −94)	−98 (−103, −89)*	−105 (−108, −94)#
CCs	−112 (−115, −107)	−108 (−112, −105)*	−114 (−117, −110)*#
ICp	−123 (−126, −118)	−120 (−125, −115)*	−126 (−131, −121)*#
CS	−121 (−124, −118)	−119 (−121, −116)*	−124 (−127, −121)*#
Fmi	−120 (−124, −117)	−117 (−123, −114)*	−122 (−128, −119)*#
Fmj	−123 (−124, −115)	−121 (−122, −113)*	−126 (−127, −117)*#
CG	−112 (−119, −98)	−105 (−113, −91)*	−109 (−115, −94)*#
SpG	−117 (−121, −102)	−110 (−115, −104)*	−114 (−118, −107)*#

*CCg, genu of the corpus callosum; CCs, splenium of the corpus callosum; ICp, posterior limbs of the internal capsule; CS, centrum semiovale; Fmi, forceps minor; Fmj, forceps major; CG, cingulate gyrus; SpG, supramarginal gyrus. Data expressed as median (Q1, Q3). *p < 0.05, refers to the bi-exponential model; #p < 0.05, refers to the conventional tri-exponential model.*

Representative parameter maps derived from the modified tri-exponential model and the conventional tri-exponential model are shown in **Figure 4**. In the white matter ROIs, the mean $ADC_{very-slow}$ values (1–7 × 10^{-6} mm^2/s) were extremely low, and the mean $f_{very-slow}$ values (11.8–18.3%) were similar to the mean f_0 values (11.9–18.7%). However, in the gray matter ROIs, the mean $ADC_{very-slow}$ values (251–445 × 10^{-6} mm^2/s) were not extremely low and the mean $f_{very-slow}$ values (11.9–15.7%) were much higher than the mean f_0 values (1.2–2.7%), shown in **Table 5**.

Figure 5 presents the whole brain f_0 maps of one volunteer. The f_0 is high in white matter, but very low in gray matter. These

TABLE 3 | Predicted error sums of squares (PRESS) of the bi-exponential, conventional tri-exponential and modified tri-exponential models in ROIs.

ROI	Bi-exponential (×10^{-5})	Conventional tri-exponential (×10^{-5})	Modified tri-exponential (×10^{-5})
CCg	2,930 (2,534, 3,864)	2,399 (1,786, 3,373)*	1,985 (1,458, 3,054)*#
CCs	1,679 (1,593, 2,327)	1,316 (1,121, 1,805)*	1,144 (1,044, 1,602)*#
ICp	861 (685, 1,038)	670 (530, 810)*	518 (489, 694)*#
CS	879 (793, 113)	715 (589, 835)*	582 (495, 759)*#
Fmi	1,006 (736, 1,203)	780 (572, 916)*	688 (454, 852)*#
Fmj	869 (728, 1,243)	619 (546, 886)*	573 (434, 807)*#
CG	1,964 (976, 3,433)	1,898 (915, 3,324)*	1,925 (989, 3,510)#
SpG	1,146 (819, 1,684)	1,073 (756, 1,621)*	1,085 (860, 1,721)

*CCg, genu of the corpus callosum; CCs, splenium of the corpus callosum; ICp, posterior limbs of the internal capsule; CS, centrum semiovale; Fmi, forceps minor; Fmj, forceps major; CG, cingulate gyrus; SpG, supramarginal gyrus. Data expressed as median (Q1, Q3). *p < 0.05, refers to the bi-exponential model; #p < 0.05, refers to the conventional tri-exponential model.*

TABLE 4 | Squared prediction errors (SPEs) of the bi-exponential, conventional tri-exponential and modified tri-exponential models in ROIs of white matter.

ROI	Bi-exponential (×10^{-5})	Conventional tri-exponential (×10^{-5})	Modified tri-exponential (×10^{-5})
CCg	500 (340, 595)	56 (31, 69)*	46 (22, 60)*
CCs	613 (462, 761)	52 (46, 110)*	50 (42, 185)*
ICp	414 (352, 488)	38 (22, 43)*	44 (31, 56)*#
CS	362 (267, 428)	38 (24, 95)*	46 (36, 104)*#
Fmi	356 (337, 403)	23 (12, 31)*	28 (20, 42)*#
Fmj	328 (293, 351)	24 (17, 31)*	33 (23, 40)*#

*CCg, genu of the corpus callosum; CCs, splenium of the corpus callosum; ICp, posterior limbs of the internal capsule; CS, centrum semiovale; Fmi, forceps minor; Fmj, forceps major. Data expressed as median (Q1, Q3). *p < 0.05, refers to the bi-exponential model; #p < 0.05, refers to the conventional tri-exponential model.*

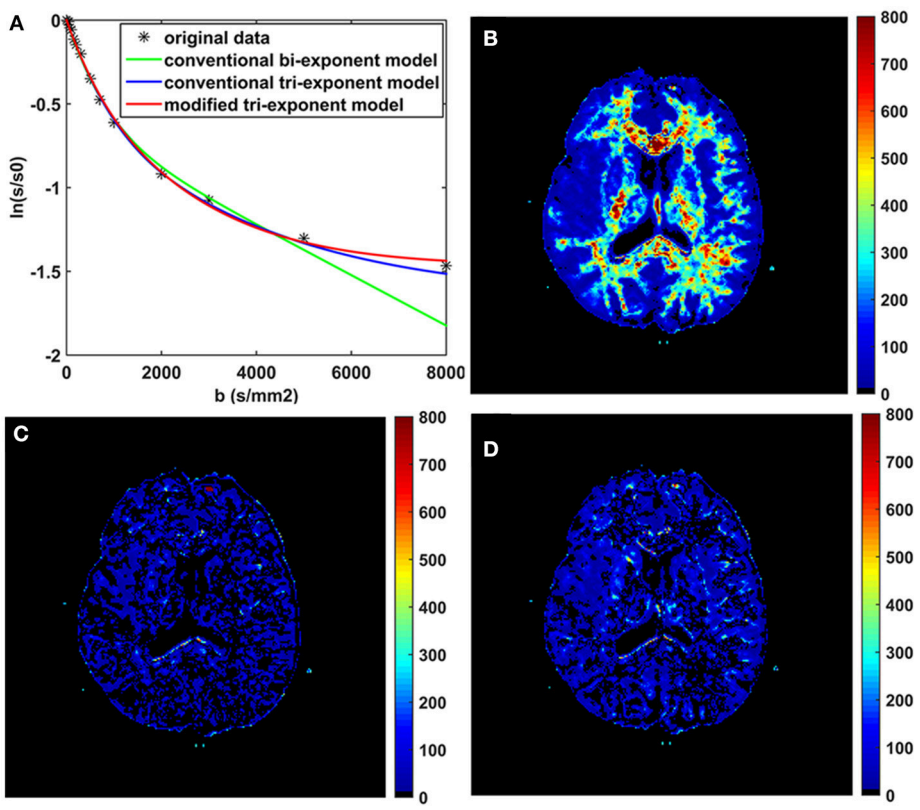

FIGURE 3 | The fitting curves of the three models with the first 16 *b*-values in a typical voxel of white matter **(A)**. The maps of the squared prediction errors (SPE) calculated by the bi-exponential model **(B)**, the conventional tri-exponential model **(C)**, and the modified tri-exponential model **(D)**. The unit for SPE is ×10^{-5}.

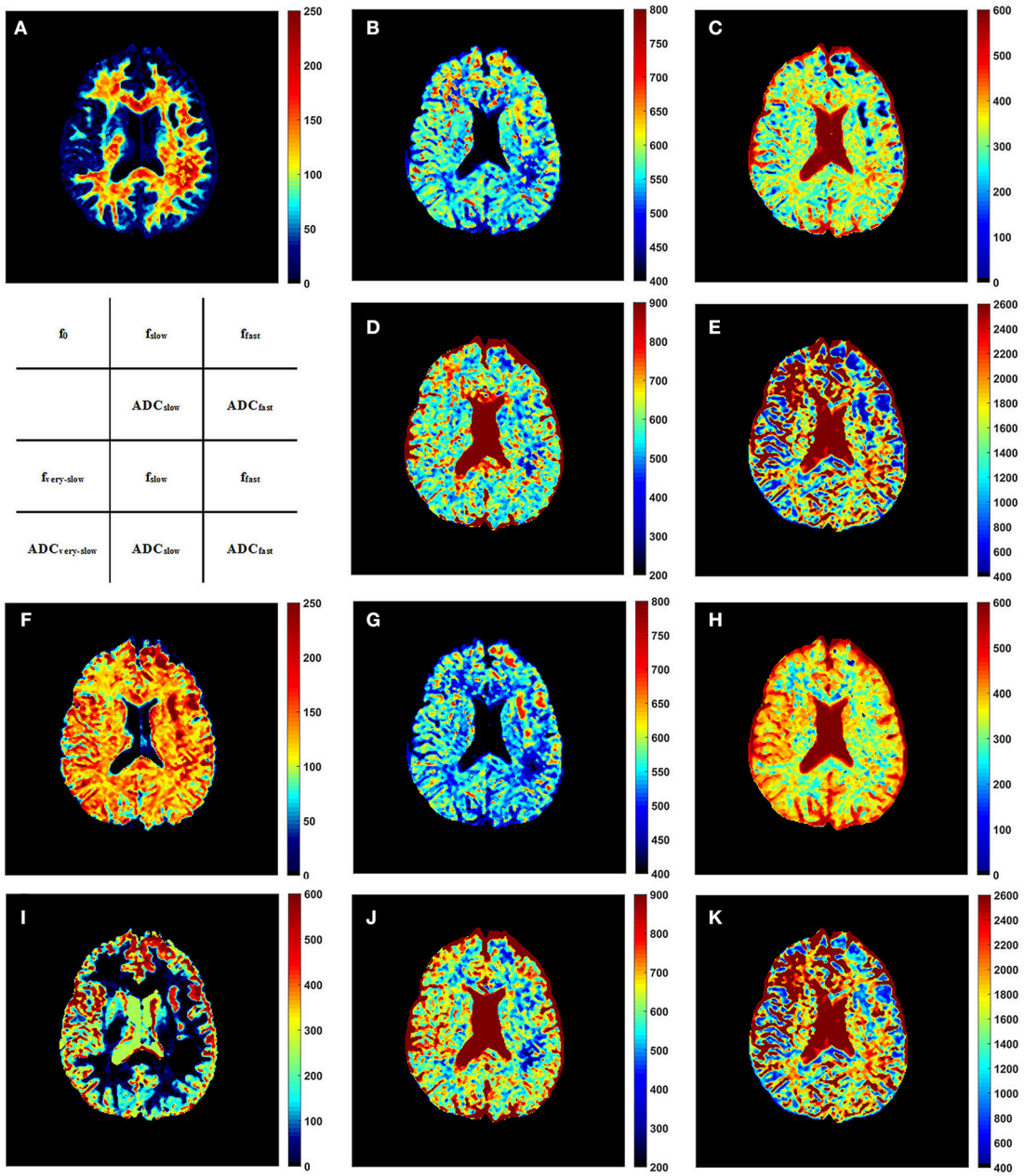

FIGURE 4 | The f_0 map **(A)**, f_{slow} map **(B)**, f_{fast} map **(C)**, ADC_{slow} map **(D),** and ADC_{fast} map **(E)** derived from the modified tri-exponential model. The $f_{very-slow}$ map **(F)**, f_{slow} map **(G)**, f_{fast} map **(H)**, $ADC_{very-slow}$ map **(I)**, ADC_{slow} map **(J),** and ADC_{fast} map **(K)** derived from the conventional tri-exponential model. The unit for f maps is ‰, and the unit for ADC maps is $\times 10^{-6}$ mm^2/s.

images show good resolution and good definition at white-gray matter interfaces.

DISCUSSION

In our study, the AICcs and PRESSs of the new model were found to be the lowest in white matter, suggesting that this new model fit better than the conventional bi-exponential and tri-exponential models and may provide more detailed information. The f_0 values were found to be very small in gray matter but ranging 10–20% in white matter. This result indicates that the strictly diffusion-limited compartment may be an important component in white matter and may need to be considered when we develop models for multi-b-value DWI.

First of all, we certified that the fraction of the strictly diffusion-limited compartment (f_0) in white matter cannot be explained only by noise. In white matter, the remaining signal

intensity ratio was as high as 18.7% at $b = 8{,}000$ s/mm^2, while the SNR was 23.7. Thus, the ratio of noise at $b = 8{,}000$ s/mm^2 to signal at $b = 0$ s/mm^2 was only 0.79%. This ratio is much lower than the fractions of the strictly diffusion-compartment in white matter which were ranging from 11.8 to 18.7%. Thus, the existence of the strictly diffusion-limited compartment in white matter is not only a result of noise.

TABLE 5 | The f_0 derived from the modified tri-exponential models, and the $f_{very-slow}$ and the $ADC_{very-slow}$ derived from the conventional tri-exponential in ROIs.

ROI	f_0 (%)	$f_{very-slow}$ (%)	$ADC_{very-slow}$ ($\times 10^{-6}$ s/mm^2)
CCg	16.9 ± 2.8	17.8 ± 0.2	7 ± 11
CCs	18.7 ± 2.0	18.3 ± 1.8	2 ± 4
ICp	15.3 ± 0.7	14.3 ± 0.9	1 ± 1
CS	14.9 ± 1.3	14.3 ± 1.1	1 ± 1
Fmi	13.2 ± 1.8	12.8 ± 1.6	4 ± 3
Fmj	11.9 ± 1.3	11.8 ± 0.8	7 ± 5
CgC	1.2 ± 1.0	15.7 ± 3.5	445 ± 144
SpG	2.7 ± 1.3	11.9 ± 1.5	251 ± 83

CCg, genu of corpus callosum; CCs, splenium of corpus callosum; ICp, posterior limbs of internal capsule; CS, centrum semiovale; Fmi, forceps minor; Fmj, forceps major; CgC, cingulate cortex; SpG, supramarginal gyrus. Data expressed as mean ± sd.

In the present study, the bi-exponential model was found to be an over-simplified model. According to the intravoxel incoherent motion (IVIM) theory, the fast ADC is thought to be linked to the microcirculatory perfusion of blood within the capillaries, while the slow ADC is related to diffusion of water molecules in the tissues (Le Bihan and Turner, 1992; Koh et al., 2011; Cercueil et al., 2015). This theory is not suitable when $b >$ 1,000 s/mm^2. Another explanation for this model is that two components represent intra- and extra-cellular compartments, respectively (Niendorf et al., 1996; Steier et al., 2012). However, researchers have found that the attenuation of DWI signal does not obey the mono-exponential model even without extra-cellular compartment or even in a single cell (Grant et al., 2001; Schwarcz et al., 2004; Steier et al., 2012). These findings of previous studies also indicate that the bi-exponential model may not be a satisfying model for explaining the attenuation of DWI signal. Models with more pools might be preferable to accurately reflect the diffusion motion of water molecules in tissues.

In the present study, we also found that the SPEs of the bi-exponential model were much higher than the other two models in white matter. As we know, the remaining signal intensity ratio will be very low at ultra-high b-value for compartments

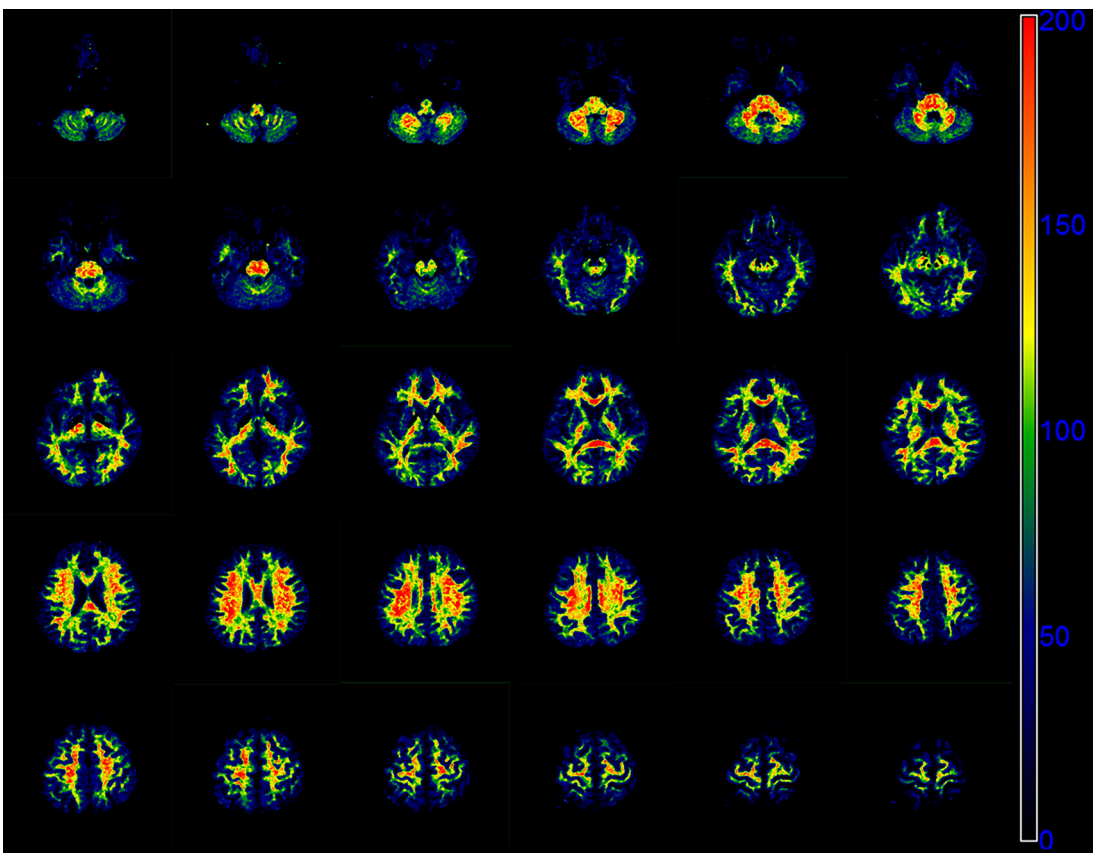

FIGURE 5 | Sequential 30 slices of the f_0 maps of one volunteer derived by the modified tri-exponential model. The f_0 maps are displayed from the top left. The unit is ‰.

with a normal ADC, while this ratio will still remain high for the compartment with an extremely low ADC. Hence, as the bi-exponential model does not contain the compartment with extremely low ADC, it is conceivable that the predicted signal at $b = 8{,}000$ s/mm^2 would be much lower than the measured value, resulting in high SPE.

When compared with the modified tri-exponential model, the conventional tri-exponential model had significantly higher AICcs in all ROIs and was considered as an over-fitting model. More importantly, the biological implications of the $ADC_{very-slow}$ compartment differed between white matter and gray matter. In the white matter ROIs, $ADC_{very-slow}$ values were extremely small, and the $f_{very-slow}$ values were found to be similar to the f_0 values. Thus, f_0 and $f_{very-slow}$ represent the fraction of the same compartment with extremely small ADC in white matter. However, when f_0 values were negligible in the gray matter ROIs, the $f_{very-slow}$ values were still as high as in white matter, while the $ADC_{very-slow}$ values were not extremely small. This finding suggests that the $ADC_{very-slow}$ compartment no longer represents the compartment with extremely small ADC in gray matter. In our view, the three compartments of the conventional tri-exponential model may represent three major proton pools in tissues, while the major proton pools may differ among tissues. Hence, the parameters derived from this model may have no specific biological implications. This might be an important limitation for the application of the conventional tri-exponential model. Generally, models with more pools may also suffer from this fatal limitation.

On the contrary, by directly setting the $ADC_{very-slow}$ to zero, the modified tri-exponential model is able to detect the volume fraction of the extremely-low ADC compartment. In the present study, the mean f_0 values were found to be non-ignorable in white matter, ranging from 11.9 to 18.7%. Ferizi et al. also found that three compartment models with a "dot" compartment (zero radius sphere) can produce better fit for diffusion MRI in white matter, suggesting the existence of the extremely-low ADC compartment (Ferizi et al., 2014). In white matter, it has been suspected that there are stationary water molecules trapped in glial cells and other small compartments or bound to membranes and other subcellular structures (Alexander et al., 2010). However, Dhita et al. recently showed that still water compartment was absent in white matte by using isotropic diffusion measurement (Dhital et al., 2017). A similar conclusion was also made by Veraart el al. using single-direction measurements (Veraart et al., 2016). Although Dhital et al. found that the slowly diffusing water pools existed in all directions, these pools were suspected to reside in separate micro-environments (Dhital et al., 2017). It is recommended that orientation dispersion of axons and glial processes should be taken into account when developing models for fitting isotropic diffusion measurement (Dhital et al., 2017). Thus, the exact biological interpretation for the strictly diffusion-limited compartment in white matter needs to be investigated further. Besides, the existence of this compartment in other normal or pathological tissue also needs to be investigated.

One limitation of the application of ultra-high *b*-value DWI is low SNR. To ensure high SNRs, the NSAs were designed very large in this study, especially for DWI images with ultra-high *b*-values. Our result showed that the SNRs of DWI maps with ultra-high *b*-values were comparable with that of DWI maps with $b = 0$ s/mm^2. However, traditional magnitude reconstruction which is used in this study, may lead to an accumulation of noise (Eichner et al., 2015). Averaging the repeat measurements in complex domain is recommend to further improve the SNR, while it requires complex phase navigation and is not normally provided by hardware vendors (Jones et al., 2013; Eichner et al., 2015).

Anisotropic resolution with a high in-plant resolution and a large slice thickness was applied in this study. Clinically, a high in-plant resolution is required to distinguish fine structure in brain. SNR has a linear relationship with voxel volume, thus a relative large slice thickness can improve the SNR. Besides, a large slice thickness can also shorten the scan time. However, anisotropic resolution can lead to differential averaging of fiber orientations (Jones et al., 2013). This effect is not accounted for in this study because the DWI images used for model fitting do not contain direction information.

There are still several limitations in this study. First, the total scan time of this sequence is too long for clinical practice. Hence, the multi-*b*-value DWI sequence should be optimized, including the selection of *b*-values and NSAs. Second, in gray matter, the SNRs of DWI maps at ultra-high *b*-values were low, which reduced the reliability of some results. However, the main focus of the study was on white matter, and the SNR still remained high at ultra-high *b*-values in white matter. Third, the impact of T2 values of different compartments were not evaluated in our study, and need further research.

In conclusion, the bi-exponential model is an over-simplified model and unable to predict the signal intensity at ultra-high *b*-values in white matter, while the conventional tri-exponential model is an over-fitting model and has no specific biological implication for each compartment. The new model fits better than the other two models, and may provide additional information.

AUTHOR CONTRIBUTIONS

QZ: Conceived the idea; BJ: Supervised the work; CL and FD: Collected the data; JZ, FD, and FS: Analyzed the data; QZ, FS, and CL: Wrote the main manuscript text. All authors reviewed the manuscript.

FUNDING

This study was supported by Zhejiang Provincial Natural Science Foundation of China (Grant number, LY13H180006).

SUPPLEMENTARY MATERIAL

The Supplementary Material for this article can be found online at: https://www.frontiersin.org/articles/10.3389/fnins.2018.00102/full#supplementary-material

REFERENCES

Akaike, H. (1974). A new look at the statistical model identification. *IEEE Trans. Autom. Control* 9, 716–723. doi: 10.1109/TAC.1974.1100705

Alexander, D. C., Hubbard, P. L., Hall, M. G., Moore, E. A., Ptito, M., Parker, G. J. M., et al. (2010). Orientationally invariant indices of axon diameter and density from diffusion MRI. *Neuroimage* 52, 1374–1389. doi: 10.1016/j.neuroimage.2010.05.043

Allen, D. M. (1974). The relationship between variable selection and data agumentation and a method for prediction. *Technometrics* 16, 125–127. doi: 10.1080/00401706.1974.10489157

Baxter, G. T., and Frank, L. R. (2013). A computational model for diffusion weighted imaging of myelinated white matter. *Neuroimage* 75, 204–212. doi: 10.1016/j.neuroimage.2013.02.076

Bennett, K. M., Hyde, J. S., and Schmainda, K. M. (2006). Water diffusion heterogeneity index in the human brain is insensitive to the orientation of applied magnetic field gradients. *Magn. Reson. Med.* 56, 235–239. doi: 10.1002/mrm.20960

Bennett, K. M., Schmainda, K. M., Bennett Tong, R., Rowe, D. B., Lu, H., and Hyde, J. S. (2003). Characterization of continuously distributed cortical water diffusion rates with a stretched-exponential model. *Magn. Reson. Med.* 50, 727–734. doi: 10.1002/mrm.10581

Bisdas, S., Koh, T. S., Roder, C., Braun, C., Schittenhelm, J., Ernemann, U., et al. (2013). Intravoxel incoherent motion diffusion-weighted MR imaging of gliomas: feasibility of the method and initial results. *Neuroradiology* 55, 1189–1196. doi: 10.1007/s00234-013-1229-7

Bourne, R. M., Panagiotaki, E., Bongers, A., Sved, P., Watson, G., and Alexander, D. C. (2014). Information theoretic ranking of four models of diffusion attenuation in fresh and fixed prostate tissue *ex vivo*. *Magn. Reson. Med.* 72, 1418–1426. doi: 10.1002/mrm.25032

Cercueil, J. P., Petit, J. M., Nougaret, S., Soyer, P., Fohlen, A., Pierredon-Foulongne, M. A., et al. (2015). Intravoxel incoherent motion diffusion-weighted imaging in the liver: comparison of mono-, bi- and tri-exponential modelling at 3.0-T. *Eur. Radiol.* 25, 1541–1550. doi: 10.1007/s00330-014-3554-6

Clark, C. A., and Le Bihan, D. (2000). Water diffusion compartmentation and anisotropy at high b values in the human brain. *Magn. Reson. Med.* 44, 852–859. doi: 10.1002/1522-2594(200012)44:6<852::AID-MRM5>3.0.CO;2-A

Dhital, B., Kellner, E., Kiselev, V. G., and Reisert, M. (2017). The absence of restricted water pool in brain white matter. *Neuroimage*. doi: 10.1016/j.neuroimage.2017.10.051. [Epub ahead of print].

Dietrich, O., Raya, J. G., Reeder, S. B., Reiser, M. F., and Schoenberg, S. O. (2007). Measurement of signal-to-noise ratios in MR images: influence of multichannel coils, parallel imaging, and reconstruction filters. *J. Magn. Reson. Imaging* 26, 375–385. doi: 10.1002/jmri.20969

Eichner, C., Cauley, S. F., Cohen-Adad, J., Moller, H. E., Turner, R., Setsompop, K., et al. (2015). Real diffusion-weighted MRI enabling true signal averaging and increased diffusion contrast. *Neuroimage* 122, 373–384. doi: 10.1016/j.neuroimage.2015.07.074

Ferizi, U., Schneider, T., Panagiotaki, E., Nedjati-Gilani, G., Zhang, H., Wheeler-Kingshott, C. A. M., et al. (2014). A ranking of diffusion MRI compartment models with *in vivo* human brain data. *Magn. Reson. Med.* 72, 1785–1792. doi: 10.1002/mrm.25080

Grant, S. C., Buckley, D. L., Gibbs, S., Webb, A. G., and Blackband, S. J. (2001). MR microscopy of multicomponent diffusion in single neurons. *Magn. Reson. Med.* 46, 1107–1112. doi: 10.1002/mrm.1306

Hayashi, T., Miyati, T., and Takahashi, J. (2013). Diffusion analysis with triexponential function in liver cirrhosis. *J. Magn. Reson. Imaging* 38, 148–153. doi: 10.1002/jmri.23966

Hayashi, T., Miyati, T., Takahashi, J., Tsuji, Y., Suzuki, H., Tagaya, N., et al. (2014). Diffusion analysis with triexponential function in hepatic steatosis. *Radiol. Phys. Technol.* 7, 89–94. doi: 10.1007/s12194-013-0235-0

Hu, Y. C., Yan, L. F., Sun, Q., Liu, Z. C., Wang, S. M., Han, Y., et al. (2017). Comparison between ultra-high and conventional mono b-value DWI for preoperative glioma grading. *Oncotarget* 8, 37884–37895. doi: 10.18632/oncotarget.14180

Hu, Y. C., Yan, L. F., Wu, L., Du, P., Chen, B. Y., Wang, L., et al. (2014). Intravoxel incoherent motion diffusion-weighted MR imaging of gliomas: efficacy in preoperative grading. *Sci. Rep.* 4:7208. doi: 10.1038/srep.07208

Hurvich, C. M., and Tsai, C. L. (1989). Regression and time series model selection in small samples. *Biometrika* 76, 297–307. doi: 10.1093/biomet/76.2.297

Jambor, I., Merisaari, H., Taimen, P., Boström, P., Minn, H., Pesola, M., et al. (2015). Evaluation of different mathematical models for diffusion-weighted imaging of normal prostate and prostate cancer using high b-values: a repeatability study. *Magn. Reson. Med.* 73, 1988–1998. doi: 10.1002/mrm.25323

Jensen, J. H., Helpern, J. A., Ramani, A., Lu, H., and Kaczynski, K. (2005). Diffusional kurtosis imaging: the quantification of non-gaussian water diffusion by means of magnetic resonance imaging. *Magn. Reson. Med.* 53, 1432–1440. doi: 10.1002/mrm.20508

Jones, D. K., Knosche, T. R., and Turner, R. (2013). White matter integrity, fiber count, and other fallacies: the do"s and don"ts of diffusion MRI. *Neuroimage* 73, 239–254. doi: 10.1016/j.neuroimage.2012.06.081

Koh, D. M., Collins, D. J., and Orton, M. R. (2011). Intravoxel incoherent motion in body diffusion-weighted MRI: reality and challenges. *Am. J. Roentgenol.* 196, 1351–1361. doi: 10.2214/AJR.10.5515

Le Bihan, D., Breton, E., Lallemand, D., Aubin, M. L., Vignaud, J., and Laval-Jeantet, M. (1988). Separation of diffusion and perfusion in intravoxel incoherent motion MR imaging. *Radiology* 168, 497–505. doi: 10.1148/radiology.168.2.3393671

Le Bihan, D., and Turner, R. (1992). The capillary network: a link between IVIM and classical perfusion. *Magn. Reson. Med.* 27, 171–178. doi: 10.1002/mrm.1910270116

Lenglet, C., Campbell, J. S. W., Descoteaux, M., Haro, G., Savadjiev, P., Wassermann, D., et al. (2009). Mathematical methods for diffusion MRI processing. *Neuroimage* 45, S111–S122. doi: 10.1016/j.neuroimage.2008.10.054

Lin, Y., Li, J., Zhang, Z., Xu, Q., Zhou, Z., Zhang, Z., et al. (2015). Comparison of intravoxel incoherent motion diffusion-weighted MR imaging and arterial spin labeling MR imaging in gliomas. *Biomed. Res. Int.* 2015, 234245–234210. doi: 10.1155/2015/234245

Ling, X., Zhang, Z., Zhao, Z., Guo, L., Tang, Y., Shi, C., et al. (2015). Investigation of apparent diffusion coefficient from ultra-high b-values in Parkinson's disease. *Eur. Radiol.* 25, 2593–2600. doi: 10.1007/s00330-015-3678-3

Müller, M. F., Prasad, P. V., and Edelman, R. R. (1998). Can the IVIM model be used for renal perfusion imaging? *Eur. J. Radiol.* 26, 297–303. doi: 10.1016/S0720-048X(97)01161-3

Niendorf, T., Dijkhuizen, R. M., Norris, D. G., van Lookeren Campagne, M., and Nicolay, K. (1996). Biexponential diffusion attenuation in various states of brain tissue: implications for diffusion-weighted imaging. *Magn. Reson. Med.* 36, 847–857. doi: 10.1002/mrm.1910360607

Ohno, N., Miyati, T., Kobayashi, S., and Gabata, T. (2016). Modified triexponential analysis of intravoxel incoherent motion for brain perfusion and diffusion. *J. Magn. Reson. Imaging* 43, 818–823. doi: 10.1002/jmri.25048

Schwarcz, A., Bogner, P., Meric, P., Correze, J. L., Berente, Z., Pál, J., et al. (2004). The existence of biexponential signal decay in magnetic resonance diffusion-weighted imaging appears to be independent of compartmentalization. *Magn. Reson. Med.* 51, 278–285. doi: 10.1002/mrm.10702

Sen, P. N., and Basser, P. J. (2005). A model for diffusion in white matter in the brain. *Biophys. J.* 89, 2927–2938. doi: 10.1529/biophysj.105.063016

Steier, R., Aradi, M., Pál, J., Perlaki, G., Orsi, G., Bogner, P., et al. (2012). A biexponential DWI study in rat brain intracellular oedema. *Eur. J. Radiol.* 81, 1758–1765. doi: 10.1016/j.ejrad.2011.03.058

Ueda, Y., Takahashi, S., Ohno, N., Kyotani, K., Kawamitu, H., Miyati, T., et al. (2016). Triexponential function analysis of diffusion-weighted MRI for diagnosing prostate cancer. *J. Magn. Reson. Imaging* 43, 138–148. doi: 10.1002/jmri.24974

van Baalen, S., Leemans, A., Dik, P., Lilien, M. R., Ten Haken, B., and Froeling, M. (2017). Intravoxel incoherent motion modeling in the kidneys: comparison of mono-, bi-, and triexponential fit. *J. Magn. Reson. Imaging* 46, 228–239. doi: 10.1002/jmri.25519

Veraart, J., Fieremans, E., and Novikov, D. S. (2016). Universal power-law scaling of water diffusion in human brain defines what we see with MRI. *arXiv arXiv:1609.09145*.

Conflict of Interest Statement: The authors declare that the research was conducted in the absence of any commercial or financial relationships that could be construed as a potential conflict of interest.

frontiers in Physics

PERSPECTIVE
published: 01 May 2018
doi: 10.3389/fphy.2018.00038

Assessing Diffusion in the Extra-Cellular Space of Brain Tissue by Dynamic MRI Mapping of Contrast Agent Concentrations

Sébastien Mériaux[1,2]*, *Allegra Conti*[1,2] *and Benoît Larrat*[1,2]

[1] NeuroSpin, Institut des Sciences du Vivant Frédéric-Joliot, Commissariat à l'Énergie Atomique et aux Énergies Alternatives, Gif-sur-Yvette, France, [2] Université Paris-Saclay, Orsay, France

The characterization of extracellular space (ECS) architecture represents valuable information for the understanding of transport mechanisms occurring in brain parenchyma. ECS tortuosity reflects the hindrance imposed by cell membranes to molecular diffusion. Numerous strategies have been proposed to measure the diffusion through ECS and to estimate its tortuosity. The first method implies the perfusion for several hours of a radiotracer which effective diffusion coefficient D^* is determined after *post mortem* processing. The most well-established techniques are real-time iontophoresis that measures the concentration of a specific ion at known distance from its release point, and integrative optical imaging that relies on acquiring microscopy images of macromolecules labeled with fluorophore. After presenting these methods, we focus on a recent Magnetic Resonance Imaging (MRI)-based technique that consists in acquiring concentration maps of a contrast agent diffusing within ECS. Thanks to MRI properties, molecular diffusion and tortuosity can be estimated in 3D for deep brain regions. To further discuss the reliability of this technique, we point out the influence of the delivery method on the estimation of D^*. We compare the value of D^* for a contrast agent intracerebrally injected, with its value when the agent is delivered to the brain after an ultrasound-induced blood-brain barrier (BBB) permeabilization. Several studies have already shown that tortuosity may be modified in pathological conditions. Therefore, we believe that MRI-based techniques could be useful in a clinical context for characterizing the diffusion properties of pathological ECS and thus predicting the drug biodistribution into the targeted area.

Keywords: brain tissue tortuosity, extracellular diffusion, MRI contrast agents, *in vivo* concentration quantification, dynamic T_1 mapping, ultrasound-induced BBB permeabilization

OPEN ACCESS

Edited by:
Itamar Ronen,
Leiden University, Netherlands

Reviewed by:
Marco Palombo,
University College London,
United Kingdom
Gisela E. Hagberg,
Universität Tübingen, Germany

***Correspondence:**
Sébastien Mériaux
sebastien.meriaux@cea.fr

Specialty section:
This article was submitted to Biomedical Physics, a section of the journal Frontiers in Physics

Received: *22 December 2017*
Accepted: *13 April 2018*
Published: *01 May 2018*

Citation:
Mériaux S, Conti A and Larrat B (2018) Assessing Diffusion in the Extra-Cellular Space of Brain Tissue by Dynamic MRI Mapping of Contrast Agent Concentrations. Front. Phys. 6:38. doi: 10.3389/fphy.2018.00038

WHY ASSESSING BRAIN TORTUOSITY?

The diffusion of substances in the brain is predominantly occurring through the narrow extracellular space (ECS) that comprises the fluid-filled spaces external to cell membranes. A consequent number of studies (see [1] for an extensive review) have already established that the ECS labyrinthine nature makes the brain act like a porous medium for substances that cannot cross cellular membranes, allowing the use of established diffusion equation [2]. Two main structural

descriptors, α and λ, are usually reported to define the diffusion processes in the ECS. The volume fraction α reflects the fact that molecules released into the ECS are restricted to a smaller volume than the entire brain volume. Furthermore, the diffusion of molecules can be considered as hindered by cells, because of the increase in path length imposed by the ECS geometry. This hindrance relatively to a free medium is quantified introducing the tissue tortuosity λ [3]:

$$\lambda = \sqrt{\frac{D_{free}}{D^*}}$$

where D_{free} is the diffusion coefficient in obstacle-free medium (water or very dilute gel), and D^* the effective diffusion coefficient in ECS.

Volume fraction α admits of a simple interpretation and its value is reported to be ∼0.2 for most regions of different studied brains [1]. Moreover, tortuosity λ, which value is around 1.6 for small molecules, remains a composite parameter as many potential mechanisms may contribute to the hindrance experienced by molecules. This parameter is commonly described as some combination of (i) an increased path length as molecules are compelled to diffuse around cellular obstructions [4, 5], (ii) a transient trapping in dead-space microdomains [6, 7], and (iii) extracellular matrix interactions [8, 9]. When considering the ECS diffusion of larger macromolecules, such as dextrans or proteins, a new behavior occurs leading to an increase of λ with the hydrodynamic diameter (d_H). In this regime, the ECS porous structure is dominating and the observed restricted diffusion of molecules is mainly influenced by (i) the steric hindrance arising from the pore's limited cross-sectional area and (ii) the drag from the pore walls. Thorne and Nicholson performed tortuosity measurements using quantum dot nanocrystals (d_H∼35 nm), and they were able to estimate that the true average ECS width in the *in vivo* rat cortex lies between 38 and 64 nm using specific pore models [10].

Although diffusion transport predominates in the ECS, it is often modified by loss of molecules through removal across the blood-brain barrier (BBB), uptake into cells, or binding to receptors. Furthermore, clearance processes may also be due to a hydrodynamic flow of fluid, but it seems likely that this bulk flow is confined to the perivascular spaces in healthy brain [11]. If the underlying mechanism, importance, and even the existence of interstitial fluid flow remain incompletely resolved, this question has become a topic of renewed interest with the introduction of the brain lymphatic drainage system, known as the glymphatic system [12–14]. This system, which involves convective transport from para-arterial to para-venous cerebrospinal fluid through ECS, has been proposed to account for solute clearance in brain, and for removing toxic metabolites from the brain [15]. However, Jin et al suggested that the glymphatic system flow is not essential, since the role of diffusion seems to remain dominant when observing the molecules dispersion in the ECS [16].

Thus, the precise determination of ECS diffusion properties represents valuable information for the understanding of brain physiology and drug delivery in normal or pathological conditions. To predict the distribution of a specific externally administered agent, it is essential to know its effective diffusion coefficient in brain tissue, as well as the relative importance of diffusion vs. clearance processes that may remove that agent from the ECS. For example, these parameters are crucial to control the dose-dependent action of pharmacological agents used to target specific brain diseases, and consequently to improve clinical treatment protocols.

WHAT ARE THE WELL-ESTABLISHED TECHNIQUES FOR ASSESSING ECS DIFFUSION PROPERTIES?

The concept underlying methods of diffusion measurements is to introduce a detectable substance into the ECS, to subsequently measure its concentration distribution in space and time. It is necessary for the measurement technique to produce concentration distribution curves rather than single values, so that the adequate diffusion equation can be applied to extract α and λ values. The choice of diffusing probe is also key: it should be small enough to explore all ECS regions, but should also not cross cellular membranes or BBB to remain predominantly in the ECS compartment. Furthermore, the probe should be nontoxic to brain tissue and its concentration should be kept sufficiently low to avoid osmolarity modifications as well as sufficiently high to exceed the sensitivity threshold of the detection technique.

Lots of reviews have been written to detail the main drawbacks and advantages of each technique implemented to measure ECS diffusion properties, as well as to compare the α and λ values obtained in various animal brains and physio-pathological conditions [1, 4, 17–19]. The first technique used radiolabeled probes, such as inulin, sulfate or dextran [20]. After several hours of probe perfusion in the ECS of anesthetized animal, its brain is removed, frozen and sectioned. The *post mortem* analysis of several brains processed at various times after perfusion allows deducing the D^* value of radiotracer from the temporal evolution of radioactivity profile. The need of one animal for each time point is the main disadvantage explaining why this technique is not in general use today.

To overcome this drawback, Nicholson and Phillips proposed a "point-source paradigm," which consists in releasing specific small ions with a glass micropipette, and then measuring the resulting concentration ∼100 μm away with an ion-selective microelectrodes (ISMs) [21]. This method is usually called Real-Time Iontophoresis (RTI) because the source micropipette emits molecules using iontophoresis, thanks to the application of a constant current pulse. If the source amplitude is accurately defined, both α and λ may be estimated. The ion employed for a vast majority of studies is the tetramethylammonium monovalent cation (TMA+). This molecule is broadly used because it does not affect physiological function at low concentrations, and it

Abbreviations: ECS, ExtraCellular Space; BBB, Blood-Brain Barrier; RTI, Real-Time Iontophoresis; TMA, TetraMethylAmmonium; IOI, Integrative Optical Imaging; MRI, Magnetic Resonance Imaging; ADC_w, water Apparent Diffusion Coefficient; Gd, Gadolinium

remains mostly extracellular for the duration of measurements. To date, RTI-TMA+ remains the predominant technique for exploring ECS diffusion properties and their changes induced by brain development and aging, as well as numerous pathological states [1]. The major advantage of RTI method is the possibility to perform real-time measurements in very small volumes of living tissue, and therefore to follow diffusion properties in specific brain regions during drug injection or other intervention. The main drawbacks concern the relatively small number of usable probes, since each ion requires a dedicated ISM, and the concentration quantification that is only performed at a single position.

Nicholson and Tao recently introduced the Integrative Optical Imaging (IOI) technique, for quantifying in 2D the diffusion properties of larger probes such as proteins and macromolecules [22]. The method requires to label the probes with fluorophores, enabling their *in vivo* follow-up with dedicated epifluorescence microscope. The labeled probes are released in the ECS from a micropipette by a pressure pulse, and by fitting a 2D Gaussian curve to the image intensity at different time points, the D^* value, and hence λ, can be estimated. The diffusion measurements performed *in vivo* with IOI technique exhibit at the same time an excellent sensitivity, a high spatial and temporal resolutions [10]. One main limitation is that optical detection can only be performed down to a depth of $\sim$400 μm [18]. Still, the RTI and IOI methods are now well-established and present in most cases the same results in terms of estimated D^* and λ values [1, 17, 18].

Water diffusion in the brain can be directly assessed with Magnetic Resonance Imaging (MRI) to probe tissue microstructure [23]. However, water is found in both intracellular and extracellular compartments, with specific exchange rates between them. The relationship between water movement, water apparent diffusion coefficient (ADC_w) maps and changes in ECS characteristics thus remains difficult to understand since changes in both α and λ are accompanied by changes in ADC_w [24]. Nevertheless, diffusion MRI of protons from extracellular molecules such as TMA+ was recently demonstrated to be a potential alternative to the RTI method [25]. Another study investigated the use of 2FDG-6P as a compartment-specific marker in normal and globally ischemic rat brain, and followed its diffusion in ECS with dedicated ^{19}F MRI strategy [26]. For these two studies, volume-localized diffusion spectroscopy sequences were chosen, leading to relatively poor spatial resolution.

In this Perspective article, we illustrate how a different MRI approach, which relies on the dynamic mapping of Gadolinium (Gd)-based contrast agent concentrations [27], could be complementary to RTI and IOI methods for studying the ECS diffusion properties in extended brain regions.

OUR APPROACH TO ASSESS BRAIN TORTUOSITY WITH MRI

In 2013, we introduced a different approach to assess brain tortuosity with MRI: a specific Gd-based contrast agent was delivered in the striatum of rat brains and its diffusion through the ECS was quantified thanks to the dynamic mapping of MRI probe concentrations using a dedicated T_1 quantification strategy [27]. Interestingly, Hagberg et al. also relied on T_1 mapping sequences to measure ECS diffusion properties from voxel-wise measurements of the temporal pharmacokinetic curve obtained after an intracerebral injection of Gd-based probe [28]. One difference between the two approaches is that ECS diffusion estimation comes from the spatial evolution of MRI signal in Marty et al. [27], rather than on the temporal one in Hagberg et al. [28]. Both studies succeeded in estimating D^* for several contrast agents and providing brain tortuosity values, thanks to sensitive quantification strategies.

MRI TORTUOSITY PROBE

As already explained, the choice of MRI probe used for λ measurements is key. We selected a clinically approved Gd-chelate named Dotarem® (Guerbet, France) that presents several advantages. It is nontoxic for brain tissue compared to other MRI contrast agents [29]. Its size ($d_H < 1$ nm) is close to the one of TMA+ ($d_H \sim 0.6$ nm) and small compared to the ECS typical width. Furthermore, Dotarem® is known to not cross cell membranes and thus remain into the extracellular compartment.

Finally, Dotarem® has a relatively good relaxivity ($r_1 = 3.4$ $mM^{-1}.s^{-1}$) at high magnetic field (7T). This ensures to detect relatively low local concentrations (down to a few μM), while maintaining sufficient spatial and temporal resolutions for detecting molecules spreading in the brain. Noticeably, Dotarem® is known to be a stable molecule that maintains its relaxivity unchanged in plasma and in several tissues [30].

MRI QUANTIFICATION STRATEGY

Quantitative techniques are requested to precisely map the distribution of MRI probe after its delivery to the brain and then estimate its D^* value. Therefore, instead of relying on T_1-weighted images which contrast may saturate at high Gd concentration, we implemented one T_1 mapping strategy based on the Inversion Recovery Fast Gradient Echo sequence presented in **Figure 1A** [31]. The sequence parameters were chosen to ensure a high sampling rate of the longitudinal magnetization recovery curve over a long time (**Figures 1B,C**): 60 images are acquired with inversion times between 45 and 5060 ms spaced by 85 ms [27]. Thus, a very accurate estimation of T_1 values for a large range of T_1 can be achieved. For example, it allows to detect *in vitro* Gd concentrations lower than 2.5 μM (**Figure 1D**). From T_1 maps acquired before and after Dotarem® injection, and knowing its r_1 value at 7T and 37°C, one can estimate *in vivo* concentration maps as illustrated on **Figure 1E**, with the addition of a dedicated realignment procedure if needed. Finally, we verified that our quantification strategy follows a linear behavior with the injected dose, while the T_1-weighted signal saturates at high concentrations as expected (**Figure 1F**).

The choice of spatial resolution is also key for a precise quantification of D^*. Indeed, low spatial resolution implies large partial volume effects leading to drastic errors in Gd

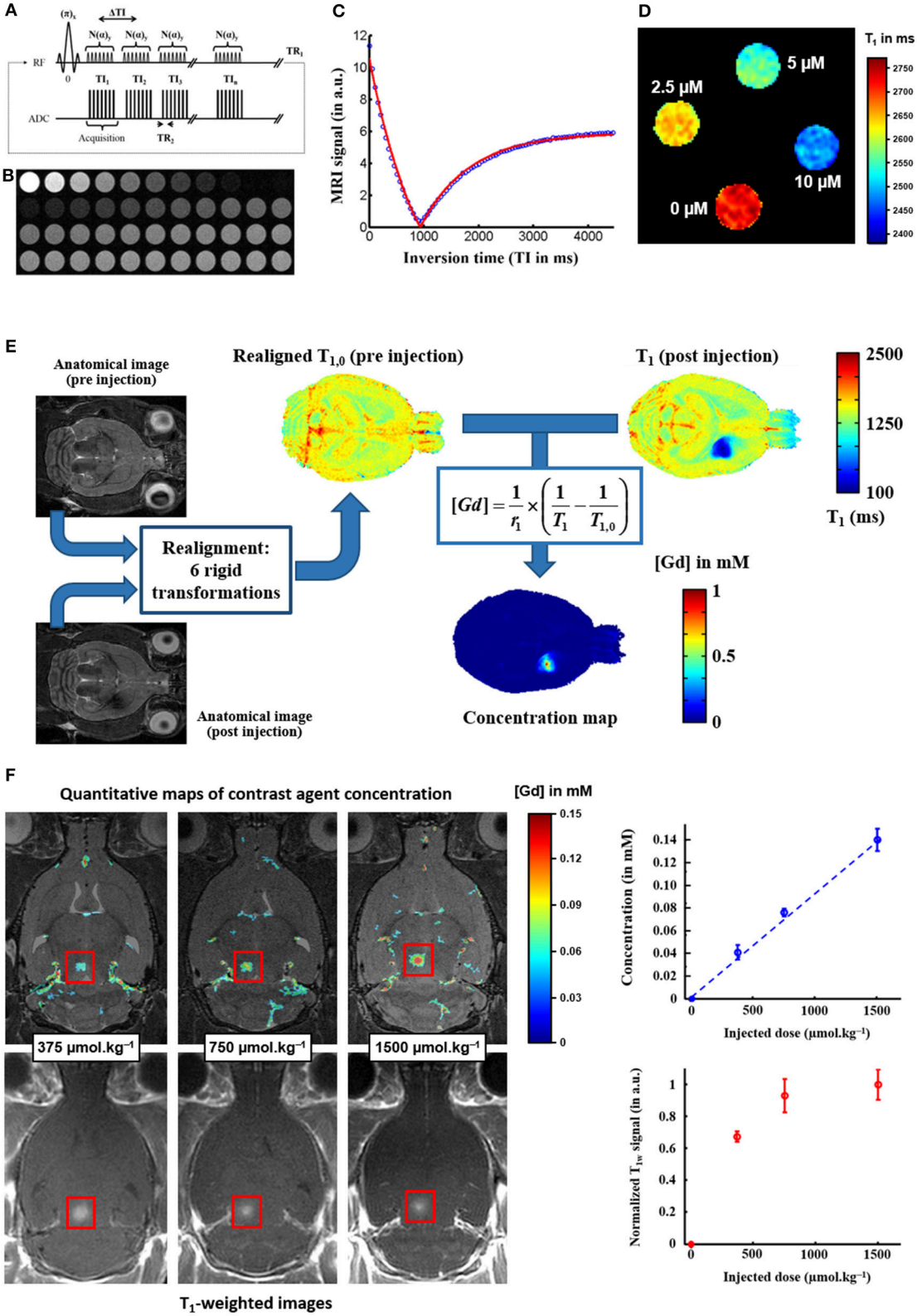

FIGURE 1 | MRI quantification of Gadolinium-based contrast agent concentration. **(A)** The T_1 mapping strategy is based on one Inversion Recovery Fast Gradient Echo sequence: it consists of a segmented series of fast gradient echo images **(B)** acquired at different time points after magnetization inversion. **(C)** The recovery of

(Continued)

FIGURE 1 | the longitudinal magnetization is fitted voxel-by-voxel as a function of the inversion time to produce a quantitative T_1 map [31]. **(D)** The sensitivity of this T_1 mapping strategy is estimated on a gallery of tubes filled with different concentrations of Dotarem® (0 / 2.5 / 5 / 10 μM). **(E)** From T_1 parametric maps acquired before and after Gd-based contrast agent injection, and knowing the longitudinal relaxivity r_1 of the agent, one can estimate *in vivo* concentration map [32], with the addition of a realignment procedure if the animal is removed from the scanner between pre- and post-injection scans. **(F)** The concentration maps estimated with this T_1 mapping strategy are proportional to the injected dose, whereas the signal in standard T_1-weighted images saturates at high injected doses (Figure adapted from Marty et al. [33]: J Cereb Blood Flow Metab (2012) 32:1948–1958).

concentration mapping, while high resolution will result in poor signal-to-noise ratio and increased errors in D^* estimation. In our case, Marty et al demonstrated from tortuosity values obtained by Thorne et al. [10] that an in-plane resolution of about 200 μm was a good compromise given our sensitivity threshold. Slice thickness could be larger since our delivery method enables us to neglect the concentration gradient along depth (**Figure 2D**).

FREE DIFFUSION COEFFICIENT MEASUREMENT

The D_{free} coefficient of Dotarem® was estimated by injecting a 5 μL aliquot with a Hamilton syringe in a tube filled with dilute agar gel (0.3% w/w) maintained at 37°C (**Figure 2A**). According to Nicholson et al., this gel can be considered as an essentially free medium for diffusion [22]. The diffusion of Dotarem® was followed during 1 h by acquiring T_1 maps as described above. A T_{10} map acquired before injection was used as a reference for estimating Gd concentration as follows [32]:

$$[Gd] = \frac{1}{r_1}\left(\frac{1}{T_1} - \frac{1}{T_{10}}\right)$$

COMPARISON OF TWO *IN VIVO* DELIVERY TECHNIQUES FOR TORTUOSITY ASSESSMENT IN RAT STRIATUM

Dotarem® was delivered *in vivo* in the striatum of Sprague Dawley rats to estimate D^*. Two delivery protocols were compared. First, a direct intracranial injection was performed using a Hamilton syringe (**Figure 2D**). Second, a more complex but less invasive method was used (**Figure 2E**): an ultrasound-induced BBB permeabilization protocol [33] was combined with an intravenous injection of Dotarem® to ensure a precise delivery where the ultrasound beam was focused [34, 35]. For both delivery methods, Dotarem® concentration maps were dynamically acquired for 1 hour as described before (**Figures 2F,G**).

DATA PROCESSING

Data analysis was performed using homemade Matlab routines (MathWorks, USA). MRI images were first reconstructed from raw K-space data, then T_1 maps were obtained using the approach proposed in Deichmann et al. [31] and Deichmann and Haase [36]. 3D Gd concentration maps were calculated from the T_1 maps acquired before and after injection (**Figure 1E**). On each slice of those maps and at every time point, the Gd spatial distribution was fitted by a 2D Gaussian function (**Figures 2B,F,G**). As illustrated on **Figures 2C,H,I**, the diffusion coefficients along X and Y were computed as:

$$D_X = \frac{\sigma_X^2}{2t} \qquad D_Y = \frac{\sigma_Y^2}{2t}$$

where t is the acquisition time, σ_X and σ_Y are the Gaussian spreads along X and Y main axes. D^* (resp. D_{free}) was taken as the average value along main axes obtained with *in vivo* (resp. *in vitro*) diffusion data.

RESULTS

The ECS tortuosity value obtained after direct intracerebral injection of Dotarem® was found equal to 3.25 ± 0.40 ($n = 2$ rats), while being equal to 1.70 ± 0.11 ($n = 3$ rats) if the probe diffuses within ECS after a local ultrasound-induced BBB permeabilization. The over-estimation of λ value observed with the first delivery method probably comes from two major drawbacks of the intracerebral injection: (i) the tip diameter of the Hamilton syringe is rather large (0.5 mm) which is unfortunately expected to induce tissue inflammation along the needle pathway and thus locally increase the hindrance of molecular diffusion; (ii) 2 μL of Dotarem® solution is injected as a bolus which induces significant changes of interstitial pressure at the injection site. For comparison, the RTI-TMA+ technique uses micropipettes and microelectrodes of 2–12 μm diameter and nanoliters only are injected at slow speed.

On the other hand, the local ultrasound-induced BBB permeabilization does not modify the ECS diffusion properties. Indeed, the λ values obtained with this delivery method are in good agreement with the ones obtained in the striatum of healthy brain with other techniques (λ = 1.59–1.60) [37, 38].

DISCUSSION AND CONCLUSION

Characterization of the diffusion in the ECS is of great importance in order to predict drug biodistribution in the brain. Our view is that non-invasive imaging technique such as MRI and non-invasive probe delivery based on ultrasound-induced BBB permeabilization can be combined to better probe brain tortuosity *in vivo*. Our ultrasound-based approach relies on the intravenous injection of the probe: its diffusion within brain tissue is thus very little disturbed as compared to a spontaneous crossing of the BBB through biochemical engineering.

Taking advantage of high field MRI acquisitions at 7T, we demonstrated that our T_1 quantification strategy reaches

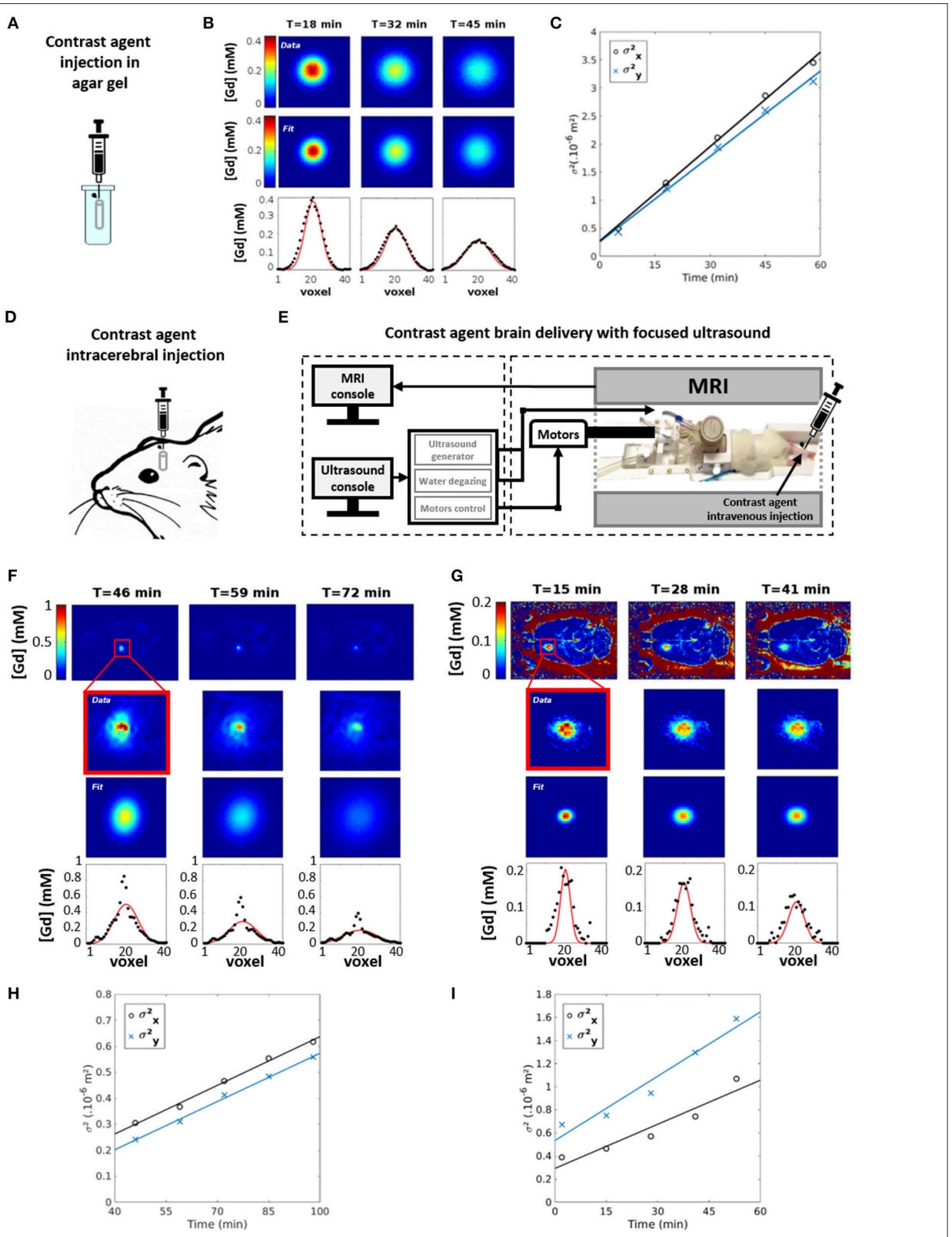

FIGURE 2 | MRI measurements of Gadolinium-based contrast agent diffusion. **(A)** The free diffusion coefficient D_{free} of Dotarem® is estimated by injecting a 5 μL aliquot with a Hamilton syringe in a tube filled with dilute agar gel (0.3% w/w) maintained at 37°C. **(B)** Concentration maps of Dotarem® (upper row) are acquired at

(Continued)

FIGURE 2 | different time points after injection with the approach described in **Figure 1**. Each slice of those maps is fitted with a 2D Gaussian function (middle row). The result of this fit is also presented for the central line of the slice (lower row). **(C)** The squares of the 2D Gaussian spreads along X and Y main axes (σ_X^2 and σ_Y^2) are fitted along time in order to estimate the diffusion coefficients D_X and D_Y: D_{free} is taken as the average value of D_X and D_Y. The effective diffusion coefficient D^* of Dotarem® is estimated *in vivo* in the striatum of Sprague Dawley rat for two delivery protocols: a direct intracranial injection of a 2 μL bolus **(D)** and an ultrasound-induced BBB permeabilization protocol [34] combined with an intravenous injection **(E)**. **(F,G)** For both protocols, concentration maps of Dotarem® (upper row) are acquired at different time points after injection with the approach described in **Figure 1**. Each slice of those maps is fitted with a 2D Gaussian function (middle row). The result of this fit is also presented for the central line of the slice (lower row). **(H,I)** For both protocols, the squares of the 2D Gaussian spreads along X and Y main axes (σ_X^2 and σ_Y^2) are fitted along time in order to estimate the diffusion coefficients D_X and D_Y: D^* is taken as the average value of D_X and D_Y.

the requirements in terms of sensitivity detection, spatial and temporal resolutions, for estimating *in vivo* tortuosity values in deep regions of the rat brain. Our diffusion measurements are not based on diffusion-weighted MRI data that probe water diffusion at a few milliseconds timescale, but rather on the dynamic acquisition at a few minutes timescale of concentration maps of a Gd-based contrast agent diffusing in brain tissue. While optical methods study 2D diffusion processes occurring up to 2–3 min, and across distances up to about 300 μm, MRI can assess in 3D long range diffusion processes that evolve over hours across several millimeters. Both information can complement each other: a slower timescale should allow for example to investigate the cellular uptake and transport, as well as the potential clearance processes related to bulk flow or glymphatic pathway.

Our method presents the great advantages of not being restricted to superficial brain structures, of being compatible with a 3D anisotropic data analysis and of being usable multiple times on the same animal opening the door to longitudinal follow-up of tortuosity. This features are particularly relevant to know more about ECS structure in pathologies such as brain tumors, during aging, or under various pharmacological conditions. Indeed, other studies have already shown that this parameter can change in case of pathologies, such as ischemia and edema [17]. Furthermore, another interest of our approach is that additional MRI sequences can be added to the protocol for correlating tortuosity with structural, vascular, morphological, spectroscopic and functional MRI data. In a clinical context, the estimated values of tortuosity could be used as additional indicators of the pathological state.

Further interest in better ways to measure ECS physical properties has recently been raised by the discovery of major changes of ECS volume during sleep [15] and its correlation with the glymphatic pulsation flow that plays a great role in the cleaning of brain. Ultrafast MRI has recently been shown to be able to catch the slow flows occurring within the ECS [39]. In this context, such flow imaging could be combined with tortuosity measurements at various stages of the day/night cycle to better understand the clinical implications of the glymphatic pathway. Finally, Frenkel et al. have recently shown with histology that low intensity pulsed ultrasound could be used to transiently enlarge ECS [40]. This could be transferred into clinical applications for facilitating drug access to targets, and the characterization of ECS diffusion properties with MRI would be of great importance to predict the drug biodistribution into the targeted area.

ETHICS STATEMENT

All *in vivo* experiments were conducted in strict accordance with the recommendations of the European Community (2010/63/EU) and the French legislation (decree no2013-118) for use and care of laboratory animals. The protocol for contrast agent injection and BBB permeabilization has been approved by the Comité d'Éthique en Expérimentation Animale du Commissariat à l'Énergie Atomique et aux Énergies Alternatives – Direction des Sciences du Vivant Ile-de-France (CETEA/CEA/DSV IdF) under protocol ID 12-058.

AUTHOR CONTRIBUTIONS

SM developed and refined the perspective. SM, AC, and BL planned the MRI experiments. AC performed MRI acquisitions and data analysis. SM provided all data analysis pipelines. SM and BL managed the overall project and provided its funding. All authors contributed to manuscript edition.

ACKNOWLEDGMENTS

This work was part of the Iseult/INUMAC project, supported by the French public agency BPI (ex-OSEO), dedicated to the support of small and medium-sized companies.

France Life Imaging is acknowledged for its support in funding the NeuroSpin platform of preclinical MRI scanners.

AC received an Enhanced Eurotalents post-doctoral fellowship (Grant Agreement n°600382), part of the Marie Sklodowska-Curie Actions Programme, co-funded by the European Commission and managed by the French Atomic Energy and Alternative Energies Commission (CEA).

The authors also thank the Health Technology Program of CEA for its support in funding some ultrasound experiments.

REFERENCES

1. Syková E, Nicholson C. Diffusion in brain extracellular space. *Physiol Rev*. (2008) **88**:1277–340. doi: 10.1152/physrev.00027.2007

2. Nicholson C, Phillips JM. Ion diffusion modified by tortuosity and volume fraction in the extracellular microenvironment of the rat cerebellum. *J Physiol.* (1981) **321**: 225–57.

3. Ernst MH, Machta J, Dorfman JR, Vanbeijeren H. Long-time tails in stationary random-media. I. *Theory. J Stat Phys* (1984) **34**:477–95. doi: 10.1007/BF01018555
4. Nicholson C. Diffusion and related transport mechanisms in brain tissue. *Rep Prog Phys*. (2001) **64**:815–84. doi: 10.1088/0034-4885/64/7/202
5. Tao L, Nicholson C. Maximum geometrical hindrance to diffusion in brain extracellular space surrounding uniformly spaced convex cells. *J Theor Biol*. (2004) **229**:59–68. doi: 10.1016/j.jtbi.2004.03.003
6. Chen KC, Nicholson C. Changes in brain cell shape create residual extracellular space volume and explain tortuosity behavior during osmotic challenge. *Proc Natl Acad Sci USA*. (2000) **97**:8306–11. doi: 10.1073/pnas.150338197
7. Hrabětová S, Nicholson C. Contribution of dead-space microdomains to tortuosity of brain extracellular space. *Neurochem Int*. (2004) **45**:467–77. doi: 10.1016/j.neuint.2003.11.011
8. Rusakov DA, Kullmann DM. Geometric and viscous components of the tortuosity of the extracellular space in the brain. *Proc Natl Acad Sci USA*. (1998) **95**:8975–80.
9. Syková E. Extrasynaptic volume transmission and diffusion parameters of the extracellular space. *Neuroscience* (2004) **129**:861–76. doi: 10.1016/j.neuroscience.2004.06.077
10. Thorne RG, Nicholson C. In vivo diffusion analysis with quantum dots and dextrans predicts the width of brain extracellular space. *Proc Natl Acad Sci USA*. (2006) **103**:5567–72. doi: 10.1073/pnas.0509425103
11. Abbott NJ. Evidence for bulk flow of brain interstitial fluid: significance for physiology and pathology. *Neurochem Int*. (2004) **45**:545–52. doi: 10.1016/j.neuint.2003.11.006
12. Iliff JJ, Wang M, Liao Y, Plogg BA, Peng W, Gundersen GA, et al. A paravascular pathway facilitates CSF flow through the brain parenchyma and the clearance of interstitial solutes, including amyloid β. *Sci Transl Med*. (2012) **4**:147ra111. doi: 10.1126/scitranslmed.3003748
13. Aspelund A, Antila S, Proulx ST, Karlsen TV, Karaman S, Detmar M, et al. A dural lymphatic vascular system that drains brain interstitial fluid and macromolecules. *J Exp Med*. (2015) **212**:991–9. doi: 10.1084/jem.20142290
14. Louveau A, Smirnov I, Keyes TJ, Eccles JD, Rouhani SJ, Peske JD, et al. Structural and functional features of central nervous system lymphatic vessels. *Nature* (2015) **523**:337–41. doi: 10.1038/nature14432
15. Xie L, Kang H, Xu Q, Chen MJ, Liao Y, Thiyagarajan M, et al. Sleep drives metabolite clearance from the adult brain. *Science* (2013) **342**:373–7. doi: 10.1126/science.1241224
16. Jin BJ, Smith AJ, Verkman AS. Spatial model of convective solute transport in brain extracellular space does not support a "glymphatic" mechanism. *J Gen Physiol*. (2016) **148**:489–501. doi: 10.1085/jgp.201611684
17. Nicholson C, Syková E. Extracellular space structure revealed by diffusion analysis. *Trends Neurosci* (1998) **21**:207–15. doi: 10.1016/S0166-2236(98)01261-2
18. Nicholson C, Kamali-Zare P, Tao L. Brain extracellular space as a diffusion barrier. *Comput Vis Sci*. (2011) **14**:309–25. doi: 10.1007/s00791-012-0185-9
19. Nicholson C, Hrabětová S. Brain extracellular space: the final frontier of neuroscience. *Biophys J* (2017) **113**:2133–42. doi: 10.1016/j.bpj.2017.06.052
20. Rall DP, Oppelt WW, Patlak CS. Extracellular space of brain as determined by diffusion of inulin from the ventricular system. *Life Sci*. (1962) **1**:43–8. doi: 10.1016/0024-3205(62)90104-2
21. Nicholson C, Phillips JM. Ion diffusion modified by tortuosity and volume fraction in the extracellular microenvironment of the rat cerebellum. *J Physiol*. (1981) **321**:225–57.
22. Nicholson C, Tao L. Hindered diffusion of high molecular weight compounds in brain extracellular microenvironment measured with integrative optical imaging. *Biophys J*. (1993) **65**:2277–90. doi: 10.1016/S0006-3495(93)81324-9
23. Le Bihan D, Mangin JF, Poupon C, Clark CA, Pappata S, Molko N, et al. Diffusion tensor imaging: concepts and applications. *J Magn Reson Imaging* (2001) **13**:534–46. doi: 10.1002/jmri.1076
24. Norris DG. The effects of microscopic tissue parameters on the diffusion weighted magnetic resonance imaging experiment. *NMR Biomed*. (2001) **14**:77–93. doi: 10.1002/nbm.682
25. Kroenke CD, Ackerman JJ, Neil JJ. Magnetic resonance measurement of tetramethylammonium diffusion in rat brain: comparison of magnetic resonance and ionophoresis *in vivo* diffusion measurements. *Magn Reson Med*. (2003) **50**:717–26. doi: 10.1002/mrm.10579
26. Duong TQ, Ackerman JJ, Ying HS, Neil JJ. Evaluation of extra- and intracellular apparent diffusion in normal and globally ischemic rat brain via 19F NMR. *Magn Reson Med*. (1998) **40**:1–13. doi: 10.1002/mrm.1910400102
27. Marty B, Djemaï B, Robic C, Port M, Robert P, Valette J, et al. Hindered diffusion of MRI contrast agents in rat brain extracellular micro-environment assessed by acquisition of dynamic T1 and T2 maps. *Contrast Media Mol Imaging* (2013) **8**:12–9. doi: 10.1002/cmmi.1489
28. Hagberg GE, Mamedov I, Power A, Beyerlein M, Merkle H, Kiselev VG, et al. Diffusion properties of conventional and calcium-sensitive MRI contrast agents in the rat cerebral cortex. *Contrast Media Mol Imaging* (2014) **9**:71–82. doi: 10.1002/cmmi.1535
29. Rogosnitzky M, Branch S. Gadolinium-based contrast agent toxicity: a review of known and proposed mechanisms. *Biometals* (2016) **29**:365–76. doi: 10.1007/s10534-016-9931-7
30. Laurent S, Elst LV, Muller RN. Comparative study of the physicochemical properties of six clinical low molecular weight gadolinium contrast agents. *Contrast Media Mol Imag*. (2006) **1**:128–37. doi: 10.1002/cmmi.100
31. Deichmann R, Hahn D, Haase A. Fast T1 mapping on a whole-body scanner. *Magn Reson Med*. (1999) **42**:206–9. doi: 10.1002/(SICI)1522-2594(199907)42:1<206::AID-MRM28>3.0.CO;2-Q
32. Swift TJ, Connick RE. NMR-Relaxation mechanisms of O17 in aqueous solutions of paramagnetic cations and lifetime of water molecules in first coordination sphere. *J Chem Phys*. (1962) **37**:307–20. doi: 10.1063/1.1701321
33. Marty B, Larrat B, Van Landeghem M, Robic C, Robert P, Port M, et al. Dynamic study of blood-brain barrier closure after its disruption using ultrasound: a quantitative analysis. *J Cereb Blood Flow Metab*. (2012) **32**:1948–58. doi: 10.1038/jcbfm.2012.100
34. Magnin R, Rabusseau F, Salabartan F, Mériaux S, Aubry JF, Le Bihan D, et al. Magnetic resonance-guided motorized transcranial ultrasound system for blood-brain barrier permeabilization along arbitrary trajectories in rodents. *J Ther Ultrasound* (2015) **3**:22. doi: 10.1186/s40349-015-0044-5
35. Conti A, Magnin R, Gerstenmayer M, Lux F, Tillement O, Mériaux S, et al. Characterization of the diffusion process of different Gadolinium-based nanoparticles within the brain tissue after ultrasound induced Blood-Brain Barrier permeabilization. In: *Ultrasonics Symposium (IUS), 2016 IEEE International*, Tours.
36. Deichmann R, Haase A. Quantification of T1 values by SNAPSHOT-FLASH NMR imaging. *J Magn Reson*. (1992) **96**:608–12. doi: 10.1016/0022-2364(92)90347-A
37. Jansson A, Mazel T, Andbjer B, Rosén L, Guidolin D, Zoli M, et al. Effects of nitric oxide inhibition on the spread of biotinylated dextran and on extracellular space parameters in the neostriatum of the male rat. *Neuroscience* (1999) **91**:69–80. doi: 10.1016/S0306-4522(98)00575-2
38. Reum T, Olshausen F, Mazel T, Vorísek I, Morgenstern R, Syková E. Diffusion parameters in the striatum of rats with 6-hydroxydopamine-induced lesions and with fetal mesencephalic grafts. *J Neurosci Res* (2002) **70**:680–693. doi: 10.1002/jnr.10332
39. Kiviniemi V, Wang X, Korhonen V, Keinänen T, Tuovinen T, Autio J, et al. Ultra-fast magnetic resonance encephalography of physiological brain activity - Glymphatic pulsation mechanisms? *J Cereb Blood Flow Metab* (2016) **36**:1033–45. doi: 10.1177/0271678X15622047
40. Frenkel V, Hersh DS, Anastasiadis P, Mohammadabadi A, Dancy J, Winkles J, et al. Pulsed focused ultrasound effects on the brain interstitium. In: *Ultrasonics Symposium (IUS), 2017 IEEE International*, Washington.

Conflict of Interest Statement: The authors declare that the research was conducted in the absence of any commercial or financial relationships that could be construed as a potential conflict of interest.

frontiers in Physics

REVIEW
published: 15 November 2017
doi: 10.3389/fphy.2017.00058

Time-Dependent Diffusion MRI in Cancer: Tissue Modeling and Applications

*Olivier Reynaud**

Centre d'Imagerie Biomédicale, Ecole Polytechnique Fédérale de Lausanne, Lausanne, Switzerland

In diffusion weighted imaging (DWI), the apparent diffusion coefficient (ADC) has been recognized as a useful and sensitive surrogate for cell density, paving the way for non-invasive tumor staging, and characterization of treatment efficacy in cancer. However, microstructural parameters, such as cell size, density and/or compartmental diffusivities affect diffusion in various fashions, making of conventional DWI a sensitive but non-specific probe into changes happening at cellular level. Alternatively, tissue complexity can be probed and quantified using the time dependence of diffusion metrics, sometimes also referred to as temporal diffusion spectroscopy when only using oscillating diffusion gradients. Time-dependent diffusion (TDD) is emerging as a strong candidate for specific and non-invasive tumor characterization. Despite the lack of a general analytical solution for all diffusion times/frequencies, TDD can be probed in various regimes where systems simplify in order to extract relevant information about tissue microstructure. The fundamentals of TDD are first reviewed (a) in the short time regime, disentangling structural and diffusive tissue properties, and (b) near the tortuosity limit, assuming weakly heterogeneous media near infinitely long diffusion times. Focusing on cell bodies (as opposed to neuronal tracts), a simple but realistic model for intracellular diffusion can offer precious insight on diffusion inside biological systems, at all times. Based on this approach, the main three geometrical models implemented so far (IMPULSED, POMACE, VERDICT) are reviewed. Their suitability to quantify cell size, intra- and extracellular spaces (ICS and ECS) and diffusivities are assessed. The proper modeling of tissue membrane permeability—hardly a newcomer in the field, but lacking applications—and its impact on microstructural estimates are also considered. After discussing general issues with tissue modeling and microstructural parameter estimation (i.e., fitting), potential solutions are detailed. The *in vivo* applications of this new, non-invasive, specific approach in cancer are reviewed, ranging from the characterization of gliomas in rodent brains and observation of time-dependence in breast tissue lesions and prostate cancer, to the recent preclinical evaluation of new treatments efficacy. It is expected that clinical applications of TDD will strongly benefit the community in terms of non-invasive cancer screening.

Keywords: diffusion, diffusion magnetic resonance imaging, temporal diffusion spectroscopy, diffusion time dependence, diffusion time, PGSE, OGSE, MRI of cancer

OPEN ACCESS

Edited by:
Julien Valette,
Commissariat à l'Energie Atomique et aux Energies Alternatives (CEA), France

Reviewed by:
Henrik Lundell,
Danish Research Centre for Magnetic Resonance (DRCMR), Denmark
Markus Nilsson,
Lund University, Sweden

***Correspondence:**
Olivier Reynaud
oli.reynaud@gmail.com

Specialty section:
This article was submitted to Biomedical Physics, a section of the journal Frontiers in Physics

Received: *19 July 2017*
Accepted: *31 October 2017*
Published: *15 November 2017*

Citation:
Reynaud O (2017) Time-Dependent Diffusion MRI in Cancer: Tissue Modeling and Applications. Front. Phys. 5:58. doi: 10.3389/fphy.2017.00058

INTRODUCTION

By probing the water molecule displacement at the microscopic scale, Diffusion Weighted Imaging (DWI) is well established as a powerful non-invasive MRI technique to characterize tissue order—or disorder. Since diffusion gradients sensitize the overall MR signal to potential fine changes occurring at cellular level, DWI has been extensively used to study the abnormal cellular growth characterizing cancer development [1] and/or predict therapeutic outcome [2].

The apparent diffusion coefficient (ADC)—a hallmark of DWI—has been recognized as a useful and sensitive surrogate for cell density [3, 4], paving the way for non-invasive tumor staging and characterization of treatment efficacy in cancer [5]. However, sensitivity does not equate with specificity, generating confusion when attempting to interpret diffusion changes in a meaningful manner. Cell size, density and/or compartmental diffusivities can all affect ADC measurements so that changes in the diffusion signal cannot be unambiguously attributed to specific tissue properties.

Diffusion is in general not Gaussian. While the reasons tissue complexity cannot be reduced to a single indirect diffusion metric are manifold, two particular aspects of non-gaussian diffusion deserve our special attention.

For a given diffusion time, the full diffusion signal S description can be written as a Taylor series, also known as cumulant expansion [6, 7]: $\ln(S/S_0) = -bD + (bD)^2K/6 + O(D^2)$, where D is the diffusion coefficient and K the kurtosis. The first-order approximation therefore only holds for $bD \ll 1/K$, i.e., small b-values (b < 1 ms/μm^2 *in vivo*). The estimation of the full kurtosis tensor can help characterize tissue structure more specifically, at the cost of extended scan time. Successful examples in cancer can be found in Jensen and Helpern [7] and Szczepankiewicz et al. [8] but fall outside the scope of this review.

Alternatively, this review focuses on time-dependent diffusion (TDD), i.e., the manifestation of tissue complexity through the dependence of the metrics previously introduced with diffusion time t: $D = D(t)$ (and $K = K(t)$), sometimes also referred to as temporal diffusion spectroscopy [9]. The objective of this review is to provide the interested reader with all the keys and tools required to design a TDD experiment in which tissue microstructure parameters can be judiciously and non-ambiguously estimated.

The main issue with TDD is that, for a biological system, there is no analytical solution for the diffusion time-dependence in general.

Starting on a positive note, there are two extreme time domains where an exact solution exists. Diffusion in the infinitely short time regime is well defined for any system, and disentangle geometric from purely diffusive tissue properties [10]. Alternatively, diffusion in the infinitely long time regime can be characterized based on universal classes of tissue disorder [11].

In-between, a simple geometrical model, for which intracellular diffusion can be conveniently derived for any given time/frequency [12, 13], is presented. For a biological system and/or cancer cells, the range of cell size to which it can be applied is discussed.

Using these results, the main models used to characterize tumor tissue using TDD are reviewed: IMPULSED [14], POMACE [15], and VERDICT [16]. Modeling cells as impermeable spheres, additional assumptions are made to describe the ECS, and finally estimate diffusivities, cell size and volume fraction *ex vivo* and *in vivo*. Non-geometrical models [17, 18] are also discussed.

Membrane permeability is a key parameter often neglected during tissue characterization. Using time dependence, we discuss how this parameter—likely to vary in tumors—can be estimated in particular time regimes [17, 19] or via novel modeling [20].

Potential issues to keep in mind when modeling tumor tissue are also discussed. Experiments should be carefully designed in order to justify any modeling assumption, avoid overfitting and optimize the fit accuracy and precision.

At last, the growing impact of TDD in the preclinical and clinical setting is reviewed. A distinction is made between highly sensitive but non-specific results, often lacking the rigor of proper tumor tissue modeling, and specific yet less sensitive studies, whose conclusions are not always backed up by different methodologies. Issues regarding clinical scanners, as well as the perspectives and potential of TDD regarding new avenues of cancer research is finally discussed.

TIME DEPENDENT DIFFUSION: FUNDAMENTAL ISSUES AND CONCEPT

There is in general no analytical solution for the time dependence of diffusion. The problem only simplifies in three particular regimes: at infinitely short times, at infinitely long times (also known as tortuosity limit), and near the long time regime. We will briefly summarize how diffusion behaves in these three time domains.

The Short Time Regime

The universal behavior of diffusion measured with Pulsed Gradient Spin Echo (PGSE, **Figure 1A**) at short times t was initially derived in porous media by Mitra et al. [10]. In a medium with free diffusivity D_0, the overall diffusion coefficient D can be written as:

$$D_{PGSE}(t) = D_0\left(1 - \frac{4}{3d\sqrt{\pi}} \cdot \frac{S}{V} \cdot \sqrt{D_0 t}\right) + O(D_0 t), \quad \text{with } O(D_0 t) \ll \sqrt{D_0 t} \text{ when } t \to 0. \tag{1}$$

with d the number of dimensions along which molecules can diffuse and S/V the surface-to-volume ratio of the

Abbreviations: ADC, apparent diffusion coefficient; DWI, diffusion-weighted imaging; ECS, extracellular space; ICS, intracellular space; IMPULSED, imaging microstructural parameters using limited spectrally edited diffusion; OGSE, oscillating gradient spin echo; PGSE, pulsed gradient spin echo; POMACE, pulsed and oscillating gradient MRI for assessment of cell size and extracellular space; RBPM, random barrier permeable model; STEAM, stimulated echo acquisition mode; VERDICT, vascular, extracellular, and restricted diffusion for cytometry in tumors; TDD, time-dependent diffusion.

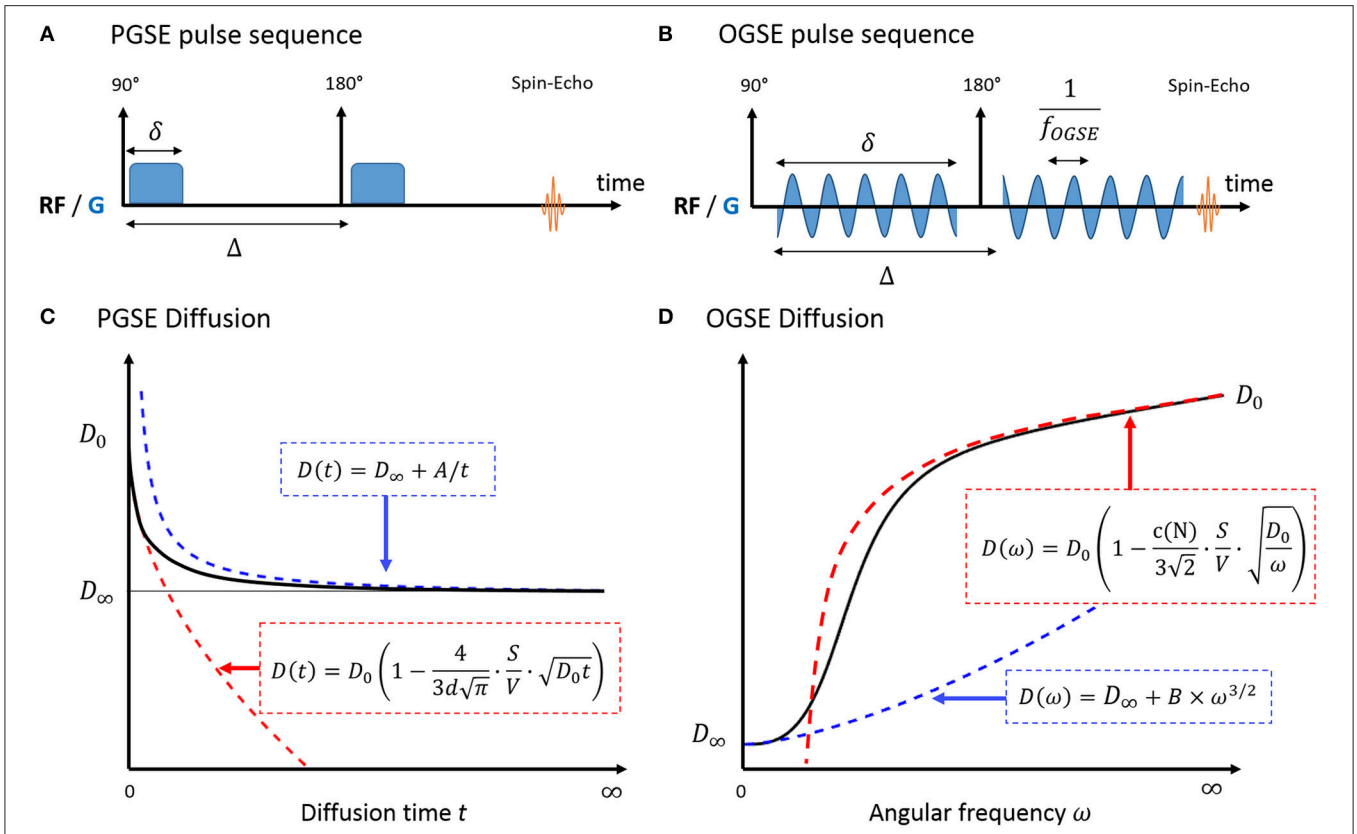

FIGURE 1 | Pulse sequence diagram for PGSE **(A)** and OGSE **(B)** and diffusion in a biological system, measured with PGSE **(C)** and OGSE **(D)**. In the short time regime (red), diffusion is fully characterized by the medium free diffusivity D_0 and the surface-to-volume ratio *S/V*. At long times (blue), diffusion reaches its tortuosity limit D_∞ with $1/t$ (PGSE) or $\omega^{3/2}$ (OGSE). There is no exact solution for the time dependence of diffusion in-between. *A* and *B* are geometry-dependent constants.

barriers/walls/cellular membranes. A similar formula was derived for Oscillating Gradient Spin Echo (OGSE, **Figure 1B**) using a cosinusoidal waveform acquired at frequency ω [21]:

$$D_{OGSE}(\omega) = D_0\left(1 - \frac{c(N)}{d\sqrt{2}}\cdot\frac{S}{V}\cdot\sqrt{\frac{D_0}{\omega}}\right) + O\left(\frac{D_0}{\omega}\right),$$
$$\text{with } O\left(\frac{D_0}{\omega}\right) \ll \sqrt{\frac{D_0}{\omega}} \text{ when } \omega \to \infty. \quad (2)$$

The correction factor $c(N)$ depends on the number of oscillations N and rapidly converges toward 1 [22].

Interestingly, this regime unambiguously decouples the medium diffusive properties D_0 from the purely geometric restrictions embedded in *S/V*. The linearity of diffusion vs. $t^{1/2}/\omega^{-1/2}$ remain valid for a typical biological system consisting of intra- and extracellular water molecules, if the short time regime is reached in both compartments.

The validity of surface-to-volume ratio estimates was first verified experimentally using stimulated echo acquisition mode (STEAM) measurements on sedimentary rocks [23, 24] and large size beads [25]. It was later verified in smaller structures [26] and solutions of packed beads of various size (radius 1–400 μm) using OGSE [27].

The short time regime is only valid if the typical restriction scale R far exceeds the NMR diffusion length $\sqrt{D_0 t}$ [10]. For small *in vivo* structures ($R < 10\,\mu m$), only OGSE can achieve sufficient diffusion strength to probe this regime, by accumulating contrast over N oscillations: $b_{total} = N \times b_{N=1}$ [27]. The linearity of D with $\omega^{-1/2}$ was recently demonstrated for $f = \omega/2\pi > 90\ Hz$ in mice brain glioma [18] with large cellular radius (GL261, $R_{cell} \sim 5\,\mu m$). The quadratic inequality $f \sim 1/t \gg D_0/R^2$ rapidly becomes impossible to satisfy for smaller structures (healthy brain tissue, astrocytes, neurons, with R∼1 μm). For these applications, dedicated and strong custom-built diffusion gradients should be used [27, 28].

The Tortuosity Limit

At very long times, diffusion lengths exceed the typical length of restriction within the medium to approach the macroscopic "tortuosity" limit $D(t) = D_\infty$ (**Figure 1C**). Diffusion becomes Gaussian, and time dependence and fine microstructural details are lost. For a non-exchanging multi-compartment system, each compartment cannot be distinguished from a homogeneous medium, and multi-exponential behavior is observed as a result. Various models used to describe white matter in this regime are detailed and reviewed in Ferizi et al. [29] and Panagiotaki et al. [30].

In a totally confined geometry, $D(t) = \langle x^2(t)\rangle/2t < 2R^2/t$. The diffusion inside closed impermeable structures converges to $D_\infty = 0$ as $1/t$.

Approaching the Long Time Regime

A perturbative solution to the time-dependence of diffusion exists near the tortuosity limit [11, 31]. In this regime, Novikov et al. [11] demonstrated that the diffusion depends on large scale structural fluctuations via the power law:

$$D_{PGSE}(t) = D_\infty + A \cdot t^{-\vartheta} \tag{3}$$

with $\vartheta = (p + d)/2$, p and d being respectively the discrete structural exponent and spatial dimensionality of the problem, as in Equations (1) and (2) in Novikov et al. [11]. The exponent p characterizes global structural complexity, opposing regular lattices ($p = \infty$) to highly disordered media ($p < 0$). The case $p = 0$ corresponds to short-range disorder, when restrictions are uncorrelated or exhibit finite correlation length. Outside three dimensional dilute structures lacking long range order, such as cancer cells, PGSE and OGSE diffusion can then be expressed as Novikov et al. [11] and deSwiet and Sen [32]:

$$D_{PGSE}(t) = D_\infty + A/t \text{ when } t \to \infty \tag{4}$$

$$D_{OGSE}(\omega) = D_\infty + B \cdot \omega^{3/2} \text{ when } \omega \to 0. \tag{5}$$

The previous equations highlight that there is no one-to-one correspondence between diffusion time and oscillation frequency. This becomes apparent when combining OGSE and PGSE measurements on similar graphs [28, 33]. A common approach when combining PGSE and OGSE is to use a single PGSE measurement as a surrogate for a diffusion measurement with zero frequency [27, 33–35]. This should be avoided as the PGSE time dependence cannot be neglected, as illustrated in **Figure 5**.

For All the Rest of Time

Both the extent of the intermediate regime and the diffusion behavior in that regime are in general unknown (**Figures 1C,D**). As an alternative, a Padé approximation [36] was considered in several studies to interpolate between the short and long time regime. Excellent agreement was found between S/V estimates from the Padé approximant and microscopy performed on monosized sphere packs [17, 37]. To date, this non-specific approach has not been applied to the characterization of cancer cells.

TUMOR TISSUE MODELING: VARIOUS APPROACHES

A Simple Model for Intracellular Diffusion

A practical solution to characterize tissue structure using TDD is to (a) model the cellular microenvironment using simple geometries, where an analytical solution for the intracellular diffusion D_{ics} exists, and (b) consider the extracellular contribution in one of the aforementioned regimes (short/long/tortuosity limit). The case of impermeable spheres, that represent the simplest three-dimensional geometrical model for characterizing cells—and therefore cancer cells (**Figure 2**)—is detailed here.

Diffusion Inside Impermeable Spheres

The signal attenuation inside impermeable spheres was first derived for PGSE by Murday and Cotts [12] and for OGSE by the Vanderbilt group [13]. The PGSE intracellular diffusion is expressed as:

$$D_{ics,PGSE}(t) = \frac{4R^2}{(\Delta - \delta/3)}\left(\frac{\tau_R}{\delta}\right)^2 \sum_n \frac{1}{\mu_n^6(\mu_n^2 - 2)}\left\{\mu_n^2\frac{\delta}{\tau_R} - 1 + exp\left(-\mu_n^2\frac{\delta}{\tau_R}\right) + exp\left(-\mu_n^2\frac{\Delta}{\tau_R}\right)\left[1 - cosh\left(\mu_n^2\frac{\delta}{\tau_R}\right)\right]\right\} \tag{6}$$

Here R is the cell radius, δ and Δ the gradient and inter-gradient duration, and $\tau_R = R^2/D_0$ the characteristic diffusion time of the cell ($R = \sqrt{D_0\tau_R}$). μ_n is numerically estimated as the nth root of $\partial j_1(\mu)/\partial\mu$, where $j_1(\mu) = (\sin(\mu) - \mu \cdot \cos(\mu))/\mu^2$ is the spherical Bessel function of the first kind. For the PGSE experiment in the narrow pulse regime, the diffusion time t equates the inter-gradient duration Δ. Finite pulse widths δ act as low-pass filter on the velocity autocorrelation function [38, 39], potentially impacting the functional form of the diffusion time–dependence (see for instance Equation 8 vs. Equation 9 in Fieremans et al. [40]—an axon study).

For OGSE, using the same formalism:

$$D_{ics,OGSE}(\omega) = 2D_0(\omega\tau_R)^2 \sum_n \frac{1}{(\mu_n^2 - 2)}\left\{\frac{1}{\mu_n^4 + (\omega\tau_R)^2} + \frac{2\mu_n^2\tau_R/\delta}{\left(\mu_n^4 + (\omega\tau_R)^2\right)^2}\left[exp\left(-\mu_n^2\frac{\delta}{\tau_R}\right) - 1 + exp\left(-\mu_n^2\frac{\Delta}{\tau_R}\right)\left[1 - cosh\left(\mu_n^2\frac{\delta}{\tau_R}\right)\right]\right]\right\} \tag{7}$$

The diffusion behavior inside impermeable spheres is illustrated in **Figure 2C**, most changes happening around the tissue characteristic frequency $1/\tau_R = D_0/R^2$.

The complete list of TDD studies and models used to characterize tissue structure based on this geometry are detailed in another section of the manuscript. In addition to the unrealistic case of infinite impermeable membranes already described by Tanner and Stejskal [41], similar expressions were derived for diffusion inside spherical shells [42] and infinite cylinders [43]. The former, in order to represent cellular nuclei and cytoplasm, adds two extra degrees of freedom to a problem already prone to overfitting [15]. The latter was shown successful in estimating the size of small cylinders in the absence of an extracellular medium [44] and could be promising for axonal size estimation but is of little use for MR in cancer.

Oscillation Frequency vs. Cell Size

Depending on cell size, the tissue characteristic frequency D_0/R^2 can remain out of reach using OGSE and conventional diffusion gradients, thus preventing a good sampling of the diffusion time-dependence. **Figure 3A** highlights the diffusion behavior over a realistic range of cellular size radii (R = 1–10 μm) and ICS free diffusivity (D_0 = 2 μm^2/ms). Without a dedicated gradient insert, the only oscillation frequencies that can be probed with sufficient

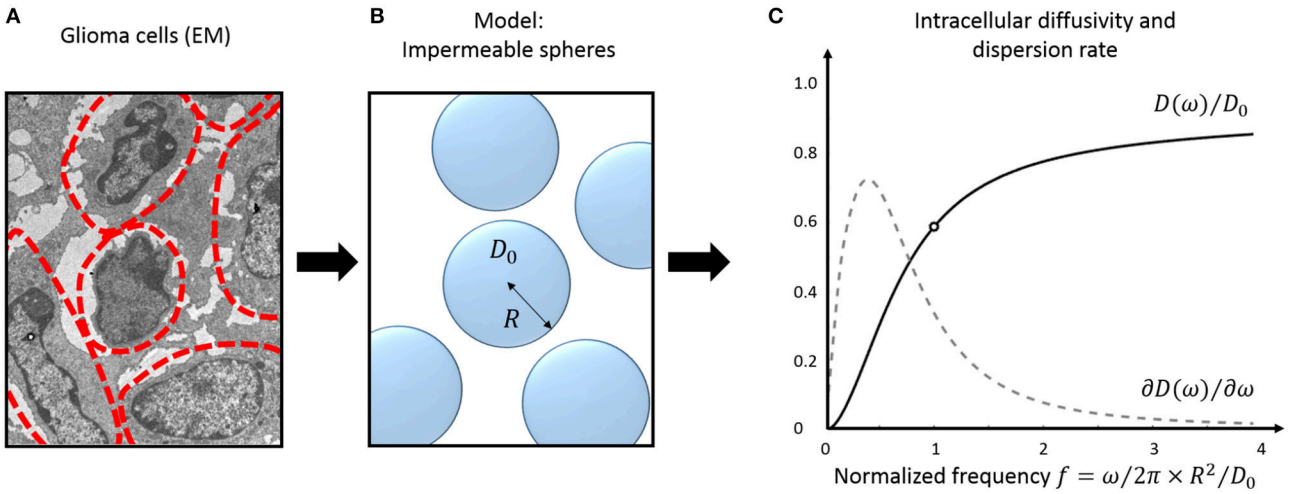

FIGURE 2 | Tumor tissue modeling: intracellular diffusion. Electron micrograph (EM) of murine glioblastoma GL261 cells **(A)**. The approximate cell contours are delineated in red. **(B)** Simple three-dimensional geometrical model for tumor cells. Cells are assumed perfectly spherical, homogeneous in size and fully impermeable. **(C)** Diffusivity inside impermeable spheres (black) and its frequency- derivative: the instantaneous dispersion rate (gray, arbitrary units). Oscillations frequencies are normalized to the tissue characteristic frequency D_0/R^2. The EM was extracted from the dataset used for cell size measurement in Reynaud et al. [15].

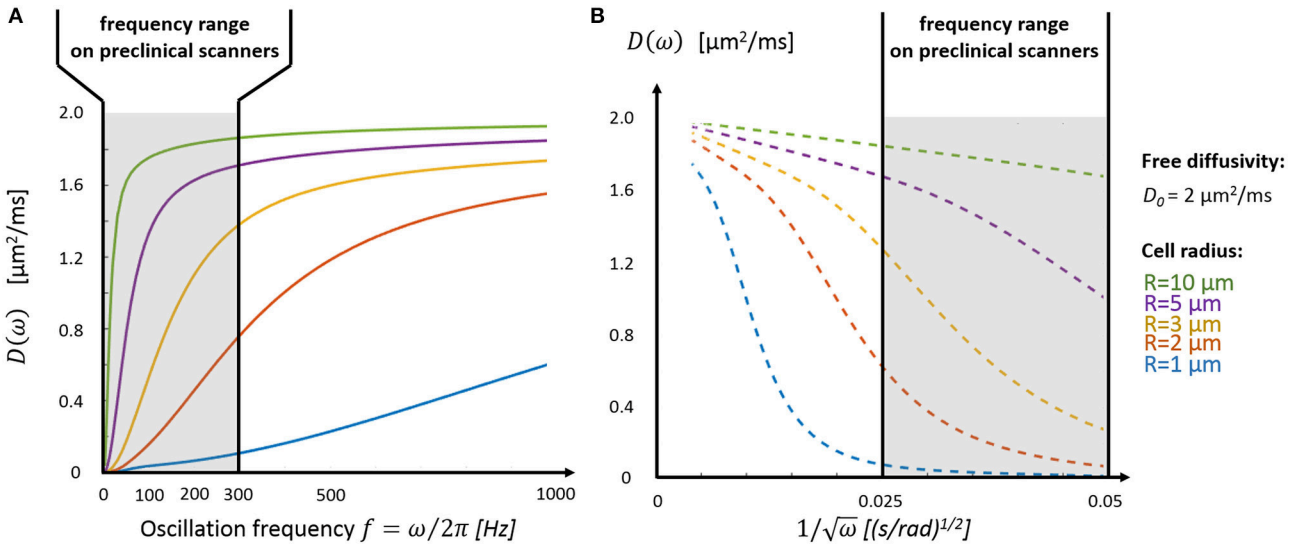

FIGURE 3 | Intracellular diffusivity and cell size. **(A)** The oscillation frequency range available on preclinical scanners (f_{OGSE} < 300 Hz, gray area) is most suited to characterize the diffusion time-dependence inside large structures ($R > 3\,\mu m$). **(B)** The short time regime, characterized by a linear dependence between D and $\omega^{-1/2}$ (Equations 1 and 2), is only accessible for very large cells ($R > 5\,\mu m$). Plots were adapted from the equations derived in Xu et al. [13].

diffusion contrast on commercial scanners are restricted to the far left side of the spectrum ($f_{OGSE} < 300$ Hz), insufficient to explore diffusion inside small structures ($R = 1$–$2\,\mu m$). On the other hand, the short-time limit—characterized by the linear relationship between D and $\omega^{-1/2}$–is already within reach for larger cells ($R = 5$–$10\,\mu m$, see **Figure 3B**), as demonstrated *in vivo* in Reynaud et al. [18].

Modeling Impermeable Tumor Tissue

A commonly used picture to describe tumor tissue is a non-exchanging multi-compartmental model distinguishing intracellular from extracellular diffusivity.

Impermeable Spheres within the Extracellular Space

At least four independent parameters (cell radius R, ICS/ECS free diffusivities D_0^{ics}/D_0^{ecs}, intracellular volume fraction f) are needed to describe the system {impermeable spheres + ECS compartment}. Additional parameters are required to describe the ECS diffusion outside the tortuosity limit (D = cste) and short-time regime (Equations 1–2), or to model additional compartments, such as vasculature with VERDICT [16]. In practice, multiple PGSE [16, 45] or a combination of PGSE and OGSE [14, 15] measurements are combined in order to probe diffusion in a specific or over several frequency/time domains.

The IMPULSED model

The IMPULSED (imaging microstructural parameters using limited spectrally edited diffusion) model combines multiple low-frequency OGSE measurements ($f_{OGSE} < 150$ Hz) and a single PGSE acquisition in the long time regime (**Figure 4A**) to quantify the characteristic size of restriction and ICS fraction [14, 46].

This approach was shown successful in estimating cancer cell size *in vitro* in the range (5–10) μm using only a small subset of measurements on murine (MEL) and human leukemia cells (K562) [14]. *In vivo*, the correlation between histology and IMPULSED-based cellularities were found superior than between histology and conventional PGSE measurements, in three different colorectal cancer xenograft tumor models (DiFi, HCT116, and SW620) [46].

This model assumes that the ECS diffusion varies linearly with frequency f_{OGSE} in the range 50–150 Hz. This assumption was motivated by (i) the empirical linear behavior of the overall ADC (intra- and extracellular) measured in the healthy mouse brain [34] and (ii) simulations in extra-axonal space derived from histology samples [43]. Unfortunately, this would only be valid of a two-dimensional problem ($d = 2$ in Equation 3) and the correct formula for the ECS diffusion around spheres at long times is given by Equation (5) instead. However, the linear approximation can be considered as an approximation in a narrow frequency range, with little impact on estimated parameters.

The POMACE model

The POMACE (Pulsed and oscillating gradient MRI for assessment of cell size and extracellular space) model combines multiple OGSE and PGSE measurements in different time domains (**Figure 4B**). Microstructural parameter estimation is performed in two steps. The surface-to-volume ratio and free diffusivity are first evaluated using high-frequency OGSE in the short-time regime [18] using Equation (2). These values are then used as constraints when fitting the low-frequency OGSE and PGSE data (**Figure 5**, $f_{OGSE} < 88$ Hz) to a model of impermeable spheres bathing in ECS [15].

Using a dedicated histology coil [47], the validity of POMACE was tested *ex vivo*. ICS maps correlated well with optical microscopy performed on the same samples used for MRI [15]. *In vivo*, ICS estimates were found in agreement with ECS estimates from an effective medium theory [25], while cell sizes matched electron microscopy measurements in mice gliomas (GL261).

The POMACE framework was later applied to the *in vivo* assessment of treatment response in GL261 gliomas and 4T1 mammary carcinomas [48]. Following tumor treatment with 5FU and bevacizumab, a significant ECS decrease was observed with POMACE, while the absence of impact on S/V or cell radius suggested partial membrane deterioration and/or a decrease of the apparent restrictive surface due to increased cell packing in both cell lines.

The VERDICT model

VERDICT (vascular, extracellular, and restricted diffusion for cytometry in tumors) is the only model to consider the impact of tumor vasculature on the directionality of diffusion (**Figure 4C**). Cancer cells are modeled by spheres, the extracellular diffusivity by an isotropic diffusion tensor, and the vascular compartment by an additional highly anisotropic tensor [16], although its precise form can vary depending on the application [49].

This more complex modeling comes at the expense of a large number of parameters to estimate. To ensure fit robustness, the free diffusivities in the ICS and ECS are fixed. Six independent parameters are estimated: intracellular and extracellular volume fractions f_{ics} and f_{ecs}, cell size R, the pseudo-diffusion coefficient of water inside blood vessels P, and two angles characterizing the directionality of the vascular compartment. The intravascular fractions is then calculated as $f_v = 1 - f_{ics} - f_{ecs}$.

This model successfully differentiated two human colorectal carcinoma cell lines based on their vascular fraction [16]: SW1222 xenografts exhibited dense perfusion ($f_v = 0.22$) while LS174T (**Figure 5**) were properly categorized as densely packed ($f_{ecs} < 0.05$) with low perfusion ($f_v = 0.12$). In addition, significant changes in intravascular and intracellular volume fractions were observed in response to a chemotoxic agent leading to cell apoptosis (gemcitabine), as confirmed by flow cytometry [16].

Focusing on PGSE acquired at several diffusion times (10–40 ms), diffusion contrast is plentiful and VERDICT can be easily adapted to a clinical setting. After preliminary work on model selection,

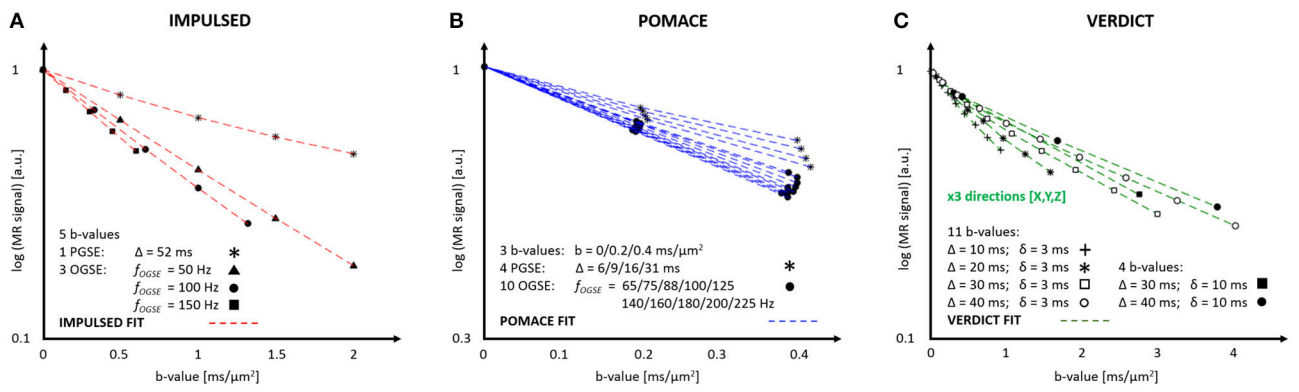

FIGURE 4 | MR parameters and diffusion signal for three geometrical models: IMPULSED **(A)**, POMACE **(B)** and VERDICT **(C).** Only 20 measurements (5 *b*-values, 4 diffusion times) are required to fit the diffusion signal with IMPULSED (red). With POMACE (blue), 42 points are acquired (3 *b*-values, 14 diffusion times), strictly restricted to the DTI regime ($b < 0.5$ ms/μm^2). The full implementation of VERDICT (green) requires 44 measurements repeated along three orthogonal axes (X/Y/Z), plus acquisitions at $b = 0$. Note the different scale of *b*-value along the horizontal axis. The plots illustrate the protocols described in Reynaud et al. [15], Panagiotaki et al. [16], Jiang et al. [46].

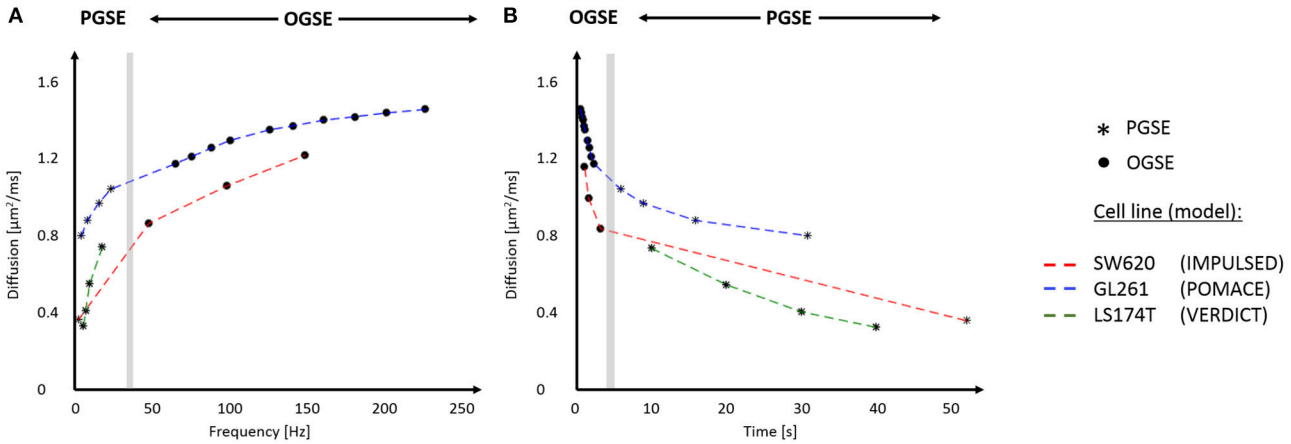

FIGURE 5 | *In vivo* time-dependent diffusion in tumors plotted vs. frequency **(A)** and diffusion time **(B).** Synthetic data for different cell lines (SW620, GL261, and LS174T) were generated using the best fits for the diffusion signals respectively reported in Reynaud et al. [15], Panagiotaki et al. [16], Jiang et al. [46]. The range of frequencies and diffusion times probed with IMPULSED (red), POMACE (blue) and VERDICT (green) can be appreciated in **(A,B)**. The gray area delineates the limit between OGSE (circles) and PGSE (stars) datapoints. For display purposes, PGSE and OGSE measurements were attributed the equivalent frequency f_{OGSE} and diffusion time t according to $f_{OGSE} = 9/64 \times t^{-1}$, as discussed in Novikov et al. [79].

the previous model was modified to (i) consider the vascular compartment as isotropic and (ii) fix the free diffusivities and pseudo-diffusion coefficient to 2 and 8 μm^2/ms, respectively. *In vivo*, the new model (with only three independent parameters) was able to distinguish tumor from benign prostatic areas in eight patients at 3T under acceptable scan times (35 min) [49].

A prospective study—INNOVATE [50]—recently started combining the VERDICT framework with novel blood and urine sampling based potential biomarkers in an attempt to affine patient screening and promote the use of multi-parametric MRI before biopsy for the diagnosis of prostate cancer. Patient follow-up is needed before assessing the potential improvement in patient care by diagnosing early aggressive prostate cancer.

ADC dispersion rate

A linear increase of ADC vs. OGSE frequency was reported in the *ex vivo* mouse brain in the range 0–150 Hz [34]. Regions of large ADC changes (Δ_f ADC) colocalized well with Nissl staining and densely packed neuronal regions, suggesting a link between ADC dispersion and ICS volume and/or cell size.

A theoretical justification for this effect can be found in Equation (7) and **Figure 3**. At low frequency OGSE, the intracellular diffusion in small structures ($R \leq 5$ μm) does not approach the asymptotic short-time limit and can be considered linear with f_{OGSE}, as a first approximation in a narrow frequency range. Fixing D_0, the slope of this linear relationship increases with cell size (**Figure 3A**) and ICS volume, assuming slower diffusion time-dependence in the ECS.

The ADC dispersion rate averaged in the range 50–250 Hz was shown sensitive to treatment of colorectal tumor SW620 with barasertib (AZD1152) [51], known to induce the formation of new chromosomic structures at subcellular level, increased cell size and eventually apoptosis [52].

A closer look on **Figure 2C** highlights that the instantaneous dispersion rate $\partial D/\partial f$ is non-monotonous with OGSE frequency. A maximum is reached around $0.4 \times D_0/R^2$, suggesting potential for characterizing the tissue characteristic restriction scale. This was demonstrated i*n vitro* using two cell lines with different radius ($R = 5/10\,\mu m$ for MEL/K562) with significantly different instantaneous dispersion rate around 60 Hz [53].

Although e*x vivo* experiments performed on kidney and liver tissue highlighted very little contrast with dispersion rate compared to conventional ADC [53], these result are dependent on sample preparation and fixation, and should be reproduced *in vivo*. Larger diffusivities might shift the oscillation frequency range of interest.

Impermeable Model-Free Approaches

Non-geometrical models can also be used to describe tumor microstructure. Systems can indeed simplify in a specific time regime, where geometry is partly irrelevant, such as the very short or long time regime. This results almost always in a more accurate estimation of a certain tissue parameter, at the expense of another.

The short time regime

As discussed in the first section, the universal behavior of short-time diffusion is described for PGSE and OGSE by Equations (1) and (2). In this regime, any system can be considered made of two spin populations. Regardless of the particular geometry, some random walkers will never experience the cell walls (and freely diffuse with D_0) while the displacement of the population within diffusion length of the wall (with volume fraction: $height \times surface/volume = \sqrt{D_0 t} \times S/V$) will be restricted. At such short times, neither the curvature nor the permeability of the cell walls impact diffusion [10, 19].

The validity of the short diffusion-time regime was demonstrated *in vivo* and *ex vivo* in mice gliomas (GL261, $R \sim 5\,\mu m$) in the range $88\,Hz \leq f_{OGSE} \leq 225\,Hz$ [18]. The decoupling of diffusive and geometric properties was assessed *ex vivo* by varying the sample temperature, only impacting the term D_0 in Equation (2). Parametric maps of S/V and D_0 were easily accessible *in vivo*, paving the way for robust—thanks to linear fitting—and unambiguous interpretation of TDD in tumors.

Potential applications in a clinical setting include characterization of breast cancer. Recently, this regime was demonstrated *in vivo* at

3T in healthy breast tissue using STEAM and diffusion times in the range 80–900 ms [54], following up on muscular studies [55, 56] with similar restriction scale (hundreds of microns).

Effective medium theory at long times

On the other side of the spectrum, the effective medium theory (EMT) only focuses on the macroscopic properties of tissue. At long times, molecules have diffused around and inside each structure, so that microscopic information such as cell size is lost. Using an EMT analogous to that of conductivity in porous media, the long time limit of diffusion in a biological system {permeable spheres + ECS} was derived [17]. In the impermeable case, Equation (2) from Latour et al. [17] becomes:

$$D_\infty = \left(1 - f\right)^{3/2} \times D_0 \tag{8}$$

where f is the ICS volume fraction and D_0 the free extracellular diffusivity. Since microstructural information is lost, changing cell shapes should not affect Equation (8).

This EMT establishes the well-known relationship between PGSE measurements at long times and cellularity for a simple system [3, 4]. Provided the cell size is of little interest, estimating the tortuosity limit with multiple PGSE in the long time regime (**Figure 1C**) is indeed an alternative way of estimating the size of the ICS. *A priori* knowledge on D_0 is however required to quantify f using Equation (8). Additional information on D_0 can be gathered in the short-time regime using Equations (1) and (2).

An EMT approach was successfully demonstrated in mice gliomas using only four diffusion times (6–31 ms) [15]. ICS estimates were found in excellent agreement with that of POMACE, fewer acquisitions were required, and fit estimates found very robust. Unfortunately, cell sizes could not be estimated using this technique.

CURRENT RESEARCH GAPS AND PITFALLS

Modeling Issues

In this section are detailed problems commonly encountered when modeling and fitting tissue microstructure. Potential solutions are discussed when available. The objective is not to compare the various fitting frameworks, but rather to discuss common flaws when modeling biological tissue.

Accuracy and Precision of Fitting

Albeit simplistic, geometrical models require the simultaneous estimation of at least four independent parameters: cell size R, ICS volume fraction f, and intra- and extracellular diffusivities D_{ics} and D_{ecs}. Additional parameters are required for modeling time-dependence in the ECS [14] and/or a vasculature compartment [16]. In practice, the narrow range of diffusion times available in most scanners (**Figure 5**) prevents the completely unambiguous estimation of all model parameters.

Accuracy

Accuracy represents the closeness of fit estimates compared to the ground truth. In the absence of a ground truth, a commonly used approach is to generate synthetic data based on the model, add noise, and compare the "noisy" fit outputs to the initial "clean" input. For preclinical brain studies, typical *in vivo* SNR values range were reported between 100 and 150 [15].

We consider here the case of impermeable spheres within the ECS. As in POMACE, the ECS is modeled in the tortuosity limit for low-frequency measurements, and in the short time regime for high-frequency OGSE acquisitions. The problem is further simplified by initiating the fitting algorithm from the ground truth in order to minimize the influence of local minima when estimating parameters. Synthetic data is generated from the parameters best describing TDD in murine glioblastoma [15].

Without PGSE, a large range of solutions emerge from noise propagation (**Figure 6A**) despite high SNR (SNR = 120) and multiple OGSE time-points (10 f_{OGSE} steps from 60 to 225 Hz). This model is obviously not well suited to characterize tumor microstructure accurately, its solutions are not centered on the ground truth.

This issue can be resolved here by increasing the SNR or incorporating additional data points (b-values and/or diffusion times), for instance PGSE measurements. Incorporating *a priori* knowledge on the system—by fixing one parameter—will also help by reducing the degree of freedom of the problem. A combination of the last two approaches was chosen to improve the robustness of the POMACE framework [15], as can be seen in **Figure 6B**. Another "angle" can be to use the directionality of diffusion, only useful when properly accounted for in tissue modeling [16].

Similarly, synthetic diffusion data was generated using the IMPULSED framework [46] in order to mimic TDD in colorectal tumors (see **Table 1**). Multiple instances of gaussian noise (typical *in vivo* SNR = 120, n = 2,500) were added to the signal before fitting. Although the distribution of fit estimates were not found normal (**Figures 6C,D**), average fit estimates matched the ground truth ($SNR = \infty$) with good accuracy for most parameters (**Table 1**, relative bias below 3/13% for f, R, D_{ics} for DiFi/HCT116 cell lines). The matlab code used to generate synthetic tumor data and plot parameter accuracy with POMACE and IMPULSED is readily available for download at https://github.com/oreynaud/FIT_TDD.

Precision

The primary objective behind the development of TDD was to attribute the changes in the diffusion signal to specific microstructural metrics, without ambiguity. Even if the fit is accurate, microstructural variations—in space or time—can only be reliably estimated if they exceed the fit precision, defined by the reproducibility of parameter estimation.

Small changes in volume fraction are likely to be picked up by POMACE (**Figure 6B** and standard deviations in **Table 1**), due to the large amount of data acquired in the long time regime. On the other hand, the IMPULSED framework is well suited to detect small variations in cell size (**Table 1**) and would benefit from a reduced scan time. Results might depend on the particular microstructure, as illustrated by the different precision available on diffusivities estimates between the two colorectal cell lines.

In general, it appears unreasonable to attempt to detect variations below the following thresholds: $\Delta f_{\min} = 3\%$ and $\Delta R_{\min} = 0.5\,\mu\text{m}$. Since low image SNR is extremely detrimental to the fit precision, smoothing and/or averaging the signal within regions of interest might be preferred to raw single-voxel parametric mapping in order to enhance the robustness and specificity of the analysis. Special care should however be taken in very heterogeneous tumors.

Fixing Parameters

Because of model over-parametrization, most TDD frameworks resort to fixing one or several parameters in order to improve the

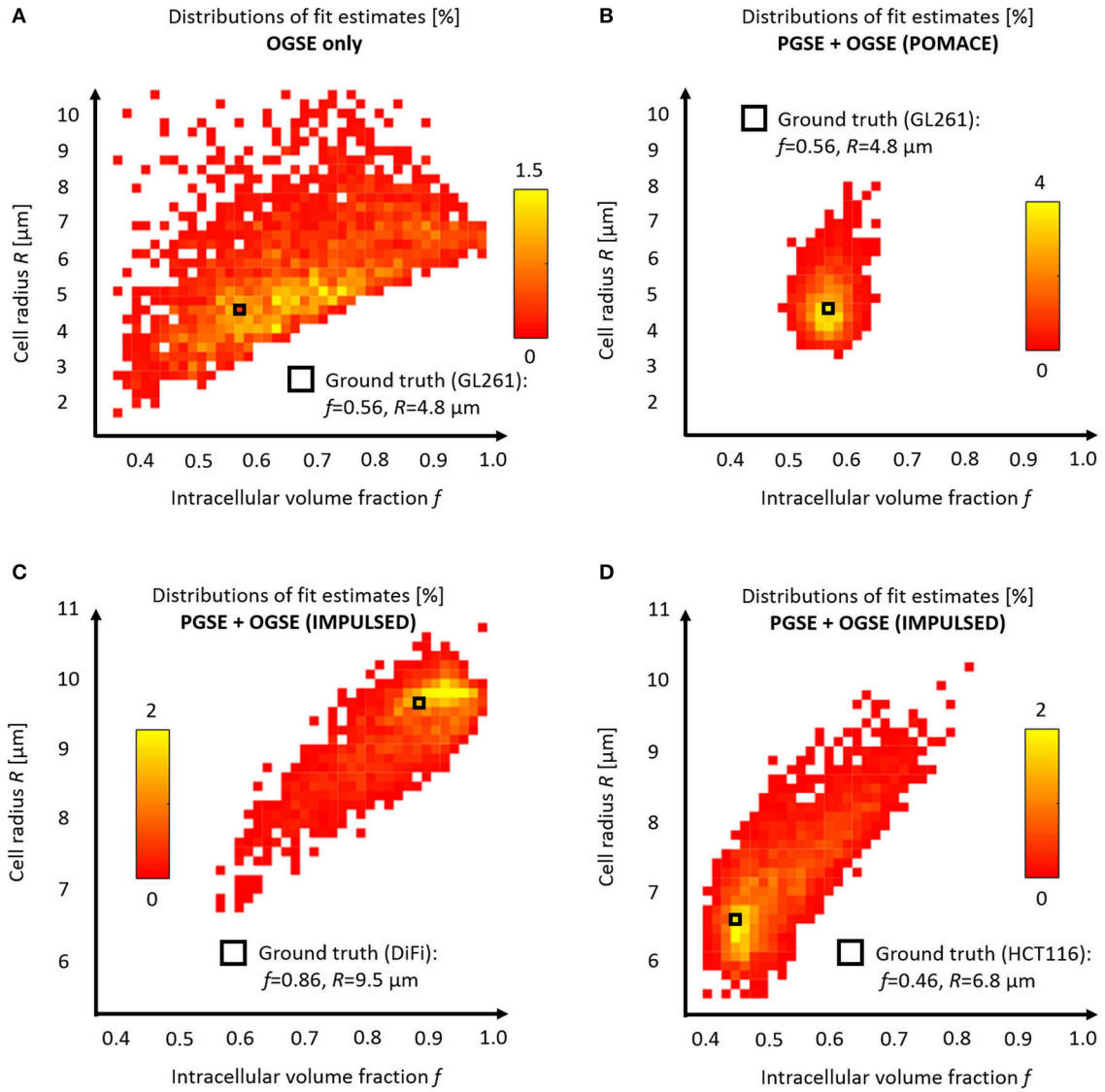

FIGURE 6 | Model accuracy and precision. Distributions of intracellular volume fractions and cell radius estimates on noisy data (synthetic GL261 glioma signal, SNR = 120, $n = 2{,}500$) using **(A)** OGSE measurements in the range (65–225) Hz, or **(B)** a combination of PGSE (Δ6/9/16/31 ms) and OGSE data as in POMACE [15]. Fit estimates distribution when characterizing tumor microstructure *in vivo* inside DiFi **(C)** and HCT116 **(D)** colorectal tumors with IMPULSED [46]. The ground truth is indicated by a black square. For each framework, the full list of fit estimates can be found in **Table 1**. The matlab code used to generate synthetic tumor data and plot parameter accuracy with POMACE and IMPULSED is readily available for download at https://github.com/oreynaud/FIT_TDD.

fit stability and precision. This comes at the expense of accuracy, because errors on fixed parameters can propagate into the remaining fit estimates.

In the first VERDICT framework, the ICS and ECS diffusivities were fixed based on fit optimization performed on preliminary data [16], and found consistent with values derived from *ex vivo* studies with high SNR [57]. To further improve the fit robustness, the pseudo-diffusion coefficient of the water inside blood vessels was also fixed when characterizing prostatic tissue lesions *in vivo* in a later study [49].

In POMACE, the extracellular free diffusivity D_0^{ecs} was also fixed ($D_0^{ecs} = 2.7/1.9$ µm^2/ms *in vivo*/*ex vivo*) and used as an additional constrain to reduce the degree of freedom to three parameters, using short time limit measurements [15].

Despite being central to the fit accuracy and precision, it is not always clear how other frameworks deal with these practical issues. Data and code sharing, a good example of which can be found in Panagiotaki et al. [16], would help increase the transparency so desperately needed when dealing with complex modeling.

Diffusion Is Not Constant in the ECS

The main three geometrical models (IMPULSED, POMACE, VERDICT) all assume that the extracellular diffusion is in the tortuosity limit for PGSE [14, 16] and/or low-frequency OGSE [15].

TABLE 1 | Accuracy and precision of all fit estimates (average ± std, $n = 2{,}500$).

Cell line (model)	SNR	f [%]	R [μm]	B_{ecs} [1,000*μm^2]	D_{ics} [μm^2/ms]	D_{ecs} [μm^2/ms]
GL261 (POMACE)	∞	56	4.8	–	0.95	2.06
	120	57 ± 3	5.0 ± 1.0	–	0.98 ± 0.11	2.09 ± 0.23
DiFi (IMPULSED)	∞	86	9.5	2.1	1.15	0.44
	120	87 ± 8	9.3 ± 0.6	5.2 ± 5.3	1.12 ± 0.09	0.58 ± 0.38
HCT116 (IMPULSED)	∞	46	6.8	2.4	1.53	0.75
	120	52 ± 8	7.2 ± 0.8	3.6 ± 1.8	1.34 ± 0.27	0.81 ± 0.13

The synthetic data was simulated based on the parameters estimated in vivo for GL261 gliomas [15], and DiFi and HCT116 colorectal tumors [46]. Good accuracy was generally observed for f, R, and D_{ics} under in vivo conditions (SNR = 120).

However, in the long time regime, Equations (6) and (7) degenerate into $D_{PGSE,ics}(t) \propto 1/t$ and $D_{OGSE,ics}(\omega) \propto \omega^2$. Therefore, the ECS time-dependence, supposedly varying as $1/t$ or $\omega^{3/2}$ using Equations (4) and (5), is not negligible when $t \to \infty$ or $\omega \to 0$. Neglecting the ECS time-dependence is in general wrong (see **Figures 1C,D**) and should be carefully justified, depending on the application.

This problem can be resolved by estimating a lower and upper bound for the extracellular diffusivity in the range where it is assumed constant. If ECS diffusion variations cannot be neglected, prior knowledge on typical restriction scales can be used to justify that intracellular changes are expected to dominate the overall time-dependence. Obviously, the validity of such an approach would only hold in a certain time/frequency range, and for a specific application.

Microscopic Heterogeneity

To date, all geometrical models have considered that each component of tissue microstructure (compartment size, diffusivities…) could be properly modeled by a single metric per voxel, fully depicting the value of a particular parameter. This can potentially lead to substantial bias, since tumor heterogeneity—revealed with histopathology—is present both at macroscopic and microscopic scale.

Because the relationship between the different estimated parameters and the resulting MR signal is not linear (see Equations 6 and 7), the various outputs of the fit procedure are likely not to represent neither the average nor the median value of any physical metric that could be measured using a more direct imaging method (electron/optical/fluorescence microscopy).

Interestingly, DWI can be used to probe intra-voxel parameter variance using conventional kurtosis imaging [7] and/or the recently introduced kurtosis-based DIVIDE technique [8]. These techniques can be used as safeguards to delineate areas of strong heterogeneity in order to minimize parameter bias with TDD due to strong intra-voxel variance. In their absence, most parameters shall be regarded as indexes, rather than specific precise markers of tumor microstructure.

Accounting for Tissue Permeability

All the models introduced so far consider cells to be fully impermeable. The present section will focus on (a) how to properly model membrane permeability κ at short and long times, (b) whether it impacts parameter estimation using geometrical models and (c) alternative models that attempted to account for permeability, using TDD and/or filter exchange imaging.

The short time limit

Cell permeability does not impact diffusion measurements at very short times: Equations (1) and (2) are always valid regardless of cell permeability κ . However, as time increases, diffusion departs from the previous equation and can be expressed as in Sen [19] and Sen [58]:

$$D_1(t) = D_1\left(1 - \frac{S_1}{V_1}\left[\frac{4\sqrt{D_1 t}}{9\sqrt{\pi}} - \frac{\sqrt{D_2}\left(\sqrt{D_2}+\sqrt{D_1}\right)}{6D_1}\kappa t - \frac{\rho t}{6} + \frac{D_1 t}{12}\left\langle\frac{1}{R_1}+\frac{1}{R_2}\right\rangle_R\right]\cdot\right) + O(D_0 t^{3/2}) \quad (9)$$

Here ρ is the surface relaxivity, and D_i, S_i/V_i, and R_i the free diffusivity, surface-to-volume ratio, and radius of curvature of compartment i = {1,2}. A similar expression describes the diffusion in the second compartment, by interchanging the subscripts {1,2} and the sign of the last term $\langle\frac{1}{R_1}+\frac{1}{R_2}\rangle_R$, representing the average inverse curvature radius over the interior surface.

The models simplifies under two assumptions: $\rho \ll \kappa$ (true for most biological systems) and $D_1 = D_2$. The curvature terms cancel each other in the overall diffusion $D = fD_1 + (1-f)D_2$. From there follow that the linear dependence of the diffusion directly represents the influence of permeability κ . Estimates are weighted by the surface-to-volume ratio counted twice, as random walkers explore the walls both from inside and outside the cells.

Using the diffusivity and permeability calculated for packed erythrocytes (red blood cells) in Latour et al. [17], Sen [19] estimated that permeability only becomes a relevant model parameter when diffusion times approach or exceed 60 ms.

Since *in vivo* diffusion deviates from the short-time limit regime around $f_{OGSE} = 88$ Hz for cancer cells [18], one could wonder whether permeability might already impact low-frequency diffusion measurements. However, the mismatch between experimental data and Equation (2) could not be fitted by a linear relationship with f_{OGSE}.

The long time regime

The impact of permeability on diffusion at long times can be derived using the EMT proposed by Latour et al. [17]:

$$\left(\frac{D_\infty - D^*}{D_{ecs} - D^*}\right) \times \left(\frac{D_{ecs}}{D_\infty}\right)^{1/3} = (1-f), \text{with}$$
$$D^* = D_{ics}\kappa R/(\kappa R + D_{ics}) \quad (10)$$

Equation (10) was successfully used to estimate membrane permeability in bovine red blood cell samples around 6.3×10^{-3} cm/s [17]. Diffusion results were found well in agreement with extensive literature in red blood cell permeability [59, 60].

This equation simplifies for $f = 1$ (i.e., no ECS) to the well-known equation derived by Tanner [61] for a stack of flat layers with characteristic length R: $D^{-1} = D_{ics}^{-1} + (\kappa R)^{-1}$. This approximation was later used to accurately measure cells permeability in yeast suspensions [62].

Permeability and geometrical models

The lesser tortuosity expected from permeable cells according to Equation (10) was observed experimentally on human leukemia K562 cells treated with saponin [63], for the multiple diffusion times and oscillation frequency available on preclinical scanners.

The impact of non-zero permeability on parameter estimation was simulated using a finite difference method within the IMPULSED framework [64]. The robustness of most fit estimates (f, R, D_{ics}) was demonstrated under two conditions: the image SNR must remain large (≥ 50) and the water exchange time τ–related to permeability via $\kappa^{-1} = 3\tau/R - R/5D_{ics}$ – must exceed 100 ms.

Such results would in all likelihood hold for other frameworks, provided tissue exchange times exceed the longest diffusion times used to probe diffusion. In cancer, water residency times were estimated around hundreds of milliseconds [65–67], suggesting that permeability could bias but not severely impact parameter estimation performed using PGSE and OGSE. However, changes of cell permeability due to treatment during longitudinal studies could impair the specificity of the model via the apparent variation of other microstructural estimates, such as cell size and ICS diffusivity.

Empirical "permeable planes/spheres" models

The analytical solutions for the diffusion inside impermeable spheres $D_{spheres}(R, D_0)$ or between planes $D_{planes}(R, D_0)$ predict $D = 0$ at infinite times. Rather than evaluating the contribution of a second—extracellular—compartment, a handful of studies attributed the disparity between these models and the observed diffusion ($D_\infty \neq 0$) to membrane permeability, and modeled the TDD of a biological system using empirical formulas such as: $D = D_\infty + D_{planes/spheres}(R, D_0 - D_\infty)$ [28, 35]. It should be noted that permeability cannot be estimated using those models.

Such models can be used to sensitize MRI to small tissue changes thanks to a restricted number of fit parameters, and were shown useful in assessing tumor treatment efficacy in two ovarian human cell lines (OVCAR-8 and NCI/ADR-RES) [35].

However, interpretation of the results is limited as only a mere qualitative insight into tissue structural changes is possible. Without ECS, the pseudo-intracellular diffusivity $D_0 - D_\infty$ is void of physical meaning. At best, R can represent a "restriction index", based on $D_0 - D_\infty$ and the characteristic oscillation frequency (**Figure 2C**).

The random permeable barrier model (RBPM)

In cancer, randomly oriented flat membranes represent a more realistic model than a stack of flat layers, for which a solution accounting for permeability can be derived [20]. Using the EMT formalism for the diffusion signal proposed in Novikov and Kiselev [31], *D(t)* is related to the dispersive diffusivity $\mathcal{D}(\omega)$ via:

$$D(t) = \frac{1}{t}\int \frac{d\omega}{2\pi} e^{-i\omega t} \frac{\mathcal{D}(\omega)}{(\omega + i0)^2} \tag{11}$$

and $\mathcal{D}(\omega)$, for random permeable barriers, is described by Novikov et al. [20]:

$$\frac{D_0}{\mathcal{D}(\omega)} = 1 + \xi + 2z_\omega(1 - z_\omega)\left[\sqrt{1 + \xi/(1 - z_\omega)^2} - 1\right] \tag{12}$$

where ξ represents the effective volume fraction of membranes via $\xi = S/V \times D_0/2\kappa d$ in d dimensions, and $z_\omega = i\sqrt{iD_0}/2\kappa$ is a dimensionless frequency.

Although never applied in tumors, the RBPM geometry is well suited for muscle studies [56], and tissue permeability and cell size were recently estimated *in vivo* and on clinical scanners [68]. This approach could provide an interesting approach to characterizing sarcomas using TDD in the near future.

Filter exchange imaging (FEXI)

A promising alternative to TDD for characterizing cell permeability might lie in apparent exchange rate/filter exchange imaging (FEXI) [69, 70]. In FEXI, a stimulated-echo double diffusion encoding sequence uses two PGSE diffusion blocks separated by a mixing time t_d, during which exchange between intra- and extracellular compartments (where diffusion is assumed to be approximately Gaussian) occur. The water exchange rate is estimated by measuring a mono-exponential decay of diffusion with mixing time t_d [69].

The clinical potential of FEXI was first assessed in the brain, in both healthy and brain cancer patients, where viable and necrotic parts of the tumor could be clearly differentiated based on exchange rate [70]. More recently, FEXI was shown capable of differentiating two brain cancer types (astrocytomas vs. meningiomas) *in vivo* based on exchange rate using only a small sample size (5–10 subjects) [71]. In breast cancer, FEXI could differentiate between multiple cell lines *in vitro*, while its potential for *in vivo* imaging was also demonstrated [72].

Time and Hardware Issues

Acquisition Time

A typical TDD experiment relies on the acquisition of multiple diffusion measurements performed when varying the diffusion time/oscillation frequency. Multiple diffusion times are required to extract relevant microstructural information from variable molecular restriction via Equations (6) and (7). It is also recommended to acquire a large range of b-values due to the large amount of parameters to estimate when fitting diffusion data to a specific model for tissue microstructure. The multiplicity of scans considerably lengthens the acquisition time dedicated to TDD.

Long scanning times are detrimental for the translation of newly-derived frameworks in a clinical setting. In that view, efforts are being made to shorten the number of measurements [46, 49].

This issue can be magnified for anisotropic media, where some compartments should be characterized by a tensor. Tissue lesions are often considered isotropic for convenience and practicality [49], potentially at the expense of specificity [57].

Frequency Range and Cell Size

The apparent mismatch between preclinical and clinical applications originates from restricted scanner capabilities.

Preclinical scanners

For a given gradient strength and duration, $b_{OGSE} \propto f_{OGSE}^{-3}$ for cosine OGSE [27]. As a result, reasonable contrast at large oscillation frequencies can only be achieved by compensating the lesser temporal window allow for molecular diffusion by stronger dephasing, i.e., stronger gradient strength.

This sets an upper bound limit for the frequency of OGSE measurements around 300–350 Hz (using $b_{OGSE} = 0.4$ ms/μm^2 and typical echo times) on preclinical scanners equipped with diffusion-friendly gradients (1 T/m). This in turns sets a lower limit for the range of restriction scales that can be probed using TDD around $R \sim \sqrt{D_0/f_{OGSE}} \sim 2\,\mu$m.

As a result, most preclinical applications of TDD so far have focused on relatively large structures, such as brain glioma or colorectal cells (R ∼ 4–20 μm). An obvious downside is that—in the brain—the comparison of diffusion-based tumor microstructural metrics with healthy tissue remains out of reach, since TDD is not adapted to characterize normal brain tissue structure (white/gray matter).

Although sinusoidal OGSE exhibit larger b-values than their cosine counterpart, a DC component is introduced into the frequency spectrum, effectively mixing conventional PGSE and OGSE

measurements [27]. Compared to cosine OGSE, the gain in diffusion contrast does not originates from the frequencies of interest.

Clinical scanners

The situation worsens for clinical scanners, where $f_{OGSE} = 100\,\text{Hz}$ can only be achieved with $b < 120\ \text{s/mm}^2$ (3T, gradient strength 80 mT/m). While intra-voxel incoherent motion effects [73] do not affect cosine modulated OGSE or other sequences with no sensitivity to the zero frequency of the diffusion spectrum relating to translation, this results in poor diffusion contrast. In addition, diffusion is in that range already highly restricted in small structures, and microstructural information cannot be retrieved using diffusion time-dependence [74]. The development and availability of high gradients systems is crucial to the eventual translation of the full TDD potential to the clinic.

On the contrary, clinical diffusion—using STEAM and PGSE—is already well adapted to characterizing breast and muscle tissues, where the restriction scale approaches hundreds of microns. TDD applications in sarcomas and breast cancer are well within reach of the current hardware systems, and are expected to flourish over the next few years.

In addition, the potential success of the INNOVATE study [50] on a large cohort could represent a tremendous springboard for prostate cancer characterization using TDD, as well as a major billboard for promoting TDD applied to various forms of cancer.

APPLICATIONS OF TIME-DEPENDENT DIFFUSION IN CANCER AND FUTURE DEVELOPMENTS

Range of Applications

The full list of studies combining TDD with *in vivo* MR of cancer can be found in **Table 2**.

At preclinical level, *in vivo* time-dependent studies have focused on brain gliomas using rat [45, 75, 76] and mice models [15, 18, 48], as well as mice xenografts models of colorectal [16, 46, 51] and ovarian cancer [35].

On the other hand, human *in vivo* applications have targeted prostatic tissue [49, 50, 77, 78] and breast lesions [54], while its potential in muscle was shown in Sigmund et al. [56].

Tumor Treatment

A distinction is made between two classes of studies. On one hand, sensitive metrics can be derived from TDD experiments without proper tissue modeling, by benefiting from a small number of degrees of freedom. Alternatively, the diffusion frameworks based on geometrical modeling and multi-compartmental approaches provide specific insight into tumor structure. This comes at the expense of parameter accuracy and precision due to the large number of estimates to quantify.

Sensitive Markers

The impact of tumor treatment on TDD measured with OGSE was first observed *in vivo* in the rat brain following the injection of BCNU in 9L gliomas [75]. A significant increase in contrast (tumor vs. healthy brain) was obtained from ADC maps at high oscillation frequencies ($f_{OGSE} = 240\,\text{Hz}$).

From the same group, Xu et al. [51] acquired the diffusion signal for a wide range of oscillation frequencies 2 and 4 days after chemotherapeutic treatment on SW620 colorectal tumors grafted in mice limbs. Results differed from the previous experiment in that the treated tumor ADC decreased for high frequencies, but still increased for PGSE and low-frequency OGSE. These observations, consistent with a decrease in cell density simultaneous to an increase in cell size following the barasertib treatment, highlighted the necessity to probe diffusion on a large time scale. Based on these findings,

TABLE 2 | List of *in vivo* applications of time-dependent diffusion in cancer.

Study	Species	Organ	Cell line	Treatment	Conclusion
[76]	Rat	Brain	C6 (glioma) ***		Increased diffusion contrast in tumor with OGSE
[75]	Rat	Brain	9L (glioma)	BCNU	Large ADC increase using OGSE (following tumor treatment)
[51]	Mice	Limb	SW620 (colorectal)	barasertib	ADC dispersion rate decrease (following tumor treatment)
[16]	Mice	Limb	LS174T, SW1222 (colorectal)	gemcitabine	Assessment of cell size and vasculature using VERDICT
[15]	Mice	Brain	GL261 (glioma) ***		Quantification of Surface-to-volume ratio in tumors
[18]	Mice	Brain	GL261 (glioma) ***		Estimation of cell size and ECS volume fraction using POMACE
[48]	Mice	Brain	GL261 (glioma), 4T1 (mammary carcinoma)	5FU + bevacizumab	ECS decrease 1–2 days following tumor treatment
[45]	Rat	Brain	GBM4 (glioma)		Non-gaussian diffusion in restricted compartment of high tumor density regions
[46]	Mice	Limb	DiFi, HCT116, SW620 (colorectal)		Cell size estimation using IMPULSED
[35]	Mice	Limb	OVCAR-8, NCI/ADR_RES (ovarian)	Nab-paclitaxel	Change in restriction size (following OVCAR-8 tumor treatment)
[49]	Human	Prostate	Manifold		Vasculature-specific tumor differentiation using VERDICT
[50]	Human	Prostate	Manifold		INNOVATE: Prospective cohort study using VERDICT for evaluating prostate cancer screening
[78]	Human	Prostate	Manifold		Model-free observation of diffusion time-dependence in prostate cancer
[54]	Human	Breast	Cyst, carcinoma, fibroadenoma		Observation of short time regime for radial diffusion in healthy breast and lesions

*** *indicates that ex vivo MRI was also performed on fixed tissue.*

the ADC dispersion rate—averaged over the range 50–250 Hz—was proposed as a promising sensitive (but unspecific) marker for treatment efficacy [51].

Recently, Jiang et al. [35] evaluated the potential of an empirical model—of the type $D = D_\infty + D_{planes/spheres}(R, D_0 - D_\infty)$–to study ovarian cancer cells (OVCAR-8 and NCI/ADR-RES) undergoing mitotic arrest. As already discussed, such models can be used to sensitize MRI to small tissue changes thanks to a restricted number of fit parameters. Significant changes of the "restriction index" and "free diffusivity" were reported following treatment of OVCAR-8 with Nab-paclitaxel [35].

In summary, TDD has been successfully used to observe a small trend in ADC and ADC dispersion rate, or using simplistic modeling. Although sensitive, the reported results remain difficult to interpret due to the non-physical origin of the measured metrics. Changes in diffusivities, compartments and cell size cannot be efficiently disentangled from the estimation of a small number of non-physical parameters.

Specific Markers

The influence of cell apoptosis on TDD was assessed *in vivo* using the VERDICT model on LS174T colorectal xenografts treated with gemcitabine [16]. The changes in cell size observed *in vitro* (on the order of 5%) were not found significant with VERDICT, likely the result of insufficient precision on fit estimates. However, significant changes in vascular and intracellular volume fractions were found. These results were found consistent with cell apoptosis, providing for once a specific insight into changes at microstructural level based on diffusion.

The POMACE framework was recently used to measure the *in vivo* microstructural changes associated with chemotherapeutic therapy on GL261 and 4T1 cell lines [48]. A small ECS decrease (−10%) was measured 2 days after injection. Interestingly, surface–to-volume ratio estimates in the short time regime did not vary significantly following 5FU treatment, likely the result of a simultaneous—but small—increase in cell size that could not be detected with POMACE.

In summary, applying the geometrical models detailed in this review often suffer from a lack of sensitivity to detect and/or reliably quantify the relatively small changes happening at microstructural level. Validation is also impaired by the difficulty of confirming MRI measurements with other imaging modalities. To date, the clear measurement of a specific change in microstructure (f, R, S/V) or medium property (D_{ics}, D_{ecs}) following tumor treatment—and fully consistent with histology and/or electron microscopy - has yet to be demonstrated and reported.

Future Developments

Although TDD has demonstrated great potential for non-invasive yet specific cancer characterization, many challenges remain before the technique can be suitable integrated into a clinical setting. Some of the questions the community will need to answer are non-specific to the field of TDD in cancer.

In the short term, future areas of research shall include the integration of permeability into geometrical models of cancer, a cautious assessment of the sensitivity and utility of each processing framework, and proper and successful validation of TDD in cancer using multimodality (MRI/microscopy/fluorescence imaging/Electron Micrography) imaging of the same tissues both *ex vivo* and *in vivo*.

Addressing the specificity issue is also of prime importance—here lies the real advantage of performing TDD compared to conventional DWI, and the number of fixed parameters shall be kept to a minimum, potentially by combining TDD with additional measurements in specific extra short/long time regimes.

The added benefit of performing TDD in terms of diagnosis and/or therapeutic follow-up shall be investigated as well. Results from the INNOVATE study will inform further about the potential of TDD in a clinical setting. Time-dependent measurements in muscle and breast are equally promising, as they can easily be performed in the clinic using the hardware (i.e., magnetic field gradients) commercially available today.

The following questions should also be addressed. How can we model healthy tissue so that we can extract meaningful parameters and compare them to those of control regions at individual level? Will TDD ever be applied for human brain cancer mapping *in vivo*? Can we find an optimal unifying framework to perform TDD?

CONCLUSION

TDD is slowly emerging as a strong contender for non-invasive tumor characterization. Despite the lack of a general analytical solution, diffusion can be probed in various regimes where systems simplify to extract relevant information about tissue microstructure. If modeling is thought adequate, Equations (1)–(8) describe how to properly model diffusion in both intracellular and extracellular compartments, or in a combined system. When it cannot be neglected, permeability should be accounted for in the short and long time regime using Equations (9) and (10), or within specific models, as seen in muscle studies. To date, preclinical TDD applications include amongst others the characterization of rodent brain gliomas, and murine xenografts of colorectal or ovarian cancer. This approach has indeed proven successful in estimating tumor intra- and extracellular volume fraction and cell size, as well as treatment efficacy. In the clinic, although probing such small restriction scales is practically impossible due to hardware constraints, it is expected that human applications on breast and prostate cancer will strongly benefit the community in terms of non-invasive cancer screening.

AUTHOR CONTRIBUTIONS

OR: Substantial contributions to the conception or design of the work; acquisition, analysis, or interpretation of data for the work; drafting the work or revising it critically for important intellectual content; final approval of the version to be published; agreement to be accountable for all aspects of the work in ensuring that questions related to the accuracy or integrity of any part of the work are appropriately investigated and resolved.

ACKNOWLEDGMENTS

This work was supported by Centre d'Imagerie BioMédicale (CIBM) of the UNIL, UNIGE, HUG, CHUV, EPFL and the Leenaards and Jeantet Foundations. The author would also like to thank Dr. Sungheon G. Kim, Dmitry S. Novikov, and Ileana O. Jelescu for stimulating discussions on the matter.

REFERENCES

1. Ross BD, Moffat BA, Lawrence TS, Mukherji SK, Gebarski SS, Quint DJ, et al. Evaluation of cancer therapy using diffusion magnetic resonance imaging. *Mol Cancer Ther*. (2003) **2**:581–7.
2. Moffat BA, Chenevert TL, Meyer CR, McKeever PE, Hall DE, Hoff BA, et al. The functional diffusion map: an imaging biomarker for the early prediction of cancer treatment outcome. *Neoplasia* (2006) **8**:259–67. doi: 10.1593/neo.05844
3. Guo AC, Cummings TJ, Dash RC, Provenzale JM. Lymphomas and high-grade astrocytomas: comparison of water diffusibility and histologic characteristics. *Radiology* (2002) **224**:177–83. doi: 10.1148/radiol.2241010637
4. Sugahara T, Korogi Y, Kochi M, Ikushima I, Shigematu Y, Hirai T, et al. Usefulness of diffusion-weighted MRI with echo-planar technique in the evaluation of cellularity in gliomas. *J Magn Reson Imaging* (1999) **9**:53–60. doi: 10.1002/(SICI)1522-2586(199901)9:1<53::AID-JMRI7>3.0.CO;2-2
5. Padhani AR, Liu G, Koh DM, Chenevert TL, Thoeny HC, Takahara T, et al. Diffusion-weighted magnetic resonance imaging as a cancer biomarker: consensus and recommendations. *Neoplasia* (2009) **11**:102–25. doi: 10.1593/neo.81328
6. Basser PJ, Mattiello J, LeBihan D. Estimation of the effective self-diffusion tensor from the NMR spin echo. *J Magn Reson Ser. B* (1994) **103**:247–54. doi: 10.1006/jmrb.1994.1037
7. Jensen JH, Helpern JA. MRI quantification of non-Gaussian water diffusion by kurtosis analysis. *NMR Biomed*. (2010) **23**:698–710. doi: 10.1002/nbm.1518
8. Szczepankiewicz F, van Westen D, Englund E, Westin CF, Ståhlberg F, Lätt J, et al. The link between diffusion MRI and tumor heterogeneity: mapping cell eccentricity and density by diffusional variance decomposition (DIVIDE). *Neuroimage* (2016) **142**:522–32. doi: 10.1016/j.neuroimage.2016.07.038
9. Gore JC, Xu J, Colvin DC, Yankeelov TE, Parsons EC, Does MD. Characterization of tissue structure at varying length scales using temporal diffusion spectroscopy. *NMR Biomed*. (2010) **23**:745–56. doi: 10.1002/nbm.1531
10. Mitra PP, Sen PN, Schwartz LM. Short-time behavior of the diffusion coefficient as a geometrical probe of porous media. *Phys Rev B* (1993) **47**:8565–74. doi: 10.1103/PhysRevB.47.8565
11. Novikov DS, Jensen JH, Helpern JA, Fieremans E. Revealing mesoscopic structural universality with diffusion. *Proc Natl Acad Sci USA*. (2014) **111**:5088–93. doi: 10.1073/pnas.1316944111
12. Murday JS, Cotts RM. Self-diffusion coefficient of liquid lithium. *J Chem Phys*. (1968) **48**:4938–45. doi: 10.1063/1.1668160
13. Xu J, Does MD, Gore JC. Quantitative characterization of tissue microstructure with temporal diffusion spectroscopy. *J Magn Reson*. (2009a) **200**:189–97. doi: 10.1016/j.jmr.2009.06.022
14. Jiang X, Li H, Xie J, Zhao P, Gore JC, Xu J. Quantification of cell size using temporal diffusion spectroscopy. *Magn Reson Med*. (2016b) **75**:1076–85. doi: 10.1002/mrm.25684
15. Reynaud O, Winters KV, Hoang DM, Wadghiri YZ, Novikov DS, Kim SG. Pulsed and oscillating gradient MRI for assessment of cell size and extracellular space (POMACE) in mouse gliomas. *NMR Biomed*. (2016a) **29**:1350–63. doi: 10.1002/nbm.3577
16. Panagiotaki E, Walker-Samuel S, Siow B, Johnson SP, Rajkumar V, Pedley RB, et al. Noninvasive quantification of solid tumor microstructure using VERDICT MRI. *Cancer Res*. (2014) **74**:1902–12. doi: 10.1158/0008-5472.CAN-13-2511
17. Latour LL, Svoboda K, Mitra PP, Sotak CH. Time-dependent diffusion of water in a biological model system. *Proc Natl Acad Sci USA*. (1994) **91**:1229–33. doi: 10.1073/pnas.91.4.1229
18. Reynaud O, Winters KV, Hoang DM, Wadghiri YZ, Novikov DS, Kim SG. Surface-to-volume ratio mapping of tumor microstructure using oscillating gradient diffusion weighted imaging. *Magn Reson Med*. (2016b) **76**:237–47. doi: 10.1002/mrm.25865
19. Sen PN. Time-dependent diffusion coefficient as a probe of geometry. *Concepts Magn Reson Part A Bridg Educ Res*. (2004a) **23**:1–21. doi: 10.1002/cmr.a.20017
20. Novikov DS, Fieremans E, Jensen JH, Helpern JA. Random walk with barriers. *Nat Phys*. (2011) **7**:508–14. doi: 10.1038/nphys1936
21. Novikov DS, Kiselev VG. Surface-to-volume ratio with oscillating gradients. *J Magn Reson*. (2011) **210**:141–5. doi: 10.1016/j.jmr.2011.02.011
22. Sukstanskii AL. Exact analytical results for ADC with oscillating diffusion sensitizing gradients. *J Magn Reson*. (2013) **234**:135–40. doi: 10.1016/j.jmr.2013.06.016
23. Fordham EJ, Gibbs SJ, Hall LD. Partially restricted diffusion in a permeable sandstone: observations by stimulated echo PFG NMR. *Magn Reson Imaging* (1994) **12**:279–84. doi: 10.1016/0730-725X(94)91536-9
24. Hürlimann MD, Helmer KG, Latour LL, Sotak CH. Restricted diffusion in sedimentary rocks. Determination of surface-area-to-volume ratio and surface relaxivity. *J Magn Reson Ser A*. (1994) **111**:169–78. doi: 10.1006/jmra.1994.1243
25. Latour LL, Mitra PP, Kleinberg RL, Sotak CH. Time-dependent diffusion coefficient of fluids in porous media as a probe of surface-to-volume ratio. *J Magn Reson Ser A* (1993) **101**:342–46. doi: 10.1006/jmra.1993.1056
26. Schachter M, Does M, Anderson, A, Gore J. Measurements of restricted diffusion using an oscillating gradient spin-echo sequence. *J Magn Reson*. (2000) **147**:232–7. doi: 10.1006/jmre.2000.2203
27. Parsons EC, Does MD, Gore JC. Temporal diffusion spectroscopy: theory and implementation in restricted systems using oscillating gradients. *Magn Reson Med*. (2006) **55**:75–84. doi: 10.1002/mrm.20732
28. Portnoy S, Flint JJ, Blackband SJ, Stanisz GJ. Oscillating and pulsed gradient diffusion magnetic resonance microscopy over an extended b-value range: implications for the characterization of tissue microstructure. *Magn Reson Med*. (2013) **69**:1131–45. doi: 10.1002/mrm.24325
29. Ferizi U, Schneider T, Witzel T, Wald LL, Zhang H, Wheeler-Kingshott CAM, et al. White matter compartment models for *in vivo* diffusion MRI at 300mT/m. *Neuroimage* (2015) **118**:468–83. doi: 10.1016/j.neuroimage.2015.06.027
30. Panagiotaki E, Schneider T, Siow B, Hall MG, Lythgoe MF, Alexander DC. Compartment models of the diffusion MR signal in brain white matter: a taxonomy and comparison. *Neuroimage* (2012) **59**:2241–54. doi: 10.1016/j.neuroimage.2011.09.081
31. Novikov DS, Kiselev VG. Effective medium theory of a diffusion-weighted signal. *NMR Biomed*. (2010) **23**:682–97. doi: 10.1002/nbm.1584
32. deSwiet TM, Sen PN. Time dependent diffusion coefficient in a disordered medium. *J Chem Phys*. (1996) **104**:206–9. doi: 10.1063/1.470890
33. Van AT, Holdsworth SJ, Bammer R. *In vivo* investigation of restricted diffusion in the human brain with optimized oscillating diffusion gradient encoding. *Magn Reson Med* (2014) **71**:83–94. doi: 10.1002/mrm.24632
34. Aggarwal M, Jones MV, Calabresi PA, Mori S, Zhang J. Probing mouse brain microstructure using oscillating gradient diffusion MRI. *Magn Reson Med*. (2012) **67**:98–109. doi: 10.1002/mrm.22981
35. Jiang X, Li H, Zhao P, Xie J, Khabele D, Xu J, et al. Early detection of treatment-induced mitotic arrest using temporal diffusion magnetic resonance spectroscopy. *Neoplasia* (2016c) **18**:387–97. doi: 10.1016/j.neo.2016.04.006
36. Bender C, Orszag S. *Advanced Mathematical Methods for Scientists and Engineers: Asymptotic Methods and Perturbation Theory*. (1999) Springer.
37. Mair RW, Sen PN, Hürlimann MD, Patz S, Cory DG, Walsworth RL. The narrow pulse approximation and long length scale determination in xenon gas diffusion NMR studies of model porous media. *J Magn Reson*. (2002) **156**:202–12. doi: 10.1006/jmre.2002.2540
38. Kiselev VG. Fundamentals of diffusion MRI physics. *NMR Biomed*. (2017) **30**:e3602. doi: 10.1002/nbm.3602
39. Lee HH, Burcaw LM, Veraart J, Fieremans E, Novikov DS. Low-pass filter effect of finite gradient duration on time-dependent diffusion in the human brain. In *Proceedings of International Society for Magnetic Resonance in Medicine*, Vol. 23. Toronto (2015). p. 2777.
40. Fieremans E, Burcaw LM, Lee HH, Lemberskiy G, Veraart J, Novikov DS. *In vivo* observation and biophysical interpretation of time-dependent diffusion in human white matter. *Neuroimage* (2016) **129**:414–27. doi: 10.1016/j.neuroimage.2016.01.018
41. Tanner JE, Stejskal EO. Restricted self-diffusion of protons in colloidal systems by the pulsed-gradient, spin-echo method. *J Chem Phys*. (1968) **49**:1768–77. doi: 10.1063/1.1670306

42. Xu J, Does MD, Gore JC. Sensitivity of MR diffusion measurements to variations in intracellular structure: effects of nuclear size. *Magn Reson Med*. (2009b) **61**:828–33. doi: 10.1002/mrm.21793
43. Xu J, Li H, Harkins KD, Jiang X, Xie J, Kang H, et al. Mapping mean axon diameter and axonal volume fraction by MRI using temporal diffusion spectroscopy. *Neuroimage* (2014) **103**:10–9. doi: 10.1016/j.neuroimage.2014.09.006
44. Li H, Gore JC, Xu J. Fast and robust measurement of microstructural dimensions using temporal diffusion spectroscopy. *J Magn Reson*. (2014) **242**:4–9. doi: 10.1016/j.jmr.2014.02.007
45. Hope TR, White NS, Kuperman J, Chao Y, Yamin G, Bartch H, et al. Demonstration of non-gaussian restricted diffusion in tumor cells using diffusion time-dependent diffusion-weighted magnetic resonance imaging contrast. *Front. Oncol*. (2016). **6**:179. doi: 10.3389/fonc.2016.00179
46. Jiang X, Li H, Xie J, McKinley ET, Zhao P, Gore JC, et al. *In vivo* imaging of cancer cell size and cellularity using temporal diffusion spectroscopy. *Magn. Reson. Med*. (2016a) **78**:156–64. doi: 10.1002/mrm.26356
47. Hoang DM, Voura EB, Zhang C, Fakri-Bouchet L, Wadghiri YZ. Evaluation of coils for imaging histological slides: signal-to-noise ratio and filling factor. *Magn Reson Med*. (2014) **71**:1932–43. doi: 10.1002/mrm.24841
48. Reynaud O, Zhang J, Winters KV, Novikov DS, Kim SG. Time-dependent diffusion for assessment of treatment response in GL261 murine glioma model. In: *Proceedings of International Society for Magnetic Resonance in Medicine*. (Singapore) (2016c). p. 1229.
49. Panagiotaki E, Chan RW, Dikaios N, Ahmed HU, O'Callaghan J, Freeman A, et al. Microstructural characterization of normal and malignant human prostate tissue with vascular, extracellular, and restricted diffusion for cytometry in tumours magnetic resonance imaging. *Invest. Radiol*. (2015) **50**:218–27. doi: 10.1097/RLI.0000000000000115
50. Johnston E, Pye H, Bonet-Carne E, Panagiotaki E, Patel D, Galazi M, et al. INNOVATE: a prospective cohort study combining serum and urinary biomarkers with novel diffusion-weighted magnetic resonance imaging for the prediction and characterization of prostate cancer. *BMC Cancer* (2016) **16**:816. doi: 10.1186/s12885-016-2856-2
51. Xu J, Li K, Smith RA, Waterton JC, Zhao P, Chen H, et al. Characterizing tumor response to chemotherapy at various length scales using temporal diffusion spectroscopy. *PLoS ONE* (2012) **7**:e41714. doi: 10.1371/journal.pone.0041714
52. Moroz MA, Kochetkov T, Cai S, Wu J, Shamis M, Nair J, et al. Imaging colon cancer response following treatment with AZD1152: a preclinical analysis of [18F]fluoro-2-deoxyglucose and 3???-deoxy-3???-[18F]fluorothymidine imaging. *Clin Cancer Res*. (2011). **17**:1099–10. doi: 10.1158/1078-0432.CCR-10-1430
53. Li H, Jiang X, Wang F, Xu J, Gore JC. Structural information revealed by the dispersion of ADC with frequency. *Magn Reson Imaging*. (2015a) **33**:1083–90. doi: 10.1016/j.mri.2015.06.009
54. Teruel JR, Cho GY, Moccaldi RTM, Goa PE, Bathen TF, Feiweier T, et al. Stimulated echo diffusion tensor imaging (STEAM-DTI) with varying diffusion times as a probe of breast tissue. *J Magn Reson Imaging* (2017) **45**:84–93. doi: 10.1002/jmri.25376
55. Marschar AM, Kuder TA, Stieltjes B, Nagel AM, Bachert P, Laun FB. *In vivo* imaging of the time-dependent apparent diffusional kurtosis in the human calf muscle. *J Magn Reson Imaging* (2015) **41**:1581–90. doi: 10.1002/jmri.24743
56. Sigmund EE, Novikov DS, Sui D, Ukpebor O, Baete S, Babb JS, et al. Time-dependent diffusion in skeletal muscle with the random permeable barrier model (RPBM): application to normal controls and chronic exertional compartment syndrome patients. *NMR Biomed*. (2014) **27**:519–28. doi: 10.1002/nbm.3087
57. Liang S, Panagiotaki E, Bongers A, Shi P, Sved P, Watson G, et al. Information-based ranking of 10 compartment models of diffusion-weighted signal attenuation in fixed prostate tissue. *NMR Biomed*. (2016) **29**:660–71. doi: 10.1002/nbm.3510
58. Sen PN. Erratum: Time-dependent diffusion coefficient as a probe of permeability of the pore wall (Journal of Chemical Physics (2003) 119 (9871)). *J. Chem. Phys*. (2004b) **119**:9871–76. doi: 10.1063/1.1756575
59. Benga G, Pop VI, Popescu O, Borza V. On measuring the diffusional water permeability of human red blood cells and ghosts by nuclear magnetic resonance. *J Biochem Biophys Methods* (1990) **21**:87–102. doi: 10.1016/0165-022X(90)90057-J
60. Benga G, Borza T. Diffusional water permeability of mammalian red blood cells. *Comp Biochem Physiol- B Biochem*. (1995) **112**:653–9. doi: 10.1016/0305-0491(95)00116-6
61. Tanner JE. Transient diffusion in a system partitioned by permeable barriers. Application to NMR measurements with a pulsed field gradient. *J Chem Phys*. (1978) **69**:1748–54. doi: 10.1063/1.436751
62. Suh K-J, Hong Y-S, Skirda VD, Volkov VI, Lee C-YJ, Lee C-H. Water self-diffusion behavior in yeast cells studied by pulsed field gradient NMR. *Biophys Chem*. (2003) **104**:121–30. doi: 10.1016/S0301-4622(02)00361-7
63. Li H, Jiang X, Xie J, McIntyre JO, Gore JC, Xu J. Time-dependent influence of cell membrane permeability on MR diffusion measurements. *Magn. Reson. Med*. (2015b) **75**:1927–34. doi: 10.1002/mrm.25724
64. Li H, Jiang X, Xie J, Gore JC, Xu J. Impact of transcytolemmal water exchange on estimates of tissue microstructural properties derived from diffusion MRI. *Magn. Reson. Med*. (2016) **77**:2239–49. doi: 10.1002/mrm.26309
65. Meier C, Dreher W, Leibfritz D. Diffusion in compartmental systems. II. Diffusion-weighted measurements of rat brain tissue *in vivo* and postmortem at very large b-values. *Magn. Reson. Med*. (2003) **50**:510–4. doi: 10.1002/mrm.10558
66. Pfeuffer J, Bröer S, Bröer A, Lechte M, Flögel U, Leibfritz D. Expression of aquaporins in Xenopus laevis oocytes and glial cells as detected by diffusion-weighted 1H NMR spectroscopy and photometric swelling assay. *Biochim Biophys Acta Mol Cell Res*. (1998) **1448**:27–36. doi: 10.1016/S0167-4889(98)00111-6
67. Quirk JD, Bretthorst GL, Duong TQ, Snyder AZ, Springer CS, Ackerman JJH, et al. Equilibrium water exchange between the intra- and extracellular spaces of mammalian brain. *Magn Reson Med*. (2003) **50**:493–9. doi: 10.1002/mrm.10565
68. Fieremans E, Lemberskiy G, Veraart J, Sigmund EE, Gyftopoulos S, Novikov DS. *In vivo* measurement of membrane permeability and myofiber size in human muscle using time-dependent diffusion tensor imaging and the random permeable barrier model. *NMR Biomed*. (2017) **30**:e3612. doi: 10.1002/nbm.3612
69. Lasic S, Nilsson M, Lätt J, Stahlberg F, Topgaard D. Apparent exchange rate mapping with diffusion MRI. *Magn Reson Med*. (2011) **66**:356–65. doi: 10.1002/mrm.22782
70. Nilsson M, Lätt J, Van Westen D, Brockstedt S, Lasič S, Ståhlberg F, et al. Noninvasive mapping of water diffusional exchange in the human brain using filter-exchange imaging. *Magn Reson Med*. (2013) **69**:1573–81. doi: 10.1002/mrm.24395
71. Lampinen B, Szczepankiewicz F, van Westen D, Englund E, Sundgren PC, Latt J, et al. Optimal experimental design for filter exchange imaging: apparent exchange rate measurements in the healthy brain and in intracranial tumors. *Magn. Reson. Med*. (2017) **77**:1104–14. doi: 10.1002/mrm.26641
72. Lasič S, Oredsson S, Partridge SC, Saal LH, Topgaard D, Nilsson M, et al. Apparent exchange rate for breast cancer characterization. *NMR Biomed*. (2016) **29**:631–9. doi: 10.1002/nbm.3504
73. Le Bihan D, Breton E, Lallemand D, Grenier P, Cabanis E, Laval_Jeantet M. MR imaging of intravoxel incoherent motions: application to diffusion and perfusion in neurologic disorders. *Radiology* (1986) **161**:401–7. doi: 10.1148/radiology.161.2.3763909
74. Nilsson M, Lasič S, Drobnjak I, Topgaard D, Westin C-F. Resolution limit of cylinder diameter estimation by diffusion MRI: the impact of gradient waveform and orientation dispersion. *NMR Biomed*. (2017) **30**:e3711. doi: 10.1002/nbm.3711
75. Colvin DC, Loveless ME, Does MD, Yue Z, Yankeelov TE, Gore JC. Earlier detection of tumor treatment response using magnetic resonance diffusion imaging with oscillating gradients. *Magn. Reson. Imaging* (2011) **29**:315–23. doi: 10.1016/j.mri.2010.10.003
76. Colvin DC, Yankeelov TE, Does MD, Yue Z, Quarles C, Gore JC. New insights into tumor microstructure using temporal diffusion

spectroscopy. *Cancer Res.* (2008) **68**:5941–7. doi: 10.1158/0008-5472.CAN-08-0832

77. Bourne R, Panagiotaki E. Limitations and prospects for diffusion-weighted MRI of the prostate. *Diagnostics* (2016) **6**:21. doi: 10.3390/diagnostics6020021
78. Lemberskiy G, Rosenkrantz AB, Veraart J, Taneja SS, Novikov DS, Fieremans E. Time-dependent diffusion in prostate cancer. *Invest. Radiol.* (2017) **52**:405–11. doi: 10.1097/RLI.0000000000000356
79. Novikov DS, Jespersen SN, Kiselev VG, Fieremans E. Quantifying brain microstructure with diffusion MRI: theory and parameter estimation. *arxiv.org* (2016) 1–38.

Conflict of Interest Statement: The author declares that the research was conducted in the absence of any commercial or financial relationships that could be construed as a potential conflict of interest.

frontiers in Neuroscience

ORIGINAL RESEARCH
published: 19 December 2017
doi: 10.3389/fnins.2017.00706

Optimizing Filter-Probe Diffusion Weighting in the Rat Spinal Cord for Human Translation

Matthew D. Budde[1], Nathan P. Skinner[1,2], L. Tugan Muftuler[1], Brian D. Schmit[3] and Shekar N. Kurpad[1]*

[1] Department of Neurosurgery, Medical College of Wisconsin, Milwaukee, WI, United States, [2] Medical Scientist Training Program, Medical College of Wisconsin, Milwaukee, WI, United States, [3] Department of Biomedical Engineering, Marquette University and the Medical College of Wisconsin, Milwaukee, WI, United States

Diffusion tensor imaging (DTI) is a promising biomarker of spinal cord injury (SCI). In the acute aftermath, DTI in SCI animal models consistently demonstrates high sensitivity and prognostic performance, yet translation of DTI to acute human SCI has been limited. In addition to technical challenges, interpretation of the resulting metrics is ambiguous, with contributions in the acute setting from both axonal injury and edema. Novel diffusion MRI acquisition strategies such as double diffusion encoding (DDE) have recently enabled detection of features not available with DTI or similar methods. In this work, we perform a systematic optimization of DDE using simulations and an *in vivo* rat model of SCI and subsequently implement the protocol to the healthy human spinal cord. First, two complementary DDE approaches were evaluated using an orientationally invariant or a filter-probe diffusion encoding approach. While the two methods were similar in their ability to detect acute SCI, the filter-probe DDE approach had greater predictive power for functional outcomes. Next, the filter-probe DDE was compared to an analogous single diffusion encoding (SDE) approach, with the results indicating that in the spinal cord, SDE provides similar contrast with improved signal to noise. In the SCI rat model, the filter-probe SDE scheme was coupled with a reduced field of view (rFOV) excitation, and the results demonstrate high quality maps of the spinal cord without contamination from edema and cerebrospinal fluid, thereby providing high sensitivity to injury severity. The optimized protocol was demonstrated in the healthy human spinal cord using the commercially-available diffusion MRI sequence with modifications only to the diffusion encoding directions. Maps of axial diffusivity devoid of CSF partial volume effects were obtained in a clinically feasible imaging time with a straightforward analysis and variability comparable to axial diffusivity derived from DTI. Overall, the results and optimizations describe a protocol that mitigates several difficulties with DTI of the spinal cord. Detection of acute axonal damage in the injured or diseased spinal cord will benefit the optimized filter-probe diffusion MRI protocol outlined here.

Keywords: diffusion tensor imaging, double diffusion encoding, spinal cord injury, magnetic resonance imaging

OPEN ACCESS

Edited by:
Sune Nørhøj Jespersen, Aarhus University, Denmark

Reviewed by:
Noam Shemesh, Champalimaud Foundation, Portugal
Henrik Lundell, Danish Research Centre for Magnetic Resonance (DRCMR), Denmark

****Correspondence:***
Matthew D. Budde
mdbudde@mcw.edu

Specialty section:
This article was submitted to Brain Imaging Methods, a section of the journal Frontiers in Neuroscience

Received: *17 July 2017*
Accepted: *01 December 2017*
Published: *19 December 2017*

Citation:
Budde MD, Skinner NP, Muftuler LT, Schmit BD and Kurpad SN (2017) Optimizing Filter-Probe Diffusion Weighting in the Rat Spinal Cord for Human Translation. Front. Neurosci. 11:706. doi: 10.3389/fnins.2017.00706

INTRODUCTION

A noninvasive biomarker of spinal cord injury (SCI) severity is a highly-sought goal that could aid clinical decision-making and facilitate clinical trial enrollment and outcomes. Diffusion weighted imaging (DWI) is a magnetic resonance imaging (MRI) technique uniquely sensitive to microscopic injury and has shown promise as a biomarker of SCI. However, although preclinical studies have consistently shown diffusion tensor imaging (DTI) captures microscopic injury not evident through other MRI contrasts (Krzyzak et al., 2005; Deo et al., 2006; Gaviria et al., 2006; Loy et al., 2007; Herrera et al., 2008; Shemesh and Cohen, 2008; Kim et al., 2010; Sundberg et al., 2010; Tu et al., 2010; Mondragon-Lozano et al., 2013; Kelley et al., 2014; Wang et al., 2014; Li et al., 2015; Patel et al., 2016; Skinner et al., 2016), the adoption of DTI to human SCI, and acute SCI in particular, has been limited to only a small number of studies (Cheran et al., 2011; Endo et al., 2011; Vedantam et al., 2015; Shanmuganathan et al., 2017). The lack of translation can be attributed to many factors, but technical challenges of imaging the spinal cord along with difficulties in interpretation are prominent hurdles to clinical feasibility and utility for DWI as well as other advanced MRI techniques (Stroman et al., 2014; Wheeler-Kingshott et al., 2014; Martin et al., 2016). Double diffusion encoding has recently been shown to be a rapid and accurate method of assessing the severity of injury in a rat model (Skinner et al., 2016). The goal of this study was to optimize the filter-probe double diffusion encoding for human translation.

Animal studies of experimental SCI convincingly demonstrate microscopic disruption to white matter tracts as detected with DTI both at the lesion site and in regions remote from the site of injury (Krzyzak et al., 2005; Ellingson et al., 2008, 2010; Sundberg et al., 2010; Jirjis et al., 2013). This is often observed as a decrease in the DTI parameter of fractional anisotropy (FA) that is attributed to white matter tract injury, although FA has poor specificity since it reflects a complex combination of multiple pathologies. A reduction in diffusion measured parallel to the fibers, or axial diffusivity (AD), has been shown to be more closely associated with axonal injury. In the acute aftermath of SCI, decreased AD is argued to be caused by the formation of axonal varicosities, or beading, that are observed in experimental SCI (Williams et al., 2014). In a recent human SCI study at 24 h post-injury, AD had a strong relationship with outcome 1 year later (Shanmuganathan et al., 2017). However, the sensitivity of AD to injury can change as the injury-to-imaging interval increases and edema evolves in the initial days to weeks after injury (Leypold et al., 2008). Thus, despite promising results as a biomarker, its use remains limited.

Improvements in the ability of DWI to capture microstructure have been introduced through advanced diffusion encoding techniques, including double diffusion encoding (DDE). DDE, as the term implies, uses two separate diffusion gradient pairs to provide contrast (Cory et al., 1990; Mitra, 1995) unattainable with the traditional Stejskal-Tanner single diffusion encoding (SDE). For a review of the history of DDE with derived measures and accepted nomenclature, see (Shemesh et al., 2016). Most related to neurological injury is the ability of DDE to estimate compartment shape anisotropy or eccentricity. In a previous simulation study (Skinner et al., 2015), microscopic anisotropy estimated from DDE was highly sensitive to axonal injury. Importantly, one DDE variant, referred to as 5-design DDE (Jespersen et al., 2013), has the benefit of being insensitive to the underlying fiber distribution and is termed orientational invariance, which is a particular confound in DTI. Thus, DDE measures of microscopic anisotropy may have a benefit in detecting acute injury to the brain and spinal cord. While DDE has been reported for materials, cells, and tissues, its application to neurological injury has been limited (Shemesh et al., 2014) although applications in aging (Lawrenz et al., 2016) have demonstrated its utility and advantages over more conventional DTI.

Another DDE variant, referred to filter-probe DDE (FP-DDE), was similarly sensitive to axonal beading (Skinner et al., 2015) in a simulation study. It was developed specifically for tissues in which the fiber organization is known a priori and largely coherent, which makes it suitable for the spinal cord but could also be a confound with improper alignment or complex fiber arrangements. In this approach, an initial diffusion "filter" perpendicular to the cord suppresses mobile spins, and a second diffusion "probe" parallel to the cord measures the diffusivity of the unsuppressed spins. It demonstrates a high sensitivity to acute SCI in a rat model and outperforms DTI in stratifying the degree of injury (Skinner et al., 2016). When coupled with a single-voxel diffusion spectroscopy localization, FP-DDE has substantially less post-processing demands than DTI, which is believed to improve its translation to clinical settings. However, FP-DDE is constrained by the requirement that the diffusion encoding directions are aligned with the spinal cord axonal fibers, and curvature of the spinal cord or user error may limit its applicability.

While our previous spectroscopic FP-DDE approach has methodological benefits over an imaging readout, the lack of spatial information limits the visualization of regional injuries that may have important benefits for outcomes along different functional domains such as motor or sensory systems (Martin et al., 2016). Another obvious challenge is that DDE pulse sequences are not readily available on most MRI systems. The inclusion of two separate diffusion encoding gradient pairs increases echo time, resulting in lower signal to noise compared to a SDE. Thus, DDE has other practical considerations that could potentially limit its adoption.

To improve the feasibility and translational potential of DDE for clinical settings, this study systematically compared several different experimental conditions with the goal of developing a protocol capable of clinically-feasible human translation. First, simulations tested the relationship of derived DWI measures with the underlying model of injury with an emphasis on reliability and effects of signal to noise ratio (SNR). Next, the *in vivo* application of alternative DDE methods was examined in a rat model of SCI to identify if orientation-invariant metrics performed as well as metrics aligned with the cord axis. Further, it was assessed whether the contrast obtained from the DDE approach could be captured with a SDE in the spinal cord. Finally, the set of optimized parameters was applied to the healthy human

cervical spinal cord to assess reliability of the obtained measures. Collectively, the results define a set of experimental parameters and considerations to provide robust measurements of spinal cord integrity in future studies of patients with spinal cord disease and injury.

METHODS

Simulations

Monte-Carlo simulations were performed to examine the response of diffusion metrics to models of microscopic injury and effects of signal to noise (SNR) using camino diffusion toolkit (Hall and Alexander, 2009) and models of healthy and injured axons as straight and beaded cylinders, respectively, as previously described (Budde and Frank, 2010; Skinner et al., 2015). A range of injured axon fractions and intracellular volume fractions were simulated, and the pulse sequences were those described in **Figure 1**, **Table 1**. The simulations each used 50,000 individual spins, 2,000 time-steps, and an intrinsic diffusivity of 1.8 um^2/ms consistent with the measured longitudinal diffusivity of healthy spinal cord white matter (Budde et al., 2007). To examine the effects of SNR, additional Gaussian noise was added to the phase-sensitive simulated signals to achieve a nominal SNR for the $b = 0$ signal, noting this results in a characteristic Rician noise profile when converted to magnitude signal. The gradient directions are specified in **Table 1** and are consistent with the previously reported conditions for the 5-design DDE (Jespersen et al., 2013). The filter-probe DDE was simulated with the gradients consecutive in time as originally proposed (Skinner et al., 2015) in which a diffusion "filter" is applied perpendicular to the known fiber axis and the diffusion "probe" samples the diffusion along the axis in a series of varying gradient amplitudes. The effects of combining the two gradients into a SDE overlapped in time was evaluated (**Figure 1** bottom) with other conditions identical.

The parameters investigated were limited to those that showed nearly perfect specificity for axonal injury in the presence of varying volume fractions in a previous simulation study (Skinner et al., 2015). A measure of microscopic anisotropy, eccentricity (ε), was derived from the 5-design DDE having the feature of orientation invariance defined by

$$\varepsilon = \frac{ln\left(S_{Parallel}\right) - ln\left(S_{Orthogonal}\right)}{q^4} \quad (1)$$

where $S_{Parallel}$ and $S_{Orthogonal}$ are the mean signal from the parallel and orthogonal diffusion encoding directions, respectively, and q is the diffusion wave vector given by $q = \frac{1}{2\pi}\gamma G\delta$ with $\boldsymbol{G}$ and δ the amplitude and duration of the diffusion encoding gradient, respectively. Notably, ε has a strong dependence on the diffusion encoding gradients and may be converted to the parameter microscopic fractional anisotropy to reduce its dependence on experimental conditions (Jespersen et al., 2013). However, the normalization factor includes mean diffusivity (MD) which introduces a minor dependence on intracellular volume fraction (Skinner et al., 2015). For the purposes of this study, ε was obtained under identical experimental conditions and was therefore sufficient to relate to the other derived metrics under the same conditions.

In the filter-probe diffusion encoding scheme (Skinner et al., 2016) a measure of apparent diffusion coefficient along the spinal cord axis ($ADC_{||}$) was obtained in the presence of a perpendicular diffusion filter under the assumption of coherent and uniformly aligned fibers by

$$S_i = S_0 \cdot exp(-b \cdot D) \quad (2)$$

where S_0 is the signal measured with without diffusion weighting. Notably, in this specific condition it reflects the signal in the presence of the diffusion "filter" but no parallel diffusion weighting. S_i reflects the measured signal at each of the b-values measured parallel to the fiber axis with $b{=}q^2(\Delta - \frac{\delta}{3})$. Likewise, a biexponential model under the same conditions and measurements is given by

$$S_i = S_0 \cdot f_R \cdot exp(-b \cdot D_R) + S_0(1 - f_R) \cdot exp(-b \cdot D_{fast}) \quad (3)$$

where D_R and D_{fast} reflect the diffusivities of the restricted and fast compartments, respectively, and f_R reflects the fraction of the restricted signal. All analyses were performed in Matlab using least-squares regression for Equation 2 and the non-linear curve fitting toolbox for Equation 3. The effect of SNR on the estimated parameters (**Figure 2**) was quantified as the relative error (%) measured as the difference between the estimated and true values (infinite SNR) normalized by the maximum across all simulated axonal and volume fractions.

Animals

All animal procedures were approved by the Institutional Animal Care and Use Committees (IACUC) at the Medical College of Wisconsin, the Clement J Zablocki VA Medical Center and Northwestern University. A total of 38 female Sprague–Dawley rats (200–250 g) were used. Contusion SCI was performed in rats at the T10 vertebral level of the spinal cord with varying levels of injury severity or sham injury as previously described (Skinner et al., 2016). Briefly, animals were anesthetized and a dorsal laminectomy was performed followed by a weight-drop to deliver a mild, moderate, or severe injury. Sham animals were identical including laminectomy but the weight was not dropped. Naïve animals were used for protocol developments and testing where indicated. Rats underwent locomotor functional assessments using the BBB scale (Basso et al., 1995) at 1 and 30 days post-injury and were scored by a blinded reviewer.

Rat Magnetic Resonance Imaging

In vivo MRI was collected 48 h following the injury procedure using a Bruker 9.4T Biospec System with Paravision (6.0.1). A quadrature volume coil was used for transmission and 4-channel surface coil array for reception centered over the lesion epicenter at the T10 thoracic vertebrae. Animal respiration and temperature were monitored for the duration of the imaging.

The DDE pulse sequence consisted of two separate Stejskal-Tanner diffusion encoding gradients (**Figure 1**), each with independent direction and amplitude (**Table 1**), while the diffusion separation and durations were identical (**Table 2**). To

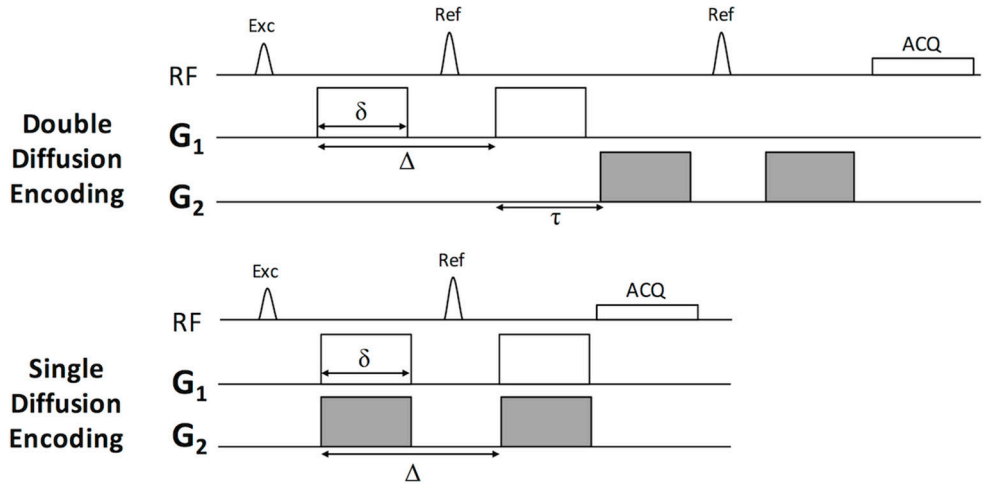

FIGURE 1 | Pulse sequence for Double and Single Diffusion Encoding Techniques. The double diffusion encoding (DDE) sequence consists of two pairs of Stejskal-Tanner diffusion weighting gradients (G_1 and G_2) independent in their orientations, timing, and amplitude. The single diffusion encoding (SDE) consists of a single gradient pair. In this work, G_1 and G_2 were either parallel or perpendicular to one another and modulated relative to the laboratory frame of reference according to **Table 1**.

TABLE 1 | Double diffusion encoding schemes and parameters.

	Orientationally Invariant[a]	**Filter-Probe[b]**
G_1 directions	Orthogonal: 60 (12 unique) Parallel: 12	Perpendicular to Cord: 2 (+ & −)
G_1 b-values (s/mm^2)	2,000	2,000
G_2 directions	Orthogonal to G_1: 60 Parallel to G_1: 12	Parallel to Cord: 2 (+ & −)
G_2 b-values (s/mm^2)	2,000	9 increments: 0–2,000
Non-DWI (b = 0)	0	0
Total Acquisitions	72	36

[a] *Jespersen et al. (2013).*
[b] *Skinner et al. (2016).*

examine the effects of different DDE approaches, a single voxel Point RESolved Spectroscopy (PRESS) acquisition (Bottomley, 1987) was used as previously described (Skinner et al., 2016), with the voxel ($10 \times 10 \times 6$ mm^3) placed at the lesion epicenter and aligned with the spinal cord main axis (**Figure 3**). The acquisition was cardiac- and respiratory-gated, and other relevant acquisition parameters included sweep width = 4,960 Hz, and number of points = 256. As shown in **Table 1**, the diffusion parameters for the DDE sequence comparison used identical parameters to the extent possible, including a maximum b-value for each diffusion encoding pair of 2000 s/mm^2.

In the naïve spinal cord at T10, the DDE sequence was compared to the SDE using identical diffusion gradients. The SDE enabled a reduction in TE from 61 to 35 ms using a 4-shot echo planar imaging (EPI) readout. Both positive and negative diffusion gradient encoding directions on each axis were acquired to mitigate any directional or cross-term dependence (Neeman et al., 1991).

A reduced field of view (rFOV) excitation scheme (Saritas et al., 2008) was implemented using a 2D excitation (2DRF) echo planar gradient trajectory. The excitation consisted of 16 Gaussian sub-pulses (time-bandwidth product of 2.74) each with 0.2 ms duration and amplitudes modulated by a Gaussian window. The total pulse duration was 6.85 ms. The sequence was evaluated in naïve animals using the DWI-EPI sequence (13.5×9.6 mm^2, 90×64 matrix), and compared to rFOV of the same resolution (13.5×13.5 mm^2, 90×90 matrix) using outer volume suppression with four 10 mm saturation bands surrounding the acquisition FOV and a separate spectral-selective fat suppression pulse. The 2DRF rFOV did not include any spatial or fat suppression. DWI consisted of 12 directions, b-value of 800 s/mm^2, with TEs of 24 and 29 ms for the OVS and rFOV, respectively, and identical acquisition times of 3:28 min. Both schemes had 150 μm^2 in-plane resolution and 2 mm slice thickness. The 2DRF excitation rFOV imaging was combined with the FP-SDE diffusion encoding scheme and applied to the rat SCI at 48 h and 30 days post-injury and performed at the T10 lesion epicenter.

Human Magnetic Resonance Imaging

All procedures were approved by the Institutional Review Board (IRB) at the Medical College of Wisconsin, and written consent was obtained from all subjects. Three subjects (age range: 28–38 years; 2 male) underwent cervical spine imaging on a 3T General Electric Discovery system using a 12 channel head, neck, and spine receive array. The DWI-EPI vendor-supplied sequence was a single-shot EPI with a 2DRF excitation rFOV. The diffusion gradient directions were modified to include the SDE filter-probe values as shown in **Table 1** along with a conventional DTI acquisition with 2 *b*-values of 1,000 and 2,000 s/mm^2 along 15 directions. Other sequence parameters are listed in **Table 2**.

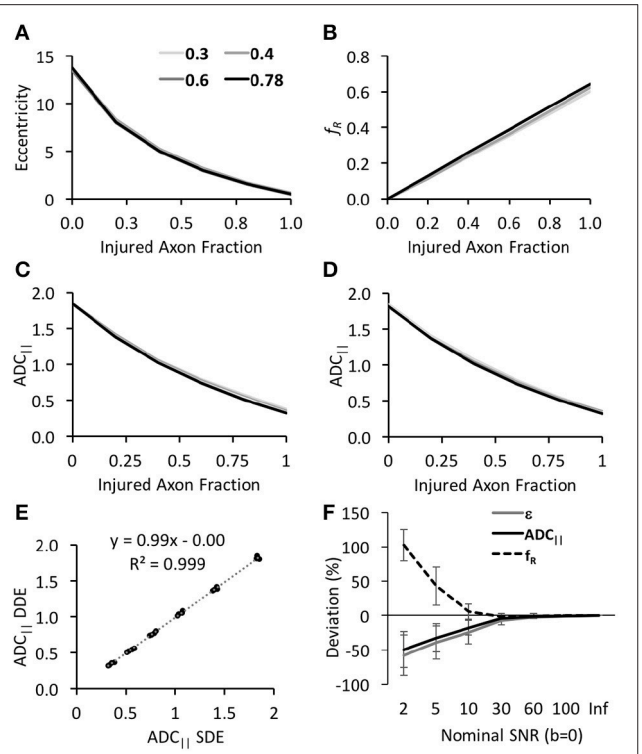

FIGURE 2 | Simulation of DWI schemes and derived parameters. All estimated DWI parameters, including eccentricity **(A)**, restricted fraction **(B)**, and $ADC_{||}$ from the DDE **(C)** or SDE **(D)**, exhibited high sensitivity to the injured axon fraction (x-axis) with minimal differences between different intra-axonal volume fractions (shown as individual lines). Notably, $ADC_{||}$ was nearly identical between the DDE and SDE **(E)** for uniformly-oriented fibers. The estimated parameters showed differential reliability under low SNR with $ADC_{||}$ being most robust to noise **(F)**.

Data Analysis

In both naïve and injured animals, maps of parallel diffusivity ($ADC_{||}$) along the spinal cord were calculated according to equation 2 and 3. Notably, S_0 reflects the absence of diffusion weighted parallel to the cord but in the presence of the perpendicular diffusion filter. Parameter maps were evaluated using whole-cord region of interest (ROI) analysis. DTI fitting was performed for comparison parameter map quality in full-FOV and rFOV DWI using FSL (Jenkinson et al., 2012). Quantification of $ADC_{||}$ in injured animals used whole-cord averages from a single slice at the T10 injury epicenter. The magnitude spectroscopic signals were integrated between ±2 ppm of the water peak. For the filter-probe DDE, the signals were fit to a monoexponential model. Spinal cord images were analyzed with regions of interest (ROI) using an approach to avoid bias in manual segmentation. $DWI_{\perp}$ images were converted to SNR maps by dividing the images by the standard deviation measured from a region of pure noise. A second ROI surrounding the whole cord was placed in the slice at the lesion epicenter, and only voxels with SNR values above 12 were included in the final mask, which was subsequently transferred to the $ADC_{||}$ map. The whole-cord mean voxel $ADC_{||}$ values were obtained.

The correlations between the resulting metrics and the compression distance (mm) at the moment of injury were assessed using a Pearson's product moment correlation. Likewise, correlations between the diffusion metrics and locomotor function (BBB score) at 30 days post-injury were evaluated with a Pearson correlation. A direct comparison of correlation coefficients between the two different diffusion methods and their relationship with outcome was carried out using the method described in Steiger (1980).

RESULTS

Simulations of DWI Scheme and SNR Dependence

As expected, the three parameters derived from the simulations, $ADC_{||}$, f_R, and ε were highly specific to axonal beading even with variations in the intracellular volume fraction (**Figure 2**). Increasing beading fraction was associated with decreased ε and $ADC_{||}$ and increased f_R. While f_R exhibited the most linear relationship with beading fraction (**Figure 2B**), its slope of 0.64 indicated it did not directly correspond to the true injured fraction. In the filter-probe scheme, $ADC_{||}$ obtained from the DDE or the SDE were identical to one another ($R^2 = 0.999$; **Figures 2C,D**), demonstrating the SDE scheme with orthogonal gradients aligned with the fiber axis is equally effective as the DDE under the same conditions. The parameters differed considerably in their accuracy under varying SNR conditions. The nominal SNR values of 10, 30, 60, and 100 for the non-diffusion weighted signals ($b = 0$ s/mm^2) equated to mean SNR values of 2.6, 7.8, 15.6, and 30.0, respectively, for the diffusion weighted signals across all directions at the highest b-values ($b = 4{,}000$ s/mm^2). Across all beading and volume fractions and the lowest SNR condition, $ADC_{||}$ exhibited a decrease of 27.3% compared the highest SNR condition whereas eccentricity decreased by 117% and f_R increased by 256%. Furthermore, $ADC_{||}$ was within 10% of its true value at a DW SNR of 11.1%, eccentricity and f_R were within 10% of their true values at SNR values of 34 and 36, respectively, further demonstrating these parameters require greater SNR for accuracy than $ADC_{||}$. It should be noted that these are relative differences and not absolute cutoffs since other factors affect the results under experimental conditions.

In Vivo Effects of DWI Scheme in SCI

The DDE-PRESS was applied to a rat model of spinal cord contusion injury (**Figure 3**) using parameters similar to those of the simulations (**Table 2** condition 1 and 2). The mean SNR across diffusion-weighted spectra at $b = 4{,}000$ s/mm^2 were 73.8 (±47.8) and 70.4 (±28.8) for the 5-design DDE and the filter-probe DDE, respectively. Across all animals with varying injury severities ($n = 17$), the average water peak linewidth (FWHM) was 36.8 (±9.3) Hz, and the average coefficient of variation across repeats was 9.8 (±8.3)%.

In a direct comparison in the same animals, $ADC_{||}$ and ε were significantly related (**Figure 4A**) to one another ($t = 2.58$, $p = 0.021$, $R^2 = 0.31$), as were f_R and ε ($t = -3.63$, $p =$

TABLE 2 | Diffusion weighted experimental parameters.

Condition	1	2	3	4	5
Application	Rat/Simulation	Rat/Simulation	Rat	Rat	Human
Readout	PRESS	PRESS	EPI	EPI	EPI
EPI Segments	–	–	4	4	1
rFOV	–	–	–	2DRF	2DRF
TR (ms)	3,000	3,000	1,500	1,500	2,000
TE (ms)	41	41	61	35	86
FOV (mm^2)	10	10	25.6×25.6	13.5×9.6	200
Voxel/Slice thickness (mm)	6	6	1.5	1.5	5
In-plane resolution	–	–	$266\times400\mu m^2$	$150\mu m^2$	1.43 mm^2
DWI Scheme[a]	5-design DDE	DDE Filter-Probe	DDE Filter-Probe	SDE Filter-Probe	SDE Filter-Probe
DWI Acquisitions	72	36	36	36	36
Max total *b*-value (s/mm^2)	4,000	4,000	4,000	3,000	3,000
Diffusion separation Δ (ms)	12	12	12	12	32.5
Diffusion duration (ms)	6	6	6	6	25.4
Mixing Time (τ; ms)	6	6	6	–	–
NEX	1	1	2	2	6
Acquisition Time	3:48	2:09	5:36	5:36	5:26
Outcome Measure(s)	Eccentricity (μm^4)	$ADC_{\|\|}$ (μm^2/ms) f_R (fraction)	$ADC_{\|\|}$ (μm^2/ms)	$ADC_{\|\|}$(μm^2/ms)	$ADC_{\|\|}$ (μm^2/ms)

[a]*From* ***Table 1***.

0.002, $R^2 = 0.47$) (**Figure 4B**). $ADC_{||}$ ($t = -2.01$, $p = 0.067$, $R^2 = 0.25$), f_R ($t = 2.39$, $p = 0.034$, $R^2 = 0.32$), and ε ($t = -1.95$, $p = 0.075$, $R^2 = 0.24$) had similar relationships with the compression (in mm) of the spinal cord at the moment of impact (**Figures 4 C,E,G**), although only f_R reached significance. $ADC_{||}$ was a significant predictive marker of locomotor outcome (**Figure 4F**) as measured by the relationship with BBB score at 30 days post-injury ($t = 3.39$, $p = 0.004$, $R^2 = 0.45$), and f_R was significant (**Figure 4H**) but had a lower relationship ($t = -2.81$, $p = 0.014$, $R^2 = 0.36$). ε ($t = 1.05$, $p = 0.31$, $R^2 = 0.07$) was not a significant predictor of locomotor outcome (**Figure 4D**). None of the measures of data quality were related to BBB score, including CoV ($t = 0.05$, $p = 0.96$) or FWHM ($t = -0.05$ $p = 0.96$). Moreover, neither CoV nor FWHM were significantly related to the outcome measures of $ADC_{||}$ (CoV: $t = -0.39$, $p = 0.70$; FWHM: $t = -0.06$, $p = 0.95$) or ε (CoV: $t = 0.18$, $p = 0.86$; FWHM $t = -1.21$ $p = 0.24$).

In Vivo Effects of Single vs. Double Diffusion Filter-Probe

As expected, diffusion weighted images from the SDE (**Figure 5A**) had a higher SNR than those with the DDE encoding due to the shorter TE for the SDE. The $ADC_{||}$ maps from both filter-probe diffusion encoding schemes were similar and were largely devoid of non-spinal cord signals, as anticipated. Across 3 naïve animals, the mean SNR of the whole cord was 1.6 times greater in the SDE than the DDE (**Figure 5B**), which is consistent with the predicted SNR increase of 1.68 based solely on the reduction in TE, using a T_2 of the spinal cord white matter of 50.2 ms. A significant increase in the white matter $ADC_{||}$ (**Figures 5C,D**) was evident in the SDE compared to the DDE in a paired *T*-test ($t = 6.04$; $p = 0.026$). The difference is likely explained by the differences in T_2 relaxation filtering. In either the SDE or DDE, no significant differences were evident from positive or negative sign combinations of diffusion gradient encoding directions.

Application of *rFOV FP-SDE* in SCI

The rFOV-DWI using 2DRF improved image quality by reducing artifacts compared to OVS (**Figure 6**). The rFOV images reflected the full FOV acquired without any cropping. Notably, OVS images contained fold-over artifacts of the lipid signal even though fat suppression and spatial saturation bands were utilized. The 2DRF images contained negligible lipid signal without separate fat suppression pulses consistent with their intrinsic suppression of lipids based on the chemical shift. The measured SNR of the rFOV-DWI (47.4) was increased by approximately 12% compared to the OVS-DWI (41.5) averaged across all diffusion weighted images from a whole-cord ROI in a single animal. The rFOV had a slight improvement in image distortion, although neither the artifacts nor distortion was quantified.

The full pulse sequence incorporating 2DRF excitation and FP-SDE diffusion encoding was applied to rats with varying injury severities (**Figure 7**). The perpendicular weighted images (DWI) revealed high signal in the white matter even in an animal with a severe injury. Qualitatively, the $ADC_{||}$ maps demonstrated a clear and pronounced effect of injury severity that was evident, with the severely-injured animal having an $ADC_{||}$ decrease in the central region of the cord and a higher $ADC_{||}$ rim along the periphery. It should be emphasized that the region along the periphery of the white matter would typically be obscured or confounded by the surrounding CSF. A decrease in $ADC_{||}$ within the ascending dorsal columns is also evident in the severe injury.

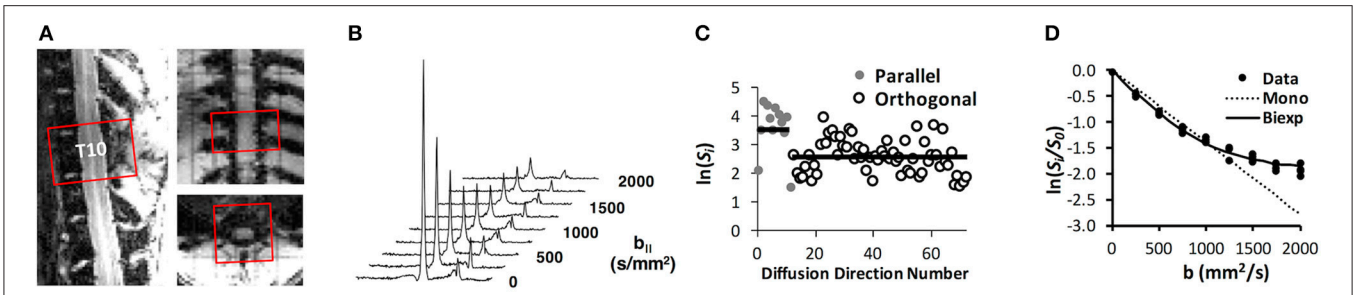

FIGURE 3 | DDE-PRESS Acquisition and Quantification. A voxel was positioned over the T10 vertebral segment **(A)** and aligned with the cord axis, shown here for a sham-injured animal. The integrated signal quantified as the area under the water peak **(B)** was obtained over the range ±2 ppm for subsequent analysis. For orientationally invariant DDE **(C)**, the mean signal from parallel and orthogonal directions were compared to derive eccentricity, whereas for the filter-probe DDE, the diffusivity and restricted fraction **(D)** were derived from a mono- and bi-exponential fit **(D)** to the signals.

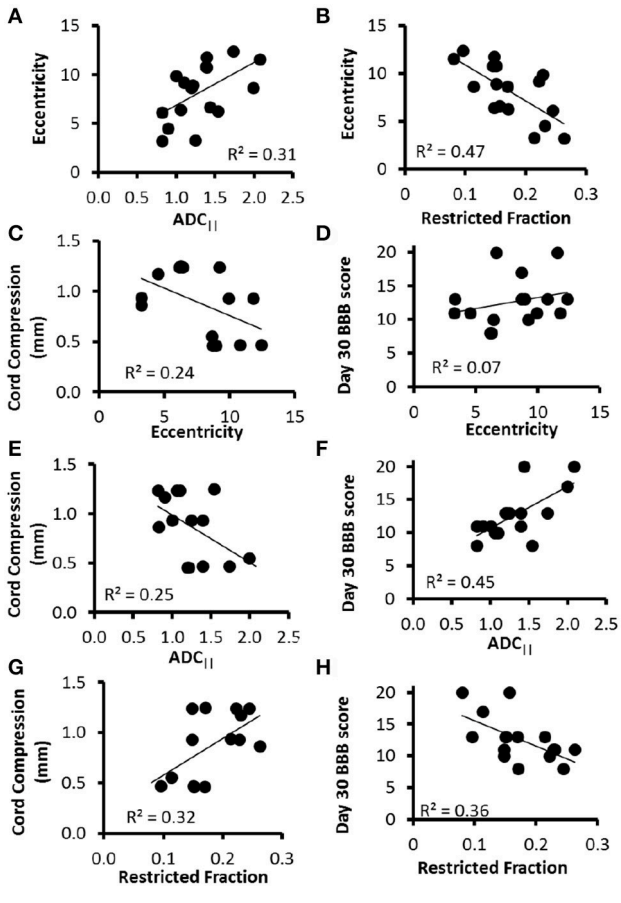

FIGURE 4 | DDE-PRESS Relationship to Severity and Outcomes. Across all animals with a range of injury severities, both $ADC_{||}$ and f_R measured at the injury site were moderately correlated with eccentricity **(A,B)**. The relationship with cord compression **(C,E,G)** were similar across all three parameters. The strength of the correlation with BBB score 30 days post-injury was lowest for eccentricity **(D)**, greatest for $ADC_{||}$ **(F)**, and in between for f_R **(H)**.

A region of interest analysis was performed to quantitatively assess the DWI measures across the full cohort of animals (**Figure 8**). Based on the simulation results, only voxels with a SNR above 12 on the DWI images were included by masking with a whole-cord ROI in conjunction with automatic thresholding. $ADC_{||}$ showed a significant effect of injury severity [$F_{(3, 18)} = 10.2$; $p = 0.001$] across all animals ($n = 16$) but was non-significant with the sham animals omitted [$F_{(2, 12)} = 0.76$; $p = 0.49$]. Single-voxel PRESS estimates of the same parameter were also obtained in the same animals, and all spectra had sufficient SNR to ensure robust estimates of both $ADC_{||}$ and f_R. (mean SNR = 69.7, range = 46.3–116.4). $ADC_{||}$ showed a strong effect of injury severity [$F_{(3, 14)} = 27.2$; $p < 0.0001$] although it was also non-significant with the sham animals excluded [$F_{(2, 12)} = 1.1$; $p = 0.37$]. f_R also had a significant effect of severity [$F_{(3, 12)} = 6.67$; $p < 0.005$], but was non-significant with the sham animals included [$F_{(3, 12)} = 2.38$; $p = 0.13$].

Human Application of *rFOV FP-SDE*

A commercially-available diffusion weighted EPI sequence with reduced field of view (rFOV) was applied to the human cervical spinal cord using the FP-SDE diffusion encoding scheme and compared to a conventional DTI acquisition at the same resolution (**Figure 9**). AD_{DTI} and $ADC_{||}$ were visually similar within the spinal cord, although as expected, $ADC_{||}$ more clearly delineated the spinal cord due to the suppression of non-cord signals, permitting visualization of the white matter boundary without partial volume contamination by CSF. The mean filter-probe SNR in the cord white matter was 10.8 (±2.3). Across three healthy subjects averaged in all 10 slices, $ADC_{||}$ in the spinal cord white matter ($1.66 \pm 0.18\,\mu m^2/ms$) was larger than AD_{DTI} ($1.32 \pm 0.15\,\mu m^2/ms$), with difference being significant in a paired t-test ($t = -5.92$; $p = 0.027$). In this limited sample, similar between-subject coefficients of variation were observed for $ADC_{||}$ (10.9%) and AD_{DTI} (11.2%).

DISCUSSION

Following from previous work (Skinner et al., 2015, 2016), the filter-probe diffusion encoding scheme demonstrates detection of microscopic injury in the spinal cord. These studies define experimental parameters to enable improved detection of injury and translation to human spinal cord. The filter-probe diffusion

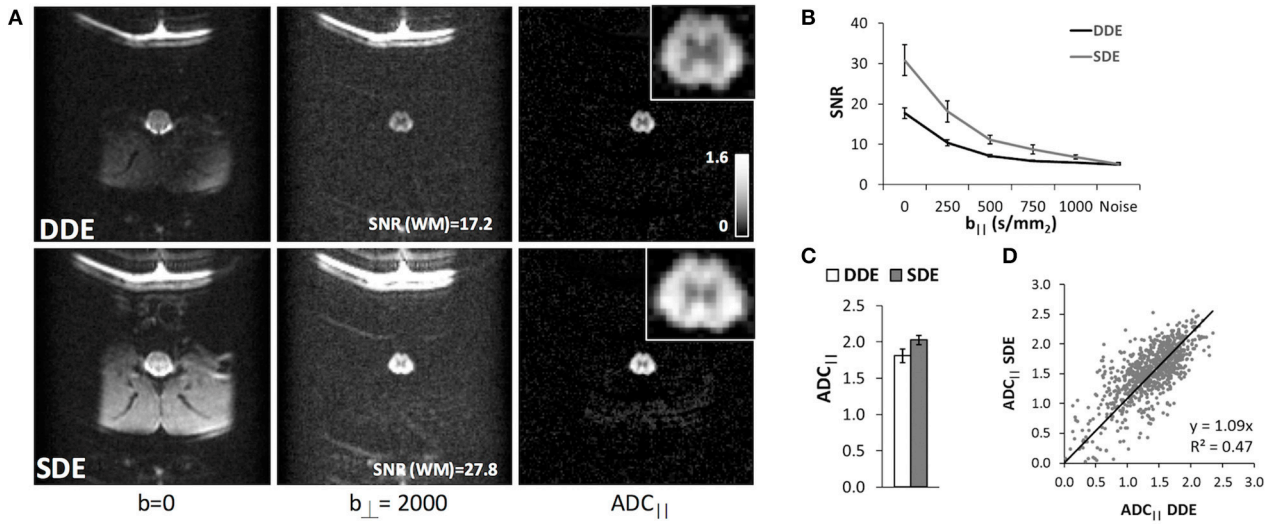

FIGURE 5 | Double and Single Filter-Probe Diffusion Encoding. Representative images **(A)** from the double (top) and single (bottom) diffusion encoding variants of the DWI sequence. As expected, the SDE had improved SNR compared to the DDE acquisition. $ADC_{||}$ maps depict primarily the spinal cord white matter along with fat. Across 3 naïve animals, the white matter signal **(B)** in the SDE remains above noise floor even at $b_{||} = 1{,}000$ s/mm^2, whereas the DDE signal was indistinguishable from the noise above $b_{||} = 500$ s/mm^2. The measured $ADC_{||}$ of the SDE and DDE were comparable **(C)**, with a slight elevation in the SDE that could be attributable to the greater SNR. In the white matter voxels across all animals **(D)**, $ADC_{||}$ values from the DDE and SDE were strongly correlated with a slope of 1.09.

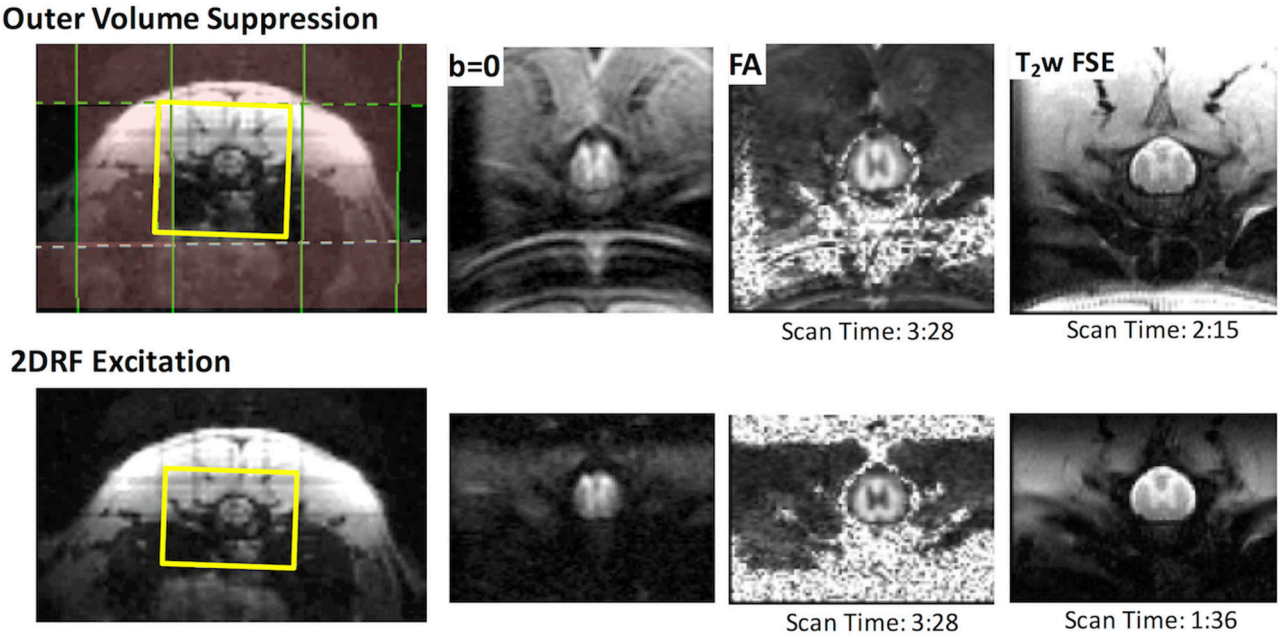

FIGURE 6 | Reduced Field of View DWI and T_2-weighted Imaging. rFOV using outer volume suppression (top) or 2DRF (bottom) provided high-quality images of the thoracic spine. Fold-over and chemical shift artifacts were evident in the OVS, which includes a separate fat-suppression module. The 2DRF with a slightly smaller FOV but an identical resolution offered similar SNR, minimal chemical shift artifacts (without separate fat suppression), and slight improvement in EPI distortion as shown by the $b = 0$ images and FA maps. In a T_2-weighted fast spin echo, the smaller FOV allowed a reduction in acquisition time with a comparable SNR.

encoding strategy is premised on the pathology of axonal injury manifesting as focal swellings or beading. Beading in traumatic SCI has been directly observed *in vivo* in a murine model (Williams et al., 2014), and axonal injury is consistently the pathological feature most related to functional outcome (Medana and Esiri, 2003). On the other hand, edema and cavitation are pathological features of acute and chronic spinal cord injury, respectively, yet they are not direct markers of axonal integrity.

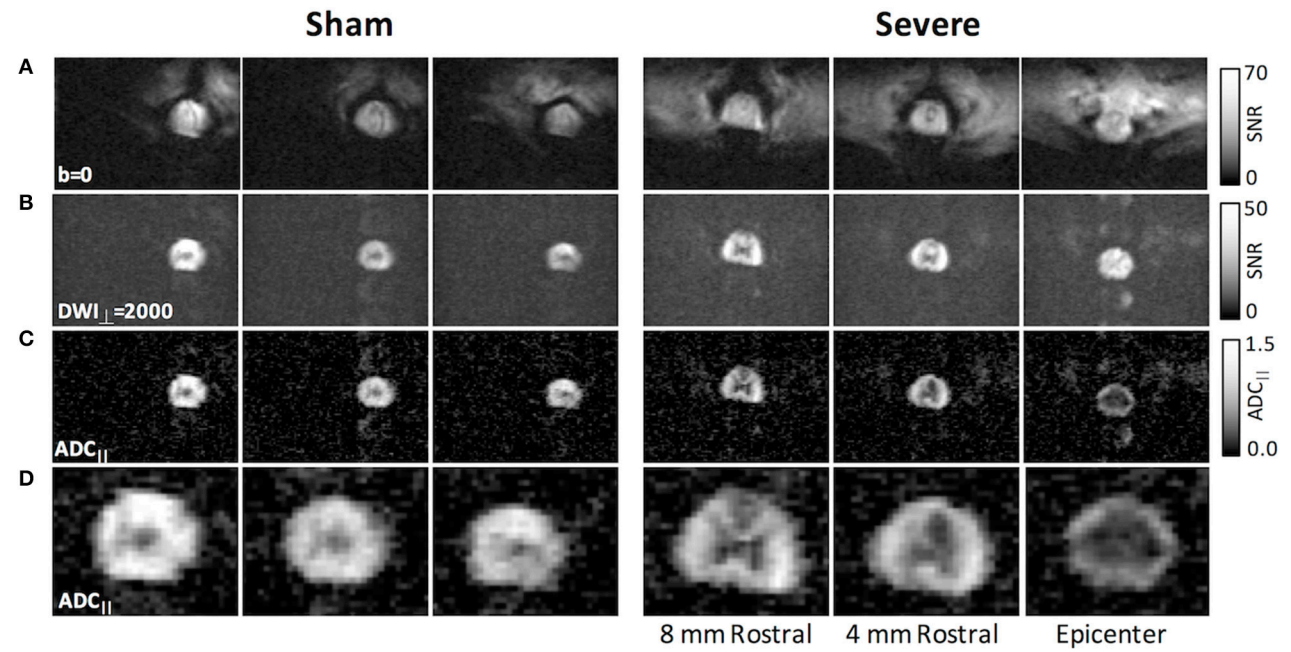

FIGURE 7 | rFOV DWI in SCI with filter-probe SDE. Compared to the non-diffusion weighted images **(A)**, the perpendicular diffusion-weighted images **(B)** were free from extraneous tissue signals, although some slight EPI ghosting was evident. The filtered $ADC_{||}$ maps **(C)** reflected primarily the intra-axonal diffusivity. In an acute severe SCI (right), the $ADC_{||}$ maps clearly demonstrated a reduction in the central region at the epicenter and in the dorsal columns rostral to the lesion. Magnification of filtered $ADC_{||}$ maps are shown in **(D)**.

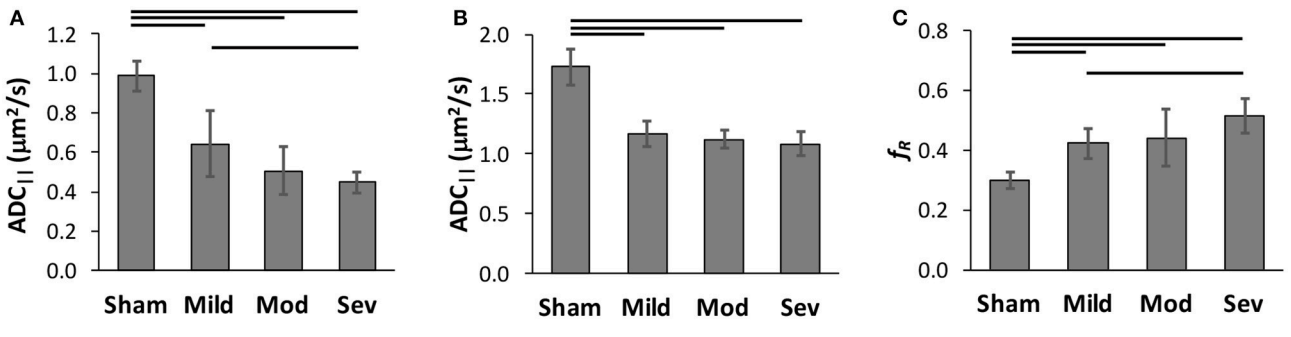

FIGURE 8 | Classification of Spinal Cord Injury Severity. Region of interest analysis of FP-SDE **(A)** was compared to DDE-PRESS **(B,C)** in the same animals across a range of injury severities. $ADC_{||}$ from imaging with a whold-cord region of interest analysis **(A)** showed an effect of injury severity. $ADC_{||}$ obtained from single voxel PRESS **(B)** was less sensitive to severity, while f_R from the same voxel **(C)** better distinguished injury severity. Lines indicate significant group differences at $p < 0.05$.

These features can confound or obscure the sensitivity of diffusion MRI to the underlying axonal injury. Edema, detected as T_2-weighted hyperintinsities, has a strong dependence on the injury-to-imaging time in SCI (Leypold et al., 2008) is not a good predictor of SCI severity (Dalkilic et al., 2017). The filter-probe design follows from prior work using diffusion weighting as a mechanism to suppress these unwanted MR signals in addition to its more common utility as a probe of diffusivity. Importantly, a high-strength diffusion gradient perpendicular to the spinal cord attenuates fast diffusing spins, which includes free CSF, the hindered extracellular water including edema. While other methods such as fluid attenuated inversion recovery diffusion imaging (DW-FLAIR) have been used to suppress CSF (Hirsch et al., 1999), it both increases scan time and does not suppress the effects of extracellular fluid and edema.

A primary limitation of the filter-probe DWI technique is the necessity that the diffusion filter gradients are aligned perpendicular to the spinal cord. Importantly, we chose to consistently employ a diffusion filter along the left-right axis, as the spinal cord has less curvature along this axis than along the anterior-posterior axis, and although spinal cord white matter fibers are primarily aligned with the cord axis, some fiber dispersion or crossing is present. Nonetheless, considering the extent of damage following a traumatic injury,

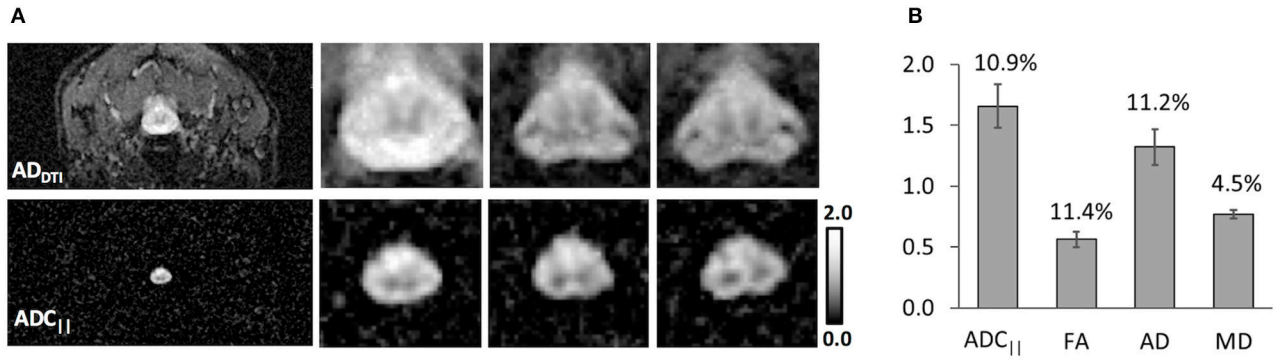

FIGURE 9 | Filter-Probe diffusion weighted imaging in Human Normal Cervical Spinal Cord. The filter-probe SDE scheme was implemented on a human 3T scanner by altering the diffusion gradient orientations of the commercially-available diffusion weighted imaging sequence. Compared with AD maps derived from DTI **(A)**, FP-SDE provided comparable $ADC_{||}$ maps but with almost complete attenuation of non-cord signals. Three of 10 slices are shown. Results from 3 healthy subjects **(B)** demonstrate similar coefficients of variation (indicated in text above bars) in the same subjects and regions of interest. $ADC_{||}$ was significantly greater than AD from DTI. Bars indicate standard deviations.

the injury is likely to be the dominant pathology affecting the diffusion measurements. The alignment of the diffusion weighted gradients relative to the underlying fibers has a $\cos^2$ dependence (Jespersen et al., 2010), indicating that angular deviations of up to 18 degrees will be within 10% of the true values. It was previously demonstrated in simulations that microscopic anisotropy (eccentricity) was both highly specific to beading and invariant to the underlying fiber direction. It was hypothesized that this metric would therefore retain sensitivity to axonal injury in the spinal cord and eliminate the directional dependence, albeit with an increase in acquisition time. Eccentricity had a correlation with injury severity similar to that of $ADC_{||}$, and the two were strongly correlated to one another, which is consistent with its similar sensitivity to axonal beading (Skinner et al., 2015) in simulations. Somewhat surprisingly, eccentricity was less reliable at predicting chronic functional outcome than $ADC_{||}$ (Skinner et al., 2015). The reasons for the discrepancy are unclear, but could be potentially related to either the underlying pathology itself or experimental and methodological considerations. The choice of diffusion weighting strength (b-value) and separation between the two DDE diffusion gradient pairs (mixing time;τ) may have affected the sensitivity of DDE. On the other hand, in SCI, diffusion parallel to the cord (axial diffusivity) is consistently a better marker of injury and a better predictor of outcome than FA (Kim et al., 2010; Tu et al., 2010; Shanmuganathan et al., 2017), suggesting there may be an underlying basis for a similar benefit of $ADC_{||}$ compared to eccentricity. Although eccentricity and f_R were strongly correlated to one another, the two parameters reflect different features of the microstructure and may be seen as complementary. $ADC_{||}$ and f_R reflect the diffusivity and restrictions, respectively, along the cord that are associated with axons, whereas eccentricity captures the shape of microstructures and may include both axonal and non-axonal features. Additional investigations into the pathophysiological basis and specificity for both DDE measures, as well as their potential applications in neurological injury and disease, are needed.

Our initial FP-DDE studies used a single-voxel encompassing the full cross section of the spinal cord at the injury site. This approach allowed rapid quantification due to its minimal and straightforward post-processing. However, as shown in **Figure 7**, imaging-based readouts enable visualization of the pattern of injury which may be more informative for tract-specific functional outcomes. While the two techniques are complementary, they both have distinct advantages and disadvantages that may find different applications to clinical situations. Most notably, there is always a balance between spatial resolution and SNR, and as expected (Jones and Basser, 2004; Farrell et al., 2010), the reliability of the estimated parameters depends greatly on SNR. The simulation results revealed $ADC_{||}$ was less affected by low SNR than either eccentricity or f_R highlighting its potential value as a reliable parameter for imaging-based DDE acquisitions where SNR and spatial resolution are in competition with one another. Imaging, compared to a single voxel readout, obviously enables spatial information to address more detailed anatomical investigation. This study utilized a whole-cord region of interest analysis approach and semi-automated methods to reduce potential bias compared to manually-defined regions (Martin et al., 2016). Although segmentation of spared vs. injured white matter has been shown to improve separation of injury groups (Kim et al., 2010), these manual methods are subjective, labor intensive, and require a separate control group to define the normal white matter values and ranges. Currently, whole-cord regions of interest are advocated by the NIH Common Data Elements (Biering-Sorensen et al., 2015). Our decision to use a single whole-cord region of interest was based on the simplest and most straightforward approach for quantification. Automated registration and tract-specific analysis methods are useful when the cord anatomy is relatively preserved (De Leener et al., 2017), but it is unclear how well these techniques will perform with significant anatomical disruptions seen in acute human DTI of spinal cord trauma (Shanmuganathan et al., 2017). Further investigations of the different quantification approaches will be

useful in combination with the optimized contrasts evaluated in this study.

Importantly, the simulations and *in vivo* results in naïve animals also demonstrated equivalence between the single and double diffusion encoding using the identical diffusion encoding schemes. The reduction in TE led to an SNR improvement of approximately 1.6. Unlike other DDE acquisitions, the SDE was only possible since the diffusion filter and probe gradients were orthogonal and assumes the fibers were coherent and aligned with the spinal cord axis. *In vivo*, a significant difference in $ADC_{||}$ was observed between the single and double diffusion encoding, which is likely due to the effects of T_2 relaxation since different TEs were used. One benefit of reduced TE with the SDE is an improved SNR. Likewise, a practical advantage of SDE is its compatibility with existing pulse sequences with only minor modifications to the diffusion encoding directions and amplitudes. Moreover, the filter-probe scheme utilizes a perpendicular diffusion weighted image for normalization rather than an unweighted ($b = 0$) image for reference as is done in most other diffusion analytical models. This also reduces artifacts associated with CSF signal such as flow or pulsation artifacts (Maier, 2007) and Gibbs ringing (Perrone et al., 2015).

The combined reduced field of view and FP-SDE scheme enabled high-resolution images of the spinal cord with prominent detection of injury severity on a per-subject basis. Notably, in one example $ADC_{||}$ map from a severely-injured animal (**Figure 7A**), a central region of decreased $ADC_{||}$ was evident, with a region of higher $ADC_{||}$ along the peripheral white matter. This pathological feature is consistent with the known pathology of contusion injury (Hausmann, 2003; Kim et al., 2006; Loy et al., 2007). Compared to DTI maps of AD, the suppression of CSF in the filter-probe scheme eliminated partial volume effects along the white matter border that would otherwise be difficult to visualize (Kim et al., 2006). The DWI images, which are a surrogate measure of axonal density, did not reveal pronounced effects of injury severity at the acute timepoint. A strong relationship between $ADC_{||}$ and injury severity was maintained in the quantitative analysis across all animals (**Figure 8**). Future studies explicitly modeling axonal density in concert with $ADC_{||}$ would be useful. Furthermore, a single post-injury timepoint was assessed in this study at 48 h post-injury, which is typically longer than the initial MRI exam in acute SCI (Talbott et al., 2015; Shanmuganathan et al., 2017). Previous studies have demonstrated that diffusion indices evolve over the initial acute post-injury period, although axial diffusivity varies less than radial diffusivity within the first week (Kim et al., 2007). A more detailed examination of the post-injury window using FP-DDE would be instrumental in assessing the role of edema in these changes and translating these techniques to clinical settings where the variability in the injury-to-imaging time is expected due to the other medical complications of SCI.

Finally, in the first application to the human spinal cord, the filter-probe diffusion approach reduced partial volume effects with CSF (**Figure 9**). Interestingly, white matter $ADC_{||}$ was greater than AD derived from DTI in the same subjects and regions. This insight has implications for modeling of the compartmental DWI signal models (Jelescu et al., 2015, 2016). However, it should be noted that the two measures were derived differently using either a single-axis ($ADC_{||}$) or tensor-based (AD) estimate and should not be considered a direct investigation of the intra/extracellular diffusion properties. Importantly, through optimization of the acquisition, the variability of $ADC_{||}$ estimates were comparable to those derived from DTI. While respiratory gating was used for all acquisitions in the rat, no gating was used for human studies despite studies demonstrating its advantages (Spuentrup et al., 2003; Mohammadi et al., 2013) evidence that CSF pulsation in the human is primarily associated with respiration (Dreha-Kulaczewski et al., 2015, 2017). However, the filter-probe approach suppresses CSF which is advantageous to reduce CSF-related artifacts (Maier, 2007). Further reliability assessments and application to patients with SCI or disease using the optimized protocol will be needed to demonstrate the reliability, applicability, and utility of the technique for research purposes or clinical diagnosis.

CONCLUSIONS

Collectively, these acquisition advances demonstrate the sensitivity of the filter-probe diffusion weighted contrast technique to spinal cord injury. Optimizations to the acquisition and contrast mechanisms have been refined and examined for human translation, culminating in implementation of the FP-SDE scheme on clinical scanner systems without significant modifications. The strong association between quantified diffusivity values and functional outcomes in a rat model of SCI shows high sensitivity to acute injury with the potential to be useful in clinical evaluation of SCI. Future applications to patients with injury and disease of the spinal cord will refine the clinical applicability filter-probe DWI to diagnosis and prognosis.

ETHICS STATEMENT

This study was carried out and approved by the Institutional Review Board of the Medical College of Wisconsin. All subjects gave written informed consent in accordance with the Declaration of Helsinki. This study was carried out and approved by the Institutional Animal Care and Use Committee of the Medical College of Wisconsin and the Clement J Zablocki VA Medical Center.

AUTHOR CONTRIBUTIONS

MDB, NS, and LM: Acquired Data. MDB, NS: Conducted Analysis. All Authors: Edited and Approved Manuscript.

FUNDING

This project was partially funded through the Research and Education Initiative Fund, a component of the Advancing a Healthier Wisconsin endowment at MCW (5520207 to MDB), funding from the Craig H. Neilsen Foundation (297024 to MDB), and supported in part by Merit Review Award I01 RX001497

from the US Department of Veterans Affairs Rehabilitation Research and Development Service (SK). Additional support received from the National Institute of Neurological Disorders and Stroke of the National Institutes of Health under Award Number F31NS096958 (NS). NS is a member of the Medical Scientist Training Program at MCW, partially supported by NIGMS T32-GM080202 training grant, and additional support was received from the National Center for Advancing Translational Sciences, National Institutes of Health, through grant numbers UL1TR001436 and 1TL1TR001437. Support from the Bryon Riesch Paralysis Foundation is gratefully acknowledged.

ACKNOWLEDGMENTS

We thank Kyle Stehlik and Natasha Beucher in the Department of Neurosurgery for experimental assistance. We thank Thomas Meade, Ph.D., Chad Haney, Ph.D., and Emily Alex Waters, Ph.D., for use of the MRI facilities at the Center for Advanced Molecular Imaging at Northewestern University.

REFERENCES

Basso, D. M., Beattie, M. S., and Bresnahan, J. C. (1995). A sensitive and reliable locomotor rating scale for open field testing in rats. *J. Neurotrauma* 12, 1–21. doi: 10.1089/neu.1995.12.1

Biering-Sorensen, F., Alai, S., Anderson, K., Charlifue, S., Chen, Y., Devivo, M., et al. (2015). Common data elements for spinal cord injury clinical research: a National Institute for Neurological Disorders and Stroke project. *Spinal Cord* 53, 265–277. doi: 10.1038/sc.2014.246

Bottomley, P. A. (1987). Spatial localization in NMR spectroscopy *in vivo*. *Ann. N. Y. Acad. Sci.* 508, 333–348. doi: 10.1111/j.1749-6632.1987.tb32915.x

Budde, M. D., and Frank, J. A. (2010). Neurite beading is sufficient to decrease the apparent diffusion coefficient after ischemic stroke. *Proc. Natl. Acad. Sci. U.S.A.* 107, 14472–14477. doi: 10.1073/pnas.1004841107

Budde, M. D., Kim, J. H., Liang, H. F., Schmidt, R. E., Russell, J. H., Cross, A. H., et al. (2007). Toward accurate diagnosis of white matter pathology using diffusion tensor imaging. *Magn. Reson. Med.* 57, 688–695. doi: 10.1002/mrm.21200

Cheran, S., Shanmuganathan, K., Zhuo, J., Mirvis, S. E., Aarabi, B., Alexander, M. T., et al. (2011). Correlation of MR diffusion tensor imaging parameters with ASIA motor scores in hemorrhagic and nonhemorrhagic acute spinal cord injury. *J. Neurotrauma* 28, 1881–1892. doi: 10.1089/neu.2010.1741

Dalkilic, T., Fallah, N., Noonan, V. K., Salimi Elizei, S., Dong, K., Belanger, L. M., et al. (2017). Predicting injury severity and neurologic recovery after acute cervical spinal cord injury: a comparison of cerebrospinal fluid and magnetic resonance imaging biomarkers. *J. Neurotrauma.* doi: 10.1089/neu.2017.5357. [Epub ahead of print].

De Leener, B., Levy, S., Dupont, S. M., Fonov, V. S., Stikov, N., Louis Collins, D., et al. (2017). SCT: Spinal Cord Toolbox, an open-source software for processing spinal cord MRI data. *Neuroimage* 145, 24–43. doi: 10.1016/j.neuroimage.2016.10.009

Deo, A. A., Grill, R. J., Hasan, K. M., and Narayana, P. A. (2006). *In vivo* serial diffusion tensor imaging of experimental spinal cord injury. *J. Neurosci. Res.* 83, 801–810. doi: 10.1002/jnr.20783

Dreha-Kulaczewski, S., Joseph, A. A., Merboldt, K. D., Ludwig, H. C., Gartner, J., and Frahm, J. (2015). Inspiration is the major regulator of human CSF flow. *J. Neurosci.* 35, 2485–2491. doi: 10.1523/JNEUROSCI.3246-14.2015

Dreha-Kulaczewski, S., Joseph, A. A., Merboldt, K. D., Ludwig, H. C., Gartner, J., and Frahm, J. (2017). Identification of the upward movement of human CSF *in vivo* and its relation to the brain venous system. *J. Neurosci.* 37, 2395–2402. doi: 10.1523/JNEUROSCI.2754-16.2017

Ellingson, B. M., Kurpad, S. N., and Schmit, B. D. (2008). *Ex vivo* diffusion tensor imaging and quantitative tractography of the rat spinal cord during long-term recovery from moderate spinal contusion. *J. Magn. Reson. Imaging* 28, 1068–1079. doi: 10.1002/jmri.21578

Ellingson, B. M., Schmit, B. D., and Kurpad, S. N. (2010). Lesion growth and degeneration patterns measured using diffusion tensor 9.4-T magnetic resonance imaging in rat spinal cord injury. *J. Neurosurg. Spine* 13, 181–192. doi: 10.3171/2010.3.SPINE09523

Endo, T., Suzuki, S., Utsunomiya, A., Uenohara, H., and Tominaga, T. (2011). Prediction of neurological recovery using apparent diffusion coefficient in cases of incomplete spinal cord injury. *Neurosurgery* 68, 329–336. doi: 10.1227/NEU.0b013e3182031ce7

Farrell, J. A., Zhang, J., Jones, M. V., Deboy, C. A., Hoffman, P. N., Landman, B. A., et al. (2010). q-space and conventional diffusion imaging of axon and myelin damage in the rat spinal cord after axotomy. *Magn. Reson. Med.* 63, 1323–1335. doi: 10.1002/mrm.22389

Gaviria, M., Bonny, J. M., Haton, H., Jean, B., Teigell, M., Renou, J. P., et al. (2006). Time course of acute phase in mouse spinal cord injury monitored by *ex vivo* quantitative MRI. *Neurobiol. Dis.* 22, 694–701. doi: 10.1016/j.nbd.2006.01.011

Cory, D. F., Garroway, A. N., and Miller, J. B. (1990). Applications of spin transport as a probe of local geometry. *Polym Preprints* 3, 149–150.

Hall, M. G., and Alexander, D. C. (2009). Convergence and parameter choice for Monte-Carlo simulations of diffusion MRI. *IEEE Trans. Med. Imaging* 28, 1354–1364. doi: 10.1109/TMI.2009.2015756

Hausmann, O. N. (2003). Post-traumatic inflammation following spinal cord injury. *Spinal Cord* 41, 369–378. doi: 10.1038/sj.sc.3101483

Herrera, J. J., Chacko, T., and Narayana, P. A. (2008). Histological correlation of diffusion tensor imaging metrics in experimental spinal cord injury. *J. Neurosci. Res.* 86, 443–447. doi: 10.1002/jnr.21481

Hirsch, J. G., Bock, M., Essig, M., and Schad, L. R. (1999). Comparison of diffusion anisotropy measurements in combination with the flair-technique. *Magn. Reson. Imaging* 17, 705–716. doi: 10.1016/S0730-725X(98)00217-3

Jelescu, I. O., Veraart, J., Adisetiyo, V., Milla, S. S., Novikov, D. S., and Fieremans, E. (2015). One diffusion acquisition and different white matter models: how does microstructure change in human early development based on WMTI and NODDI? *Neuroimage* 107, 242–256. doi: 10.1016/j.neuroimage.2014.12.009

Jelescu, I. O., Veraart, J., Fieremans, E., and Novikov, D. S. (2016). Degeneracy in model parameter estimation for multi-compartmental diffusion in neuronal tissue. *NMR Biomed.* 29, 33–47. doi: 10.1002/nbm.3450

Jenkinson, M., Beckmann, C. F., Behrens, T. E., Woolrich, M. W., and Smith, S. M. (2012). Fsl. *Neuroimage* 62, 782–790. doi: 10.1016/j.neuroimage.2011.09.015

Jespersen, S. N., Bjarkam, C. R., Nyengaard, J. R., Chakravarty, M. M., Hansen, B., Vosegaard, T., et al. (2010). Neurite density from magnetic resonance diffusion measurements at ultrahigh field: comparison with light microscopy and electron microscopy. *Neuroimage* 49, 205–216. doi: 10.1016/j.neuroimage.2009.08.053

Jespersen, S. N., Lundell, H., Sonderby, C. K., and Dyrby, T. B. (2013). Orientationally invariant metrics of apparent compartment eccentricity from double pulsed field gradient diffusion experiments. *NMR Biomed.* 26, 1647–1662. doi: 10.1002/nbm.2999

Jirjis, M. B., Kurpad, S. N., and Schmit, B. D. (2013). *Ex vivo* diffusion tensor imaging of spinal cord injury in rats of varying degrees of severity. *J. Neurotrauma* 30, 1577–1586. doi: 10.1089/neu.2013.2897

Jones, D. K., and Basser, P. J. (2004). "Squashing peanuts and smashing pumpkins": how noise distorts diffusion-weighted MR data. *Magn. Reson. Med.* 52, 979–993. doi: 10.1002/mrm.20283

Kelley, B. J., Harel, N. Y., Kim, C. Y., Papademetris, X., Coman, D., Wang, X., et al. (2014). Diffusion tensor imaging as a predictor of locomotor function after experimental spinal cord injury and recovery. *J. Neurotrauma* 31, 1362–1373. doi: 10.1089/neu.2013.3238

Kim, J. H., Budde, M. D., Liang, H. F., Klein, R. S., Russell, J. H., Cross, A. H., et al. (2006). Detecting axon damage in spinal cord from a mouse model of multiple sclerosis. *Neurobiol. Dis.* 21, 626–632. doi: 10.1016/j.nbd.2005.09.009

Kim, J. H., Loy, D. N., Liang, H. F., Trinkaus, K., Schmidt, R. E., and Song, S. K. (2007). Noninvasive diffusion tensor imaging of evolving white matter

pathology in a mouse model of acute spinal cord injury. *Magn. Reson. Med.* 58, 253–260. doi: 10.1002/mrm.21316

Kim, J. H., Loy, D. N., Wang, Q., Budde, M. D., Schmidt, R. E., Trinkaus, K., et al. (2010). Diffusion tensor imaging at 3 hours after traumatic spinal cord injury predicts long-term locomotor recovery. *J. Neurotrauma* 27, 587–598. doi: 10.1089/neu.2009.1063

Krzyzak, A. T., Jasinski, A., Weglarz, W. P., Adamek, D., Sagnowskil, P., and Baj, M. (2005). Visualisation of the extent of damage in a rat spinal cord injury model using MR microsopy of the water diffusion tensor. *Acta Neurobiol. Exp.* 65, 255–264.

Lawrenz, M., Brassen, S., and Finsterbusch, J. (2016). Microscopic diffusion anisotropy in the human brain: age-related changes. *Neuroimage* 141, 313–325. doi: 10.1016/j.neuroimage.2016.07.031

Leypold, B. G., Flanders, A. E., and Burns, A. S. (2008). The early evolution of spinal cord lesions on MR imaging following traumatic spinal cord injury. *AJNR Am. J. Neuroradiol.* 29, 1012–1016. doi: 10.3174/ajnr.A0962

Li, X. H., Li, J. B., He, X. J., Wang, F., Huang, S. L., and Bai, Z. L. (2015). Timing of diffusion tensor imaging in the acute spinal cord injury of rats. *Sci. Rep.* 5:12639. doi: 10.1038/srep12639

Loy, D. N., Kim, J. H., Xie, M., Schmidt, R. E., Trinkaus, K., and Song, S. K. (2007). Diffusion tensor imaging predicts hyperacute spinal cord injury severity. *J. Neurotrauma* 24, 979–990. doi: 10.1089/neu.2006.0253

Maier, S. E. (2007). Examination of spinal cord tissue architecture with magnetic resonance diffusion tensor imaging. *Neurotherapeutics* 4, 453–459. doi: 10.1016/j.nurt.2007.05.003

Martin, A. R., Aleksanderek, I., Cohen-Adad, J., Tarmohamed, Z., Tetreault, L., Smith, N., et al. (2016). Translating state-of-the-art spinal cord MRI techniques to clinical use: a systematic review of clinical studies utilizing DTI, MT, MWF, MRS, and fMRI. *Neuroimage Clin.* 10, 192–238. doi: 10.1016/j.nicl.2015.11.019

Medana, I. M., and Esiri, M. M. (2003). Axonal damage: a key predictor of outcome in human CNS diseases. *Brain* 126, 515–530. doi: 10.1093/brain/awg061

Mitra, P. P. (1995). Multiple wave-vector extensions of the NMR pulsed-field-gradient spin-echo diffusion measurement. *Phys. Rev. B Condens. Matter* 51, 15074–15078. doi: 10.1103/PhysRevB.51.15074

Mohammadi, S., Freund, P., Feiweier, T., Curt, A., and Weiskopf, N. (2013). The impact of post-processing on spinal cord diffusion tensor imaging. *Neuroimage* 70, 377–385. doi: 10.1016/j.neuroimage.2012.12.058

Mondragon-Lozano, R., Diaz-Ruiz, A., Rios, C., Olayo Gonzalez, R., Favila, R., Salgado-Ceballos, H., et al. (2013). Feasibility of *in vivo* quantitative magnetic resonance imaging with diffusion weighted imaging, T2-weighted relaxometry, and diffusion tensor imaging in a clinical 3 tesla magnetic resonance scanner for the acute traumatic spinal cord injury of rats: technical note. *Spine* 38, E1242–E1249. doi: 10.1097/BRS.0b013e31829ef69c

Neeman, M., Freyer, J. P., and Sillerud, L. O. (1991). A simple method for obtaining cross-term-free images for diffusion anisotropy studies in NMR microimaging. *Magn. Reson. Med.* 21, 138–143. doi: 10.1002/mrm.1910210117

Patel, S. P., Smith, T. D., Vanrooyen, J. L., Powell, D., Cox, D. H., Sullivan, P. G., et al. (2016). Serial diffusion tensor imaging *in vivo* predicts long-term functional recovery and histopathology in rats following different severities of spinal cord injury. *J. Neurotrauma* 33, 917–928. doi: 10.1089/neu.2015.4185

Perrone, D., Aelterman, J., Pizurica, A., Jeurissen, B., Philips, W., and Leemans, A. (2015). The effect of Gibbs ringing artifacts on measures derived from diffusion MRI. *Neuroimage* 120, 441–455. doi: 10.1016/j.neuroimage.2015.06.068

Saritas, E. U., Cunningham, C. H., Lee, J. H., Han, E. T., and Nishimura, D. G. (2008). DWI of the spinal cord with reduced FOV single-shot EPI. *Magn. Reson. Med.* 60, 468–473. doi: 10.1002/mrm.21640

Shanmuganathan, K., Zhuo, J., Chen, H. H., Aarabi, B., Adams, J., Miller, C., et al. (2017). Diffusion tensor imaging parameter obtained during acute blunt cervical spinal cord injury in predicting long term outcome. *J. Neurotrauma* 34, 2964–2971. doi: 10.1089/neu.2016.4901

Shemesh, N., and Cohen, Y. (2008). The effect of experimental parameters on the signal decay in double-PGSE experiments: negative diffractions and enhancement of structural information. *J. Magn. Reson.* 195, 153–161. doi: 10.1016/j.jmr.2008.09.006

Shemesh, N., Jespersen, S. N., Alexander, D. C., Cohen, Y., Drobnjak, I., Dyrby, T. B., et al. (2016). Conventions and nomenclature for double diffusion encoding NMR and MRI. *Magn. Reson. Med.* 75, 82–87. doi: 10.1002/mrm.25901

Shemesh, N., Rosenberg, J. T., Dumez, J. N., Muniz, J. A., Grant, S. C., and Frydman, L. (2014). Metabolic properties in stroked rats revealed by relaxation-enhanced magnetic resonance spectroscopy at ultrahigh fields. *Nat. Commun.* 5, 4958. doi: 10.1038/ncomms5958

Skinner, N. P., Kurpad, S. N., Schmit, B. D., and Budde, M. D. (2015). Detection of acute nervous system injury with advanced diffusion-weighted MRI: a simulation and sensitivity analysis. *NMR Biomed.* 28, 1489–1506. doi: 10.1002/nbm.3405

Skinner, N. P., Kurpad, S. N., Schmit, B. D., Tugan Muftuler, L., and Budde, M. D. (2016). Rapid *in vivo* detection of rat spinal cord injury with double-diffusion-encoded magnetic resonance spectroscopy. *Magn. Reson Med.* 77, 1639–1649. doi: 10.1002/mrm.26243

Spuentrup, E., Buecker, A., Koelker, C., Guenther, R. W., and Stuber, M. (2003). Respiratory motion artifact suppression in diffusion-weighted MR imaging of the spine. *Eur. Radiol.* 13, 330–336. doi: 10.1007/s00330-002-1603-z

Steiger, J. H. (1980). Tests for comparing elements of a correlation matrix. *Psychol. Bull.* 87, 245–251. doi: 10.1037/0033-2909.87.2.245

Stroman, P. W., Wheeler-Kingshott, C., Bacon, M., Schwab, J. M., Bosma, R., Brooks, J., et al. (2014). The current state-of-the-art of spinal cord imaging: methods. *Neuroimage* 84, 1070–1081. doi: 10.1016/j.neuroimage.2013.04.124

Sundberg, L. M., Herrera, J. J., and Narayana, P. A. (2010). *In vivo* longitudinal MRI and behavioral studies in experimental spinal cord injury. *J. Neurotrauma* 27, 1753–1767. doi: 10.1089/neu.2010.1369

Talbott, J. F., Whetstone, W. D., Readdy, W. J., Ferguson, A. R., Bresnahan, J. C., Saigal, R., et al. (2015). The Brain and Spinal Injury Center score: a novel, simple, and reproducible method for assessing the severity of acute cervical spinal cord injury with axial T2-weighted MRI findings. *J. Neurosurg. Spine* 23, 495–504. doi: 10.3171/2015.1.SPINE141033

Tu, T. W., Kim, J. H., Wang, J., and Song, S. K. (2010). Full tensor diffusion imaging is not required to assess the white-matter integrity in mouse contusion spinal cord injury. *J. Neurotrauma* 27, 253–262. doi: 10.1089/neu.2009.1026

Vedantam, A., Eckardt, G., Wang, M. C., Schmit, B. D., and Kurpad, S. N. (2015). Clinical correlates of high cervical fractional anisotropy in acute cervical spinal cord injury. *World Neurosurg.* 83, 824–828. doi: 10.1016/j.wneu.2013.09.017

Wang, F., Huang, S. L., He, X. J., and Li, X. H. (2014). Determination of the ideal rat model for spinal cord injury by diffusion tensor imaging. *Neuroreport* 25, 1386–1392. doi: 10.1097/WNR.0000000000000278

Wheeler-Kingshott, C. A., Stroman, P. W., Schwab, J. M., Bacon, M., Bosma, R., Brooks, J., et al. (2014). The current state-of-the-art of spinal cord imaging: applications. *Neuroimage* 84, 1082–1093. doi: 10.1016/j.neuroimage.2013.07.014

Williams, P. R., Marincu, B. N., Sorbara, C. D., Mahler, C. F., Schumacher, A. M., Griesbeck, O., et al. (2014). A recoverable state of axon injury persists for hours after spinal cord contusion *in vivo*. *Nat. Commun.* 5, 5683. doi: 10.1038/ncomms6683

Conflict of Interest Statement: The authors declare that the research was conducted in the absence of any commercial or financial relationships that could be construed as a potential conflict of interest.

frontiers in Neuroscience

ORIGINAL RESEARCH
published: 21 February 2018
doi: 10.3389/fnins.2018.00092

On the Viability of Diffusion MRI-Based Microstructural Biomarkers in Ischemic Stroke

Ilaria Boscolo Galazzo[1]*, *Lorenza Brusini*[1], *Silvia Obertino*[1], *Mauro Zucchelli*[1], *Cristina Granziera*[2] and *Gloria Menegaz*[1]

[1] Department of Computer Science, University of Verona, Verona, Italy, [2] Translational Imaging in Neurology Group, Department of Neurology, Basel University Hospital, Basel, Switzerland

Recent tract-based analyses provided evidence for the exploitability of 3D-SHORE microstructural descriptors derived from diffusion MRI (dMRI) in revealing white matter (WM) plasticity. In this work, we focused on the main open issues left: (1) the comparative analysis with respect to classical tensor-derived indices, i.e., Fractional Anisotropy (FA) and Mean Diffusivity (MD); and (2) the ability to detect plasticity processes in gray matter (GM). Although signal modeling in GM is still largely unexplored, we investigated their sensibility to stroke-induced microstructural modifications occurring in the contralateral hemisphere. A more complete picture could provide hints for investigating the interplay of GM and WM modulations. Ten stroke patients and ten age/gender-matched healthy controls were enrolled in the study and underwent diffusion spectrum imaging (DSI). Acquisitions at three and two time points (*tp*) were performed on patients and controls, respectively. For all subjects and acquisitions, FA and MD were computed along with 3D-SHORE-based indices [Generalized Fractional Anisotropy (GFA), Propagator Anisotropy (PA), Return To the Axis Probability (RTAP), Return To the Plane Probability (RTPP), and Mean Square Displacement (MSD)]. Tract-based analysis involving the cortical, subcortical and transcallosal motor networks and region-based analysis in GM were successively performed, focusing on the contralateral hemisphere to the stroke. Reproducibility of all the indices on both WM and GM was quantitatively proved on controls. For tract-based, longitudinal group analyses revealed the highest significant differences across the subcortical and transcallosal networks for all the indices. The optimal regression model for predicting the clinical motor outcome at *tp3* included GFA, PA, RTPP, and MSD in the subcortical network in combination with the main clinical information at baseline. Region-based analysis in the contralateral GM highlighted the ability of anisotropy indices in discriminating between groups mainly at *tp1*, while diffusivity indices appeared to be altered at *tp2*. 3D-SHORE indices proved to be suitable in probing plasticity in both WM and GM, further confirming their viability as a novel family of biomarkers in ischemic stroke in WM and revealing their potential exploitability in GM. Their combination with tensor-derived indices can provide more detailed insights of the different tissue modulations related to stroke pathology.

Keywords: diffusion propagator, tensor model, 3D-SHORE model, reproducibility, tract-based, gray matter, ischemic stroke

OPEN ACCESS

Edited by:
Julien Valette, Commissariat à l'Energie Atomique et aux Energies Alternatives (CEA), France

Reviewed by:
Matthew D. Budde, Medical College of Wisconsin, United States
Alexandru Vlad Avram, National Institutes of Health (NIH), United States

***Correspondence:**
Ilaria Boscolo Galazzo
ilaria.boscologalazzo@univr.it

Specialty section:
This article was submitted to Brain Imaging Methods, a section of the journal Frontiers in Neuroscience

Received: *30 November 2017*
Accepted: *05 February 2018*
Published: *21 February 2018*

Citation:
Boscolo Galazzo I, Brusini L, Obertino S, Zucchelli M, Granziera C and Menegaz G (2018) On the Viability of Diffusion MRI-Based Microstructural Biomarkers in Ischemic Stroke. Front. Neurosci. 12:92. doi: 10.3389/fnins.2018.00092

INTRODUCTION

In the last 30 years, diffusion magnetic resonance imaging (dMRI) has been proven to be a valuable tool for characterizing physiological and pathological conditions *in-vivo* (Le Bihan et al., 1986; Beaulieu, 2002). An increasing number of modeling methods have been proposed for inferring tissue microstructural properties from the acquired diffusion signal (for a detailed overview see Novikov et al., 2016), many of which rely only on the reconstruction of the ensemble average propagator (EAP), i.e., the probability distribution function of the water molecules displacements. The EAP, under some optimality assumptions, contains the full information about the diffusion process and therefore can inform about the underlying tissue architecture (Zucchelli et al., 2016b), leading to numerical indices that can indirectly quantify the different microstructural features.

Diffusion Tensor Imaging (DTI) (Basser et al., 1994a) was the first EAP model introduced to describe the anisotropic nature of the diffusion process in biological tissues and is still the preferred method in clinical settings thanks to its ability to estimate the principal diffusion direction from very few dMRI measurements. The scalar indices obtained from DTI, mainly the mean diffusivity (MD) and the fractional anisotropy (FA) (Pierpaoli and Basser, 1996), have become precious tools for characterizing pathological conditions such as tumors, stroke and neurodegenerative disorders (Sundgren et al., 2004). Nonetheless, DTI has an inherent strong modeling constraint related to the description of the EAP as a single multivariate Gaussian function. This assumption is rarely adequate in real conditions where complex white matter (WM) topologies featuring crossing, fanning and kissing fibers are most often encountered, severely limiting its applicability. Among the widespread EAP models proposed for circumventing this limitation, one of the most accurate is the Simple Harmonic Oscillator Based Reconstruction and Estimation (SHORE), firstly introduced in Özarslan et al. (2008). 3D-SHORE and its extensions, as Mean Apparent Propagator (MAP)-MRI (Özarslan et al., 2013), demonstrated good performance in detecting multiple diffusion directions and are among the most promising EAP-based models for characterizing the tissue microstructure, as recently highlighted at the SPARC-dMRI contest (Ning et al., 2015). Under some assumptions, reliable measures of tissue anisotropy can be derived from these EAP models, such as the Generalized Fractional Anisotropy (GFA) and the Propagator Anisotropy (PA), along with measures of the EAP variance (Mean Square Displacement, MSD). In addition, they provide indices that quantify various features of the three-dimensional diffusion process, namely the Return to the Origin Probability (RTOP), the Return To the Axis Probability (RTAP) and the Return To the Plane Probability (RTPP). When the diffusion time is long enough and under narrow pulse assumptions (Özarslan et al., 2013), these indices reflect the degree of restriction of the water molecules in the voxel, which is linked to the underlying pore shape and thus represent relevant descriptors of the microstructural properties (Zucchelli et al., 2016a).

Since their first introduction, 3D-SHORE indices have been increasingly explored as novel potential biomarkers of brain microstructure. This has been shown both on synthetic data and in *ex-vivo* experiments on a marmoset brain (Özarslan et al., 2013) as well as in *in-vivo* studies on healthy subjects (Avram et al., 2014; Fick et al., 2015; Mendez et al., 2016; Zucchelli et al., 2016a). Very few studies have tried to pursue their potentialities as clinical biomarkers in pathologies, with promising results to date only on Alzheimer's animal models (Fick et al., 2016) and on ischemic stroke (Brusini et al., 2015; Obertino et al., 2016). In the latter case, albeit DTI scalar indices have been used to assess stroke features in several longitudinal studies (Maniega et al., 2004; Yu et al., 2009), the characterisation of the network pathophysiology with advanced EAP-based indices would add insights into the reorganization processes that can be combined with clinical information to draw a more precise picture of the disease. A recent study (Brusini et al., 2016) investigated these aspects on a group of ischemic stroke patients and assessed the performance of selected 3D-SHORE indices along WM tracts of different motor networks (cortical, subcortical, and transcallosal circuits). Results highlighted how 3D-SHORE-based indices (mainly GFA, PA, RTAP, and RTPP) could provide measurements featuring high precision and allow discriminating patients from controls, supporting their suitability for mapping longitudinal changes after stroke.

Although the available findings for these numerical indices are encouraging, a quantitative comparison with the classical tensor-derived metrics is currently lacking but essential to further probing their potentialities as biologically specific markers. Indeed, MD and FA remain the standard measures in clinical settings, especially for acute stroke imaging. Therefore, 3D-SHORE-based indices have to be carefully related to tensor-derived indices in terms of precision, consistency, discriminative and predictive power in patients, all essential requirements to be eligible as numerical biomarkers. Avram et al. (2016) reported a first attempt to assess the feasibility of novel EAP-indices (from MAP-MRI modeling rather than 3D-SHORE) in comparison to classical DTI indices, demonstrating good consistency across subjects and reproducibility in test–retest experiments on three controls. However, despite the promising results, the authors dealt with a very limited number of healthy subjects and relied only on qualitative visual comparisons, acknowledging the need for further studies on patient populations that, to the best of our knowledge, are still missing in recent literature.

Whereas a great research effort has been devoted to dMRI signal modeling in WM, its exploitability for characterizing gray matter (GM) structures is still largely unexplored. In fact, there is a growing need for a more comprehensive assessment of GM tissue changes using dMRI. The intrinsic complexity of GM microstructure which, as opposed to WM, lacks coherent tissue orientation complicates the modeling and interpretation of the diffusion process, and casts shadows on the suitability of the currently available models. Some previous studies with classical DTI indices have highlighted MD as a promising marker of GM diffusivity changes in several pathologies such as Alzheimer's disease (Weston et al., 2015), multiple sclerosis (Ceccarelli et al., 2007), and Parkinson (Kim et al., 2013). However, DTI is scarcely employed in the assessment of GM regions, especially in the cortex, and its ability of capturing

microstructural features and feature modulations in GM is still under debate. Conversely, thanks to the ability of capturing the EAP in complex tissue microstructures, the 3D-SHORE model might allow characterizing the signatures of hindered diffusion in GM regions as well as providing information about GM changes occurring over time.

The goal of this study was twofold. First, to complete the assessment of the potential of the 3D-SHORE-derived indices in capturing the microstructural feature modulations induced by ischemic stroke in WM by providing a comparative analysis of their performance with respect to the classical DTI-based FA and MD indices. Second, to start bridging WM and GM modeling by investigating the ability of the considered models (DTI and 3D-SHORE) for the identification of microstructural feature variations in GM, possibly hinting at plasticity processes.

TABLE 1 | Signal-to-Noise (SNR) ratio for the diffusion datasets.

SNR-corpus callosum		
Controls	*tp1*	28.47 ± 5.33
	tp2	28.63 ± 4.38
Patients	*tp1*	28.21 ± 4.60
	tp2	29.65 ± 6.24
	tp3	27.25 ± 4.55

SNR values were calculated on the b0 volume of each subject. In particular, a uniform ROI in the background was chosen for estimating the noise standard deviation while the mean signal was extracted from the corpus callosum, selected as representative ROI for the SNR calculation. Mean ± standard deviation values across subjects are reported, considering each time point and group separately.

MATERIALS AND METHODS

Dataset

Ten ischemic stroke patients (6 males, mean age: 60.3 ± 12.3 years) and ten age- and gender-matched healthy subjects were enrolled in the study and underwent longitudinal MRI acquisitions on a 3T Siemens scanner (Trio, Siemens, Erlangen, Germany), as firstly reported in Granziera et al. (2012b). Of note, an optimized protocol and a dedicated 32-channel head coil with excellent signal-to-noise (SNR) properties (based on Wiggins et al., 2006) were employed, aiming at maximizing the SNR in the acquired data (as in Granziera et al., 2009). Acquisitions were performed at three time points in patients (within 1 week (*tp1*), 1 month (± 1 week, *tp2*), and 6 months (± 15 days, *tp3*) after the injury), and at two time points in controls (1 month apart, *tp1c*, and *tp2c*). The same structural imaging protocol was used in all cases. In particular, Diffusion Spectrum Imaging (DSI), a high angular resolution diffusion technique (Wedeen et al., 2005), was performed using a single-shot spin-echo echo-planar imaging (EPI) product sequence and the following parameters: TR/TE = 6,600/138 ms, FOV = 212 × 212 mm^2, 34 slices, 2.2 × 2.2 × 3 mm^3 resolution, GRAPPA = 2, scan time = 25.8 min. The sampling scheme consisted of a keyhole Cartesian acquisition with 258 diffusion directions covering a half q-space 3D grid with radial grid size of 5. Thirty-four different *b*-values (from 300 up to 8,000 s/mm^2) were included in the acquisition and one image was acquired at $b = 0$ s/mm^2 (b0 volume). Because of the inherent antipodal symmetry, the signal was duplicated on the other hemisphere yielding to 515 points.

In order to provide a measure of the diffusion data quality, SNR values were calculated for all the b0 volumes as the ratio of the mean of the signal divided by the standard deviation of the underlying Gaussian noise (Descoteaux et al., 2011). A uniform ROI in the background was chosen for deriving the noise standard deviation while the mean signal was extracted from the corpus callosum, selected as representative ROI for the SNR calculation. The estimated values are reported in **Table 1**. High-resolution 3D T1-weighted images were also added to the protocol (TR/TE = 2,300/3 ms, FOV = 256 × 256 mm^2, 160 slices, 1 × 1 × 1.2 mm^3 resolution, scan time = 6.13 min). Besides MRI acquisitions, patients underwent clinical neurological assessment following the National Institutes of Health Stroke Scale (NIHSS) at each *tp*. Only the motor part of the NIHSS score was retained for further analysis. Stroke volumes were derived from the individual high-resolution T1-weighted images using the statistical parametric mapping (SPM) lesion segmentation toolbox (www.fil.ion.ucl.ac.uk/spm/). All the subjects signed the written informed consent to the imaging in accordance with the Declaration of Helsinki and the Lausanne University Hospital approved the protocol. Patient demographics and main clinical information are reported in Supplementary Table 1.

Signal Modeling and Microstructural Descriptors

The classical DTI (Basser et al., 1994a,b) and the 3D-SHORE (Özarslan et al., 2008, 2013) models were used to reconstruct the EAP from which the microstructural descriptors were then derived.

The EAP can be recovered from the diffusion weighted signal attenuation $E(q)$ under the narrow pulse assumption (Stejskal and Tanner, 1965) via the Fourier relationship:

$$P(\boldsymbol{r}) = \int_{\boldsymbol{q}\in R^3} E(\boldsymbol{q})\, e^{i2\pi \boldsymbol{q}\boldsymbol{r}} d\boldsymbol{q} \tag{1}$$

where $P(\boldsymbol{r})$ is the EAP, indicating the likelihood for a particle to undergo a net displacement $\boldsymbol{r}$ in the unit time and $\boldsymbol{q} = q\boldsymbol{u}$ is the sampling position, with $\boldsymbol{u}$ being unit vector of the reciprocal space, or *q*-space.

DTI assumes that the diffusion propagator can be described by a single 3D Gaussian distribution (Basser et al., 1994a,b) from which a 3 × 3 symmetric positive-definite matrix is derived (*D*, diffusion tensor) and used to compute the classical tensor-based indices (MD and FA) as follows:

$$MD = \frac{(\lambda_1 + \lambda_2 + \lambda_3)}{3} \tag{2}$$

$$FA = \sqrt{\frac{1}{2}\frac{(\lambda_1 - \lambda_2)^2 + (\lambda_2 - \lambda_3)^2 + (\lambda_1 - \lambda_3)^2}{\lambda_1^2 + \lambda_2^2 + \lambda_3^2}} \tag{3}$$

where λ_1, λ_2, λ_3 are the eigenvalues of D. Only $b < 1{,}500$ mm^2/s were used for the DTI analysis, corresponding to 32 gradient directions.

The novel microstructural indices explored in this work were calculated by fitting the SHORE model (Özarslan et al., 2008, 2013) based on the solutions of the 3D quantum harmonic oscillator in the formulation using the orthonormalized basis:

$$E(\boldsymbol{q}) = \sum_{l=0,even}^{N_{max}} \sum_{n=l}^{\frac{(N_{max}+l)}{2}} \sum_{m=-l}^{l} c_{nlm} \Phi_{nlm}(\boldsymbol{q}) \tag{4}$$

In this equation, N_{max} is the maximal order of the functions, $\Phi_{nlm}(\boldsymbol{q})$ are the functions forming the 3D-SHORE orthonormal basis and are given by:

$$\Phi_{nlm}(\boldsymbol{q}) = \left[\frac{2(n-l)!}{\zeta^{\frac{3}{2}}\Gamma\left(n+\frac{3}{2}\right)}\right]^{\frac{1}{2}} \left(\frac{q^2}{\zeta}\right)^{\frac{l}{2}} exp\left(\frac{-q^2}{2\zeta}\right) L_{n-l}^{l+\frac{1}{2}}\left(\frac{q^2}{\zeta}\right) Y_l^m(\boldsymbol{u}) \tag{5}$$

where Γ is the Gamma function and ζ is a scaling parameter determined by the diffusion time and the mean diffusivity (Merlet and Deriche, 2013; Zucchelli et al., 2016a). For the 3D-SHORE model, the EAP is obtained by plugging Equation (4) into Equation (1) (Özarslan et al., 2013; Zucchelli et al., 2016a). Due to the linearity of the Fourier transform, the EAP basis is thus expressed in terms of the same set of coefficients c_{nlm} as the diffusion signal.

RTAP and RTPP (Özarslan et al., 2013) represent the integral of the EAP along the main diffusion direction and over the plane passing through the origin and perpendicular to the main diffusion direction, respectively:

$$RTAP = \int_R P(\boldsymbol{r}_{\|})\, d\boldsymbol{r}_{\|} \tag{6}$$

$$RTPP = \int_{R^2} P(\mathbf{r}_{\perp})\, d^2\mathbf{r}_{\perp} \tag{7}$$

where $\boldsymbol{r}_{\|}$ is the main diffusion direction, and $\boldsymbol{r}_{\perp}$ indicates the plane orthogonal to the main diffusion direction and passing through the origin. It has been shown (Özarslan et al., 2013; Zucchelli et al., 2016b) that, under the assumptions of narrow pulses and long diffusion time, RTAP and RTPP are proportional to the inverse of the mean apparent cross-sectional area and length of the compartment where diffusion takes place, respectively.

The MSD represents the mean square displacement of the water molecules in the unit time and is computed as follows:

$$MSD = \int_{R^3} P(\boldsymbol{r})\, r^2 d^3\boldsymbol{r} \tag{8}$$

MSD has been proven to be closely related to the classical MD index, sharing similar patterns (Wu and Alexander, 2007).

From the EAP it is possible to derive a propagator anisotropy index, depending on the angular distance between the isotropic part of the EAP, that is encoded in the coefficients c_{n00}, and the full EAP as in Özarslan et al. (2013):

$$PA = \sqrt{1 - \frac{\sum_{n=0}^{N_{\max}} c_{n00}^2}{\sum_{n,l,m}^{N_{\max}} c_{nlm}^2}} \tag{9}$$

Finally, the Orientation Distribution Function (ODF) can be analytically obtained from the 3D-SHORE by taking the radial integral of the EAP along a given direction (Merlet and Deriche, 2013; Özarslan et al., 2013). From the ODF it is possible to derive another measure of anisotropy, the GFA index, which can be viewed as the normalized variance of the ODF:

$$GFA = \sqrt{\frac{n\sum_{i=1}^{n}(ODF(\boldsymbol{u}_i) - \langle ODF\rangle)^2}{(n-1)\sum_{i=1}^{n} ODF(\boldsymbol{u}_i)^2}} \tag{10}$$

where $ODF(\boldsymbol{u}_i)$ is the value of the ODF in the direction $\boldsymbol{u}_i$, and $\langle ODF\rangle$ is the mean ODF value across all directions.

In this work, we used both classical tensor-based indices (MD, FA) along with the aforementioned 3D-SHORE-based indices (RTAP, RTPP, MSD, PA, and GFA) to detect microstructural modulations by both tract-based analyses in WM and by ROI-based analyses in GM, respectively. While the first allowed assessing the performance of the 3D-SHORE-based indices with respect to FA and MD in the motor cortical and subcortical networks, the second targets the GM in order to provide a more complete picture of changes occurring after stroke and possibly pointing at plasticity processes.

Tract-Based Analysis of WM

The tractogram was obtained via a streamline-based algorithm with diffusion tensor ODFs computed from the DSI images (Diffusion Toolkit, CMTK, www.connectomics.org). Individual high-resolution T1-weighted images were parcellated using Freesurfer (http://surfer.nmr.mgh.harvard.edu/) and the Desikan-Killiany anatomical atlas at 83-region scale (sixty-four cortical and nineteen subcortical regions) plus the corpus callosum was employed. The FLIRT tool from the FMRIB FSL software (www.fmrib.ox.ac.uk/fsl) was used for the linear (affine) registration of the T1-weighted scan to diffusion data. In particular, the diffusion baseline images (b0 volumes) were considered as reference images for estimating the registration transformation subsequently applied to back-project the subject-specific anatomical parcellation into the DSI space.

Among all the parcels, a subset of the motor regions of interest (ROIs) was considered for the analyses. For the cortical area we selected the primary motor area (M1), supplementary motor area (SMA), somatosensory cortex (SC) and premotor area (PM), which was considered as a unique region given by the joint combination of the dorsal and ventral parts from the Freesurfer parcellation, while thalamus (Thl), caudatus (Cau), putamen (Put), and globus pallidus (GPi) were selected for the subcortical part. Then, three loops involved in the motor network and linking these cortical-subcortical ROIs were considered in the analysis as in Brusini et al. (2016). In details, the transcallosal circuit (CC) gathers the set of fibers linking the corpus callosum

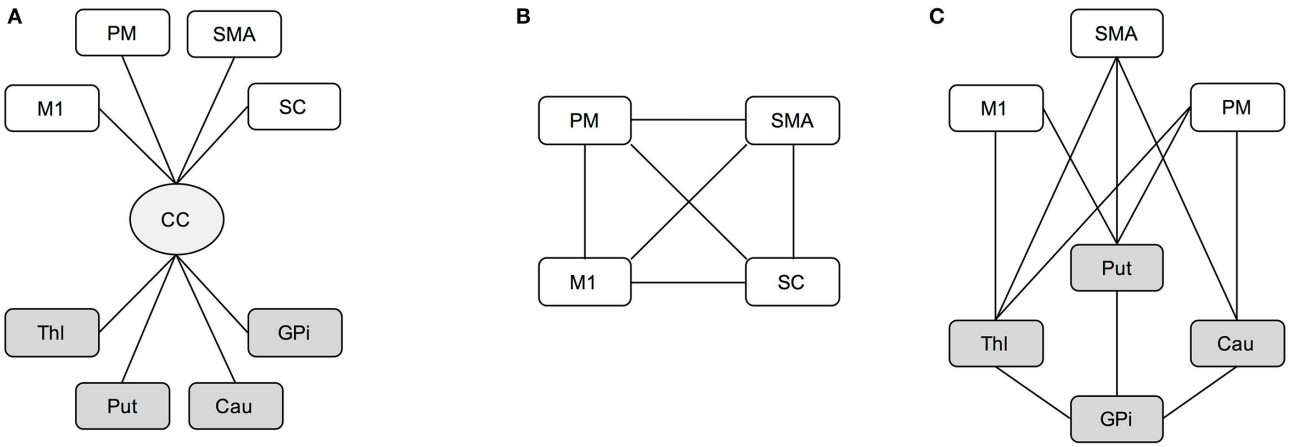

FIGURE 1 | Schematic representation of transcallosal **(A)**, cortical **(B)**, and subcortical **(C)** networks. Cortical areas (white): M1, primary motor area; SMA, supplementary motor area; SC, somatosensory cortex; PM, premotor area. Subcortical nuclei (gray): Thl, thalamus; Cau, caudatus; Put, putamen; GPi, globus pallidus. Bundle of neural fibers (light gray): CC, corpus callosum.

with each considered ROI (**Figure 1A**). The cortical loop (CORT) consists of fibers linking the four cortical ROIs (**Figure 1B**), while the subcortical loop (SUBCORT) includes the set of fibers linking cortical (except SC) with subcortical ROIs (**Figure 1C**).

Tensor-based and 3D-SHORE-based indices were finally calculated along each fiber bundle linking every pair of regions in the proposed networks. To this end, the values of the considered microstructural parameter were firstly mapped onto each fiber connecting two specific ROIs, then averaged across the whole fiber bundle. In this way, a representative microstructural value was derived for each connection of the considered network.

Region-Based Analysis of GM

The individual high-resolution T1-weighted images were segmented into WM, GM, and cerebrospinal fluid (CSF) tissues using the SPM toolbox (Friston et al., 1995). A binary mask was derived for GM using a conservative 95% threshold on the individual probability maps.

Eighty regions from the Freesurfer parcellation were considered (brainstem and corpus callosum were excluded) and masked with the binary GM mask. Four small subcortical regions per hemisphere resulted to be empty after GM masking and were excluded from further analyses, for a total of seventy-two regions. For all indices, the mean GM value across each masked ROI was then calculated. In particular, average measures were calculated across corresponding regions in both hemispheres for controls, while averaging was constrained to the contralateral hemisphere for patients, leading in both cases to thirty-six representative GM values for each index and subject. The list of the considered regions and relative abbreviations is provided in Supplementary Table 2.

Test–Retest Reproducibility Analysis

Before comparing the performance of the indices in the two groups and assessing their discriminative/predictive power, a preliminary step for analyzing their variability and longitudinal stability was performed following the test-retest paradigm on controls (*tp1c* and *tp2c*). This allowed to quantitatively assess their reproducibility in physiological conditions and thus to estimate the precision of the measurements. These elements were quantified for all the microstructural indices, relying on all the representative measures coming from both tract-based and region-based analysis.

The following metrics were computed for each measure to assess the reproducibility: the intraclass correlation coefficients (ICC) and the intra- and inter-subject coefficients of variation (CV_{intra} and CV_{inter}) (Bland and Altman, 1996; Chen et al., 2011; Pinto et al., 2016). ICC is one of the most important methods to assess the reliability of a measure, reflecting both intra- and inter-subject variability. It allows evaluating how measurements derived from the same subject are reproducible across sessions, taking into account the intra/inter-subject variability as follows:

$$ICC = \frac{\sigma_{bs}^2}{\sigma_{bs}^2 + \sigma_{ws}^2} \tag{11}$$

where σ_{bs} is the between-subject standard deviation and σ_{ws} is the within-subject standard deviation for repeated measurements. ICC levels and reliability can be evaluated using the following recommendations: poor (<0.4), fair (0.41–0.59), good (0.60–0.74) and excellent (>0.75) (Fleiss, 1981; Cicchetti, 2010).

The CV_{intra} (within-subject CV) measures the variability between sessions of the same subject, reflecting both physiological variations that can occur in a natural way and possible measurement errors (Pinto et al., 2016). CV_{intra} was computed as:

$$CV_{intra} = \frac{\sigma_{ws}}{\mu} \cdot 100\,[\%] \tag{12}$$

where μ is the mean value of the parameter across subjects and sessions (overall mean). Since only two measurements per subject

were available, σ_{ws} can be calculated as:

$$\sigma_{ws} = \sqrt{\left(\frac{\sum_{i=1}^{k}\left(a_{itp1} - a_{itp2}\right)^2}{2 \times k}\right)} \quad (13)$$

where k is the number of subjects, and $a_{itp1}$and a_{itp2} are the measurements for subject i on test (*tp1*) and retest (*tp2*) sessions, respectively (Bland and Altman, 1996).

Finally, the CV_{inter} (between-subject CV) measures the stability across the group, reflecting the inter-individual variability. For each index, the CV_{inter} was initially computed for each session as follows:

$$CV_{inter_j} = \frac{\sigma_{tpj}}{\mu_{tpj}} \cdot 100\,[\%] \quad (14)$$

where *tpj* represents the session j ($j = 1, 2$), μ_{tpj} and σ_{tpj} are the mean and standard deviation values, respectively, calculated across all the subjects for the considered session *tpj*. The representative CV_{inter} measure was then computed as the mean of the CV_{interj} from the two sessions.

For biological measurements from MRI, $CV_{intra} \leq 10\%$ and $CV_{inter} < 15\%$ are considered as acceptable (Heiervang et al., 2006; Marenco et al., 2006).

For tract-based measures, ICC and CV_{intra} were a single measure for each loop, as all the connections belonging to the corresponding network were grouped for providing a global representative measure of network reproducibility, in line with (Brusini et al., 2016). Conversely, the representative CV_{inter} metric was first computed for each tract and then summarized for each loop by the mean ± standard deviation (SD) values across connections. This allowed to evaluate the stability across subjects and also the inter-subject variability across the different structural links of each network.

For region-based analysis, CV_{intra} and ICC were computed for each ROI individually (mean ± SD values across GM ROIs), while the representative CV_{inter} metric was initially calculated for each region and then reported as mean ± SD values across GM ROIs. This again allowed to appreciate the variability across the GM structures.

Statistical Analysis on Tract-Based Outcomes–Patients and Controls

After the reproducibility analysis, the outcome measures from tract-based analysis were assessed for depicting possible differences between patients and controls and determining the discriminative power of the different indices. In particular, for each index and network, the percentage absolute changes in mean values between *tp* (Δ_{tp}) were calculated as in Brusini et al. (2016).

Since the Kolmogorov–Smirnov normality test confirmed the normal distribution of the percentage values, statistical comparisons with the unpaired *t*-test were performed to detect significant differences between delta changes in controls (Δ_{tp12c}) and Δ_{tp12}, Δ_{tp23}, Δ_{tp13} calculated in the patient cohort. While in our previous work (Brusini et al., 2016) the False Discovery Rate (FDR) correction was applied to the statistical results, here a more conservative Bonferroni adjustment ($\alpha = 0.05$) was used to correct for multiple comparisons across indices. This approach was chosen in order to further strengthen the statistical findings and highly reduce false positive results.

In addition, in order to assess the predictive power of both tensor-derived and 3D-SHORE-derived indices, different linear regression models were considered and their performance in predicting the clinical motor outcome at 6 months (NIHSS at *tp3*) was tested. First, a linear regression model including only clinical information at baseline (age, stroke size, and NIHSS motor scores at *tp1*) as predictors was calculated for reference. Then, for each network, three types of regression models were built and compared as opposed to what was done in our previous work (Brusini et al., 2016), where a single model combining clinical information with a set of 3D-SHORE-based descriptors (GFA, PA, R, RTAP, RTOP, RTPP) was considered. In detail, the following models were considered:

1) *Tensor-based model (TBM)*: the average across all the connections of the considered loop at *tp1* was calculated for each index (MD, FA) and both mean values were included as predictors along with age, stroke size and NIHSS at *tp1*.
2) *3D-SHORE-based model (SBM)*: the average across all the connections of the considered loop at *tp1* was calculated for each index (GFA, PA, RTAP, RTPP, MSD) and these mean values were included as predictors along with age, stroke size and NIHSS at *tp1*.
3) *Global microstructural model (GBM)*: all the indices at *tp1* (both tensor-derived and 3D-SHORE-derived) were included as predictors, after having calculated their individual mean value across all the connections of the considered loop. No clinical information was included.

All the linear regression analyses were performed in SPSS, version 18 (SPSS, Inc., Chicago, Illinois), setting $p = 0.05$ as significance threshold of the overall *F*-test to determine whether the regression model significantly predicts the clinical motor outcome. A backward elimination strategy was utilized to obtain a parsimonious regression model. In details, a full model that includes all the predictor variables was initially created. Then, each subsequent step removed the least significant variable in the model until all the remaining variables had individual *p*-values smaller than the selected criterion. The default criterion in SPSS (based on the probability of F-to-remove, with $pout = 0.10$) was chosen for deleting a predictor that had little or no influence on the dependent variable. For each optimal model, the calculated R^2 value was adjusted for the number of predictors included, in order to perform a valid comparison across the different regression models and penalize the addition of extraneous predictors. The following equation, as implemented in SPSS (Ezekiel, 1930; Kirk, 1996), was applied:

$$R^2_{adj} = 1 - \frac{(1 - R^2)(N - 1)}{N - k - 1} \quad (15)$$

where N is the sample size and k is the number of predictors in the corresponding model, i.e., those that were not deleted by the backward selection process, excluding the constant.

Statistical Analysis on GM Region-Based Outcomes–Patients and Controls

In order to compare the GM region-based measures, a three-way mixed (within-between) analysis of variance (ANOVA) was firstly performed for each microstructural index to test the significance of different factors, using the mean index value as dependent variable. Three independent variables were considered: Time with two levels and Region with thirty-six levels (within-subject factors) plus Group with two levels as between-subject factor. In addition, a further two-way repeated measures ANOVA was performed on the patient group data in order to assess for the presence of longitudinal changes in contralateral GM structures across all temporal scales. Also in this case the mean value for each index was used as dependent variable in the corresponding ANOVA, while two independent variables were included: Time with three levels and Region with thirty-six levels.

For each ANOVA, Mauchley test was used to assess the sphericity assumption and Greenhouse-Geisser epsilon adjustments for non-sphericity were applied where appropriate. *Post-hoc* tests adjusted for multiple comparisons with the Bonferroni correction were used when significant interactions were found. For all statistical tests, performed in SPSS v.18, $p < 0.05$ was considered to be significant.

RESULTS

Qualitative Assessment of dMRI-Based Indices

Classical tensor-derived and 3D-SHORE-derived indices were estimated in all subjects and *tp*. **Figures 2**, **3** show the different maps calculated for each index across times in a representative control and a representative ischemic stroke patient, respectively. For ease of visualization and for the sake of clearer presentation, the three anisotropy measures were normalized to the respective maximum index value, while the square-root of the RTAP maps was extracted to report the values in the same range of RTPP, as in Avram et al. (2016).

All the anisotropy measures as well as RTAP and RTPP maps revealed high values in WM, while lower values were reached in GM and especially in voxels with strong CSF contribution. The opposite pattern was visible in MD and MSD maps, where WM appeared to be hypointense due to restricted diffusion while higher values were reached in GM and CSF tissues. These patterns were consistent across subjects and temporal scales. Comparing GFA, PA, and FA, both control and patient representative slices revealed a higher WM/GM contrast for the normalized 3D-SHORE-derived anisotropy measures that also appeared to be less noisy and more uniform throughout WM in comparison to the classical FA. Moreover, FA appeared to have lower values in regions with large fiber orientation dispersions where the single tensor representation precludes the possibility to cope with complex structures leading to drops. RTAP maps were hyperintense in regions of coherently packed WM fibers, while RTPP was similar in GM and WM tissues. Finally, MSD, and MD visually demonstrated a correlated behavior, appearing brighter in regions where water particles are free to diffuse like ventricles and darker in regions of restriction like WM.

In the stroke patient reported in **Figure 3**, a large ischemic lesion can be appreciated in the left hemisphere (cortico-subcortical areas) and the modulation of tissue microstructure is visible across the different *tp*. The lesion was hypointense in GFA, PA, MSD, FA, and MD at *tp1*, while markedly brighter than the other tissues in RTAP and RTPP. After 1 month from the injury (*tp2*), the contrast was reversed for these two indices, such that the lesion appeared hypointense as in the anisotropy measures, where hyperintensities within the lesion became visible in MSD and MD. Such a trend persisted at 6 months after the initial brain damage (*tp3*).

For all the subsequent quantitative analyses, we investigated the contralateral hemisphere only, where microstructural changes after stroke might be subtle and not visually detectable.

Test-Retest Reproducibility on Healthy Controls

In terms of test-retest reproducibility, tract-based results highlighted excellent consistency across sessions in the three networks for tensor-derived as well as 3D-SHORE indices, with ICC > 0.8 in almost all cases and values close to unity for the SUBCORT loop (Supplementary Table 3). Indeed, the highest ICC was obtained for PA in SUBCORT (ICC $= 0.96$), followed by MSD in the same network (ICC $= 0.95$). Conversely, MSD together with RTPP reached the lowest values in CORT, although still amenable to be judged as having good reliability (ICC $= 0.67$ and ICC $= 0.59$, respectively). This high reliability was matched with high intra-subject stability across sessions as measured by CV_{intra} values, well below 10% and, in most of the cases, also below 5%. The lowest stability was found in the CC loop for MD ($CV_{intra} = 7.7\%$), while MSD resulted to be the index with the highest stability in all the loops, reaching a remarkable 1.1% within-subject variability in the SUBCORT network.

GM region-based reproducibility results are reported in **Table 2** in terms of mean and SD values across ROIs. RTAP, RTPP, MSD, and MD reached excellent consistency, with mean ICC > 0.90 and very low SD across ROIs (<0.10). Conversely, all the anisotropy measures showed only good reliability and more variability across the different GM structures. This was further confirmed by the CV_{intra} measure, reporting mean values $<10\%$ in all cases albeit higher for GFA, PA, and FA in comparison to the other microstructural indices. Also in this case, MSD reached the lowest variability values with a limited spread around the mean.

Figure 4 shows the inter-subject variability results (CV_{inter}) represented as mean $\pm$ SD across all the connections of a given loop for tract-based analysis, and across ROIs for region-based analysis on GM. As expected, the between-subject variability was higher than the within-subject, although the mean CV_{inter} values were $\leq 15\%$ in all cases. Regarding the network analysis, similar patterns in the three loops were observed for each index, with RTPP and MSD featuring the lowest variability across subjects (RTPP: $CV_{inter} = 4.67 \pm 2.53$ % in CORT; MSD: $CV_{inter} = 2.36 \pm 1.82$ % in SUBCORT). Conversely, RTAP was the index showing

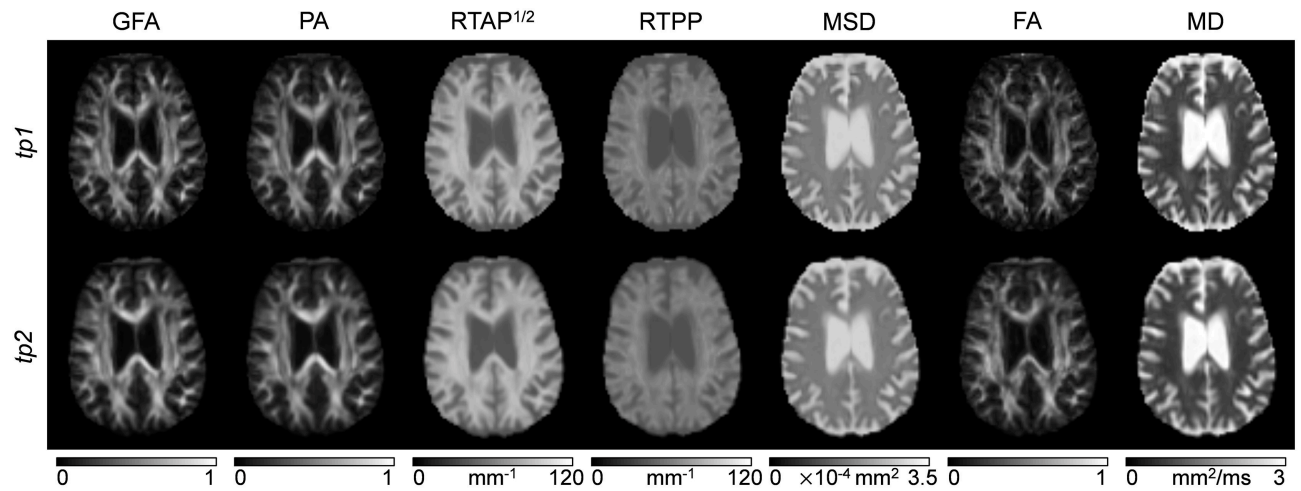

FIGURE 2 | dMRI-based indices on a representative control. Axial slices of a representative control are reported for each index (columns) and each time point (rows). Images are displayed in radiological convention.

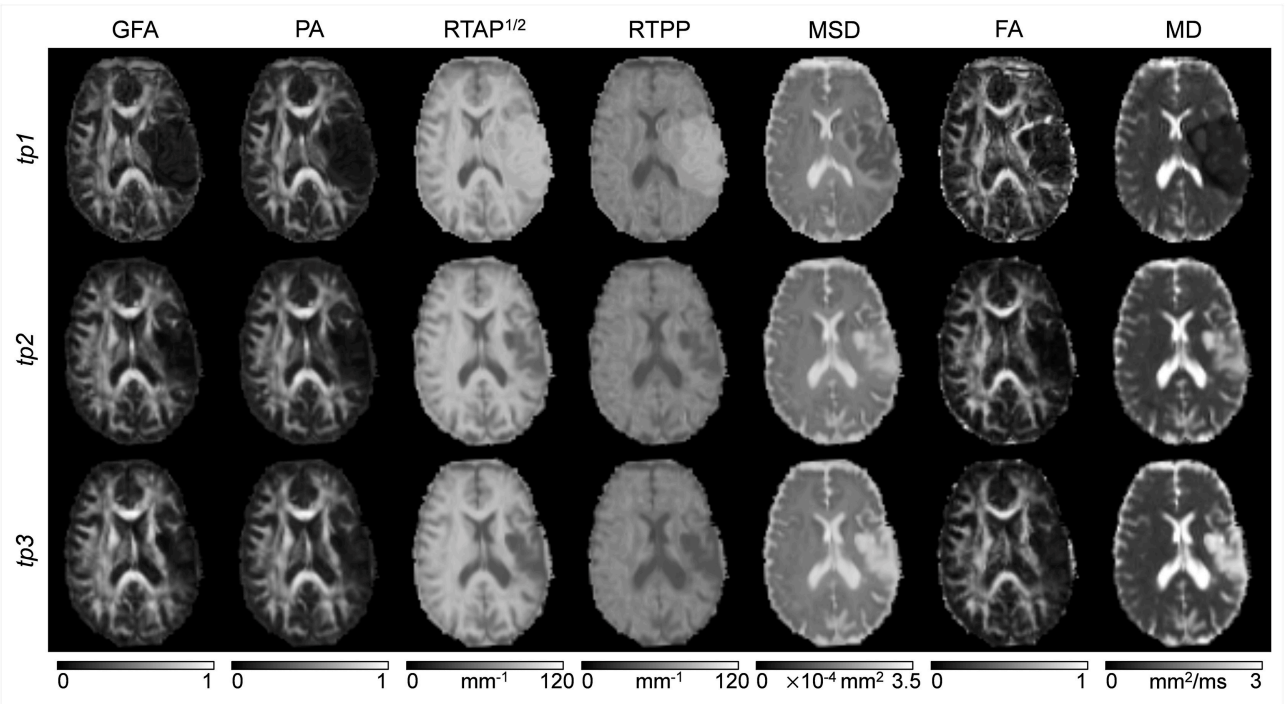

FIGURE 3 | dMRI-based indices on a representative patient. Axial slices of a representative patient (ischemic stroke in left cortico-subcortical areas) are reported for each index (columns) and each time point (rows). Images are displayed in radiological convention.

more variability in all loops, especially in CC. The same trend was observed in the ROI-based analysis on GM, where the CV_{inter} values were similar to those resulting from tract-based analysis with RTPP and MSD reaching the highest stability (RTPP: $CV_{inter} = 4.87 \pm 1.34$ %; MSD: $CV_{inter} = 6.49 \pm 1.72$ %). It is worthy of note that all the values were within the recommended 15% range (Heiervang et al., 2006; Marenco et al., 2006), even though tensor-derived indices featured relatively lower stability across subjects in GM, with the highest values reached by FA ($CV_{inter} = 11.68 \pm 3.09$ %).

Quantitative Assessment on Tract-Based Outcomes–Patients and Controls

For each index and network, the mean of the percentage absolute changes between *tp* is reported in **Figure 5** along with SD across subjects. The *p*-values resulting from the statistical analysis are

shown as stars with three levels of significance ($^{*}p < 0.05$, $^{**}p < 0.01$, $^{***}p < 0.001$). In all cases, data from the control group confirmed the limited percentage changes between time points, with mean values <5%, in agreement with the reproducibility results from the previous section.

Regarding the CC network, all the anisotropy measures (GFA, PA, and FA) reached the highest significance when comparing Δ_{tp12c} and Δ_{tp12} as well as Δ_{tp12c} and Δ_{tp13} ($p < 0.001$). Moreover, GFA and FA showed higher significance than the other microstructural indices in the comparison between Δ_{tp12c} and Δ_{tp23} ($p < 0.01$). MSD and MD highlighted the same patterns across time and the same statistical differences, with no significant changes between Δ_{tp12c} and Δ_{tp23}. In the CORT network, only few significant differences were detected between controls and patients (Δ_{tp12}) by GFA and RTAP, while for all the other indices the longitudinal changes, although appreciable, did not reach the statistical threshold. Conversely, several significant differences were detected again in the SUBCORT loop by all the indices at multiple time scales, except for RTAP and RTPP which did not depict significant changes between Δ_{tp12c} and Δ_{tp23}. All the anisotropy measures confirmed the presence of marked changes over time involving also this network, with similar patterns to the findings shown in CC.

Extending the preliminary analyses on predictive models reported in Brusini et al. (2016), the tract-based results in patients were further used to predict the clinical motor outcome at *tp3* by relying on several regression models. The reference linear regression model including only clinical variables at baseline (age, stroke size and NIHSS motor score at *tp1*) and avoiding microstructural indices could predict the NIHSS outcome at *tp3* with low correlation ($R^2 = 0.546$; adjusted $R^2 = 0.489$; $p < 0.05$). The TBM, enclosing MD-FA at *tp1* plus the clinical variables, allowed increasing the prediction capability of the reference model in the CORT and SUBCORT networks (**Figure 6**, first row). In detail, the TBM for SUBCORT presented the best performance ($R^2 = 0.975$; adjusted $R^2 = 0.955$; $p < 0.001$) holding MD, FA, stroke size and age as relevant predictors. In the case of the CORT network, a higher correlation than the reference model was found with the TBM retaining only stroke size and MD as significant predictors ($R^2 = 0.700$; adjusted $R^2 = 0.614$; $p < 0.05$). Conversely, the TBM for CC did not include any microstructural index, returning the reference model as the optimal one.

The SBM, embedding the five 3D-SHORE indices at *tp1* plus the clinical variables, reached the highest correlation in the SUBCORT network ($R^2 = 1$; adjusted $R^2 = 0.998$; $p < 0.001$) (**Figure 6**, second row). The optimal predictive model held clinical variables plus GFA, MSD, RTPP, and PA as significant predictors. The SBM for CORT excluded all the microstructural indices, leading to the reference model as the optimal one. Finally, in the CC network the SBM presented a slightly lower correlation than the reference ($R^2 = 0.454$; adjusted $R^2 = 0.385$; $p < 0.05$) but highlighting RTPP as the only significant predictor.

The GBM, including only the dMRI-based indices, allowed to substantially increase the capability to timely predict the motor outcome compared to the clinical reference model (**Figure 6**, third row). In detail, the SUBCORT network provided again the highest correlation ($R^2 = 0.728$; adjusted $R^2 = 0.694$; $p < 0.01$) keeping only RTPP as significant predictor. The predictive

TABLE 2 | Reproducibility for gray matter (GM) outcomes.

	ICC	CV_{intra} %
GFA	0.63 ± 0.22	7.36 ± 2.96
PA	0.61 ± 0.24	6.82 ± 2.42
RTAP	0.91 ± 0.07	3.40 ± 1.63
RTPP	0.92 ± 0.07	1.73 ± 0.78
MSD	0.93 ± 0.09	1.97 ± 0.75
FA	0.66 ± 0.17	9.25 ± 3.59
MD	0.94 ± 0.08	3.09 ± 1.71

Results are quantified in terms of intra-class correlation coefficient (ICC) and intra-subject coefficient of variation (CV_{intra}) for all the indices. In particular, mean ± standard deviation values across all the considered GM regions are reported.

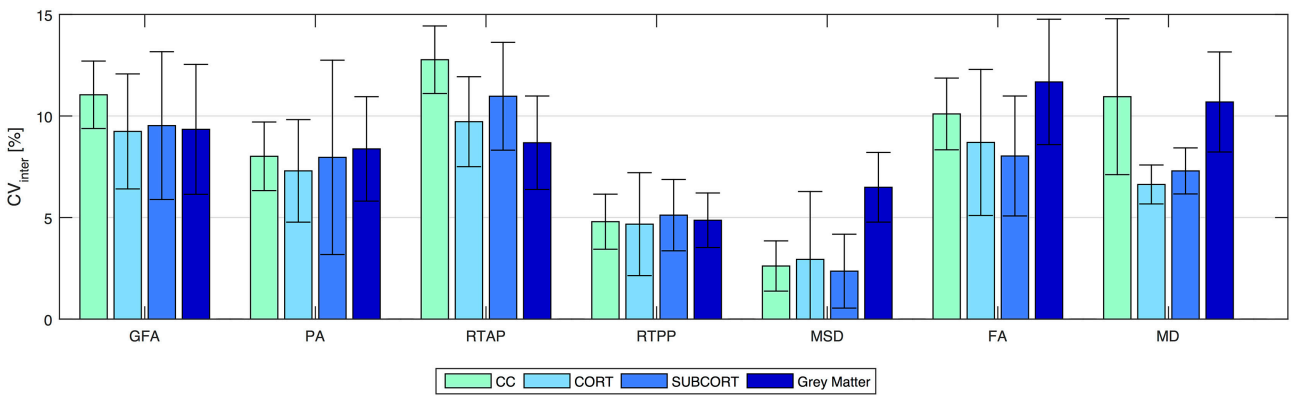

FIGURE 4 | Reproducibility in terms of inter-subject coefficient of variation (CV_{inter}) for all the indices and for all the outcome measures. Results are expressed as percentage and reported as mean ± standard deviation across connections (for tract-based) and regions (for region-based on gray matter), respectively. CC, transcallosal network; CORT, cortical network; SUBCORT, subcortical network.

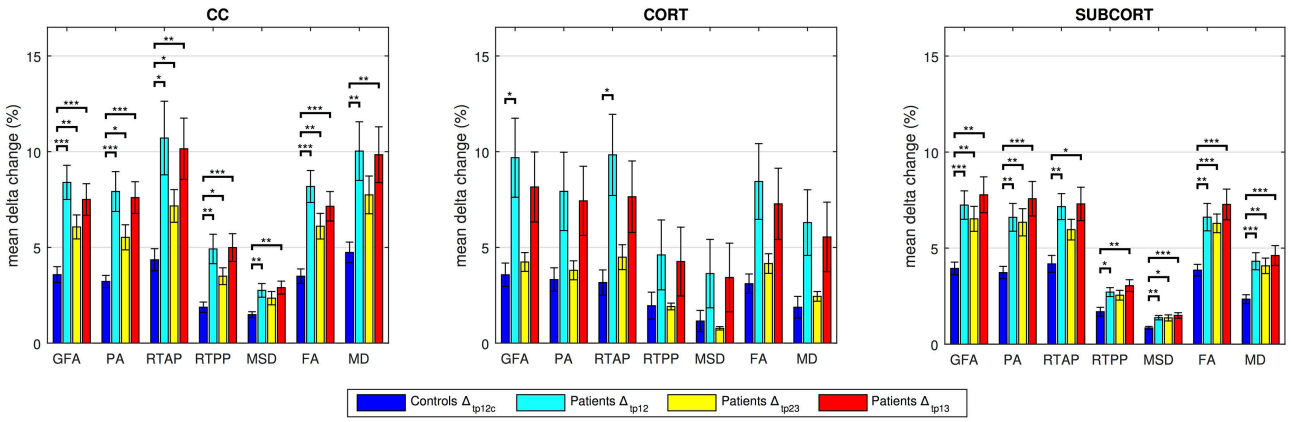

FIGURE 5 | Group-based analyses on controls and patients over time**.** Longitudinal changes in percent absolute values in controls and patients are reported. The significant differences between cohort distributions are indicated in figure (*$p < 0.05$, **$p < 0.01$, ***$p < 0.001$) for each index in transcallosal (CC), cortical (CORT), and subcortical (SUBCORT) networks. Mean ± standard deviation values across subjects are reported.

model for the CC network also featured high correlation ($R^2 = 0.713$; adjusted $R^2 = 0.631$; $p < 0.05$) maintaining MD and RTPP as predictors, while GFA, RTAP, and MD were retained in the predictive model for CORT. This network led to the GBM with the lowest correlation ($R^2 = 0.724$; adjusted $R^2 = 0.586$; $p < 0.05$), but still higher than the reference model. Further details on the predictive models and the retained predictors are reported in the Supplementary Tables 4.

Quantitative Assessment on GM Region-Based Outcomes–Patients and Controls

Regarding the control vs. patient analyses on the outcomes from the region-based quantification in GM tissues, the mixed ANOVA revealed a significant three-way interaction between Group, Time (TP) and Region (ROI) for all the anisotropy measures (GFA, PA, and FA) and RTPP. Details about these statistical results are reported in **Table 3**. For the four indices, *post-hoc* Bonferroni tests revealed significant between-group differences in several regions at both time scales, showing in these cases higher values in patients than controls (**Figure 7**). While the most widespread changes were detected in terms of anisotropy at *tp1*, four common regions were identified as significantly altered (Patients > Controls) also by RTPP. In detail, the inferior temporal gyrus (ITG) and the lateral occipital cortex (LOC) were in common at both *tp*, while the lateral orbitofrontal cortex (lOFC) and the middle temporal gyrus (MTG) presented high significance ($p \leq 0.01$) at *tp1* and *tp2* in GFA, PA, and RTPP and only at *tp1* in FA (**Figure 7**). RTPP changes were more visible at *tp2,* with several regions showing higher values in patients compared to controls and non-significant anisotropic differences. The remaining indices failed to reach a significant three-way interaction even though control vs. patient differences can be visually appreciated in **Figure 7A**. In particular, for RTAP a similar trend to the anisotropy measures was detected in all the regions, especially at *tp1* over motor areas and subcortical nuclei as PM, SMA, SC, M1 and Thal, Cau and Put (Patients > Controls). For MSD, while few ROIs presented relatively higher values in patients at *tp1,* there was an overall increase in all regions at *tp2* (Patients > Controls), except for the temporal pole where lower values were found over time in this group. Finally, MD patterns were in line with MSD results, although with less marked changes between groups.

Moving a step backward in the mixed ANOVA, all the indices except RTAP revealed a significant two-way interaction between Group and ROI confirming that, considering the overall time scales, there were differences in specific GM regions between the two groups (**Table 3**; Supplementary Figure 1). The anisotropy measures were highly consistent, with FA highlighting more widespread increased values in GM for patients as before. Finally, only GFA, PA, and FA revealed an overall significant main effect of Group (between-subject factor), as reported in **Table 3**.

Considering the longitudinal analysis on the patient measures only, again all the anisotropy indices along with RTPP and MD revealed a significant interaction between TP and ROI. In details, for GFA $F_{(70, 630)} = 1.61$, $p = 0.002$; for PA $F_{(70, 630)} = 1.52$, $p = 0.006$; for RTPP $F_{(70, 630)} = 1.47$, $p = 0.01$; for FA $F_{(70, 630)} = 1.92$, $p < 0.0001$; and for MD $F_{(70, 630)} = 1.76$, $p = 0.0003$ (Supplementary Table 5). *Post-hoc* Bonferroni tests (**Figure 8**) highlighted for the three anisotropy measures consistently significant differences over the lingual gyrus (LgG) for *tp1* vs. *tp2*, and in the medial orbitofrontal cortex (mOFC) for *tp1* vs. *tp3*. Moreover, FA presented LgG differences for *tp1* vs. *tp3*, and in the precuneus (PCN) for both *tp1* vs. *tp2* and *tp1* vs. *tp3*. In all these statistically significant changes, higher values were detected just after the stroke event (*tp1*) in comparison to *tp2* and *tp3*. Conversely, an opposite trend was found for RTPP detecting a single region [frontal pole (FP)] with higher values at *tp2* compared to *tp1*. For MD, despite the significant interaction no regions survived the Bonferroni corrections of the *post-hoc* paired tests (**Figure 8**). When using a less conservative approach [Least Significant Different (LSD) *post-hoc* tests], five regions, including PM, SC, and Thal, turned

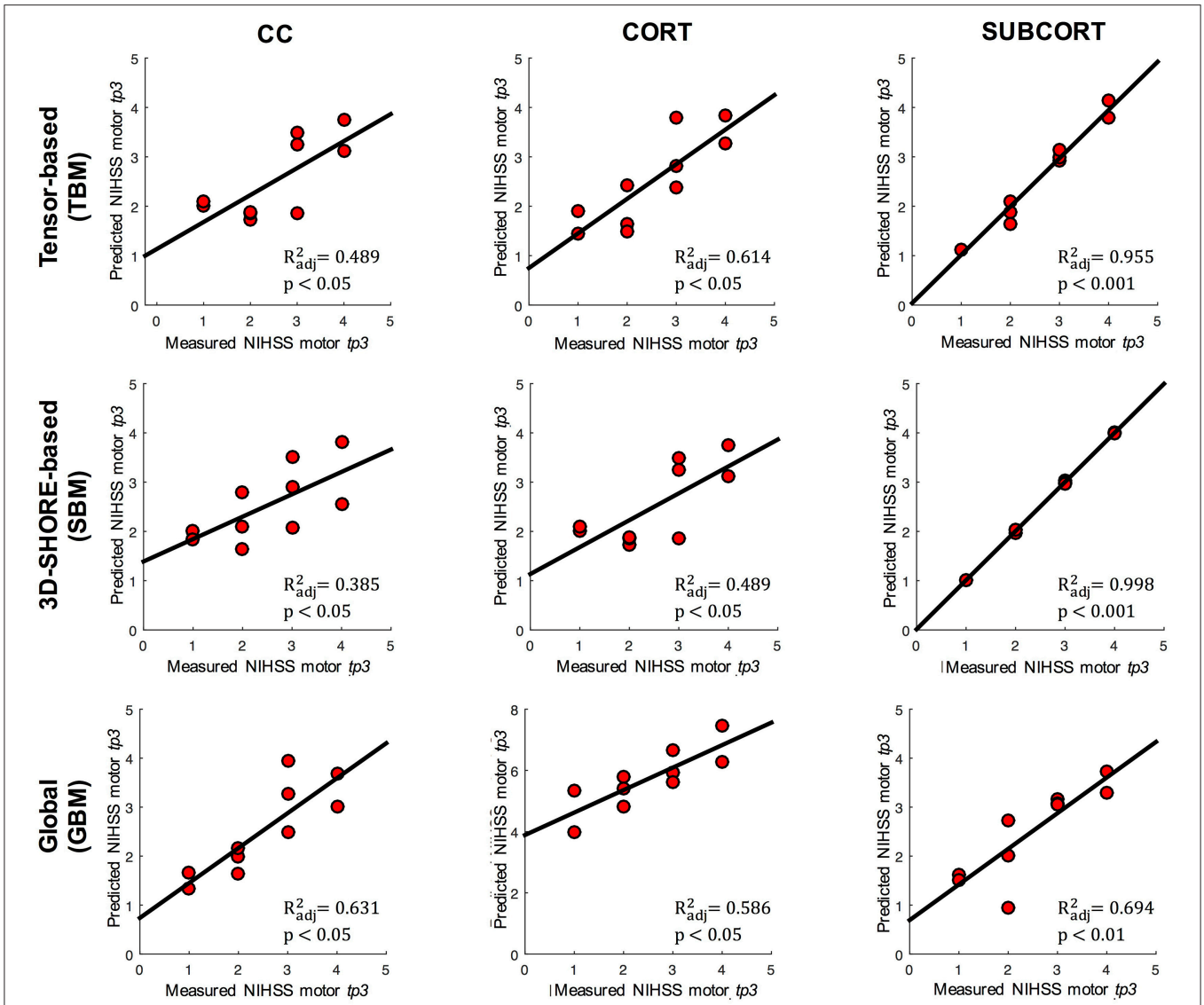

FIGURE 6 | Linear regression models. Representation of the measured and predicted NIHSS-motor score at *tp3* using tensor-based (TBM), 3D-SHORE-based (SBM), and global (GBM) predictive models. For each model, the adjusted R^2 and corresponding *p*-values are reported.

out to be significantly increased at *tp3* compared to *tp2* and *tp1* (Supplementary Figure 2). Applying LSD *post-hoc* tests also to the other indices, the anisotropy measures revealed more widespread regions of increased values in the early phase (*tp1*) in comparison to the other two time points, consistently with the results from the mixed ANOVA. GFA and PA, in addition, showed higher values at *tp3* compared to *tp2* over two motor regions, e.g., Put and M1, respectively. Finally, RTPP confirmed a significant increase over time (both *tp2* and *tp3*) in comparison to *tp1* in the FP region.

Regarding the other two indices that did not show a significant interaction (RTAP and MSD) and were thus precluded to be evaluated with *post-hoc* tests, a different trend was visible across time with a series of appreciable longitudinal differences (**Figure 8A**). In particular, RTAP revealed a similar behavior to the anisotropy measures, with higher values at *tp1* that decreased over time, especially at *tp3*. Conversely, MSD highlighted higher values over time, as in the case of MD, with marked visual increases at *tp3* over several regions (as PM, SC, FP, Thal, Put, Cau).

DISCUSSION

In this study, our results suggest that 3D-SHORE-based microstructural descriptors obtained from DSI data are capable to quantify the remodeling of WM tracts and GM regions involved in motor recovery after ischemic stroke. 3D-SHORE-based indices proved to perform similarly to the classical DTI indices (FA and MD) and revealed common patterns across the networks and ROI evaluated in the analyses.

TABLE 3 | ANOVA results (three-way mixed ANOVA) for the control vs. patient comparison of gray matter outcomes.

	Between-subject		Within-subject			
	Group		Group*ROI		Group*TP*ROI	
	F-ratio (1, 18)	*p*-value	F-ratio (35, 630)	*p*-value	F-ratio (35, 630)	*p*-value
GFA	6.205	0.023*	2.340	<0.001*	2.235	<0.001*
PA	6.256	0.022*	2.218	<0.001*	1.669	0.010*
RTAP	1.548	0.229	1.249	0.157	1.326	0.102
RTPP	2.064	0.168	2.152	<0.001*	1.843	0.003*
MSD	2.681	0.119	2.601	<0.001*	0.552	0.990
FA	7.346	0.014*	2.082	<0.001*	2.731	<0.001*
MD	0.186	0.671	1.825	0.003*	1.105	0.314

*The three independent variables were Group (between-subject factor), Time Point (TP) and Region (ROI) (within-subject factors), while the dependent variable was the mean index value. Group, along with Group*ROI and Group*TP*ROI interactions, are expressed in terms of F-ratio (degree of freedom, error) and p-values. *, significant values.*

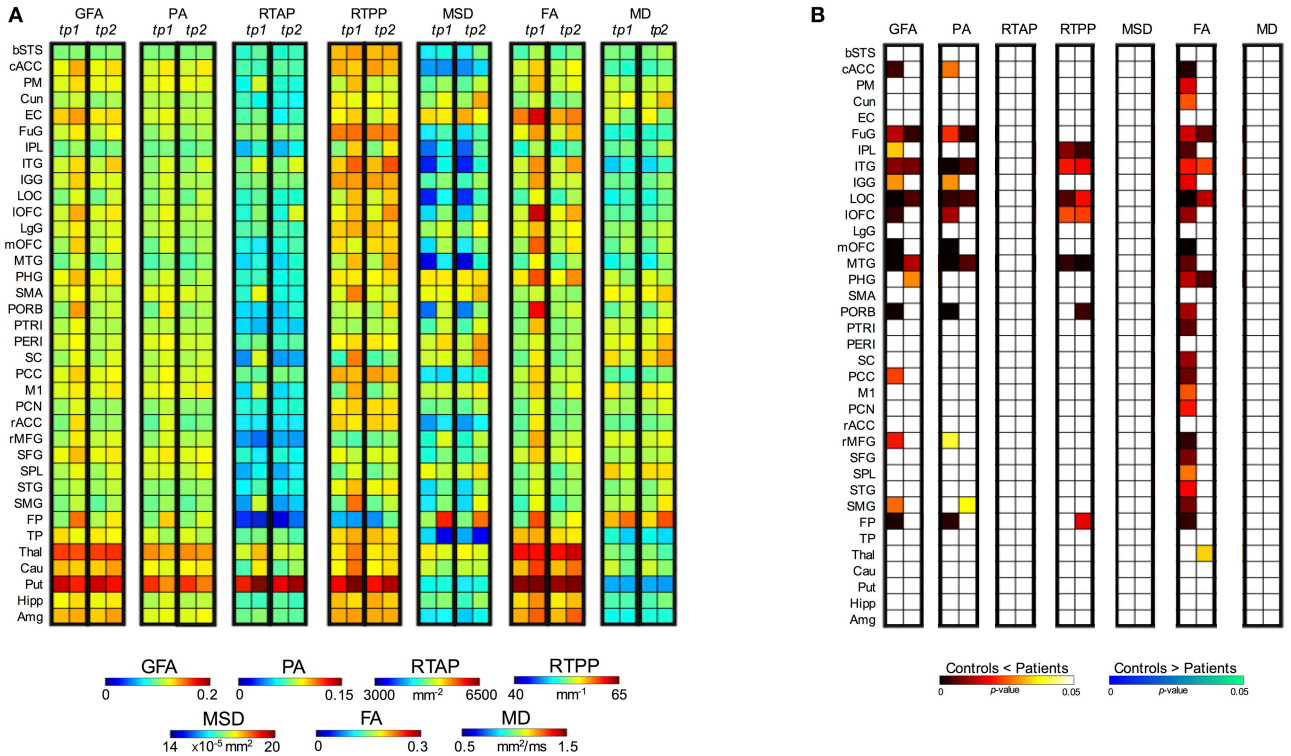

FIGURE 7 | *Post-hoc* test results for the three-way mixed ANOVA (controls vs. patients). **(A)** For each index and each time point (*tp*) block, the first column represents the mean values for the controls while the second column the mean values for the patients. **(B)** *Post-hoc* results expressed in terms of *p*-values for the significant interactions between Group, TP and Region (ROI). Two different colormaps are used to display the *p*-values for the ROIs with significant differences between control and patient mean values (hot: Controls < Patients; cold: Controls > Patients). These values ($p < 0.05$) are Bonferroni corrected for multiple comparisons.

Considering their performance and different nature, their combination in clinical studies would allow to provide a more detailed and specific tissue characterization, allowing to disentangle different conditions where tensor-based indices take the same values. For instance, DTI cannot distinguish between a reduction of FA caused by crossing fibers and one caused by a decrease of neural density in a voxel. Conversely, the joint exploitation of RTAP and RTPP can allow disentangling such ambiguity, as RTAP and RTPP both diminish in the case of neuronal density reduction, while RTAP decreases and RTPP increases for crossing fibers, as previously reported (Zucchelli et al., 2016a). In addition, the combination of tensor-based and SHORE-based indices in the linear regression models allowed to greatly increase their ability to predict the clinical motor outcome in all the considered networks. To the best of our knowledge, this is the first study focusing on the

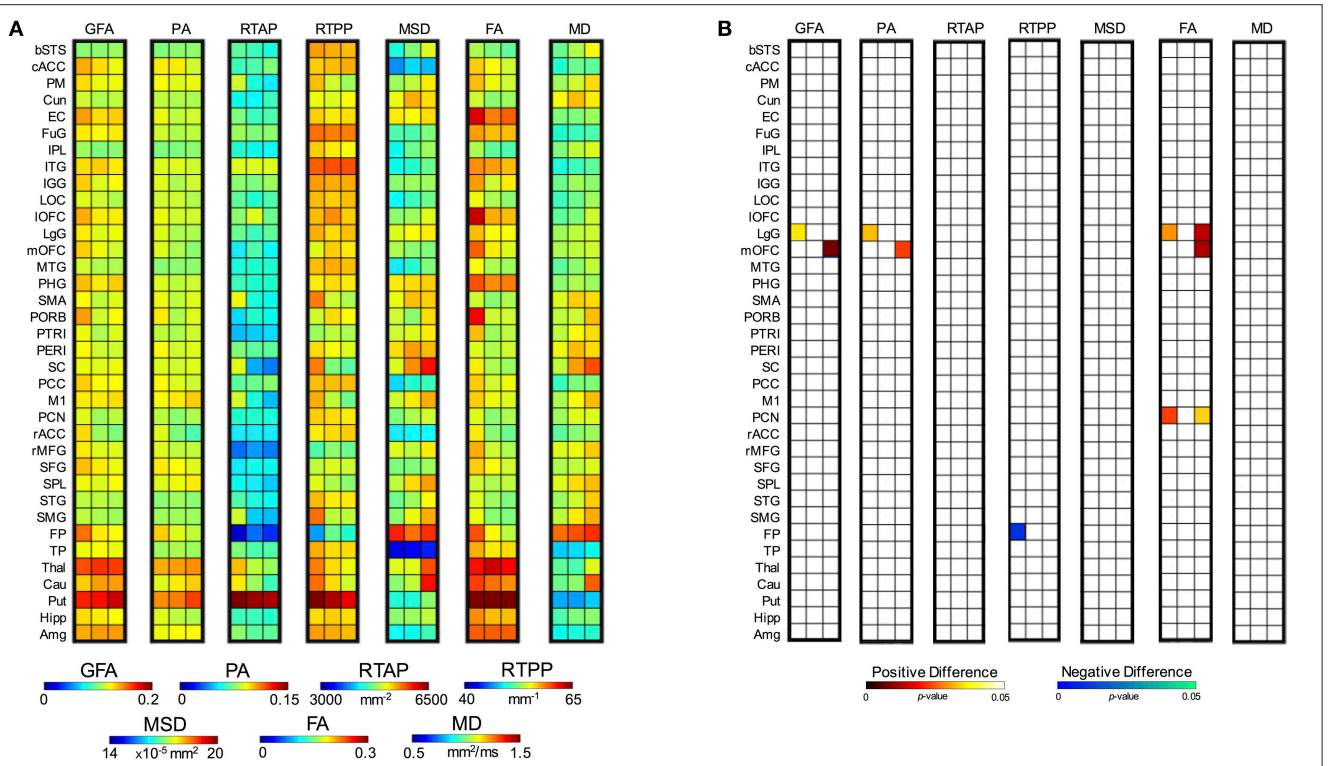

FIGURE 8 | *Post-hoc* test results for the two-way ANOVA for repeated measures on patients. **(A)** For each index, the first column represents the mean values at *tp1*, the second column at *tp2* and the third at *tp3*. **(B)** *Post-hoc* results expressed in terms of *p*-values for the significant interactions between Time Point (TP) and Region (ROI). Each column in the matrix refers to a specific statistical comparison between time scales, i.e. *tpi* vs. *tpj* with $i = 1, 2$ and $j = 2, 3$ (first: *tp1* vs. *tp2*; second: *tp2* vs. *tp3*; third: *tp1* vs. *tp3*). Two different colormaps are used to display the *p*-values for the ROIs with significantly different values between the considered time scales (hot: positive difference, $tpi > tpj$; cold: negative difference, $tpi < tpj$). These values ($p < 0.05$) are Bonferroni corrected for multiple comparisons.

quantitative comparison between 3D-SHORE-based and tensor-based descriptors in healthy subjects and in a patient population, aiming at demonstrating their behavior in different brain conditions/tissues and accomplishing an essential step toward their applicability as viable tissue markers.

Qualitative Assessment of dMRI-Based Indices

A growing body of literature is currently reporting the advantages of using multiple b-values in terms of both detecting fiber crossings (Sotiropoulos et al., 2013; Jeurissen et al., 2014) and recovering the tissue microstructure (Assaf and Basser, 2005; Zhang et al., 2012; Kaden et al., 2016). Because of these facts, nowadays, sampling schemes presenting higher b-values (as DSI and multi-shell) are becoming popular in research and started to appear also in clinical application. In order to fully exploit advanced dMRI datasets, reconstruction models that require multiple b-values such as the 3D-SHORE are necessary and therefore will become more common in this field. In this context, it is therefore necessary to provide an extensive characterization of these indices in describing tissues in physiological and pathological condition, as we did for stroke patients. In line with the findings firstly described by Özarslan et al. (2008, 2013), our results suggest that 3D-SHORE-based indices can provide a wide set of information, reflecting meaningful tissue properties as visually appreciable from the different maps. In particular, the values estimated in our healthy population for each index and their spatial distribution across the different anatomical structures appear to be in agreement with the available literature results (Özarslan et al., 2013; Avram et al., 2016; Zucchelli et al., 2016a), with a high consistency across subjects and time. These 3D-SHORE-based metrics are able to provide accurate microstructural information especially in brain regions characterized by complex architectures and geometries, to which the classical indices have low sensitivity. GFA and PA represent alternative measures of anisotropy to the classical FA, based on different mathematical formulations. Indeed, while GFA is a measure of the ODF variance, PA is derived from the EAP as a measure of its deviation from the isotropic component, and FA is computed from the tensor eigenvalues. In consequence, they provide different descriptors of the diffusion anisotropy with a high degree of correlation. However, GFA and PA are able to more properly quantify the anisotropy, presenting more contrast between the GM and regions with multiple fiber crossings in which the FA usually results in the same value. The two zero-displacement probability measures derived from SHORE reflect diffusion restriction in different directions, respectively radially (RTAP) and axially (RTPP) to the main diffusion direction (Özarslan et al., 2013). Consistently, RTAP maps exhibited high values in regions of coherently packed WM fibers, as the corpus

callosum which is less contaminated by partial volume effects. RTPP values were similar in both GM and WM tissues featuring less WM/GM contrast. This could suggest similar apparent axial diffusivity for WM and GM, even though the mapping of this measurement to real tissue microstructural properties is still an open issue. Finally, MSD and MD were consistently higher in regions featuring free diffusion, like the CSF and in areas with ischemic oedema (Alexander et al., 2007). These two indices are directly related via the Einstein diffusion equation as reported in the works of Wu and Alexander (2007) and Hosseinbor et al. (2013) and, accordingly, are visually correlated.

Evaluating qualitatively the longitudinal maps derived from the stroke patients, the microstructural indices exhibited a different behavior in the voxels belonging to the damaged area but with a consistent pattern. Indeed, while all the anisotropy measures revealed low values within the lesion that persisted over time, RTAP and RTPP shifted from initial hyperintensities toward hypointensities after 1 month from the event (*tp2*), highlighting an opposite trend for anisotropy and restriction. This stresses the complementarity of the information brought by those indices. Furthermore, considering their opposite trend in comparison to MSD and MD (from hypo- to hyperintensities) and the ischemic nature of the stroke, these findings support the hypothesis of Avram et al. (2016) according to which the zero-displacement measures are more specific biomarkers of the presence of restricting barriers to diffusion. Interestingly, RTAP and RTPP featured the highest values at *tp1* highlighting restricted diffusion in the lesion. Moreover, we found MSD to be more contrasted than MD inside the ischemic lesion in all cases. In particular, this index seems to identify and characterize different portions of the lesion, while MD appears to be more homogeneous in the same areas. Some patients (mainly those with extensive lesions) also revealed increased MSD values in the periphery. However, as this pattern was not confirmed in all cases, a larger sample size and more focused analyses on the stroke lesion would be necessary to draw robust conclusions on this aspect, possibly pointing at an inflammatory reaction which has been previously described (Wang et al., 2007; Kim et al., 2016). Finally, the heterogeneous patterns of RTAP, RTPP, and MSD visible within the lesion 1 week after stroke could be of help for distinguishing the ischemic core from the penumbra area. This issue deserves further investigation.

Reproducibility Analyses on Controls

The quantitative analysis of possible plasticity processes was focused on the contralateral hemisphere to the stroke. The contralesional GM and WM tissues have been widely considered as normal appearing, although the plasticity and compensatory processes that might take place in the non-injured areas are still not well understood. First of all, several complementary aspects were evaluated on healthy controls in order to quantify the reliability of these microstructural indices through a test-retest paradigm and their potentialities as novel biomarkers for stroke recovery. In particular, both 3D-SHORE-based and DTI indices exhibited high reproducibility, as quantified by ICC, and high stability, as quantified by intra/inter-subject CV parameters, on both tract and region-based outcomes.

Interestingly, for tract measures the 3D-SHORE index MSD, rarely considered in previous studies, showed the lowest intra-subject variability (CV_{intra}) in all cases, and the highest reliability (ICC) in CC and SUBCORT. Conversely, it revealed lower, although still good, ICC values in CORT along with RTPP that resulted to be the index with the lowest reliability in this network. This is possibly related to the fact that these two indices exhibited here a relatively higher within-subject SD for repeated measurements than in the other cases, which resulted to be closer to the between-subject SD values and therefore led to lower ICC values for this loop. Despite this consideration concerning the CORT loop only, the reliability and discriminative power of MSD and RTPP were not compromised as further proven by the other group-based analyses performed in this study. To note that beside Brusini et al. (2016), where some of these indices were initially evaluated along WM tracts, no other studies have quantified the reproducibility of 3D-SHORE-based metrics across subjects and sessions. Moreover, the previous reports aiming at quantifying the reliability of classical tensor-based measures generally focused only on few major fiber tracts (e.g., corpus callosum, cingulum, fornix and arcuate fasciculus) (Heiervang et al., 2006; Danielian et al., 2010; Wang et al., 2012) rather than considering specific brain networks with different sets of tracts. Despite this main difference, our findings are in line with the results of these studies, which demonstrated reliable measurements for FA and MD featuring both inter-session $CV_{intra} \leq 10\%$ and $ICC \geq 0.70$, with some variability related to the considered tract.

Regarding region-based outcomes, the reproducibility analysis in GM ROIs revealed a higher intra-subject variability for the three anisotropy measures (GFA, PA, and FA) in comparison to the other indices, with mean values still well within the 10% range, matched with a good reliability from ICC. This is possibly due to the lack of directed orientation in a tissue as GM (Basser and Ozarslan, 2009) and is in agreement with previous studies showing a two-three times higher variation of FA in regions of GM compared to WM structures (Vollmar et al., 2010; Bouix et al., 2013). Conversely, MSD and RTPP appeared again as featuring the lowest intra-subject variability and, along with MD, reached the highest ICC reliability values. The performance of FA for GM ROIs appears to be in line with previous reports evaluating DTI indices in this tissue (Veenith et al., 2013; Grech-Sollars et al., 2015), showing higher CV_{intra} values for the whole GM than for MD (8–11% vs. 2–5%, respectively) and a wide range of variation across the different GM structures (3.3–19.2%). Conversely, no studies have previously quantified the measurement precision of 3D-SHORE-based indices in GM regions, therefore our findings add an important step to the current literature on the topic and their reassurance in terms of reliability encourages their use for evaluating GM tissues as well.

Considering as additional reliability measure the between-subject variability, we found average CV_{inter} values well below the 15% threshold for both tract- and region-based outcome. Among the seven variables, RTPP and MSD generally had lower CV_{inter} than the other metrics with average values $\leq 6\%$. Tensor-based measures revealed overall lower between-subject stability than 3D-SHORE-based indices, especially in the GM ROIs where the

average values were around 10%. Previous studies have indicated FA and MD as the measures with lower CV_{inter} in different WM fiber tracts, for example Wang et al. (2012) reported average values in the range 2.4–7.6% for FA and 1.7–9.9% for MD respectively, while Grech-Sollars et al. (2015) showed mean inter-subject values <6% for the whole GM and WM regions (not tracts). Our results confirmed the good inter-subject stability for FA and MD but demonstrated that the 3D-SHORE-based indices improve on the classical measures in terms of between-subject variability in most of the cases. The latter observation demonstrated the gain in using a multi-b-values model such as 3D-SHORE. In particular, GFA and MSD were already defined the analogs of FA and MD for multi-b-values acquisitions by Hosseinbor et al. (2013). The combined high stability over time, relatively higher inter-subject variability ($CV_{intra} << CV_{inter}$) shown by the 3D-SHORE based indices, which is a pattern that can help detecting group differences between subjects, and excellent inter-session ICC values for most of the cases reinforce their potentialities as microstructural biomarkers for revealing longitudinal changes.

Quantitative Analyses on Tract-Based Outcomes of WM

Longitudinal group-based analyses were performed to statistically compare the mean absolute changes between time points calculated for each network. Regarding 3D-SHORE-based indices, the Bonferroni corrected *t*-tests revealed several highly significant differences between patients and controls in the SUBCORT and CC networks, also for the newly introduced MSD index. These findings further confirm and strengthen our preliminary results on a subset of 3D-SHORE indices (Brusini et al., 2016), where the *t*-tests were corrected for multiple comparisons with FDR. Conversely, a more conservative correction was employed here in order to quantify with additional confidence the longitudinal changes detected by the different indices and to reduce false positive results. Tensor-derived indices also exhibited similar patterns to 3D-SHORE descriptors, in terms of both evolutions of changes over time and level of significance.

In all cases, the highest levels of significance were reached in the patient group for the *tp1-tp2* and *tp1-tp3* relative changes, suggesting the presence of marked modifications in the contralateral hemisphere just 1 week after the stroke event (*tp1*). Interestingly, 3D-SHORE-based indices appeared to be the only capable of depicting statistically significant changes across the CORT loop. Indeed, only GFA and RTAP found a significant patient vs. control difference in the first phase (*tp1-tp2*), further highlighting the relevance of this time scale in the course of the disease.

These findings are in line with the few previous works reporting changes in the WM tracts of the contralesional hemisphere after stroke. Indeed, the possible modifications in the contralateral hemisphere with respect to the lesion have been scarcely investigated in literature, especially in humans, as these tissues have been widely disregarded as considered healthy and not directly involved in any rearrangement process (Maniega et al., 2004; Ozsunar et al., 2004). However, as the field moved forward, it became apparent that also the non-injured hemisphere undergoes marked changes and has a fundamental role in stroke recovery, as recognized by several authors relying on different MRI techniques (Ward et al., 2003; Gerloff et al., 2006; Crofts et al., 2011; Granziera et al., 2012b; Lin et al., 2015). Specifically, Crofts et al. (2011) showed how communicability values, derived from complex network analysis, were reduced in both ipsilateral and homologous contralateral regions. Moreover, Granziera et al. (2012a) reported significantly increased apparent diffusion coefficient (ADC) values in the infarct region (in both GM and WM tissues) moving from acute to chronic, whereas WM FA significantly decreased in the mirror regions. Our study extends the available literature on the topic and the novel biomarkers derived by the 3D-SHORE model possibly add new metrics that can be employed in this context (for a detailed overview see Kim and Winstein, 2017).

In addition, the predictive power of all the microstructural indices for patient motor outcome at *tp3* were investigated relying on the tract-based values and comparing several regression models for the prediction. Notably, among the three loops, the SUBCORT was the only one for which all the three types of models created (tensor-based model, 3D-SHORE-based model, global microstructural model) reached excellent performance. In particular, the 3D-SHORE-based model, combining a subset of these indices together with clinical patient information, led to the best linear regression model featuring a very high predictive power ($R^2_{adj} = 0.998, p < 0.001$), which slightly outperformed the optimal model we found in our previous work ($R^2_{adj} = 0.988$, $p = 0.009$) (Brusini et al., 2016). The set of indices in the optimal model of this work embeds MSD, suggesting that this index holds a higher potential in probing stroke-induced microstructural changes during the early phase.

The model using all the microstructural indices led to the best performance in the SUBCORT loop, reaching the highest correlation score ($R^2_{adj} = 0.694$, $p < 0.01$) and keeping RTPP as key predictor. The relevance of RTPP for subcortical WM tracts appears to be coherent with another observation of Avram et al. (2016) according to which RTPP is very sensitive to deep structures, showing higher intensity in nuclei like thalamus. RTPP also highlighted high predictive power in CC, contributing to the optimal model for both the 3D-SHORE-based and global model, in combination with MD in this latter case. These results, jointly with the high precision and the ability to detect significant changes between patients and controls, stress the potential of this index in the considered task.

Quantitative Analyses on ROI-Based Outcomes of GM

Besides evaluating the performance of the different indices along the WM connections of specific brain networks, we performed a quantitative comparison of their patterns within contralateral GM regions. GM tissue changes related to the disease are generally quantified by volume or density analyses and are very rarely investigated with dMRI-based indices. A growing body of literature is emerging to endorse the use of dMRI techniques for detecting microscopic changes in GM in different disorders.

Indeed, the analysis of diffusivity GM changes using MD has shown to be promising for detecting abnormalities in Alzheimer disease (Weston et al., 2015) and multiple sclerosis (Ceccarelli et al., 2007). GM FA alterations were also demonstrated in schizophrenic patients in Situ et al. (2015), reporting increased MD and decreased FA values in patients compared to controls. In stroke patients, studies in GM are less consistent and generally consider the tissues in the contralateral hemisphere as normal appearing, although regions remote (upstream or downstream) from the infarct have been demonstrated to undergo marked changes over a time course of 2 days to 1 year (Sotak, 2002). In one of these studies using the contralateral part as reference, Maniega et al. (2004) showed a trend of increased MD/decreased FA values within the lesion, which just started the first week from the event.

In our study, the longitudinal analyses on the patient group demonstrated a similar pattern but in the contralateral hemisphere, revealing an increase in MD values over time which mainly involved GM motor regions. Conversely, FA exhibited an initial widespread increase at *tp1* over temporo-frontal and motor areas, followed by a gradual decrease toward normality at *tp3*. This was further confirmed by the group-based comparisons with ANOVA, highlighting in most of these regions significantly higher FA values at *tp1* in patients vs. controls, whereas the increased pattern remained restricted to few ROIs when *tp2* values were evaluated. Similar patterns of alterations were detected also by SHORE-based indices, in particular by GFA, PA, RTPP and MSD. The group comparisons 1 week after the stroke revealed several GM regions (cACC, FuG, IGG, mOFC, PORB, rMFG, FP, ITG, LOC, IOFC, MTG) in which the patients exhibit significantly higher values for all the anisotropy indices (GFA, PA, FA) with respect to the controls. Considering that in the same regions, at the same time point, the MD and MSD appear to be increasing (**Figure 7A**), although not significantly, we can speculate that we are observing a general increase of the diffusivity along the main diffusion direction in the GM. More difficult to interpret is the simultaneous increase of the RTPP in some of these regions (ITG, LOC, IOFC, MTG). RTPP is generally inversely proportional to anisotropy in WM, e.g., RTPP is low in single fiber bundle areas such as the CC, and higher in crossing regions (Özarslan et al., 2013; Avram et al., 2016; Zucchelli et al., 2016a). Understanding the possible causes of this contemporary increase of RTPP and anisotropy in the GM will be one of the aims of our future works.

Contralateral changes in GM involved not only regions in the motor systems, but also areas playing an important role in cognition and behavior, as the FP and frontal areas, supporting the hypothesis of extensive rearrangements during stroke recovery. These indices therefore confirm their potentialities in describing not only WM but also GM properties, with high reliability and discriminative power. However, RTAP and MSD, which resulted to be suitable to characterize WM tracts in all the networks, appeared to be less sensitive to GM changes. Indeed, these indices failed to highlight statistically significant differences in the GM areas, especially when comparing the patient data over time. However, they deserve further investigations considering their good stability over time and their physiological relevance.

It is worth mentioning that the impact of partial volume effects was minimized by restricting the analysis to voxels where the GM contribution was above the 95%. This further enhances the hypothesis of extensive contralateral changes involving also the GM, reducing the contamination by other tissues.

As a side note, we also extracted for each patient and time point the average volumes of GM ROIs (results not shown). However, when statistically compared by means of a two-way repeated measure ANOVA, no significant changes were detected, possibly because of the small sample size and the limitations of such morphometric measure that might be not sensitive enough to subtle changes in the contralateral hemisphere. A larger sample size and more sophisticated analyses, for example based on cortical thickness measures or voxel-based morphometry, might be more suitable for depicting GM longitudinal changes following stroke, as often done in literature (Stebbins et al., 2008; Brodtmann et al., 2012). Our results, though preliminary, support the hypothesis that SHORE-based indices might hold the potential of revealing GM plasticity processes in the contralesional stroke area. We are aware of the fact that the interpretation in terms of geometrical restriction of the diffusion of the SHORE-derived indices in GM is prone to criticism because the real tissue architecture cannot be directly mapped to the underlying reference model (i.e., the pore). However, the fact that differences across time within a patient population and across groups can be detected using such indices provide evidence in favor of their exploitability as potential numerical biomarkers for GM plasticity in disease, leaving their interpretation in terms of microstructural properties an open issue.

Some limitations have to be acknowledged. This work has to be considered as a preliminary comparison between DTI and SHORE-based EAP derived indices in stroke. Here, we considered only the two most used DTI derived indices (FA and MD) and some of the principal EAP derived indices (RTAP, RTPP, MSD, PA, GFA). However, it will be interesting to extend the analyses to further indices that can be derived, e.g., the radial and axial diffusivity for the DTI, RTOP and the MAP-MRI non-gaussianity for the EAP. Moreover, our findings are based on the comparison between 10 healthy subjects and 10 ischemic stroke patients. A higher number of subjects would be necessary in future studies to fully exploit the potentialities and discriminative/predictive power of these rather novel indices. In particular, the linear regression analyses have to be carefully evaluated bearing in mind they are preliminary, although encouraging, findings. Indeed, the limited sample size precluded the possibility of identifying the optimal model in a subset of the population and testing it in a different validation cohort, as normally does in the machine learning/classification field. Moreover, a large number of predictors was initially included in the models, possibly leading to over-fitting problems that should be carefully considered when dealing with a limited number of subjects. Adding more data will allow to increase the power of the statistical analyses performed in this work and to further validate the promising findings about contralateral WM and GM changes suggesting the presence of plasticity processes.

CONCLUSIONS

In conclusion, this work provided new evidence in favor of the suitability of dMRI-based microstructural indices for probing WM modifications and highlighted their potential as descriptors of microstructural feature changes in GM in ischemic stroke patients. To the best of our knowledge this is the first attempt of using 3D-SHORE-derived indices for studying microstructure in GM in both controls and patients, contributing a first step in bridging WM and GM diffusion signal modeling. In particular, the RTPP seems to be able to convey relevant information while being consistent across groups and time.

From the clinical point of view, our results provide additional evidence in favor of the hypothesis of the contralateral remodeling after stroke. The 3D-SHORE-derived indices performed as well as classical tensor-derived indices (FA and MD), achieving a high predictive power for clinical outcome over cortico-subcortical connections and a good discrimination between patients and controls at different time scales, further confirming their viability in ischemic stroke. Their combination can allow to convey a more detailed microstructural description, marking a step forward in the definition of a novel family of biomarkers. Finally, the detection of significant changes in GM across groups and in the patient longitudinal comparison provides a new perspective along the path of characterizing disease-related microstructural modulations which deserves further investigation.

AUTHOR CONTRIBUTIONS

IBG and GM conceived and designed the experiments, interpreted the results of experiments and wrote the manuscript. IBG performed part of the statistical analyses. LB and SO analyzed the data and drafted the manuscript. MZ wrote the code for deriving all the indices, interpreted the results and drafted the manuscript. CG was involved in the design of the study and in data acquisition, interpreted the results of experiments, and drafted the manuscript.

SUPPLEMENTARY MATERIAL

The Supplementary Material for this article can be found online at: https://www.frontiersin.org/articles/10.3389/fnins.2018.00092/full#supplementary-material

REFERENCES

Alexander, A. L., Eun Lee, J., Lazar, M., and Field, A. S. (2007). Diffusion tensor imaging of the brain. *Neurotherapeutics* 4, 316–329. doi: 10.1016/j.nurt.2007.05.011

Assaf, Y., and Basser, P. J. (2005). Composite hindered and restricted model of diffusion (CHARMED) MR imaging of the human brain. *Neuroimage* 27, 48–58. doi: 10.1016/j.neuroimage.2005.03.042

Avram, A. V., Barnett, A. S., and Basser, P. J. (2014). "The Variation of MAP—MRI Derived Parameters Along White Matter Fiber Pathways in the Human Brain," in *ISMRM 22nd Annual Meeting*, (Milan), 2587.

Avram, A. V., Sarlls, J. E., Barnett, A. S., Özarslan, E., Thomas, C., Irfanoglu, M. O., et al. (2016). Clinical feasibility of using mean apparent propagator (MAP) MRI to characterize brain tissue microstructure. *Neuroimage* 127, 422–434. doi: 10.1016/j.neuroimage.2015.11.027

Basser, P. J., Mattiello, J., and Le Bihan, D. (1994a). Estimation of the effective self-diffusion tensor from the NMR spin echo. *J. Magn. Reson. B* 103, 247–254. doi: 10.1006/jmrb.1994.1037

Basser, P. J., Mattiello, J., and Le Bihan, D. (1994b). MR diffusion tensor spectroscopy and imaging. *Biophys. J.* 66, 259–267. doi: 10.1016/S0006-3495(94)80775-1

Basser, P. J., and Ozarslan, E. (2009). "Introduction to diffusion MR," in *Diffusion MRI: From Quantitative Measurement to In-vivo Neuroanatomy*, eds H. Johansen-Berg and E. J. Timothy (Oxford: Academic Press), 2–10.

Beaulieu, C. (2002). The basis of anisotropic water diffusion in the nervous system–a technical review. *NMR Biomed.* 15, 435–455. doi: 10.1002/nbm.782

Bland, J., and Altman, D. (1996). Statistics notes: measurement error. *BMJ* 312:774.

Bouix, S., Pasternak, O., Rathi, Y., Pelavin, P. E., Zafonte, R., and Shenton, M. E. (2013). Increased gray matter diffusion anisotropy in patients with persistent post-concussive symptoms following mild traumatic brain injury. *PLoS ONE* 8:e66205. doi: 10.1371/journal.pone.0066205

Brodtmann, A., Pardoe, H., Li, Q., Lichter, R., Ostergaard, L., and Cumming, T. (2012). Changes in regional brain volume three months after stroke. *J. Neurol. Sci.* 322, 122–128. doi: 10.1016/j.jns.2012.07.019

Brusini, L., Obertino, S., Boscolo Galazzo, I., Zucchelli, M., Krueger, G., Granziera, C., et al. (2016). Ensemble average propagator-based detection of microstructural alterations after stroke. *Int. J. Comp. Assist. Radiol. Surg.* 11, 1585–1597. doi: 10.1007/s11548-016-1442-z

Brusini, L., Obertino, S., Zucchelli, M., Galazzo, I. B., Krueger, G., Granziera, C., et al. (2015, October). "Assessment of mean apparent propagator-based indices as biomarkers of axonal remodeling after stroke," in *International Conference on Medical Image Computing and Computer-Assisted Intervention.* Munich: Springer International Publishing, 199–206.

Ceccarelli, A., Rocca, M. A., Falini, A., Tortorella, P., Pagani, E., Rodegher, M., et al. (2007). Normal-appearing white and grey matter damage in MS. *J. Neurol.* 254, 513–518. doi: 10.1007/s00415-006-0408-4

Chen, Y., Wang, D. J., and Detre, J. A. (2011). Test–retest reliability of arterial spin labeling with common labeling strategies. *J. Magn. Reson. Imaging* 33, 940–949. doi: 10.1002/jmri.22345

Cicchetti, D. V. (2010). Methodological commentary the precision of reliability and validity estimates re-visited: distinguishing between clinical and statistical significance of sample size requirements. *J. Clin. Exp. Neuropsychol.* 23, 695–700. doi: 10.1076/jcen.23.5.695.1249

Crofts, J. J., Higham, D. J., Bosnell, R., Jbabdi, S., Matthews, P. M., Behrens, T. E. J., et al. (2011). Network analysis detects changes in the contralesional hemisphere following stroke. *Neuroimage* 54, 161–169. doi: 10.1016/j.neuroimage.2010.08.032

Danielian, L. E., Iwata, N. K., Thomasson, D. M., and Floeter, M. K. (2010). Reliability of fiber tracking measurements in diffusion tensor imaging for longitudinal study. *Neuroimage* 49, 1572–1580. doi: 10.1016/j.neuroimage.2009.08.062

Descoteaux, M., Deriche, R., Le Bihan, D., Mangin, J. F., and Poupon, C. (2011). Multiple q-shell diffusion propagator imaging. *Med. Image Anal.* 15, 603–621. doi: 10.1016/j.media.2010.07.001

Ezekiel, M. (1930). *Methods of Correlation Analysis*. New York, NY: John Wiley and Sons.

Fick, R. H. J., Daianu, M., Pizzolato, M., Wassermann, D., Jacobs, R. E., Thompson, P. M., et al. (2016). "Comparison of biomarkers in transgenic Alzheimer rats using multi-shell diffusion MRI," in *MICCAI 2016 Workshop on Computational Diffusion MRI (CDMRI'16)* (Athens).

Fick, R. H. J., Zucchelli, M., Girard, G., Descoteaux, M., Menegaz, G., and Deriche, R. (2015). "Using 3D-SHORE and MAP-MRI to obtain both tractography and microstructural constrast from a clinical DMRI acquisition," in *Biomedical Imaging (ISBI), 2015 IEEE 12th International Symposium on IEEE* (New York, NY), 436–439.

Fleiss, J. L. (1981). *Methods for Rates and Proportions, 2nd Edn*. New York, NY: Wiley.

Friston, K. J., Holmes, A. P., Worsley, K. J., Poline, J.-P., Frith, C. D., and Frackowiak, R. S. J. (1995). Statistical parametric maps in functional imaging: a general linear approach. *Hum. Brain Mapp*. 2, 189–210. doi: 10.1002/hbm.460020402

Gerloff, C., Bushara, K., Sailer, A., Wassermann, E. M., Chen, R., Matsuoka, T. D., et al. (2006). Multimodal imaging of brain reorganization in motor areas of the contralesional hemisphere of well recovered patients after capsular stroke. *Brain* 129, 791–808. doi: 10.1093/brain/awh713

Granziera, C., Ay, H., Koniak, S. P., Krueger, G., and Sorensen, A. G. (2012a). Diffusion tensor imaging shows structural remodeling of stroke mirror region: results from a pilot study. *Eur. Neurol*. 67, 370–376. doi: 10.1159/000336062

Granziera, C., Daducci, A., Meskaldji, D. E., Roche, A., Maeder, P., Michel, P., et al. (2012b). A new early and automated MRI-based predictor of motor improvement after stroke. *Neurology* 79, 39–46. doi: 10.1212/WNL.0b013e31825f25e7

Granziera, C., Schmahmann, J. D., Hadjikhani, N., Meyer, H., Meuli, R., and Wedeen, V., et al (2009). Diffusion spectrum imaging shows the structural basis of functional cerebellar circuits in the human cerebellum *in vivo*. *PLoS ONE* 4:e5101. doi: 10.1371/journal.pone.0005101

Grech-Sollars, M., Hales, P. W., Miyazaki, K., Raschke, F., Rodriguez, D., Wilson, M., et al. (2015). Multi-centre reproducibility of diffusion MRI parameters for clinical sequences in the brain. *NMR Biomed*. 28, 468–485. doi: 10.1002/nbm.3269

Heiervang, E., Behrens, T. E. J., Mackay, C. E., Robson, M. D., and Johansen-Berg, H. (2006). Between sessions reproducibility and between subject variability of diffusion MR and tractography measures. *Neuroimage* 33, 867–877. doi: 10.1016/j.neuroimage.2006.07.037

Hosseinbor, A. P., Chung, M. K., Wu, Y. C., and Alexander, A. L. (2013). Bessel fourier orientation reconstruction (bfor): an analytical diffusion propagator reconstruction for hybrid diffusion imaging and computation of q-space indices. *Neuroimage* 64, 650–670. doi: 10.1016/j.neuroimage.2012.08.072

Jeurissen, B., Tournier, J. D., Dhollander, T., Connelly, A., and Sijbers, J. (2014). Multi-tissue constrained spherical deconvolution for improved analysis of multi-shell diffusion MRI data. *Neuroimage* 103, 411–426. doi: 10.1016/j.neuroimage.2014.07.061

Kaden, E., Kelm, N. D., Carson, R. P., Does, M. D., and Alexander, D. C. (2016). Multi-compartment microscopic diffusion imaging. *Neuroimage* 139, 346–359. doi: 10.1016/j.neuroimage.2016.06.002

Kim, B., and Winstein, C. (2017). Can neurological biomarkers of brain impairment be used to predict poststroke motor recovery? A Systematic Review. *Neurorehabil. Neural. Repair* 31, 3–24. doi: 10.1177/1545968316662708

Kim, H. J., Kim, S. J., Kim, H. S., Choi, C. G., Kim, N., Han, S., et al. (2013). Alterations of mean diffusivity in brain white matter and deep gray matter in Parkinson's disease. *Neurosci. Lett*. 550, 64–68. doi: 10.1016/j.neulet.2013.06.050

Kim, J. Y, Park, J., Chang, J. Y., Kim, S. H., and Lee, J. E. (2016). Inflammation after ischemic stroke: the role of leukocytes and glial cells. *Exp. Neurobiol*. 25, 241–251. doi: 10.5607/en.2016.25.5.241

Kirk, R. E. (1996). Practical significance: a concept whose time has come. *Educ. Psychol. Meas.* 56, 746–759. doi: 10.1177/0013164496056005002

Le Bihan, D., Breton, E., Lallemand, D., Grenier, P., Cabanis, E., and Laval-Jeantet, M. (1986). MR imaging of intravoxel incoherent motions: application to diffusion and perfusion in neurologic disorders. *Radiology* 161, 401–407. doi: 10.1148/radiology.161.2.3763909

Lin, Y. C., Daducci, A., Meskaldji, D. E., Thiran, J. P., Michel, P., Meuli, R., et al. (2015). Quantitative analysis of myelin and axonal remodeling in the uninjured motor network after stroke. *Brain Connect*. 5, 401–412. doi: 10.1089/brain.2014.0245

Maniega, S. M., Bastin, M. E., Armitage, P. A., Farrall, A. J., Carpenter, T. K., Hand, P. J., et al. (2004). Temporal evolution of water diffusion parameters is different in grey and white matter in human ischaemic stroke. *J. Neurol. Neurosurg. Psychiatry* 75, 1714–1718. doi: 10.1136/jnnp.2003.033852

Marenco, S., Rawlings, R., Rohde, G. K., Barnett, A. S., Honea, R. A., Pierpaoli, C., et al. (2006). Regional distribution of measurement error in diffusion tensor imaging. *Psychiatry Res*. 147, 69–78. doi: 10.1016/j.pscychresns.2006.01.008

Mendez, A., Obertino, S., and Menegaz, G. (2016). "Shore-based microstructural indices: do they tell us more?" in *Pattern Recognition in Neuroimaging (PRNI), 2016 International Workshop on IEEE* (Trento), 1–4.

Merlet, S. L., and Deriche, R. (2013). Continuous diffusion signal, EAP and ODF estimation via compressive sensing in diffusion MRI. *Med. Image Anal*. 17, 556–572. doi: 10.1016/j.media.2013.02.010

Ning, L., Laun, F., Gur, Y., DiBella, E. V., Deslauriers-Gauthier, S., Megherbi, T., et al. (2015). Sparse reconstruction challenge for diffusion MRI: validation on a physical phantom to determine which acquisition scheme and analysis method to use? *Med. Image Anal*. 26, 316–331. doi: 10.1016/j.media.2015.10.012

Novikov, D. S., Jespersen, S. N., Kiselev, V. G., and Fieremans, E. (2016). Quantifying brain microstructure with diffusion MRI: theory and parameter estimation. *arXiv*:1612.02059.

Obertino, S., Brusini, L., Boscolo Galazzo, I., Zucchelli, M., Granziera, C., and Cristani, M., et al (2016). "Shore-based biomarkers allow patient versus control classification in stroke," in *Biomedical Imaging (ISBI), 2016 IEEE 13th International Symposium on IEEE* (Prague), 1097–1100.

Özarslan, E., and Koay, C. G., Basser, P. J. (2008). "Simple harmonic oscillator based estimation and reconstruction for one-dimensional q-space MR," in *Proceedings of the International Society for Magnetic Resonance in Medicine* (Toronto, ON), Vol 16. 35.

Özarslan, E., Koay, C. G., Shepherd, T. M., Komlosh, M. E., Irfanoglu, M. O., Pierpaoli, C., et al. (2013). Mean apparent propagator (MAP) MRI: a novel diffusion imaging method for mapping tissue microstructure. *Neuroimage* 78, 16–32. doi: 10.1016/j.neuroimage.2013.04.016

Ozsunar, Y., Grant, P. E., Huisman, T. A., Schaefer, P. W., Wu, O., Sorensen, A. G., et al. (2004). Evolution of water diffusion and anisotropy in hyperacute stroke: significant correlation between fractional anisotropy and T2. *AJNR Am. J. Neuroradiol*. 25, 699–705.

Pierpaoli, C., and Basser, P. J. (1996). Toward a quantitative assessment of diffusion anisotropy. *Magn. Reson. Med.* 36, 893–906. doi: 10.1002/mrm.1910360612

Pinto, J., Jorge, J., Sousa, I., Vilela, P., and Figueiredo, P. (2016). Fourier modeling of the BOLD response to a breath-hold task: optimization and reproducibility. *Neuroimage* 135, 223–231. doi: 10.1016/j.neuroimage.2016.02.037

Situ, W., Liao, H., Zhou, B., Xia, X., and Tan, C. (2015). Application of diffusion tensor imaging for detecting structural changes in the brain of schizophrenic patients. *Int. J. Psychiatry Clin. Pract*. 19, 114–118. doi: 10.3109/13651501.2014.988270

Sotak, C. (2002). The role of diffusion tensor imaging in the evaluation of ischemic brain injury a review. *NMR Biomed*. 15, 561–569. doi: 10.1002/nbm.786

Sotiropoulos, S. N., Jbabdi, S., Xu, J., Andersson, J. L., Moeller, S., Auerbach, E. J., et al. (2013). Advances in diffusion MRI acquisition and processing in the human connectome project. *Neuroimage*. 80, 125–143. doi: 10.1016/j.neuroimage.2013.05.057

Stebbins, G. T., Nyenhuis, D. L., Wang, C., Cox, J. L., Freels, S., and Bangen, K., et al (2008). Gray matter atrophy in patients with ischemic stroke with cognitive impairment. *Stroke* 39, 785–793. doi: 10.1161/STROKEAHA.107.507392

Stejskal, E., and Tanner, J. (1965). Spin diffusion measurements: spin echoes in the presence of a time-dependent field gradient. *J. Chem. Phys*. 42, 288–292. doi: 10.1063/1.1695690

Sundgren, P. C., Dong, Q., Gómez-Hassan, D., Mukherji, S. K., Maly, P., and Welsh, R. (2004). Diffusion tensor imaging of the brain: review of clinical applications. *Neuroradiology* 46, 339–350. doi: 10.1007/s00234-003-1114-x

Veenith, T. V., Carter, E., Grossac, J., Newcombe, V. F., Outtrim, J. G., Lupson, V., et al. (2013). Inter subject variability and reproducibility of diffusion tensor imaging within and between different imaging sessions. *PLoS ONE* 8:e65941. doi: 10.1371/journal.pone.0065941.

Vollmar, C., O'Muircheartaigh, J., Barker, G. J., Symms, M. R., Thompson, P., Kumari, V., et al. (2010). Identical, but not the same: intra-site and inter-site reproducibility of fractional anisotropy measures on two 3.0 T scanners. *Neuroimage* 51, 1384–1394. doi: 10.1016/j.neuroimage.2010.03.046

Wang, J. Y., Abdi, H., Bakhadirov, K., Diaz-Arrastia, R., and Devous, M. Sr. (2012). A comprehensive reliability assessment of quantitative diffusion tensor tractography. *Neuroimage* 60, 1127–1138. doi: 10.1016/j.neuroimage.2011.12.062

Wang, Q., Tang, X. N., and Yenari, M. A. (2007). The inflammatory response in stroke. *J. Neuroimmunol.* 184, 53–68. doi: 10.1016/j.jneuroim.2006.11.014

Ward, N. S., Brown, M. M., Thompson, A. J., and Frackowiak, R. S. J. (2003). Neural correlates of motor recovery after stroke: a longitudinal fMRI study. *Brain* 126, 2476–2496. doi: 10.1093/brain/awg245

Wedeen, V. J., Hagmann, P., Tseng, W. Y., Reese, T. G., and Weisskoff, R. M. (2005). Mapping complex tissue architecture with diffusion spectrum magnetic resonance imaging. *Magn. Reson. Med.* 54, 1377–1386. doi: 10.1002/mrm.20642

Weston, P. S. J., Simpson, I. J. A., Ryan, N. S., Ourselin, S., and Fox, N. C. (2015). Diffusion imaging changes in grey matter in Alzheimer's disease: a potential marker of early neurodegeneration. *Alzheimers Res. Ther.* 7, 47–55. doi: 10.1186/s13195-015-0132-3

Wiggins, G. C., Triantafyllou, C., Potthast, A., Reykowski, A., Nittka, M., and Wald, L. L. (2006). 32-channel 3 Tesla receive-only phased-array head coil with soccer-ball element geometry. *Magn. Reson. Med.* 56, 216–223. doi: 10.1002/mrm.20925

Wu, Y. C., and Alexander, A. L. (2007). Hybrid diffusion imaging. *Neuroimage* 36, 617–629. doi: 10.1016/j.neuroimage.2007.02.050

Yu, C., Zhu, C., Zhang, Y., Chen, H., Qin, W., Wang, M., et al. (2009). A longitudinal diffusion tensor imaging study on Wallerian degeneration of corticospinal tract after motor pathway stroke. *Neuroimage* 47, 451–458. doi: 10.1016/j.neuroimage.2009.04.066

Zhang, H., Schneider, T., Wheeler-Kingshott, C. A., and Alexander, D. C. (2012). NODDI: practical *in vivo* neurite orientation dispersion and density imaging of the human brain. *Neuroimage* 61, 1000–1016. doi: 10.1016/j.neuroimage.2012.03.072

Zucchelli, M., Brusini, L., Méndez, C. A., Daducci, A., Granziera, C., and Menegaz, G. (2016a). What lies beneath? Diffusion EAP-based study of brain tissue microstructure. *Med. Image Anal.* 32, 145–156. doi: 10.1016/j.media.2016.03.008

Zucchelli, M., Fick, R. H. J., Deriche, R., and Menegaz, G. (2016b). "Ensemble average propagator estimation of axon diameter in diffusion MRI: implications and limitations," in *Biomedical Imaging (ISBI), 2016 IEEE 13th International Symposium* (Prague), 465–468.

Conflict of Interest Statement: The authors declare that the research was conducted in the absence of any commercial or financial relationships that could be construed as a potential conflict of interest.

Advantages of publishing in Frontiers

OPEN ACCESS
Articles are free to read for greatest visibility and readership

FAST PUBLICATION
Around 90 days from submission to decision

HIGH QUALITY PEER-REVIEW
Rigorous, collaborative, and constructive peer-review

TRANSPARENT PEER-REVIEW
Editors and reviewers acknowledged by name on published articles

Frontiers
Avenue du Tribunal-Fédéral 34
1005 Lausanne | Switzerland

Visit us: www.frontiersin.org
Contact us: info@frontiersin.org | +41 21 510 17 00

REPRODUCIBILITY OF RESEARCH
Support open data and methods to enhance research reproducibility

DIGITAL PUBLISHING
Articles designed for optimal readership across devices

FOLLOW US
@frontiersin

IMPACT METRICS
Advanced article metrics track visibility across digital media

EXTENSIVE PROMOTION
Marketing and promotion of impactful research

LOOP RESEARCH NETWORK
Our network increases your article's readership